NASA/TM-1999-209554

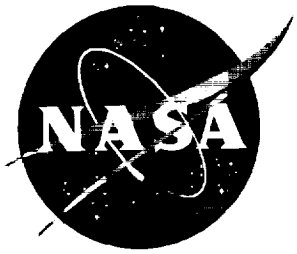

Models and Measurements Intercomparison II

Edited by
Jae H. Park
NASA Langley Research Center, Hampton, Virginia

Malcolm K. W. Ko
Atmospheric and Environmental Research, Inc., Cambridge, Massachusetts

Charles H. Jackman
NASA Goddard Space Flight Center, Greenbelt, Maryland

R. Alan Plumb
Massachusetts Institute of Technology, Cambridge, Massachusetts

Jack A. Kaye
Headquarters, National Aeronautics and Space Administration, Washington, D.C.

Karen H. Sage
SAIC, Hampton, Virginia

September 1999

The NASA STI Program Office . . . in Profile

Since its founding, NASA has been dedicated to the advancement of aeronautics and space science. The NASA Scientific and Technical Information (STI) Program Office plays a key part in helping NASA maintain this important role.

The NASA STI Program Office is operated by Langley Research Center, the lead center for NASA's scientific and technical information. The NASA STI Program Office provides access to the NASA STI Database, the largest collection of aeronautical and space science STI in the world. The Program Office is also NASA's institutional mechanism for disseminating the results of its research and development activities. These results are published by NASA in the NASA STI Report Series, which includes the following report types:

- TECHNICAL PUBLICATION. Reports of completed research or a major significant phase of research that present the results of NASA programs and include extensive data or theoretical analysis. Includes compilations of significant scientific and technical data and information deemed to be of continuing reference value. NASA counterpart or peer-reviewed formal professional papers, but having less stringent limitations on manuscript length and extent of graphic presentations.

- TECHNICAL MEMORANDUM. Scientific and technical findings that are preliminary or of specialized interest, e.g., quick release reports, working papers, and bibliographies that contain minimal annotation. Does not contain extensive analysis.

- CONTRACTOR REPORT. Scientific and technical findings by NASA-sponsored contractors and grantees.

- CONFERENCE PUBLICATION. Collected papers from scientific and technical conferences, symposia, seminars, or other meetings sponsored or co-sponsored by NASA.

- SPECIAL PUBLICATION. Scientific, technical, or historical information from NASA programs, projects, and missions, often concerned with subjects having substantial public interest.

- TECHNICAL TRANSLATION. English-language translations of foreign scientific and technical material pertinent to NASA's mission.

Specialized services that complement the STI Program Office's diverse offerings include creating custom thesauri, building customized databases, organizing and publishing research results . . . even providing videos.

For more information about the NASA STI Program Office, see the following:

- Access the NASA STI Program Home Page at ***http://www.sti.nasa.gov***

- Email your question via the Internet to help@sti.nasa.gov

- Fax your question to the NASA STI Help Desk at (301) 621-0134

- Telephone the NASA STI Help Desk at (301) 621-0390

- Write to:
  NASA STI Help Desk
  NASA Center for AeroSpace Information
  7121 Standard Drive
  Hanover, MD 21076-1320

NASA/TM-1999-209554

Models and Measurements Intercomparison II

Edited by
Jae H. Park
NASA Langley Research Center, Hampton, Virginia

Malcolm K. W. Ko
Atmospheric and Environmental Research, Inc., Cambridge, Massachusetts

Charles H. Jackman
NASA Goddard Space Flight Center, Greenbelt, Maryland

R. Alan Plumb
Massachusetts Institute of Technology, Cambridge, Massachusetts

Jack A. Kaye
Headquarters, National Aeronautics and Space Administration, Washington, D.C.

Karen H. Sage
SAIC, Hampton, Virginia

National Aeronautics and
Space Administration

Langley Research Center
Hampton, Virginia 23681-2199

September 1999

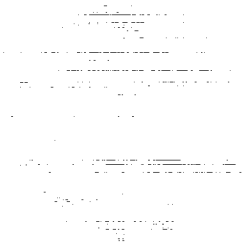

Available from:

NASA Center for AeroSpace Information (CASI)
7121 Standard Drive
Hanover, MD 21076-1320
(301) 621-0390

National Technical Information Service (NTIS)
5285 Port Royal Road
Springfield, VA 22161-2171
(703) 605-6000

Preface

Jae H. Park, Malcolm K. W. Ko, Charles H. Jackman, R. Alan Plumb, Jack A. Kaye, and Karen H. Sage

The activity and publication of this "Models and Measurements Intercomparison II (MM II)" during the three-year period starting in November of 1996 was made possible by the unselfish hard work of many international modeling groups and atmospheric scientists. Altogether, 28 atmospheric simulation models were used for model intercomparisons. The model run (starting) conditions were prescribed in order to minimize the differences and identify the causes of differences in the models. The modelers have reviewed their results critically and discussed the causes of differences between modeled and measured results as well as between results from different models. This MM II report should help in evaluating the results from various predictive models for assessing humankind perturbations of the stratosphere.

A kick-off meeting was held on November 4, 1996, at NASA Headquarters, Washington, D.C., to discuss the goals of a model and measurement intercomparison exercise. Several topics and topics' leaders were chosen at this initial meeting. The next months were spent in preparation of the model experiments, including much discussion at the Atmospheric Effects of Aviation Project (AEAP) Global Modeling Initiative (GMI) meeting held February 24-26, 1997, in San Diego, California. The model exercises were finalized by June 25, 1997, and sent to interested modeling groups. A preliminary analysis meeting was held at the end of the AEAP GMI meeting on August 27, 1997, in Fairfax, Virginia. Further analysis continued at the more comprehensive MM II meeting held November 3-5, 1997, in Williamsburg, Virginia. The final analysis meeting was held on March 4-5, 1998, in Satellite Beach, Florida. Participating scientists attending the annual meeting for AEAP in Virginia Beach, Virginia, also attended an evening meeting on April 27, 1998, to discuss the Executive Summary and publication of the MM II report. The rest of 1998 and early 1999 was spent finalizing figures to be included and writing and re-writing text for the final MM II report.

The editors would like to express sincere thanks to all of the participants who made the activity successful, especially in light of the fact that they were not directly supported financially. Also, the editors would like to thank Kathy Wolfe (CSC) and her staff for meeting support, and NASA Langley's Technical Editing and Publishing Services, who made publication of the MM II report possible. A list of contributors, who participated directly, reviewed the report, and provided necessary data, is given at the end of this report.

Table of Contents

Executive Summary

Malcolm.K.W. Ko,[1] R.Alan Plumb,[2] and Charles H. Jackman[3]

1. Atmospheric and Environmental Research, Inc.
2. Massachusetts Institute of Technology
3. NASA Goddard Space Flight Center

The Second Workshop on Stratospheric Models and Measurements Workshop (M&M II) is the continuation of the effort previously started in the first Workshop (M&M I, Prather and Remsberg [1993]) held in 1992. As originally stated, the aim of M&M is to provide a foundation for establishing the credibility of stratospheric models used in environmental assessments of the ozone response to chlorofluorocarbons, aircraft emissions, and other climate-chemistry interactions. To accomplish this, a set of measurements of the present day atmosphere was selected. The intent was that successful simulations of the set of measurements should become the prerequisite for the acceptance of these models as having a reliable prediction for future ozone behavior.

The choice of the measurements for M&M I was limited by data availability, and the emphasis on 2-D and 3-D assessment models. Other models such as climate models, air-trajectory models and assimilation models were not included in the consideration. In M&M II, the GSFC DAO assimilation model provided results for a number of transport experiments. In this report, we emphasize what was accomplished beyond M&M I.

A. New Data Used for M&M II

Almost all the data sets that were used for M&M I have been revised or replaced with better and more complete compilations. UARS satellite data sets are the primary ones being used for the middle and upper stratosphere. We chose to use the 1992 data as the basis for our comparison because it is the only full year for which there is CLAES data available, The CLAES data provide the very useful global coverage of N_2O, CH_4, HNO_3, and $ClONO_2$. In addition, data for O_3, ClO, H_2O and CH_4 were available from MLS and HALOE. Many of the evaluations in M&M II relied on individuals to compile the UARS datasets for comparisons with the models. Future model comparisons will benefit from the climatological datasets constructed by the UARS Science Team, which were not available for M &M II but are now accessible (see http://hyperion.gsfc.nasa.gov/Analysis/UARS/urap/home.html).

The M&M II exercise has also benefited from additional data from various ER-2 aircraft campaigns (AASE II 91/92; SPADE 92/93; ASHOE/MAESA 94; STRAT 95/96; POLARIS 96/97) and balloon launches from the OMS program (Brazil, Alaska, Bill Brune, Geoff Toon). New data on SF_6, CO_2 and H_2O provide diagnostics for transport rates, mean age of air, and propagation of seasonal cycles into the tropical lower stratosphere. Enhanced payload of the ER-2 provided in situ measured concentrations of OH and HO_2. Data from the new $ClONO_2$ instrument also place additional contraints on partitioning of the chlorine species. Simultaneous measurements of NOx and NOy allow determination of the NOx/NOy ratio. New data on aerosol surface areas and photolysis rates measurements provide additional constraints on our understanding of photochemical partitionings.

A climatology for ozone, consisting of monthly zonal mean column ozone and monthly ozone profiles as a function of latitude, was put together for M&M II. The column ozone climatology is based on ozone column data from 1988 to 1996 using TOMS on Nimbus-7, Meteor 3 and Earth Probe. The ozone profile is based on ozone sonde data between 0 and 28 km and SAGE II data between 20 and 60 km. In

the region where the two datasets overlap (20-30 km), a weighted average is used with a heavier weighting for the sonde data at lower altitudes and a heavier weighting for the SAGE II data at higher altitudes.

B. Strategy for Model Testing

Ozone is the only species where there is long-term global coverage to derive a reliable climatology. However, using ozone by itself as a guide to choose the best transport and chemistry representations in a model is problematic since it is never clear whether a good ozone simulation in a particular model is achieved by having the correct combination of transport and chemistry or simply good fortune. A wrong transport rate in the model will give erroneous Cly and NOy, which will produce an incorrect local ozone removal rate. The combination of the wrong transport with the wrong ozone removal rate could fortuitously result in a "correct" ozone simulation. This makes it impossible to use the agreement between observed and calculated ozone as the only criterion for having the correct transport.

Direct comparison of model simulated tracer distributions with observed distributions has limited value. In the case of observations from satellite platforms, one must take into account that the observations represent a specific year while the model results represent a climatological mean. Comparison of 3-D data with 2-D model results requires additional work since straight zonal averaging of the observation may overlook the effects from the wave motions that should be taken into account. This is particularly important for the winter hemisphere where planetary wave activities are stronger. In those cases, averaging by potential vorticity (PV) may help (see e.g. Randel et al., 1998). Finally, observations from aircraft and balloon platforms may be affected by short term motions so that observations taken at a particular latitude and altitude may be sampling air that has been transported from another location. In those cases, use of alternative co-ordinates such as N_2O and PV would also help.

Comparison of radical species with model results are even more problematic. For example, discrepancies between model calculated and observed NO_2 concentration at a particular location could be due either to differences in NOy concentrations, differences in partitioning (because of differences in local temperature, overhead ozone or air trajectory, treatments of heterogeneous reactions), or a combination of the two. In this report, the simulation is carried out for 1992, a period when the stratosphere was heavily perturbed by Pinatubo aerosols. Hence, the exercise provides a test bed for volcanic perturbations to stratospheric chemistry and the ways in which it is described in the models. However, the approaches to polar stratospheric cloud and volcanic heterogeneous chemistry were not 'standardized', and each modelling group made their own choices.

A number of theoretical developments enable us to develop a new strategy for model testing. Successful simulation of ozone depends on several processes. Therefore, it is difficult to identify the causes of the discrepancy between model results and observation. The current approach in M&M II identifies a number of independent tests for individual process simulated in the model (see Figure 1 and discussion below). Having the independent tests for the components provides a theoretical framework in which further adjustments could be made.

B.1 Focus on Transport

Current thinking considers the lower stratosphere as being separated into the tropics, extra-tropics and the polar regions. The tropical lower stratosphere is dominated by upwelling from the tropopause. It is the region where source gases from the troposphere are transported into the stratosphere. In this region, the local concentration of ozone is maintained by a balance between net photochemical production and transport away from the region. Downward motions occur in the extra-tropics and the polar

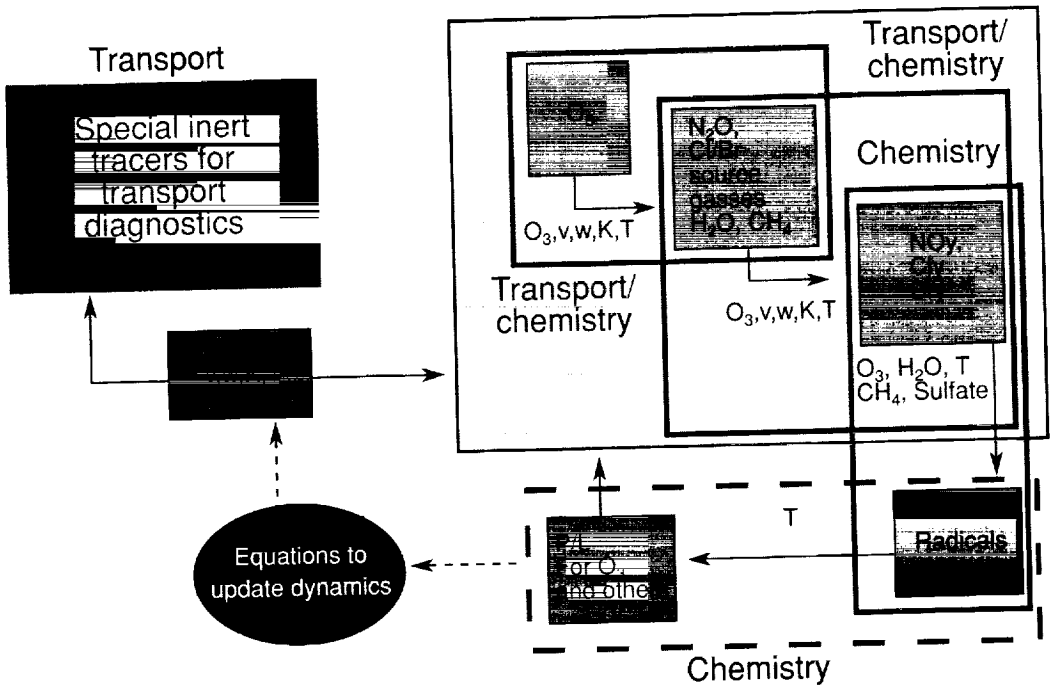

Figure 1. Testing different components of the model.

region. In both regions, local ozone concentration is determined by the balance between photochemical removal and transport into the region. In addition to the large scale motion as determined by advection, neighboring regions also communicate by irreversible transport associated with wave motions. In 2-D models, these are simulated by exchange of air between the two regions along isentropes whose rate is related to the horizontal eddy diffusion coefficient (K_{yy}). If the mixing ratio of a species is different in two neighboring regions, this exchange of air will lead to a net transport of the species. Vertical motion (downward) and vertical mixing will carry material out of the extra-tropical lower stratosphere into the troposphere. Exchange along isentropes across the middle world is also thought to be important. This mixing connects the extra-tropical lower stratosphere and the tropical upper troposphere. Within this framework, the transport can be described by specifying the upwelling in the tropics, downward motions in the extra-tropics and polar regions, vertical mixing in each region, and the values of K_{yy} linking neighboring regions.

Progress has been made on understanding the individual components of transport in 2-D models. Heating rates calculated from observed ozone, temperature and aerosol (Eluszkiewicz et al., 1996; Jackman et al., 1996; Rosenlof, 1995) can be used to verify the heating rates associated with the residual circulation used in the models. In fact, several models (e.g. CSIRO, GSFC and LLNL) use heating rates calculated using observed fields to derive the residual circulation. Work by Minschwaner et al. (1996), Volk et al. (1996) and Schoeberl et al. (1997) provide a quantitative measure of the mixing rate between the tropics and mid-latitudes. Work by Hall et al. (1997) and Mote et al. (1998) provide measures of K_{zz} in the tropics in addition to upwelling velocity and mixing rate from mid-latitudes. With these works, a conceptual framework has been developed to identify the key transport processes in the lower stratosphere. Some of these parameters are related directly to observations (e.g., SF_6, CO_2) on the one hand, and can be derived as diagnostics from model output. Comparison of these model diagnostics with the values derived from observations provides a measure of how well the transport processes are simulated in each model.

The combinations of the data on long-lived tracers from satellite, aircraft and balloon platforms provide ample opportunity to study the correlation diagram for these species. As shown by Plumb and Ko (1992) and Plumb (1996), the slope of the correlation curve can be related to the ratio of the stratospheric lifetimes of the two species. The knowledge on the tropospheric growth rate of SF_6 allows one to translate relative lifetime to absolute lifetimes for comparison with model calculations (Volk et al., 1997).

B.2 Focus on Chemistry

The local production and removal rates of long-lived species such as ozone, N_2O, and CH_4 depend on the local concentrations of the radicals and photolysis rates. Partitioning of the radicals in an air parcel is determined by the local concentration of ozone, H_2O, Cly, NOy, Bry and CH_4; and the solar illumination to which it is exposed. The solar illumination depends on the overhead column ozone and the exact trajectory of the motion. This is particularly important near the terminator as excursions in latitude would bring the parcel in and out of sunlight. Away from the terminator, the observed concentrations of the radicals at a particular latitude and longitude are found to correspond to the partitioning calculated for the air-parcel by assuming that the parcel is in photochemical equilibrium while executing exact zonal motion at the same latitude and altitude.

In situ observations of atmospheric trace species provided data for process studies of the partitioning of the radical species over a range of conditions with different sulfate loading and solar illumination. In a series of studies performed by Ross Salawitch (see e.g. Salawitch et al., 1994), it was demonstrated that a photostationary box model constrained by observed values of sulfate surface area, temperature, NOy, Cly, Bry, H_2O, ozone, overhead column ozone and CH_4 can produce the observed partitioning of the radical species under a range of conditions. This method has been validated in the lower stratosphere using the data from the AASE II, ASHOE/MAESA, SPADE and POLARIS aircraft campaigns, and in the mid- to upper stratosphere using balloon data.

The above approach used to analyze the observations can be modified to examine photochemical partitioning in the models. Specifically, appropriate parameters are taken from the outputs of the assessment models to constrain the photostationary model. The radical concentrations calculated by the constrained photostationary model can be compared to the radical concentrations calculated by the assessment models. To the extent that the photostationary model can simulate the observed radicals using appropriate rate data, this provides verification of the photochemical solvers in the assessment models. The production and removal rates of the reservoir species calculated by the assessment models are also partially verified since they are determined by the radicals. The limitations of this approach are discussed in section 5.2.

C. Results of M&M II

The numerical experiments for M&M II were chosen so that the results from different models could be easily compared and that specific diagnostics which can be related to observations provide guidelines for the correct answers. The experiments can be separated into two groups. The first group involves simulations of chemical inert tracers and is used to provide diagnostics for transport. The second group uses the distributions (as functions of latitude, height and seasons) of chemical tracers simulated in the models (H_2O, Cly, NOy, various source gases and ozone) for comparison with observations.

C.1 Transport Exercises

The transport exercises include the following:

(1) simulation of a special tracer for diagnosing the age spectrum, and seasonal variation of the transport parameters (A-1 and A-2),

(2) simulation of the distribution of an inert tracer using the boundary condition corresponding to the emission history of SF_6 (A-5),

(3) simulation of the distribution of an inert tracer using the seasonally varying boundary condition corresponding to that of CO_2 (A-6),

(4) simulation of the distributions of inert tracers released in the lower stratosphere, which represent HSCT emissions (A-3 and A-4).

The age spectrum (Hall and Plumb, 1994) encapsulates all the information required to reconstruct the stratospheric response to any tropospheric time series of a conserved tracer, and as such it summarizes transport in a chemistry-independent way. From this, the mean age can be directly determined and compared with determinations from observations of SF_6 (e.g., Elkins et al., 1996; Harnisch et al., 1996) and from the observed trend in CO_2 (Boering et al., 1995, 1996). The response to a seasonally varying source can also be reconstructed. In principle, the full seasonal variation of the age spectrum, which cannot be fully determined from the single experiment A-1, is required to do this, and so experiment A-2 was designed to simulate seasonal tracers explicitly. However, it was found that the results of the seasonal tracer experiments could be reconstructed with little error from the age spectrum derived from experiment A-1.

The model calculations of mean age for the stratosphere were found to vary widely, by as much as a factor of 4. Moreover, compared to mean ages determined from observed SF_6 and CO_2 data, most models produced air that is too young throughout the stratosphere. Theoretical arguments indicate that stratospheric ages that are too young could result from a mean meridional circulation that is too strong, horizontal mixing between tropics and middle latitudes that is too weak, or vertical diffusion that is too strong [analyses of observed tracers indicates that vertical diffusion is negligible in the tropical atmosphere (Hall and Waugh 1997), but this may not be true of all the models]. Controlled comparisons between models differing in one or more of these circulation features are consistent with these arguments. A contribution from numerical errors (to which age calculations may be sensitive) cannot be ruled out, as no experiments were designed to compare transport schemes, but it is noteworthy that one pair of models, essentially identical except for their advection schemes, produced very similar magnitudes and distributions of stratospheric age.

The observation of propagation of the seasonal cycle of CO_2 (Boering et al., 1996), and that of H_2O (Mote et al., 1998) allows one to examine the upward propagation of a signal into the tropical lower stratosphere. Most models attenuated the signal too quickly; those that did not showed too rapid upward phase propagation. From the phase velocity and attenuation, and a third measurement such as mean age, one can deduce the tropical upwelling rate, the vertical eddy diffusion coefficient, and the rate extratropical air mixes into the tropics (Hall and Waugh, 1997; Mote et al., 1998). Compared to such deductions from observations, tropical upwelling in most models is too fast, consistent with the circulation being too strong from the age comparison. Vertical diffusion is also too large in many 2D models. Compared to the mixing rate time constant of about 15 months derived from several independent analyses of

observations, most models are mixing the tropics and mid-latitudes too fast. This suggests that weak horizontal mixing is not the reason for the excessively young ages in most models.

Boering et al. (1996) suggested that the model-calculated mean age should be related to the residence time of materials deposited at the same rate (in mixing ratio unit) in the whole stratosphere. Indeed, it was found that model simulations of trace gases, not only of those with stratospheric sources, but also those with tropospheric sources, correlated extremely well with the age simulations. Model-to-model variation for tropospheric source gases is modest, but that for gases with stratospheric sources is substantial, being as large as a factor of 2 for Cly in the lower stratosphere and as much as a factor of 3 for the idealized HSCT emission simulation (experiments A-3 and A-4). Thus, model deficiencies in the simulation of age are indicative of serious transport errors that may impact the models' ability to simulate stratospheric composition, especially the stratospheric burden of HSCT emissions. This is an important step in the verification of model-computed changes in NOy and H_2O due to aircraft emission, and these results indicate that improvements in the simulation of stratospheric transport should be a high priority in future model development.

C.2 Chemistry Partitioning

Testing chemistry partitioning in the models is performed as follows. First, the individual model was asked to simulate the 1992 atmosphere providing the calculated concentrations of the trace gases including the radical species. Appropriate parameters are taken from the outputs of the individual model to constrain the photostationary model of Salawitch. The radical concentrations calculated by the constrained photostationary model are used to verify the radical concentrations calculated by the assessment models.

The M&M I report identified a 30% difference in model calculated partitioning. Two separate photochemical benchmark exercises were carried out in 1994 to resolve this. As a result of these calculations, the participating models have identified the causes of these differences for their own models and modified them accordingly so that they produce the correct benchmark answers. As expected, the comparison with the constrained photostationary model confirms that the photochemical solvers used in most assessment models are in good agreement with the photostationary model.

In interpreting the chemistry test, one should be aware of the following two caveats. First, results of the photostationary model depend on the reaction rate constants used. With the current JPL-97 recommendation, some discrepancies between calculated results and observed results still exist. Most notable of these is the model ozone deficit at 40 km (Clancy et al. 1987 and references cited; Natarajan and Callis, 1991; Eluszkiewicz and Allen, 1993; Crutzen et al., 1995; Dessler et al., 1996; Osterman et al., 1997; Summers et al., 1997). There are indications that models may underestimate the NOx/NOy ratio in the summer lower extra-tropical stratosphere (Sen et al., 1998, Gao et al., 1999, Danilin et al., 1999). Recent laboratory measurements (Brown et al. 1999 a,b) suggest that the rate recommendations for $OH + NO_2$ and $OH + HNO_3$ in JPL-97 may have to be revised. Second, the above procedure provides a valid test only for situations where heterogeneous chemistry is easily parameterized and where local photochemistry is rapid. It is well-known that behavior of the radicals depends on the air-parcel trajectory (temperature and solar illumination) in regions when the temperature is cold enough to trigger heterogeneous chemistry on surfaces. In addition, the long phtochemical lifetimes of some reservoirs in the lowermost stratosphere (such as HNO_3 and HCl) imply that transport can influence chemical partitioning, and the local photostationary solution may not be appropriate. There remains a need to find ways to verify the PSC treatments in the models.

C.3 Chemical Tracers

In the following comparison, we emphasize specific aspects rather than direct comparison with observed concentrations:

- The model calculated atmospheric lifetimes of N_2O and several CFCs from the models are longer than those derived from observations by Volk et al. (1997) and Minschwaner et al. (1998). Assuming that the photolysis rates are correct, the models would need a stronger upwelling in the tropics and/or less mixing between the tropics and mid-latitudes to get longer lifetimes. Unfortunately, this conflicts with the requirement to get greater mean age of air at mid-latitudes.

- Because of zonal asymmetric motions, computation of the zonal mean of observed N_2O and CH_4 would underestimate the latitudinal gradient across the tropical barrier and polar vortex. The alternative way is to use PV to define an equivalent latitude. The gradient across the barrier defined this way is more pronounced. It is likely that unsuccessful simulations of the correct gradients across the region boundaries would imply incorrect exchange rates across the boundary.

- Analyses of the HNO_3 and N_2O measurements in the polar vortex suggest that correlative measurements of those two species provides an indication of removal of gas-phase HNO_3 by heterogeneous reactions and recovery of HNO_3 on the polar region.

- Model results show significant differences in NOy and Cly (>50% at mid-latitudes, larger in the polar region) in the lower stratosphere. Differences in model calculated NOy and Cly computed using specified source gases (N_2O for NOy, CFCs for Cly) are even larger, indicating differences in transport as a major contributor.

- The UARS measurements provide information on seasonal behavior of NO, NO_2, HNO_3, HCl, $ClONO_2$, and ClO. The differences among model calculated concentrations for these species are large, reflecting the differences in NOy and Cly, and different partitionings because of different local ozone. Given the large ranges covered by the model calculated values, the observed values generally lie within the model ranges most of the time. However, there is no one model that matches the observation in a consistent way.

C.4 Ozone Comparison

The comparison between model ozone and the ozone climatology shows the following:

- The model predicted columns are within ±5% of the climatology in the tropics, ±15% at mid-latitudes, and as much as 30% in polar region. The general tendency is to underestimate the tropical column and overestimate the column in the extra-tropics, consistent with too strong a circulation.

- Models that follow the JPL recommendation underestimate the ozone amount above 40 km (about 10% too little around 40km, up to 30% less at 60km). Calculations have shown that including a 6% yield of HCl from OH + ClO will increase the model calculated ozone in this region.

- The calculated ozone is within 10% of the climatology between 25 km and 35 km in the tropics and mid-latitudes. The differences are as large as 30% at high latitudes in some models. Larger differences also occur in the lower stratosphere. The differences are largest in the extra tropics below 20 km where some models overestimate ozone by as much as 100% around 14 km.

- Concentrations of tropospheric ozone are more than a factor of 2 too low for many of the models.

Several other exercises were also included. While these results cannot be easily compared to observations, they provide some useful insights.

- The local ozone production and removal rates for the simulation of the 1992 atmosphere from different models were compared to each other. In spite of the large differences in NOy, Cly, Bry and H_2O concentrations, the calculated production and removal rates show many similarities. This suggests that there is internal buffering of the system.

- In another exercise, all the models used the same fixed ozone production and loss rates to compute ozone. This exercise highlighted how differences in transport affect the model computed ozone. Generally, the column ozone computed in this exercise for a model was fairly close to the column ozone calculated by the same model for the 1992 atmosphere even though the ozone production and loss rates used in two simulations were quite different.

References

Boering, K.A., E.J. Hinsta, S.C. Wofsy, J.G. Anderson, B.C. Daube, Jr., A.E. Dessler, M. Lowenstein, M.P. McCormick, J.R. Podolske, E.M. Weinstock, and G.K. Yue, Measurements of stratospheric carbon dioxide and water vapor at northern mid-latitudes: Implications for troposphere-to-stratosphere transport, *Geophy. Res. Lett.*, **22**, 2737-2740, 1995.

Boering, K.A., S.C. Wofsey, B.C. Daube, H.R. Schneider, M. Lowenstein, and J.R. Podolske, Stratospheric transport rates and mean age distribution derived from observations of atmospheric CO_2 and N_2O, *Science*, **274**, 1340-1343, 1996.

Brown, S.S., R.K. Talukdar, and A.R. Ravishankara, Rate constants for the reaction $OH + NO_2 + M \rightarrow HNO_3 + M$ under atmospheric conditions, *Chem. Phys. Lett.*, **299**, 277-284, 1999a.

Brown, S.S., R.K. Talukdar, and A.R. Ravishankara, Reconsideration of the rate constant for the reaction of hydroxyl radicals with nitric acid, *J. Phys. Chem.*, in press, 1999b.

Clancy, R.T., D.W. Rusch, R.J. Thomas, M. Allen, and R.S. Eckman, Model ozone phtotochemistry on the basis of Solar Mesospheric Explorers mesospheric observations, *J. Geophys. Res.*, **92**, 3067-3080 1987.

Crutzen, P.J., J.-U. Grooz, C. Bruhl, R. Muller, J.M. Russell III, A reevaluation of the O_3 budget with HALOE UARS data: no evidence for the O_3 deficit, *Science*, **268**, 705-708, 1995.

Danilin, M.Y., J.M. Rodriguez, W. Hu, M.K.W. Ko, D.K. Weisenstein, J.B. Kumer, J.L. Mergenthaler, J.M. Russel III, M. Koike, G.K. Yue, N.B Jones, and P.V. Johnston, Nitrogen species in the post-Pinatubo stratosphere: Model analysis utilizing UARS measurements, *J. Geophys. Res.*, **104**, 8247-8262, 1999.

Dessler, A.E., S.R. Kawa, D.B. Considine, J.W. Waters, L. Froidevaux, and J.B. Kumer, 393 UARS measurements of ClO and NO_2 at 40 km and 46 km and implications for the 394 model "ozone deficit", *Geophy. Res. Lett.*, **23**, 339-342, 1996.

Elkins, J. W., D.W. Fahey, J.M. Gilligan, G.S. Dutton, T.J. Baring, C.M. Volk, R.E. Dunn, R.C. Meyers, S.A. Montzka, P.R. Wamsley, A.H. Hayden, J.H. Butler, T. M. Thompson, T.H. Swanson, E.J. Dlugokencky, P.C. Novelli, D.F. Hurst, J.M. Lobert, S.J. Ciciora, R.J., McLaughlin, T.L. Thompson, R.H., Winkler, P.J. Fraser, L.P. Steele, and M.P. Lucarelli, Airborne gas chromatograph for in situ measurements of long-lived species in the upper troposphere and lower stratosphere, *Geophy. Res. Lett.*, **23**, 347-350, 1996.

Eluszkiewicz, J., and M. Allen, A global analysis of ozone deficit in the upper stratosphere and lower mesosphere, *J. Geophys. Res.*, **98**, 1069-1082, 1993.

Eluszkiewicz, J., D. Crisp, R. Zurek, L. Elson, E. Fishbein, L. Froidevaux, J. Waters, R.Grainger, A. Lambert, R. Harwood, and G. Peckham, Residual circulation in the stratosphere and lower mesosphere as diagnosed from Microwave Limb Sounder Data, *J. Atmos. Sci.*, 53, 217-240, 1996.

Gao, R.S., D.W. Fahey, L.A. Del Negro, S. G. Donnelly, E.R. Keim. J.A. Neuman, E. Teverovski, P.O. Wennberg, T.F. Hanisco, E.J. Lanzendorf, M.H. Proffitt, J.J. Margitan, J.C. Wilson, J.W. Elkins, R.M. Stimpfle, R.C. Cohen, C.T. McElroy, T.P. Bui, R.J. Salawitch, S.S. Brown, A.R. Ravishankara, R.W. Portman, M.K.W. Ko, D.K. Weisensten, and P.A. Newman, A comparison of observations and model simulations of NOx/NOy in the lower stratosphere, *Geophys. Res. Lett.*, **26**, 1153-1156, 1999.

Geller, L.S., J.W. Elkins, J.M. Lobert, A.D. Clarke, D.F. Hurst, J.H. Butler, and R.C. Meyers, Tropospheric SF_6: Observed latitudinal distribution and trends, derived emissions, and interhemispheric exchange time, *Geophy. Res. Lett.*, **24**, 675-678, 1997.

Hall, T.M., and R.A. Plumb, Age as a diagnostic of stratospheric transport, *J. Geophys. Res.*, **99**, 1059-1070, 1994.

Hall, T.M., and D.W. Waugh, Tracer transport in the tropical stratosphere due to vertical diffusion and horizontal mixing, *Geophy. Res. Lett.*, **24**, 1383-1386, 1997.

Jackman, C. H., E. L. Fleming, S. Chandra, D. B. Considine, and J. E. Rosenfield, Past, present, and future modeled ozone trends with comparisons to observed trends, *J. Geophys. Res.*, **101**, 28,753- 28,767, 1996.

Minschwaner, K., A.E. Dessler, J.W. Elkins, C.M. Volk, D.W. Fahey, M. Lowenstein, J.R. Podolske, A.E. Roche, and K.R. Chen, Bulk properties of isotropic mixing into the tropics in the lower stratosphere, *J. Geophys. Res.*, **101**, 9433-9439, 1996.

Minschwaner, K.,R.W. Carver, and B.P. Briegleb, Infrared radiative forcing and atmospheric lifetimes of trace species based on observations form UARS, *J. Geophys. Res.*, **103**, 23243-23253, 1998.

Mote, P.W., T.J. Dunkerton, M.E. McIntyre, E.A. Ray, P.H. Haynes, and J.M. Russell III, Vertical velocity, vertical diffusion, and dilution by mid-latitude air in the tropical lower stratosphere, *J. Geophys. Res.*, **103**, 8651-8666, 1998.

Natarajan, M. and L.B. Callis, Stratospheric Photochemical studies with Atmospheric Trace Molecule Spectroscopy (ATMOS) measurements, *J. Geophys. Res.*, **96**, 9361-9370, 1991.

Osterman G.B., R.J. Salawitch, B. Sen, G.C. Toon, R.A. Stachnik, H.M. Pickett, J.J. Margitan, J.-F. Blavier, and D.B. Peterson, Balloon-borne measurements of stratospheric radicals and their precursors: Implications for the production and loss of ozone, *Geophy. Res. Lett.*, **24**, 1107-1110, 1997.

Prather, M.J. and Remsberg, E.E., The atmospheric effects of stratospheric aircraft: Report of the 1992 models and measurements workshop, 3 volumes, NASA Reference Publication 1292, 1993.

Randel, W.J., F. Wu, J.M. Ruussell, A. Roche, and J.W. Waters, Seasonal cycles and QBO variations in stratospheric CH4 and H2O observed in UARS HALOE data, *J. Atmos. Sci.*, 55, 163-184, 1998.

Rosenlof, K.H., Seasonal cycle of residual mean meridional circulation the stratosphere, *J. Geophys. Res.*, **100**, 5173-5191, 1995.

Salawitch, R.J., S.C. Wofsy, P.O. Wennberg, R.C. Cohen, J.G. Anderson, D.W. Fahey, R.S. Gao, E.R. Keim, E. L. Woodbridge, R.M. Stimpfle, J.P. Koplow, D.W. Kohn, C.R. Webster, R.D. May, L. Pfister, E.W. Gottlieb, H.A. Michelsen, G.K. Yue, J.C. Wilson, C.A. Brock, H.H. Jonsson, J.E. Dye, D. Baumgardner, M.H. Proffitt, M. Loewenstein, J.R. Podolske, J.W. Elkins, G.S. Dutton, E.J. Hisntsa, A.E. Dessler, E.M.Wienstock, K.K. kelly. K.A. Boering, B.C. Daube, K.R. Chan, S.W. Bowen, The distribution of hydrogen, nitrogen, and chlorine radicals in the lower stratosphere: Implications for changes in O_3 due to emission of NOy from supersonic aircraft, *Geophys. Res. Lett.*, **21**, 2547-2550, 1994.

Sen, B., G.C. Toon, G.B. Osterman, J-F Blavier, J.J. Margitan, R.J. Salawitch, and G.K. Yue, Measurements of reactive nitrogen in the stratosphere, *J. Geophys. Res.*, **103**, 3571-3585, 1998.

Schoeberl, M.R., A.E. Roche, J.M. Russell III, D. Ortland, P.B. Hays, and J.W. Waters, An estimation of the dynamical isolation of the tropical lower stratosphere using UARS wind and trace gas observations of quasi-biennial oscillation, *Geophys. Res. Lett.*, **24**, 53-56, 1997.

Summers, M.E., R.R. Conway, D.E. Siskind, M.H. Stevens, D. Offermann, M. Riese, P. Preusse, D.F. Strobel, J.M. Russell III, Implications of Satellite OH observations for middle atmospheric H_2O and Ozone, *Science*, **277**, 1967-1970, 1997.

Volk, C. M., J.W. Elkins, D.W. Fahey, R.J. Salawitch, G.S. Dutton, J.M. Gilligan, M.H. Profitt, M. Lowenstein, J.R. Podolske, K. Minschwaner, J.J. Margitan, and K.R. Chen, Quantifying transport between the tropical and mid-latitude lower stratosphere, *Science*, **272**, 1763-1768, 1996.

Volk, C.M J.W. Elkins, D.W. Fahey, G.S. Dutton, J.M. Gilligan, M. Lowenstein, J.R. Podolske, K.R. Chen, and M.R. Gunson, Evaluation of source gas lifetimes from stratospheric observations, *J. Geophys. Res.*, **102**, 25543-25564, 1997.

1. Model Experiments and Model Descriptions

Charles H. Jackman[1] and Malcolm K. W. Ko[2]

1. NASA Goddard Space Flight Center

2. Atmospheric and Environmental Research, Inc.

1.1 Model Experiments

The planning of the Model and Measurement Workshop started with the kick-off meeting in November 1996 at NASA Headquarters. Participants were given the charge to design a number of experiments that would use observations to test whether models are using the correct mechanisms to simulate the distributions of ozone and other trace gases in the atmosphere. The purpose is closely tied to the needs to reduce the uncertainties in the model predicted responses of stratospheric ozone to perturbations. The set of numerical experiments was finalized in a meeting in February 1997. People were identified with each experiment. One was given the responsibility of defining the boundary conditions for the simulation and specifying the content and format of the model outputs for analyses. The others were to lead the analysis of the results for the experiment. The specifications for the experiments were sent out to the modeling community in June 1997. The list of experiments, along with the definition leads and the analysis leads are given in Table 1.1.1. Descriptions of each experiment are given in section 1.2.

Twenty eight modeling groups responded to the requests for input. Table 1.1.2 lists the participating modeling group, along with the experiments performed. Table 1.1.3 gives the short hand designations of each model that will be used in labeling the results. Brief descriptions of each model as provided by the individual modeling groups are given in section 1.3. The model results were archived in the specified format at UADP at Langley Research Laboratory. The collection of the results at one location in a common format make it possible to analyze the results. Throughout the exercise, the modelers worked closely with the analysis leads to examine the model results. The discussions of the results took place in two meetings, August 1997 and November 1997. A draft report was put together by the analysis leads and the draft was discussed in a meeting held in March 1998. The draft report was revised and sent to copy-edit at the end of 1998.

1.1.1 Introduction

Since the Models and Measurements Workshop held in 1992 (Prather and Remsberg, 1993), additional progress has been made in understanding model differences. A photolysis benchmark (Stolarski et al. 1995) and a chemistry benchmark have been instituted. The photolysis benchmark led to improvements in the computations in 2-D models of radiative transfer with a very large reduction in model-model differences (Stolarski et al. 1995). The chemistry benchmark has been used by modellers to check their chemistry solvers with subsequent improvements in some models.

Some transport differences among the models were highlighted in Prather and Remsberg (1993) with model simulations of C-14, Sr-90, and two idealized tracers. Recent measurements of SF_6 and CO_2 with subsequent derivations of "age of air" have prompted a renewed interest in modelled transport. The model exercises for Models and Measurements II include both "transport" and "chemistry" parts.

The information about the transport and chemistry runs is given below for two reasons: 1) to assist the reader in understanding the enclosed analysis of the model simulations; and 2) to assist modellers, who did not take part in the original Models and Measurements II workshops, in repeating the model simulations for their own benefit.

References

Prather, M. J., and E. E. Remsberg, The Atmospheric Effects of Stratospheric Aircraft: Report of the 1992 Models and Measurements Workshop, 3 volumes, NASA Reference Publication 1292, 1993.

Stolarski, R. S., S. L. Baughcum, W. H. Brune, A. R. Douglass, D. W. Fahey, R. R. Friedl, S. C. Liu, R. A. Plumb, L. R. Poole, H. L. Wesoky, and D. R. Worsnop, 1995 Scientific Assessment of the Atmospheric Effects of Stratospheric Aircraft, NASA Reference Publication 1381, 1995.

1.1.2 Information on the Transport and Chemistry Runs

1.1.2.1 Baseline Transport Runs

1.1.2.1.1 A-1. Age Diagnostic

Definition Lead: R. Alan Plumb

The main purpose of this experiment is to have a delta function source in order to generate the age spectrum in the atmospheric model. The age spectrum at a particular location is the distribution of transport times from the troposphere to that location; the age is the first moment of this spectrum (see Hall and Plumb, JGR, 99, 1059, 1994). The age spectrum carries much more information about transport than age alone.

Proposed Run A-1

The tracers should be exactly conserved, except within a source region near the surface. Within this source region only, the mixing ratio is specified as a function of time. The precise spatial location of the source is not really critical, but it should be consistent between models (and must be in the troposphere). The target should be the lowest 2 km of the troposphere and 10 degrees width in latitude centered on the equator. In terms of the UADP grid (see below), it will be the lowest grid boxes centered on 5S, equator and 5N. Note that the edges of the region are at 7.5S and 7.5N. You should pick a box in your model grid that is LARGER than the region defined in UADP grid, but MUST lie below 500 mbar and within 20 degrees of the equator. For 3D models, all longitudes should be specified identically. The model should be run for 20 years, beginning on January 1 of year 1.

The boundary condition for this run is as follows: For the whole first month (starting at t=0, Jan 1, year 1), X1 = 1 (mixing ratio of tracer within box) at every time step. All subsequent time steps after the first month: X1 = 0.0

Proposed output from Run A-1

Model fields should be output on the UADP standard grid (see below) every half-month (on the first and 15th of the months) for the entire 20 years of the run. Having the full time series is essential to deriving the age spectrum. 3D model results should first be zonally averaged.

Modellers need to provide Temperature, w* (in cm/s), v* (in m/s), K_{yy} (in cm^2/s), K_{zz} (in cm^2/s), and K_{yz} (in cm^2/s) twice monthly. Please output at the beginning and middle of the month for one year. This information should help in the analysis of A-1 model results.

1.1.2.1.2 A-2. Seasonal Transport Diagnostics

Definition Lead: R. Alan Plumb

These runs are designed to focus on the seasonal transport in the models, and will form a fundamental basis on which CO2 concentrations can be understood.

Proposed Run A-2

Two runs, with tropical sources (see note above on source regions - use same target box as for age diagnostic run A-1) whose seasonal cycles are 90 degrees out of phase should be done:

a. X2(t) = 1 + sin(2*pi*t/T) where T = 1 model year

b. X3(t) = 1 + cos(2*pi*t/T)

The boundary condition will be applied for the full five years. The constant term of one is included to avoid negative mixing ratios. The basic conditions for these runs will be the same as for the age diagnostic (A-1). These runs need only be integrated for five years, however.

Initial condition: Outside the target box, the mixing ratios should be set to X2=1, X3=1, at all latitudes and heights, at t=0.

Proposed output from Model Run A-2

Model fields should be output on the UADP standard grid (see below) every half-month (on the first and 15 of the months) for the entire 5 years of the run. 3D model results should first be zonally averaged.

Temperature would also be useful to have every half-month. If temperatures repeat annually, then one year of temperature output is sufficient.

1.1.2.1.3 A-3. Artificial Tracers with Stratospheric Sources; HSCT Emission; Case I

Definition Lead: Donald J. Wuebbles

The idea of these experiments is to test model transports in general, and in particular to test transport from natural and aircraft sources in a chemistry-independent way. These experiments will also help define model stratospheric residence times for various sources. One of these runs will help assess the way in which material is transported from mid-latitudes into the tropics. It is intended that results from these calculations, along with the associated model-model comparisons of results, will allow assesment of model-to-model transport differences on the simulations of real tracers.

Proposed Run A-3

This scenario will involve the simulation of emissions of a hypothetical tracer from a projected fleet of HSCTs. Model input will be mapped to the specified grid for your model and provided as a function of longitude, latitude, and altitude. Emissions will be zonally averaged for 2-D models. The gridded emission will correspond to the NOx emissions for the case of 500 HSCTs at Mach 2.4 and E.I.=10. However, you are to treat the NOx emissions as if this were a tracer. The stratospheric sources are constant in time. Surface destruction is imposed by setting the mixing ratio of the hypothetical tracer below 6 km to zero at every time step. There are no other destruction processes for these tracers, however. The experiments should be initialized on January 1, year 1, with zero mixing ratio everywhere, and run to equilibrium.

The supersonic fleet scenario needed for this model experiment is in your directories; it is named hsct_2015_ei10_500.*. You may get the data from anonymous ftp on uadp1.larc.nasa.gov. If you are doing only MMII then the file will be in mm1997/MMII/your_model_name. If you are doing IPCC and MMII, the file will be in mm1997/IPCC/your_model_name.

Proposed output from Run A-3

Output the steady state concentration of NOx for 1 year. 2D model output should be submitted on the UADP latitude/altitude grid (defined below) and 3D model output on the UADP longitude/latitude/altitude grid for each month. A midmonth value is preferred for 2D models.

Temperature would also be useful to have every mid-month. If temperatures repeat annually, then one year of temperature output is sufficient.

1.1.2.1.4 *A*-4. Artifical Tracers with Stratospheric Sources; HSCT Emission; Case II

Proposed Run A-4

For case A-4, same as A-3 but include only emissions at latitudes greater than 30 degrees North. The emission of the tracer from the HSCT scenario should be truncated so that there is no emission of the tracer at latitudes south of 30 degrees north (no emission in tropics, northern sub-tropics, or in southern hemisphere). All other aspects of this run will be identical to the baseline HSCT scenario (above).

1.1.2.1.5 A-5. Focused Simulation: SF_6

Definition Lead: Malcolm K. W. Ko

Proposed Run A-5

Simulate SF_6 concentration between 1966 to 2000.

Emission: restrict emission to between 30N to 60N, uniform emission rate per unit area (independent of land/ocean for 3-D models), total annual emission set equal to 0.2[t-1966] Ggm/yr. 1 Ggm is 1e9 gm. If you want to reduce the length of the run, you can start with year N, sum all emissions prior to year N to be released in year N, then run to 1996. Sink: no sink, i.e. no in situ chemical removal, no deposition. Therefore, your result should conserve mass.

The recommendation is to keep the emission constant through each year. But if you are particular, you can go through the following: If you are updating your emission rate every DS(in second), you will be changing your emission N=Sy/DS times a year where Sy is the number of seconds in a 365 day year, the amount emitted during the nth interval in a particular year is given by

{0.2*(T-1966+1)/N + 0.2*[n-(N+1)/2]/(N*N)} Ggm

and the emission rate is

{0.2*(T-1966+1)/N + 0.2*[n-(N+1)/2]/(N*N)}/DS Ggm/sec.

In the above equation T is an integer for the year. "n" goes from 1 to N.

Proposed output from A-5

Output: zonal mean distribution of SF_6 in UADP (see below) grid 4 times a year (March 15, June 15, September 15, December 15) for the entire model run; AND global averaged concentration of SF_6 in the troposphere and concentration of SF_6 at the tropical tropopause. Also provide your steady state zonal-mean distribution of N_2O for the same four months and the global average concentration of N_2O in the troposphere. We may use N_2O as the vertical co-ordinate in our analysis. The global averaged tropospheric concentration of N_2O provided by you will be used to scale the N_2O concentrations in the stratosphere if it is necessary to worry about long-term trend in N_2O.

Temperature would also be useful to have 4 times a year (March 15, June 15, September 15, December 15). If temperatures repeat annually, then one year of temperature output is sufficient.

Anticipated analysis: compare tropospheric concentration of SF_6 with various data, stratospheric concentration of SF_6 with ATMOS and aircraft data. We may do some age of air type comparison.

1.1.2.1.6 A-6. Focused Simulations: CO_2

Definition Lead: Timothy M. Hall

The main purpose of this run is to simulate CO_2 as realistically as possible.

Proposed Run A-6

Here is information on specification of the CO_2 surface boundary conditions (in mixing ratio):

1) Set the CO_2 in the atmosphere everywhere equal to 337 ppm at the beginning of 1979 and before; and

2) Set the CO_2 in the atmosphere to boundary conditions based on CMDL maritime measurements for 17 years from 1979 through 1995 (inclusive). These values are based on data provided by Pieter Tans and Ken Masarie at NOAA CMDL and are given every 10 degrees latitude from 90S to 90N (19 latitudes).

To get this CO_2 input data, grab Appendix A via ftp:

ftp uadp1.larc.nasa.gov

Name: anonymous
Password: <your e-mail address>

ftp> cd mm1997/MMII/input_data
ftp> get Appendix_A_CO2.dat
ftp> bye

Modellers should aim to specify these mixing ratio values over the first 2 km (approximately) of the model atmospheres. 3D models should use equal values at all longitudes.

There is no steady state condition, due to the nonrepeating boundary condition. However, from the age spectrum runs, it should be possible to tell when the startup transients become negligible (possibly by year 10 for most models).

Proposed output from Run A-6

Model fields of CO_2 should be output on the UADP standard grid (see previous message) every half-month (on the first and 15th of the months) for the final 6 years of the 17 year run (i.e., 1990 to 1995 inclusive).

Temperature would also be useful to have every half-month. If temperatures repeat annually, then one year of temperature output is sufficient.

1.1.2.2 Baseline Chemistry Runs

1.1.2.2.1 B-1 Baseline Runs for 1992

Definition Lead: David B. Considine

The objective of this run is for each modeling group to provide their "best" simulation of 1992, however they see fit.

Proposed Run B-1

1. Run B-1 should include PSCs. Groups willing to provide output for Run E-1, Polar Processes, should repeat this run without PSCs (see run E-1 below).

2. Sulfate aerosol surface area densities for 1992 are very high due to the eruption of Mt. Pinatubo in 1991. The surface area densities used in the models should not be a background distribution but should be elevated. A three year zonal and monthly mean climatology (1990-1992) of sulfate aerosol SAD derived from SAGE II observations has been constructed and is available from the UADP for those interested in using it (file sage2sad_uadp.dat). See information under "Constrained Chemistry Run B-2" to retrieve this file.

3. Because the 1992 sulfate aerosol SAD is decaying from highly elevated values, running a 2D model to an annually repeating steady state for 1992 would not be legitimate. 2D models should therefore run to an annually repeating steady state for 1990, and then integrate an extra 2 years through the eruption of Mt. Pinatubo. Output from the last year only is requested.

4. Model temperatures should correspond to 1992 if possible. A zonal and monthly mean temperature file taken from 1992 NCEP data and the 1986 CIRA reference model is available on the UADP data base (Temperature_92.dat). See information under "Constrained Chemistry Run B-2" to retrieve this file.

5. Boundary Conditions: You may use whatever source gas boundary conditions you feel are appropriate for 1992. Here is a table of source gas boundary conditions that are believed to be reasonably close to 1992 conditions. These are generally taken from Table 6-3, WMO (1994) for the year 1990. Source gas CH_3Br is taken from the IS92a scenario given in Table 2.2 of "Climate Change 1995." The CO_2 boundary condition is taken from Figure 5, p.23, of "Climate Change 1995."

Species	Value
CFC-10 (CCl_4)	108 pptv
CFC-11 ($CFCl_3$)	270 pptv
CFC-12 (CF_2Cl_2)	465 pptv
CFC-113 ($C_2F_3Cl_3$)	70 pptv
HCFC-22 (CHF_2Cl)	106 pptv
CH_3CCl_3	153 pptv
H-1301 (CF_3Br)	1.7 pptv
H-1211 (CF_2ClBr)	2.9 pptv
CH_3Cl	600 pptv
CH_3Br	10 pptv
CH_4	1715 ppbv
N_2O	310 ppbv
CO_2	356 ppmv

6. Reaction rates, heterogeneous reaction rates, and photolysis cross sections should be consistent with JPL-97 (see below to retrieve this information).

Proposed output from Run B-1

2D model output should be submitted on the UADP latitude/altitude grid (defined below) and 3D model output on the UADP longitude/latitude/altitude grid at the beginning and middle of each month of 1992. An output of the daytime average value is preferred for 2D models. An output at 12Z would be best for 3D models. Please output the following, if calculated:

a. Source Gases/Tracers (in mixing ratio):

CF_2Cl_2, CF_2Cl_3, CCl_4, CH_3Cl, CH_3CCl_3, $CHClF_2$, $C_2Cl_3F_3$, CClFO, CF_2O, N_2O, CH_4, H_2O, HF, CH_3Br

b. Column ozone (in Dobson Units) - by latitude and month

c. Medium Lived/Reservoir (in mixing ratio):

O_3, HCl, $ClONO_2$, HNO_3, N_2O_5, HBr, $BrONO_2$, H_2O_2

d. Short Lived/Radical (in mixing ratio):

$O(^3P)$, $O(^1D)$, NO, NO_2, OH, HO_2, HOCl, ClO, BrO, Cl_2O_2, HOBr

e. Families (in mixing ratio): NOy, Cly, Bry

f. Other: CH_2O & CO (in mixing ratio),
M (total number density in #/cm+3),
Temperature (Kelvin)

g. Ozone loss rates (in mixing ratio per second) for NOx, HOx, ClOx, BrOx, and Ox

h. Ozone production rates (in mixing ratio per second) for
1. $J(O_2)$ and 2. a sum of the rest

i. For N_2O, CH_4, $CFCl_3$, CF_2Cl_2, CCl_4, CH_3Cl, CH_3Br, CH_3CCl_3, $C_2Cl_3F_3$, $CHClF_2$, and any other CFC or HCFC in your model simulation, please provide:
1. Global yearly average atmospheric abundance (in # of molecules);
2. total global yearly average atmospheric loss rate (in # of molecules per second);
3. total global yearly average stratospheric loss rate (in # of molecules per second).

1.1.2.2.2 B-2 Constrained Runs: Fixed Inputs

Definition Lead: Charles H. Jackman

Here is additional information on Constrained Chemistry Run B-2. The "Proposed Model Run" and "Proposed Model Run Output" are given below.

Simulate 1992 with fixed 1) zonal-mean temperature; 2) aerosol; and 3) ozone, water vapor, and several source gases. These model parameters will be fixed to values constrained as much as possible by observations.

Data to Constrain the Run B-2

The data to constrain this run are located at the Upper Atmosphere Data Pilot (UADP) at NASA Langley Research Center. To retrieve these data, do the following:

ftp uadp1.larc.nasa.gov

Name: anonymous
Password: <your e-mail address>

ftp> cd mm1997/MMII/input_data
ftp> get README
ftp> get Constrained_species_92.dat
ftp> get Temperature_92.dat
ftp> get sage2sad_uadp.dat
ftp> bye

1) Zonal-mean Temperature

These data are located in "Temperature_92.dat"

Temperature data for 1992 was taken from the National Centers for Environmental Prediction (NCEP) for 1000-1 mbar and the CIRA (1986) empirical reference model for the mesosphere above 1 mbar.

2) Zonal-mean Aerosol

These data are located in "sage2sad_uadp.dat"

The 1990-1992 surface area density data set was constructed from calculations of aerosol surface area density made by Larry Thomason of the NASA Langley Research Center using SAGE II satellite data. These calculations are described in Thomason, L. W., L. R. Poole, and T. Deshler, "A global climatology of stratospheric aerosol surface area density deduced from Stratospheric Aerosol and Gas Experiment II measurements: 1984-1994," J. Geophys. Res., 102, 8967-8976, 1997. The Thomason et al. calculations have been modified in the following ways: 1. Only data from 1990, 1991, and 1992 are included in this data set; 2. A time interpolation was used between −65 and +65 degrees to eliminate occasional data gaps; 3. In the areas where the SAGE II instrument was saturated after the eruption of Mt. Pinatubo in June, 1991, midlatitude values of surface area density have been interpolated through the tropics. This interpolation fills the region from −15 to +15 degrees and 5.5 to 25.5 kilometers during the months from June, 1991 to August, 1992; 4. During months where there was no data in the −80 to −70 and 70 to 80 degree bins, values from the −70 to −60 and 60 to 70 degree bins were used; 5. The −90 to −80 and 80 to 90 degree latitude bins were filled with values from the −80 to −70 and 70 to 80 degree bins; 6. The resulting 36 month by 18 latitude (10 degree resolution) by 36 altitude (1 kilometer resolution from 5.5 to 40.5 kilometers) was interpolated to the standard UADP 37 latitude by 31 altitude grid.

3) Zonal-mean Ozone, Water Vapor, and Several Source Gases

These data are located in "Constrained_species_92.dat"

The GSFC 2D model (e.g., Jackman et al. 1996) was used in a ""data assimilation" mode. The UARS MLS instrument version 3 measurements were used for O_3 and H_2O. The UARS CLAES instrument version 7 measurements were used for N_2O, CH_4, and CFC-12. The model was fixed to these measurements where they are dependable and was fixed to 1990 boundary conditions in Table 6-3 of WMO (1994) at the ground for N_2O, CH_4, and CFC-12. The model with these constraints was run for

twenty years to a steady-state annually repeating condition. Gas amounts were thus computed over the whole domain of the model.

The constrained source gases CFC-11, CCl_4, CH_3CCl_3, CFC-113, and CH_3Br are computed by using the N_2O values as a tranfer standard [e.g., (Constrained CFC-11) = (Model CFC-11) * (CLAES N_2O)/(Model N_2O)]. The constrained source gas HCFC-22 is not constrained in any way by UARS measurements but is computed in the free-running model. Boundary conditions for CFC-11, CCl_4, CH_3CCl_3, CFC-113, CH_3Br, and HCFC-22 are also taken from year 1990 of Table 6-3 of WMO (1994).

References

Jackman, C. H., E. L. Fleming, S. Chandra, D. B. Considine, and J. E. Rosenfield, Past, Present, and Future Modeled Ozone Trends With Comparisons to Observed Trends, *J. Geophys. Res.*, **101**, 28,753-28,767, 1996.

WMO, Scientific Assessment of Ozone Depletion: 1994, World Meteorological Organization, Global Ozone Research and Monitoring Project, Report No. 37, 1994.

Special Instructions

Modellers are urged to linearly interpolate in time between the monthly intervals to get out these gases on a finer interval.

Modellers are encouraged to run their model to an approximate steady-state condition with the fixed temperature and source gases AND a near background sulfate surface area. Modellers are then encouraged to run their model in a time-dependent manner for three years (1990-2) using the monthly changing, but prescribed, sulfate surface areas.

Proposed output from Run B-2

2D model output should be submitted on the UADP latitude/ altitude grid (defined below) and 3D model output on the UADP longitude/latitude/altitude grid for each month of 1992. A midmonth daytime average value is preferred for 2D models. A midmonth day at 12Z would be best for 3D models. Please output the following, if calculated:

a. Medium Lived/Reservoir (in mixing ratio):

   HCl, $ClONO_2$, HNO_3, N_2O_5, HBr, $BrONO_2$, H_2O_2

b. Short Lived/Radical (in mixing ratio):

   $O(^3P)$, $O(^1D)$, NO, NO_2, OH, HO_2, $HOCl$, ClO, BrO, Cl_2O_2, $HOBr$

c. Families (in mixing ratio): NOy, Cly, Bry

d. Other: CH_2O & CO (in mixing ratio),
   M (total number density in #/cm+3),
   Temperature (Kelvin)

e. Ozone loss rates (in mixing ratio per second) for NOx, HOx, ClOx, BrOx, and Ox

f. Ozone production rates (in mixing ratio per second) for
1. $J(O_2)$ and 2. a sum of the rest

g. For N_2O, CH_4, $CFCl_3$, CF_2Cl_2, CCl_4, CH_3Cl, CH_3Br, CH_3CCl_3, $C_2Cl_3F_3$, $CHClF_2$, and any other CFC or HCFC in your model simulation, please provide:
1. Global yearly average atmospheric abundance (in # of molecules);
2. total global yearly average atmospheric loss rate (in # of molecules per second);
3. total global yearly average stratospheric loss rate (in # of molecules per second).

1.1.2.2.3 B-3 Constrained Runs: Prescribed Ozone P/L

Definition Lead: Malcolm K. W. Ko

Here is additional information on Constrained Chemistry Run B-3. The "Proposed Model Run" and "Proposed Model Run Output" are given below.

Proposed Run B-3

The input file provides:
O3: ozone mixing ratio
O3P: in units of mixing ratio per sec
O3L: loss frequency in unit of 1/sec
O3Q: quadratic loss frequency in unit of 1/sec

Data to Constrain the Run -
The data to constrain this run are located at the Upper Atmosphere Data Pilot (UADP) at NASA Langley Research Center. To retrieve these data, do the following:

ftp uadp1.larc.nasa.gov

Name: anonymous
Password: <your e-mail address>

ftp> cd mm1997/MMII/input_data
ftp> get O3.dat
ftp> get O3Prod.dat
ftp> get O3LLoss.dat
ftp> get O3QLoss.dat
ftp> bye

We suggest that you use O3L and O3Q and write the chemical tendency in your model at each time step as
O3P - O3model*O3L - O3model*O3model*O3Q (eq 1),
where O3model is the model calculated ozone at each time step.

The net chemical tendency in each time step can be reconstructed by
O3P - O3*O3L -O3*O3*O3Q (eq 2).
Some modelers may be tempted to use the values defined by eq 2 as the fixed net tendency term at each time step and the given O3 distribution on January 1 as initial condition and solve the equation as an initial value problem. Since we do not do our model that way, we are not sure how well this works.

However, this may not work because the net tendency depends on the transport terms in the AER model. Since your model has different transport tendencies, the system may not reach steady state.

Proposed output from Run B-3

Proposed model output:

2D model output should be submitted on the UADP latitude/ altitude grid (defined below) and 3D model output on the UADP longitude/latitude/altitude grid for each month of 1992. A mid-month daytime average value is preferred for 2D models. A mid-month day at 12Z would be best for 3D models. Please output the following, if calculated:

a. Column ozone (in Dobson units by month and latitude)

b. O_3 mixing ratio

1.1.2.2.4 B-4 High Speed Civil Transport (HSCT)

Definition Lead: Donald J. Wuebbles

Here is additional information on HSCT Run B-4. The "Proposed Model Run" and "Proposed Model Run Output" are given below.

Proposed Run B-4

The emissions input of HSCTs only will be based on the new NASA database for HSCTs projected to 2015. We will consider NOx emissions only for the case of 500 HSCTs at Mach 2.4 and E.I.=10. We will consider only NOx emissions so as to avoid interpretation problems with the analyses of the results and because some models may not be able to include water vapor emissions. The E.I. = 10 case is chosen to try to ensure a perturbation that is statistically meaningful. The recommended source gas boundary conditions for 2015 are given below. Modellers are asked to do the 2015 perturbed run for BOTH sulfate aerosol amounts of SA0 and SA1.

Two runs will be needed:

I) A 2015 base run with no emissions of NOx.

II) A 2015 perturbed run with emissions of NOx.

The supersonic fleet scenario needed for this model experiment is in your directories; it is named hsct_2015_ei10_500.*. You may get the data from anonymous ftp on uadp1.larc.nasa.gov. If you are doing only MMII then the file will be in mm1997/MMII/your_model_name. If you are doing IPCC and MMII, the file will be in mm1997/IPCC/your_model_name.

Proposed output from Run B-4

2D model output should be submitted on the uadp latitude/ altitude grid (defined below) and 3D model output on the uadp longitude/latitude/altitude grid for each month of 1992. A midmonth daytime average value is preferred for 2D models. A midmonth day at 12Z would be best for 3D models. Please output the following, if calculated:

a. Source Gases/Tracers (in mixing ratio):

N_2O, CH_4, H_2O

b. Column ozone (in Dobson Units) - by latitude and month

c. Medium Lived/Reservoir (in mixing ratio):

O_3, HCl, $ClONO_2$, HNO_3, N_2O_5, HBr, $BrONO_2$, H_2O_2

d. Short Lived/Radical (in mixing ratio):

$O(^3P)$, $O(^1D)$, NO, NO_2, OH, HO_2, HOCl, ClO, BrO, Cl_2O_2, HOBr

e. Families (in mixing ratio): NOy, Cly, Bry

f. Other: CO (in mixing ratio),
M (total number density in #/cm+3),
Temperature (Kelvin)

g. Ozone loss rates (in mixing ratio per second) for NOx, HOx, ClOx, BrOx, and Ox

h. Ozone production rates (in mixing ratio per second) for
1. $J(O_2)$ and 2. a sum of the rest

Recommendations for Source Gas Boundary Conditions

Use "2015 - 3 ppbv Cly" boundary conditions (see below; same as being used in IPCC assessment).

The halogen source gases are taken from the "1995 Scientific Assessment of the Atmospheric Effects of Stratospheric Aircraft", NASA Reference Publication 1381, 1995. Source gases CH_4 and N_2O are taken from the IS92a scenario given in Tables 2.5a and 2.5b of "Climate Change 1995." Source gas CO_2 is taken from the IS92a scenario given in Figure 5, p. 23, of "Climate Change 1995." Source gas CH_3Br is taken from the IS92a scenario given in Table 2.2 of "Climate Change 1995."

Table - Recommendations for species concentrations in 2015

Species	2015 ("3 ppbv Cly")
CFC-11	220 pptv
CFC-12	470 pptv
CFC-113	80 pptv
CCl_4	70 pptv
HCFC-22	250 pptv
CH_3CCl_3	3 pptv
[a]HCFC-141b	12 pptv
Halon-1301	1.4 pptv
Halon-1211	1.1 pptv
CH_3Cl	600 pptv
CH_3Br	10 pptv
CH_4	2052 ppbv
N_2O	333 ppbv
CO_2	405 ppmv

[a] If your model cannot handle HCFC-141b, we recommend putting it in as CH_3CCl_3 after adjusting for the number of chlorine atoms per molecule, i.e., multiply the HCFC-141b mixing ratio by 2/3 and add to CH_3CCl_3. The stratospheric lifetimes for CH3CCl3 and HCFC-141b are 50 years and 75 years, respectively. These lifetimes are sufficiently close so supplementing CH_3CCl_3 with HCFC-141b should be a reasonable approximation.

Use sulfate surface area SA0 (labelled SAunep) and SA1, which are available at the NASA Langley UADP. SA0 (SAunep) is the WMO background sulfate surface area. SA1 corresponds to the surface area obtained by adding to the WMO background sulfate surface area the increase in surface area calculated by Wiesenstein et al. (J. Geophys. Res., "A two dimensional model of sulfur species and aerosols," in press) 1997 caused by a 500 aircraft fleet with sulfur EI=0.4 and assuming 50% of the SO_2 is converted to sulfate particles in the plume.

To access surface area SA1:

ftp uadp1.larc.nasa.gov

Name: anonymous
Password: <your e-mail address>

ftp> cd mm1997/IPCC/input_to_model_runs
ftp> get README
ftp> get SURFACE_AREA.dat
ftp> bye

1.1.2.2.5 E-1 Modified Runs of B-1

Definition Lead: David B. Considine

Proposed Run E-1

This run is very similar to run B-1, except heterogeneous chlorine activation SHOULD NOT BE included. The reactions

1) $N_2O_5 + H_2O \rightarrow HNO_3 + HNO_3$

and

2) $BrONO_2 + H_2O \rightarrow HOBr + HNO_3$

SHOULD BE included in this run.

Proposed output from Run E-1

2D model output should be submitted on the UADP latitude/altitude grid (defined below) and 3D model output on the UADP longitude/latitude/altitude grid at the beginning and middle of each month of 1992. An output of the daytime average value is preferred for 2D models. An output at 12Z would be best for 3D models. Please output the following, if calculated:

a. Source Gases/Tracers (in mixing ratio):

CF_2Cl_2, $CFCl_3$, CCl_4, CH_3Cl, CH_3CCl_3, $CHClF_2$, $C_2Cl_3F_3$, CClFO, CF_2O, N_2O, CH_4, H_2O, HF, CH_3Br

b. Column ozone (in Dobson Units) - by latitude and month

c. Medium Lived/Reservoir (in mixing ratio):

O_3, HCl, $ClONO_2$, HNO_3, N_2O_5, HBr, $BrONO_2$, H_2O_2

d. Short Lived/Radical (in mixing ratio):

$O(^3P)$, $O(^1D)$, NO, NO_2, OH, HO_2, HOCl, ClO, BrO, Cl_2O_2, HOBr

e. Families (in mixing ratio): NOy, Cly, Bry

f. Other: CH_2O & CO (in mixing ratio),
M (total number density in #/cm+3),
Temperature (Kelvin)

g. Ozone loss rates (in mixing ratio per second) for NOx, HOx, ClOx, BrOx, and Ox

h. Ozone production rates (in mixing ratio per second) for 1. $J(O_2)$ and 2. a sum of the rest

i. For N_2O, CH_4, $CFCl_3$, CF_2Cl_2, CCl_4, CH_3Cl, CH_3Br, CH_3CCl_3, $C_2Cl_3F_3$, $CHClF_2$, and any other CFC or HCFC in your model simulation, please provide:
   1. Global yearly average atmospheric abundance (in # of molecules);
   2. total global yearly average atmospheric loss rate (in # of molecules per second);
   3. total global yearly average stratospheric loss rate (in # of molecules per second).

Modellers should update their chemistry to JPL Publication 97-4, published January 15, 1997. Copies of this publication are available from:

Jet Propulsion Laboratory
California Institute of Technology
Secondary Distribution, MS 512-110
4800 Oak Grove Drive Pasadena, CA 91109
Phone: (818)397-7952

The JPL Publication 97-4 kinetics data base can be obtained electronically at http://remus.jpl.nasa.gov/jpl97/ or via ftp at host remus.jpl.nasa.gov.

This electronic means of receiving the 1997 kinetics data base would be much faster than through the regular mail.

1.1.3 The Langley Upper Atmosphere Data Pilot (UADP) Information

The following information is similar to that sent out for the 1995 assessment. The file naming convention has been altered to fit the requested model runs. Don Brown will be working on this effort with me. Linda Hunt is no longer with this project. Please review this document and if you have any questions, please let us know.

Here is some information about the model run results you will be returning to us. Since you have done this before you probably know that we're not real picky about the file format used. What we do ask is that once you start using a format that you stick with it.

The file format below is identical to the one used for supersonic aircraft scenario computations. If you can use it easily, please do. If you have a format you have sent to us previously, feel free to use that format. Once again, we will handle the data in whatever format you send. However, once you use a particular format, please stick with that format for all the data submitted for a particular effort.

The file name should indicate the scenario involved. Here's a suggested file naming convention:

QUANTITY.YEAR.MODELrun.MODEL

where:

QUANTITY =	o3col	(column O3, DU)
	ox o3 ch4 noy n2o ...	(species mixing ratio)
	P.total P.jo2 P.ch3o2+no ...	(Ox production, mixing ratio/s)
	L.total L.ox L.noy L.o.no2 ...	(Ox loss, mixing ratio/s)
	etc	

YEAR = 1992

MODEL RUN = b1,b2,b3,b4

MODEL = csiro csiro1 csiro2 csiro2b ... (for different model versions)
llnl ... gsfc ...
etc

Hence a name might turn out to be something like:
O3col.1992.b2.gsfc

It is not necessary for you to have each parameter in its own file, in which case you could use "species" in the file name (or use some other indicator). However, column data should be in a separate file from data on a lat/alt grid.

Please let us know if you have any questions or suggestions. Thanks!

General UADP Model Data Submission Info (Revised 5/95)

1. GENERAL: Data can be transferred to the UADP via electronic file transfer (TCP/IP protocol). Electronic addresses are as follows:
   uadp1.larc.nasa.gov 146.165.21.96
   uadp2.larc.nasa.gov 128.155.17.46
   Anonymous ftp accounts (user name anonymous or ftp, password is your internet address) are available on both machines.

***NOTE: Some of you are participating in the IPCC and the M&MII efforts. For those of you participating in BOTH efforts, we have made directories for your models on uadp1 and uadp2 in mm1997/MMII. If you would please put your MMII results in those directories on one of the machines and send us email letting us know they are there, we would appreciate it.

Those of you participating in ı 1&MII effort exclusively, please put your results in your model directory under mm1997/MMII on ıer uadp1 or uadp2. And let us know via email that the results files are there.

We are going to try to keep an eye on disk space, please let us know if you run into any problems with "disk full" messages.

2. DESCRIPTIVE TEXT: A set of free format character data records (up to 80 characters per line) should begin each file. The following information should be included:
   a. an initial record specifying the number of lines of descriptive text
   b. brief (1 to 5 lines) description of the model and technique
   c. names and institutions of principal investigator(s)
   d. journal reference for model documentation (where available)
   e. name, telephone number, and electronic address (if available) of data contact
   f. units for each parameter (parameter name followed by units)
   g. information about the time and range of time steps for the data set (i.e. mid-month data for twelve months of 1990)

***If items b-e are the same for all data in the current submission, you can put this information in a separate file rather than repeating it in each file.

3. DATA RECORDS: The information below illustrates how these records (parts 3A and 3B) should be written.

4. DATA GRID: Data should be provided on the following standard grid:
   Latitude - 37 latitudes (90S to 90N at 5 degree increments)
   Longitude (if appropriate) - 19 longitudes (180W to 180E at 20 degree increments)
   Vertical - 31 levels in z* (z* = 16*log10(1000/p)) (0 to 60 in increments of 2 km) for profiles
   Time - mid-month (15th of month preferred, otherwise monthly mean)

5. INFORMATION/QUESTIONS: Questions or inquiries about use of the system, data submittal, and the like should be adressed to either Don Brown (757-864-5855) or Karen Sage (757-894-5857). Electronic mail to the UADP can be addressed to brown@uadp1.larc.nasa.gov or sage@uadp2.larc.nasa.gov. FAX service is available at 757-864-7790. Our mailing address is:

   MS 401A
   21 Langley Blvd
   NASA Langley Research Center
   Hampton, Virginia USA 23681-0001

Model Data Submission File Specification

1. FILE DESCRIPTIVE TEXT
   - Value indicating number of lines (up to 80 characters per line) of descriptive text
   - Descriptive text

2. FILE HEADER LINE
   - Four values indicating number of parameters, number of latitudes (=37), number of levels (=31 for profiles or arrays, =1 for columns), and number of time steps. For example, this line would be 20 37 31 12 for 20 parameters, 37 latitudes, 31 levels, and 12 months.

3A. PARAMETER DATA HEADER LINE
   - Two values indicating parameter name and time step (for example CH_4 15-JAN-81) separated by at least one blank

3B. PARAMETER DATA:

2d models (zonally averaged output)--
   DATA FOR I LATITUDES FOR J LEVELS
   - Array of parameter values written in order of
   (((I,J), J=1,Num. of Z* levels), I=1,Num. of latitudes)

(Repeat 3A and 3B for each parameter)

1.1.4 Modeling Groups and Proposed Experiments

Individual model's running experiments are summarized in Table 1.1.2, and shorthand designation of each model is summarized in Table 1.1.3.

Descriptions of each model are given in the following section.

Table 1.1.1 List of Experiments, Definition and Analysis Leads

Experiments	Definition Lead	Analysis Lead(s)	Results
Transport Experiment			
A1 Age Diagnostics: simulation the distributions of an inert tracer with specific initial condition to generate model output for age analysis	Plumb	Hall	2.3
		Waugh, Hall	2.6
A2 Seasonal transport diagnostics: simulation of the distributions of an inert tracer with seasonally varying boundary condition to simulate the seasonal cycle of CO_2.	Plumb	Hall	2.3, 2.5
		Boering	2.4
		Plumb	2.7
A3 NOy-1: simulation the steady state distribution of an inert tracer with an injection similar to that of the projected HSCT fleet	Wuebbles	Rind, Hall, Wuebbles	2.8
A4 NOy-2: similar to A3 except that the injection are limted to mid-latitudes	Wuebbles	Rind, Hall, Wuebbles	2.8
A5 SF_6: simulation of SF_6 distributions from 1966-2000 using surface concentrations from observations	Ko	Hall	2.3
		Boering	2.4
		Waugh, Hall	2.6
A6 CO_2: simulation of the atmospheric distribution of CO_2 1979-1995 using the surface concentrations from NOAA CMDL	Hall	Hall	2.3
		Boering	2.4
		Waugh, Hall	2.6
Chemistry Experiment			
B1 1992 atmosphere: simulation of the chemical trace gases in the 1992 atmosphere	Considine	Waugh, Hall	2.6
		Remsberg, Scott, Ko, Tie, Brasseur, Huang	Chapter 3
		Logan, McPeters	Chapter 4
		Ko, Salawitch	5.2
		Jackman	5.3
		Considine	5.5
B2 constrained simulation for 1992: simulation of the 1992 atmosphere using fixed zonal-mean temperature, aerosol surface area, ozone, water vapor, N_2O, CH_4, CFC-11, CFC-12, CH_3CCl_3, CFC-113, and CH_3Br	Jackman	Tie, Brasseur, Huang	3.5
B3 constrained ozone: simulation of the ozone distribution using prescribed production and removal rates	Ko	Jackman, Fleming, Ko	5.4
B4 ozone response to injected NOx: simulations of the 2015 atmosphere to determine the ozone response to injction of NOx from HSCT	Wuebbles	Wuebbles	Chapter 6
E1 PSC treatment: similar to B1 except assume no PSC formation and reactions	Considine	Douglass	5.6

Table 1.1.2 Matrix of models and experiments.

2D Model	A1	A2	A3	A4	A5	A6	B1	B2	B3	B4	E1
AER	X	X	X	X	X	X	X	X	X	X	X
CSIRO	X	X					X	X		X	
GSFC-2D	X	X	X	X	X	X	X	X	X	X	X
GSFC-2Dint	X	X	X	X	X	X					
HARVARD	X	X	X	X	X	X	X		X	X	
LLNL	X	X	X	X	X	X	X	X	X	X	X
MGO-UIUC-2D	X	X	X	X	X	X					
NCAR-2D	X	X	X	X							
NOCAR	X	X	X	X	X		X				
SUNY_SPB	X	X	X	X	X	X	X	X	X	X	X
UNIVAQ-2D	X	X	X	X	X	X	X	X	X	X	X
WISCAR	X	X									
3D Model											
ECHAM3/CHEM							X			X	
GISS-3D			X	X							
GISS8X10	X	X			X	X					
GMI-DAO	X	X	X	X	X	X					
GMI-GISS	X		X		X						
GMI-NCAR	X	X	X	X	X	X					
GMI-NCARcon	X	X				X					
GSFC-3D	X	X	X	X	X	X	X				
LARC-3D							X				
MONASH1		X	X	X	X	X					
MONASH2		X	X	X	X	X					
NCAR-3D		X	X	X							
SLIMCAT								X			
UCI21	X										
UCI23	X	X	X	X	X	X					
UIUC-3D	X	X	X	X	X	X					
UNIVAQ-3D		X	X	X	X	X			X	X	

Table 1.1.3 Model names and designations.

Model "official" designation	Four character (or less) shorthand designation
AER	AER
CSIRO	CSI
ECHAM3/CHEM	E3CH
GISS-3D	GIS3
GISS8X10	GISS
GMI-DAO	GMDA
GMI-GISS	GMGI
GMI-NCAR	GMNC
GMI-NCARcon	GMND
GSFC-2D	GS2
GSFC-2Dint	GS2i
GSFC-3D	GS3
HARVARD	HARV
LARC-3D	LARC
LLNL	LLNL
MGO-UIUC-2D	MUI2
MONASH1	MON1
MONASH2	MON2
NCAR-2D	NCA2
NCAR-3D	NCA3
NOCAR	NOCR
SLIMCAT	SLIM
SUNY_SPB	NYSP
UCI21	UCIA
UCI23	UCIB
UIUC-3D	UIU3
UNIVAQ-2D	UAQ2
UNIVAQ-3D	UAQ3
WISCAR	WCAR

1.2 Model Descriptions

1.2.1 Description of the AER 2-D Photochemical Transport Model

Malcolm Ko, Debra Weisenstein, Courtney J. Scott,
Run-Lie Shia, Jose Rodriguez, N.D. Sze
Atmospheric and Environmental Research, Inc
840 Memorial Dr., Cambridge, MA 02139
(email: mko@aer.com, weisenstein@aer.com, scott@aer.com)

General Information

The AER 2-D photochemical transport model participated in both M&M I, M&M II, and photolysis and chemical solver intercomparisions sponsored by the AESA project. References to the model formulation are listed near the end of this document.

Domain and Grid Sizes

The AER 2-D model domain extends from south pole to north pole and approximately from the ground to 60 km. Latitude and log-pressure are used as coordinates, with horizontal resolution of 9.5 and vertical resolution of 0.167 in units of ln(1000/p(mb)), equivalent to approximately 1.2 km. The center of each latitude band in degrees is given by (180./19)*(i-10), where i is the latitude index ranging from 1 to 19. The pressure in mb at the center of each altitude bin is given by 1000.*exp(-0.167*(j-0.5)), where j is the altitude index ranging from 1 to 51.

Transport and Temperature

The dynamical transport occurs through the zonal-mean diabatic circulation, by quasi-horizontal diffusion along isentropic surfaces, and by vertical diffusion in the troposphere and upper stratosphere. Circulation and diffusion in the AER model are non-interactive and are specified independently of each other and the adopted temperature fields. The diabatic circulation used was based on the calculated heating rates of Murgatroyd and Singleton (1961) for the upper stratosphere and Dopplick (1979) for the lower stratosphere, and resembles that derived by Rosenfield et al. (1987) in both structure and magnitude. Temperatures are an 8 year average of NMC monthly-mean zonal-mean temperatures for the 1979-1986 period. Temperature distributions, based on the same 8 years of NCEP/NCAR Reanalysis data (Kalnay et al., 1996), are used to account for deviations from the zonal and monthly mean temperature in the calculation of reaction rates and PSC formation probabilities. Daily temperatures are interpolated from monthly mean fields. The shape of the temperature distribution is retained for a full month but is shifted in temperature to match the zonal-mean temperature for that day. Tropopause heights are based on temperature gradients and vary seasonally from 10.2 to 12.3 km at 45 N.

The horizontal eddy diffusion coefficient, K_{yy}, is a function of latitude, altitude, and season. It has the value 1.5×10^{10} cm^2/sec in the troposphere. In the lower statosphere, we simulate a tropical barrier circulation (Plumb, 1996) by employing low values of K_{yy} in the tropics. These values are based on fits of model transport to tropical/midlatitude exchange rates derived from observations (Minschwaner et al., 1996; Volk et al., 1996; Schoeberl et al., 1997). In the tropical lower stratosphere below 23 km, the value of K_{yy} is 1.3×10^9 cm^2/sec and from 23 to 35 km is 0.7×10^9 cm^2/sec (Shia et al., 1998). Midlatitude values of K_{yy} in the stratosphere range from $3\text{-}10 \times 10^9$ cm^2/sec. The value of K_{yy} in the

stratosphere above 35 km is $3x10^9$ cm^2/sec for all latitudes and seasons, based on the work of Kida (1983) and Tung (1984). A K_{yz} term is calculated based on a translation of the horizontal diffusion, which is assumed to be acting along isentropic surfaces, to the model's log-pressure grid.

The vertical diffusion coefficient, K_{zz}, is $1x10^5$ cm^2/sec in the troposphere, $1x10^3$ cm^2/sec in the stratosphere below 40 km and $1x10^4$ cm^2/sec above 40 km. The relatively large vertical diffusion coefficient in the troposphere simulates convective overturning and synoptic scale eddies. Stratospheric vertical diffusion was estimated by Kida (1983) to be $1x10^3$ cm^2/sec. Enhanced vertical mixing above 40 km is based on the work of Garcia and Solomon (1985) regarding gravity wave breaking.

Photochemistry

The model contains 62 chemical species, including complete diurnal chemistry for the NOy, Clx, Brx, Fx, HOx, Ox, methyl and ethyl families. Source gases include N_2O, CH_4, C_2H_6, H_2, CO, CCl_4, CFC-11, CFC-12, CFC-113, HCFC-22, CH_3Cl, CH_3CCl_3, Halon-1211, Halon-1301, and CH_3Br. The family chemistry approach is used for the transport of NOy, Clx, Brx, and Ox, but HNO_3 is transported separately from other members of the NOy family. When the lifetime of HNO_3 becomes short, it is solved using chemical equilibrium, and then the total NOy family is transported together. Explicit diurnal calculations are performed for the short-lived species every day of model simulation. An iterative Newton/Raphson scheme is used to solve for all the short-lived species simultaneously, using 12 time intervals for the daylight hours and 5 intervals for the nighttime hours.

The kinetic reaction rates and absorption cross-sections are taken from NASA/JPL (1997). The solar fluxes are from WMO/NASA (1982). The spectral resolution is 5 nm or less over the wavelength range from 178 nm to 330 nm. Longer intervals are used from 330 nm up to 805 nm. Solar zenith angle is a function of altitude. The photolysis code, which includes calculation of multiple scattering in a spherical atmosphere, was provided by M. Prather (UCI) and is known to agree with the codes of Anderson and Lloyd (1990) and Dahlback and Stamnes (1991). O_2 absorption in the Schumann-Runge band is based on Minschwaner et al. (1992). Washout and rainout provide removal of H_2O_2, CH_3OOH, CH_2O, HNO_3, HCl, HBr, and HF in the troposphere below 10 km with lifetimes ranging from 5 days at the surface to 40 days at 10 km.

Heterogeneous Chemistry

The following heterogeneous reactions on sulfate and PSC particles are included in the model:

1. $N_2O_5 + H_2O = 2HNO_3$
2. $ClONO_2 + H_2O = HOCl + HNO_3$
3. $ClONO_2 + HCl = Cl_2 + HNO_3$
4. $HOCl + HCl = Cl_2 + H_2O$
5. $HOBr + HCl = BrCl + H_2O$
6. $BrONO_2 + H_2O = HOBr + HNO_3$
7. $N_2O_5 + HCl = ClNO_2 + HNO_3$

Heterogeneous reaction rates, k, are calculated as first-order loss rates proportional to particle surface area:

$$k = \gamma v A/4,$$

where γ is the reaction probability or sticking coefficient, v is the thermal velocity of the gas molecule, and A is the surface area density of the aerosol particles. On sulfate aerosols, reaction 1 uses a constant γ of 0.1, while reactions 2-4 follow Hanson et al. (1994). Reaction 5 follows Hanson and Ravishankara (1995) and reaction 6 follows Hanson et al. (1996). Reactions 4 and 5 account for possible reaction within the particle volume, with volume obtained from surface area by assuming a particle radius of 0.1 mm. Reaction 7 applies only to PSCs.

Parameterized PSC chemistry is included for NAT and ice, assuming a unimodal radius of 0.5 mm for NAT and 7 mm for ice particles. The calculation assumes thermodynamic equilibrium between the gas and the condensed phase for HNO_3 and H_2O, with no supersaturation required. The temperature probability distribution is employed to obtain PSC surface areas for each temperature in the distribution. PSC and sulfate surface areas are independent in the model, but sulfate reaction rates are reduced to zero when the PSC surface area exceeds 50% of the sulfate surface area to simulate coating of sulfate by NAT or ice. Rates of PSC reactions are obtained for each temperature in the distribution, the net rate being obtained as the integral of the probability of occurrence of a particular temperature multiplied by the rate and the surface area at that temperature. Reaction probabilities for PSC reactions are taken from NASA/JPL (1997). Reactions 5 and 6 do not occur on PSC-type 1 particles. All PSC reactions are assumed to have a constant g except for reaction 3 on PSC-type 1.

Time Steps and Transport Scheme

Production and loss terms for the long-lived species are updated every day and are calculated as diurnal averages of the product of the rate and the radical species densities over the 17 diurnal time intervals. Lightning is included as a source of NOY in the tropical troposphere, with a source strength of 2 MT/yr. Concentrations of long-lived atmospheric species are integrated forward in time using the iterative upstream scheme of Smolarkiewicz (1984). The scheme is positive definite with small implicit diffusion. The advective time step is 6 hours. The water vapor concentration is calculated for the stratosphere only. The tropospheric values of H_2O vary seasonally depending on the parameterized value of relative humidity and the assigned temperature.

Sulfate Aerosol Microphysics

Sulfate aerosol concentrations and surface area can be calculated by the AER sulfate aerosol microphysics model. This model is built on the same framework as the 2-D CTM but operates as a separate model, interacting with the CTM by use of off-line ozone and OH fields. Gas phase species included in the sulfate model are CS_2, H_2S, DMS, MSA, OCS, SO_2, SO_3, and H_2SO_4. Particles are resolved into 40 size bins ranging from 0.39 nm to 3.2 mm in radius by volume doubling. Each aerosol size bin is transported separately, with the appropriate sedimentation rate applied. New nanometer-sized sulfate particles are formed by homogeneous nucleation of H_2SO_4 and H_2O in the tropopause and polar regions and grow to micron-sized particles by condensation of H_2SO_4 and H_2O vapor in the lower stratosphere. The aerosols interact through coagulation, which decreases aerosol number density while conserving volume. Sulfate particles which are transported above 35 km experience evaporation and release H_2SO_4 vapor, which may dissociate into SO_3 and SO_2. Tropospheric washout applies to aerosol particles, MSA, SO_2, and H_2SO_4. Sulfate surface area density fields calculated by the sulfate model can be used in the CTM to calculate rates of heterogeneous reactions which determine ozone concentration. For M&M II exercises, sulfate surface area density was specified and therefore not calculated.

References Cited

Anderson, D.E., Jr., and S.A. Lloyd, Polar twilight UV-visible radiation field: Perturbations due to multiple scattering, ozone depletion, stratospheric clouds, and surface albedo, *J. Geophys. Res., 95*, 7429-7434, 1990.

Dahlback, A., and K. Stamnes, A new spherical model for computing the radiation field available for photolysis and heating at twilight, *Planet. Space Sci., 39*, 671-683, 1991.

Dopplick, T.G., Radiative heating of the global atmosphere: Corrigendum, *J. Atmos. Sci., 36*, 1812-1817, 1979.

Garcia, R.R., and S. Solomon, The effect of breaking gravity waves on the dynamics and chemical composition of the mesosphere and lower thermosphere, *J. Geophys. Res., 90*, 3850, 1985.

Hanson, D.R., A.R. Ravishankara, and S. Solomon, Heterogeneous reactions in sulfuric acid aerosols: A framework for model calculations, *J. Geophys. Res., 99*, 3615-3629, 1994.

Hanson, D.R., and A.R. Ravishankara, Heterogeneous chemistry of bromine species in sulfuric acid uner stratospheric conditions, *Geophys. Res. Lett., 22*, 385-388, 1995.

Hanson, D.R., A.R. Ravishankara, and E.R. Lovejoy, Reactions of $BrONO_2$ with H_2O on submicron sulfuric acid aerosol and the implications for the lower stratosphere, *J. Geophys. Res., 101*, 9063-9069, 1996.

Kalnay, E., et al., The NCEP/NCAR 40-year reanalysis project, *Bull. Am. Met. Soc., 77*, 437-471, 1996.

Kida, H. General circulation of air parcels and transport characteristics derived from a hemispheric GCM, Part 1, A determination of advective mass flow in the lower stratosphere, *J. Meteorol. Soc. Japan, 61*, 171-185, 1983.

Minschwaner, K., G.P. Anderson, L.A. Hall, and K. Yoshino, Polynomial coefficients for calculating O_2 Schumann-Runge cross sections at 0.5 cm^{-1} resoltuion, *Journal of Geophysical Research, 97*, 10,103-10,108, 1992.

Minschwaner, K., A.E. Dessler, J.W. Elkins, C.M.Volk, D.W. Fahey, M. Loewenstein, J.R. Podolske, A.E. Roche, and K.R. Chan, Bulk properties of isentropic mixing into the tropics in the lower stratosphere, *J. Geophys. Res., 101*, 9433-9439, 1996.

Murgatroyd, R.J., and F. Singleton, Possible meridional circulation in the stratosphere and mesosphere, *Quart. J. Roy. Meteor. Soc., 87*, 125-135, 1961.

NASA/JPL, Chemical kinetics and photochemical data for use in stratospheric modeling, Evaluation Number 12, *JPL Publication 97-4*, 1997.

Plumb, R.A., A "tropical pipe" model of stratospheric transport, *J. Geophys. Res., 101*, 3957-3972, 1996

Rosenfield, J.E., M.R. Schoeberl, and M.A. Geller, A computation of the stratospheric diabatic residual circulation using an accurate radiative transfer model, *J. Atmos. Sci., 44*, 859-876, 1987.

Schoeberl, M. R., et al., An estimation of the dynamical isolation of the tropical lower stratosphere using UARS wind and trace gas observations of the quasi-biennial oscillation, *Geophys. Res. Lett., 24*, pp. 53-56, 1997.

Shia, R.L., M.K.W. Ko, D.K. Weisenstein, C. Scott, and J. Rodriguez, Transport between the tropical and mid latitude lower stratosphere: Implications for ozone response to high-speed civil transport emissions, *J. Geophys. Res.*, **103**, 25435-25446, 1998.

Smolarkiewicz, P.K. A simple positive definite advection scheme with small implicit diffusion, *Mon. Weather Rev., 111*, 479-487, 1984.

Tung, K.K. Modeling of tracer transport in the middle atmosphere. In *Dynamics of the Middle Atmosphere*, J.R. Holton and T. Matsuno (eds.), pp. 412-444, Terra Scientific Publishing, Tokyo, Japan, 1984.

Volk, C.M., et al., Quantifying transport between the tropical and mid-latitude lower stratosphere, *Science, 272*, 1763-1768, 1996.

WMO/NASA, *The Stratosphere 1981: Theory and measurements*, WMO Global Ozone Monitoring Project Report No. 11, 1982.

References to AER 2-D Model Formulation

Ko, M.K.W., N.D. Sze, M. Livshits, M.B. McElroy, J.A. Pyle, The seasonal and latitudinal behavior of trace gases and O_3 as simulated by a two-dimensional model of the atmosphere, *J. Atmos. Sci., 41*, 2381-2408, 1984

Ko, M.K.W., K.K. Tung, D.K. Weisenstein, N.D. Sze, A zonal mean model of stratospheric tracer transport in isentropic co-ordinates: Numerical simulations for nitrous oxide and nitric acid, *J. Geophys. Res., 90*, 2313-2329, 1985

Ko, M.K.W., M.B. McElroy, D.K. Weisenstein, and N.D. Sze, Lightning: A possible source of stratospheric odd nitrogen, *J. Geophys. Res., 91*, 5395-5404, 1986.

Ko, M.K.W., N.D. Sze and D.K. Weisenstein, The roles of dynamical and chemical processes in determining the stratospheric concentration of ozone in one-dimensional and two-dimensional models, *J. Geophys. Res., 94*, 9889-9896, 1989.

Ko, M.K.W., N.D. Sze, and D.K. Weisenstein, Use of satellite data to constrain the model-calculated atmospheric lifetime for N_2O: Implications for other trace gases, *J. Geophys. Res., 96*, 7547-7552, 1991.

Kotamarthi, V.R., M.K.W. Ko, D.K. Weisenstein, J.M. Rodriguez, and N.D. Sze, The effect of lightning on the concentration of odd nitrogen species in the lower stratosphere: An update. *J. of Geophys. Res., 99*, 8167-8174, 1994.

Plumb, R.A. and M.K.W. Ko, Interrelationships between mixing ratios of long-lived stratospheric constituents, *J. Geophys. Res., 97*, 10,145-10,156, 1992.

Rodriguez, J.M., M.K.W. Ko, N.D. Sze, Role of heterogeneous conversion of N_2O_5 on sulphate aerosols in global ozone losses, *Nature, 352*, 134-137, 1991.

Rodriguez, J.M., M.K.W. Ko, N.D. Sze, C.W. Heisey, G.K. Yue, and M.P. McCormick, Ozone response to enhanced heterogeneous processing after the eruption of Mt. Pinatubo, *Geophys. Res. Lett., 21*, 209-212, 1994.

Shia, R.L., M.K.W. Ko, M. Zou, and V.R. Kotamarthi, Cross-tropopause transport of excess ^{14}C in a two-dimensional model, *J. Geophys. Res., 98*, 18,599-18,606, 1993.

Shia, R.-L., M. K. W. Ko, D. K. Weisenstein, C. Scott and J. Rodriguez, Transport between the tropical and mid-latitude lower stratosphere: Implications for ozone response to HSCT emissions, *J. Geophys. Res., 103*, 25,435-25,446, 19978

Weisenstein, D.K., M.K.W. Ko, J.M. Rodriguez, and N.D. Sze, Impact of heterogeneous chemistry on model-calculated ozone change due to high speed civil transport aircraft, *Geophys. Res. Letters, 18*, 1991-1994, 1991.

Weisenstein, D.K., M.K.W. Ko, N-D Sze, and J.M. Rodriguez, Potential impact of SO_2 emissions from stratospheric aircraft on ozone. *Geophys. Res. Lett., 23*, 161-164, 1996.

Weisentein, D.K., G.K. Yue, M.K.W. Ko, N.D. Sze, J.M. Rodriguez, and C.J. Scott, A two-dimensional model of sulfur species and aerosols, *J. Geophys. Res., 102*, 13,019-13035, 1997.

References to AER 2-D Model Applications

Danilin, M.Y., J.M. Rodriguez, M.K.W. Ko, D.K. Weisenstein, R.C. Brown, R.C. Miake-Iye, and M.R. Anderson, Aerosol particle evolution in an aircraft wake: implications for the HSCT fleet impact on ozone *J. Geophys. Res. 102*, 21,453-21,463, 1997.

Fahey et al. In situ observations of NOy, O_3, and the NOy/O_3 ratio in the lower stratosphere. *Geophys. Res. Lett., 23*, 1653-1656, 1996.

Fisher, D.A., C.H. Hales, D.L. Filkin, M.K.W. Ko, N.D. Sze, P.S. Connell, D.J. Wuebbles, I.S.A. Isaksen and F. Stordal, Model calculations of the relative effects of CFCs and their replacements on stratospheric ozone. *Nature, 344*, 508-512, 1990.

Gunson, M.R., M.C. Abrams, L.L. Lowes, E. Mahieu, R. Zander, C.P. Rinsland, M.K.W. Ko, N.D. Sze, and D.K. Weisenstein, Increase in levels of stratospheric chlorine and fluorine loading between 1985 and 1992. *Geophys. Res. Lett., 21*, 2,223-2,226, 1994.

Keim, E.R., M.Lowenstein, J.R. Podolske, D.W. Fahey, R.S. Gao, E.L. Woodbridge, R.C. Wamsley, S.G. Donnelly, L.A. Del Negro, C.D. Nevison, S. Solomon, K.H. Rosenslof, C.J. Scott, M.K.W. Ko, D.Weisensten, and K.R. Chen, Measurements of NOy-N_2O correlation in the lower stratopshere: latitudinal and seasonal changes and model comparisons, *J. Geophys. Res., 102*, 13,193-13,212, 1997.

Ko, M.K.W., J.M. Rodriguez, N.D. Sze, M.H. Profitt, W.L. Starr, A. Krueger, E. V. Browell, and M.P. McCormick, Implications of AAOE observations for proposed chemical explanations of the seasonal and interannual behavior of Antarctic ozone. *J. Geophys. Res., 94*, 16,705-16,715, 1989.

Ko, M.K.W., N-D. Sze, C. Scott, and D.K. Weisenstein, On the relation between stratospheric chlorine/bromine loading and short-lived tropospheric source gases, *J. Geophys. Res., 102*, 25507-25517, 1997.

Plumb, R. A., M.K.W. Ko, and R.L. Shia, Representation of localized aircraft NOy emissions in a two-dimensional model of stratospheric ozone. *J. Geophys. Res., 100*, 20,901-20,911, 1995.

Prather, M.J., M.M. Garcia, A.R. Douglass, C.H. Jackman, M.K.W. Ko, and N.D. Sze, The space shuttle's impact on the stratosphere. *J. Geophys. Res., 95*, 18,583-18,590, 1990.

Rinsland, C.P., J.S. Levine, A. Goldman, N.D. Sze, M.K.W. Ko, and D.W. Johnson, Infrared measurements of HF and HCl total column abundances above Kitt Peak, 1977-1990: Seasonal cycles, long-term increases, and comparisons with model calculations. *J. Geophys. Res., 96*, 15,523-15,540, 1991.

Rinsland, C.P., M.R. Gunson, M.C. Abrams, R. Znader, E. Mahieu, A. Goldman, M.K.W. Ko, J. M. Rodriguez, and N. D. Sze, Profiles of stratospheric chlorine nitrate ($ClONO_2$) from atmospheric trace molecule spectroscopy/ATLAS 1 infrared solar occultation spectra, *J. Geophys. Res., 99*, 18,895-18,900, 1994.

Rinsland, C.P., M.C. Abrams, L.L. Lowes, R. Zander, E. Mahieu, A. Goldman, M.K.W. Ko, J.M. Rodriguez, and N.D. Sze, Heterogeneous conversion of N_2O_5 to HNO_3 in the post-Mount Pinatubo eruption stratosphere, *J. Geophys. Res., 99*, 8213-8220, 1994.

Rinsland, C.P., M.R. Gunson, M.K.W. Ko, D.K. Weisenstein, R. Zander, M.C. Abrams, A. Goldman, N.D. Sze, and G.K. Yue, H_2SO_4 photolyis: A source of sulfur dioxide in the upper stratosphere. *Geophys. Res. Lett., 22*, 1109-1112, 1995.

Rodriguez, J.M., M.K.W. Ko, and N.D. Sze, Antarctic chlorine chemistry: Possible global implications, *Geophys. Res. Lett., 15*, 257-260, 1988.

Rodriguez, J.M., M.K.W. Ko, N.D. Sze, S.D.. Pierce, J.G. Anderson, D.W. Fahey, K. Kelly, C.B. Farmer, G.C. Toon, M.T. Coffey, L.E. Heidt, W.G. Mankin, K.R. Chan, W.L. Starr, J.F. Vedder, M.P. McCormick, Nitrogen and chlorine species in the spring Antarctic stratosphere: Comparison of models with AAOE observations. *J. Geophys. Res., 94*, 16,683-16,703, 1989.

Rodriguez, J.M., M.K.W. Ko, and N.D. Sze, Role of heterogeneous conversion of N_2O_5 on sulfate aerosols in global ozone losses. *Nature, 352*, 134-137, 1991.

Rodriguez, J.M., M.K.W. Ko, N.D. Sze, C.W. Heisey, G.K. Yue, and M.P. McCormick, Ozone response to enhanced heterogeneous processing after the eruption of Mt. Pinatubo, *Geophys. Res. Lett., 21*, 209-212, 1994.

Sze, N.D., M.K.W. Ko, D.K. Weisenstein, J.M. Rodriguez, R.S. Stolarski, and M.R. Schoeberl, Antarctic ozone hole: Possible implications for ozone trends in the southern hemisphere, *J. Geophys. Res., 94*, 11521-11528, 1989.

Weisenstein, D., M.K. Ko, and N.D. Sze, The chlorine budget of the present day atmosphere: A modeling study, *J. Geophys. Res., 97*, 2547-2559, 1992.

Weisenstein, D.K., M.K.W. Ko, J.M. Rodriguez, and N.D. Sze, Effects on stratospheric ozone from high speed civil transport: Sensitivity to stratospheric aerosol loading. *J. Geophys. Res., 98*, 23133-23140, 1993.

Weisenstein, D.K., M.K.W. Ko, N-D Sze,a nd J.M. Rodriguez, Potential impact of SO_2 emissions from stratospheric aircraft on ozone. *Geophys. Res. Lett., 23*, 161-164, 1996.

Weisenstein, D. K., M.K.W. Ko, I.G. Dyominov, G. Pitari, L. Ricciardulli, G. Visconti, and S. Bekki, The effect of sulfur emissions from HSCT aircraft: A 2-D model intercomparison, *J. Geophys. Res, 103, 1527-1547,* 1998.

Zander, R., C.P. Rinsland, E. Mahieu, M.R. Gunson, C.B. Farmer, M.C. Abrams, and M.K.W. Ko, Increase of carbonyl fluoride (COF_2) in the stratosphere and its contribution to the 1992 budget of inorganic fluorine in the upper stratosphere. *J. Geophys. Res.*, *99*, 16,737-16,743, 1994.

1.2.2 CSIRO 2-D Chemical-Transport Model, Version Number 94, October 1998

Peter Vohralik, Lakshman Randeniya, Ian Plumb, Keith Ryan
CSIRO Telecommunications and Industrial Physics
P.O. Box 218, Lindfield, NSW 2070, Australia
For more information contact Dr Keith Ryan at: Keith.Ryan@tip.csiro.au

General Information

The CSIRO 2-D model has been described briefly by Vohralik et al. (1998) and in more detail by Randeniya et al. (1997). An earlier version of the CSIRO 2-D model, which included a less rigorous treatment of the eddy diffusion terms K_{yy}, was described by Randeniya et al. (1996) and in the 1995 report on the Atmospheric Effects of Stratospheric Aircraft (Stolarski et al. (1995)). The improved treatment of the eddy diffusion terms leads to a good representation of the mixing between the tropics and midlatitudes, as reported by Vohralik et al. (1998). The current version of the CSIRO 2-D model, which is described in detail below, was used to obtain the results reported in the M&M II Technical Report (1999, ref?), the IPCC Special Report on Aviation and the Global Atmosphere (1999, ref?) the NASA High Speed Research Program report on the Atmospheric Effects of Stratospheric Aircraft (1999, ref?), and the WMO/UNEP 1998 Ozone Assessment (1999, ref?). The model domain extends from 90 S to 90 N in 5 degree steps and from the ground to 80 km with a vertical resolution of approximately 2 km (log pressure). Zonal mean diabatic circulation, together with appropriate diffusion terms, provide the model transport. The chemistry module is family based and employs full diurnal averaging methods.

Photodissociation

The solar radiation module in the CSIRO 2-D model includes fully interactive multiple scattering calculations and allowance for the curvature of the Earth. The method of Meier et al. (1982) is employed to account for the effects of multiple scattering, while the spherical atmosphere treatment uses ray-tracing techniques. The model uses 158 wavelengths from 175 to 850 nm, as defined by WMO (1986). Cross sections are from the JPL97 database (DeMore et al. (1997)).

Chemistry

The chemical module is family based, with a total of 67 species and 213 reactions. The species included in the model and the family definitions are as follows:

Fixed Species: N_2, O_2, CO_2

Transported families: Ox, NOy, Cly, Bry, where:

$Ox = O + O(^1D) + O_3$
$NOy = N + NO + NO_2 + NO_3 + HONO + HNO_3 + HNO_4 + 2 \times N_2O_5 + ClONO_2 + BrONO_2$
$Cly = Cl + 2 \times Cl_2 + ClO + ClO_2 + OClO + 2 \times Cl_2O_2 + HOCl + HCl + ClONO_2$
$Bry = Br + BrO + HOBr + HBr + BrONO_2$

Other transported species: N_2O, CH_4, CO, H_2O, H_2, $CFCl_3$, CF_2Cl_2, CFC_113, CFC_114, CFC_115, CCl_4, HCFC_22, CH_3CCl_3, CH_3Cl, CF_3Br, CF_2ClBr, CH_3Br, HF, CF_2O, CClFO

Equilibrium species not in transported families: H, OH, HO_2, H_2O_2, HCO, CH_2O, CH_3, CH_3O, CH_3O_2, CH_3OOH

Rate coefficients conform to the recommendations in JPL97.

The model includes the heterogeneous hydrolysis of N_2O_5, $ClONO_2$ and $BrONO_2$ with sulphuric acid aerosols, with the following reaction probabilities. A reaction probability of 0.1 is used for the hydrolysis of N_2O_5. For $ClONO_2$ the reaction probability is calculated using equation (4) of Hanson and Ravishankara (1991). A reaction probability of 0.8 is used for $BrONO_2$ hydrolysis. Other heterogeneous reactions, including those on polar stratospheric clouds, are not included in the version of the CSIRO 2-D model used to obtain the results reported in the M&M II Technical Report.

Zonal-mean temperatures (discussed further below) are used when calculating reaction rates.

The mixing ratios of N_2, O_2 and CO_2 are held fixed throughout the model atmosphere, and their concentrations are determined from the hydrostatic equation. The concentrations of N_2O, CO, H_2, CH_3Cl, CCl_4, CH_3Br, the halons, the chlorofluorocarbons and the hydrochlorofluorocarbons are all set at the ground at values appropriate to the particular calculation. Tropospheric H_2O is set to values determined by the Oort (1983) climatology where available and SAGE-II from Prather and Remsberg (1992) otherwise. The stratospheric concentrations of H_2O are calculated by setting the volume mixing ratio at the tropopause to $3x10^{-6}$ and then allowing the concentration to vary in the stratosphere as a result of chemistry and transport. The model also includes an upper tropospheric source of NOy between 30 S and 30 N from 4 to 12 km, and between 25 S and 25 N from 12 to 14 km. The NOy source strength used is 1100 cm^{-3} s^{-1}, corresponding to a total source of approximately 2 Tg N y^{-1}.

Production and loss terms for the long-lived species are updated every 10 days. This is done by first carrying out a full diurnal integration to establish the 24-hour behaviour of all of the species. The diurnal coefficients derived from this integration are then multiplied by noon rate coefficients to obtain diurnally-averaged reaction rate coefficients. These are used in a constrained equilibrium calculation to determine the diurnal-average concentrations of species in the Ox, NOy, Cly and Bry families, together with those of the equilibrium species not included in transported families. During the constrained equilibrium calculation the family total concentrations are held constant.

Rainout and Surface Deposition

Rainout rates are included for transported family totals NOy, Cly and Bry and for H_2O_2, CH_2O, CH_3OOH, HF, CClFO and CF_2O for model grid cells below 10 km which are also more than 3 km below the tropopause. Rainout rates for individual members of NOy, Cly and Bry are not explicitly included when partitioning these family totals. Rainout rates for model levels at z = 1, 3, 5, 7 and 9 km are $3.74x10^{-6}$, $3.98x10^{-6}$, $2.96x10^{-6}$, $1.38x10^{-6}$ and $0.42x10^{-6}$ s^{-1} respectively. In addition to these rainout processes, the following surface deposition rates are included: $6.7x10^{-6}$ s^{-1} for NOy, OH, HO_2, H_2O_2, HCO, CH_3 and $3.3x10^{-8}$ s^{-1} for CH_2O. (Surface deposition is not applied to Ox, Cly, Bry, H_2 and CO as these species are held fixed at the ground by the model.)

Dynamics

The transport in the CSIRO 2-D model is derived diagnostically, using observed temperatures and ozone mixing ratio profiles. Temperatures from the ground to 60 km are 8-year zonal and monthly mean National Meteorological Center (NMC) values obtained from the 1992 Models and Measurements

database (Prather and Remsberg (1993)). From 60 to 80 km, temperatures are from the Middle Atmosphere Program database (Barnett and Corney (1995)). Radiative heating rates from the ground to 60 km are as calculated by Rosenfield and obtained from the 1992 Models and Measurements database. Above 60 km, because of the breakdown of local thermodynamic equilibrium assumptions, cooling rates are calculated using a Newtonian cooling approximation with Newtonian cooling coefficients from Holton and Wehrbein (1980), and heating rates are calculated using parameterisations developed by Strobel (1978) and Schoeberl and Strobel (1978). Because there are inevitable discontinuities in both temperatures and heating rates at 60 km, values for both of these quantities are joined smoothly over a transition region which extends from 60 to 70 km by linear interpolation between the data sets over this region. Numerical experiments have shown that the ozone column is quite insensitive to details of this matching procedure, as is to be expected since there is little mass transport at altitudes greater than 60 km. In the troposphere, latent and sensible heating rates are added to the radiative heating rates to obtain net heating rates. Sensible and latent heating rates are obtained from Dopplick (1974).

Residual mean vertical velocities are calculated from the transformed Eulerian mean (TEM) energy conservation equation (including the dT/dt term), by first assuming zero meridional velocities. Meridional velocities are then derived from the continuity equation, and these meridional velocities are used to obtain improved estimates of vertical velocities, as described by Solomon et al. (1986). This process is repeated until a self-consistent set of residual circulation velocities is obtained.

The Eliassen-Palm flux divergence required for the calculation of horizontal eddy diffusion coefficients Kyy is evaluated from the left-hand side of the TEM zonal momentum equation. Zonal winds are calculated from the temperatures using gradient wind balance. Because of the breakdown of the geostrophic approximation in the tropics, zonal winds at latitudes less than 15 degrees latitude are calculated from the curvature expression. Stratospheric K_{yy} values are calculated diagnostically as the ratio of the EP flux divergence to the meridional gradient of potential vorticity, where the E ux divergence is obtained by evaluating the left-hand side of the TEM zonal momentum equation. Where calculated values fall outside the range $1x10^4 < K_{yy} < 3x10^6$ m^2 s^{-1}, they are reset to these limiting values; K_{yy} values are also set to the lower limit where zonal winds are easterly, in line with current understanding of planetary wave propagation. Tropospheric K_{yy} values are set to $1x10^6$ m^2 s^{-1} to simulate rapid convective mixing. Values of K_{yz} are obtained by projecting the K_{yy} from isentropic surfaces to pressure surfaces. The CSIRO model uses an annually averaged zonal mean tropopause height distribution obtained by averaging daily NMC tropopause data for the period 1983-1993. K_{zz} values are set to 4 m^2 s^{-1} in the troposphere, 0.25 m^2 s^{-1} between 21 and 42 km and 0.1 m^2 s^{-1} throughout the remainder of the stratosphere. Off-diagonal components of the diffusion tensor are included by assuming that diffusion occurs predominantly along isentropes.

Advection in the model uses the variable-order Bott (1989) scheme. This method, which is a high-order implementation of the upwind scheme, is conservative and positive definite and produces only small numerical diffusion. Tests in this laboratory and elsewhere (Strand and Hov (1993)) have shown that the Bott scheme compares favourably with other modern advection algorithms in terms of both accuracy and computational efficiency. The calculations reported here used a second-order Bott scheme with a 6-hour time step. For a given model run, vertical velocities are calculated for each of the 12 months of the year at the beginning of the run and stored in a three-dimensional array. Vertical velocities and temperatures are obtained at 10-day intervals by interpolation of the monthly values. Horizontal velocities are then computed from the vertical velocities using continuity. Small mass conservation correction factors are derived to correct for departures from mass conservation (< 1%) due to the process-splitting algorithm used to integrate the continuity equation. Eddy diffusion coefficients K_{yy} are derived self-consistently with the residual circulation as described above. This procedure is repeated at each transport time step.

References

Barnett, J.J., and M. Corney, A middle atmosphere temperature reference model from satellite measurements, Adv. Space Res., 5, 125-134, 1985.

Bott, A., A positive definite advection scheme obtained by nonlinear renormalization of the advective fluxes, Mon. Weather Rev., 117, 1006-1015, 1989.

DeMoore et al., Chemical kinetics and photochemical data for use in stratospheric modeling, JPL Publication 97-4, 1997.

Dopplick, T.G., The heat budget, in "The General Circulation of the Tropical Atmosphere", vol. 2, edited by R.E. Newell et al., pp. 27-94, MIT Press, Cambridge, Mass., 1974.

Hanson D.R., and A.R. Raviskankara, The reaction probabilities of $ClONO_2$ and N_2O_5 on 40 to 75% sulfuric acid solutions, J. Geophys. Res., 96, 17307-17314, 1991.

Hanson D.R. et al., Reaction of $BrONO_2$ with H_2O on submicron sulfuric acid aerosol and the implications for the lower stratosphere, J. Geophys. Res., 101, 9063-9070, 1996.

Holton, J.R. and W.M. Wehrbein, A numerical model of the zonal mean circulation of the middle atmosphere, Pure Appl. Geophys., 118, 284-306, 1980.

Meier, et al., Radiation field in the troposphere and stratosphere from 240-1000 nm, I, General analysis, Planet. Space Sci., 30, 923-933, 1982.

Oort, Global Atmospheric Circulation Statistics, 1958-1973, NOAA NOAA Prof. Pap. 14, U.S. Dep. of Commer., Rockville, Md., 1983.

Prather, M., and E.E. Remsberg (Eds.), The atmospheric effects of stratospheric aircraft: Report of the 1992 models and measurements workshop, Nasa Ref. Publ. 1292, 1993.

Randeniya, L.K., P.F. Vohralik, I.C. Plumb, and K.R. Ryan, Impact of the heterogeneous hydrolysis of $BrONO_2$ on calculated ozone changes due to HSCT aircraft and increased sulphate aerosol levels, Geophys. Res. Lett., 23, 343-346, 1996.

Randeniya, L.K., P.F. Vohralik, I.C. Plumb, and K.R. Ryan, Heterogeneous $BrONO_2$ hydrolysis: effect on NO_2 columns and ozone at high latitudes in summer, J. Geophys. Res., in press, 1997.

Solomon, S., J.T. Kiehl, R.R. Garcia, and W. Grose, Tracer transport by the diabatic circulation deduced from satellite observations, J. Atmos. Sci., 43, 1603-1617, 1986.

Stolarski, R.S. et al., 1995 Scientific assessment of the atmospheric effects of stratospheric aircraft, Nasa Ref. Publ. 1381, 1995.

Strand, A., and O. Hov, A two-dimensional zonally averaged transport model including convective motions and a new strategy for the numerical solution, J. Geophys. Res., 98, 9023-9037, 1993.

Strobel, D.F., Parameterization of the atmospheric heating rate from 15 to 120 km due to O_2 and O_3 absorption of solar radiation, J. Geophys. Res., 83, 6225-6230, 1978.

Schoeberl, M.R. and D.F. Strobel, The zonally averaged circulation of the middle atmosphere, J. Atmos. Sci., 35, 577-591, 1978.

Vohralik, P.F., L.K. Randeniya, I.C. Plumb, and K.R. Ryan, Use of correlations between long-lived atmospheric species in assessment studies, J. Geophys. Res., 103, 3611-3627, 1998.

WMO, Atmospheric Ozone 1985, WMO Report No. 16, 1986.

1.2.3 GSFC 2D Model Description

Charles H. Jackman
Code 916
NASA/GSFC
Greenbelt, MD 20771
E-mail: jackman@assess.gsfc.nasa.gov
TEL: (301) 614-6053
FAX: (301) 614-5903

David B. Considine
same address and FAX as above
E-mail: dbc@welkin.gsfc.nasa.gov
TEL: (301) 614-5992

Eric L. Fleming
same address and FAX as above
E-mail: fleming@welkin.gsfc.nasa.gov
TEL: (301) 614-5983

General Information

Much information about the model used in these Models and Measurements II model experiments is discussed in Jackman et al. [1996].

Domain and Grid Sizes

Latitude - From 85S to 85N with 10 °g latitude bands (85S,75S,...75N,85N)

Altitude - From the ground to 0.0024 hPa - Equally spaced in log pressure - Approximately a 2 km spacing

Circulation and Diffusion

A meridional stream function is calculated to obtain the transformed Eulerian circulation. The coefficients of the elliptic stream function equation depend on the zonal mean temperature and zonal wind, which are based on the 17-year average (1979-95) of temperature data from the National Centers for Environmental Prediction (NCEP) for 1000^{-1} mbar, and the CIRA [1986] empirical reference model for the mesosphere above 1 mbar. Zonal wind is derived from temperature using the gradient wind relation. Forcing of the stream function is proportional to the vertical gradient of the mechanical forcing from planetary waves, gravity waves, and equatorial Kelvin waves and the latitudinal gradient of the total heating rate. We have computed diabatic heating rates following Rosenfield et al. [1994] utilizing climatological distributions of temperature, ozone, and water vapor. The climatological latent heating rate distribution is adapted from Newell et al. [1974]. Forcing from plantary waves is proportional to the Eliassen-Palm (E-P) flux divergence, which we have computed offline from the 17-year NCEP three-dimensional analyses for 1000^{-1} mbar and from the CIRA [1986] planetary wave climatology for the mesosphere above 1 mbar.

Latitudinal eddy diffusion (K_{yy}) is obtained self-consistently as the ratio of the E-P flux divergence to the latitudinal gradient of zonal mean potential vorticity. The parameterization of Holton and Zhu [1984] is used to obtain the distributions of vertical eddy diffusion (K_{zz}) and mechanical forcing from the gravity waves. The empirical zonal mean temperature and zonal wind fields are used to compute the latitudinal, seasonal, and vertical distributions of gravity wave drag and diffusion based on a given set of gravity wave parameters. The equatorial semiannual oscillation (SAO) is approximated using the methodology of Gray and Pyle [1987] along with the empirical zonal mean wind field to diagnose the mechanical forcing from thermally damped equatorial Kelvin waves.

Among the features of source gases simulated in the model are the sharp gradients between the tropics and subtropics, a relatively weak gradient between the subtropics and mid-latitudes, and a strong descent in the late winter polar vortex with large horizonal gradients across the vortex edge near about 60 deg.

Transport Scheme

The numerical advection scheme is based on Lin and Rood [1996] and utilizes the piecewise parabolic method (PPM). The PPM is highly accurate and is capable of preserving sharp tracer gradients.

Time Steps

The species continuity equations are solved by operator splitting; that is, by assuming that the continuity equation may be factored into a product of difference operators [McRae et al., 1982]. First the advection field is applied to the constituent distributions; second the vertical eddy diffusion (K_{zz}); third the horizontal eddy diffusion (K_{yy}); and fourth the chemistry operators are implemented. The time steps vary for each operator such that the advection field is applied with a 1/2 day step, the K_{zz} with a 1/8 day step, and the K_{yy} and chemistry both with a 1 day step.

Photochemistry

All photochemical reaction rates are updated at 1 day intervals and the rates are all taken from JPL 97-4 [DeMore et al. 1997].

Heterogeneous Chemistry on Sulfate Aerosols and PSCs

The following reactions on aerosol particles are included in the model:

1. $ClONO_2 + HCl \rightarrow HNO_3 + Cl_2$
2. $ClONO_2 + H_2O \rightarrow HNO_3 + HOCl$
3. $N_2O_5 + H_2O \rightarrow 2HNO_3$
4. $HOCl + HCl \rightarrow Cl2 + H_2O$
5. $BrONO_2 + H_2O \rightarrow HNO_3 + HOBr$
6. $HOBr + HCl \rightarrow BrCl + H_2O$

Heterogeneous reaction rates are calculated as first-order loss rates for $ClONO_2$, N_2O_5, HOCl, $BrONO_2$, and HOBr using the formula:

$k=\gamma vA/4$,

where γ is a "sticking coefficient" which can be interpreted as the probability of uptake to the aerosol and subsequent reaction, v is the thermal velocity of the gas phase molecule, and A is the surface area density of the aerosol particles.

On sulfate aerosols, the sticking coefficients for reactions 1 and 2 are calculated using the methodology of Hanson and Ravishankara [1994]. The sticking coefficient for reaction 3 is set to 0.1. The sticking coefficient for reaction 4 is calculated as in Hanson et al. [1994]. The sticking coefficients for reactions 5 and 6 are 0.8 and 0.2 respectively, as in DeMore et al., [1997].

The above reactions are also included on the surfaces of Type 1 (nitric acid trihydrate) and Type 2 (water ice) PSCs. The rates for these reactions are as specified in DeMore et al., [1997].

Polar Stratospheric Clouds

Polar stratospheric clouds (PSCs) are included using the methodology explained in Considine et al. [1994]. Both Type 1 and Type 2 PSCs are simulated. Type 1 PSCs are assumed to be composed of nitric acid tryhydrate and Type 2 PSCs are assumed to be water ice. The amount of HNO_3 and H_2O condensed into PSCs in each gridbox is calculated using saturation vapor pressure measurements of HNO_3 over HNO_3-$3H_2O$ made by Hanson and Mauersberger [1988] and saturation vapor pressure measurements of H_2O over H_2O-ice made by Marti and Mauersberger [1991]. Supersaturation ratios of 10 and 1.4 are requred before Type 1 and Type 2 PSCs form, resulting in a reduction in PSC nucleation temperatures of approximately 3K and 2K for Type 1 and Type 2 PSCs, respectively [Peter et al., 1991]. Integrals over climatological temperature probability distributions are used to account for variations of temperature away from the zonal mean values in the calculation of condensed phase HNO_3 and H_2O. The temperature distributions are monthly climatologies of temperature variation taken from 14 years (1979 - 1992) of NCEP temperature data, and vary with latitude, pressure, and month of year. Particle size distributions are assumed for both Type 1 and 2 PSCs. Type 1 PSCs are assumed to follow a log-normal distribution with a mode radius of 1 micron and a standard deviation of 1.8. Type 1 PSCs are assumed to follow a lognormal distribution with a mode radius of 10 microns and a standard deviation of 1.8. Sedimentation of Type 1 and Type 2 PSCs is included, with sedimentation velocities calculated according to Kasten [1968].

Treatment of Solar Radiance and Photodissociation

A look-up table is used for the photolytic source term (PST) and photolysis of O_2 [$J(O_2)$]. This table was developed by D. Anderson and coworkers at the Johns Hopkins University Applied Physics Laboratory [Anderson and Lloyd, 1990]. The PST and $J(O_2)$ table is a function of wavelength, solar zenith angle, and column ozone and is given on the pressure grid of the GSFC 2D model. The PST is computed for the particular wavelength, solar zenith angle, column ozone, and pressure of interest and is multiplied by the solar irradiance at the top of the model to compute the reduced (or enhanced) flux at the point of interest. The reduced (or enhanced) flux is then used with the photodissociation cross section for a particular constituent to derive the photolysis rate of interest.

Family Chemistry and Transported Constituents or Families

Well-known family chemistry approximations are used to reduce the number of transported species in the model. Thirty-one chemical species or families are currently transported in our model simulations. These include Ox (O_3, $O[^1D]$, $O[^3P]$), NOz (N, NO, NO_2, NO_3, HO_2NO_2), N_2O_5, $ClONO_2$, HNO_3, Clz (Cl, ClO, HOCl, HCl), Bry (Br, BrO, HBr, $BrONO_2$, HOBr), N_2O, CH_4, H_2O, CO_2, H_2,

CO, CH_3OOH, $CFCl_3$, CF_2Cl_2, CH_3Cl, CCl_4, CH_3CCl_3, CH_3Br, $CHClF_2$, $C_2Cl_3F_3$, $C_2Cl_2F_4$, C_2ClF_5, $CBrClF_2$, $CBrF_3$, HF, CClFO, CF_2O, solid HNO_3, and solid H_2O. The HOx (H, OH, HO_2) species, H_2O_2, and the hydrocarbons CH_3, CH_3O, CH_3O_2, CH_2O, and CHO are calculated using photochemical equilibrium assumptions.

Nighttime Chemistry

Some constituents that vary significantly over the diurnal time period are treated with a special nighttime calculation. The nighttime calculation is applied to constituents N_2O_5, $ClONO_2$, ClO, BrO, and $BrONO_2$, utilizing 24 time steps during each night. This methodology is explained further in Douglass et al. [1989].

References

Anderson, D. E., Jr., and S. A. Lloyd, Polar twilight UV-visible radiation field: Perturbations due to multiple scattering, ozone depletion, stratospheric clouds, and surface albedo, J. Geophys. Res., 95, 7429-7434, 1990.

Considine, D. B., A. R. Douglass, and C. H. Jackman, Effects of a polar stratospheric cloud parameterization on ozone depletion due to stratospheric aircraft in a two-dimensional model, J. Geophys. Res., 99, 18,879-18,894, 1994.

DeMore, W. B., S. P. Sander, D. M. Golden, R. F. Hampson, M. J. Kurylo, C. J. Howard, A. R. Ravishankara, C. E. Kolb, and M. J. Molina, Chemical kinetics and photochemical data for use in stratospheric modeling, Evaluation number 12, JPL Publication 97-4, Jet Propulsion Laboratory, NASA, January 15, 1997.

Douglass, A. R., C. H. Jackman, and R. S. Stolarski, Comparison of model results transporting the odd nitrogen family with results transporting separate odd nitrogen species, J. Geophys. Res., 94, 9862-9872, 1989.

Gray, L. J., and J. A. Pyle, Two-dimensional model studies of equatorial dynamics and tracer distributions, Q. J. R. Meteorol. Soc., 113, 635-651, 1987.

Hanson, D., and K. Mauersberger, Laboratory studies of the nitric acid trihydrate: Implications for the south polar stratosphere, Geophys. Res. Lett., 15, 855-858, 1988.

Hanson, D. R., and A. R. Ravishankara, Reactive uptake of $ClONO_2$ onto sulfuric acid due to reaction with HCl and H2O, J. Phys. Chem., 98, 5728-5735, 1994.

Hanson, D. R., A. R. Ravishankara, and S. Solomon, Heterogeneous reactions in sulfuric acid aerosols: A framework for model calculations, J. Geophys. Res., 99, 3615-3629, 1994.

Holton, J. R., and X. Zhu, A further study of gravity wave induced drag and diffusion in the mesosphere, J. Atmos. Sci., 41, 2653-2662, 1984.

Jackman, C. H., E. L. Fleming, S. Chandra, D. B. Considine, and J. E. Rosenfield, Past, present, and future modeled ozone trends with comparisons to observed trends, J. Geophys. Res., 101, 28,753-28,767, 1996.

Kasten, F., Falling speed of aerosol particles, J. Appl. Meteorol., 7, 944-947, 1968.

Lin, S.-J., and R. B. Rood, Multidimentional flux-form semi-Lagrangian transport schemes, Mon. Weather Rev., 124, 2046-2070, 1996.

McRae, G. J., W. R. Goodin, and J. H. Seinfeld, Numerial solution of the atmospheric diffusion equation for chemially reacting flows, J. Comput. Phys., 45, 1-42, 1982.

Newell, R. E., J. W. Kidson, D. G. Vincent, and G. J. Boer, The General Circulations of the Tropical Atmosphere, vol. 2, chap. 7, MIT Press, Cambridge, Mass., 1974.

Peter, Th., C. Bruhl, and P.J. Crutzen, Increase in the PSC-Formation Probability Caused by High-Flying Aircraft, Geophys. Res. Lett., 18, 1465-1468, 1991.

Rosenfield, J. E., P. A. Newman, and M. R. Schoeberl, Computations of diabatic descent in the stratospheric polar vortex, J. Geophys. Res., 99, 16,677-16,689, 1994.

1.2.4 GSFC-INT 2D Model Description

Joan E. Rosenfield, David B. Considine, Julio T. Bacmeister

Code 916
NASA/GSFC
Greenbelt, MD 20771
E-mail: rose@euterpe.gsfc.nasa.gov
TEL: (301) 614-5986
FAX: (301) 614-5903

General Information

The model consists of three separate modules - chemistry (including the photolysis rate calculation), radiation (which computes the heating and cooling rates), and dynamics. The dynamics uses heating rates computed in the radiation module. The dynamics computes temperatures, residual circulation, and diffusion coefficients which are used in the chemistry module. The radiation uses the temperatures from the dynamics code and the ozone and water vapor from the chemistry module. References describing the model and its applications are Rosenfield et al. [1997], Rosenfield et al. [1998a], and Rosenfield and Douglass [1998b].

Domain and Grid Sizes

Chemistry Module:
Latitude - From 85S to 85N with 10 deg latitude bands (85S,75S,...75N,85N)
Altitude - From the ground to 0.0024 hPa - Equally spaced in log pressure - Approximately a 2 km spacing

Dynamics Module:
Latitude - From 85.1S to 85.1N with 4.86 deg latitude bands
Altitude - From 2.66 km to 106.4 km, at a resolution of 2.66 km

Radiation Module:
Latitude - Same as dynamics module
Altitude - 45 levels from the ground to 0.0018 hPa - equally spaced in ln p, approximately a 2 km spacing

Circulation and Temperature

The dynamics model is similar to that described in Bacmeister et al. [1995]. The residual circulation is driven by radiative heating and cooling rates which are calculated with the model predicted temperatures, ozone, and water vapor, using the parameterizations discussed in Rosenfield et al. [1994]. Latitudinally dependent effective tropospheric cloud heights and amounts are specified [Rosenfield et al.,1997] in such a way that the outgoing longwave flux agrees with satellite observations.

The linear model of planetary wave drag and horizontal diffusion is as described in Bacmeister et al. [1995]. A new parameterization of gravity wave drag and vertical mixing [Summers et al., 1997] is

included. To obtain simulations that are valid in the tropics, both zonally averaged momentum and potential temperature are advected by the meridional residual circulation.

Time Steps and Transport Scheme

In the chemistry module, the numerical advection scheme is based on Lin and Rood [1996] and utilizes the piecewise parabolic method (PPM). The PPM is highly accurate and is capable of preserving sharp tracer gradients. The species continuity equations are solved by operator splitting; that is, by assuming that the continuity equation may be factored into a product of difference operators [McRae et al., 1982]. First the advection field is applied to the constituent distributions; second the vertical eddy diffusion (K_{zz}); third the horizontal eddy diffusion (K_{yy}); and fourth the chemistry operators are implemented. The time steps vary for each operator such that the advection field is applied with a 1/2 day step, the K_{zz} with a 1/8 day step, and the K_{yy} and chemistry both with a 1 day step.

In the dynamics module, the numerical advection scheme is that of Prather [1986], modified for atmospheres with exponentially decreasing density by Shia et al. [1990]. The heating rates are updated once a day, while the dynamics calculation is done every two hours.

Photochemistry

Well-known family chemistry approximations are used to reduce the number of transported species in the model. Thirty-one chemical species or families are currently transported in our model simulations. These include Ox (O_3, $O[^1D]$, $O[^3P]$), NOz (N, NO, NO_2, NO_3, HO_2NO_2), N_2O_5, $ClONO_2$, HNO_3, Clz (Cl, ClO, HOCl, HCl), Bry (Br, BrO, HBr, $BrONO_2$, HOBr), N_2O, CH_4, H_2O, CO_2, H_2, CO, CH_3OOH, $CFCl_3$, CF_2Cl_2, CH_3Cl, CCl_4, CH_3CCl_3, CH_3Br, $CHClF_2$, $C_2Cl_3F_3$, $C_2Cl_2F_4$, C_2ClF_5, $CBrClF_2$, $CBrF_3$, HF, CClFO, CF_2O, solid HNO_3, and solid H_2O. The HOx (H, OH, HO_2) species, H_2O_2, and the hydrocarbons CH_3, CH_3O, CH_3O_2, CH_2O, and CHO are calculated using photochemical equilibrium assumptions.

Some constituents that vary significantly over the diurnal time period are treated with a special nighttime calculation. The nighttime calculation is applied to constituents N_2O_5, $ClONO_2$, ClO, BrO, and $BrONO_2$, utilizing 24 time steps during each night. This methodology is explained further in Douglass et al. [1989].

All photochemical reaction rates are updated at 1 day intervals and the rates are all taken from JPL 94-26 [DeMore et al. 1994]. The photolysis rate is calculated at 39 wavelengths between 1215 and 7300 nm. The mean intensity, or photolytic source term, is the sum of the attenuated direct beam and the diffuse beam. The attenuation of the direct beam is calculated by using spherical geometry, while the diffuse beam is calculated with plane parallel geometry only. We use the two-stream Eddington approximation multiple-scattering algorithm described by Toon et al. [1989], together with the delta scalings of Joseph et al. [1976] to treat the anisotropic scattering associated with aerosols. The photolysis computations use the model generated ozone.

Heterogeneous Chemistry

The heterogeneous chemistry parameterizations are the same as those used in the GSFC 2D fixed transport model.

References

Bacmeister, J. T., M. R. Schoeberl, M. E. Summers, J. E. Rosenfield, and X. Zhu, Descent of long-lived trace gases in the winter polar vortex, J. Geophys. Res., 100, 11,669-11,684, 1995.

DeMore, W. B., et al., Chemical kinetics and photochemical data for use in stratospheric modeling, Evaluation number 11, JPL Publication 94-26, Jet Propulsion Laboratory, NASA, 1994.

Douglass, A. R., C. H. Jackman, and R. S. Stolarski, Comparison of model results transporting the odd nitrogen family with results transporting separate odd nitrogen species, J. Geophys. Res., 94, 9862-9872, 1989.

Jackman, C. H., E. L. Fleming, S. Chandra, D. B. Considine, and J. E. Rosenfield, Past, present, and future modeled ozone trends with comparisons to observed trends, J. Geophys. Res., 101, 28,753-28,767, 1996.]

Joseph, J. H., W. J. Wiscombe, and J. A. Weinman, The delta-Eddington approximation for radiative flux transfer, J. Atmos. Sci., 33, 2452-2459, 1976.

Lin, S.-J., and R. B. Rood, Multidimentional flux-form semi-Lagrangian transport schemes, Mon. Weather Rev., 124, 2046-2070, 1996.

McRae, G. J., W. R. Goodin, and J. H. Seinfeld, Numerial solution of the atmospheric diffusion equation for chemially reacting flows, J. Comput. Phys., 45, 1-42, 1982.

Prather, M. J., Numerical advection by conservation of second-order moments, J. Geophys. Res., 91, 6671-6681, 1986.

Rosenfield, J. E., P. A. Newman, and M. R. Schoeberl, Computations of diabatic descent in the stratospheric polar vortex, J. Geophys. Res., 99, 16,677-16,689, 1994.

Rosenfield, J. E., D. B. Considine, P. A. Meade, J. T. Bacmeister, C. H. Jackman, and M. R. Schoeberl, Stratospheric effects of Mount Pinatubo aerosol studied with a coupled two-dimensional model, J. Geophys. Res., 102, 3649-3670, 1997.

Rosenfield, J. E., D. B. Considine, M. R. Schoeberl, and E. V. Browell, The impact of subvisible cirrus clouds near the tropical tropopause on stratospheric water vapor, Geophys. Res. Lett., 25, 1883-1886, 1998a.

Rosenfield, J. E., and A. R. Douglass, Doubled CO2 effects on NOy in a coupled 2D model, Geophys. Res. Lett., 1998b, in press.

Shia, R. L., Y. L. Ha, J. S. Wen, and Y. L. Yung, Two-dimensional transport and chemistry model: Numerical experiments with a new advection algorithm, J. Geophys. Res., 95, 7467-7483, 1990.

Summers, M. E., D. E. Siskind, J. T. Bacmeister, and R. R. Conway, Seasonal variation of middle atmosphere CH4 and H2O with a new chemical-dynamical model, J. Geophys. Res., 102, 3503-3526, 1997.

Toon, O. B., C. P. McKay, T. P. Ackerman, and K. Santhanam, Rapid calculation of radiative heating rates and photodissociation rates in inhomogeneous multiple scattering atmospheres, J. Geophys. Res., 94, 16,287-16,301, 1989.

1.2.5 HARVARD 2D Model Description

Hans R. Schneider
Center for Earth & Planetary Physics
Pierce Hall
Harvard University
29 Oxford St.
Cambridge, MA 02138-2901
E-mail: hrs@io.harvard.edu
TEL: (617) 495-0810
FAX: (617) 495-4551

Dylan B. A. Jones
same address and FAX as above
E-mail: dbj@io.harvard.edu
TEL: (301) 286-4299

Larissa Kogan
same address and FAX as above
E-mail: lar@io.harvard.edu
TEL: (301) 286-3923

General Information

The model is an interactive 2-D residual circulation model. Circulation and temperatures are calculated using heating rates derived from model temperatures and model ozone. Eddy diffusion coefficients, K_{yy}, are externally specified. The residual circulation calculated by the dynamics module is consistent with the diffusive tracer transport.

Details and first applications of the model are described in forthcoming papers.

Domain and Grid Sizes

Latitude - Pole to pole with a resolution of 5 degrees. A staggered grid is used for the dynamics module, the latitudes of the chemistry/transport grid are -87.5S, -82.5S, ..., 82.5N, 87.5N.

Altitude - Equally spaced in log pressure, z*, from the ground to z* = 81km. Level spacing is dz*=2.0 km. The first chemistry level is at z* = 1 km, i.e. the center of the lowest grid box. Dynamical quantities are staggered in height.

Circulation and Diffusion

The model residual mean meridional circulation and temperatures are calculated using a primitive equation dynamics module (Schneider and Geller, 1985). Heating rates are calculated with a full radiative transfer scheme (an updated version of Shi, 1981) using model temperatures and model ozone as well as CO_2. The calculated heating rates are not used in the troposphere. There, they are replaced by a heating rate parameterization adopted from Cunnold et al. (1975) with some modifications to account for asymmetries between the Northern and Southern hemisphere.

The transition from calculated to parameterized heating rates near the tropopause is somewhat ambiguous. The altitude and depth of the transition region have been adjusted such that reasonable tropical temperature profiles are produced by the model.

Nonzero diabatic heating rates and a finite residual circulation are only obtained in the presense of time dependent and nonconservative processes. These processes are parameterized and we have tried to keep the parameterization as simple as possible. The model includes two dissipative processes to drive its circulation: (1) gravity wave drag, parameterized by Rayleigh friction and (2) the potential vorticity flux associated with breaking planetary waves, parameterized as K_{yy} times the gradient of the zonal mean potential vorticity. The parameters have been chosen as follows:

Gravity wave drag has to be strong enough to close the stratospheric jets in the mesosphere. Planetary waves add to the deceleration of the winter jet, the easterly summer jet is, however, only subject to gravity wave drag. The Rayleigh friction is assumed to be independent of latitude. It is largest above 50 km in altitude. In the lower stratosphere, i.e. the altitude region between 10 and 20 km, coefficients have been reduced to ensure a frictional damping time scale that is longer than a season (close to one year in the middle of the layer).

The structure of the prescribed distribution of K_{yy} follows loosely the analysis of NMC data by Newman et al. (1986, 1988). A maximum in K_{yy} of is specified near the center of the polar night jet in winter. A second maximum in K_{yy} is specified in the lower stratosphere in summer to account for the action of trapped planetary waves.

The magnitude of the upper maximum in the Northern Hemisphere winter varies from 3×10^6 m^2/sec (low K_{yy} case) to 6×10^6 m^2/sec (large K_{yy} case). The K_{yy} maximum in the Southern winter is assumed to have half the amplitude in order to account for the difference in planetary wave structures between the hemispheres. The lower stratospheric summer maxima are set to 0.75×10^6 for the low K_{yy} case and 1.5×10^6 m^2/sec for the high K_{yy} case. The strength of these maxima is the same in the Northern and Southern Hemisphere. The stength of K_{yy} falls off exponentially in latitude and altitude away from the maxima. Values of K_{yy} for the Northern Hemisphere midlatitudes at 30 km in altitude are typically 5×10^5 m^2/sec in winter.

The K_{yy}'s are set to zero equatorward of 15 degrees. This defines a 'pipe' structure in the model. However, the walls of the pipe are not well defined as K_{yy} increases gradually poleward of 15 degrees. Furthermore, the rate of increase varies with season. At some altitudes, the pipe extends all the way to the pole in summer. Due to our choice of representing the distribution of K_{yy} as a superposition of seasonally varying maxima, the values of the diffusion coefficients are comparatively small in the high latitude lower stratosphere, resulting in a 'stagnation zone' with the oldest air in this region.

The mass exchange between tropics and midlatitudes is determined by the model calculated residual circulation which depends on K_{yy} in midlatitudes. Increasing the extratropical large scale mixing increases the flow across the subtropical regions.

All results submitted for this intercomparison workshop were obtained with the low values of K_{yy} as described above.

Transport Scheme

The numerical advection scheme is the Square Root scheme (Schneider, 1985) using fourth order spatial differencing.

The large scale eddy diffusion coefficients, K_{yy}, are assumed to represent the one non-zero component of the diffusion tensor in isentropic coordinates. The diffusion tensor in pressure coordinates is determined by calculating the slope of isentropic surfaces at every grid point and rotating the isentropic center accordingly.

An additional vertical diffusion of 10. m^2/sec is specified below the tropopause of the model to represent tropospheric vertical exchange processes. The timescale of diffusive transport between the surface and the tropopause is of the order of a month. In the stratosphere, a background vertical diffusion of 0.1 m^2/sec is used to account for the vertical mixing introduced by breaking gravity waves.

The tropopause height is set to 16 km in the tropics. In midlatitudes, it is 12 km in the summer and 10 km in winter. No attempts have been made to fine tune tropopause heights in order to generate realistic ozone coulmn amounts.

Time Steps

Starting from day N, the dynamics is integrated forward for 5 days, using a split explicit time stepping scheme. Time steps are half an hour for the external step and 8 minutes for the internal steps. The dynamical fields are saved at the beginning and the end of the 5-day interval.

Using interpolated dynamical fields for the 5-day interval, the tracer transport equation is integrated forward for each transported species, using 3 hour timesteps.

Using the updated transported species concentrations, the remaining species are determined by requiring photochemical equilibrium. To calculate equilibrium, a diurnal cycle (24-hour) integration is performed with all chemical species. Diurnal coefficients are then determined from the diurnal calculation and the system of equations (Pi - Li) = 0, (i=1,number of species) is solved using rates that have been multiplied by the appropriate diurnal coefficients. New production rates and loss frequencies are calculated for the transported species, including the families.

Using the updated ozone of day+5, heating rates are recalculated, and the dynamics is integrated forward again.

Photochemistry

Reaction rates and photo dissociation cross sections are taken from JPL 97-4 [DeMore et al. 1997].

Heterogeneous Chemistry on Sulfate Aerosols and PSCs

The following heterogeneous reactions are included in the model:

$N_2O5 + H_2O \quad = 2 \times HNO_3$
$ClONO_2 + H_2O = HNO_3 + HOCl$

Polar Stratospheric Clouds

Polar stratospheric clouds are not included in the model.

Treatment of Solar Radiance and Photodissociation

For the photodissociation calculation we assume that the direct solar beam is attenuated by gas absorption and in situ Rayleigh scattering. The radiative transfer equation is solved using a 6-stream approximation for clear sky conditions in a multiple scattering atmosphere. We use the radiative transfer code from the Harvard photochemical model (Salawitch et al. [1994]). The incident solar flux specified at the top of the atmosphere was taken from WMO [1986]. Cross sections for Rayleigh scattering and for absorption in the Herzberg continuum (for wavelengths greater than 202.5 nm) of O_2 were taken from WMO [1986]. For absorption in the Schumann-Runge bands of O_2 we use the cross section parameterization of Minchwaner et al. [1992], with the the underlying Herzberg continuum included in the parameterization.

Family Chemistry and Transported Constituents or Families

The chemistry module solves for 71 species. Four of them are fixed (N_2, O_2, H_2 and H_2O), 28 are transported and 39 are assumed to be in photochemical equilibrium. Four of the transported species are families:

$Ox = O + O(^1D) + O_3 + NO_2 + ClO + BrO + HO_2$

$NOy = N + NO + NO_2 + NO_3 + HONO + HNO_3 + HNO_4 + 2 \times N_2O_5 + ClONO_2 + ClNO + ClNO_2 + ClONO + BrONO_2$

$Cly = Cl + ClO + HCl + HOCl + ClONO_2 + ClNO + 2 \times Cl_2 + ClNO_2 + ClONO + ClOO + 2 \times ClOOCl + OClO + BrCl$

$Bry = Br + BrCl + BrO + HBr + HOBr + BrONO_2$

Members of the following two families are treated as equilibrium species.

$HOx = OH + H + HO_2 + H_2O_2$

$CHx = HCO + CH_2O + CH_3 + CH_3O + CH_3O_2 + CH_3OOH$

Daytime Concentrations

The daytime average species concentrations, submitted to this workshop, have been diagnosed at every timestep by calculating daytime averages in addition to the 24-hour averages needed for the determination of our diurnal coefficients. These daytime averages do not represent an exact daytime photochemical equilibrium state. They are reasonably close to equilibrium but should not be used to recalculate production or loss rates.

References

Cunnold, D., F. Alyea, N. Phillips, and R. Prinn: A three-dimensional dynamical-chemical model of atmospheric ozone, J. Atmos. Sci., 32, 170-194, 1975

DeMore, W. B., S. P. Sander, D. M. Golden, R. F. Hampson, M. J. Kurylo, C. J. Howard, A. R. Ravishankara, C. E. Kolb, and M. J. Molina, Chemical kinetics and photochemical data for use in stratospheric modeling, Evaluation number 12, JPL Publication 97-4, Jet Propulsion Laboratory, NASA, January 15, 1997.

Minschwaner, K., G. P. Anderson, L. A. Hall, and K Yoshino, Polynomial coefficients for calculating O_2 Schumann-Runge cross sections at 0.5 cm^{-1} resolution, J. Geophys. Res., 97, 10103-10108, 1992.

Newman, P. A., M. R. Schoeberl, and R. A. Plumb, Horizontal mixing coefficients for two-dimensional chemical models calculated from National Meteorological Center data, J. Geophys. Res., 91, 7919-7924, 1986.

Newman, P. A., M. R. Schoeberl, R. A. Plumb, and J. E. Rosenfield, Mixing rates calculated from potential vorticity, J. Geophys. Res., 93, 5221-5240, 1988.

Salawitch, R. J., et al., The distribution of hydrogen, nitrogen, and chlorine radicals in the lower stratosphere: Implications for changes in O_3 due to emission of NOy from supersonic aircraft, Geophys. Res. Lett., 21, 2547-2550, 1994.

Schneider, H. R. and M. A. Geller, A comparison of two- and three-dimensional transport within a stratospheric circulation model, J. Atmos. Sci., 42, 1792-1808, 1985.

Schneider, H. R., D. B. A. Jones, G.-Y. Shi, and M. B. McElroy: Analysis of residual mean transport in the stratosphere. Part 1: Model description and comparison with satellite data. Submitted to J. Geophys. Res., 1998.

Schneider, H. R., D. B. A. Jones, S. C. Wofsy, and M. B. McElroy: Analysis of residual mean transport in the stratosphere. Part 2: Distributions of CO_2 and mean age. Submitted to J. Geophys. Res., 1998.

Shi, Guang-Yu, An accurate calculation and representation of the infrared transmission function of the atmospheric constitutes, Ph.D. thesis, Dept. of Science, Tohoku University of Japan, 191pp, 1981.

1.2.6 LLNL 2-D Model

Douglas E. Kinnison
Atmospheric Chemistry Division
National Center for Atmospheric Research
P. O. Box 3000
Boulder, CO 80307-3000
E-mail: dkin@acd.ucar.edu
Telephone: (303)497-1469
Fax: (303)497-1400

Peter S. Connell
Global Climate Research Division, L-240
Lawrence Livermore National Laboratory
7000 East Avenue
P. O. Box 808
Livermore, CA 94550-9900
E-mail: connell2@llnl.gov
Telephone: (510)422-1811
Fax: (510)422-5844

General Information

The LLNL 2-D chemical-radiative-transport (CRT) model, or LOTUS (Livermore Operator-split Two-dimensional Zonal-average (U) System), calculates zonal average atmospheric distributions of chemically active trace constituents in the troposphere and stratosphere, based on numeric representations of chemical and physical atmospheric processes. The processes represented include; (a) thermal kinetic chemical reactions with rate constants based on climatological zonal temperature distributions, (b) photolytic chemical reactions, (c) advection and diffusion driven by climatological zonal average temperature, radiative transfer of energy, and orographic forcing, (d) surface emission and in situ production of active trace constituents, and (e) dry and wet deposition or removal of active species.

The model has been developed partially from various components of the previous LLNL 2-D CRT model (Kinnison et al., 1994; Patten et al., 1994), that have been improved and modularized. The model domain extends from pole to pole, and from the surface to 85 km. The horizontal resolution is 5 degrees in latitude and the vertical coordinate is logarithmic in pressure, with an approximate vertical resolution of 1.5 km. As implemented for this application, the model treats 46 chemically active species.

Chemistry Mechanism and Solution

The model integration procedure is based on the split operator approach, with a central time step that can be made appropriate for either a diel[1]-average chemistry solution technique (e.g. 1 day) or a direct diel solution (e.g. 900 seconds). Chemistry, transport, and physical process operators interact on multiples of the central time step. Within the chemistry operator, species are integrated with SMVGEAR II, a grouped stiffness-ordered, sparse matrix implementation of the variable internal time-step, variable order, implicit, error-controlled Gear solution technique (Jacobson, 1995). The continuity

[1]The word 'diel' denotes the 24 hour diurnal/nocturnal cycle.

equation is solved for each species individually; no lumping of species into chemical families or steady-state approximations is made. Although the model can be run either in direct diel mode or as a diel average integration, diel averaging is based on scaling with coefficients determined in a direct diel run that properly account for diel correlations among species concentrations and solar insolation.

The photochemical mechanism represents the tropospheric and stratospheric interactions of actinic solar flux and the species families Ox, NOy, ClOy, HOy, BrOy, and CH_4 and its oxidation products. The chemical mechanism incorporates 46 transported and chemically active trace constituent species. There are 118 thermal, both homogenous and heterogeneous, and 38 photolytic reactions. Source gases present in the model include N_2O, CH_4, the chlorine containing compounds CFC-11, -12, -113, HCFC-22, CCl_4, CH_3CCl_3, CH_3Cl, and the bromine containing compounds CH_3Br, CF_2ClBr, and CF_3Br. Surface and in situ emissions of NOx, CO, and HCl are included. CO_2 abundance is an input to the radiative heating calculation. Most of the thermal reaction rate constants were taken from the NASA Panel recommendations provided in JPL Publication 97-4 (DeMore et al., 1997). Direct hydrolysis of $ClONO_2$, N_2O_5, and $BrONO_2$ on the surface of stratospheric sulfate aerosol is included, as are the reactions of $ClONO_2$, HOCl, and HOBr with HCl on aerosol surfaces. Representation of the rate constants for these the above heterogeneous reactions follow the work of Hanson et al. (1994).

Thermal kinetic processes with larger activation energies and heterogeneous processes with threshold temperatures have a nonlinear response to temperature variations, which is inconsistent with simple rate constant determination based on a zonal average temperature. In calculating thermal rate constants in LOTUS, and following the sense of Portmann et al. (1996), we account for both the climatological zonal average temperature and for spatial/temporal variability in temperature in the zonal dimension. Using output of the assimilation model of the NASA Data Assimilation Office for the year 1995-6 (DAO STRAT), we evaluated zonal temperature distributions on the LOTUS grid using ten variable width temperature bins. The means of these distributions are co-located with the Fleming climatological temperatures and the rate constants are determined as a distribution average over values calculated for each temperature bin.

The recognition of the effects of zonal temperature variability appears to be able to account for a significant portion of the heterogeneous activation of chlorine, even with climatological background sulfate aerosol surface area density. However, satellite climatologies of aerosol are based on sparse information near the poles, so we enforce a minimum surface area density of 1(-8) cm^2/cm^3 within 25 degrees of the poles when the frequency of polar stratospheric cloud occurrence exceeds 0.08 in the climatology of Poole and Pitts (1994). Loss of water and HNO_3 from the stratosphere through gravitational sedimentation of ice particles is represented through time constants for first order loss applied whenever the partial pressure of water exceeds to saturation vapor pressure over ice.

Absorption cross section information was assembled from a variety of sources, including JPL 97-4. These cross sections, as functions of temperature, are combined with a tabulated radiative source function as a function of wavelength, solar zenith angle, pressure, and overhead ozone column, provided by Kawa (personal communication, 1997) to produce the photolysis frequencies. The wavelength bin structure is more highly resolved at shorter wavelengths and includes 79 bins between 180 and 760 nm. Kawa also provided tabulated oxygen photolysis frequencies directly, calculated by the method of Minschwaner, et al. (1992 and 1993). The effect of clouds on tropospheric photolysis frequencies is treated simply as a process that partially obscures the lowest atmospheric layers. Additionally, air parcels near the edge of polar night may be alternately exposed and shadowed. This is represented in the model by a sinusoidal average over neighboring latitude zones for latitudes within 30 degrees of the pole and in the winter season when waves are more active.

Dynamics Model

The dynamical representation is based on the approach of Garcia and Solomon (1983). Both the temperature and zonal mean wind field vary continuously over the annual cycle. The temperature field is based on climatology of Fleming (personal communication, 1997), while the zonal mean wind is based on data from Fleming et al. (1988). The method used to obtain the circulation is based on the combination of the zonal mean momentum equation and the thermodynamic equation into a form that, along with the thermal wind equation, yields a second order diagnostic equation for the residual mean meridional stream function. This stream function is defined so that the continuity equation is solved exactly. The coefficients in front of the stream function terms on the left side of the equation are functions of known quantities, namely, the Coriolis force, zonal mean wind, scale height, temperature field, a global reference altitude dependent temperature field, and the Brunt-Vaisala frequency. The model seasonally averages the known temperature fields to provide an altitude dependent reference temperature field from which an altitude dependent Brunt-Vaisala frequency is calculated. The right hand side of the stream function equation includes the net heating rate term and the Eliassen-Palm flux representing wave driving. The net heating rate is calculated knowing the temperature and radiative chemical species distribution and includes latent heating. This is done by simply calculating the left hand side of the zonal mean momentum equation using the known zonal mean wind field and approximate values of v* and w*. These approximate values of v* and w* are obtained from a diagnostic approach of iteration between the continuity and thermodynamic equations with a known temperature field. The right hand side also includes a very small value of Rayleigh friction (value of about 0.1 day^{-1}) to account for small scale disturbances. With all terms known, the second order equation for the stream function is evaluated from which the velocity fields are then obtained.

The transport of chemical species is accomplished through both advection and turbulent eddy transport. Advection terms are treated using the second order, two dimensional transport algorithm of Smolarkiewicz (1984). The transport caused by sub-grid scale processes is parameterized through the diffusion coefficients, K_{yy} and K_{zz}. The coefficients of this motion are derived from treatment of planetary waves (both wave number 1 and 2), based on the ground breaking work of Garcia (1991) and Garcia et al. (1992), and the gravity wave effects following Lindzen (1981).

Radiative Transfer Models

The infrared model that we have been using for several years is a version of the model described by Harshvardhan et al. (1987). We have modified the model to improve the accuracy in the upper stratosphere. It includes absorption and emission by CO_2, O_3, and H_2O. It is based on wide-band parameterizations fit to line-by-line calculations. Inhomogeneous absorption paths are included by pressure- and temperature-weighted scaling of trace gas absorber amounts. The model provides for specification of fractional cloud cover within each vertical model layer. Separate fractions can be specified for convective (deep, overlapping) and randomly overlapped clouds.

References

DeMore, W.B., S.P. Sanders, D.M. Golden, R.F. Hampson, M.J. Kurylo, C.J. Howard, A.R. Ravishankara, C.E. Kolb, and M.J. Molina, Chemical Kinetics and Photochemical Data for Use in Stratospheric Modeling, Eval. No. 12, JPL Publication 97-4, January 15, 1997.

Fleming, E.L., S. Chandra, M.R. Schoeberl, and J.J. Barnett, Monthy mean global climatology of temperature, wind geopotential height, and pressure for 0-120 km, NASA Tech. Memo. 1000697, 1988.

Garcia, R.R., and S. Solomon, A numerical model of the zonally averaged dynamical and chemical structure of the middle atmosphere, *J. Geophys. Res.*, 88, 1379-1400, 1983.

Garcia, R.R., Parameterization of planetay wave breaking in the middle atmosphere, *J. Atmos. Sci.*, 1991.

Garcia, R. R., F. Stordal, S. Solomon, and J.T. Kiehl, A new numerical model of the middle atmosphere, 1, Dynamics and transport of tropospheric source gases, *J. Geophys. Res.*, 97, 12967, 1992.

Hanson, D.R.., and A.R. Ravishankara, Reactive uptake of $ClONO_2$ onto sulfuric acid due to reaction with HCl and H_2O, *J. Phys. Chem.*, 98, 5728-5735, 1994.

Harshvardhan, R. Davis, D.A. Randall, and T.G. Corset, A fast radiation parameterization for atmospheric circulaton models, *J. Geophys. Res.*, 92, 1009-1016, 1987.

Jacobson, M.Z., Computation of global photochemistry with SMVGEARII, *Atm. Env.*, 29, 2541-2546, 1995.

Kinnison, D.E., K.E. Grant, P.S. Connell, D.A. Rotman, and D.J. Wuebbles, The chemical and radiative effects of the Mt. Pinatubo eruption, *J. Geophys. Res.*, 99, 25705-25731, 1994.

Lindzen, R.S., Tubulence and stress owing to gravity wave and tidal breakdown, *J. Geophys. Res.*, 86, 9707, 1981.

Minschwaner, K., G.P. Anderson, L.A. Hall, and K. Yoshino, Polynomial coefficients for calculating O_2 Schumann-Runge cross sections at 0.5 cm^{-1} resolution, *J. Geophys. Res.*, 97, 10103-10108, 1992.

Minschwaner K., R.J. Salawitch, and M.B. McElroy, Absorption of solar radiation by O_2: implications for O_3 and lifetimes of N_2O, $CFCl_3$, and CF_2Cl_2, *J. Geophys. Res.*, 98, 10543-10561, 1993.

Patten, K.O., Jr., P.S. Connell, D.E. Kinnison, D.J. Wuebbles, T.G. Slanger, and L. Froidevaux, Effect of vibrationally excited oxygen on ozone production in the stratosphere, *J. Geophys. Res.*, 99, 1211-1224, 1994.

Poole, L.R., and M.C. Pitts, Polar stratospheric cloud climatology based on Stratospheric Aerosol Measurement II observations from 1978 to 1989, *J. Geophys. Res.*, 99, 13083-13089, 1994.

Portmann, R.W., S.Solomon, R.R. Garcia, L.W. Thomason, L.R. Poole, and M.P. McCormick, Role of aerosol variations in anthropogenic ozone depletion in the polar regions, *J. Geophys. Res.*, 101, 22991-23006, 1996.

Smolarkiewicz, P.K., A fully multidimensional positive definitive advection transort algorithm with small implicit diffusion, *J. Comput. Phys.*, 54, 325-362, 1984.

1.2.7 MGO/UIUC: Description of the 2-D Zonally Averaged Transient Model of Photochemical Dynamical and Radiative Processes in the Troposphere and Stratosphere

VLADIMIR ZUBOV and IGOR KAROL
Main Geophysical observatory,
194021, Karbyshev 7, S.Petersburg, Russia.
(email: zubov@main.mgo.rssi.ru, karol@main.mgo.rssi.ru)

EUGENE ROZANOV
Department of Atmospheric Sciences
University of Illinois at Urbana-Champaign
105 S. Gregory Ave, Urbana, IL 61801, USA.
(email: rozanov@atmos.uiuc.edu)

Domain and Grid Sizes

The MGO/UIUC 2-D model domain extends from south pole to north pole and approximately from the ground to 66 km. Latitude and log-pressure altitude are used as coordinates, with horizontal resolution of 10 deg. and vertical resolution of 2 in units of 7xln(1013/p(mb)), equivalent to approximately 2 km. The center of each latitude in degrees is given by -85+10x(i-1), where i is the latitude index ranging from 1 to 18. The pressure in mb at the center of each altitude bin is given by 1013./exp(1+2x(j-1)/7.) where j is the altitude index ranging from 1 to 33.

Transport and Temperature

The dynamical part includes the numerical solution of the dynamical equations system in the stratosphere by approach used in [Garcia and Solomon, 1983]. The stratospheric temperature fields are obtained from the energy balance equation. The zonal winds are evaluated from the thermal wind relation and from the calculated temperature. The mean meridional stream-function of the residual circulation is determined by vertical gradient in dynamical forcing and by horizontal gradient of the radiative heating and cooling from the elliptic stream-function equation. Dynamical forcing depend on the gravity and planetary wave dissipation. Gravity wave dissipation is treated as the Rayleigh friction as a function of latitude, height and day of the year. We have used the modified Rayleigh friction coefficient from [Holton and Wehrbein, 1980]. The planetary wave dissipation is inferred from the generalized Eliassen-Palm relation according of [Hitchman and Brasseur, 1988] parametrization. At the bottom of the stratosphere, at 16 km in height, the vertical velocity has been specified as a function of latitude and day of the year [Brasseur at al., 1990] and the stream function is obtained from vertical velocity field, taking care of the integral mass conservation. The tropospheric circulation has been derived from these specification by interpolating linearly down to the ground level. Temperatures in the troposphere are an 4 year average of MAP monthly-mean zonal-mean temperatures for the 1979-1982 period [Barnett and Corney, 1985]. Daily temperatures are interpolated from monthly mean fields. Tropopause heights are calculated from the temperature gradients. The tropospheric water vapor mixing ratios are prescribed on the base of Oort's statistics [Oort 1983].

The horizontal eddy diffusion coefficient, K_{yy}, is a function of latitude, altitude, and season. The background K_{yy} values in the stratosphere are 3×10^5 m^2/s [Atmospheric Ozone,1985] or larger and

related to the Rossby wave dissipation [Hitchman and Brasseur, 1988]. In the troposphere value K_{yy} has been adopted as 1x106 m2/s.

The vertical diffusion coefficient, K_{zz}, is 1x10 m^2/sec in the troposphere. Between the tropopause and 65 km altitude K_{zz} increases from 0.1 m^2/s up to 16 m^2/s. The relatively large vertical diffusion coefficient in the troposphere simulates convective overturning and synoptic scale eddies. Enhancing vertical mixing with altitude in the stratosphere is based on the work of [Garcia and Solomon, 1985] regarding gravity wave breaking.

Radiation

The radiation scheme is to supply the photolysis rates and the net heating rates.

Photolysis rates

Photolysis rates are calculated every seventh model day for solar zenith angles related to the two hours time steps. The calculations use 61 spectral intervals in the UV and Visible region with boundaries every 2 nm between 175.4 and 204.1 nm in the Schumann-Runge bands, and every 5 nm between 205 and 410 nm. The Chappuis region is subdivided into 3 broad bands between 410, 470, 630, and 750 nm. Absorption cross sections and quantum yields are mainly taken from DeMore et al.[1997]. Within the model atmosphere O_2,O_3,NO_2 and clouds are considered as absorbers influencing the transmission down to ground and the upward reflection. Taking the distribution of the absorbing atmosphere and the albedo of the ground, the radiation available for the photolysis processes is directly calculated for intervals between 175.4 and 285 nm. For larger wave lengths the Rayleigh scattering is taken into account and the photon fluxes are calculated using the Delta-Eddington scheme [Joseph et al., 1976]. The O_2 and the NO photolysis rates calculations in the Schumann-Runge bands follow the special treatment in [Allen and Frederic, 1982].

Net heating

The radiation code calculates net heating rates every one model day according to the scheme described in [Frolkis and Rozanov, 1993]. The net heating rates are obtained by calculating separately the short wave heating in the UV plus Visible and the NIR regions, and the long wave cooling rates in the IR region.

Short wave heating

The heating calculations in the UV and visible are done for 13 intervals, ranging from 197.5 to 750 nm. Interval boundaries are every 10 nm between 197.5 and 297.5 nm, 312.5, 450, and 750 nm. For the two larger intervals in the Huggins and Chappuis bands, the Rayleigh scattering is accounted for and the Delta-Eddington scheme is used. For the 11 lower intervals the up- and down-fluxes are calculated directly taking care of the albedo of clouds and of the ground as well as the absorption by O_2,O_3, and NO_2 as done for photolysis rates calculations. The heating from the NIR radiation is calculated using 12 interval with boundaries 0.7519, 0.8929, 0.9259, 0.9804, 1.099, 1.163, 1.299, 1.315, 1.724, 2, 2.326, 2.941, and 4 mu. Proceeding in principle as for the UV heating calculations, the relative spectral solar fluxes are calculated at the top of the model atmosphere for all intervals. The optical properties of clouds and of air in terms of the integrated optical depths, the single scattering albedo and the asymmetry coefficients of all layers are determined and the Delta-Eddington scheme is used to find the transmission and reflection coefficients. The absorption and scattering by H_2O, CO_2, CH_4, and N_2O are then

accounted for taking also care of the temperature dependent optical parameters of these species [Frolkis and Rozanov, 1993].

Longwave radiation

The radiative cooling in the absorbing atmosphere is calculated according to [Frolkis and Rozanov, 1992] and take care of the gases H_2O, CO_2, O_3, CH_4, N_2O, O_2, $CFCl_3$, CF_2Cl_2, and NO_2 as well as of aerosols, clouds and surface albedo. The IR region is divided into 17 intervals with boundaries 4.425, 4.545, 5.952, 7.042, 7.353, 7.692, 8.065, 8.475, 9.434, 10.20, 13.16, 14.29, 15.63, 17.24, 20.83, 35.71, 71.43, and 1000 mu. The transmission function calculations account for the continuum and the temperature dependent band absorption [Frolkis and Rozanov, 1993] utilizing Goody's statistical model.

Photochemistry

We have adopted as our photochemical algorithm the algorithm developed by Karol et al. [1992], which was used for a box model and later modified and introduced into a 2-D photochemical-radiative-transport model [Zubov et al., 1995]. The algorithm includes a total of 55 species from the oxygen, hydrogen, nitrogen, carbon, chlorine and bromine families. More than 100 gas-phase and 5 heterogeneous reactions are included. The set of photochemical equations for the considered species is solved by using the implicit Newton-Raphson numerical scheme proposed for atmospheric chemistry by Ozolin [1992] and Stott and Harwood [1993]. This scheme has first-order accuracy in time, is very stable and does not produce negative concentrations. The core of the photochemical module is a specially designed Generator of Chemical Routines (GCR) which is based on non-numerical algorithms. The GCR was designed to: (1) process the photochemical reaction set, (2) determine the set of independent variables, and (3) create the FORTRAN code that performs the photochemical calculations in the model.

Heterogeneous Chemistry

The heterogeneous reactions in and on stratospheric sulfate aerosol and polar stratospheric cloud (PSC) particles have been included according to state-of-the-art parameterizations [Hanson et al., 1994 and DeMore et al., 1997]. The diagnostic thermodynamic scheme for predicting PSC events has been incorporated following Hanson and Maursberger [1988], Muller and Crutzen [1993], and Chipperfield et al. (1993). This scheme describes the condensation, sedimentation and evaporation of PSC type I and II particles in simplified form without any microphysical calculations. When the clouds evaporate, the condensed species transform back to the gaseous phase. The following heterogeneous reactions on sulfate and PSC particles are included in the model:

1. $N_2O_5 + H_2O = 2HNO_3$
2. $ClONO_2 + H_2O = HOCl + HNO_3$
3. $ClONO_2 + HCl = Cl_2 + HNO_3$
4. $HOCl + HCl = Cl_2 + H_2O$
5. $N_2O_5 + HCl = ClNO_2 + HNO_3$

Time Steps and Transport Scheme

The time step is 2 hours for photochemical and gas transport calculations, one day for the integration of the dynamics equations of the model and net heating rates. The diurnal course of photolysis rates is recalculated every 7th day.

The fields of the temperature and long-lived species are advected by a residual mean meridional circulation. Advection terms are treated using the Prather's scheme [Prather, 1986]. Explicit centered differencing is used for computing diffusion [Fletcher, 1991].

Applications of the model

The model validation against UARS ozone data has been presented by Egorova et al. (1998). The model has been used for the simulation of present day, pre-industrial and Last Glacial Minimum stratospheric species and temperature (Karol et al, 1996, 1997), and for estimation of ozone changes due to NOx emission from subsonic aircrafts (Rozanov et al., 1996, Egorova et al.,1997).

References Cited

Allen, M. and J.E. Frederic, Effective photodissociation cross section for molecular oxygen and nitric oxide in the Shumann-Runge bands. J.Atm Sci.,39, 2066-2075, 1982.

Atmospheric Ozone 1985, World Meteorological Organization-Report, N 16, Geneva, World Meteorological Organization, 1986, -1181 p.

Barnett, J.J. and M.Corney, Middle atmosphere reference model derived from satellite data, Handbook for MAP, 16, 47-85, 1985.

Brasseur,G., M.H.Hitchman, S.Walters, M.Dymek, E.Falise and M.Pirre, An interactive chemical dynamical radiative two-dimensional model of the middle atmosphere. J.Geophys.Res., 95, 5639-5655, 1990.

Chipperfield, M., D. Cariolle, P. Simon, R. Ramaroson, and D. Lary, A three-dimensional modeling study of trace species in the Arctic lower stratosphere during winter 1989-1990, J. Geophys. Res., 98, 7199-7218, 1993.

DeMore, W.B., S.P.Sander, D.M.Golden, R.F.Hampson, M.J.Kurilo, C.J.Horward, A.R.Ravishankara, C.E.Colb, and M.J.Molina, Chemical kinetics and photochemical data for use in stratospheric modeling, Evaluation 12, J.P.L. Publ., 1997.

Fletcher K., Numerical methods in the fluid dynamics, Moscow, Mir, v.% 1,2, (Russian translation), 1991.

Frolkis, V.A. and E.V. Rozanov, Radiation code for climate and general circulation models. In IRS'92: Current problems in atmospheric radiation. Proceedings of the International radiation Symposium,Tallinn, Estonia, August 1992, A. Deepak Publ., 101-105, 1993.

Garcia,R.R, and S. Solomon, A numerical model of the zonally averaged dynamical and chemical structure of the middle atmosphere, J.Geophys.Res., 88, 1379-1400,1983.

Garcia, R.R., and S. Solomon, The effect of breaking gravity waves on the dynamics and chemical composition of the mesosphere and lower thermosphere, J. Geophys. Res., 90, 3850, 1985.

Hanson, D., and K. Maursberger, Laboratory studies of the nitric acid trihydrate: Implications for the south polar stratosphere, Geophys. Res. Lettr., 15, 855-858, 1988.

Hanson, D., A. Ravishankara, and S. Solomon, Heterogeneous reactions in sulfuric acid aerosols: A framework for model calculations, J. Geophys. Res., 99 (D2), 3615-3629, 1994.

Hitchman, M.H., and G.Brasseur, Rossby wave activity in a two-dimensional model: closure for wave driving and meridional eddy diffusivity, J.Geophys.Res., 93, 9405-9417, 1988.

Holton, J.R., and W.M. Wehrbein, The role of forced planetary waves in the annual cycle of the zonal mean circulation of the middle atmosphere, J.Atm. Sci., 37, 1968-1983, 1980.

Joseph ,J.H., W.J. Wiskombe, and J.A.Weinman, The Delta-Eddington approximation for radiative flux transfer, J.Atm Sci., No.12, 2452-2459, 1976.

Karol, I.L., (Ed.), Radiative-Photochemical models of the atmosphere (in Russian), Gidrometeoizdat, Leningrad, 1986, 192 p.

Karol, I. L., Y. E. Ozolin, and E. V. Rozanov, Effect of space rocket launches on ozone, Ann. Geophys., 10, 810-814, 1992.

Muller, R., and P. Crutzen, A possible role of galactic cosmic rays in chlorine activation during polar night, J. Geophys. Res., 98 (D20), 20,483-20,490, 1993.

Oort A.N. Global atmospheric circulation statistics, 1958-1973. NOAA, Princeton N.J., Professional paper 14, 1983, 423 p.

Ozolin, Y. E., Modelling of diurnal variations of gas species in the atmosphere and diurnal averaging in photochemical models, Izv. RAN, PAO, 28 (12), 135-143, 1992.

Prather, M.J., Numerical advection by conservation of second-order moments, J. Geophys. Res., 91, 6671-6681, 1986.

Rozanov, E. V., and V. A. Frolkis, Radiation code for climate and general circulation models, in International Radiation Symposium, pp. 101-105, A. Deepak Publ., Tallinn, Estonia, 1992.

Stott, P. A., and R. S. Harwood, An implicit time-stepping scheme for chemical species in a global atmospheric circulation model, Ann. Geophys., 11, 377-388, 1993.

Talukdar, R. K., C. A. Longfellow, M. K. Gilles, and A. R. Ravishankara, Quantum yields of O(1D) in the photolysis of ozone between 289 and 329 nm as a function of temperature, Geophys. Res. Lettr., 25 (143-146), 1998.

References to MGO/UIUC 2-D Model Formulation and Applications

Karol I.L., Yu.E. Ozolin, E.V. Rozanov and V.A. Zubov. The zonally-averadged model of the photochemical, radiative and dynamical processes in the troposphere and stratosphere. Study of aircraft emission impact on O3. - In Research activities in Atmospheric and Oceanic Modeling" Ed. by G.J. Boer, WMO, Rep. No. 19, p. 7.15, Feb. 1994.

Zubov V.A., I.L.Karol, Y.E.Ozolin, and E.V.Rozanov, Global zonally averaged non stationary model of photochemistry, radiative and dynamic processes in the troposphere and stratosphere. Part I: Description of the model and its verification. (In Russian), Izvestia RAN, Physics of atmosphere and ocean, 31, 469-476, 1995.

Karol I.L.,E.V.Rozanov and V.A.Zubov. Model reconstruction of stratospheric composition and air transport during the preindustrial and last glacial periods. Atmospheric ozone. Proceedings of the XVIII quadrennial ozone symposium, L'Aquila, Italy 12-21 September 1996, Ed. R.Bojkov, G.Visconti,v.2, pp. 743-746, 1996.

Rozanov E.V., V.A.Zubov, T.A. Egorova and Y.E.Ozolin, Model evaluation of subsonic aircraft effect on the gas distribution and radiative forcing.), Proceedings of International Colloquium: "Impact of Aircraft emissions upon the Atmosphere", Paris, France, 1996, Oct. 15-18, vol. II, pp. 641-646.

Karol I.L., V.A. Zubov, E.V. Rozanov, Ch. Bruehl and A. Zieger Model reconstruction of seasonal and latitudinal changes of temperature gas transport and composition in the stratosphere of the preindustrial and last glacial periods., Doklady RAN, v. 357, N1, pp. 99-103, 1997

Egorova T. A., V.A. Zubov, E.V.Rozanov, Y. E. Ozolin and S. Jagovkina. The Model evaluation of Subsonic Aircraft Effect on Ozone and Radiative Forcing. Research Activities in atmospheric and ocean modeling, Ed. by A. Staniforth, Rep. 25, WMO/TD - No. 792, pp. 7.58-7.59, 1997.

Egorova T., V. Zubov,S. Jagovkina, and E.Rozanov, Simulation of the atmospheric ozone distributions with the 2D model and validations against UARS and TOMS data, Physics and Chemistry of the Earth, (in press), 1998

1.2.8 NCAR 2D Model

G. Brasseur, X. Tie, and R. Khosravi
National Center for Atmospheric Research
Boulder, Colorado

T. Huang
Jet Propulsion Laboratory
Pasadena, California

The NCAR 2-D model, which is named SOCRATES (Simulation Of Chemistry, RAdiation, and Transport of Environmentally important Species), is an interactive chemical, dynamical, radiative model. The spatial domain of the model is from the surface to 120 km in altitude and from 85 S to 85 N in latitude. The vertical and horizontal resolutions are 1 km and 5 degrees, respectively.

The model chemistry includes 52 species, and 137 gas phase, 5 heterogeneous (PSC/aerosol), and 46 photolysis reactions. The reaction rate coefficients and absorption cross sections are taken from JPL 1997 compilation. The chemistry solver is based on a Backward Euler scheme in which the full set of nonlinear ordinary differential equations for the concentrations of the species is solved simultaneously (i.e., the family method is not used). Diurnal variations in the density of species are also calculated.

The dynamical fields of velocity and potential temperature are obtained by solving the thermodynamic, zonal momentum, mass continuity, and thermal wind equations in the transformed Eulerian mean formulation. For planetary wave forcing the model of Matsuno and Andrews (1987) is adopted, and for gravity wave forcing the Lindzen parameterization (1981) is used (option to use the model of Fritts and Lu (1993) exists).

Radiative cooling calculations in the IR are based on the broad band model of the NCAR climate community model (CCM 3). Cooling by CO_2, H_2O, O_3, N_2O, CH_4, CFC11, and CFC12 are accounted for in the stratosphere, and the formulation of Fomichev (1998) for the NLTE cooling by CO_2 in the mesosphere is included. The total heating rate calculations include multiple scattering by air molecules and aerosol and cloud particles in the lower atmosphere, as well as chemical heating rates due to Ox and HOx reactions in the mesosphere and lower thermosphere regions. Photolysis of O_2 in the Schumann-Runge bands is based on Kockarts' (1994) parameterization.

1.2.9 NOCAR 2D Model

Rolando Garcia
National Center for Atmospheric Research
Boulder, Colorado

Susan Solomon
National Oceanic & Atmospheric Administration/Aeronomy Laboratory
Boulder, Colorado

This is a 2D, zonally-averaged model based on the diagnostic streamfunction equation plus prognostic equations for zonal wind and temperature. It uses the Transformed Eulerian Mean (TEM) formulation for all of the zonally-averaged equations. A wave-1, quasi-geostrophic planetary wave model is coupled to the zonal-mean model, so the interaction between this wave and the zonal mean state can be calculated explicitly. Diffusion and zonal mean forcing due to gravity wave breaking are parameterized after Lindzen (1981). Breaking of the explicitly computed planetary wave is parameterized using the method of Garcia (1991), which yields estimates of the EP-flux and diffusion due to breaking. The chemical scheme includes gas phase and heterogeneous reactions for all of the species/families of importance in the middle atmosphere. The influence of wave temperature perturbations on reaction rates is taken into account. Reaction rates are taken mainly from the JPL 1997 compilation.

References

Garcia, JAS, 48, 1405-1419 (1991)

Garcia et al., JGR, 97, 12967-12991 (1992)

Garcia and Solomon, JGR, 99, 12937-12951 (1994)

JPL Evaluation Number 12, JPL Pub. 97-4, 15 Jan 1997

Lindzen, R.S., JGR, 86, 9707-9714 (1981)

1.2.10 SUNY-SPb 2D Model Description

Sergey P. Smyshlyaev (1), Victor L. Dvortsov (2), Valery A. Yudin (1,2), and Marvin A. Geller (2)

AFFILIATION: (1) Russian State Hydrometeorological Institute
St. Petersburg, Russia
(2) State University of New York at Stony Brook
Stony Brook, New York

DATA CONTACT: Victor Dvortsov
phone: (516) 632-8228
fax: (516) 632-6251
E-mail: vdvor@dombai.uars.sunysb.edu

General Information

The SUNY-SPb 2-D photochemical transport model participated in photolysis and chemical solver intercomparisons sponsored by the AESA project. References to the model description can be found at the end of this document.

Domain and Grid Sizes

The model domain extends from the surface up to 0.027 mbar (approximately 74 km), and from 87.5 degrees South to 87.5 degrees North. Latitude is used as horizontal coordinate with 5 degree resolution. Vertical grid is equally spaced in log-pressure (approximately 2 km spacing).

Circulation and Diffusion

A self-consistent set of zonally-averaged transport parameters (residual circulation and diffusivity tensor) was derived from MA CCM2 using the extension of Plumb and Mahlman [1987] technique developed by Yudin et. al. [1997].

Briefly, this was done by applying flux-gradient relationship to the results of the 3-D transport numerical experiments with the two artificial orthogonal tracers. We had shown that 2-D model with the transport parameters derived in such a way is capable to reproduce reasonably well zonally-averaged fields of "real" tracers obtained from the parent 3-D model [Yudin et. al., 1997].

Transport Scheme

Using operator splitting approach, we solve continuity equations separately for advection and diffusion plus chemistry. Prather's second-order moments scheme [Prather, 1986] is used to advect tracers in the model. The equations for diffusion and chemistry are solved by the alternating directions implicit method [Smyshlyaev, 1991]. All modeled species are transported independently, with a correction at each time step to conserve mass within families.

Time Steps

The model time step is 1 day. To account for the diurnal variations of short-lived gases, the detailed photochemical calculations are performed every 15 days with time steps varying from 15 min to 2 hours depending on the rate of change of the atmospheric optical depth. The derived concentrations of the short-lived gases are then used to calculate daily mean rates of photochemical production and destruction. This procedure is also used when the change of daily mean optical depth exceeds 50 percent, and during the transition between polar day and night.

Photochemistry

The model features sixty chemical species. The rates of chemical reactions included in the model are based on the JPL 97-4 compilation [De More et al.,1997]. Ox, NOy, Cly and Bry families are considered. Hydrogen species are calculated separately. To solve the stiff system of continuity equations we use an original technique [Smyshlyaev,1991 and Smyshlyaev and Yudin,1995] which is based on the "family conservation method" [Turco and Whitten,1974] and methods for solving stiff differential equations [Hall and Watt, 1976].

Boundary conditions are specified according to WMO [1994], and water vapor is taken from MA CCM2 simulations. Lightning is included as a source of NOY in the tropical troposphere, with a source strength of 2 MT/yr.

The model has passed chemical benchmark [Stolarski et. al., 1995].

Heterogeneous Chemistry on Sulfate Aerosols and PSCs

The following reactions on stratospheric sulfate aerosol (SAA) and PSC particles are included in the model:

1. $ClONO_2 + HCl \rightarrow HNO_3 + Cl_2$
2. $ClONO_2 + H_2O \rightarrow HNO_3 + HOCl$
3. $N_2O_5 + H_2O \rightarrow 2HNO_3$
4. $HOCl + HCl \rightarrow Cl_2 + H_2O$
5. $HOBr + HCl \rightarrow BrCl + H_2O$
6. $BrONO_2 + H_2O \rightarrow HNO_3 + HOBr$
7. $N_2O_5 + HCl \rightarrow ClONO + HNO_3$

Heterogeneous reaction rates are calculated as first-order loss rates:

$k=\gamma v A/4,$

where γ is a "sticking coefficient" which can be interpreted as the probability of uptake to the aerosol and subsequent reaction, v is the thermal velocity of the gas phase molecule, and A is the surface area density of the aerosol particles.

Sticking coefficients for heterogeneous reactions on the SSA are taken from JPL 97-4 [DeMore et al.,1997], except for the reactions of $ClONO_2$ and HOCl with HCl and H_2O which are from Hanson and Ravishankara [1994] and Hanson et al., [1994]. Under low temperatures, the SSA is assumed to be

frozen and the surface area is recalculated according to [Danilin and McConnell, 1995]. The reaction rates for frozen sulfuric acid are calculated as defined by Hanson and Ravishankara [1993].

The last reaction (7) occurs only on PSC particles. All the above reactions (1) to (7) apply to PSCI and PSCII. The rates for the reactions on PSC particles are as specified in [DeMore et al., 1997].

Polar Stratospheric Clouds

Calculations of PSCI and PSCII surface areas are based on the Danilin and McConnell [1994] parameterizations. PSCI particles are assumed to be composed of nitric acid tryhydrate. PSCI are formed when the temperature drops below the point at which air becomes supersaturated with respect to NAT. The equilibrium value of HNO_3 is defined as a function of temperature according to Hanson and Mauersberger [1988]. We used a supersaturation ratio 8 for the PSCI, which approximately corresponds to 3K overcooling [Peter et al., 1991]. Type II PSCs start to form when the H_2O concentration exceeds the equilibrium value above ice given by Marti and Maursberger [1993]. The PSCII overcooling is taken to be 1.8K according to Peter et al. [1991], which corresponds to a supersaturation ratio of 1.4. NAT and ice sedimentation velocities are calculated according to Kasten [1968].

To account for temperature variations with longitude, we employ a superposition of planetary waves with zonal wave number from one to three. The wave amplitudes and phases as function of day, altitude and latitude are calculated using the Fourier transform of the MA CCM2 3-D daily mean temperature fields [Smyshlyaev et al., 1997].

Treatment of Solar Radiance and Photodissociation

Modified delta-Eddington method [Dvortsov et al.,1992] is used to calculate solar fluxes in 81 spectral intervals from 175 to 850 nm. The solar fluxes at the top of the atmosphere are from Solar Ultraviolet Spectral Irradiance Monitor (SUSIM) data [VanHoosier et. al., 1988] for wavelengths shorter than 400 nm, and from measurements of Neckel and Labs [1984] for the longer wavelengths, as recommended by JPL 97-4 [DeMore et al., 1997]. Absorption cross sections are also from [De More et al., 1997]. Direct solar fluxes are calculated for spherical atmosphere; scattered radiation is obtained in plane-parallel approximation. Our algorithm accounts for the effects of multiple scattering on air molecules, aerosol and cloud particles.

Solar fluxes in the Schumann-Runge bands are calculated for 500 cm^{-1} intervals using Kockarts's [1994] algorithm implemented by S. Madronich.

The model has passed photolysis benchmark [Stolarski et. al., 1995].

References

DeMore, W. B., S. P. Sander, D. M. Golden, R. F. Hampson, M. J. Kurylo, C. J. Howard, A. R. Ravishankara, C. E. Kolb, and M. J. Molina, Chemical kinetics and photochemical data for use in stratospheric modeling, Evaluation number 12, JPL Publication 97-4, Jet Propulsion Laboratory, NASA, January 15, 1997.

Danilin, M.Y., and J.C. McConnell, Heterogeneous reactions in a stratosperic box model: a sensitivity study, J.Geophys.Res., 99, 25681-25696, 1994.

Dvortsov V.L., S.G.Zvenigorodsky, and S.P.Smyshlyaev, On the use of Isaksen-Luther method of computing photodissociation rates in photochemical models, J.Geophys.Res., 97, 7593-7601, 1992.

Hall, G., and J.M.Watt, Modern numerical methods for ordinary differential equations, Clarendon Press, Oxford, 312 pp., 1976.

Hanson, D., and K. Mauersberger, Laboratory studies of the nitric acid trihydrate: Implications for the south polar stratosphere, Geophys. Res. Lett., 15, 855-858, 1988.

Hanson, D. R., and A. R. Ravishankara, Reactive uptake of ClONO2 onto sulfuric acid due to reaction with HCl and H2O, J. Phys. Chem., 98, 5728-5735, 1994.

Hanson, D. R., A. R. Ravishankara, and S. Solomon, Heterogeneous reactions in sulfuric acid aerosols: A framework for model calculations, J. Geophys. Res., 99, 3615-3629, 1994.

Hanson, D.R., and A.R.Ravishankara, Reaction of ClONO2 with HCl on NAT, NAD, and frozen sulfuric acid and hydrolysis of N2O5 and ClONO2 on frozen sulfuric acid, J.Geophys.Res., 98, 22931-22936, 1993.

Kasten, F., Falling speed of aerosol particles, J.Appl.Meteorol., 7, 944-947, 1968.

Kockarts G., Penetration of solar radiation in the Schumann-Runge bands of molecular oxygen: A robust approximation, Annales Geophysicae, v12, n12, pp. 1207 ff., Dec 1994.

Marti J., and K.Mauersberger, A survey and new measurements on ice vapor pressure at temperatures between 170 and 250 K, Geophys.Res.Lett., 20, 363-366, 1993.

Neckel H. and D.Labs, The Solar Radiation Between 3300 and 12500 A, Solar Physics v.90, pp.205-258, 1984.

Peter Th., C.Bruhl, and P.J.Crutzen, Increase in the PSC-formation probability caused by highflying aircraft, Geophys.Res.Lett.,18, 1465-1468, 1991.

Plumb, R. A., and J. D. Mahlman, The zonally averaged transport characteristics of the GFDL general circulation/transport model, J. Atmos. Sci., 44, 298-327.

Prather, M. J., Numerical advection by conservation of second-order moments, J. Geophys. Res., 91, 6671-6681, 1986.

Smyshlyaev S.P. Optimization of the numerical solution algorithms of the two-dimensional zonaly average photochemical model, in Atmosfernyy Ozon, 45-54, Politekhnichesky Institut, Leningrad, 1991.

Smyshlyaev S.P., and V.A.Yudin, Numerical simulation of the impact of aircraft exhaust on the ozone layer, Atmospheric and Oceanic Physics, 31, 116-125, 1995.

Smyshlyaev S.P., V.L.Dvortsov, M.A.Geller and V.A.Yudin, A two-dimensional model with input parameters from a GCM: Ozone sensitivity to different formulation for the longitudinal temperature variation, submitted to J. Geophys. Res., 1997.

Stolarski, R. S., S. L. Baughcum, W. H. Brune, A. R. Douglass, D. W. Fahey, R. R. Friedl, S. C. Liu, R. A. Plumb, L. R. Poole, H. L. Wesoky, and D. R. Worsnop: 1995 Scientific Assessment of the Atmospheric Effects of Stratospheric Aircraft, NASA Reference Publication 1381.

VanHoosier, M. E., J.-D. F. Bartoe, G. E. Brueckner, and D. K. Prinz, Absolute solar spectral irradiance 120 nm - 400 nm (Results from the Solar Ultraviolet Spectral Irradiance Monitor - SUSIM- Experiment on board Spacelab 2), Astro. Lett. and Communications, 1988, vol. 27, pp. 163-168.

World Meteorological Organization/United Nations Environment Programme (WMO/UNEP), Scientific assessment of ozone depletion: 1994, Rep.37, World Meteorol. Org., Geneva, 1994.

Yudin, V. A., S. P. Smyshlyaev, M. A. Geller, and V. Dvortsov, Transport diagnostics of GCMs and implications for 2-D chemistry-transport model of troposphere and stratopshere, submitted to J. Atmos. Sci., 1997.

1.2.11 UNIVAQ-2D Photochemical Transport Model

Giovanni Pitari, Barbara Grassi, Lucrezia Ricciardulli
Universita' degli Studi L'Aquila
via Vetoio, 67010 Coppito L'Aquila, Italy
(email: pitari@aquila.infn.it)

The University of L'Aquila (Italy) two-dimensional model ('univaq-2d') is a 2D photochemical-transport model extending from pole to pole with a 10 degree latitudinal resolution, and from the ground to about 71 Km altitude with 26 log-pressure levels correspondent to an approximate altitude resolution of 2.84 Km, for a total of 19x26 grid-points. The pressure levels are specified as p(j)=p(j-1)/1.5, with p(0)=1000 hPa. The main features of this model have been described in Pitari et al. (1993).

All transport fields are taken off-line and are not interactive. The advective transport formulation is based on the paper of Holton (1981): a monthly-averaged residual circulation is calculated off-line from the daily output of a low-resolution spectral GCM (Pitari et al., 1992), as well as the antisymmetric components of the diffusion tensor. The symmetric components are calculated following the technique described in Newman et al. (1986) for K_{yy} and K_{yz}, with the monthly-averaged flux-to-gradient ratio of quasi-geostrophic potential vorticity calculated from the same GCM output. A constant value of 2E05 m^2/s is added everywhere to K_{yy} for removing negative values (located mostly in the polar latitudes) and for controlling too small K_{yy} values, except in the tropical lower stratosphere where the calculated K_{yy} is kept (typically of the order of 0.1-0.5 x 1E05 m^2/s). No special treatment is adopted for the polar vortices. K_{zz} is assigned with large tropospheric values (10-30 m^2/s) decreasing to about 0.1-0.3 m^2/s in the lower stratosphere. The effect of gravity wave breaking is simulated by increasing K_{zz} in the upper stratosphere and mesosphere.

The numerical scheme for transport is Eulerian fully explicit, with a four-cycle time integration scheme using a 2.0 hour time increment (Lorenz, 1971).

All chemical species are diurnally-averaged. Diurnal variations are parameterized using the scheme described in Brasseur and Solomon (1984) for N_2O_5 and assuming that a number of species are only present during daytime ($O,O(^1D),H,OH,HO_2,NO,Cl,ClO,Br,BrO$). The 24-hr averaged photodissociation rates are calculated daily (i.e. every 24 model hours) and include the effects of Rayleigh and Mie scattering.

All medium and short-lived chemical species are grouped in families: Ox, NOy=NOx+HNO_3, NOx, HOx, CHOx, Cly, Bry, SOx, aerosols. The chemical species in the families are the following:

Ox: $O(^1D),O,O_3$
NOx: $NO,NO_2,NO_3,N_2O_5,HNO_4,ClONO_2,BrONO_2$,PAN
HOx: H,OH,HO_2,H_2O_2
CHOx: CH_3O_2,CH_3OOH,CH_2O,
$CH_3CHO,CH_3CO_3,CH_3COOOH,C_2H_5O_2,C_2H_5OOH$,
$C_3H_6OHO_2,C_3H_6OHOOH,C_5H_8OHO_2$
Cly: $Cl,ClO,ClOOCl,HOCl,ClONO_2,HCl$
Bry: $Br,BrO,HOBr,BrONO_2,HBr$
SOx: SO_2,H_2SO_4
Aerosols: Aitken-nuclei, Sulfate, NAT, Ice.

Long-lived and surface-flux species are the following:
N_2O,H_2O,CH_4,CO,

C_2H_6,C_2H_4,C_3H_6,C_5H_8,$C_{10}H_{16}$,other hydrocarbons,
CF_2C_{12},CFC_{13},CC_{14},CH_3CC_{13},CFC-113,CH_3Cl,HCFC-22,CH_3Br,Halon-1211,Halon-1301,
OCS,CS2,DMS,H_2S.

All photochemical data are taken from JPL (1997). The heterogeneous reactions on sulfate aerosols included in the model are the following:
$N_2O_5 + H_2O \rightarrow 2HNO_3$
$ClONO_2 + H_2O \rightarrow HOCl + HNO_3$
$ClONO_2 + HCl \rightarrow Cl_2 + HNO_3$
$HOCl + HCl \rightarrow Cl_2 + H_2O$
$BrONO_2 + H_2O \rightarrow HOBr + HNO_3$
The size distribution of both sulfate and PSC aerosols (NAT + ice) may be calculated using a fully interactive and mass conserving microphysical code for aerosol formation and growth. Denitrification and dehydration due to PSC sedimentation are calculated explicitly from the NAT and ice aerosols size distribution.

The 2D temperature field is taken from time-zonally averaged NMC data and is used in all photochemical calculation; the effects of temperature zonal asymmetries are included only in the calculation of the heterogeneous reaction rates, by means of temperature standard deviations taken from climatological data or again calculated from the output of the GCM (Pitari, 1993).

References

Brasseur, G. and S. Solomon: Aeronomy of the Middle Atmosphere, D.Reidel, 1984.

Holton, J.R.: An Advective Model for Two-Dimensional Transport of Stratospheric Trace Species, J. Geophys. Res., 86, 11989-11994, 1981.

JPL: Chemical Kinetics and Photochemical Data for Use in Stratospheric Modeling, JPL publ. 97-4, 1997.

Lorenz, E.: An N-Cycle Time Differencing Scheme for Stepwise Numerical Integration, Mon. Weather Rev., 99, 644-648, 1971.

Newman, P.A., M.R. Schoeberl, and R.A. Plumb: Horizontal Mixing Coefficients for Two-Dimensional Chemical Models Calculated From National Meteorological Center Data, J. Geophys. Res., 91, 7919-7924, 1986.

Pitari, G., S. Palermi, G. Visconti and R.G. Prinn: Ozone Response to a CO2 Doubling: Results From a Stratospheric Circulation Model With Heterogeneous Chemistry, J.Geophys.Res., 97, 5953-5962, 1992.

Pitari, G., V. Rizi, L. Ricciardulli, and G. Visconti: High-Speed Civil Transport Impact: Role of Sulfate, Nitric Acid Trihydrate, and Ice Aerosols Studied With a Two-Dimensional Model Including Aerosol Physics, J.Geophys.Res., 98,23141-23164, 1993.

Pitari, G.: Contribution to th Ozone Trend of Heterogeneous Reactions of ClONO2 on the Sulfate Aerosol Layer, Geophys.Res.Lett., 20, 263-2666, 1993.

1.2.12 WISCAR 2D Model

M. H. Hitchman
University of Wisconsin
Madison, Wisconsin

The WISCAR model was designed at NCAR by Guy Brasseur and collaborators. Several additions were made by Hitchman and collaborators at UW-Madison, hence the name. The zonal mean model features interactive wave dynamics, climatological aerosol amounts by season and phase of the QBO, and analytic QBO forcing methods. For this run, aersols and the QBO are turned off. The WISCAR model extends from the surface to 85 km, and from 85S to 85N in latitude.

Brasseur, G., M.H. Hitchman, S. Walters, M. Dymek, E. Falise, and M. Pirre, An interactive chemical dynamical radiative two-dimensional model of the middle atmosphere. J. Geophys. Res., 95, 5639-5656, 1990.

Politowicz, P.A. and M.H. Hitchman, Exploring the effects of forcing quasibiennial oscillations in a two-dimensional model, J. Geophys. Res., 102, 16,481-16,497, 1997.

1.2.13 ECHAM3/CHEM

Dr. Volker Grewe
DLR Oberpfaffenhofen
D-82234 Wessling
Germany
Volker.Grewe@dlr.de

1. MMII model name, affiliation(s), general references:

ECHAM3/CHEM

PIs: B. Steil[1], M. Dameris[2], Ch. Bruehl[1], P.J. Crutzen[1],
V. Grewe[2], M. Ponater[2], R. Sausen[2], E. Roeckner[3]

1: MPI for chemistry, 55020 Mainz, Germany
2: DLR Oberpfaffenhofen, 82234 Wessling, Germany
3: MPI for meteorology, 20146 Hamburg, Germany

Model description and validation:

Steil et al., Development of a chemistry module for GCMs: First results of a multi-annual integration, Ann. Geophys., in press, 1997.

Roeckner et. al. 1992 for GCM ECHAM3.

Description of submitted experiments and interpretation:

Dameris et al., Impact of aircraft NOx-emissions on tropospheric and stratospheric ozone. Part II: 3-D model results, Atmos. Environm., in press, 1997.

2. Class of model (e.g., off-line CTM, free-running GCM, assimilation): coupled dynamic-chemical GCM.

BUT: the feedback of H_2O and O_3 on the radiation is switched off. In this sense it is similar to a CTM with a GCM input,
BUT: EXTENSIVE USE OF DETAILED MODEL PHYSICS in the chemistry module (e.g. to simulate wash-out, separation of gaseous and liquid water content for OH calculations, clouds for photolysis rates)

3. Meteorological data source (if off-line CTM):

see 2. Each experiment consists of 4+10 different years representing the climatological situation of 1992 or 2015.

4 years spin up time and 10 years for interpretation.

4. Sub-grid scale mixing parameterization in troposphere:

Convection: according to Tiedtke (1989)

Hor. Diffusion: implicit in semi-lagrangian scheme (only for tracer)

Ver. Diffusion: Louis (1979)

5. Sub-grid scale mixing in stratosphere:

Hor./Ver. Diff. see 4.

6. If grid-point model, number gridpoints longitude by latitude:
several processes are described in the grid-space: 64x32

7. Latitude values at centers of grid points:
85.76058712, 80.26877907, 74.74454037, 69.21297617, 63.67863556,
58.14295405, 52.60652603, 47.06964206, 41.53246125, 35.99507841,
30.45755396, 24.91992863, 19.38223135, 13.84448373, 8.30670286,
2.76890301
for both hemispheres

8. If spectral model, truncation:
T21

9. Number vertical levels:
19

10. Vertical coordinate (e.g., pressure, sigma, hybrid, theta):
hybrid sigma-p

11. Vertical coordinate values at centers of levels:
1009hPa, 996 hPa, 968 hPa, 921 hPa, 857 hPa, 779 hPa,
690 hPa, 594 hPa, 499 hPa, 409 hPa, 326 hPa, 253 hPa,
191 hPa, 141 hPa, 103 hPa, 74 hPa, 51 hPa, 30 hPa, 10 hPa.

12. Numerical advection scheme:
Semi-lagrange (Rasch & Williamsen, 1990)

13. Advection timestep:
40 min.

14. Nature of chemical reaction for active species
(e.g., production/loss tables or explicit interaction?):
family-concept: explicit interaction.

15. If production/loss tables, source:
---

16. If explicit interaction,
(a) number of transported species and families:
12

(b) List transported species/families:
H_2O, CH_4, N_2O, H_2O_2, CO, CH_3O_2H, $ClONO_2$, HNO_3+NAT,
PSC type2 (Ice), ClOx(=Cl+ClO+ClOH+2*Cl_2O_2+2*Cl_2),
NOx(=N+NO+NO_2+NO_3+2*N_2O_5+HNO_4), and Ox(O_3+O(^{3}P)+O(^{1}D)).

(c) Reaction rate source:
DeMore et al. 1994

(d) Numerical chemical solver:
Longlived species and families: semi-implicit approach
species within families ("medium lived"): semi-analytic exponential approach
short-lived: steady state.

These three approaches are used to solve algebraic solutions of a coupled system of differential equations, which take into account the interaction of various species.

17. Heterogeneous chemistry parameterization:
PSCs: Hanson & Mauersberger (1988) using T, vmr(H_2O) and vmr(HNO_3). with nucleation barrier (dT=3K) to account for observed supersaturation.
Assumptions:
Type 1: spherical with monodisperse size distribution particle number density 1cm-3
Existence only at radii above 0.07 micrometer.
Type 2: dT=1.8K (Nucleation barrier) particle number density 0.1cm-3
Existence only at radii above 0.7 micrometer.

18. Aerosol physics:
Stratospheric aerosol is prescibed according to WMO(1992) background aerosol conditions. The enlargement of the aerosol surface areas due to admittance of water at very low temperatures is considered interactively (Luo et al., 1996).

1.2.14 GISS GCMAM

David Rind and Jean Lerner
NASA/Goddard Institute for Space Studies
New York

1. This particular model has been used, although not extensively described, in the following references:

Koch,D. and D. Rind, 1998: 10Be/7Be as a tracer of stratospheric transport. JGR, .103, 3907-3917. Hannegan, B., S. Olsen, M. Prather, X. Zhu, D. Rind and J. Lerner, 1998: The dry stratosphere: a limit on cometary influx. Geophys. Res. Lett.,25, 1649-1652.

The version used for these experiments is an update of the original model described in detail in the following references:

Rind, D., R. Suozzo, N.K. Balachandran, A. Lacis and G. L. Russell, 1988: The GISS Global Climate/Middle Atmosphere Model Part I: Model structure and climatology. J. Atmos. Sci., 45, 329-370.

Rind, D., R. Suozzo and N.K. Balachandran, 1988: The GISS Global Climate/Middle Atmosphere Model Part II: Model variability due to interactions between planetary waves, the mean circulation and gravity wave drag. J. Atmos. Sci., 45, 371-386.

2. Class of model (e.g., off-line CTM, free-running GCM, assimilation): free-running GMC

3. Meteorological data source (if off-line CTM):

4. Wind data frequency (off-line CTMs); e.g., instantaneous 6 hourly samples, averaged 12 hourly samples:

5. Sub-grid scale mixing parameterization in troposphere: None

6. Sub-grid scale mixing in stratosphere: None

7. If grid-point model, number gridpoints longitude by latitude: 72 X 46

8. Latitude values at centers of grid points:

Our grid is 5 deg longitude by 4 deg latitude (72x46 points).

The center of the latitude zone J is located at:

-90 +(J-1)*4

i.e., -90,-86,-82,-78,.....78,82,86,90

9. If spectral model, truncation: NA

10. Number vertical levels: 31

11. Vertical coordinate (e.g., pressure, sigma, hybrid, theta): sigma coordinates to 150 mb; constant pressure above

12. Vertical coordinate values at centers of levels:

layer	center
31	.00439
30	.00781
29	.0139
28	.0247
27	.0439
26	.0781
25	.139
24	.247
23	.439
22	.781
21	1.390
20	2.470
19	4.390
18	7.810
17	13.90
16	24.70
15	43.90
14	71.20
13	101.6
12	133.5
11	171.0
10	218.5
9	279.5
8	369.5
7	497.5
6	640.5
5	764.0
4	851.5
3	906.5
2	944.5
1	972.0

13. Numerical advection scheme: Quadratic upstream scheme (similar to the second order moments scheme of Prather, M., 1986: JGR, 91, 6671-6681

14. Advection timestep: Forward leapfrog timestep=112.5 sec

15. Nature of chemical reaction for active species production/loss tables

16. If production/loss tables, source: CTM results of Prather

17. If explicit interaction,

(a) number of transported species and families:

(b) List transported species/families:

(c) Reaction rate source:

(d) Numerical chemical solver:

18. Heterogeneous chemistry parameterization:

19. Aerosol physics:

Model includes parameterized gravity wave drag associated with model resolved sources in the troposphere: flow over mountains, convection, shear and frontogensis. There is no diffusive mixing of tracers associated with these parameterizations.

1.2.15 "GISS8x10" 3D CTM

M. Prather
University of California-Irvine
Irvine, California

1. MMII model name, affiliation(s), general references:

The "GISS8x10" model was developed by Michael Prather, and is used at U.C. Irvine and the Goddard Institute for Space Studies (GISS). A description of the tropospheric version is found in Prather et al, JGR, 92, 6579, 1987. This troposphere/stratosphere version is discussed in Hall and Prather, JGR, 100, 16699, 1995.

2. Class of model (e.g., off-line CTM, free-running GCM,assimilation):

Off-line Chemical Transport Model (CTM).

3. Meteorological data source (if off-line CTM):

GISS troposphere/stratosphere GCM (Rind et al, JAS, 47, 475, 1990)

4. Wind data frequency (off-line CTMs); e.g., instantaneous 6 hourly samples, averaged 12 hourly samples:

Instantaneous, 8-hourly samples.

5. Sub-grid scale mixing parameterization in troposphere:

Monthly mean wet and dry convection statistics archived by GCM act to mix tracer every 8 hours in the CTM (Prather et al, JGR, 92, 6579, 1987).

6. Sub-grid scale mixing in stratosphere:

None

7. If grid-point model, number gridpoints longitude by latitude:

36x24

8. Latitude values at centers of grid points:

j	latitude_j
1	-87.5
2	-82.2
3	-74.4
4	-66.5
5	-58.7
6	-50.9
7	-43.1
8	-35.2

 9 -27.4
10 -19.6
11 -11.7
12 -3.9
13 3.9
14 11.7
15 19.6
16 27.4,
17 35.2
18 43.1
19 50.9
20 58.7
21 66.5
22 74.4
23 82.2
24 87.5

9. If spectral model, truncation:

10. Number vertical levels: 21

11. Vertical coordinate (e.g., pressure, sigma, hybrid, theta):

pure sigma surface to 100mbar (9 levels), pure pressure above 100mb (12 levels)

12. Vertical coordinate values at centers of levels:

sigma at layer edges: edge pressure = p_surf(mb)*sigma + 100mb

sigma = 1.000000 0.973233 0.938102 0.886877 0.788246 0.637943 0.459962 0.278312 0.116969 0.000000

sigma for level edges at pressures less than 100mb: pressure = 100mb*sigma

sigma = 0.464147 0.215393 0.099976 0.046413 0.021550 0.010000 0.004642 0.002155 0.001000 0.000466 0.000215 0.000022

13. Numerical advection scheme:

Second-order moments (quadratic upstream). See Prather, JGR, 91, 6671, 1986.

14. Advection timestep:

4 hours

15. Nature of chemical reaction for active species (e.g., production/loss tables or explicit interaction?):

Production/Loss look-up tables (zonally-averaged, monthly-mean).

16. If production/loss tables, source:

Photochemical model described in Remsberg and Prather, MMI report, NASA Ref. Publ. 1292, 1993.

17. If explicit interaction,

(a) number of transported species and families:

(b) List transported species/families:

(c) Reaction rate source:

(d) Numerical chemical solver:

18. Heterogeneous chemistry parameterization:

19.Aerosol physics:

1.2.16 NASA Global Modeling Initiative (GMI) Assessment Model

Jose Rodriguez
University of Miami
Miami, Florida

Doug Rotman
Lawrence Livermore National Laboratory
Livermore, California

The NASA AEAP (Atmospheric Effects of Aviation Program) GMI model is an off-line chemical transport model designed for the assessment of atmospheric chemical impacts from aircraft emissions [Rotman, et al, 1999; Rodriguez, et al, 1999; Kinnison et al, 1999; Douglass et al, 1999; Considine, et al, 1999; and NASA Report No. 1385, 1996]. It uses input meteorological fields from three datasets: assimilated meteorological fields from the NASA GEOS (Goddard Earth Observing System) assimilation system (DAO, 1997); the output from the MACCM2 (Middle Atmospheric version of the NCAR Community Climate Model, version 2); and output from the NASA GISS (Goddard Institute for Space Studies) climate model, version 2 prime. All three meteorological datasets contain fields at 6 hour increments at 4 degrees by 5 degrees horizontal resolution. Vertical resolution varies with DAO data in 29 levels to 0.1 mb, MACCM2 data in 44 levels to 0.025 mb and GISS data in 28 levels to 0.01 mb. Cell center pressure levels (in a global averaged sense) are as follows,

NCAR MACCM2: 992.528, 970.4456, 930.0657, 869.3587, 792.5497, 704.6883, 611.0972, 516.8513, 427.4154, 349.9381, 286.5047, 234.5705, 192.0498, 157.2374, 128.7351, 105.3994, 86.2938, 70.6514, 57.8444, 47.2408, 38.3885, 31.0394, 24.9721, 19.9905, 15.9229, 12.6197, 9.9518, 7.8088, 6.0968, 4.7363, 3.6611, 2.8158, 2.1549, 1.6409, 1.2433, 0.9373, 0.7031, 0.5248, 0.3898, 0.2747, 0.1751, 0.101, 0.0527, 0.0249

GISS II': 987.7698, 959.7423, 921.0133, 864.9579, 776.2889, 649.4005, 504.1665, 373.7107, 281.9842, 219.8143, 171.403, 132.4764, 100.4261, 69.60201, 42.14166, 23.71667, 13.34166, 7.49667, 4.21416, 2.371665, 1.33416, 0.74967, 0.42141, 0.237165, 0.13341, 0.07497, 0.042135, 0.00807

NASA DAO STRAT: 921.9549, 771.3622, 648.0737, 547.7227, 447.2133, 346.4099, 273.8615, 223.6068, 187.0824, 162.0186, 139.6422, 118.0002, 100.0002, 87.99999, 77.00004, 68.12923, 56.99993, 46.41585, 31.62289, 21.54425, 14.67804, 10.00012, 6.81304, 4.64152, 3.16225, 2.15436, 1.46783, 0.68133, 0.20761

Transport

The model uses a fixed horizontal grid. Although resolution is dependent on input data, most often model simulations are carried out at 4 by 5 degrees (46 points from –90 to +90 latitude and 72 points from 0 to 355 longitude). Vertical coordinates use the hybrid ETA style vertical grid (i.e., pressure at vertical level is given as a function of surface pressure and a constants). Advection is carried out using the variable order multidimensional flux form semi-Lagrangian method (Lin and Rood, 1996) using 30 minute time steps. Additional capabilities exist for transport using semi-Lagranigan methods (Williamson and Rasch, 1990) and the Second Order method of Prather (1986). Sub-grid scale mixing is accomplished by convective transport and vertical diffusion.

Photochemistry

The chemistry equations are solved using either SMVGEAR II (Jacobson, 1995) or the ONERA solver of Ramaroson (1989). SMVGEAR II is a version of the original predictor/corrector, backward differentiation code of Gear (1971) and uses a variable time step, variable order, implicit technique for solving stiff numerical systems with strict error control. ONERA is a semi-implicit solver that shows very good comparison to the SMVGEAR II solution. Chemistry includes a complete interactive stratospheric chemical package using reaction rates of DeMore, et al 1997. Photolysis rates are obtained by a clear-sky lookup table where normalized radiative fluxes are a function of cross section (a function of temperature, species, and wavelength), pressure, solar zenith angle, and column ozone. Temperature dependent cross sections, quantum yields and solar flux are tabulated separately (DeMore, et al, 1997). The GMI model uses a chemical time step of 30 minutes.

Chemical species and transported species

List of 46 active chemical species

O, $O(^1D)$, O_3, N_2O, N, NO, NO_2, NO_3, N_2O_5, HNO_3, HO_2NO_2, H_2O, H, OH,
HO_2, H_2O_2, H_2, CH_4, CH_3O_2, CH_3OOH, CH_2O, CO, Cl, Cl_2, ClO, $OClO$,
Cl_2O_2, HCl, $HOCl$, $ClONO_2$, Br, $BrCl$, BrO, HBr, $HOBr$, $BrONO_2$, CH_3Cl,
CH_3Br, $CFCl_3$, CF_2Cl_2, $CFC11_3$, $CHClF_2$, CCl_4, CH_3CCl_3, CF_3Br, CF_2ClBr

List of transported species:

All of the above, except O, $O(^1D)$, N, H_2O, H

List of heterogeneous reactions

$N_2O_5 + H_2O$
$ClONO_2 + H_2O$
$ClONO_2 + HCl$
$HOBr + HCl$
$HOCl + HCl$
$BrONO_2 + H_2O$

Possible surfaces are STS, NAT and ice.

The GMI model includes a parameterization of polar stratospheric clouds that will respond to increases in HNO_3 and H_2O produced by aircraft emissions. Both type 1 and type 2 PSCs are considered. For the HSCT assessment simulations, type 1 PSCs were assumed to be totally STS and type 2 were assumed as ice. The parameterization also accounts for PSC sedimentation, which can produce denitrification and dehydration at the poles.

The GMI model currently does not include explicit aerosol microphysics.

References

Considine, et al, to be submitted to JGR

DAO, 1997, Algorithm and Theoretical basis documents of the Data Assimilation Office, 1997.

DeMore, W. B., S. P. Sander, D. M. Golden, R. F. Hampson, M.J. Kurylo, C.J. Howard, A.R. Ravishankara, C.E. Kolb, and M.J. Molina, Chemical Kinetics and Photochemical Data for Use in Stratospheric Modeling, Eval. 12, JPL Publication 97-4, 1997.

Douglass, et al, submitted to JGR

Gear, C.W., 1971: Numerical initial value problems in ordinary differential equations. Prentice-Hall, Englewood Cliffs, NJ.

Jacobson, M.A., 1995: Computation of global photochemistry with SMVGEAR II, *Atmos. Environ.*, **29A**, 2541-2546.

Kinnison, et al, to be submitted to JGR

Lin, S.J. and R.B. Rood, 1996: A fast flux form semi-Lagrangian transport scheme on the sphere, *Mon. Wea. Rev.*, **124**, 2046-2070.

NASA Report, No. 1385, 1996, Atmospheric Effects of Aviation: First report of the subsonic assessment project, May 1996

Prather, 1986: Numerical advection by conservation of second-order moments, *J. Geophys. Res.*, **91**, 6671-6681.

Rasch and Williamson, 1990: Computational aspects of moisture transport in global models of the atmosphere, Q.J.R Meteorol. Soc., 116, 1071-1090.

Rodriguez, et al, to be submitted to JGR

Rotman, et al, to be submitted to JGR

1.2.17 GSFC 3D Chemistry and Transport Model

Anne R. Douglass and S. Randy Kawa
Code 916 NASA Goddard Space Flight Center
Greenbelt MD 20771
(email: douglass@persephone.gsfc.nasa.gov kawa@maia.gsfc.nasa.gov)

The Goddard Space Flight Center Three Dimensional Chemistry and Transport Model (GSFC-3D) is an off-line chemistry and transport model which uses winds and temperatures from the Goddard Earth Observing System Data Assimilation System (GEOS DAS) (DAO, 1997). GSFC-3D, which contains a complete representation of stratospheric chemistry, has evolved from a chemistry and transport model which used parameterizations for chemical processes [e.g., Rood et al., 1989; Douglass et al., 1991; Weaver et al., 1996; Douglass et al., 1996] and is described by Douglass et al. [1997].

Transport

Winds and temperatures are updated every 6 hours using instantaneous output from the assimilation system. There is no explicit sub-grid scale paramaterization for mixing in the stratosphere or troposphere. The model uses a fixed horizontal grid at 2 degree latitude by 2.5 degree longitude resolution (91 points from -90 to +90; 144 points from 0 to 357.5). There are 28 vertical levels, with 10 sigma levels in the troposphere and lower stratosphere,17 stratospheric levels, and a boundary at 130 hPa. The spacing is about 1.5 km up to 20 km, and increases to 4 km above 30 km. Advection is accomplished using the numerical scheme developed by Lin and Rood [1996]. The transport and photochemical contributions to the constituent continuity equation in the model are solved sequentially (process splitting).

Photochemistry

The photolysis rate routine is based on the radiative transfer calculations from the model of Anderson and Lloyd (1990), which are used to determine the solar flux at any model location and solar zenith angle using a table lookup. Constituent cross sections which may be temperature dependent are taken from DeMore et al. (1994). The photolysis rates calculated in this way compare favorably with the photolysis benchmark which was developed as part of the Atmospheric Effects of Aircraft Program (Stolarski et al., 1995). Reaction rates are taken from DeMore et al. (1994). The photochemical production and loss are calculated using a predictor-corrector scheme with a time step of 15 minutes.

Constituents

Transported Constituents and Families

Ox	$O(^1D)$, $O(^3P)$, O_3
NOx	NO, NO_2, NO_3
HNO_3	
N_2O_5	
HO_2NO_2	
$ClONO_2$	
Clx	Cl, ClO, Cl_2O_2
HCl	
HOCl	

H_2O_2
Br_x Br, BrO
N_2O
Cl_2
OClO
BrCl
HBr
$BrONO_2$
CH_4
HOBr
CH_3OOH
CO

Steady State

NAT, ICE
CH_3, CH_3O_2, CH_3O, CH_2O, CHO
H, OH, HO_2

Constant

H_2O
SA

Heterogeneous Chemistry

The following heterogeneous reactions are included:

1. $N_2O_5+H_2O$
2. $ClONO_2+H_2O$
3. $ClONO_2+HCl$
4. N_2O_5+HCl
5. $HOCl+HCl$
6. $BrONO_2+H_2O$

Possible surfaces are liquid sulfate, NAT, and ice.

The liquid sulfate aerosol surface area (SA) is specified based on SAGE II data [Thomason and Poole, 1993] and (when appropriate) a climatology for volcanically clean air [Albritton and Watson, 1992], independent of model temperature variations. HNO_3 uptake is not considered. Particle composition is assumed to be liquid sulfate and water, depending on temperatures in the model, down to 1 K below the equilibrium formation temperature for nitric acid trihydrate (NAT). At temperatures below this, NAT and subsequently ice are assumed to occupy all of the particle surface. No externally mixed particle compositions are possible. Sulfate mean particle size is calculated from the SA assuming a fixed particle number density of 10 cm^{-3}. Temperature and relative humidity-dependent sticking coefficients are calculated from the model H_2O, T, and HCl according to Hanson and Ravi [1994] for reactions 2 and 3 and Hanson et al. [1994] for reaction 5. Reactions 1 and 6 use fixed sticking coefficients of 0.2 and 0.4, respectively. The sticking coefficient for reaction 4 on sulfate is 0.

Solid particle volume growth occurs at vapor pressure equilibrium controlled by the model T, HNO_3, and H_2O distributions. Model temperatures are raised by 1 K for calculation of the HNO_3 saturation vapor pressure over NAT [Hanson and Mauersberger, 1988], simulating a 1 K temperature barrier to NAT formation. The water saturation vapor pressure over ice is calculated directly from model T using Marti and Mauersberger [1993]. Particle condensed mass is calculated from the instantaneous difference between the total ambient mixing ratio and the saturation mixing ratio for these molecules. Condensed HNO_3 is removed from the gas phase for chemical reactions; H_2O is not. Surface area is obtained from volume assuming a fixed particle number density of 10 cm^{-3}, a variable nucleation fraction (set to 1 in these cases), and particle densities. Sticking coefficients for reactions 1-6 on ice are fixed according to JPL 94. The relative humidity dependence of the sticking coefficient for reaction 3 on NAT is from Hanson and Ravi [1993] while the remainder are fixed according to JPL 94.

Collision frequencies for all reactions depend on T, SA, and molecular weight. For stability, all heterogeneous reaction coefficients are limited to not exceed a rate equivalent to a reactant lifetime of approximately two model time steps (30 minutes) to maintain stability in the photochemical integration.

References

Albritton, D. L., and R. T. Watson, Co-Chairs, Scientific Assessment of Ozone Depletion: 1991, World Meteorological Organization Global Ozone Research and Monitoring Project - Report No. 25, 1992.

Algorithm and Theoretical Basis Documents of the Data Assimilation Office, 1997

Anderson, D. E., Jr., and S. A. Loyd, Polar twilight UV visible radiation field: perturbations due to multiple scattering, ozone depletion, stratospheric clouds, and surface albedo, J. Geophys. Res., 95, 7429-7434, 1990.

Douglass, A. R., R. B. Rood, J. A. Kaye, R. S. Stolarski, D. J. Allen, E. M. Larson, The influence of polar heterogeneous processes in reactive chlorine at middle latitudes: three-dimensional model implications, Geophys. Res. Lett., 18, 25-28, 1991.

Douglass, A. R., C. J. Weaver, R. B. Rood, and L. Coy, A three dimensional simulation of the ozone annual cycle using winds from a data assimilation system, J. Geophys. Res., 101, 1463-1474, 1991.

Douglass, A. R., R. B. Rood, S. R. Kawa and D. J. Allen, A three-dimensional simulation of the evolution of the middle latitude winter ozone in the middle stratosphere, J. Geophys. Res., 102, 19,217-19,232, 1997.

Hanson, D., and K. Mauersberger, Laboratory studies of the nitric acid trihydrate: implications for the south polar stratosphere, Geophys. Res. Lett., 15, 855-859, 1988.

Hanson, D. R., and A. R. Ravishankara, Reaction of ClONO2 with HCl on NAT, NAD, and frozen sulfuric acid and hydrolysis of N2O5 and ClONO2 on frozen sulfuric acid, J. Geophys. Res., 98, 22,931-22,936, 1993.

Hanson, D.R., A.R. Ravishankara, and S. Solomon, Heterogeneous reactions in sulfuric acid aerosols: A framework for model calculations, J. Geophys. Res., 99, 3615-3629, 1994.

Hanson, D. R., and A. R. Ravishankara, Reactive uptake of ClONO2 onto sulfuric acid due to reaction with HCl and H2O, J. Phys. Chem., 98, 5728-5735, 1994.

Lin, S. J., and R. B. Rood, Multidimensional flux form semi-Lagrangian transport schemes, Mon. Weather Rev., 124, 2046-2070, 1996.

Marti, J. J., and K. Mauersberger, Laboratory simulations of PSC particle formation, Goephys. Res. Lett., 20, 359-362, 1993.

Rood, R. B., D. S. Allen, W. E. Baker, D. J. Lamich and J. A. Kaye, The use of assimilated data in constituent transport experiments, J. Atmos. Sci, 46, 687-701, 1989.

Thomason, L. J., and L. R. Poole, Use of stratospheric aerosol proporeties as diagnostics of Antarctic vortex processes, J. Geophys. Res., 98, 23,003-23,012, 1993.

Weaver, C. J., A. R. Douglass, D. B. Considine, A 5-year simulation of supersonic aircraft emission transport using a three-dimensional model, J. Geophys. Res., 101, 20,975-20,984, 1996.

1.2.18 Langley 3-D Model

William L. Grose, Richard S. Eckman, R. Bradley Pierce
NASA Langley Research Center
Hampton, Virginia

The Langley Interactive Modeling Project for Atmospheric Chemistry and Transport (IMPACT) model is a general circulation model (GCM) with coupled chemistry extending from the surface (24 levels, sigma coordinates) to approximately 60 kilometers. The GCM is a global spectral model based on the primitive equations. The dependent variables in the model are represented by a truncated series of surface spherical harmonics at each model level (triangular truncation at wavenumber 32). Vertical differencing is approximated by finite difference techniques. The chemistry module consists of 23 mass continuity equations for individual constituents and/or families. The computed ozone distribution is used in the radiative heating calculation in the GCM.

The model includes full tropospheric physics with cloud-radiative feedbacks. The model can also be run "off line" as a CTM driven either by wind and temperature fields from the GCM or by analyzed meteorological fields.

Dynamics and Radiative Modules

The dynamics module is based on that described by Blackshear et al. [1987], Grose et al. [1989] and Pierce et al. [1993], which was originally developed from the model of Hoskins and Simmons [1975]. The semi-implicit integration scheme of Robert et al. [1972] is used with a 15-minute time step. A 1-2-1 time filter is applied every six time steps to control time splitting. Orographic forcing is represented by a smoothed spectral representation of the Earth's topography. A biharmonic diffusion is applied to the models temperature, vorticity and divergence fields to represent sub-grid scale diffusion and to inhibit spectral blocking.

A recent major development includes incorporation of moist physics, explicit cloud liquid water, and physical parameterizations for planetary boundary layer (PBL) exchange processes and radiative heating, appropriate for full, seasonal-cycle simulations. The tropospheric radiation scheme is that of the NCAR Community Climate Model (CCM1) [Williamson et al., 1987]. The planetary boundary layer is a bulk parametrization scheme taken from the Goddard Laboratory for Atmospheric Science (GLAS) 4^{th}-order GCM [Kalnay et al., 1983]. The large-scale explicit cloud scheme is based on the University of Wisconsin hybrid model [Zapotocny et al., 1991]. The moist convection scheme is based on that of Kuo [1974] with closure described by Molinari [1982]. The gravity wave drag scheme [McFarlane, 1987] is adapted from the Community Climate Model (Version 2), as is the nonlinear, timesplit, vertical diffusion scheme.

In the stratosphere, radiative heating is computed using the scheme of Shine [1987]. This scheme incorporates the absorption of solar UV radiation by ozone and molecular oxygen and the infrared contributions due to CO_2, H_2O, and O_3. The stratospheric and tropospheric radiative heating rates are smoothly blended together at 100 hPa. This procedure is currently being modified so that the stratospheric heating code will include contributions from the upwelling radiation from the troposphere, rather than from a specified climatology as is presently done.

Chemistry Module

Chemical calculations span the altitude range from the surface to approximately 60 km in 24 levels. Vertical resolution for the 14 stratospheric levels is approximately 3 km. Time integration of the constituent mass continuity equations is achieved explicitly with a leapfrog time-step of 15 minutes. Twenty-three chemical families or individual constituents are represented, namely Ox, NOy, HNO_3, Cly, N_2O_5, H_2O_2, HCl, $ClONO_2$, N_2O, $CFCl_3$, CF_2Cl_2, CCl_4, CH_3Cl, CH_3CCl_3, NAT, Bry, CH_3Br, CF_3Br, CF_2BrCl, CH_4, CF_2O, CFClO, and HF [Eckman et al., 1995]. The inclusion of bromine chemistry and the explicit transport of methane in the model are recent and noteworthy developments. The chemical families are partitioned into 53 species using photochemical equilibrium assumptions with 41 photolytic reactions and 107 chemical reactions. Odd hydrogen (HOx) is assumed to be in photochemical equilibrium throughout the model domain. A simplified methane oxidation scheme is included through the representation of CHx chemistry [Eckman et al. 1995]. The explicit transport of H_2O will be added to the model this year.

Photodissociation rates are obtained using a table lookup method to reduce computational time [Kawa, private communication, 1995]. Cross sections and quantum yields are being updated based on the recommendations of DeMore et al. [1997]. The rates include the effects of multiple scattering and surface reflection. Kinetic rates are taken from the compilation of DeMore et al. [1997].

The model includes a parameterization that represents the impact of polar stratospheric cloud chemistry [M. P. Chipperfield, private communication, 1996]. Sulfate aerosol chemistry is currently included using a zonal-mean aerosol climatology [WMO, 1991] and the parameterization of Hanson et al. [1994].

An initial attempt at adding an NOx source due to lightning has been implemented in the model following the scheme of Ko et al. [1986]. More elaborate parameterizations are being studied.

References

Blackshear, W. T., W. L. Grose, and R. E. Turner, Q. J. R. Meteorol. Soc., 113, 815-846, 1987.

DeMore, W. B., et al. JPL Publ. 97-4, Jet Propul. Lab., Pasadena, Calif., 1997.

Eckman, R. S., W. L. Grose, R. E. Turner, W. T. Blackshear, J. M. Russell III, L. Froidevaux, J. W. Waters, J. B. Kumer, A. E. Roche, J. Geophys. Res., 100, 13951-13966, 1995.

Eckman, R. S., W. L. Grose, R. E. Turner, W. T. Blackshear, J. Geophys. Res., 101, 22977-22989, 1996.

Grose, W. L., R. S. Eckman, R. E. Turner, and W. T. Blackshear, Global modeling of ozone and trace gases, in Atmospheric Ozone Research and its Policy Implications, edited by T. Schneider et al., pp. 1021-1035, Elsevier Science Publishers, Amsterdam. 1989.

Hanson, D. R., A. R. Ravishankara, and S. Solomon, J. Geophys. Res., 99, 3615-3629, 1994.

Hoskins, B.J., and A.J. Simmons, Q. J. R. Meteorol. Soc., 101, 637-655, 1975.

Kalnay, E., R. Balgovind, W. Chao, D. Edelmann, J. Pfaendtner, L. Takacs, and K. Takano, NASA Tech. Mem. 86064, NASA Goddard Space Flight Center, Greenbelt, MD 20771.

Ko, M. K. W., M. B. McElroy, D. K. Weisenstein, and N. D. Sze, J. Geophys. Res., 5395-5404, 1986.

Kuo, H.L., J. Atmos. Sci., 31, 1232-1240, 1974.

McFarlane, N.A., J. Atmos. Sci., Vol. 44, No 14, 1775-1800, 1987.

Molinari, J., Mon. Wea. Rev., 110, 1527-1534, 1982.

Pierce, R. B., W. T. Blackshear, T. D. Fairlie, W. L. Grose, R. E. Turner, J. Atmos. Sci., 50, 3829-3851, 1993.

Robert, A. J., J. Henderson, and C. Turnbull, Mon. Wea. Rev., 100, 329-335, 1972.

Shine, K.P., Q.J.R. Meteorol. Soc.,113, 605-633, 1987.

Williamson, D. L., et al., NCAR Technical Note 285, Boulder, Colo., 1987.

World Meteorological Organization (WMO), Rep. 25, World Meteorol. Org., Geneva, 1991.

Zapotocny, T. H., D. R. Johnson, F. M. Reames, R. B. Pierce, and B. J. Wolf, J. Atmos. Sci., Vol. 48, 2025-2043, 1991.

1.2.19 "MONASH1" Model

Darryn Waugh (*)
Meteorology CRC, Monash University,
Victoria, Australia
(*) Now at
Department of Earth and Planetary Sciences
Johns Hopkins University
Baltimore MD 21218
Email: waugh@jhu.edu

General Information:

The MONASH1 model is described in Waugh et al. (1997) (see also Hall & Waugh 1997). The model is an off-line chemical transport model based on the model developed at National Center for Atmospheric Research (NCAR) by [Rasch & Williamson 1990] and [Rasch et al. 1994]. The CTM is driven by wind fields from the Middle Atmosphere version of the NCAR Community Climate Model version 2 (MACCM2) [Boville-1995].

Specific Information:

This model uses a semi-Lagrangian transport scheme, which preserves shapes of tracer distributions and minimizes numerical diffusion [Williamson & Rasch 1989]. The scheme is not implicitly mass conservative, and a "mass fixer" is employed after advection to keep global tracer mass constant (see Appendix of [Rasch et al. 1995].

The CTM is driven using 1 year of winds from a MACCM2 simulation with T42 horizontal resolution (128 X 64 longitude by latitude points, giving an approximate horizontal resolution of 2.8 degrees), and there are 44 vertical levels from the surface to p approx 0.01 hPa (80 km). A hybrid vertical co-ordinate system is used, with upper 28 levels (above 100 hPa) at fixed pressure; the vertical resolution in the lower stratosphere is approximately 1.4 km. The climatology of the above configuration of MACCM2 is described by [Boville 1995]. Note that this is not the same MACCM2 dataset used in the GMI-NCAR simulations (see MONASH2 description).

Daily-averaged horizontal winds from MACCM2 are used, and vertical velocities are calculated within the CTM (using continuity). A one hour time step is used. No sub-grid scale parameterizations are used in the model (troposphere and stratosphere).

N_2O simulations use a loss rate look up table, using loss rates from [Garcia & Solomon 1983]. This is the same loss rates as used in the on-line MACCM2 N_2O simulations [e.g., Randel et al. 1994].

References:

Boville, B. A., Middle atmosphere version of the CCM2 (MACCM2): Annual cycle and interannual variability, J. Geophys. Res., 100, 9017-9039, 1995.

Garcia, R. R. and S. Solomon, A numerical model of the zonally averaged dynamical and chemical structure of the middle atmosphere, J. Geophys. Res., 88, 1379-1400, 1983.

Hall, T. M. and D. W. Waugh, Timescales for the stratospheric circulation derived from tracers, J. Geophys. Res., 102, 8991-9001, 1997.

Randel, W.J., et al., Simulation of stratospheric N2O in the NCAR CCM2: Comparison with CLAES data and global budget analysis, J. Atmos. Sci., 51, 2834-2845, 1994.

Rasch, P. J. and D. L. Williamson, On shape-preserving interpolation and semi-Lagrangian transport, SIAM, J. Sci. Stat. Comput., 11, 656-687, 1990.

Rasch, P. J., et al., A three-dimensional transport model for the middle atmosphere, J. Geophys. Res., 99, 999-1017, 1994.

Rasch, P. J., et al., A three-dimensional general circulation model with coupled chemistry for the middle atmosphere, J. Geophys. Res., 100, 9041-9071, 1995.

Waugh, D. W., et al., Three-dimensional simulations of long-lived tracers using winds from MACCM2, J. Geophys. Res., 102, 21493-21513 , 1997.

1.2.20 "MONASH2" Model

Darryn Waugh (*)
Meteorology CRC, Monash University,
Victoria, Australia
(*) Now at
Department of Earth and Planetary Sciences
Johns Hopkins University
Baltimore MD 21218
Email: waugh@jhu.edu

General Information:

The MONASH2 model is the same CTM as used in MONASH1 simulations, but is driven by a wind fields from a different version of the Middle Atmosphere version of the NCAR Community Climate Model version 2 (MACCM2). Results from MONASH2 are shown in Figure 2 of Waugh et al. (1997) and in Hall & Waugh (1998).

Specific Information:

Details are as in MONASH1 description except where mentioned below.

The winds used in MONASH2 come from a MACCM2 simulation with the same vertical grid as that used in MONASH1 but lower horizontal resolution (64 x 64 longitude by latitude points, giving an approximate horizontal resolution of 5.6 x 2.8 degrees). This version of MACCM2 included addition gravity wave parameterisations to that described in [Boville 1995], and used in MONASH1, and has a significantly different circulation. A description of this version of MACCM2 is in preparation (B. Boville, person. comm.)

The MACCM2 dataset used in MONASH2 is the same as used in the GMI-NCAR simulations.

Six-hourly averaged horizontal and vertical winds from MACCM2 are used, with a one hour time step is used. Sub-grid scale parameterizations are used in the troposphere, using parameters for convection and vertical diffusion archived from MACCM2.

References:

Hall, T. M. & Waugh, D. W., The influence of nonlocal chemistry on tracer distributions: Inferring the mean age of air from SF6. J. Geophys. Res, 103, 13327-13336, 1998.

Waugh, D. W., et al., Three-dimensional simulations of long-lived tracers using winds from MACCM2, J. Geophys. Res., 102, 21493-21513 , 1997.

1.2.21 NCAR-3D

Guy Brasseur and Xue Xi Tie
National Center for Atmospheric Research
Boulder, Colorado

The NCAR-3D chemical transport model is global and extends from the surface to the approximate altitude of 80 km. The spatial resolution is 2.8 degrees in latitude and 5.6 degrees in longitude, with 44 levels in the vertical (approximately 13 in the troposphere, 25 in the stratosphere, and 6 in the mesosphere). The timestep used to solve the continuity equations associated with each chemical compound or chemical family is 30 minutes.

The transport of tracers is performed by using the three-dimensional semi-Lagrangian formulation with shape-preserving interpolation of Rasch and Williamson (1991). The meteorological fields used to drive the model are taken from a simulation using the middle atmosphere version of CCM2 (Boville, 1995) that includes an important modification to the gravity wave drag formulation. In this version of CCM2 the momentum deposition by gravity waves is modified to include not only the previous representation of stationary gravity waves which are forced by flow over orography (McFarlane, 1987), but also a background gravity wave source designed to include non-stationary gravity wave arising from other sources (convection, shear, frontal propagation). These modifications have resulted in dramatic improvements to the model circulation in the southern polar region, which were critical to the success of the chemical simulation described here. The chemical-transport model also includes a representation of boundary layer exchanges (Holstag and Boville, 1993) and of convective transport (Hack, 1994), based on the dynamical output of CCM2. As we are focussing here on the distribution of chemical compounds in the stratosphere, the role of these tropospheric processes will not be further discussed in the present study.

The chemical scheme implemented in the model includes 46 species with a representation of 154 chemical and photochemical reactions that affect the oxygen, hydrogen, nitrogen, chlorine, and bromine families in the stratosphere (see e.g., Brasseur and Solomon, 1986). Major constituents (N_2 =78% and O_2=21%) are fixed and the mixing ratio of H2 is prescribed (0.5 ppmv). The distribution of water vapor in the troposphere is taken from the CCM2 simulation, while, in the stratosphere and mesosphere, it is calculated explicitly by the chemical-transport model. Photodissociation frequencies are interpolated from a pre-calculated look-up table as a function of pressure, ozone column abundance, and solar zenith angle. Wash-out of soluble nitrogen and chlorine compounds in the troposphere is crudely parameterized by adding a linear loss process below the tropopause. Heterogeneous processes occurring on the surface of sulfate aerosol particles (which play a considerable role in the lower stratosphere at all latitudes) and of PSC particles (which are of considerable importance in polar regions) are explicitly represented. Surface area densities associated with the presence of background (non volcanic) aerosol are specified as a function of latitude and height (for non volcanic conditions) according to the satellite observations by SAGE (WMO, 1994). In the case of PSC particles, surface area densities are calculated as a function of temperature and water and nitric acid concentrations, using the simple microphysics model developed by Chipperfield et al. (1993). The saturation pressure for type I (nitric acid trihydrate or NAT) and type II (ice) particles is derived from the expression of Hanson and Mauersberger (1988) and of Jansco et al., (1970), respectively. Condensation (evaporation) take place when ambient densities of gas phase nitric acid and water become larger (smaller) than saturation conditions. It is assumed, for the calculation of surface area density, that the effective radii of the particles are 1 um and 10 um for type I and type II PSCs, respectively. Sedimentation velocities for these particles are expressed according to Kasten (1968). In MM2 calculations, only tracer type chemical species (such as NOy etc.) are included in the model.

The chemical transport equations are solved by a splitting operator technique; at each timestep, the mixing ratios of the chemical species are successively updated in the following order: (1) advection by the semi-Lagrangian technique, (2) chemical transformations, (3) mixing accounting for vertical sub-grid transport, and (4) redistribution by convection. Initial conditions for the concentration of chemical compounds are representative of June, and are taken from zonally averaged concentration provided by our 2-D model (Brasseur et al., 1990; Granier and Brasseur, 1992).

References

Boville B., Middle atmosphere version of community climate model 2: Annual cycle and interan nual variability, J. Geophy. Res., 100, 9017-9040, 1995.

Brasseur, G., and P. C. Solomon, Aeronomy of the middle atmosphere, Second Edition, Published by D. Reidel Publishing Company, P. O. Box 17, 3300 AA Dordrecht, Holland, 1986.

Brasseur, G., M. H. Hitchman, S. Walters, M. Dymek, E. Falise, and M. Pirre, An interactive chemical dynamical radiative two-dimensional model of the middle atmosphere, J. Geophys. Res., 95, 5639-5655, 1990.

Chipperfield, M. P., D. Carriolle, P. Simon, R. Ramaroson, and D. J. Lary, A three-dimensional modeling study of trace species in the Arctic lower stratosphere during winter 1989-1990, J. Geo phys. Res., 98, 7199-7218, 1993.

DeMore, W. B., et al., Chemical kinetics and photochemical data for use in stratospheric modeling, JPL Publication 94-26, 1994.

Granier, C. and G. Brasseur, Impact of heterogeneous chemistry on model predictions of ozone changes, J. Geophys. Res., 97, 18015-18033, 1992.

Hack, J. J., B. A. Boville, B. P. Briegleb, J. T. Kiehl, P. J. Rasch, and D. L. Williamson, Description of the NCAR community climate model (CCM2), Tech Note, NCAR/TN-382+STR, 108 pp, Natl. Cent. for Atmos. Res., Boulder, CO, 1993.

Hanson, D. R., A. R. Ravishankara, and S. Solomon, Heterogeneous reactions in sulfuric acid aerosols: A framework for model calculations, J. Geophy. Res., 99, 3615-3629, 1994.

Holtslag, A. A. M., and B. A. Boville, Local versus nonlocal boundary-layer diffusion in a global climate model, J. Clim., 6, 1825-1842, 1993.

Jancso, G., J. Pupezin, and W. A. Van Hook, The vapor pressure of ice between +10-2o and 102o, J. Phys. Chem., 74, 2984-2989, 1970.

Kasten, F., Falling speed of aerosol particles, J. Appl. Meteorol., 7, 944-947, 1968.

McFarlance, N. A., The effect of orographically excited gravity wave drag on the general circulation of lower stratosphere and troposphere, J. Atmos. Sci., 44, 1775-1800, 1988.

Rasch, P.J., and D.L. Williamson, Sensitivity of a general circulation model climate to the moisture transport formulation, J. Geophy. Res., 96, 13123-13137, 1991.

Williamson, D. L., and P. J. Rasch, Two-dimensional semi-Lagrangian transport with shape preserving interpolation, Mon. Wea. Rev., 117, 102-129, 1989.

WMO, Scientific Assessment of ozone depletion: 1991, 1992.

1.2.22 SLIMCAT 3-D Chemical Transport Model

Martyn Chipperfield
University of Cambridge
Cambridge, UK

SLIMCAT is a 3D off-line stratospheric chemical transport model. The model uses an isentropic vertical coordinate and has a lower boundary near 10 km. Horizontal winds and temperatures are specified from meteorological analyses, while the vertical (diabatic) motion is calculated from a radiation scheme within the model. The chemistry and transport (advection) are treated separately using an 'split operator' approach.

Chemistry Mechanism and Solution

The model contains the principal stratospheric chemical species in the Ox, HOx, NOy, Cly, Bry groups, as well as source gases (e.g. N_2O, CH_4, $CFCl_3$, CF_2Cl_2, CH_3Br) and a treatment of CH4 oxidation. The model calculates the full diurnal cycle of chemical species with a timestep of 20 minutes. The model uses a limited number of chemical families for species which are in rapid photochemical equilibrium, and for which the partitioning can be calculated even at night (i.e., N + NO + NO_2; Br + BrO; Cl + ClO + Cl_2O_2; $O(^3P)$ + $O(^1D)$ + O_3). Otherwise, all species are integrated separately, except for H, OH, and HO_2 which are assumed to be in photochemical equilibrium (and are not transported). The chemistry is integrated using the 'Semi-Implicit Symmetric' method of Ramaroson et al. [1992]. Gas phase chemical data is taken from JPL 1997.

For heterogeneous chemistry, the model contains an equilibrium treatment of reactions on liquid sulfuric acid aerosols and on solid nitric acid trihydrate (NAT) and ice particles. The treatment of liquid aerosols requires the H2SO4 loading of atmosphere. This field is specified month-by-month from detailed two-dimensional (latitude-height) time-dependent calculations [Bekki and Pyle, 1994] and advected as a passive tracer. The composition of liquid $H_2O/H_2SO_4/HNO_3$/HCl aerosols is then calculated from the analytical scheme of Carslaw et al. [1995a, b] using this H_2SO_4 field along with the CTM fields of temperature and other chemical species. This scheme also calculates the solubilities of HBr, HOBr, and HOCl.

For NAT PSCs ($HNO_3.3H_2O$) the model mixing ratios of HNO_3, H_2O, and temperature are used with the expression of Hanson and Mauersberger [1988] to predict when they are thermodynamically possible. The available surface area is calculated from the amount of HNO_3 condensed assuming that there are 10 NAT particles cm^{-3}. Ice particles are assumed to form when they are thermodynamically possible. HNO_3 is removed from the gas phase in the presence of ice particles using the equilibrium NAT expression [Hanson and Mauersberger, 1988]. This assumes a NAT coating (as opposed to a liquid coating) to the ice particles. The available surface area is calculated from an estimate of the amount of H_2O which is condensed and assuming that the radius of the ice particles formed is 10 um.

The model has a simple treatment of denitrification and dehydration. When formed, NAT and ice particles are sedimented from the model with fall velocities appropriate for particles of radius 1 and 10 um, respectively. The NAT and ice particles are transported to the model level below where they may evaporate, depending on the ambient temperature.

Details of the chemical rates used in the heterogeneous calculations are given in Chipperfield [1999].

The photolysis rates (J values) are calculated using a scheme based on Lary and Pyle [1991], which in turn was based on Meier et al. [1982] and Nicolet et al. [1982]. The scheme uses a four-dimensional look-up table (which has coordinates of pressure altitude, temperature, O_3 column, and zenith angle) to interpolate precomputed J values to a particular location and time in the atmosphere. The scheme takes account of multiple scattering and spherical geometry and can calculate photolysis rates for zenith angles up to 96 degrees. The J rates are updated every 2 chemical timesteps (i.e. 2 times per hour).

Dynamics

The CTM uses meteorological analyses (or GCM output) to specify the horizontal winds and temperatures. These analyses are read in every meteorological cycle (e.g. every 6 or 24 hours) and averaged from the (higher resolution) analysis grid to the CTM grid.

The standard model uses the MIDRAD radiation scheme [Shine, 1987] to calculate heating rates for the vertical transport in isentropic coordinates. The thermal infrared scheme is as described by Shine [1987] although Curtis matrices are not used and so nonlocal thermodynamic equilibrium (non-LTE) is not accounted for. The solar scheme is that of Shine and Rickaby [1989]. The model radiation scheme employs two dummy levels above and below the actual model domain to account for the rest of the atmosphere. The bottom dummy level extends down to 700 hPa where monthly varying upward longwave fluxes are specified. The model-calculated O_3 field can be used interactively with MIDRAD (as in the simulations described below) allowing a degree of coupling between the model chemistry and transport, otherwise a monthly varying climatological field is used.

The SLIMCAT CTM contains a range of tracer advection schemes. In the standard model (used here) the chemical tracers are advected using the second-order moments scheme of Prather [1986]. This scheme has low numerical diffusion and performs well in maintaining strong gradients. This is particularly useful at the low model resolutions.

The simulations used in this report used a horizontal resolution of 7.5 x 7.5 (T15 Gaussian grid) and were run on 12 isentropic levels from 335 to 2700 K. The vertical resolution in the lower stratosphere was about 3 km. The runs were forced using the U.K. Meteorological Office (UKMO) Analyses [Swinbank and O'Neill, 1994] for the year 1992. The model's dynamical time step was 60 min.

References

Bekki, S., and J.A. Pyle, A two-dimensional modeling study of the volcanic eruption of Mount Pinatubo, *J. Geophys. Res., 99,* 18,861-18,869, 1994.

Carslaw, K., B. Luo, and T. Peter, An analytic expression for the composition of aqueous HNO_3-H_2SO_4 stratospheric aerosols including gas phase removal of HNO3, *Geophys. Res. Lett., 22,* 1877-1880, 1995a.

Carslaw, K.S., S.L. Clegg, and P. Brimblecome, A thermodynamic model of the system HCl-HNO_3-H_2SO_4-H_2O, including solubilities of HBr, from <200 K to 328 K, *J. Phys. Chem., 99,* 11,557-11,574, 1995b.

Chipperfield, M.P., Multiannual Simulations with a Three-Dimensional Chemical Transport Model, *J. Geophys. Res., 104,* 1781-1805, 1999.

Hanson, D., and K. Mauersberger, Laboratory studies of the nitric acid trihydrate: Implications for the south polar stratosphere, *Geophys. Res. Lett., 15,* 855-858, 1988.

Lary, D.J., and J.A. Pyle, Diffuse radiation, twilight and photochemistry, *J. Atmos. Chem., 13,* 373-392, 1991.

Meier, R.R., D.E. Anderson, and M. Nicolet, Radiation field in the troposphere and stratosphere from 240-1000 nm, I, General analysis, *Planet. Space Sci., 30,* 923-933, 1982.

Nicolet, M., R.R. Meier, and D.E. Anderson, Radiation field in the troposphere and stratosphere from 240-1000 nm, I, Numerical analysis, *Planet. Space Sci., 30,* 935-983, 1982.

Prather, M.J., Numerical advection by conservation of second-order moments, *J. Geophys. Res., 91,* 6671-6681, 1986.

Ramaroson, R., M. Pirre and D. Cariolle, A box model for on-line computations of diurnal variations in a 1D model: Potential for application to multidimensional cases, *Ann. Geophysicae., 10,* 416-428, 1992.

Shine, K.P., The middle atmosphere in the absence of dynamical heat fluxes, *Q. J. R. Meteorol. Soc., 113,* 603-633, 1987.

Shine, K.P., and J.A. Rickaby, Solar radiative heating due to absorption by ozone, in Proceedings of Quadrennial Ozone Symposium, Gottingen, pp 597-600, A. Deepak, Hampton, Va., 1989.

Swinbank, R., and A. O'Neill, A stratosphere-troposphere data assimilation system, *Mon. Weather Rev., 122,* 686-702, 1994a.

1.2.23 UCI23 Chemistry Transport Model

Michael Prather, Xin Zhu, Bryan Hannegan
Department of Earth System Science, University of California, Irvine
220 Rowland Hall, Irvine, CA, 92697-3100
(email: mprather@uci.edu, xzhu@uci.edu, bjhanneg@uci.edu)

General Information:

The "UCI23" chemistry transport model is the latest in a generation of CTMs developed by Michael Prather and used at UCI and the Goddard Institute for Space Studies (GISS). Previous versions of the CTM have been used in studies of stratospheric trace gases over the past decade, including the fate of meteoritic metals (Prather and Rodriguez, 1988), correlations between N_2O and several long-lived trace gases, including halocarbons (Hall and Prather, 1995; Avallone and Prather, 1997), and previous intercomparison projects and assessment studies (MMI, WCRP, IPCC).

Meteorological Input:

UCI23 is an offline chemistry transport model which uses meteorological fields from the new GISS general circulation middle-atmosphere model II' described in Koch and Rind (1998; see also documentation in Rind and Lerner, 1996). Meteorological data are saved every 6 hours as a combination of instantaneous and averaged quantities.

Grid/Resolution:

UCI23 has a horizontal resolution of 4 degrees latitude by 5 degrees longitude, with 2 degree latitude boxes at each pole. This yields 72 longitudinal grid points and 46 latitudinal grid points, centered as follows:

J	Latitude	J	Latitude	J	Latitude	J	Latitude
1	-89	13	-42	25	6	37	54
2	-86	14	-38	26	10	38	58
3	-82	15	-34	27	14	39	62
4	-78	16	-30	28	18	40	66
5	-74	17	-26	29	22	41	70
6	-70	18	-22	30	26	42	74
7	-66	19	-18	31	30	43	78
8	-62	20	-14	32	34	44	82
9	-58	21	-10	33	38	45	86
10	-54	22	-6	34	42	46	89
11	-50	23	-2	35	46		
12	-46	24	2	36	50		

The model has 23 vertical layers extending from the surface to 90km (0.002 mbar), using a hybrid sigma coordinate system with fixed pressure levels above 150 mbar. Pressure at the lower edge of each vertical level is given by the expression $p = \eta_a + (\eta_b * psfc)$.

L	η_a	η_b	L	η_a = p(mbar)
1	.0000000	1.0000000	12	150.0000000
2	4.3165505	.9712230	13	116.9999994
3	9.8920763	.9340528	14	86.1999954
4	17.9856151	.8800959	15	56.2000005
5	29.6762556	.8021583	16	31.5999954
6	49.2805839	.6714628	17	17.8000009
7	74.4604290	.5035971	18	9.9999991
8	100.5395696	.3297362	19	5.6200021
9	120.5035977	.1966427	20	3.1600022
10	132.9136692	.1139089	21	1.7799953
11	142.4460433	.0503597	22	1.0000038
			23	.5619941
			TOP	.0020576

Physics

UCI23 uses the UC Irvine transport shell (Prather et al., 1987; Jacob et al., 1997) as its numerical advection scheme, with an advective timestep of 6 hours. Advective mass fluxes are provided from the GCM, and a quadratic upstream numerical method is used for advection, utilizing the mean, first, and second moments of the species distribution in each grid cell to ensure numerical stability and mass conservation.

No explicit diffusion is included in either the troposphere or stratosphere. In each column, the planetary boundary layer is completely mixed up to the PBL height given in the GCM data. Archived convective mass fluxes allow for transport of trace species via wet and dry convection in the troposphere.

Removal of species can occur via wet deposition (a specified fraction of species mass is removed from the updraft), or dry deposition (a specified deposition velocity is applied to the lowest model layer).

Chemistry

Linearized stratospheric chemistry is parameterized using look-up production and loss tables from the PRATMO photochemical box model (Remsberg and Prather, 1993). Mean SBUV ozone and NCEP temperature climatologies are used to determine photochemical production and loss rates for species as a function of time, latitude, and altitude. No heterogeneous chemistry is included, nor are aerosol physics.

References

Avallone, L.M. and M.J. Prather, Tracer-tracer correlations: Three-dimensional model simulations and comparisons to observations, J. Geophys. Res., 102, 19233-19246, 1997.

Hall, T.M. and M.J. Prather, Seasonal evolutions of N_2O, O_3 and CO_2: Three-dimensional simulations of stratospheric correlations, J. Geophys. Res., 100, 16699-16720, 1995.

Jacob, D.J. et al., Evaluation and intercomparison of global atmospheric transport models using 222Rn and other short-lived tracers, J. Geophys. Res., 102, 5953-5970, 1997.

Koch, D., and D. Rind, 10Be/7Be as a tracer of stratospheric transport, J. Geophys. Res., 103, 3907-3917, 1998.

Prather, M.J., Numerical advection by conservation of second-order moments, J. Geophys. Res., 91, 6671-6681, 1986.

Prather, M.J. and J.M. Rodriguez, Antarctic ozone: meteoritic control of HNO_3, Geophys. Res. Lett., 15, 1-4, 1988.

Remsberg, E.E. and M.J. Prather, eds., The atmospheric effects of stratospheric aircraft: Report of the 1992 models and measurements workshop, NASA Ref. Publ. 1292, 1993.

Rind, D. and J. Lerner, Use of on-line tracers as a diagnostic tool in general circulation model development, 1, Horizontal and vertical transport in the troposphere, J. Geophys. Res., 101, 12667-12675, 1996.

1.2.24 UIUC-3D Model

E. V. Rozanov, M. E. Schlesinger, F. Yang, and N. Andronova

Climate Research Group, Department of Atmospheric Sciences
University of Illinois at Urbana-Champaign
105 S. Gregory Street
Urbana, Illinois 61801

V. A. Zubov

A. I. Voeikov Main Geophysical Observatory
7 Karbyshev Street
St. Petersburg, 194021, Russia

General Information

The UIUC 3-D photochemical transport model participated in the M&M II. References to the model formulation are listed near the end of this document.

Domain and Grid Sizes

The UIUC 3-D model domain extends from the South Pole to the North Pole and from the ground to approximately 50 km (1 mb). The horizontal resolution of the model is 4° latitude x 5° longitude, and in the vertical direction the model uses sigma coordinate with sigma = 1 at the earth's surface and sigma = 0 at the top of the model:

$$\sigma = \frac{p - p_{top}}{p_s - p_{top}},$$

where p is atmospheric pressure in mb, p top = 1 mb is the pressure at the top of the model, and p_s is the atmospheric pressure at the surface. For the calculation of sigma values, the pressures at the half-integer levels above 100 mbar were set as follow:

$$p_{k+1/2} = p_{k-1/2} e^{d},$$

where $d = \ln(p_{10+1/2}) - \ln(p_{top})$ and $p_{10+1/2} = 100$ mb. The 14 pressure values below 100 mb are prescribed at 150, 200, 250, 350, 450, 550, 650, 750, 850 and 1000 mb.

Transport and Temperature

For the description of vertical transport in the troposphere, the eddy diffusion approach, with $K_{zz} = 0.1\ m^2 s^{-1}$, has been used to enable vertical mixing of tropospheric air. The transport of species in the stratosphere is purely advective and we did not use any parameterization for horizontal diffusion. The velocity, temperature and tropospheric water vapor mixing ratio required by the ACTM have been taken from a simulation by our 24-layer stratosphere/troposphere general circulation model (Yang and Schlesinger, 1998). These prescribed fields vary with latitude, longitude, altitude and time, and they are

redefined every day at midnight UTS. The monthly mean 3-D fields of trace-gas mixing ratios are stored for each month of the simulation. Trace-gas mixing ratios are also stored for 12 UTS at the middle of each month to analyze the instantaneous geographical distributions of the species.

Photochemistry

The current version of the photochemical routine (Rozanov et al., 1998a,b) takes into account 28 species of the oxygen, nitrogen, hydrogen, carbon and chlorine cycles with O_3, $O(^3P)$, NO, NO_2, N_2O_5, HNO_3, HNO_4, N_2O, H_2O_2, H_2O, H_2, HCl, HOCl, $ClNO_3$, Cl_2, Cl_2O_2, F-11, F-12, CO, and CH_4 being transported. It describes the main chemical processes responsible for the production and destruction of ozone in the stratosphere. The photochemical routine includes more than 100 gas-phase reactions (DeMore et al., 1997) and 4 heterogeneous reactions on the surface of sulfate aerosol and polar stratospheric clouds (PSC) particles, as well as a simple thermodynamic scheme for PSC diagnosis.

The core of the photochemical module is a specially designed Generator of Chemical Routines (GCR) which is based on non-numerical algorithms. The GCR was designed to: (i) process the photochemical reaction set, (ii) determine the set of independent variables, and (iii) create the FORTRAN code that performs the photochemical calculations in the model.

The implicit numerical scheme proposed for atmospheric chemistry by Ozolin (1992) and Stott and Harwood (1993) and the backward implicit Eulerian scheme are applied to solve the photochemical equation set. For long-lived species, such as CH_4 and N_2O, a simple explicit scheme is used instead of the reference implicit scheme. For some of the short-lived species, such as $O(^1D)$ and OH, the steady-state approximation is applied. For the other gases the reference Newton-Raphson scheme has been changed by simplifying the iterative routine such that, during 'quiet periods' when the changes of gas concentrations are small, the maximum number of iterations is limited.

Photodissociation rates are parameterized as functions of O_2 and O_3 amounts. To take the multiple scattering in the atmosphere into account, dissociation rates are calculated using the full scheme described by Rozanov et al., (1998a) as $J_x q_x$, where q_x is the concentration of molecule x and J_x represents the coefficient or probability of photodissociation,

$$j_x(z, \theta) = \int_{\lambda_1}^{\lambda_2} \varepsilon_x(\lambda)\sigma_x(\lambda)s_\lambda(z, \theta)d\lambda,$$

where (λ_1,λ_2) is the spectral region where molecule x can be dissociated, $s_\lambda(z, \theta)d\lambda$ is the photon flux at altitude z and zenith angle θ, $\sigma_x(\lambda)$ is the absorption cross-section in cm^2, and $\varepsilon_x(\lambda)$ represents the quantum yield or efficiency. To compute the photodissociation rates, the spectral interval from 175 nm to 750 nm is divided into 61 subintervals with a resolution of about 5 nm in the shortwave part (from 175 to 400 nm) and a lower resolution in the visible part. Cross-sections and quantum yields are taken from DeMore et al. (1997). Allen and Frederic's (1982) parameterization scheme is used for O_2 and NO in the Schumann-Runge region. Oxygen and ozone amounts are calculated for all model grid cells, with their photodissociation rates being determined by bilinear interpolation of tabulated precalculated photodissociation rate vectors. The accuracy of this parameterization has been examined (Schlesinger, 1976) for oxygen and ozone photodissociation. It was found that the error for ozone dissociation with production of atomic oxygen does not exceed 20%. Further examination indicates that with modifications that partially include multiple scattering in the atmosphere, the error does not exceed 15%.

The following heterogeneous reactions on sulfate and PSC particles are included in the model:

1. $N_2O_5 + H_2O = HNO_3 + HNO_3$
2. $ClNO_3 + H_2O = HOCl + HNO_3$
3. $ClNO_3 + HCl = Cl_2 + HNO_3$
4. $HOCl + HCl = Cl_2 + H_2O$

The heterogeneous reaction probabilities for PSC I & II are calculated according to DeMore et al. (1997) and for sulfates according to the state-of-the-art parameterization by Hanson et al. (1994). The diagnostic thermodynamic scheme for predicting PSC events has been incorporated following Hanson and Maursberger (1988) and Müller and Crutzen (1993).

Time Steps and Transport Scheme

The ACT model is integrated with a 2-hour time step for the chemistry and transport calculations. A hybrid transport (HT) model (Zubov et al., 1996, 1997, 1998) has been developed for the advective transport calculations. The HT model is a combination of the Prather scheme (Prather, 1986), which is used in the vertical direction, and a semi-Lagrangian (SL) scheme, which is used for horizontal advection on a sphere (Williamson and Rasch, 1989). The use of the SL scheme for the horizontal transport allows a significantly larger time step, and smaller dependence on any increase of horizontal resolution, than would use of the Prather scheme. Furthermore, use of the Prather scheme for transport in only a single direction (vertical) instead of three directions reduces from 10 to 3 the number of moments that define the distribution of species in each model grid box. Moreover, combination of the SL scheme with the Prather scheme yields a significant economy in the transport calculation compared to using the Prather scheme alone, but attains an accuracy higher than that of the semi-Lagrangian scheme alone.

In the present version of the model the lower boundary conditions for source gases (N_2O, CFC-11, and CFC-12) are prescribed as fixed zonally homogeneous, seasonally independent mixing ratios based on the observational data for 1995 (Hofman and Peterson, 1996). The surface mixing ratio of CFC's is scaled by a factor of 1.8 to account for other sources of active chlorine. The CO_2 mixing ratio is set equal 335 ppmv everywhere. Tropospheric water vapor is taken from the UIUC 24-layer AGCM. The initial mixing ratio fields for other species in the model were taken mainly from a 10-year steady-state run of our 2-D model (Zubov et al., 1995), except water vapor, N_2O and methane in the stratosphere whose zonal-mean distributions for January were taken from the UARS dataset (Park et al., 1996; Roche et al., 1996). The annual cycle of the surface source of CO and NOx, and the NOx source from lightning are prescribed according to RIVM datasets (Müller and Brasseur, 1995; Olivier et al., 1996). The subsonic aircraft source of NOx is prescribed from a NASA dataset and the latitudinal distribution of the surface mixing ratios of the source gas CH_4 is set according to the published data for 1995 (Hein and Crutzen, 1997; Hofmann and Peterson, 1996).

References

Allen, M., and J. E. Frederick, Effective photodissociation cross section for molecular oxygen and nitric oxide in the Schumann-Runge bands, J. Atmos. Sci., 39, 2066-20 75, 1982.

DeMore, W., et al., Chemical kinetics and photochemical data for use in stratospheric modeling, in Evaluation 12, NASA Jet Propulsion Laboratory, Pasadena, California, 1997.

Hanson, D., A. Ravishankara, and S. Solomon, Heterogeneous reactions in sulfuric acid aerosols: A framework for model calculations, J. Geophys. Res., 99 (D2), 3615-3629, 1994.

Hanson, D., and K. Maursberger, Laboratory studies of the nitric acid trihydrate: Implications for the south polar stratosphere, Geophys. Res. Lettr., 15, 855-858, 1988.

Hein, R., and P. J. Crutzen, An inverse modeling approach to investigate the global atmospheric methane cycle, Global Biogeochemical Cycles, 11 (1), 43-76, 1997.

Hofman, D. J., and J. T. Peterson (Eds.), Climate Monitoring and Diagnostics Laboratory, No. 23, Summary Report 1994-1995, pp. 161, NOAA Environmental Research Laboratories, Boulder, CO, 1996.

Müller, R., and P. Crutzen, A possible role of galactic cosmic rays in chlorine activation during polar night, J. Geophys. Res., 98 (D20), 20,483-20,490, 1993.

Muller, J.-F., and G. Brasseur (1995): IMAGES: A three-dimensional chemical transport model of the global troposphere, J. Geophys. Res., 100, 16,445-16,490.

Olivier, J. G. J., et al., (1996): Description of EDGAR version 2.0: A set of global emission inventories of greenhouse gases and ozone depleting substances for all anthropogenic and most natural sources on a country bases on 1x1° grid, RIVM rep 771060002/TNO MEP rep R96/119, Natl. Inst. for Public Health and Environ., Bilthoven, the Netherlands, 1996.

Ozolin, Y. E., Modelling of diurnal variations of gas species in the atmosphere and diurnal averaging in photochemical models, Izv. RAN, PAO, 28 (12), 135- 143, 1992.

Roche, A. E., J. B. Kummer, R. W. Nightingale, J. L. Mergenthaler, G. A. Ely, P. L. Bailey, S. T. Massie, J. C. Gille, D. P. Edwards, M. R. Gunson, M. C. Abrams, G. C. Toon, C. R. Webster, W. A. Traub, K. W. Jucks, D. G. Johnston, D. G. Murcray, F. H. Murcray, A. Goldman, and E. C. Zipf, Validation of CH_4 and N_2O measurements by the cryogenic limb array Etalon spectrometer instrument on the Upper Atmosphere Research Satellite, J. Geophys. Res., 101, 9679-9710, 1996.

Rozanov, E., V. Zubov, M. Schlesinger, F. Yang and N. Andronova (1998a), Simulation of trace-gas distributions with the UIUC 3-D atmospheric chemical transport model: Model description and comparison of the source-gas distributions with observations. J. Geophys. Res., (submitted).

Rozanov, E., V. Zubov, M. Schlesinger, F. Yang and N. Andronova (1998b), Three-Dimensional Simulations of Ozone in the Stratosphere and Comparison with UARS Data, submitted to Physics and Chemistry of the Earth.

Park, J. H., J. M. Russell III, L. L. Gordley, S. R. Drayson, D. C. Benner, J. M. McInerney, M. R. Gunson, G. C. Toon, B. Sen, J.-F. Blavier, C. R. Webster, E. C. Zipf, P. Erdman, U. Schmidt, and C. Shiller, Validation of Halogen Occultation Experiment CH_4 measurements from UARS, J. Geophys. Res., 101, 10,183-10,203, 1996.

Prather, M. J., Numerical advection by conservation of second-order moments, J. Geophys., Res., 91, 6671-6681, 1986.

Schlesinger, M. E., A numerical investigation of the general circulation of atmospheric ozone, 376 pp., Ph.D. Dissertation thesis, University of California, Los Angeles, Los Angeles, 1976.

Stott, P. A., and R. S. Harwood, An implicit time-stepping scheme for chemical species in a global atmospheric circulation model, Ann. Geophys., 11, 377 - 388, 1993.

Williamson, D. L., and P. J. Rasch, Two-dimensional semi-Lagrangian transport with shape-preserving interpolation, Mon. Wea. Rev., 117, 102-129, 1989.

Yang, F., and M. E. Schlesinger, Description and performance of the UIUC 24-layer stratosphere/troposphere general circulation model, J. Climate, (to be submitted), 1998.

Zubov, V. A., I. L. Karol, Y. E. Ozolin, and E. V. Rozanov, The zonally averaged model of the photochemical, radiative and dynamical processes in the troposphere and stratosphere. Part 1: The description of the model and model validation, Izvestiya RAN Physics of Atmosphere and Ocean, 31 (N4), 469-476, 1995.

Zubov, V. A., E. V. Rozanov, and M. E. Schlesinger, Hybrid scheme for 3-dimensional advective transport, Mon. Wea. Rev. (in press), 1998.

Zubov, V., E. Rozanov, M. Schlesinger, and N. Andronova, Hybrid Scheme for 3-dimensional Transport of Chemical Species, Proceedings of the First SPARC General Assembly, WCRP-99, WMO-TD-No. 814, 1997, 421-424.

Zubov, V., E. Rozanov, M. Schlesinger, and N. Andronova, Hybrid advection scheme for 3-dimensional atmospheric models: testing and application for a study of NOx transport, Proceedings of International Colloquium "Impact of Aircraft emissions upon the Atmosphere", Paris, France, 1996, Oct. 15-18, v. II, pp. 647-652.

1.2.25 UNIVAQ-3D Photochemical Transport Model

Giovanni Pitari, Barbara Grassi, Guido Visconti
Universita' degli Studi L'Aquila
via Vetoio, 67010 Coppito L'Aquila, Italy
(email: gianni.pitari@aquila.infn.it)

The University of L'Aquila (Italy) three-dimensional model ('univaq-3d') is a 3D photochemical-transport model using a horizontal grid of 19 points in latitude and 16 in longitude (10 and 22.5 degrees resolution, respectively) and extending from the ground to about 71 Km altitude with 26 log-pressure levels correspondent to an approximate altitude resolution of 2.84 Km, for a total of 19x16x26 grid-points. The pressure levels are specified as p(j)=p(j-1)/1.5, with p(0)=1000 hPa. The main features of this model have been described in Pitari et al. (1997).

All transport fields are taken off-line and are not interactive. The advective transport is formulated in flux form with the horizontal velocity fields u,v calculated in terms of a velocity stream-function and a velocity potential, both taken from the daily output of a low-resolution spectral GCM (Pitari et al., 1992). The vertical velocity w is calculated from the mass continuity equation.

A small horizontal diffusion (1.E05 m^2/s) is used for numerical stability purposes, while a vertical diffusion coefficient K_{zz} is used for simulate those transport processes not explicitly included in the model (i.e. tropospheric convection and mesospheric gravity wave breaking). K_{zz} is assigned with large tropospheric values (10-30 m^2/s) decreasing to about 0.1-0.3 m^2/s in the lower stratosphere. The effect of gravity wave breaking is simulated by increasing K_{zz} in the upper stratosphere and mesosphere.

The zonally-averaged temperature field is taken from time-zonally averaged NMC data, while the eddy deviations are taken from the output of the GCM.

The numerical advection scheme is Eulerian fully explicit, with a four-cycle time integration scheme using a 1.0 hour time increment (Lorenz, 1971).

All chemical species interact explicitly in the model and are diurnally-averaged. Diurnal variations are parameterized using the scheme described in Brasseur and Solomon (1984) for N_2O_5 and assuming that a number of species are only present during daytime (O,O(^{1}D),H,OH,HO_2,NO,Cl,ClO,Br,BrO). The 24-hr averaged photodissociation rates are calculated daily (i.e. every 24 model hours) and include the effects of Rayleigh and Mie scattering.

All medium and short-lived chemical species are grouped in families:

Ox, NOy=NOx+HNO_3, NOx, HOx, CHOx, Cly, Bry, SOx, aerosols.

The chemical species in the families are the following:

Ox: O(^{1}D),O,O_3
NOx: NO,NO_2,NO_3,N_2O_5,HNO_4,$ClONO_2$,$BrONO_2$,PAN
HOx: H,OH,HO_2,H_2O_2
CHOx: CH_3O_2,CH_3OOH,CH_2O,
CH_3CHO,CH_3CO_3,CH_3COOOH,$C_2H_5O_2$,C_2H_5OOH,
$C_3H_6OHO_2$,C_3H_6OHOOH,$C_5H_8OHO_2$
Cly: Cl,ClO,ClOOCl,HOCl,$ClONO_2$,HCl

Bry: Br,BrO,HOBr,$BrONO_2$,HBr
SOx: SO_2,H_2SO_4
Aerosols: Aitken-nuclei, Sulfate, NAT, Ice.

Long-lived and surface-flux species are the following:

N_2O,H_2O,CH_4,CO,
C_2H_6,C_2H_4,C_3H_6,C_5H_8,$C_{10}H_{16}$,other hydrocarbons,
CF_2Cl_2,$CFCl_3$,CCl_4,CH_3CCl_3,CFC-113,CH_3Cl,HCFC-22,
CH_3Br,Halon-1211,Halon-1301,
OCS,CS_2,DMS,H_2S.

In total there are 40 transported species and families plus aerosol particles (44 size categories in total) and 26 species calculated at photochemical equilibrium. The chemical solver has been developed independently. All photochemical data are taken from JPL (1997).

Photochemical equilibrium applies to HOx, CHOx species and in the partition of NOx, Ox, Cly, Bry families:

H, OH, HO_2, CH_3O_2, CH_3OOH, CH_2O, $C_2H_5O_2$, C_2H_5OOH, CH_3CHO, CH_3CO_3,
CH_3COOOH, $C_3H_6OHO_2$, C_3H_6OHOOH, $C_5H_8OHO_2$,
NO, NO_2, NO_3, O, O(^{1}D), Cl, ClO, Cl_2O_2, Br, BrO, $BrONO_2$, HOBr

The heterogeneous reactions included in the model are the following:

$N_2O_5 + H_2O \rightarrow 2HNO_3$
$ClONO_2 + H_2O \rightarrow HOCl + HNO_3$
$ClONO_2 + HCl \rightarrow Cl_2 + HNO_3$
$HOCl + HCl \rightarrow Cl_2 + H_2O$
$BrONO_2 + H_2O \rightarrow HOBr + HNO_3$
$N_2O_5 + HCl \rightarrow ClNO_2 + HNO_3$

Heterogeneous reaction rates are calculated as first-order loss rates proportional to particle surface area (see JPL-97). On sulfate aerosols, reaction 1 uses a constant γ of 0.1, while reactions 2-4 follow Hanson et al. (1994). Reaction 5 follows follows Hanson et al. (1996). Reaction 6 applies only to PSCs.

The size distribution of both sulfate and PSC aerosols (NAT + ice) may be calculated using an interactive and mass conserving microphysical code for aerosol formation and growth. Denitrification and dehydration due to PSC sedimentation are calculated explicitly from the NAT and ice aerosol size distribution.

The microphysics code includes homogeneous/heterogeneous nucleation, condensation/evaporation, coagulation, sedimentation, rainout. The microphysics code is fully interactive with the CTM. Particles are resolved in 15 size bins ranging from 0.31 nm to 10 um in radius by doubling the particle radius. Each aerosol size bin is transported separately, for a total of 44 aerosol size categories including Aitken, sulfate and PSC particles. Tropospheric washout applies to all aerosol particles and also to SO_2 and H_2SO_4. Calculated sulfate and PSC surface area density fields can be used in the CTM to calculate rates of heterogeneous reactions. For M&M II exercises sulfate surface area density was specified.

References

Brasseur, G. and S. Solomon: Aeronomy of the Middle Atmosphere, D. Reidel, 1984.

JPL: Chemical Kinetics and Photochemical Data for Use in Stratospheric Modeling, JPL publ. 97-4, 1997.

Hanson, D.R., A.R. Ravishankara, and S. Solomon, Heterogeneous reactions in sulfuric acid aerosols: A framework for model calculations, *J. Geophys. Res., 99,* 3615-3629, 1994.

Hanson, D.R., A.R. Ravishankara, and E.R. Lovejoy, Reactions of $BrONO_2$ with H_2O on submicron sulfuric acid aerosol and the implications for the lower stratosphere, *J. Geophys. Res., 101,* 9063-9069, 1996.

Lorenz, E.: An N-Cycle Time Differencing Scheme for Stepwise Numerical Integration, *Mon. Weather Rev., 99,* 644-648, 1971.

Pitari, G., S. Palermi, G. Visconti and R.G. Prinn: Ozone Response to a CO2 Doubling: Results From a Stratospheric Circulation Model With Heterogeneous Chemistry, *J. Geophys. Res., 97,* 5953-5962, 1992.

Pitari, G., B. Grassi, and G. Visconti: Results of a Chemical-Transport Model with Interactive Aerosol Microphysics, R.D. Bojkov and G. Visconti Eds., **XVIII O3symp Proc.**, 759, 1997.

2. Transport Experiments

Timothy M. Hall,[1] Donald J. Wuebbles,[2] Kristie A. Boering,[3] Richard S. Eckman,[4] Jean Lerner,[1]
R. Alan Plumb,[5] David H. Rind,[1] Curtis P. Rinsland,[4] Darryn W. Waugh,[6] Chu-feng Wei[7]

1. NASA Goddard Institute for Space Studies
2. University of Illinois
3. University of California-Berkley
4. NASA Langley Research Center
5. Massachusetts Institute of Technology
6. Johns Hopkins University

Note on Authorship

All of the authors are responsible for this chapter, which has been written as a single document rather than separately authored sections. However, we have listed at the beginning of each section and subsection an author or authors to whom comments and questions are most conveniently addressed.

Table of Contents

2.1 Executive Summary (Hall)

MM2 defined a series of experiments to better understand and characterize model transport and to assess the realism of this transport by comparison to observations. Measurements from aircraft, balloon, and satellite, not yet available at the time of MM1 [Prather and Remsberg, 1993], provide new and stringent constraints on model transport, and address the limits of our transport modeling abilities. Simulations of the idealized tracers the age spectrum, and propagating boundary conditions, and conserved HSCT-like emissions probe the relative roles of different model transport mechanisms, while simulations of SF_6 and CO_2 make the connection to observations. Some of the tracers are related, and transport diagnostics such as the mean age can be derived from more than one of the experiments for comparison to observations.

We draw several general conclusions:

(1) There is large variation in transport among models, producing fields of mean age that vary by more than a factor 2, and fields of "ΔNOy" (conserved HSCT emission tracer) that vary by more than a factor 4. These variations are evident both locally and globally.

(2) Model-to-model variations in mean age are reflected, although reduced, in simulations of long-lived photochemically active species, such as N_2O, NOy and Cly. This suggests that uncertainty in model transport is a major factor determining uncertainty in the background chemical state of model stratospheres, and limits our ability to assess the environmental impact of HSCT fleets.

(3) Nearly all models have mean age magnitudes too small throughout the lower and middle stratosphere compared to observations, in some models and locations by a factor greater than 2.

(4) Most models have one of several unrealistic features in the shapes of their zonal-averaged mean age contour shapes.

In addition, a number of more specific conclusions may be made:

(5) Some 2D models have too large explicit vertical diffusion (too large K_{zz}).

(6) 2D models that compute planetary wave propagation and breaking interactively with the circulation have small quasi-horizontal mixing in the midlatitude stratosphere (small K_{yy}) compared to other 2D models. This may be responsible for these models' tendency to have a lower stratosphere high latitude mean age maximum, which is not observed.

(7) The vertical phase velocity in the tropics of an annual cycle tracer such as H_2O+2CH_4 is too rapid for most models, indicating either too rapid vertical advection in the tropics, too much vertical diffusion, or both.

(8) Many models have tropics that are not isolated enough, as seen in the overattenuation per wavelength of the annual cycle and in the unrealistically "flat" mean age contours. For some models vertical diffusion within the tropics may be responsible for the overattenuation.

(9) A positive correlation exists across models between mean age and ΔNOy tracer in the lower midlatitude stratosphere. Given (3) above, this suggests that most models underestimate the stratospheric residence time of HSCT emissions. This relationship needs to be explored further, however, before conclusions may be drawn from it.

We have not systematically examined the impact on long-lived tracer transport of numerical aspects of model formulation such as advection algorithm, grid resolution, and coordinate system. Such a study would be worthwhile. Nonetheless, some conclusions can be drawn with regards to certain models. The mean age distributions are similar for the three-dimensional models MONASH2 and GMI-NCAR, which differ only in their advection algorithm. On the other hand, models having the same advection algorithm, resolution, and other aspects of numerical formulation, but differing in their large scale circulation (e.g., MONASH1 and MONASH2), have significant mean age differences. This suggests that the choice of advection algorithm plays only a minor role in long-lived tracer transport for at least some of the models. As for model resolution, increasing the horizontal grid resolution in one model tested (LARC) resulted in only a small increase of stratospheric residence time of the HSCT emission tracer compared to the variation across models. However, simulations of long-lived tracers by other models, for example those models having lower resolution, may be more sensitive to numerical formulation.

It is important to appreciate that components of transport, such as advection by the residual circulation and mixing of extratropical air into the tropics, are highly coupled. The coupling is dynamical for models that compute the circulation in a self-consistent way. However, even for models that prescribe the components explicitly, their effects on tracers are not separable. For example, slowing the residual

circulation and enhancing the mixing of extratropical air into the tropics both increase the magnitude of mean age in models, which is desirable. However, changing either of these transport components independently (which may not even be possible in dynamically self-consistent models) could have detrimental effects on other characteristics of tracer distributions. The tropical stratosphere would be less isolated, when it is already not isolated enough for many models, as seen in mean age and N_2O contour shapes. In addition, slowing tropical upwelling would increase the global photochemical lifetimes of N_2O and certain CFCs, which models already overestimate (see section C-2).

2.2 Introduction (Hall and Wuebbles)

A series of experiments have been designed to evaluate the treatment of stratospheric transport processes within current two-dimensional (2D) and three-dimensional (3D) models used to study the chemistry and physics of the troposphere and stratosphere. These experiments are designed to examine model performance against observations and also to evaluate model-to-model differences. As shown in this chapter, the current treatment of transport by models causes large differences in the distributions of inert and chemically long-lived tracers among models and between models and observations.

The goals of the transport experiments are:

(1) To isolate the effects of transport in models from other processes;

(2) To assess model transport for realistic tracers (such as SF_6 and CO_2) for comparison to observations;

(3) To use certain idealized tracers to isolate model mechanisms and relationships to atmospheric chemical perturbations;

(4) To identify strengths and weaknesses of the treatment of transport processes in the models;

(5) To relate evaluated shortcomings to aspects of model formulation.

Each of the participating models was asked to provide analysis for the following six transport experiments (see the section of run specifications for detailed definitions):

(A1) The "age spectrum," the stratospheric response to an approximate delta function time-dependent mixing ratio boundary condition in the tropical troposphere near the surface.

(A2) Tropical troposphere and time-dependent mixing ratio boundary condition near the surface.

(A3) Inert tracer representing NOx emissions from 500 HSCTs. Source distribution provided by NASA database. Zero boundary condition below 6 km in troposphere. Models run to steady-state. The resulting distributions are referred to here as "ΔNOy."

(A4) As in (A3), but no emissions south of 30°N.

(A5) Simulated SF_6 concentrations from 1966 to 2000. Time-dependent surface flux boundary condition specified.

(A6) Simulated CO_2 concentrations from 1979 to 1995. Time and latitude-dependent surface mixing ratio boundary condition specified, based on observations.

The model participating in the transport experiments are given in Table 2.1. In total, 24 different models are represented, although in a number of cases different versions of the same basic model are

counted separately (e.g., NCAR-3D, MONASH1, MONASH2, and GMI-NCAR; GISS 4x5, UCI23, and GMI-GISS; GSFC-3D and GMI-DAO). This interdependence of 3D models means there are fewer wind data sets and numerical methods employed than there are models listed. It should therefore not be surprising if results from certain of these models are similar. There are several classes of approach taken in treating transport among the participating 2D models, with some models having entirely externally prescribed circulation and diffusion (e.g., AER), while others have internally consistent derivations (e.g., LLNL), up to fully interactive (e.g., GSFC-2Dint). These differences affect the "tunability" of transport among the models.

The transport information contained in simulations A1 through A6 is not mutually independent. As we shall show, basic features of the SF_6, CO_2, sin and cos simulations can be inferred from the age spectrum. Given the wide range of model performances in these transport experiments, these first order features deserve the greatest attention. Thus, in this report, not all experiments are given equal weight of analysis, and features of model transport to be compared to SF_6 and CO_2 observations are most often derived from the age spectrum. This choice of emphasis is driven primarily by convenience: similar conclusions about model transport would be reached if, for example, the direct SF_6 and sin simulations, or CO_2, had been analyzed instead. The NOx tracers do not have tropospheric source and, therefore, cannot be reconstructed from the age spectrum. They are treated separately.

In section 2.3 we examine model results of the age spectrum, and discuss its relationship to other tracers. We then present, in section 2.4, a range of recent observations, with special attention given to the mean age and propagation into the tropical stratosphere of annual cycles in tracer mixing ratio. Section 2.5 focuses on the tropical stratosphere of models, comparing model transport properties to inferences from observations, and discussing model deficiencies. In section 2.6 we present the global mean age distribution, compare models to observations, and explore possible reasons for model inaccuracies. Section 2.7 examines effects due to seasonal covariance of transport and source. In section 2.8, model results for the ΔNOy tracers are presented, and sensitivity to model resolution analyzed. Here, we also discuss possible relationships between ΔNOy tracer and mean age. We conclude and summarize in section 2.9.

2.3 Age Spectrum (Hall)

The age spectrum in the stratosphere $G(\mathbf{x}, t'|\mathbf{R}, t_0)$ is a type of Green function that propagates a tropospheric mixing ratio boundary condition specified in a region **R** into the stratosphere, and thus it may be used to reconstruct the stratospheric response to an arbitrary time variation of a conserved tracer in **R** by convolution of G with that time-variation. (Here, **x** indicates a position, and **R** a region, in two or three dimensions.) $G(\mathbf{x}, t'|\mathbf{R}, t_0)$ may be interpreted as the probability distribution function for an irreducible fluid element at **x** and time t' in the stratosphere to have last made contact with the region **R** a time $t' - t_0$ ago. The age spectrum is discussed by Kida [1983], Hall and Plumb [1994], and Hall and Waugh [1997a]. Here, we briefly focus on several features which have received less attention.

$G(\mathbf{x}, t'|\mathbf{R}, t_0)$ is determined in a model as the response to the time-dependent boundary condition $\delta(t' - t_0)$ specified over **R** in the troposphere (see section on run specification). The "forcing region" **R** varies somewhat from model to model, depending on particular grid spacings. For stratospheric studies, the details of **R** are unimportant as long as it is within the troposphere, as nearly all air and tracers enter the stratosphere in the tropics, regardless of their sources within the troposphere. The delta function in time is approximated by holding the forcing region at a finite value for one month, and zero for the duration of the simulation. (Note that the magnitude of the first month value is arbitrary, as G is afterwards normalized such that $\int_0^\infty G(\mathbf{x}, t'|\mathbf{R}, t_0)dt' = 1$.)

In general G is a function of both t' and t_0 (or $t' - t_0$ and t_0) separately. In this inter-comparison, the month corresponding to t_0 is January, and a different start month would yield a different result. Only for stationary transport does G depend exclusively on the elapsed time $t' - t_0$. However, as we will illustrate below, seasonality of transport for these models plays only a secondary role in determining many of the annually averaged properties of G. We would get similar results if a different start month had been chosen. Therefore, from here on we write $G = G(\mathbf{x}, t)$, where $t = t' - t_0$ is the elapsed time, and the separate dependence on t_0 and $\mathbf{R}$ is suppressed. If it were our goal, however, to analyze seasonal variations in G, we would need to perform separate simulations for several source times t_0 throughout the year. For tropospheric studies, the dependence of the age spectrum on $\mathbf{R}$ and t_0 is of comparable importance to $\mathbf{x}$ and $t' - t_0$, and a more complete version of G must be considered (e.g., Holzer and Hall [1999]).

Figure 2.1 shows examples of $G(\mathbf{x}, t)$ for (a) GSFC-3D, (b) GSFC-2Dint, and (c) MONASH2 at the equator and 60°N and pressure altitudes z of 18 km and 26 km. (Note that we use as a vertical coordinate $z = 16 \log(1000/p)$, where p is in millibars and z in kilometers.) The age spectra are broad, indicating a range of transit times from the troposphere. The spectra tend to be most peaked, and have the shortest transit times, near the tropical tropopause. The first moment, or mean age $\Gamma(\mathbf{x})$, is shown by the vertical dashed line. This quantity can be compared to mean ages derived from observations of temporally-increasing tracers such as CO_2 and SF_6. For example, to the extent that SF_6 is a conserved tracer whose mixing ratio is increasing linearly in time, its time lag at $\mathbf{x}$ in the stratosphere from its tropospheric time series is $\Gamma(\mathbf{x})$ [Hall and Plumb, 1994]. In fact, the tendency of SF_6 is slowly nonlinear, so the stratospheric response is actually a convolution of $G(\mathbf{x}, t)$ with this this nonlinear trend, and the stratospheric lag of SF_6 from the tropospheric history is not identically equal to the mean age [Volk et al., 1997]. However, for our purposes, the difference of SF_6 from linearity is small [Volk et al., 1997; Hall and Waugh, 1998], and Γ in the stratosphere is well approximated as the simple time lag of SF_6 from the tropospheric trend [Elkins et al., 1996; Volk et al., 1997]. The same is true for CO_2, once the annual cycle has damped out above about 19 km at midlatitudes [Bischof et al., 1985; Schmidt and Khedim, 1991; Boering et al., 1996]. Annual cycles of conserved tracers (oscillations of period one year, such as those of CO_2 or H_2O+2CH_4) in the model stratospheres may also reconstructed from $G(\mathbf{x}, t)$.

Normal Mode Analysis of the Age Spectrum

Examination of the model results for $G(\mathbf{x}, t)$ reveals that all models assume a simple exponential decay after several years, illustrated for several models in Figure 2.2, a logarithmic version of Figure 2.1. While the timeconstant for this decay, τ_0, varies from model to model, within a model it is universal, i.e., τ_0 does not depend on location in the model atmosphere. This universality may be understood by considering a normal mode analysis of models' $G(\mathbf{x}, t)$, similar to that used by Prather [1996] to analyze coupled chemical systems in a simple one-dimensional model. If an annually averaged perspective is taken, so that transport may be considered stationary, $G(\mathbf{x}, t)$ can be decomposed as $\sum_0^N \psi_n(\mathbf{x}) e^{-t/\tau_n}$. In principle, N is as large as the number of degrees of freedom of the system, at least the number of model grid-points. However, for large enough times, only the basest mode is significant; i.e., as $t \to \infty$, $G(\mathbf{x}, t) \sim a_0 \psi_0(\mathbf{x}) e^{-t/\tau_0}$. All points $\mathbf{x}$ decay at the same rate τ_0.

Table 2.2 lists τ_0 for the MM2 models, showing a range of values from 1.40 years (GSFC-2Dint) to 5.41 years (MONASH1). As will be discussed in Section 5, τ_0, $\psi_0(\mathbf{x})$, and $\Gamma(\mathbf{x})$ are related, and their variations from model to model are comparable.

Relation to Other Transport Experiments

As noted above, the formulation of the age spectrum employed here has neglected explicit dependence on time, leaving only dependence on elapsed time from the January source. In the real atmosphere, transport varies seasonally and inter-annually, while in these models, transport varies seasonally. Thus, one may ask how faithfully the fields from explicit tracer simulations (e.g., SF_6 and CO_2) can be reconstructed from $G(\mathbf{x}, t)$, given the particular January start date. At best, $G(\mathbf{x}, t)$ reconstruction can provide an annual mean picture of the fields. At worst, strong covariances between transport and surface sources could create large differences between the actual field and the reconstruction.

Figures 2.3(a) through (e) show scatter plots for 5 models of Γ as derived from the annual mean troposphere-to-stratosphere lag time of a full seasonally varying simulation of SF_6 (see section on run specifications for details) versus Γ as the first moment of $G(\mathbf{x}, t)$. The correlation is high. This near equivalence can also be seen in Figures 2.4(e) and (f), which show the height-latitude distributions of $\Gamma(\mathbf{x})$ for MONASH2 derived from the two techniques. Close agreement of the annually-averaged SF_6 lag and the mean of the age spectrum does not imply, however, that seasonal variations in Γ are small. In Figure 2.3(f), the scatter plot of 3(e) (MONASH2) is repeated, except that the SF_6 lag is for January, rather than an annual mean. The correlation breaks down due to large seasonal motions of the mean age isopleths, which cannot be reproduced from the age spectrum for the single value t_0. These isopleth motions can be seen in Figures 2.4(a) through (d), the zonal-mean mean age from MONASH2 for January, April, July, and October.

We have also compared the reconstruction of a sinusoid using $G(\mathbf{x}, t)$ with the actual sin and cos runs of A2. The amplitude $A(\mathbf{x})$ and phase lag time $\tau_\omega(\mathbf{x})$ from the sin and cos runs and as reconstructed from $G(\mathbf{x}, t)$ are plotted as tropical profiles in Figure 2.5 for the AER, GMI-NCAR, and SUNY-SPB results. The reconstructed profiles are not identical to those of the sin and cos simulations, as all models have some covariance between the oscillating source and transport, resulting in a rectification of the background mixing ratio, which cannot be reproduced from $G(\mathbf{x}, t)$ (see Section 6). However, we will show that the differences are smaller than the spread among models, and also smaller than the model-observation differences. This is true even for the models with the largest rectification, about 20% (i.e., the models' source-transport temporal covariance contributes to about 20% of the background state for the sin and cos runs).

We conclude that age spectral reconstructions of model tracers may be compared to appropriate annual mean observations, even though the age spectra have not been determined as a function of source time t_0. However, for situations in which transport seasonality is important and comparisons to observations at particular dates are made, model data from the explicit seasonally varying simulation for the date in question will be used.

2.4 Observations (Boering)

Since the first Models and Measurements Report was published six years ago [Prather and Remsberg, 1993], extensive observations have been made from satellites (e.g., UARS), from aircraft (e.g., ER-2 flights during SPADE, ASHOE-MAESA, STRAT, and POLARIS), and from balloons (e.g., the OMS campaign). The measurements of long-lived tracers have significantly improved our understanding of transport in the stratosphere, allowing us to quantify transport timescales and to constrain models more strictly.

Two categories of long-lived tracers have been particularly useful: (1) tracers of tropospheric origin whose mixing ratios at the tropical tropopause are increasing approximately linearly over time; and (2) tracers whose mixing ratios at the tropical tropopause vary approximately periodically with a dominant annual cycle. SF_6 [Elkins et al., 1996; Maiss et al., 1996; Geller et al., 1997; Harnisch et al., 1996] and annually-averaged CO_2 [Bischof et al., 1985; Schmidt and Khedim, 1991; Boering et al., 1996] are examples of (1). The annual cycle of CO_2 [Boering et al., 1994; Boering et al., 1995; Boering et al., 1996], forced at the Earth's surface, and "total hydrogen" $\hat{H}$ =H_2O+2CH_4 [Mote et al., 1995; Mote et al., 1996], forced by the annual cycle in tropical tropopause temperatures, are examples of (2). The fundamental features of linearly increasing and seasonally-varying tracers that constrain model transport are summarized by the mean age Γ (from SF_6 and CO_2) and the phase lag time τ_ω and amplitude A of the annual cycle (from $\hat{H}$ and CO_2). In this section, we summarize observations of CO_2, SF_6, and $\hat{H}$ =H_2O+2CH_4, against which models will be compared in subsequent sections. We focus first on the tropics, and then on middle and high latitudes.

Tropics

From the time series of observations of vertical profiles for CO_2 and $\hat{H}$ in the tropics, phase lag times can be determined (i.e., the time required for the extrema in the periodically-varying tracer mixing ratios to reach a given altitude from the tropical tropopause). The observed phase speeds are approximately equal to the upwelling rates in the tropical stratosphere [Hall and Waugh, 1997b; Mote et al., 1996] and can therefore be used to test models' vertical transport rates. Tropical phase lag times as a function of potential temperature and altitude are shown in Figure 2.6. The phase lag times shown by the dotted line are based on 4 years of H_2O and CH_4 "version 18 level 2" data (about 1.3 km resolution) from the HALOE instrument on the UARS satellite by Mote et al. [1998], who used an empirical orthogonal function (EOF) analysis to estimate the phase speed $c(z)$ as a function of height (data provided courtesy of Philip Mote). We have integrated $c^{-1}(z)$ over z to obtain $\tau_\omega(z)$. These data represent annual mean phase lag times and can therefore be compared to annual mean model results (or age spectral reconstructions). For comparison, the open square symbol is the 1-year phase lag time from HALOE data derived from examination of Plate 1 from Mote et al. [1998], and the black square symbol is the 11-month phase lag time from HALOE data derived by Randel et al. [1998], who used a harmonic regression analysis of the version 18 level 3a data (about 2.5 km resolution).

Phase lag times determined from in situ measurements of CO_2 from aircraft and balloons [Boering et al., 1996; Boering et al., 1998] and of H_2O and CH_4 from balloons [Voemel et al., 1998] are also shown in Figure 2.6. The CO_2 transit times were derived from knowledge of the boundary condition for CO_2 mixing ratios entering the tropical stratosphere [Boering et al., 1996; Boering et al., 1998] and extrema observed in the vertical profiles measured up to 20 km in October 1994, November 1995, February 1996, July 1996, and September 1997 (typically between 2°S and 4°N) and up to 26 km in February 1997 at 7°S. The $\hat{H}$ phase lag times were determined from extrema in vertical profiles up to 25 km in February 1997 and November 1997 at 7°S and assuming that minimum and maximum water vapor mixing ratios enter the stratosphere January 15 and August 1, respectively. Note that these times are consistent with the boundary condition determined by Weinstock et al. [1998] from ER-2 H_2O measurements and with the lowest water vapor minimum for the OMS flight of 970214 having already propagated to 417 K by February 14 (see Figure 2.6). However, balloon observations during the CEPEX campaign in March 1993 [Voemel et al., 1995] and the HALOE time series suggests that minimum water vapor mixing ratios may enter as late as mid-March. Reflecting these uncertainties, the horizontal error bars for the highest altitude in situ $\hat{H}$ minimum in Figure 2.6 include a +2 to -1 month uncertainty.

The in situ τ_ω show a clear seasonal dependence, with shorter τ_ω at a given altitude in northern winter than at other times of year. The magnitude of the seasonal difference is similar to that derived from

HALOE data by Mote et al. [1996]. The annually averaged phase lag times are very similar to the HALOE data. Overall, despite the lower spatial resolution of the satellite data versus the noncontinuous time series (in some cases single "snapshots") provided by the in situ observations, the agreement in phase lag times between the different observations is remarkably good, and the observations may therefore be used with confidence to evaluate model transport.

A comparison of τ_ω and Γ from tropical observations is given in Figure 2.7. Mean ages shown are the average of mean ages derived from recent CO_2 [Boering et al., 1998] and SF_6 [Elkins et al., 1998] measurements from the OMS campaign at 7°S in February and November 1997. Mean ages from CO_2 are derived as a time lag with respect to the linearized, deseasonalized boundary condition for CO_2 mixing ratios entering the stratosphere (see Boering et al. [1996], Boering et al. [1998]); mean ages from SF_6 are derived as a time lag with respect to tropical tropopause values by the method described in Volk et al. [1997]. The divergence of the phase lag times and mean ages increases with altitude, resulting from the mixing of older midlatitude air into the tropics. Note that for mean ages less than 1 year, a rigorous comparison of the magnitude of the mean ages and phase lag times cannot be made due to the precision limits of the SF_6 measurements and uncertainties in its stratospheric boundary condition and due to seasonal and interannual variations in CO_2 mixing ratios. Constraints such as those provided by empirical age spectra derived from a time series of CO_2 observations [Andrews et al., 1998] are required to determine reliable mean ages for the lowest 3 km of the tropical stratosphere. Comparison of the observations in Figure 2.7 with model results on the larger vertical scale, however, are straightforward.

The degree to which the annual cycles are attenuated as a function of altitude has also been determined from the in situ CO_2 and $\hat{H}$ and remote $\hat{H}$ observations, and in principle can be used to test how accurately the models simulate the relative rates of tropical upwelling, vertical diffusion, and entrainment of midlatitude air into the tropics. Figure 2.8 shows the observed amplitude attenuation, plotted as a fraction of its peak-to-peak amplitude at the tropical tropopause (390K for the in situ measurements and 100 mbar for the HALOE measurements). Although the remote and in situ phase lag times are in agreement (Figure 2.6), the in situ CO_2 and $\hat{H}$ observations indicate a much more pronounced attenuation with altitude above 20 km than the HALOE observations. It is not immediately clear which dataset should be given more weight, as they both have potential complications. On the one hand, HALOE retrievals below 20 km near the tropopause are difficult and more suspect than at higher altitudes, and representing the amplitude as a fraction of that at the tropopause could be biasing the attenuation significantly. In particular, the HALOE analyses derive a peak-to-peak amplitude in the water vapor annual cycle of only about 1.5 ppmv at the tropical tropopause [Mote et al., 1998; Randel et al., 1998], while in situ measurements suggest an amplitude of about 3 ppm [Weinstock et al., 1998]. For example, the HALOE H_2O tropical profile shown by Mote et al. [1996] (their Figure 2.1) displays a significant "compression" of the cycle maxima and minima compared to simultaneous ER-2 measurements, while Randel et al. [1998] (their Figure 2.15) note that HALOE is not able to account for all of the observed H_2O variability near the tropical tropopause. On the other hand, the in situ data above 20 km (the data points showing the most disagreement with the HALOE data) come from single profiles (the CO_2 datum from Feb 1997 and the $\hat{H}$ datum from Nov 97) at 7°S in a region shown by other simultaneous measurements to be perturbed by filamentary intrusions of midlatitude air [Jost et al., 1998], while the HALOE values come from 5 years of continuous data across the entire tropical region. Thus, the possibility exists that interannual variations and/or the sampling of subtropical air masses have significantly skewed the attenuations derived from the in situ observations. At the present time and for this report, then, we choose to weight the ampltiude attenuation towards the HALOE data but recognize that uncertainties remain.

Extratropics: the Global Mean Age Distribution

There are no global observations of tracers throughout the stratosphere from which mean age may be directly inferred. Thus, we do not, as yet, have a complete picture of the mean age distribution in the atmosphere. However, the in situ campaigns mentioned above have provided high quality, high resolution measurements of CO_2 and SF_6 from aircraft and balloon platforms over a variety of seasons and latitudes, from which mean age may be inferred. These measurements, taken together, form a picture of the mean age in the lower stratosphere, and a partial picture in the middle stratosphere, allowing us to rule out many model distributions as unrealistic.

Figure 2.9 shows the latitudinal variation of Γ in the lower stratosphere at 19 to 20 km inferred from aircraft SF_6 and CO_2 measurements obtained over a 3-week period in October-November 1994. Ages from the SF_6 measurements were calculated as a time lag with respect to the value at the tropical tropopause, about 0.8 yr as seen in the time lag from the global surface mean SF_6 time series, and include a small correction for its quadratic growth. (The quadratic correction increases with age, reaching about 6 months for ages of 6 years [Volk et al., 1997].) Ages from CO_2 were derived by accounting for CH_4 oxidation, then calculating a time lag with respect to a linear fit to the deseasonalized stratospheric boundary condition obtained from observations from 1992 to 1997 [Boering et al., 1996; Boering et al., 1998]. Note that the annual cycle in CO_2 results in seasonal oscillations in the apparent mean age, but that these are significantly attenuated by about 20 km in the tropics and 19 km in the extratropics (see below).

Balloon observations at discrete latitudes allow extension of the mean age distribution to higher altitudes. Figures 2.10a and 2.10b show vertical profiles of Γ in the tropics and at middle and high latitudes, inferred from SF_6 and CO_2 measurements from balloons. Ages from SF_6 measured in samples collected by a balloon-borne cryogenic whole air sampler (CWAS) were reported by Harnisch et al. [1996] as a time lag with respect to the northern hemisphere surface mean of SF_6 of Maiss et al. [1996]. In order to compare these ages with the in situ data reported relative to the tropical tropopause, a value of 1.4 years has been subtracted from the CWAS SF_6 ages (comprised of a 0.6 yr lag between the northern hemisphere and global surface SF_6 means [Geller et al., 1997] and a 0.8 yr lag between the global surface mean and tropical tropopause SF_6 values [Volk et al., 1997]). Note that an intercomparison of SF_6 calibration standards for the NOAA/CMDL (i.e., OMS) and the University of Heidelberg (i.e., CWAS) laboratories agreed to better than 1%, and that the adjusted CWAS ages at the tropopause and in the upper troposphere agreed well with ER-2 SF_6 ages for the same latitudes and seasons. The data labeled "Tropics" were obtained from OMS flights at 7°S in February and November 1997 and from a CWAS flight at 17°N. The flight at 17°N should be considered as subtropical, particularly given its vertical structure above 24 km (see below), and even the OMS flights at 7°S show some filamentary structure that is likely air from the subtropics or midlatitudes [Jost et al., 1998]. The data labeled "Midlatitude" were obtained from an OMS flight at 34°N in September 1996 and from a CWAS flight at 44°N in 1993. The data labeled "High Latitude" were obtained from an OMS flight at 62°N in June 1997, during which some vortex remnants were still apparent, and from a series of CWAS flights at 68°N in winters from 1992 to 1995, which often penetrated the polar vortex.

From the measurements, we can make the following observations about the global Γ distribution:

(1) At a given altitude in the lower and middle stratosphere, Γ is smallest in the tropics, i.e., a given Γ contour is higher in the tropics than at midlatitudes.

(2) In the subtropics (20°N) and midlatitudes (40°N), above about 24 km, Γ changes little with height, although it increases with latitude; i.e., Γ contours are oriented near vertically.

(3) However, in the subtropics and midlatitudes, below about 24 km, Γ increases with height. Thus, Γ contours which may be vertically oriented aloft, tilt poleward below.

(4) At high northern latitudes, Γ increases monotonically with height, at least through to 25 km, with the exception of the presence of vortex remnants observed in summer.

(5) In the lower stratosphere, latitudinal Γ gradients are largest equatorward of about $\pm 30°$.

(6) The magnitude of Γ can be 4 or more years (with respect to the tropical tropopause) in the tropics at 30 km and at high latitudes at 20 km.

These observations suggest the picture of the mean age distribution in the lower and middle stratosphere shown in Figure 2.11, which is derived by contouring the in situ data.

A complementary composite of the aircraft and balloon data can be derived by looking at the mean ages in the extratropics (i.e., polewards of 20°) on N_2O surfaces. Except when mixing of vortex and midlatitude air has occurred, creating "mixing lines" in the N_2O:CO_2 relationship [Waugh et al., 1997], a reasonably compact relationship exists between N_2O and mean age from SF_6 observations and for CO_2 observations, once the annual cycle has damped out. Figure 2.12 shows mean ages from over 1400 in situ SF_6 measurements and over 82,000 in situ CO_2 measurements from both aircraft and balloons (i.e., all extratropical measurements from SPADE, ASHOE-MAESA, STRAT, POLARIS, and OMS), binned and averaged in 5 ppb intervals from 10 to 320 ppb of N_2O [Boering et al., 1998]. The CO_2 and SF_6 ages are very similar, indicating that interannual variations in the CO_2 growth rate introduce negligible errors in determining a mean age. Thus, in the extratropical lower and middle atmosphere, the relationship between mean age and N_2O is evidently fairly constant, despite interhemispheric and seasonal differences in the N_2O distribution.

2.5 Tropical Transport in Models (Hall)

Transport in the tropics of the stratosphere critically affects the distribution of trace gases and the dispersal of aircraft pollutants, and observations of $\Gamma(\mathbf{x})$, $A(\mathbf{x})$, and $\tau_\omega(\mathbf{x})$ represent stringent constraints on modeled transport in this region. To appreciate this, consider the simplest one-dimensional "tropical leaky pipe" (TLP) model of tropical transport for a conserved tracer mixing ratio $\chi(z, t)$

$$\frac{\partial \chi}{\partial t} + w\frac{\partial \chi}{\partial z} - e^{z/H}\frac{\partial}{\partial z}\left(e^{-z/H}K\frac{\partial \chi}{\partial z}\right) = -\frac{1}{\tau}(\chi - \chi_e) \qquad (1)$$

Here w is a vertical velocity, K a vertical diffusion coefficient, H the air density scale height, and τ a relaxation time-constant to a specified extratropical value χ_e, which summarizes the rate at which upwelling tropical air entrains extra-tropical air. Such a model has been used by Minschwaner et al. [1996] and Volk et al. [1996] (with K assumed zero), by Hall and Waugh [1997b] (with constant coefficients, but K allowed to be nonzero), and Mote et al. [1998] (with w, K, and τ allowed to vary spatially). For the simple TLP model of (1) with constant coefficients, given χ_e and H, values of w, K, and τ completely specify $\Gamma(z)$, $A(z)$, and $\tau_\omega(z)$ and vice-versa. Clearly, real atmospheric and 2D and 3D model transport is more complicated. Nonetheless, this simple model is useful to guide interpretation of differences between models and observations.

Figure 2.13a shows tropical profiles of $A(z)$ for models and for inferences from satellite and in situ observations. The observations are also shown in Figure 2.8. Most models results are summarized by the shaded region, while the heavy solid line is derived from the analysis of Mote et al. [1998] of $\hat{H}$

time series from the UARS HALOE (courtesy Philip Mote). The symbols are in situ estimates, as described in Section 3. From 16 km to about 20 km the wide range of model performances brackets the HALOE amplitude, while above about 21 km most models have significantly smaller amplitude than HALOE.

The observed and modeled $\tau_\omega(z)$ are shown in Figure 2.13b. In situ and remote inferences are in good agreement, both showing that most models propagate the annual cycle too rapidly in the vertical. This has consequences for the models' annual cycle amplitude: although at first sight the models do not appear to have a general bias in $A(z)$ (Figure 2.13a), we argue below that after accounting for the unrealistically rapid phase speeds most models are seen to effectively over-attenuate the signal.

Figure 2.14 shows profiles of $\Gamma(z)$ in the tropics. Models are summarized by the shaded region, and mean ages inferred from CO_2 and SF_6 observations of three recent balloon flights at 7°S from the Observations of the Middle Stratosphere (OMS) campaign are shown as symbols. These data are shown and discussed in Section 3. Most models significantly underestimate Γ, which will be discussed further in Section 5. MONASH1 and UCI23, plotted separately in Figure 2.14, come closest to matching the tropical observations. Note that the model $\Gamma(z)$ profiles are derived from $G(\mathbf{x}, t)$, rather than the SF_6 simulations for the dates corresponding to the balloon flights in November and February. However, this introduces little error, as models show only small seasonal variation in tropical Γ. Moreover, there is little variation in the observed profiles of Γ.

As a convenient way to summarize modeled and observed tropical characteristics, consider the average behavior of $\Gamma(z)$, $A(z)$, and $\tau_\omega(z)$ over the tropical stratosphere from 100 mbar (16 km) to 24 mbar (26 km). Each modeled $A(z)$ may be fit to an exponential decay with height and each $\tau_\omega(z)$ to a linear increase with height (i.e., a constant phase velocity c). A convenient measure of the mean age distribution is $dz/d\Gamma$, which gives units of velocity for ease of comparison to c. These choices of fits for $A(z)$ and $\tau_\omega(z)$ are guided by the TLP model in which (assuming constant coefficients) the amplitude decays exponentially as e^{-z/H_a} and the phase speed $c = dz/d\tau_\omega$ is constant, with H_a and c depending on the model parameters w, K, τ [Hall and Waugh, 1977b].

Table 2.2 shows the values of H_a and c for MM2 models, the scale height fit to the HALOE analysis of Mote et al. [1998] and the scale height fit to the in situ observations. Also shown are $dz/d\Gamma$ for the models and from OMS SF_6 and CO_2 balloon measurements, as seen in Figures 2.14 and 2.10a. The models attenuate the cycle amplitude with scale heights ranging from 2.2 km to 8.7 km, while for observations $H_a = 7.6$ km for the HALOE analysis and $H_a = 3.8$ km for the in situ analysis. Note that the data used for the in situ analysis range only up to about 21 km, since the two highest altitude points have been excluded as they are derived from very few balloon flights and are likely contaminated by intrusions of midlatitude air [Jost et al., 1998]. When only the HALOE points through this height are used, the exponential fit produces $H_a = 5.4$ km, in somewhat better agreement with the in situ observations. Greater attenuation in the lower region is consistent with estimates of entrainment by Minschwaner et al. [1996], Schoeberl et al. [1997], and Mote et al. [1998], which suggest more rapid rates near the tropopause than above.

Using the HALOE τ_ω up to 26 km, an average phase speed, c, of 0.33 mm/s is obtained ($\Delta z/\Delta\tau_\omega$ from Figure 2.13). When only HALOE τ_ω data to 21 km are used, $c = 0.22$ mm/s is obtained, indicating slower upwelling in the lower tropical stratosphere than aloft [Mote et al., 1998]. Fitting a straight line through all the in situ data below 21 km yields $c = 0.23$ mm/s. (Recall that the vertical coordinate is $16 \log(1000/p)$. A more accurate relationship between altitude and pressure results in somewhat different values of c.) Overall, there is good agreement between in situ and satellite observations of annual

cycle phase, as seen in Figure 2.13b. The phase speeds of the models from 16 km to 26 km range from 0.30 mm/s to 1.09 mm/s (Table 2.2). Most models propagate the annual cycle too rapidly.

The model values of $dz/d\Gamma$ range from 0.12 mm/s to 0.42 mm/s, all larger than the value of 0.11 mm/s deduced from OMS SF_6 and CO_2. In general, models predict younger air than observed, in some cases by a factor of 2 or more. However, for all models, the phase speed c is at least larger than $dz/d\Gamma$, as the observations show. In fact, Hall and Waugh [1997a] showed that $c \geq dz/d\Gamma$ as long as $G(t)$ is positively asymmetric, or has a "long tail," as will generally be the case when diffusive flow components are present. Note that for the TLP model, $c \geq \omega \geq dz/d\Gamma$, which reduces to $c = w = dz/d\Gamma$ for a perfectly isolated tropical pipe ($\tau = \infty$ in (1)) with no vertical diffusion.

At first sight, although there is a wide range of modeled H_a, there appears to be no strong overall bias. However a better measure of the amplitude attenuation is $R = H_a/\lambda$, where $\lambda = c \times (1\text{year})$ is the vertical wavelength of the annual cycle. What we would most like to infer from $A(z)$ are the rates of processes such as diffusion and entrainment that cause the attenuation of $A(z)$. Normalizing by the wavelength allows each model an equivalent amount of time (one year) for its attenuating processes to act. Values of R are also listed in Table 2.2 and range from 0.2 to 0.5, compared to 0.7 for the HALOE analyses and 0.5 for the in situ analysis. On a per wavelength basis, most models over-attenuate the annual cycle.

Figure 2.15 summarizes Table 2.2 graphically. The top panel is a scatter plot of model values of $dz/d\Gamma$ versus c, while the bottom panel shows $R = H_a/\lambda$ versus c. The numbers indicate the models as listed in the Table 2.2, while the symbols indicate the values estimated from satellite and in situ observations. There is some correlation between model values of $dz/d\Gamma$ and c, as both increase with the rate of vertical advection in a model. However, the correlation is not perfect. The quantity $dz/d\Gamma$ is strongly affected by the transport of extratropical air into the upwelling tropical plume, while is only weakly affected.

In order to understand the difference between the model results and the tropical observations, we look at the relative roles of specific transport mechanisms. A natural tool to aid interpretation is the TLP model, the simplest model that still includes three relevant mechanisms: vertical advection, vertical diffusion, and mixing of extratropical air into the tropics. Hall and Waugh [1997b] solved the TLP model analytically to estimate w, K, and τ, given HALOE $\hat{H}$ values of H_a and c, values of Γ deduced from ER-2 aircraft SF_6, and assuming no cycle amplitude in the extratropics (reasonable for this simple model, given the rapid latitude attenuation of cycles of CO_2 [Boering et al., 1994] and $\hat{H}$ [Randel et al., 1998]). Hall and Waugh [1997b] deduced that vertical diffusion in the tropics plays nearly no role in propagating $\hat{H}$ from 16 km to 24 km, and a secondary role in attenuating the signal, implying values of $K << 0.1$ m^2/s. Most of the attenuation is due to extratropical air mixing into the tropics, with a timescale $\tau \approx 1.3$ years, in agreement with independent estimates [Minschwaner et al., 1996; Volk et al., 1996]. Nearly all vertical transport appears to be due to advection at the average rate $w \approx 0.3$ mm/s, also in approximate agreement with independent heating rate calculations [Rosenlof, 1995; Eluszkiewicz et al., 1996]. Thus, in the context of the TLP model, $H_a \sim \tau w$ and $c \sim w$. (In this low diffusion limit, therefore, $R \sim \tau/(1\text{ year})$, the entrainment timescale in years.)

Mote et al. [1998] matched a TLP model with height varying coefficients and a photochemical model to HALOE H_2O and CH_4. They observed that in the region 20 km to 24 km, the HALOE $\hat{H}$ amplitude attenuates much less than above or below, leading the authors to deductions of τ up to 6.7 years locally. Over this region, Mote et al. [1998] found that even a small K (~ 0.03 m^2/s) plays a significant role in the little attenuation that does occur. However, taking the average $\bar{\tau}^{-1} = \int \tau^{-1} w^{-1} dz / \int w^{-1} dz$ from the tropopause to 26 km yields $\bar{\tau} \approx 1.6$ year, where the $w^{-1}(z)$ factor appropriately weights altitudes at which more time is allowed for entrainment to act (τ and w values

courtesy Philip Mote). Thus, the average entrainment timescale, at least, of Mote et al. [1998] is not so different than the estimates of Minschwaner et al. [1996], Volk et al. [1996], and Hall and Waugh [1997b]. Overall, then, from 16 km through 32 km, entrainment of extratropical air appears to be the primary attenuating mechanism.

The role of vertical diffusion in propagating and attenuating a sinusoid of period 1 year is illustrated explicitly in Figure 2.16 for the TLP model, from the solution of Hall and Waugh [1997b]. The curves in the figure correspond to $w = 0.3$ mm/s, and would shift somewhat for different w. In Figure 2.16a, c/w is plotted versus K for values of the entrainment timescale τ from 0.5 years to 8.0 years. For $K < 0.1$ m^2/s, diffusion plays only a small role in the propagation. At higher K values (typical of several 2D models, as shown below), diffusion plays a significant role. Entrainment has little effect; the extratropics adds air with no cycle amplitude, increasing c only to second order.

Figure 2.16b shows $R = H_a/\lambda$ versus K. For R, there are three diffusion regimes: (1) For $K < 0.01$ m^2/s (and $\tau \leq 2$ years), diffusion plays little role in attenuating the signal. The attenuation is due mostly to dilution by extratropical air. This is the regime of the estimate by Hall and Waugh [1997b], based on HALOE data. (2) For $0.01 < K < 0.3$ m^2/s, H_a (and therefore the amplitude) decreases with increasing diffusion. Here, the amplitude is attenuated by both diffusion and dilution, but it is more sensitive to the dilution. (3) For $K > 0.3$ m^2/s, H_a increases with diffusion, with little dilutional influence. In this "diffusive-regime," the TLP model's atmosphere gets progressively closer to an equilibrium with the source, in which the signal diffuses outward to much of the atmosphere within one cycle period (1 year). Although the diffusive regime is not realistic, several 2D models may be close to it (see below).

Figure 2.17 illustrates the relative roles vertical diffusion and advection play in transporting the annual cycles in four 2D MM2 models. The quantities plotted are: (1), annually-averaged K_{zz}, the vertical component of the model's diffusivity tensor (interpreted as K in the context of the TLP model); (2), annually-averaged model τ_ω, whose slope is c; (3), τ_ω from the HALOE $\hat{H}$ analysis; and (4), the timescale for advection by the models' vertical residual circulation $\bar{w}^*$. For GSFC-2D (Figure 2.17a), $K_{zz} < 0.1$ m^2/s throughout the tropical stratosphere, putting it in the low diffusion regime of the TLP model (Figure 2.16a), so that $c \approx \bar{w}^*$. Moreover, the upwelling rate agrees fairly well with HALOE $\hat{H}$ analyses. For GSFC-2Dint (Figure 2.17b) $K_{zz} >> 0.1$ m^2/s below 22 km. As a consequence, the τ_ω profile is significantly steeper than the advective time (i.e., $c > \bar{w}^*$). In this regime, diffusion plays a large role in transporting the signal (Figure 2.16a), contrary to the estimates from observations. CSIRO (Figure 2.17c) is an intermediate case. The advective time is close to the phase lag from HALOE, suggesting a realistic $\bar{w}^*$. However, $K_{zz} > 0.1$ m^2/s, and $c > \bar{w}^*$. SUNY-SPB (Figure 2.17d) has $K_{zz} \approx 0.5$ m^2/s, which again results in $c > \bar{w}^*$. (More typical implementations of the SUNY-SPB model use much smaller K_{zz}, as discussed in Yudin et al. [1998].) Note that the 2D residual circulation of SUNY-SPB has a zero point in the lower tropical stratosphere, visible as a flattening of the advective time profile just below 24 km. Some type of diffusive transport, either vertical or horizontal, may be necessary in SUNY-SPB to propagate through this region. The origin of the zero-point is not known, but it can be seen in the residual circulation of the MACCM2 GCM (see Figure 2.25), from which the SUNY-SPB fields are derived.

From this analysis, we conclude that several 2D models have explicit values of K_{zz} that are too large, in some cases by more than an order of magnitude. For models whose diffusion coefficients are explicitly set, this may be a straightforward correction. For models whose coefficients are determined interactively with a representation of propagating and breaking planetary waves, the physical reasons for such large values of vertical diffusion should be identified and changes considered.

3D models have no explicit vertical diffusion. A few 3D models (UCI23, GMI-NCAR, MONASH1) have values of c that are not too far from that observed (see Table 2.2), while others propagate the signal too quickly (GMI-DAO, GSFC-3D, MONASH2, UNIVAQ-3D, GISS8x10). A large values of c could be due to an overly vigorous residual circulation, too much diffusion associated with resolved features of the flow, or too much diffusion implicit in the numerical advection scheme. Numerical diffusion depends on the particular advection scheme and resolution employed by the model. We have not systematically tested the schemes employed by MM2 models, a study which would be valuable. However, one-dimensional tests show that the second-order moments scheme [Prather, 1986], at least, does not significantly attenuate a sinusoid with as few as 4 grid points per wavelength. Thus, for example, numerical diffusion should not be an issue for UCI23. Recently, Yudin et al. [1998] have derived 2D transport fields from the 3D fields of MACCM2 (equivalent to MONASH2 and GMI-NCAR). They deduce $K_{zz} \approx 0.5$ m^2/s near the tropical tropopause, decreasing to less than 0.1 m^2/s above about 20 km, suggesting a small but non-negligible role for vertical diffusion in propagating the annual cycle through the lower stratosphere in MACCM2.

2.6 Global Mean Age in Models (Waugh and Hall)

The MM2 models exhibit a wide range of mean age distributions for both 2D and 3D models, as seen in Figures 2.18 and 2.19. These differences are reduced in N_2O simulations (see Figures 2.28 and 2.29), thus illustrating the role of age in highlighting and assessing model transport. In the tropics at 40 km, Γ ranges from under 2 years (UIUC-3D, GSFC-2Dint, and models using DAO winds) to over 5 years (UCI23). Although all models show the upwelling in the tropics characteristic of long-lived tracers of tropospheric origin, the tropical-extratropical gradients vary widely. Vertical age gradients at high latitudes don't everywhere agree on sign. Some models have local age maxima in the high latitude lower stratosphere (which is not observed), while others have local maxima higher up at high latitudes, or have age increasing monotonically with height throughout the atmosphere.

Figure 2.20 shows vertical profiles of models' Γ at different latitudes and a latitudinal profile in the lower stratosphere. Also shown are the observations from Section 3 for comparison. Most model profiles are indicated by the shaded regions, but several profiles lie outside these regions, and are plotted individually. Models are generally too young overall, in some places by more than factors of 2. The lower stratosphere Γ maximum at middle and high latitude in several models is a feature not present in observations, with the exception of a single polar vortex profile suggesting a weak maximum around 25 km. In latitudinal profiles, only three models (HARVARD, MONASH2, MONASH1) capture the sharp gradients observed between 10° and 30° from the equator.

For a first attempt at understanding the variation among models, it is useful to categorize them based on the orientation of their Γ contours. Figure 2.21 shows schematics of 3 conceivable global Γ orientations. The middle schematic, "class B", is the most consistent with observed $\Gamma(\mathbf{x})$ features (1) through (5), discussed in Section 3 and shown in Figure 2.11. In class A, Γ has a lower stratospheric maximum at high latitudes, in violation of feature (5). In class C, there are no regions of near zero $d\Gamma/dz$, in violation of feature (2).

The models are classified as follows:

Class A: GSFC-2Dint, HARVARD, LLNL, NOCAR

Class B: AER, CSIRO, GSFC-2D, SUNY, GMI-NCAR, MONASH1, MONASH2

Class C: NCAR-2D, MGO-UIUC-2D, UNIVAQ-2D, WISCAR, GISS8x10, GMI-DAO, GSFC-3D, UCI23, UIUC-3D, UNIVAQ-3D

There is a continuum from A to B to C, making the classification of models arbitrary in some cases. For example, LLNL could be either A or B, while SUNY could be B or C. Moreover, other classes could be defined based on different characteristics of the Γ distribution, and models would be grouped differently. In particular, the present classification scheme is determined only by the contour shapes, and not by the magnitude of Γ or its gradients, which varies widely among models. Nonetheless, the class definitions A, B, and C suggest variations among models of certain transport mechanisms, which we now discuss.

The presence of relatively flat contours (class C in Figure 2.21) is consistent with weak isolation of the tropics. If wave activity, parameterized as diffusion in 2D models, reaches too far and too often from the midlatitude "surf-zone" into the tropics, the observed sharp gradients of the mean age (and other long-lived tracers; see below) between the tropics and extratropics will not be realized. For very rapid and uniform mixing, the "global diffuser" limit is reached [Plumb and Ko, 1992; Plumb, 1996]. To illustrate this point, Figure 2.22 compares three versions of the AER model: the "tropical pipe", the "leaky tropical pipe", and the "no-pipe" models [Weisenstein et al., 1996]. In the tropical pipe model, the tropics are isolated by setting latitudinal diffusion (with coefficient K_{yy}) to near zero equatorward of 20°, whereas in the no-pipe model, transport by K_{yy} is significant at all latitudes. The leaky pipe model, the AER version submitted to MM2, is an intermediate case. In the tropical pipe, Γ contours bulge up the most in the tropics, so that the extratropical cross-isopleth gradients are the most latitudinally oriented.

Mixing of extratropical air into the tropics also increases the mean age throughout the stratosphere by allowing more air to recirculate before exiting the stratosphere. In Figure 2.22, the no-pipe model has the oldest air overall. Thus, added mixing would seem advantageous, as most MM2 models are too young overall. However, additional extratropical air in the tropics can have the detrimental effects of (1) flattening Γ contours of models in the extratropics, whose contours may already not be steep enough; and (2) further attenuating the amplitude of $\hat{H}$ and the CO_2 cycle, which may already be overattenuated (see Section 4).

Counterintuitively, mixing of extratropical air into the tropics has little effect on the magnitude of latitudinal mean age gradients. For example, while the orientation of Γ contours varies, $d\Gamma/dy$ varies little among the three AER models in Figure 2.22. Recently, Neu and Plumb [1998] have shown for a simple model that $\Delta\Gamma$ (the difference between extratropical and tropical mean age) is independent of such mixing. This can be appreciated heuristically in the following way: when there is no mixing of extratropical air into the tropics, $\Delta\Gamma$ is given by the transit time for one circuit about the Brewer-Dobson cell, which is approximated by the residual circulation. If some mixing is added, a fraction δ of tropical air now has extratropical age, increasing Γ overall in the tropics. However, the extratropical mean age increases by an equivalent amount, as the fraction δ recirculates to the extratropics. $\Delta\Gamma$ is unchanged.

In contrast, horizontal mixing by K_{yy} diffusion in midlatitudes strongly affects the orientation of mean age contours. Figure 2.23 shows latitudinal profiles of K_{yy} for several 2D models, averaged from 18 km to 24 km. There is wide variation in the magnitudes and gradients. For example, HARVARD and GSFC-2Dint, both class A models, have much smaller midlatitude values than the others. To appreciate the transport role of K_{yy}, compare the mean age distribution to the distribution of transit times obtained from back-trajectories using the residual circulation alone. Figure 2.24 shows these two quantities for GSFC-2Dint and GSFC-2D. For both models the oldest air from the trajectory calculations is in the high latitude lower stratosphere, as this represents the longest trajectory along residual circulation

streamlines from the tropical tropopause. This distribution is very different from the GSFC-2D mean age, for which K_{yy} transport prevents isolation of old air at high latitudes. On the other hand, there is little mixing in GSFC-2Dint, the mean age is more similar to the transit time distribution, and the model exhibits a high latitude lower stratospheric Γ maximum. We note that unrealistic features in the spatial structure of the residual circulation could also cause a high latitude lower stratospheric Γ maximum.

The mean age distribution is also strongly affected by the magnitude of the residual circulation. Figure 2.25 compares the residual circulations and mean age distributions of MONASH1 and MONASH2. These simulations use the same transport model, but wind data from two versions of the NCAR MACCM2 differing in their gravity wave drag. MONASH2 has a more vigorous circulation, and as a result, its mean age is lower throughout the atmosphere. Countour shapes appear to change only little between the models, and the ratio of MONASH2 to MONASH1 mean age, about 0.8, is fairly uniform through the lower and middle stratosphere.

We have not systematically examined the impact on the mean age of numerical aspects of model formulation. The simulation of advection introduces diffusion ("numerical diffusion") whose magnitude depends on the advection algorithm, the grid resolution, the coordinate system, and the time step. Diffusion, in turn, affects the global distribution and magnitude of mean age and other tracers. However, at least for MONASH2 and GMI-NCAR the advection algorithm plays only a small role in determing mean age. These models are CTMs driven by the same set of GCM wind data (NCAR MACCM2) but employ different advection algorithms ("semi-Lagrangian" [Rasch, 1994] for MONASH2 and "flux-form semi-Lagrangian" [Lin and Rood, 1996] for GMI-NCAR). Their mean age fields show differences that are much smaller than differences with other models. However, numerical diffusion may play a role in determing mean age in other models. For example, models with lower resolution than the CTMs driven by MACCM2 wind data are likely more sensitive to the choice of advection algorithm. On the other hand, it is clear that the large scale stratospheric circulation strongly affects mean age. As the comparison discussed above between MONASH1 and MONASH2 and among the three versions of AER show, models that have identical numerical formulations but different circulations have much different mean age distributions.

Using the normal mode decompositions of $G(\mathbf{x}, t)$ (see Section 2.3) the first moment of $G(\mathbf{x}, t)$, the mean age $\Gamma(\mathbf{x})$, can also be expressed as a sum over normal modes. Because $\Gamma(\mathbf{x})$ is strongly influenced by the tail region of $G(\mathbf{x}, t)$, which is, in turn, dominated by a single exponential decay mode $\psi_0(\mathbf{x})e^{-t/\tau_0}$ (see Section 2), we expect a close connection between $\Gamma(\mathbf{x})$, τ_0, and $\psi_0(\mathbf{x})$. The timescale τ_0 displays similar magnitude variation among models as $\Gamma(\mathbf{x})$. In Figure 2.26 we plot $\bar{\Gamma}$ versus τ_0 for the models of Table 2.2, where $\bar{\Gamma}$ is the mass weighted integral of $\Gamma(\mathbf{x})$, for $z > 20$ km. There is strong correlation between the two transport timescales for 3D models (top panel). For 2D models (bottom panel), there is more scatter, but the correlation is still evident. Apparently, in 2D models, the relative roles of the basest and higher order modes vary more. Recall, however, that 3D MM2 models are not as independent as 2D models. Many share the same or similar driving meteorological fields.

The spatial distribution of $\Gamma(\mathbf{x})$ is for most models very similar to that of $\psi_0(\mathbf{x})$, as shown in Figure 2.27 for LLNL and GMI-NCAR. Differences between $\Gamma(\mathbf{x})$ and $\psi_0(\mathbf{x})$ are most significant at high latitudes. $\psi_0(\mathbf{x})$ tends to have a local maximum in the high latitude lower stratosphere, which is particularly pronounced for class A models. The maximum is either not present or weaker in $\Gamma(\mathbf{x})$.

Comparison with Other Long-Lived Tracers (Waugh)

The previous discussion has shown there is a large variation in the simulated mean age between models, and that the simulated mean age generally differs greatly from that observed. A similar can also

be seen in simulations of long-lived tracers with significant photochemical loss in the stratosphere, although the magnitude of the differences is typically reduced.

Figures 2.28 and 2.29 show the annual-mean zonal-mean N_2O from all models. There is a large variation in N_2O between models, both in isopleth shape and magnitude. For example, the isopleths bulge upward sharply in the tropics of HARVARD, while in UCI23, they are relatively flat. The N_2O magnitude at 40 km in the tropics varies from 20 ppb (NCAR-2D) to 100 ppb (GMI-NCAR). The observed N_2O from the CLAES instrument on UARS [Randel et al., 1994], is shown at the bottom of Figure 2.29. Comparison with the simulated fields shows that although there is some large-scale qualitative agreement for most models, there are large quantitative differences. For example, HARVARD has too little N_2O in the upper stratosphere and the lower high latitude stratosphere, while GMI-DAO has too much in both places.

Comparing the N_2O of Figures 2.28 and 2.29 to the mean age of Figures 2.18 and 2.19 shows that the model-model variation of these two quantities is similar. Equatorward of 40° the N_2O and mean age isopleths for a given model are nearly parallel, and models with young air generally have high N_2O. At high latitudes N_2O and mean age isopleth shapes within a model differ more, particularly for class A models (GSFC-2DINT, HARVARD, LLNL, NOCAR). Because of photochemical loss in the upper stratosphere, N_2O falls off with altitude in all models, whereas the sign of $d\Gamma/dz$ varies among models. Therefore the N_2O loss hides some of the transport differences between models, and between models and observations. Overall, however, N_2O simulations display differences consistent with those of mean age.

Other long-lived tracers also show consistent model-model differences. For example, Figure 2.30 compares NOy and Cly for the AER and NCAR-2D models. These families of active chemical species have isopleth shapes similar to those of N_2O and Γ: for AER they bulge up sharply in the tropics of the lower and middle stratosphere, while for NCAR-2D they are more flat. Clearly, variations in transport affect the chemical background state of the models.

2.7 Source-Transport Covariance (Plumb)

Seasonality of model transport causes large time-variations in tracer distributions, as is seen for example in the seasonal motion of Γ contours (Figure 2.4). Such seasonality can also affect the annually averaged tracer distribution through rectification due to covariance of transport and source. We have argued that $G(\mathbf{x}, t)$ may be used to reconstruct annually averaged Γ, A, and τ_ω, even though transport seasonality is not properly included, given the single source time t_0 (January). However, the ability to reconstruct annual-mean Γ does not necessarily imply small rectification for other tracers. SF_6 has little seasonality of source, and thus no opportunity for covariance with transport. As for A and τ_ω from a periodic source, all that is required for faithful reconstruction by G for a single t_0 is that the spatial gradients of rectification be small. In principle, the stratosphere could experience large uniform rectification due to covariance between source and cross-tropopause transport, which would not be evident in A and τ_ω.

To ascertain the degree of rectification in the models, we analyze the sin and cos simulations of experiment A2. For these simulations the boundary condition fixes the annually-averaged mixing ratio to be unity at the surface. If no rectification occurred, the annually-averaged mixing ratio everywhere in a model's atmosphere would also be unity. In fact, rectification occurs to some degree throughout all the model atmospheres. However, the magnitudes are small, typically several percent. Rectification is

therefore most apparent relative to the propagating sin and cos signals where the signals' amplitudes are smallest—at high latitudes and in the upper stratosphere.

Figure 2.31 illustrates two examples: the first 5 years from the 10 year AER simulation, and the last 5 years from GSFC-2Dint. The time series for the sin experiment and the cos experiment is shown at 22 km altitude and the latitudes 50°S, the equator, and 50°N. In the AER model, relatively little rectification is evident in the long term, though there are transient effects as the initial pulse is distributed through the model, especially for the sin tracer. The stronger initial surge in the tropics of sin, as opposed to cos, indicates seasonal variation of the upwelling. Note that at high latitudes, the initial pulse of sin tracer builds up through the winter in each hemisphere. It subsequently decays, and after 3 to 4 years the annual mean offset is almost gone. One of the largest examples of rectification among the MM2 models is in the GSFC-2Dint model at high northern latitudes: source-transport covariance results in a rectification effect on tracer mixing ratio of about 20% for the cos experiment and 10% for the sin experiment. Transport seasonality in the GSFC-2Dint model is also revealed by the nonharmonic appearance of these signals at high latitude.

We have little basis to judge the realism of model rectification other than noting that the effect does not appear to play a dominant role in determining the distribution of observed stratospheric tracers. Among the MM2 models there is no obvious similarity in the spatial distribution of rectification, except that for most models the magnitude is everywhere well under 10%. For both models and the real atmosphere, rectification introduces no complication in interpreting time series of annual cycles at fixed locations. However, in regions of small cycle amplitude, spatial gradients of rectification could, in principle, complicate the interpretation in terms of annual cycle properties of tracer mixing ratio profiles measured at a single time. In addition, for a tracer having an annual cycle and a long term trend in its forcing (e.g., CO_2), rectification in the stratosphere could, in principle, complicate interpretation of the background state. It would be difficult to isolate the component of the annual mean distribution due to the secular trend alone from the component due to rectification. For example, the mean age inferred from the GSFC-2D model's simulation of CO_2 (not shown) appears smaller in the southern hemisphere than the northern hemisphere due to covariance of the CO_2 annual cycle with transport seasonality. The extent to which this is occurs in the real atmosphere is unknown, although close agreement in mean age inferred from CO_2 and SF_6 (see Figure 2.20, as well as Boering et al. [1998] and Elkins et al. [1998]) suggests a minor role at most in the stratosphere.

2.8 HSCT "ΔNOy" Tracer Distributions (Rind, Hall, and Wuebbles)

Emissions of a tracer were prescribed corresponding to NOx from a fleet of 500 High Speed Civil Transport (HSCT) aircraft. The total release was 1.75×10^6 kg d^{-1} with a latitudinal distribution mimicking that of prospective HSCT flight paths, i.e., peaking at northern hemisphere middle latitudes over the north Atlantic. Maximum releases occur around 18.5 km altitude. The participating models advect the tracer through the atmosphere, and instantaneously remove it below approximately 6 km. The experiments test model transport treatment of a stratospheric perturbation, highlighting in particular the role of stratosphere-troposphere exchange. Experiment A3 includes the full source, while A4 only includes emissions north of 30°N.

Twenty-three models performed the A3 experiment, and 21 performed A4. They all differed in their vertical resolution, with the number of layers varying from 25 to 44. Horizontal resolution varied from 2° latitude in the finest 3D model to 10° latitude in some 2D models. All output was interpolated to a grid of 37 latitudes (5° latitude) and 31 layers from the surface to 60 km (2 km spacing).

Although each modeling group was instructed to integrate until an annually-repeating steady-state was achieved, a perusal of the monthly data shows that in several cases such a state was not quite reached. When an explicit duration of run was indicated, it was generally in the range of 10 to 12 years. Model output was most usually reported for the 15th of each month; some models reported values for the 1st and 15th, while the GISS model, the only model with the ΔNOy tracers run on-line in the GCM, reported monthly averaged values. GSFC-3D produced results only for June and December.

Effects of Grid Resolution (Wuebbles)

While only a single HSCT emission source scenario was specified, the effective source distribution varied among models due to their differing vertical resolutions. Figure 2.32 shows the distribution of the A3 (and A4) source for most of the models. The data are plotted as the value input to the respective model layers. When mass weighted according to the thickness of the layers, each of the models is seen to inject accurately the desired total amount; however, as shown in the figure, the vertical distribution of the source differed.

The impact of horizontal resolution was examined for the LARC 3D model by performing two runs of the HSCT tracer, one at T16 (triangular truncation to wave number 16) resolution and one at T32 resolution. These simulations correspond approximately to $5.5° \times 5.5°$ at T16 and $2.8° \times 2.8°$ at T32. Each simulation was run in an off-line mode using the same annually repeating wind and temperature fields derived from a T32 GCM simulation. For the T16 run, the T32 input fields were degraded to the appropriate resolution. The runs were otherwise identical, with the exception that the numerical time-step in the T32 model was 30 minutes, half that used in the T16 model.

Figures 2.33 and 2.34 show the calculated ΔNOy tracer fields at 69 hPa resulting from the specified HSCT injections. Both simulations were run for 27 model years to ensure a cyclically repeating steady-state solution. In Figure 2.33 (T32) the ΔNOy mixing ratio peaks above 1.8 ppbv in the northern mid-latitudes. Comparison Figure 2.34 shows that the T16 ΔNOy distribution is up to 15% less in some regions than T32. While the overall distribution of the ΔNOy tracer is very similar in both simulations, the high resolution simulation retains about 10% more ΔNOy in the zonal mean. Globally integrated ΔNOy is 9% larger in the T32 simulation. The results indicate that the differences in horizontal resolution yield a small but non-negligible impact on the distribution of ΔNOy from aircraft effluents.

Annually-Averaged Distributions (Rind)

The annual average latitude/altitude distributions of HSCT ΔNOy tracer concentrations are given in Figures 2.35a and b for tracer A3 and Figure 2.36a and b for tracer A4. The 3D models are shown together (35a, 36a), as are the 2D models (35b, 36b). Table 2.3 lists the total integrated mass for the tracer in cases A3 and A4. Significant differences from model to model are apparent. For example, total burdens of the tracer differ by nearly a factor of 4 for A3. The 3D models look more similar than the 2D models; part of this is because a number of the 3D models use similar wind fields (e.g., MONASH1, MONASH2, and GMI-NCAR all use variants of the NCAR 3D model wind fields; GSFC-3D and GMI-DAO use the Goddard 3D assimilated wind data; and GISS-3D, GMI-GISS and UCI23 use the GISS II' winds).

Transport Between the Stratosphere and Troposphere (Rind)

Also shown in Table 2.3 is the models' ΔNOy tracer mass below and above 100 mb, as well as the ratio. These values are displayed graphically in Figures 2.39 and 2.40. (As the LARC T16 values are

close to those of the LARC T32, only the later are shown in the table; only A3 is available for the GMI-GISS, whose values are often close to those of the UCI23 model using the GISS winds, so the GMI-GISS results are not shown in all the figures.) The ratio of ΔNOy at altitudes above and below 100 mb varies between 2.0 and 5.5, i.e., they vary by almost a factor of 3. For the individual regions, the amount in the "stratosphere" (approximated as the amount above 100 mb in altitude) typically varies over a factor of 2, and the amount in the "troposphere" (below 100 mb in altitude) varies by a factor of 2 to 3. Similar magnitudes of variations arise for A4. Several models differ by even greater amounts. GSFC-2D has very large values of mass at all levels, while the HARVARD model has very high values in the stratosphere (true for both A3 and A4). In addition, UNIVAQ-3D has extremely low values in the troposphere, and hence a very high strat/trop ratio.

The relationship between these results and the altitude distribution of the sources (Figure 2.35) is complicated. The UNIVAQ model and NCAR-3D have sources in layers at the highest altitude. These models do have large strat/trop ratios, but their stratospheric values are not particularly large, implying rapid transport down through the tropopause. In comparison, GMI-NCAR has a somewhat lower altitude source, and does have a lower strat/trop ratio, but actually has a larger stratospheric mass of ΔNOy. HARVARD and GSFC-2D have similarly large high altitude sources and large stratospheric loadings, but their strat/trop ratios differ by more than 50%. NOCAR, LLNL, and GMI-DAO have somewhat lower altitude sources; only the last two of these have low strat/trop ratios, and only the first and third have relatively low stratospheric values. The layering seems to have some effect, but differing model transport is also quite important.

The strat/trop ratio for the 2D models (3.78 average for A3) is not significantly different from that of the 3D models (average 4.10). The 2D model ratios have a somewhat higher standard deviation, but this may simply indicate results from the fact that a number of 3D models use similar wind fields. The average strat/trop ratio for A3 (3.95) is higher than that for A4 (3.00). With the source extending equatorward of 30°N, the A3 tracer can be more easily caught in the tropical upwelling branch of the stratospheric circulation, resulting in a longer stratospheric residence time.

Latitudinal Transport (Rind)

Another important question is how much of the tracer is spread equatorward into the southern hemisphere. Table 2.4 gives the ratios between the two hemispheres at 20 km altitude, near the location of the peak loading. The mean ratio and standard deviation among the models for A3 is 2.76 ± 0.74; 19 of the models are within one standard deviation of the mean. In comparison to some of the other results, this A3 diagnostic shows relatively good agreement among the models. For A4 the mean and standard deviations (21.6 ± 32.9) are dominated by the outlier results, as several models have very little southern hemisphere A4 tracer. The largest ratios for A4 generally occur with the 2D models, although not all of the 2D models have large ratios. The 3D models generally have ratios between 2 and 3 for A3, and between 6 and 9 for A4.

Also shown in the table is the season when the ratio is a maximum. One might expect that the wintertime residual circulation within the stratosphere to be associated with poleward advection of tracers, and hence maximum ratio during that season, or perhaps cumulatively, the following spring. However, there is no agreement on this whatsoever, with each season represented approximately equally.

Stratospheric Vertical Transport (Rind)

To characterize the vertical distribution within the northern hemisphere stratosphere, we calculate the ratio between the peak value at 30 km, 40 km, and 50 km to the absolute peak value, which occurs near the source in the lower stratosphere. Values are given in Tables 2.5 for A3 and A4, taken from the season of maximum concentration in the lowest stratosphere, and choosing the maximum value at the given altitudes. The ratios are therefore meant to be primarily illustrative; different choices for season and location yield different magnitudes. As seen through these ratios, the vertical distribution within the stratosphere differs greatly between models. The mean value and the standard deviation of the ratio for A3 (A4) at 30 km is 0.46 ± 0.19 (0.27 ± 0.15); at 40 km is 0.36 ± 0.13 (0.17 ± 0.10); and at 50 km is 0.33 ± 0.14 (0.14 ± 0.08). The ratio tends to be lower for 2D models, indicating overall slower upward transport. The smaller value of the ratio for A4 is consistent with the lack of a source equatorward of 30°N, the region of maximum upward velocity in the stratosphere.

Other components of the vertical distribution within the stratosphere are visible in Figures 2.35 and 2.36. GSFC-2D has relatively large A3 values in the upper stratosphere/lower mesosphere in both hemisphere, while the HARVARD model has relatively large values at these levels only in the northern hemisphere. Only the HARVARD model maintains a strong hemispheric gradient above 30 km.

Also shown in Table 2.4 is the season of maximum upper to lower stratospheric ratio in the northern hemisphere, a measure of the season of maximum vertical extent of ΔNOy tracer. Most models have an autumn maximum or no significant seasonal variation at all, although a few models have peak summertime values, especially for A4. The tracer abundance in the middle and upper stratosphere is governed by the upward velocity in the tropics. In the real world the season of maximum tropical upward velocity in the lower stratosphere is the northern hemisphere winter, associated with its stronger residual circulation [Rosenlof, 1995]. In the GISS models for example, the vertical velocities in the tropical low-to-middle stratosphere are on the order of 0.5 mm/s. To rise 10 km would then take about 7 months, so a summer/fall maximum in the middle stratosphere may be realistic. The autumn maximum is also in accordance with the seasonal variation of the peak lower stratosphere tracer mass in some models, as discussed below.

Seasonal Variation (Rind)

Another diagnostic of model transport is the seasonal distribution of the total tracer mass, which, as indicated in Table 2.4 and Figures 2.35 and 2.36, is dominated by the lower stratospheric amounts. The season of maximum total ΔNOy mass is indicated in Figure 2.41 for A3; values are generally similar for A4.

The predominant time of year for peak values to occur in the models is autumn to early winter. Only one model had a peak in the summer (LARC) and only one in the late winter (GSFC-2Dint). As the source was constant throughout the year, the peak in the lower stratosphere occurs when the cumulative mixing into the troposphere is weakest. Since downward mixing in the extratropics is thought to occur in conjunction with the stratospheric residual circulation and extratropical storms, both of which maximize in winter, a peak concentration in autumn is reasonable. Note that the peak ozone transport into the troposphere, which occurs in spring, is not a suitable analog, since the lower stratospheric ozone source, associated with transport to high latitudes, maximizes during the winter season, unlike the source used here.

The magnitude of the seasonal variation also differs among models, as seen in Figure 2.41, which shows as a percentage maximum minus minimum values divided by the annual mean. The average

model amplitude is $11 \pm 9\%$; the fact that the standard deviation is almost as large as the mean illustrates the great disparity in seasonal amplitudes. Note that the models using the NCAR-3D winds have larger variations than the other 3D models. The GSFC-2D model has very little seasonal variation.

Summary of A3/A4 Distributions (Rind)

This section has quantified the large differences among model results really in just about every aspect of transport: exchange between the stratosphere and troposphere, between the northern and southern hemispheres, and within the stratosphere. In most of these areas, differences of a factor of 2 or 3 are evident. Given that there is no obvious "right" answer, this degree of uncertainty should be factored into any analysis of aircraft impacts.

What causes the model differences? Model vertical resolution likely plays some role; the differing vertical distribution of the source shown in Figure 2.32 indicates how model layering differs. Model vertical transport, either the diffusion coefficient and the residual circulation in 2D models or the winds in 3D models, are undoubtedly also important. Vertical transport coefficients are for many 2D models "tuned" to observations of long-lived tracer distributions, but apparently this does not result in agreement for the HSCT NOx source. These inert HSCT emission tracers test model transport severely and are likely more sensitive to variations in model formulations than tracers which have tropospheric source and photochemical loss in the middle and upper stratosphere. GCM winds used in the 3D models are compared with observations during the course of development, but there is generally less room for calibration, given the more complete physical representation of many transport processes.

An additional characteristic of importance is the numerical advection scheme utilized. When the GMI-GISS model was run with two different vertical advection schemes, it produced a factor of 2 difference in the peak stratospheric loading of ΔNOy (Rotman, personal communication). This difference is generally reduced at higher resolution (Rasch, personal communication).

The A3 and A4 tracers have no atmospheric counterpart, and thus there is no absolute "right" answer. In the next section we will discuss suggestive relationships between these idealized HSCT tracers and mean age, so that model performance may be indirectly assessed, at least partially. First, however, some comments can be made directly. For troposphere/stratosphere exchange the latitudinal spread of volcanic aerosols implies that high latitude sources have difficulty getting into the opposite hemisphere; thus, especially for A4, a greater NH/SH ratio (within reason) is probably more accurate. (Volcanic aerosols are not a perfect analog because their fall velocity limits their stratospheric lifetime.) The upward vertical advection within the stratosphere should be dominated by tropical upwelling, which appears to be the case in all the models. Given that this upwelling should maximize in the northern hemisphere winter, there should be a seasonal variation in middle stratospheric concentrations, perhaps delayed by the slow rate of transport until the summer or autumn. Some upward advection should occur in any case, so exceedingly low values of tracer mass in the middle stratosphere are probably unreasonable. The seasonal maximum in total concentration in most of the models occurs in late fall, which is reasonable, given that the stratospheric residual circulation, which produces downwelling in the northern hemisphere extratropics, and extratropical storms with associated tropopause folds, should maximize during northern hemisphere winter.

ΔNOy-Γ Relationship (Hall)

Despite the fact that the ΔNOy tracers of experiments A3 and A4 are not real atmospheric tracers, there exist connections between their distributyons in model simulations and distributions of tracers that do have real atmospheric counterparts, such as $\Gamma(\mathbf{x})$. To the extent these relationships are robust,

ΔNOy($\mathbf{x}$) distributions can be assessed indirectly, by comparing simulated and observed $\Gamma(\mathbf{x})$, as has been done in Sections 4 and 5. Boering et al. [1996] noted that in certain limits, $\Gamma(\mathbf{x})$ and ΔNOy($\mathbf{x}$) are closely related. In particular, if the mixing ratio $\chi(\mathbf{x}_0, t)$ of a conserved tracer is linearly increasing in a region $\mathbf{x}_0$, as is SF_6 in the troposphere, then at some other $\mathbf{x}$, $\chi(\mathbf{x}, t) \propto t - \Gamma(\mathbf{x})$. Substituting into the continuity equation for yields

$$\frac{\partial \Gamma}{\partial t} + \mathcal{L}(\Gamma) = 1 \tag{2}$$

where $\mathcal{L}$ is the linear transport operator, and the boundary condition is $\Gamma(\mathbf{x}_0) = 0$. (Γ is a function of t, because transport varies seasonally. If we restrict ourselves to an annually averaged perspective then $\partial\Gamma/\partial t = 0$). Thus, the lag time of a linearly increasing tracer (the mean age) is equivalent to the steady state atmospheric response to a uniform, constant tracer source and a zero boundary condition at the surface. This equivalence suggests a relationship between $\Gamma(\mathbf{x})$ and the distributions of tracers of HSCT emission, such as ΔNOy($\mathbf{x}$), which have stratospheric sources and tropospheric sinks [Boering et al., 1996].

The correspondence cannot be perfect. The source of ΔNOy($\mathbf{x}$) is not uniform, but is instead strongly peaked in the midlatitude lower stratosphere of the northern hemisphere. The approximation of uniform source is only valid to the extent the stratosphere is well-mixed compared to its exchange time with the troposphere, which is not the case. Nonetheless, useful ΔNOy($\mathbf{x}$)-$\Gamma(\mathbf{x})$ relationships may still hold locally within some region about the source. In addition, the ΔNOy that is transported to the rest of the stratosphere may have aspects of its distribution similar to $\Gamma(\mathbf{x})$. The extent this is true will vary among models.

On a global basis, certain similarities between $\Gamma(\mathbf{x})$ and ΔNOy($\mathbf{x}$) are seen by comparing the zonal mean plots in Figures 2.18 and 2.19 and Figures 2.33 and 2.34. In the northern hemisphere lower stratosphere, just below the region of peak forcing, ΔNOy and Γ contours are roughly parallel. In the southern hemisphere, although there is generally much less ΔNOy, the contours are also parallel.

The total amount of ΔNOy in the southern hemisphere is also related to the global $\Gamma(\mathbf{x})$ distribution, at least in certain instances. GSFC-2Dint, HARVARD, and NOCAR, the three models with the largest ratios of northern to southern hemisphere ΔNOy for A3 and A4, are all "class A" models (Figure 2.21). These models have small K_{yy} throughout the stratosphere (Figure 2.23), thereby allowing old air to remain isolated at high latitudes, resulting in the high latitude lower stratospheric Γ maxima, and preventing ΔNOy from reaching the southern hemisphere.

In Figures 2.42 (2D models) and 43 (3D models), we examine more closely northern hemisphere $\Gamma(\mathbf{x})$ and ΔNOy by plotting profiles through the upper troposphere and lower stratosphere. Values are averages from 35°N to 55°N. For most models, $\Gamma(\mathbf{x})$ and ΔNOy($\mathbf{x}$) are well correlated below the ΔNOy($\mathbf{x}$) peak. Moreover, many models have similar $\Gamma(\mathbf{x})/\Delta$NOy($\mathbf{x}$) ratios. This relationship is summarized in Figure 2.44, a scatter plot of $\bar{\Gamma}$ versus $\overline{\Delta NOy}$, where the overbar indicates averaging over the region 16 km to 22 km and 35°N to 55°N. There is a strong correlation in 2D models (bottom panel). 3D models show a somewhat weaker correlation.

The ΔNOy($\mathbf{x}$) distribution in the lower stratosphere is sensitive to several transport mechanisms, and to understand the distributions within models, it is necessary to examine these mechanisms in detail. One mechanism is the mixing of midlatitude air into the tropics, where it can upwell. As noted above, models with weak horizontal mixing tend to have little ΔNOy in the southern hemisphere. Other factors equal, these models will tend to have little ΔNOy in the stratosphere as a whole, because ΔNOy will be transported through the midlatitude tropopause into the troposphere before it can reach other

stratospheric regions. However, other factors are rarely equal among models, and beyond a few extreme cases, there is not a strong relationship between total stratospheric ΔNOy and horizontal mixing rates, or tropical entrainment of extratropical air.

In particular, the rate of transport across the midlatitude tropopause also varies among models. A critical factor determining this transport is simply the height of the source (typically peaking at 18 km) from the tropopause. For this purpose, in 2D models the tropopause is the height of onset of rapid vertical diffusion, which parameterizes vertical mixing processes in the troposphere. The closer the source to the tropopause, the less ΔNOy can reach other stratospheric regions, other things equal. A second factor is the average rate of downward vertical advection by the residual circulation, which carries ΔNOy to tropopause. Again, other things equal, rapid downwelling means less ΔNOy elsewhere in the stratosphere.

Figure 2.45 shows profiles of annually averaged $-\bar{w}^*$ and K_{zz} for several 2D models. Values are averaged from 35°N to 55°N, and panels in the figure correspond to those of Figure 2.42. For example, GSFC-2D has small K_{zz} down to 14 km, below which K_{zz} increases abruptly. This onset of larger K_{zz} is significantly below the peak source level. Moreover, GSFC-2D has relatively slow downwelling. As a consequence, GSFC-2D has one of the highest ΔNOy peak values, and the most ΔNOy over the whole stratosphere. HARVARD has a somewhat higher onset of troposphere-like K_{zz}, but it is still below the source. HARVARD's downwelling rate is the slowest among 2D models. As a consequence, HARVARD has the highest peak value of ΔNOy. The very small values of K_{zz} in HARVARD help to keep the peak ΔNOy high, but also prevent ΔNOy from reaching other parts of the atmosphere. HARVARD's global stratospheric ΔNOy is high, but less than GSFC-2D.

On the other extreme, although GSFC-2Dint has relatively slow downwelling throughout the lower stratosphere and upper troposphere, the transition from low to high K_{zz} is significantly higher and more gradual than other models. In fact, it begins above 18 km, the height of peak ΔNOy source. The resulting ΔNOy peak is smaller than most models. The small peak, combined with small values of K_{zz}, results in GSFC-2Dint having the least ΔNOy in the stratosphere among 2D models.

A similar comparison of 3D MM2 models would be more difficult, but worthwhile. The processes controlling the lower stratospheric ΔNOy(**x**) distributions are both more varied and more difficult to quantify. Stratospheric wave driving is believed to be responsible for the residual circulation ("downward control") [Haynes et al., 1991] and therefore is ultimately responsible for the transport of air from the overworld (the region of exclusively stratospheric potential temperature, in which most HSCT gases are emitted) to the lower-most stratosphere (the region of the stratosphere having potential temperature values whose isopleths cross into the troposphere). However, the fate of air in the lower-most stratosphere is determined by complex tropospheric meteorology [Holton et al., 1995]. The transport across the tropopause associated with upper tropospheric events is not modeled well by diffusion.

Although the processes governing ΔNOy(**x**) are complex, and difficult to assess individually in models, these comparisons have shown a good correlation between ΔNOy(**x**) and Γ(**x**). This implies that despite ΔNOy not being an observable tracer, we can partially assess the realism of its simulation by assessing the realism of simulated Γ(**x**), for which observations exist. Figure 2.46 shows several model Γ(**x**) profiles at 35°N through the upper troposphere and lower stratosphere. The symbols are Γ inferred from SF_6 measurements from an OMS balloon flight at similar latitude (see Section 3). Here, Γ from models is derived from the SF_6 simulations, rather than $G(\mathbf{x}, t)$, so that the values correspond to the month of flight (September) rather than an annual mean. Most models underestimate $d\Gamma/dz$ through the region, and hence have air in the lower stratosphere that is too young. To the extent that the ΔNOy(**x**)-Γ(**x**) relationship is robust, the Γ underestimate implies that most models also underestimate ΔNOy in the lower stratosphere, as has been suggested by Boering et al. [1996].

3D models may have a different $\Delta NOy(\mathbf{x})$-$\Gamma(\mathbf{x})$ relationship than 2D models. For example, transport into the troposphere along middle-world isentropes carries lower stratospheric tracers further into the tropics of the troposphere than does the rapid vertical diffusion of 2D models. This would imply younger air in the lower midlatitude stratosphere for the same amount of ΔNOy, as the pathway to the "age sink" (near the tropical surface for experiment A1) would be more direct. Such a difference is hinted at in Figure 2.42, which shows the 3D models having a more shallow ΔNOy-Γ slope (and displaying more scatter). In order to establish a more reliable ΔNOy-Γ relationship, experiments should be performed with more realistically prescribed tropospheric sources and sinks of ΔNOy and Γ.

2.9 Summary and Conclusions (Hall)

In this chapter we have reported on model simulations of idealized and realistic conserved tracers in order to better understand model transport and evaluate model transport against observations. Two general observations may be made:

(1) There is large variation in model transport, producing mean age fields that vary by more than a factor 2, both locally and integrated, and ΔNOy fields that vary by factors of 4 or more, both locally and integrated.

(2) Model-to-model variations in mean age are reflected, although reduced, in simulations of long-lived photochemically active species, such as N_2O, NOy, and Cly. This suggests that uncertainty in model transport is a major factor determining uncertainty in the background chemical state of model stratospheres.

In addition to these observations, we draw several more specific conclusions and isolate aspects of model transport that need improving:

(3) All models have too low mean age throughout the lower and middle stratosphere compared to observations, in some models and locations by a factor more than 2.

(4) Several models (AER, CSIRO, GSFC-2D, SUNY, GMI-NCAR, MONASH1, MONASH2) have realistic zonally-averaged contour shapes of mean age ("class B" in the nomenclature of Section 5), but their mean age magnitude is still too small. Other models have unrealistic features in their contour shapes ("class A" or "class C" depending on features), in addition to low mean age.

(5) Many 2D models have too large explicit vertical diffusion (too large K_{zz}).

(6) Models that compute planetary wave propagation and breaking interactively with the circulation tend to have too little quasi-horizontal mixing in the stratosphere (too small K_{yy}).

(7) The vertical phase velocity in the tropics of the annual cycle tracer such as H_2O+2CH_4 is too rapid for most models. This fact, combined with low mean age indicates too rapid vertical upwelling in the tropics, although some of the phase velocity is due to the high vertical diffusion.

(8) Many models have tropics that are not isolated enough, as seen in the overattenuation (per wavelength) of the annual cycle tracer and in the unrealistically "flat" mean age contours (class C models). For some models vertical diffusion may be responsible for the overattenuation.

(9) For most models, mean age should be increased by reducing the residual circulation magnitude. Increased mixing of extratropical air into the tropics would also increase mean age overall, but this would detrimentally affect the tropics for most model (point (8)).

We have not systematically examined the impact on long-lived tracer transport of numerical aspects of model formulation such as advection algorithm, grid resolution, and coordinate system. Such a study would be worthwhile. Nonetheless, some conclusions can be drawn with regards to certain models. The mean age distributions are similar for the three-dimensional models MONASH2 and GMI-NCAR, which differ only in their advection algorithm. On the other hand, models having the same advection algorithm, resolution, and other aspects of numerical formulation, but differing in their large scale circulation (e.g., MONASH1 and MONASH2), have significant mean age differences. This suggests that the choice of advection algorithm plays only a minor role in long-lived tracer transport for at least some of the models. As for model resolution, increasing the horizontal grid resolution in one model tested (LARC) resulted in only a small increase of stratospheric residence time of the HSCT emission tracer compared to the variation across models. However, simulations of long-lived tracers by other models, for example those models having lower resolution, may be more sensitive to numerical formulation.

It is important to appreciate that transport "mechanisms," such as residual circulation advection and mixing of extratropical air into the tropics, are highly coupled. The coupling is dynamical for models that compute these phenomena in a self-consistent way. However, even for models which prescribe the mechanisms explicitly, their effects on tracers are coupled. Thus, for example, one might strive to slow the residual circulation in order to increase mean age, and end up with older air but a poorly isolated tropics, as seen in the mean age contour shapes. One would need to find the proper balance of residual circulation magnitude and extratropical to tropical transport. This is difficult enough for highly "tunable" models, having explicit mechanism prescriptions. For more realistic models, in which the mechanisms are not truly separable in a dynamic sense, it is still more difficult. Nonetheless, given observation (2) above, this is the task ahead.

Finally, we observed a suggestive positive correlation across models between ΔNOy and mean age in the lower midlatitude stratosphere. In fact, idealized arguments hint that such a relationship might be expected. The "integrated mean age" $\bar{\Gamma}$ of the stratosphere (the mean time since air in the stratosphere was last in contact with the troposphere) equals the residence time $\bar{\tau}_R$ of the stratosphere (the mean time since air in the stratosphere next makes contact with the troposphere). If the stratosphere were a well-mixed reservoir in contact with a lower boundary (the troposphere), then a tracer emitted locally in the stratosphere at steady flux F would have total stratospheric abundance given simply by $F\bar{\tau}_R$, which equals $F\bar{\Gamma}$. Alternatively, instead of assuming "well-mixedness", an identical conclusion is reached if the tracer is assumed to be emitted uniformly through the stratosphere [Boering et al., 1996].

Clearly, the stratosphere is not well mixed and HSCT emissions are highly localized. Nonetheless, certain transport mechanisms push both the mean age and the residence time of tracers released in the lower midlatitude stratosphere in the same direction. Other factors equal, the more rapid the mixing of extratropical air into the tropics, the greater the overall mean age and the greater the residence time, as air and emission tracer are more likely to recirculate about the Brewer-Dobson cell before exiting the stratosphere. Again, other factors equal, the slower the rate of midlatitude stratosphere to troposphere transport, the greater the mean age and residence time, as more time is available for air and tracer in the lower midlatitude stratosphere to enter the tropics. Both effects push the stratosphere closer to being well-mixed compared to timescales for transport into the troposphere. At the other extreme, in the limit of pure advection by the residual circulation, the residence time and mean age must be very different, as the tracer emitted in the lower midlatitude stratosphere is much closer to exiting the stratosphere than is air newly entering the stratosphere in the tropics. Still, the slower the residual circulation, the greater both the residence time and the mean age.

It is tempting, therefore, to extrapolate the ΔNOy-Γ correlation and conclude that because models underestimate mean age, they underestimate ΔNOy. However, such a conclusion must presently be treated with great caution. The idealized arguments above have not been quantified, and take no account of the complex coupling between transport mechanisms. Moreover, we observed a poorer correlation among 3D models than 2D models, which is not understood. Until the relationship between conserved tracers of different point source locations has a more reliable theoretical underpinning, the ΔNOy-Γ relationship must be viewed as merely suggestive.

References

Andrews, A. E., K. A. Boering, B. C. Daube, and S. C. Wofsy, Empirical age spectra from observations of stratospheric CO_2: mean ages, vertical ascent rates, and dispersion in the lower tropical stratosphere, *J. Geophys. Res.*, 1998, (submitted).

Bischof, W., R. Borchers, P. Fabian, and B. C. Kruger, Increased concentration and vertical distribution of carbon dioxide in the stratosphere, *Nature*, *316*, 708–710, 1985.

Boering, K. A., B. C. Daube, S. C. Wofsey, M. Loewenstein, J. R. Podolske, and E. R. Keim, Tracer-tracer relationships and lower stratospheric dynamics: CO_2 and N_2O correlations during SPADE, *Geophys. Res. Lett.*, *21*, 2567–2570, 1994.

Boering, K. A., et al., Measurements of stratospheric carbon dioxide and water vapor at northern midlatitudes: Implications for troposphere-to-stratosphere transport, *Geophys. Res. Lett.*, *22*, 2737–2740, 1995.

Boering, K. A. et al., Timescales for stratospheric transport inferred from in situ observations of CO_2 from aircraft and balloons, *J. Geophys. Res.*, 1998, (to be submitted).

Boering, K. A., S. C. Wofsy, B. C. Daube, H. R. Schneider, M. Loewenstein, and J. R. Podolske, Stratospheric mean ages and transport rates derived from observations of CO_2 and N_2O, *Science*, *274*, 1340–1343, 1996.

Elkins, J. W., et al., Airborne gas chromatograph for in situ measurements of long-lived species in the upper troposphere and lower stratosphere, *Geophys. Res. Lett.*, *23*, 347–350, 1996.

Elkins, J. W., et al., Mean age of air in the lower and middle stratosphere fom 1991 through 1998, *J. Geophys. Res.*, 1998, (to be submitted).

Eluszkiewicz, J., et al., Residual circulation in the stratosphere and lower mesosphere as diagnosed from microwave limb sounder data, *J. Atmos. Sci.*, *53*, 217–240, 1996.

Geller, L. S., J. W. Elkins, R. C. Myers, J. M. Lobert, A. D. Clarke, D. H. Hurst, and J. H. Butler, Tropospheric SF_6: Observed latitudinal distribution and trends, derived emissions, and interhemispheric exchange time, *Geophys. Res. Lett.*, *24*, 675–678, 1997.

Hall, T. M., and R. A. Plumb, Age as a diagnostic of stratospheric transport, *J. Geophys. Res.*, *99*, 1059–1070, 1994.

Hall, T. M., and D. W. Waugh, Timescales for the stratospheric circulation derived from tracers. *J. Geophys. Res.*, *102*, 8991–9001, 1997a.

Hall, T. M., and D. W. Waugh, Tracer transport in the tropical stratosphere due to vertical diffusion and horizontal mixing, *Geophys. Res. Lett.*, *24*, 1383–1386, 1997b.

Hall, T. M., and D. W. Waugh, The influence of nonlocal chemistry on tracer distributions: inferring the mean age of air from SF_6, *J. Geophys. Res.*, pages 13,327–13,336, 1998.

Harnisch, J., R. Borchers, P. Fabian, and M. Maiss, Tropospheric trends for CF_4 and C_2F_6 since 1982 derived from SF_6 dated stratospheric air, *Geophys. Res. Lett.*, *23*, 1099–11002, 1996.

Haynes, P. H., C. J. Marks, M. E. McIntyre, T. G. Shepherd, and K. P. Shine, On the downward control of extratropical diabatic circulations by eddy-induced mean zonal forces, *J. Atmos. Sci.*, *48*, 651–678, 1991.

Holton, J. R., P. H. Haynes, M. E. McIntyre, A. R. Douglass, R. R. Rood, and L. Pfister, Stratosphere-troposphere exchange, *Rev. Geophys.*, *33*, 403–439, 1995.

Holzer, M., and T.M. Hall, Transit-time and tracer-age distributions in geophysical flows, *J. Atmos. Sci.*, 1999 (submitted).

Jost, H., et al., Filaments in the tropical middle atmosphere: Origin and age estimation, *Geophys. Res. Lett.*, 1998, (to be submitted).

Kida, H., General circulation of air parcels and transport characteristics derived froma hemispheric GCM, Part 2, Very long-term motions of air parcels in the troposphere and stratosphere, *J. Meteorol. Soc. Jpn.*, *61*, 510–522, 1983.

Lin, S. J., and R. B. Rood, Multidimensional flux-form semi-Lagrangian transport schemes, *Mon. Weather Rev.*, *124*, 2046–2070, 1996.

Maiss, M., L. P. Steele, R. J. Francey, P. J. Fraser, R. L. Langenfelds, N. B. A. Trivett, and I. Levin, Sulfer hexafluoride: A powerful new atmospheric tracer, *Atmos. Environ.*, *30*, 1621 –1629, 1996.

Minschwaner, K., A. E. Dessler, J. W. Elkins, C. M. Volk, D. W. Fahey, M. Lowenstein, J. R. Podolske, A. E. Roche, and K. R. Chan, The bulk properties of isentropic mixing into the tropics in the lower stratosphere, *J. Geophys. Res.*, *101*, 9433–9439, 1996.

Mote, P. W., T. J. Dunkerton, M. E. McIntyre, E. A. Ray, and P. H. Haynes, Vertical velocity, vertical diffusion, and dilution by midlatitude air in the tropical lower stratosphere, *J. Geophys. Res.*, *103*, 8651–8666, 1998.

Mote, P. W., K. H. Rosenlof, J. R. Holton, R. S. Harwood, and J. W. Waters, Seasonal variations of water vapor in the tropical lower stratosphere, *Geophys. Res. Lett.*, *22*, 1093–1096, 1995.

Mote, P. W., K. H. Rosenlof, M. E. McIntyre, E. S. Carr, J. C. Gille, J. R. Holton, J. S. Kinnersley, H. C. Pumphrey, J. M. Russell, and J. W. Waters, An atmospheric tape recorder: the imprint of tropical tropopause tempertures on stratospheric water vapor, *J. Geophys. Res.*, *101*, 3989–4006, 1996.

Neu, J., and R. A. Plumb, 1998. The age of air in a "leaky pipe" model of stratospheric transport, *J. Geophys. Res.*, 1999 (in press).

Plumb, R. A., A tropical pipe model of stratsopheric transport, *J. Geophys. Res.*, *101*, 3957–3972, 1996.

Plumb, R. A., and M. K. W. Ko, Interrelationships between mixing ratios of long-lived stratsopheric constituents, *J. Geophys. Res.*, *97*, 10,145–10,156, 1992.

Plumb, R. A., and D. D. McConalogue, On the meridional structure of long-lived tropospheric constituents, *J. Geophys. Res.*, *93*, 15,897–15,913, 1988.

Prather, M. J., Numerical advection by conservation of second-order moments, *J. Geophys. Res.*, *91*, 6671–6681, 1986.

Prather, M. J., Time scales in atmospheric chemistry: Theory, GWPs for CH_4 and CO, and runaway growth, *Geophys. Res. Lett.*, *23*, 2597–2600, 1996.

Prather, M. J., and E. Remsberg, The Atmospheric Effects of Stratospheric Aircraft: Reports of the 1992 Models and Measurements Workshop, *NASA Ref. Publ.*, *1292*, 1993.

Randel, W. J., B. A. Boville, J. C. Gille, P. L. Bailey, S. T. Massie, J. B. Kumer, J. L. Mergenthaler, and A. E. Roche, Simulation of stratospheric N_2O in the NCAR CCM2: Comparison with CLAES data and global budget analysis, *J. Atmos. Sci.*, *51*, 2834–2845, 1994.

Randel, W. J., F. Wu, J. M. Russell, A. Roche, and J. W. Waters, Seasonal cycles and qbo variations in stratospheric CH_4 and H_2O observed in UARS HALOE data, *J. Atmos. Sci.*, 55, 163–184, 1998.

Rasch, P. J., Conservative shape-preserving two-dimensional transport on a spherical reduced grid, *Mon. Weather Rev.*, *122*, 1337–1350, 1994.

Rosenlof, K. H., Seasonal cycle of the residual mean circulation in the stratosphere, *J. Geophys. Res.*, *100*, 5173–5191, 1995.

Schmidt, U., and A. Khedim, In situ measurements of carbon dioxide in the winter arctic vortex and at midlatitudes: An indicator of the age of stratospheric air, *Geophys. Res. Lett.*, *18*, 763–766, 1991.

Schoeberl, M. R., A. E. Roche, J. M. R. III, D. Ortland, P. B. Hays, and J. W. Waters, An estimation of the dynamical isolation of the tropical lower stratosphere using UARS wind and trace gas observations of the quasi-biennial oscillation, *Geophys. Res. Lett.*, *24*, 53–56, 1997.

Voemel, H., Hasebe, Shiotani, and S. J. Oltmans, Balloon-borne measurements of lower stratospheric water vapor in tropical regions, *J. Geophys. Res.*, 1998, (to be submitted).

Voemel, H., S. J. Oltmans, D. Kley, and P. J. Crutzen, New evidence for the stratospheric dehydration mechanism in the equatorial Pacific, *Geophys. Res. Lett.*, *22*, 3235–3238, 1995.

Volk, C. M., J. W. Elkins, D. W. Fahey, G. S. Dutton, J. M. Gilligan, M. Lowenstein, P. R. Podolske, K. R. Chan, and M. R. Gunson, Evaluation of source gas lifetimes from stratospheric observations, *J. Geophys. Res.*, *102*, 25,543–25,564, 1997.

Volk, C. M., J. W. Elkins, D. W. Fahey, R. J. Salawitch, G. S. Dutton, J. M. Gilligan, M. H. Proffitt, M. Lowenstein, P. R. Podolske, K. Minshwaner, J. J. Margitan, and K. R. Chan, Quantifying transport between the tropical and mid-latitude lower stratosphere, *Science*, *272*, 1763–1768, 1996.

Waugh, D. W., et al., Mixing of polar vortex air into middle latitudes as revealed by tracer-tracer scatterplots, *J. Geophys. Res.*, *102*, 13,119–13,134, 1997.

Weinstock, E. M., E. J. Hintsa, J. G. Anderson, R. L. Herman, R. D. May, C. R. Webster, and T. P. Bui, Evaluation of the seasonal cycle of water vapor in the stratosphere derived from monthly average tropical tropopause temperatures using a CO photochemical clock, *J. Geophys. Res.*, 1998, (submitted).

Weisenstein, D. W., M. K. W. Ko, N. D. Sze, and J. M. Rodriguez, Potential impact of SO_2 emissions from stratospheric aircraft on ozone, *Geophys. Res. Lett.*, *23*, 161–164, 1996.

Yudin, V. A., S. P. Smyshlyaev, M. A. Geller, and V. L. Dvortsov, Transport diagnostics of GCMs and implications for 2D chemistry-transport model of troposphere and stratosphere, *J. Atmos. Sci.*, 1998, (submitted).

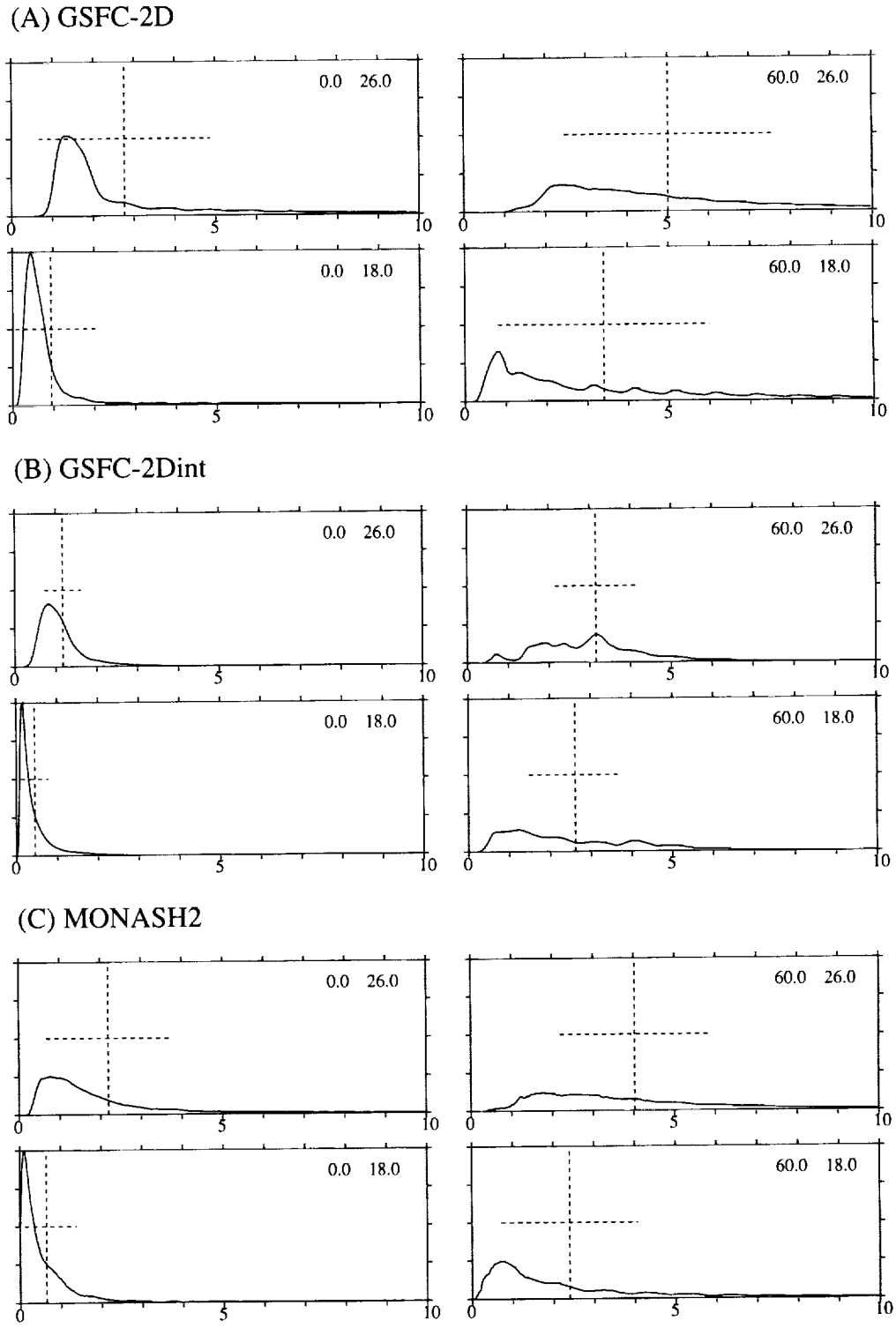

Figure 2.1. The age spectra for 3 models at 4 locations in the latitude-height plane: the equator at 18 km and 26 km, and 60°N at 18 km and 26 km. The models are (a) GSFC-2D, (b) GSFC-2Dint, and (c) MONASH2. The mean age is indicated by the vertical dashed line, and the spectral width by the horizontal dashed line.

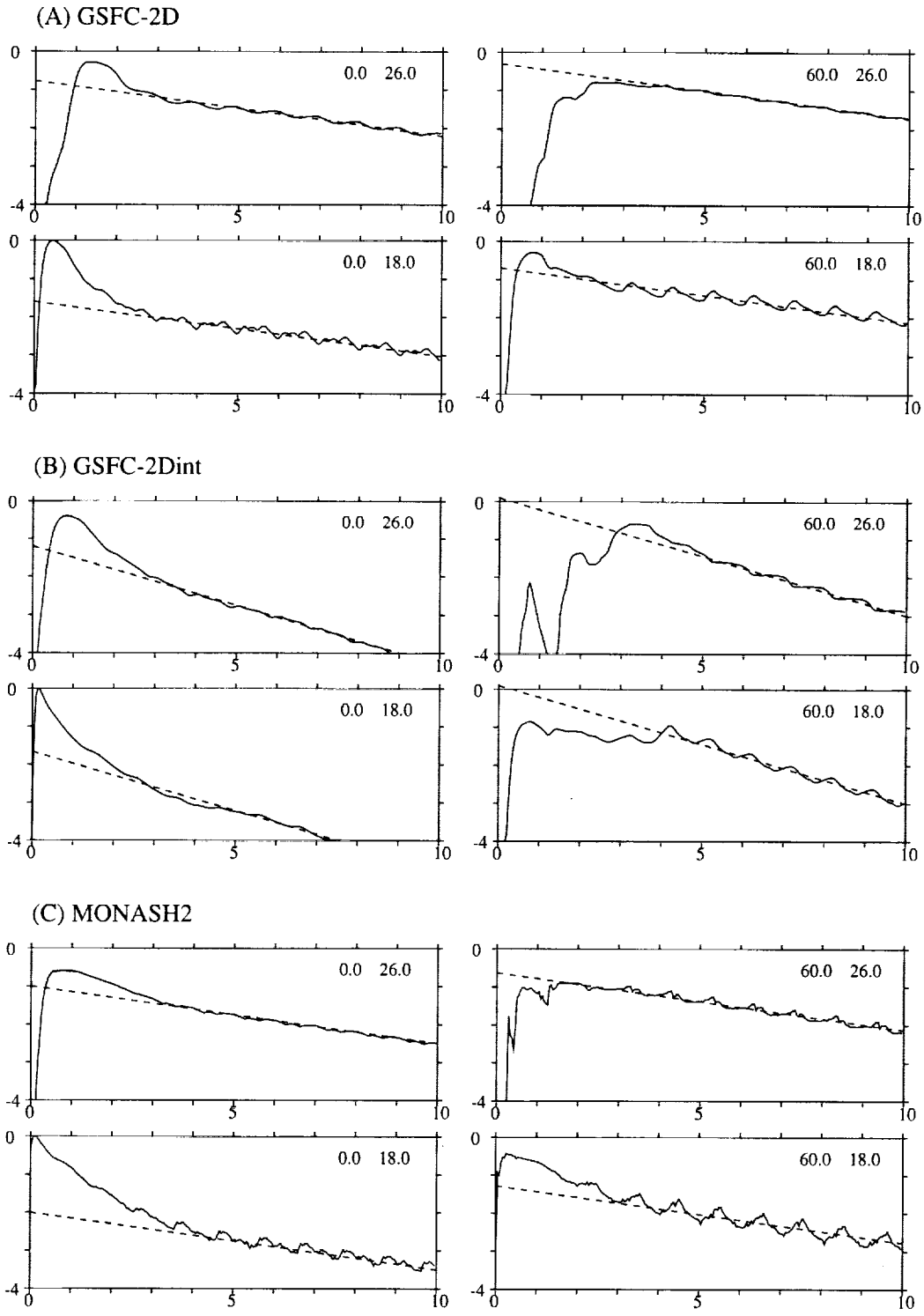

Figure 2.2. The same as in Figure 1, but here the vertical axes are log scale to emphasize the universal exponential decay time τ_0. The decay mode τ_0, as listed in Table 2.2, is illustrated by the dashed lines.

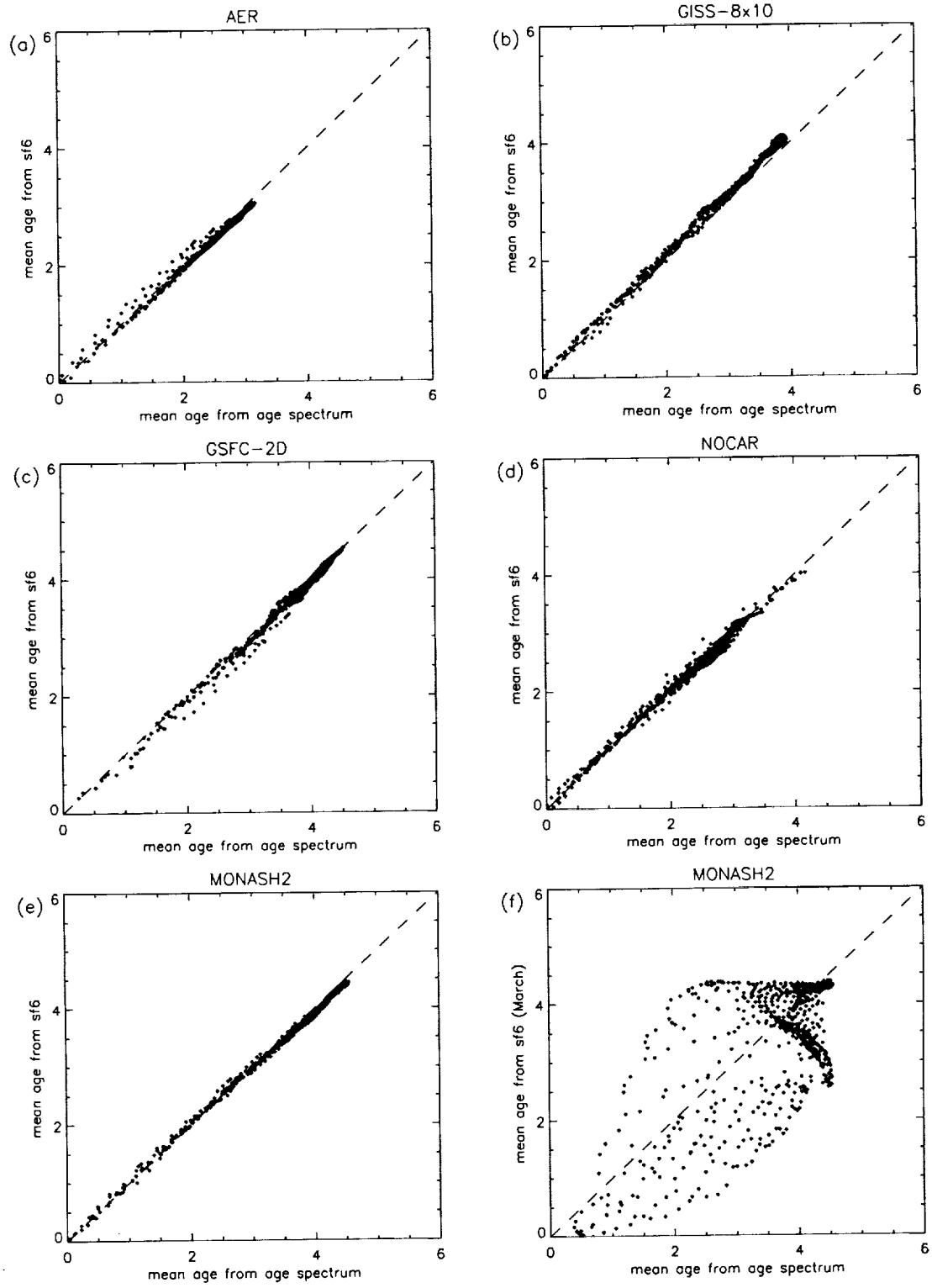

Figure 2.3. Scatter plots of mean age deduced from the SF_6 simulations (vertical axes) and the age spectrum (horizontal axes). The models are (a) AER, (b) GISS8x10, (c) GSFC-2D, (d) NOCAR, and (e) MONASH2. For (a) through (e), the SF_6 age is an annual mean. Panel (e) represents MONASH2, but this time the SF_6 lag is for January only.

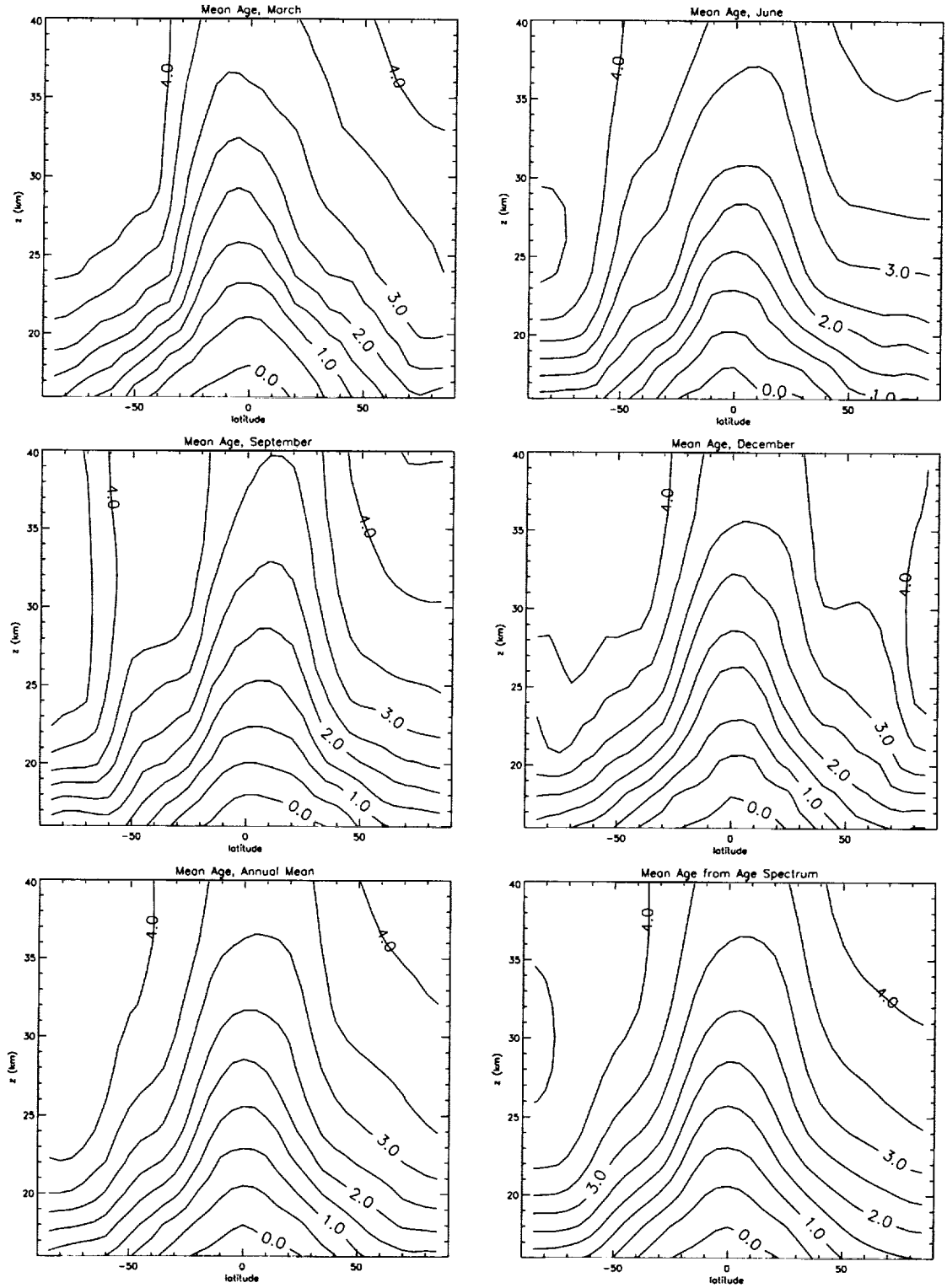

Figure 2.4. Zonally-averaged mean age distribution from MONASH2 for the individual months March, June, September, December, the annual mean, and the age spectral mean, as indicated.

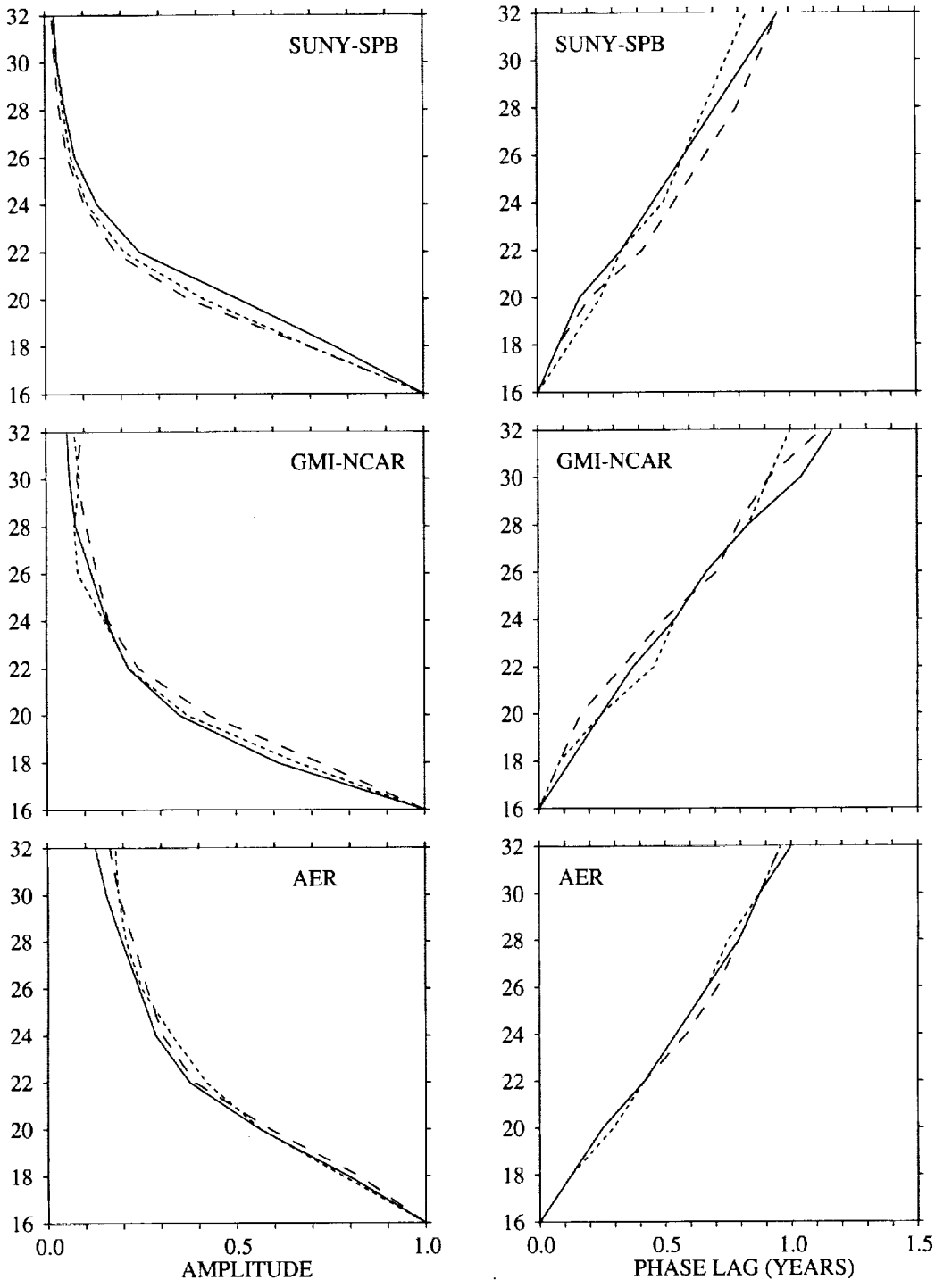

Figure 2.5. Profiles of $A(z)$ (left column) and $\tau_\omega(z)$ (right column) as reconstructed from the age spectrum (solid) and from the sine (short-dash) and cosine (long-dash) experiments. Each row is a different model: SUNY-SPB (top), GMI-NCAR (middle), and AER (bottom).

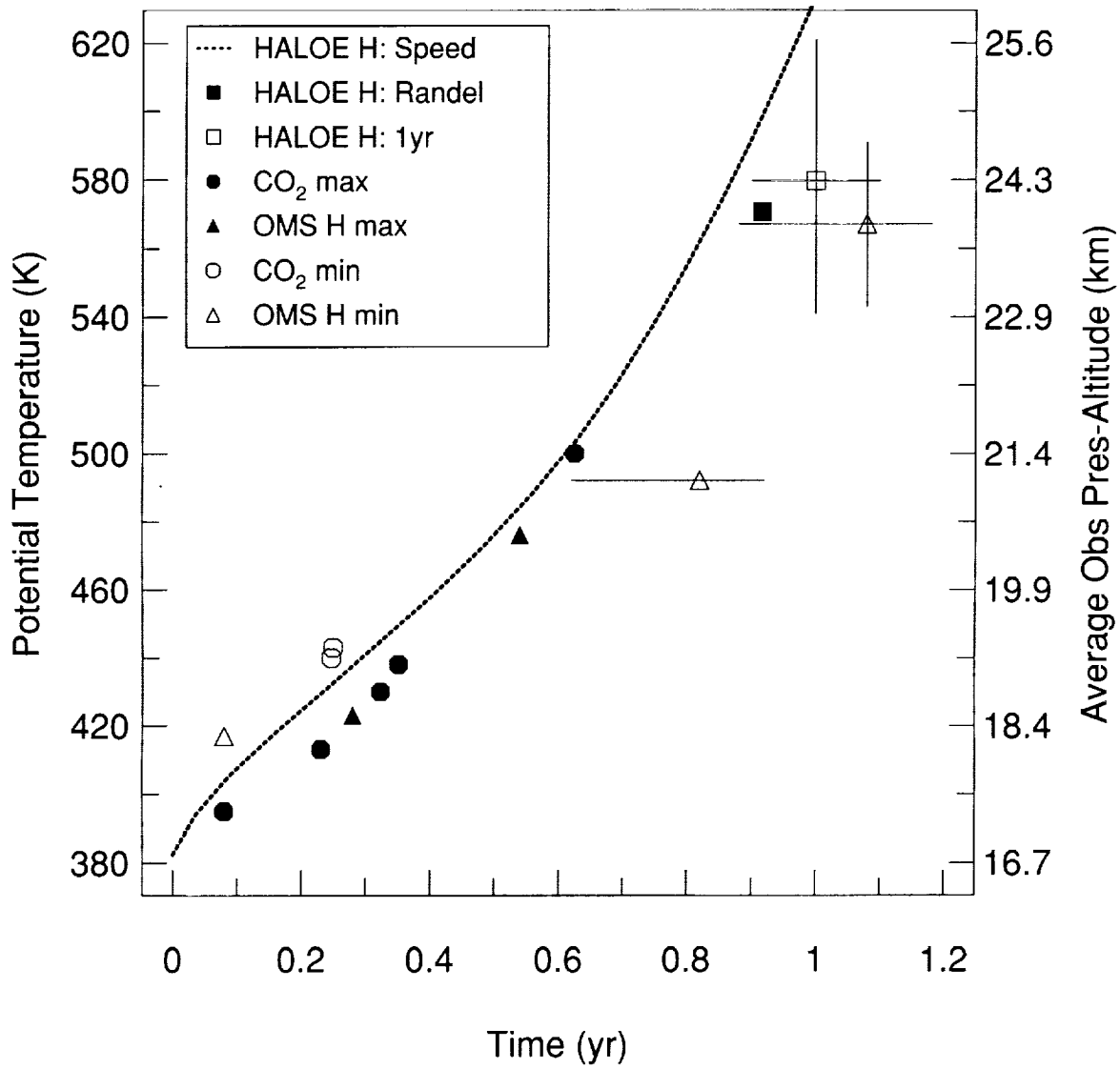

Figure 2.6. Tropical profiles of phase lag times (τ_ω) from both remote ($\hat{H}$) and in situ ($\hat{H}$ and CO_2) observations (see text for details of the observations). For the in situ observations, the measured potential temperature is represented on the left y-axis and an average tropical pressure-altitude derived from the potential temperature:pressure altitude relationships from the in situ campaigns is represented on the right y-axis. For the HALOE observations, the observed pressure-altitudes have been converted into potential temperatures using the in situ potential temperature:pressure altitude relationship.

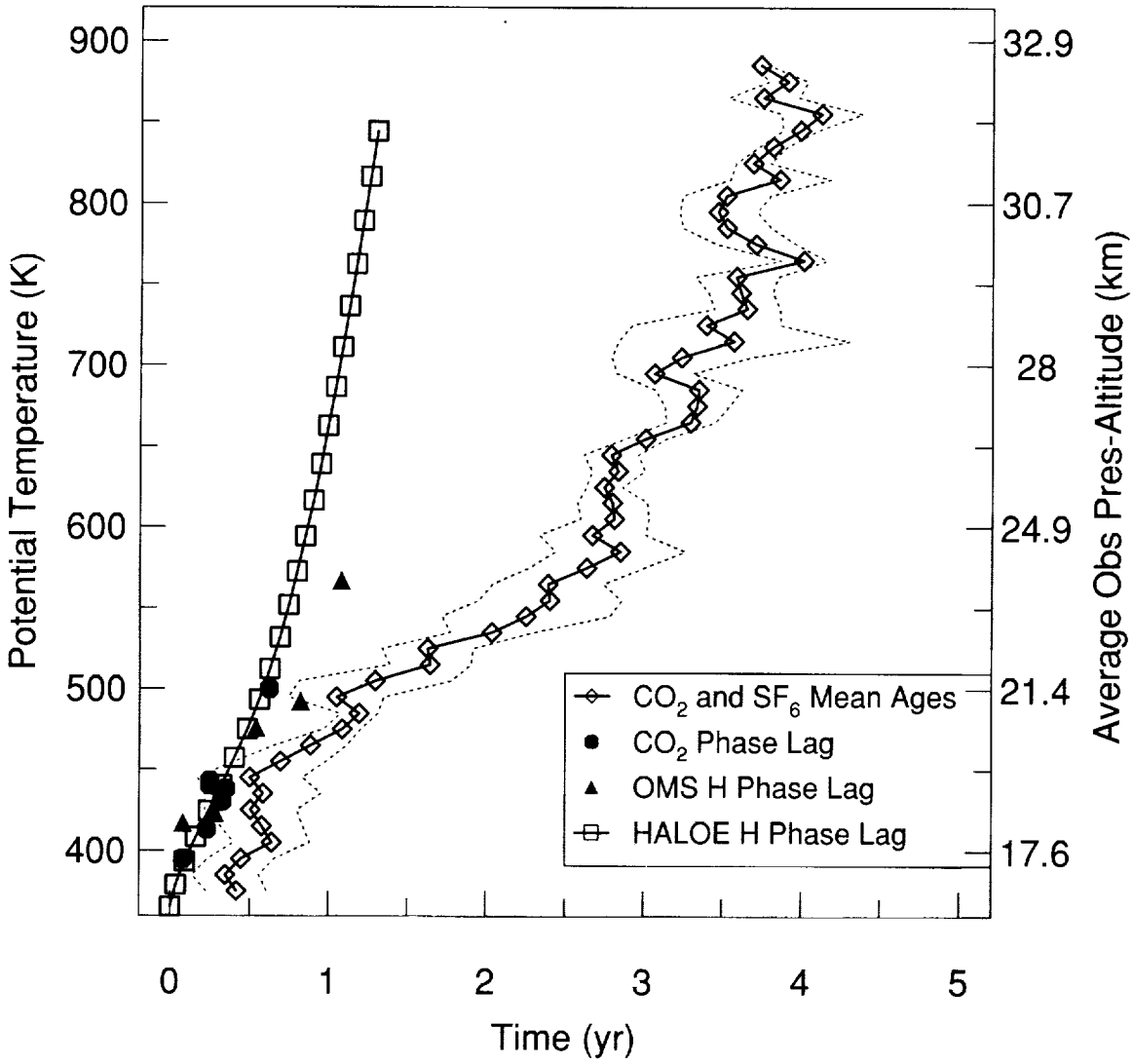

Figure 2.7. Tropical profiles of phase lag times (τ_ω) from in situ and remote observations and mean age (Γ) from in situ observations. The mean age profile (diamonds) is an average of the mean ages derived from in situ CO_2 observations (3 profiles: 970214, 971111, 971120) and SF_6 observations (2 profiles: 970214, 971111) at 7S in Juazeiro do Norte, Brazil. Dotted lines are the 1-sigma standard deviation of the average of the 5 profiles. Note that mean ages from SF_6 were set to zero at the tropical tropopause and that seasonal variations in CO_2 in the lowest 4 km of the stratosphere largely cancel out between the November and February profiles.

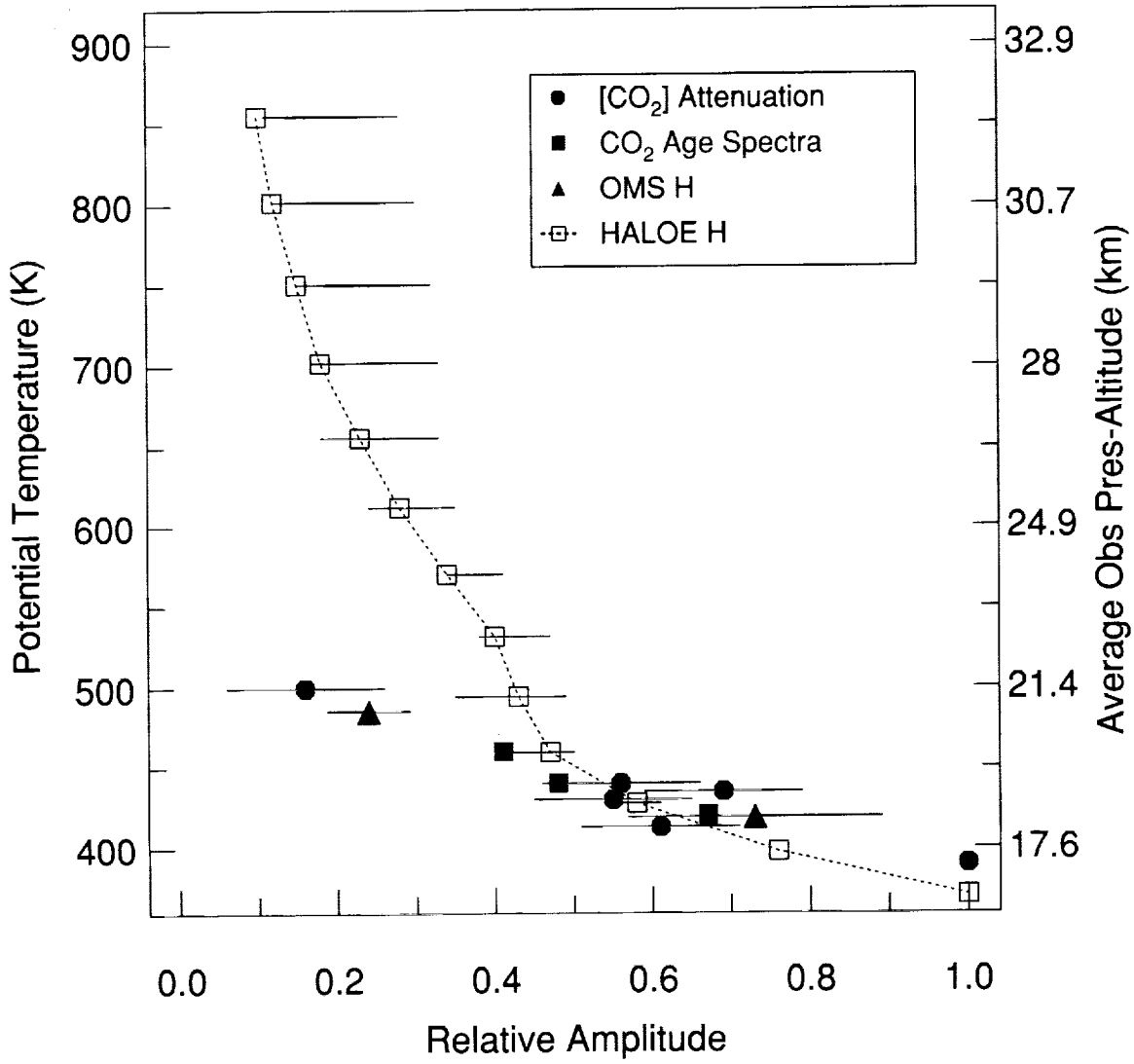

Figure 2.8. Tropical profiles of $A(z)$. All amplitudes are normalized to unity at the tropical tropopause (taken as 390K for in situ data and 100 mb for HALOE). The open squares represent the analysis of HALOE $\hat{H}$ by Mote et al. [1998]. The circles represent the attenuation of the CO_2 annual cycle from 6 aircraft and 2 balloon deployments between 1994 and 1997 [Boering et al., 1996; Boering et al., 1998]. Gray squares are the amplitude from empirical age spectra determined from a time series of 9 profiles in the lower tropical stratosphere from 1994 through 1997 at 420, 440, and 460K [Andrews et al., 1998]. The triangles are attenuations derived from observations of H-hat from these same 2 balloon deployments in 1997 [Voemel et al., 1998].

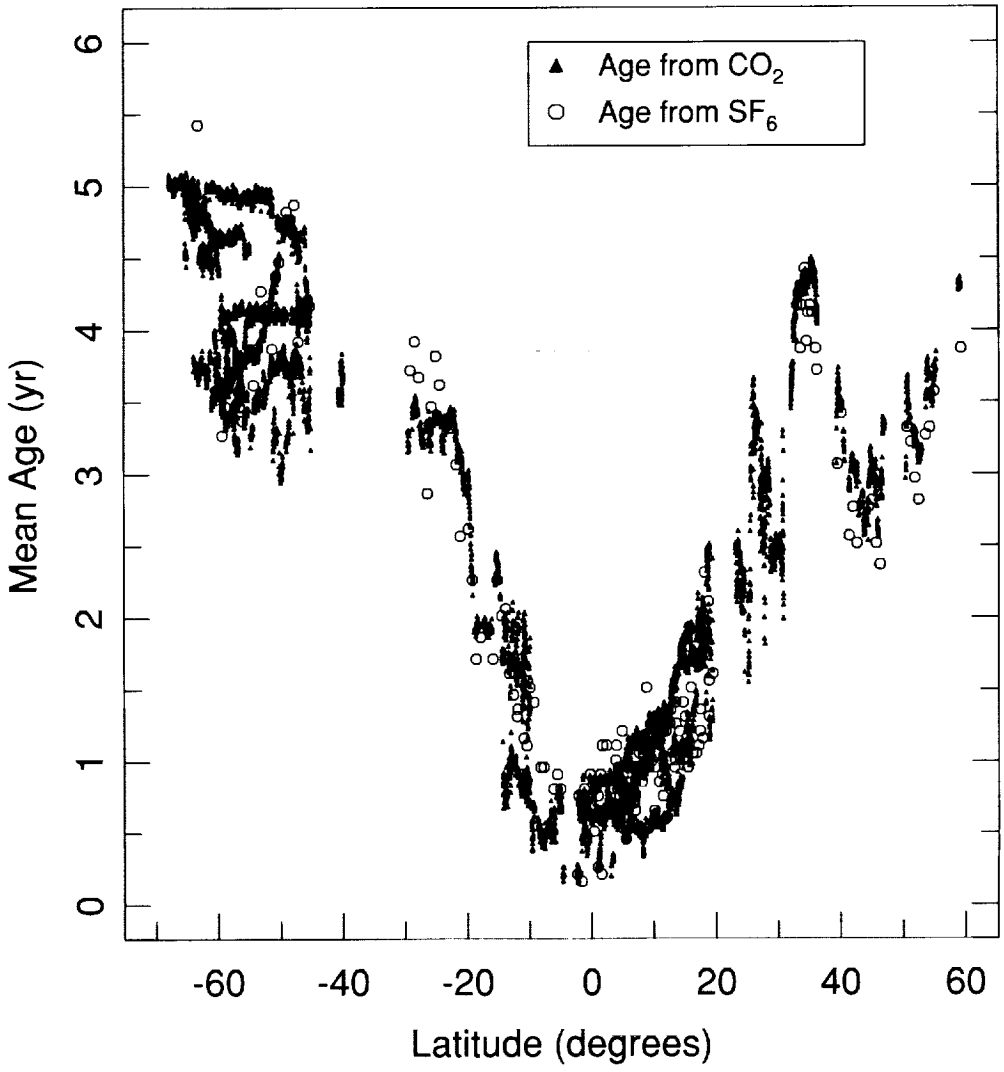

Figure 2.9. Mean age variations with latitude at 19-20 km over a 3-week period in October-November 1994. Circles are mean ages derived from SF_6 observations and triangles are mean ages derived from CO_2 observations.

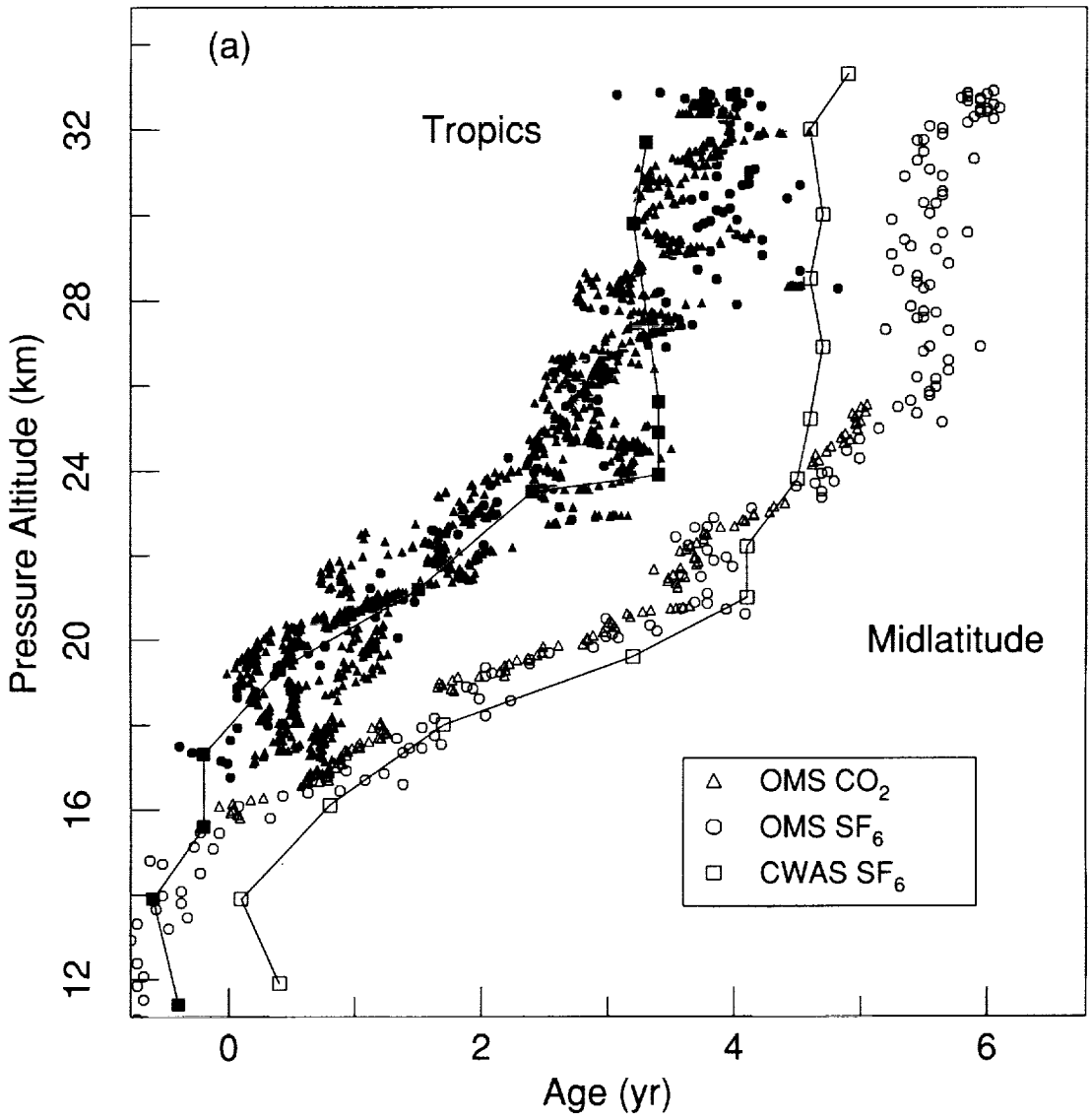

Figure 2.10. Mean age profiles from balloon observations (a) in the tropics and middle latitudes and (b) in middle and high latitudes, including vortex data. Data labeled "OMS" are in situ balloon measurements of CO_2 (triangles) and SF_6 (circles) while data labeled "CWAS" are laboratory measurements of SF_6 collected from a balloon-borne cryogenic whole air sampler (squares). The color coding is as follows: (a) black points are from the OMS flight of 970214 at 7°S and from a CWAS flight at 17°N in 1987; red points are from the OMS flight of 971111 and 981120 at 7°S; open symbols are for the OMS flight of 960921 at 34°N and for the CWAS flight at 44°N in 1993; (b) Open black symbols are the same as in (a); pink points are for the OMS flight of 970630 at 64°N and from a CWAS flight at 68°N in 1995; red squares represent CWAS data obtained in the Arctic vortex at 68°N. Note that filaments of Arctic vortex air were encountered in the OMS flight of 970630, although they are not color-coded as such. The CWAS data have been shifted by -1.4 years (see text).

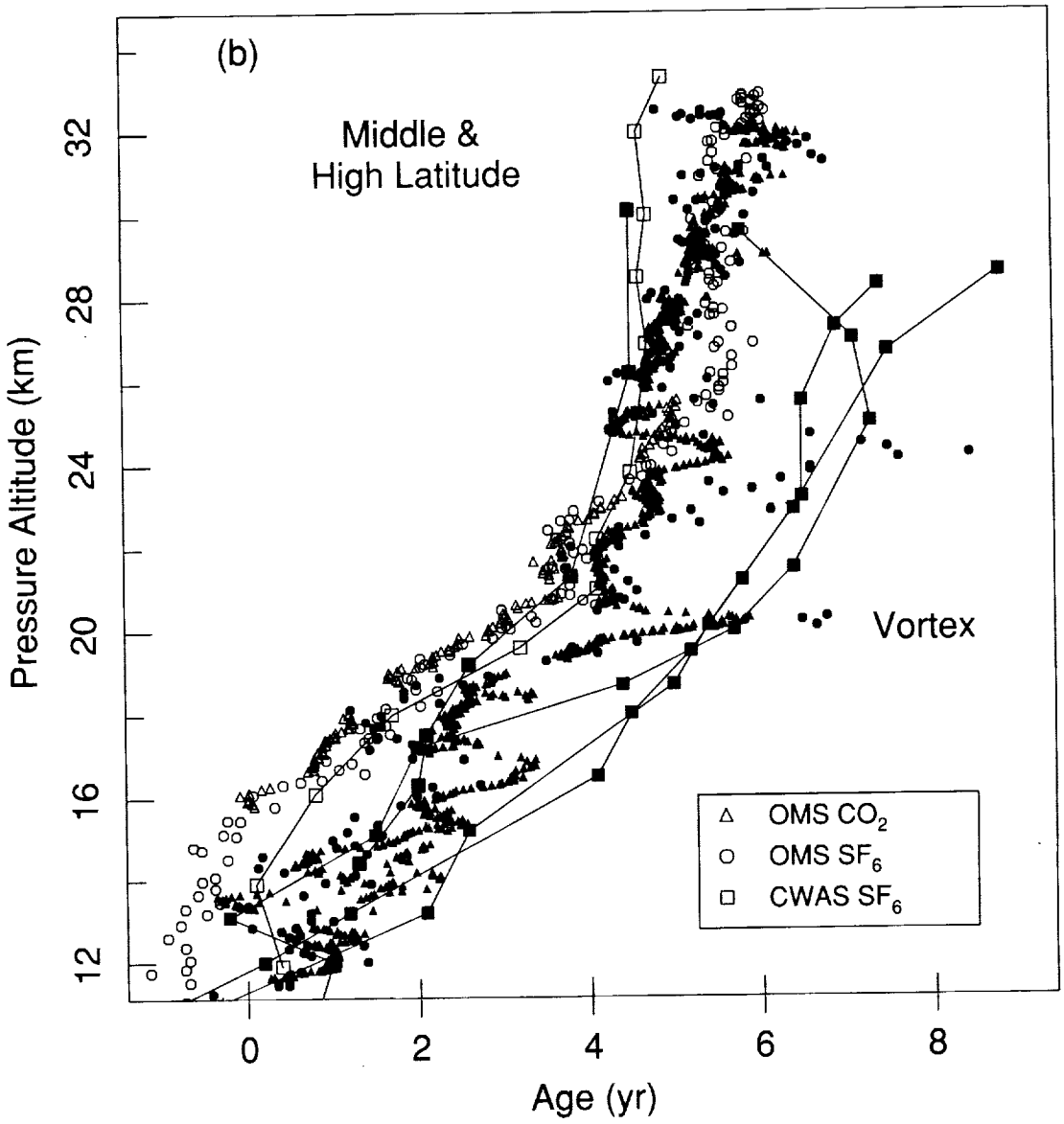

Figure 2.10. Concluded.

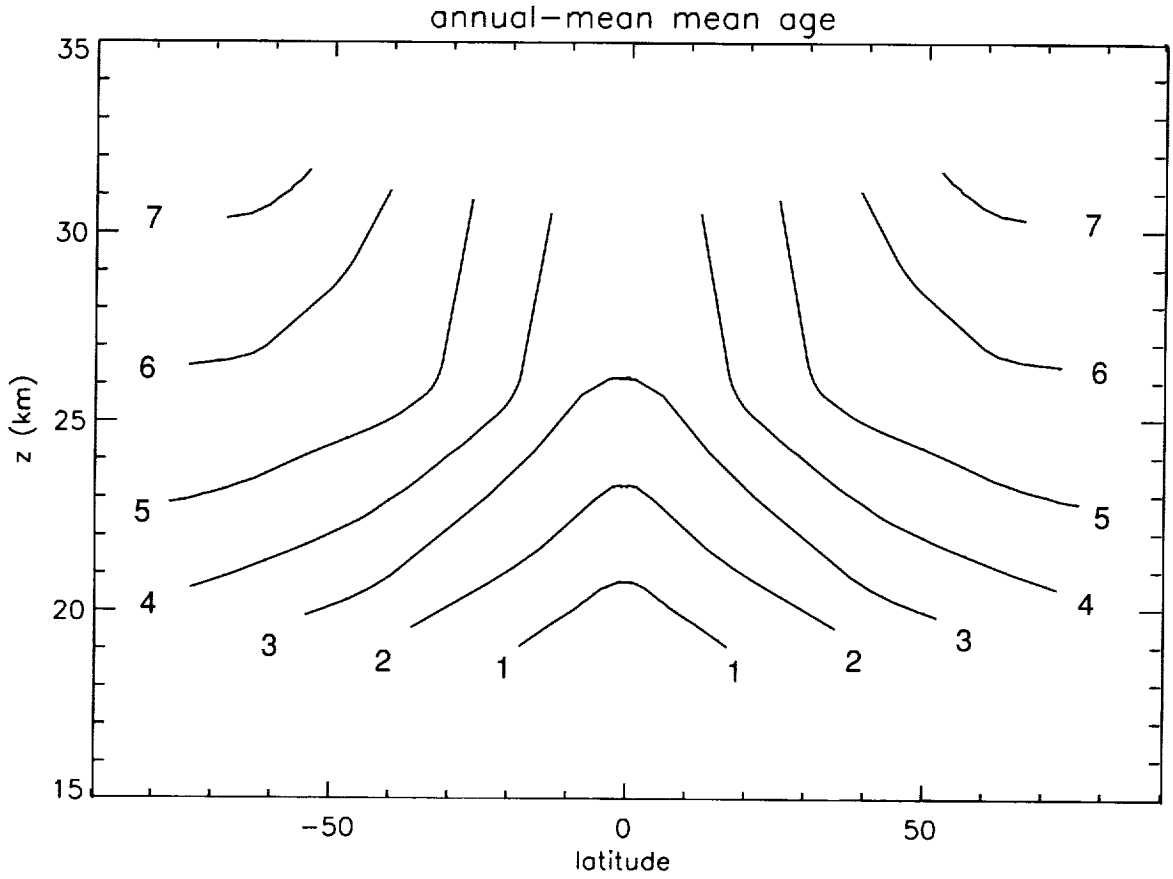

Figure 2.11. A schematic of the annually-averaged mean age distribution (in years) made from a composite of balloon and aircraft observations.

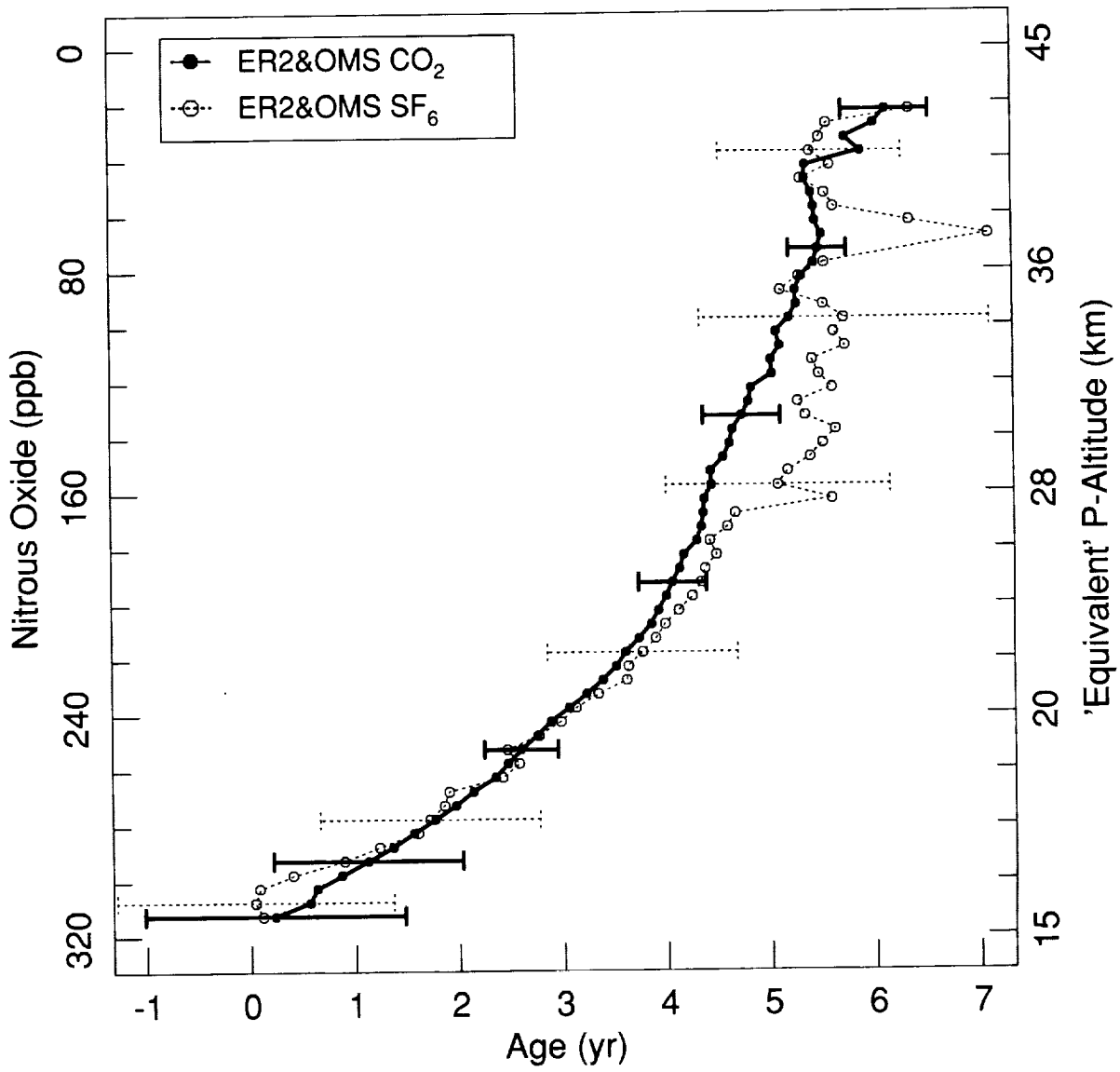

Figure 2.12. Mean ages in the extratropics (polewards of 20 degrees in both hemispheres) derived from over 1400 in situ SF_6 measurements (open circles) and over 82,000 in situ CO_2 measurements (solid circles) from both aircraft and balloons (from SPADE, ASHOE-MAESA, STRAT, POLARIS, and OMS), binned and averaged in 5 ppb intervals of N_2O from 10 to 320 ppb [Boering et al., 1998]. Horizontal bars represent the 2-sigma standard deviations of the averages (solid=CO_2; dotted=SF_6). The right y-axis represents a mapping of N_2O at midlatitudes from ATMOS and CLAES data onto a pressure altitude coordinate.

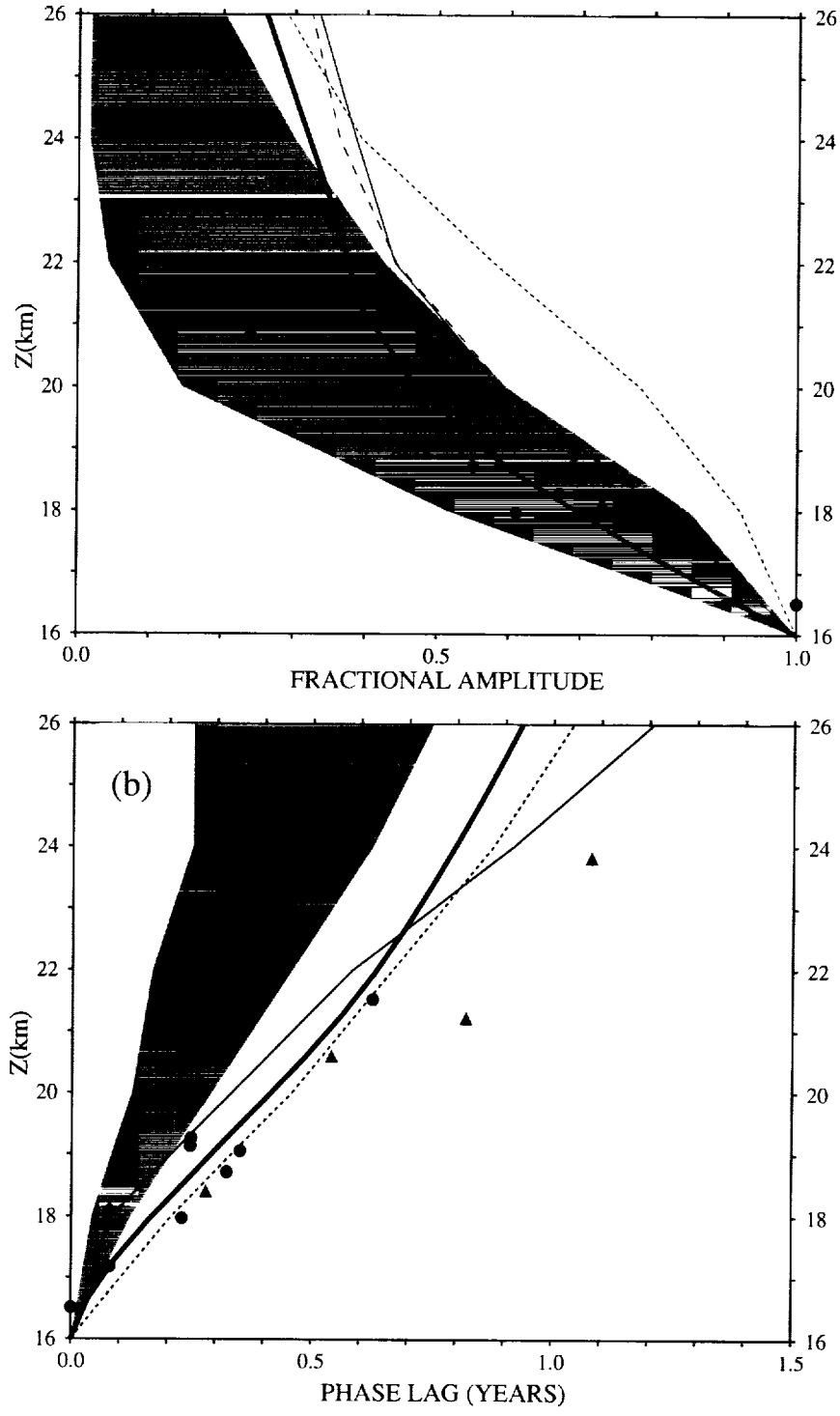

Figure 2.13. Equatorial profiles of (a) $A(z)$ and (b) $\tau_{\omega}(z)$ for a range of models and for the observational analyses. All amplitudes are normalized to unity and the phase lag taken as zero at 16 km. The shaded region indicates the range covered by (a) 19 models and (b) 20 models, while the individual lines represent several models falling outside the range: in (a), GMI-DAO (solid), GSFC-2Dint (short-dash), and GSFC-3D (long-dash); and in (b), HARVARD (solid), and GSFC-2D (short-dash). The heavy solid line represents the analysis of HALOE $\hat{H}$ [Mote et al., 1998]. The symbols represent analyses of in situ CO_2 (circles) and $\hat{H}$ (triangles) measurements (CO_2 from 6 aircraft and 2 balloon deployments between 1994 and 1997 and $\hat{H}$ from the same 2 balloon deployments in 1997).

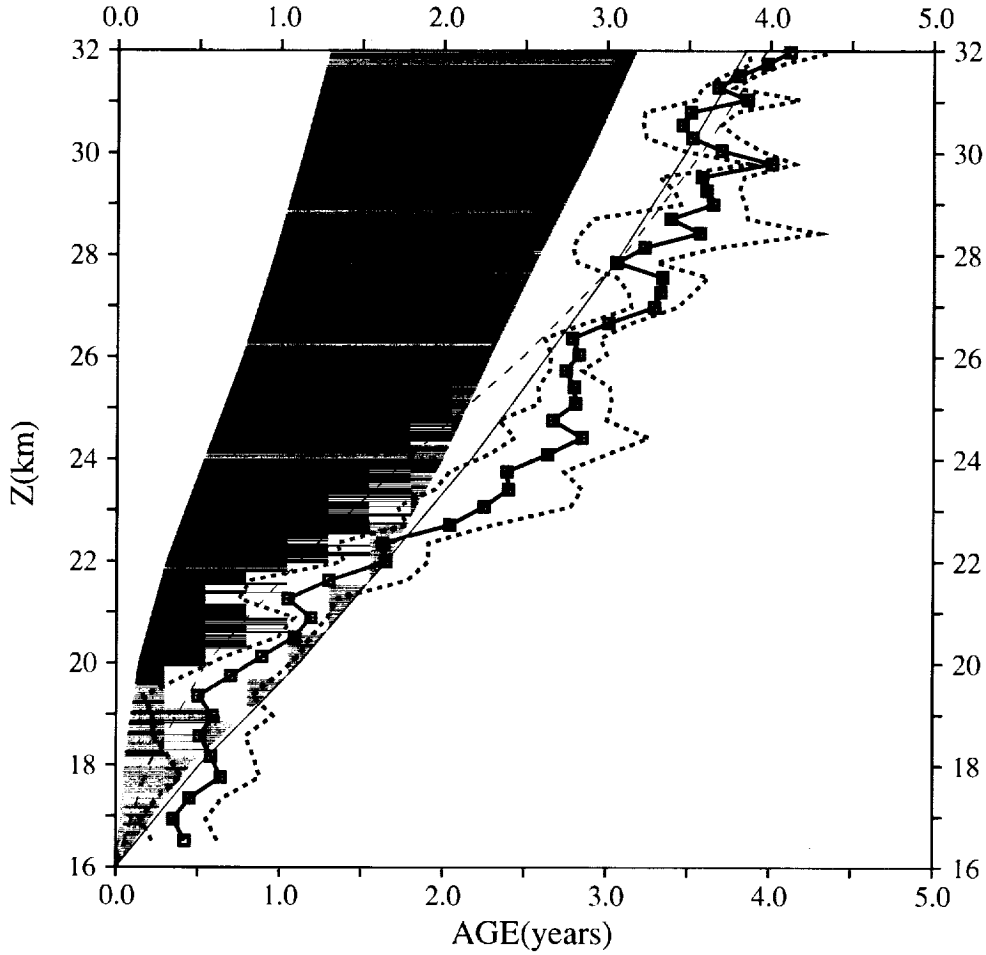

Figure 2.14. Tropical profiles of $\Gamma(z)$ from models and observations. The shaded region represents the range covered by 20 model profiles, while the light individual lines indicate several models falling outside the range: MONASH1 (solid) and UCI23 (long-dashed). The connected symbols are the averages (over 10K potential temperature bins) of mean age values inferred from CO_2 and SF_6 measurements from OMS balloon flights on the dates 970217, 971111, and 971120. The mean age has been referenced to zero at the tropical tropopause. Note that seasonal variations in CO_2 between February and November (discernible to about 21 km during these flights) largely cancel. Short-dashed lines indicate one standard deviation.

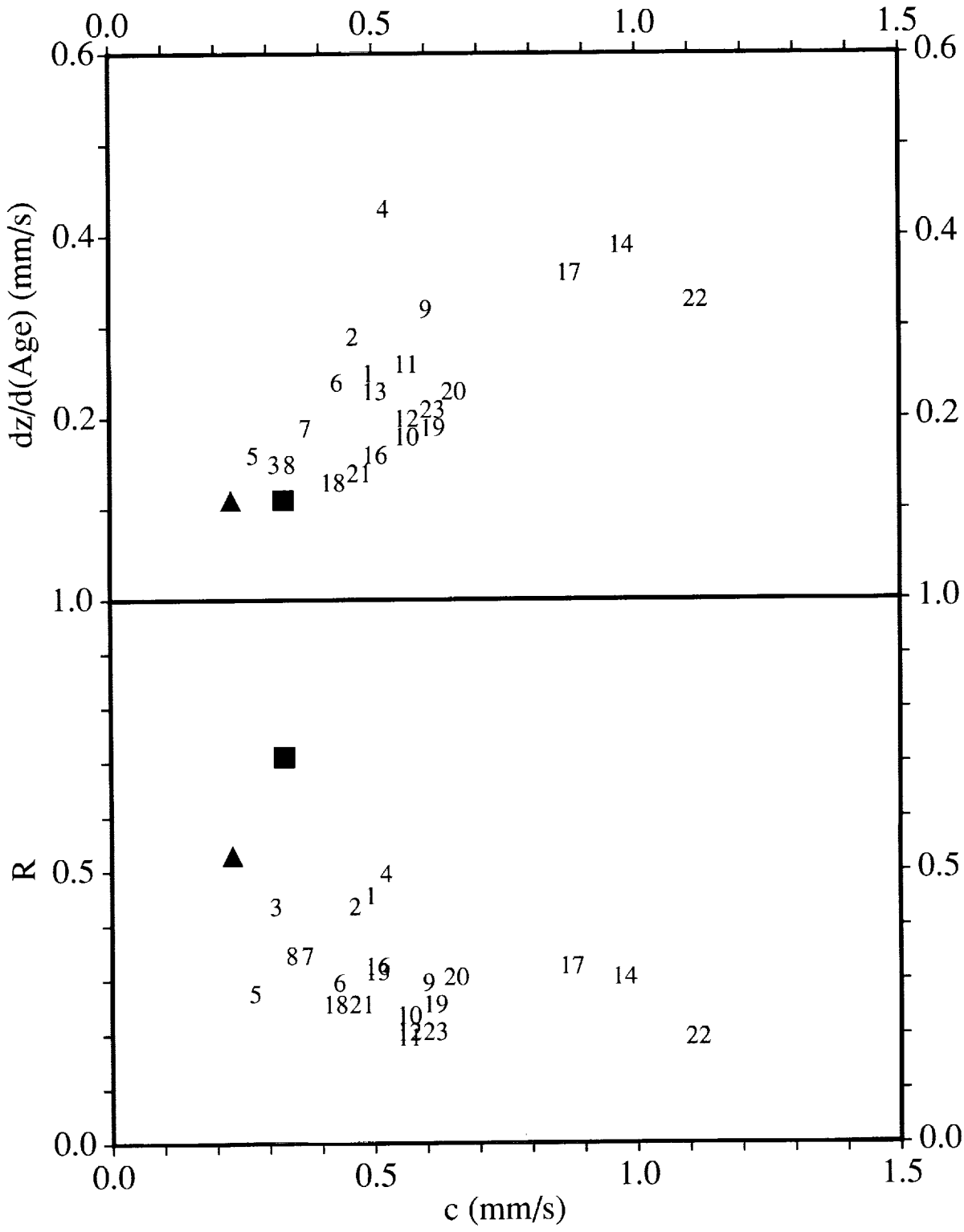

Figure 2.15. Scatter plots of $dz/d\Gamma$ versus c (top panel) and R versus c (bottom panel). Model values are indicated by numbers, as listed in Table 2.2. The square symbols represent values derived from HALOE $\hat{H}$ (for R) and in situ SF_6 and CO_2 (for $dz/d\Gamma$), while the triangles represent estimates from in situ CO_2 and $\hat{H}$ (for R) and CO_2 and SF_6 (for $dz/d\Gamma$).

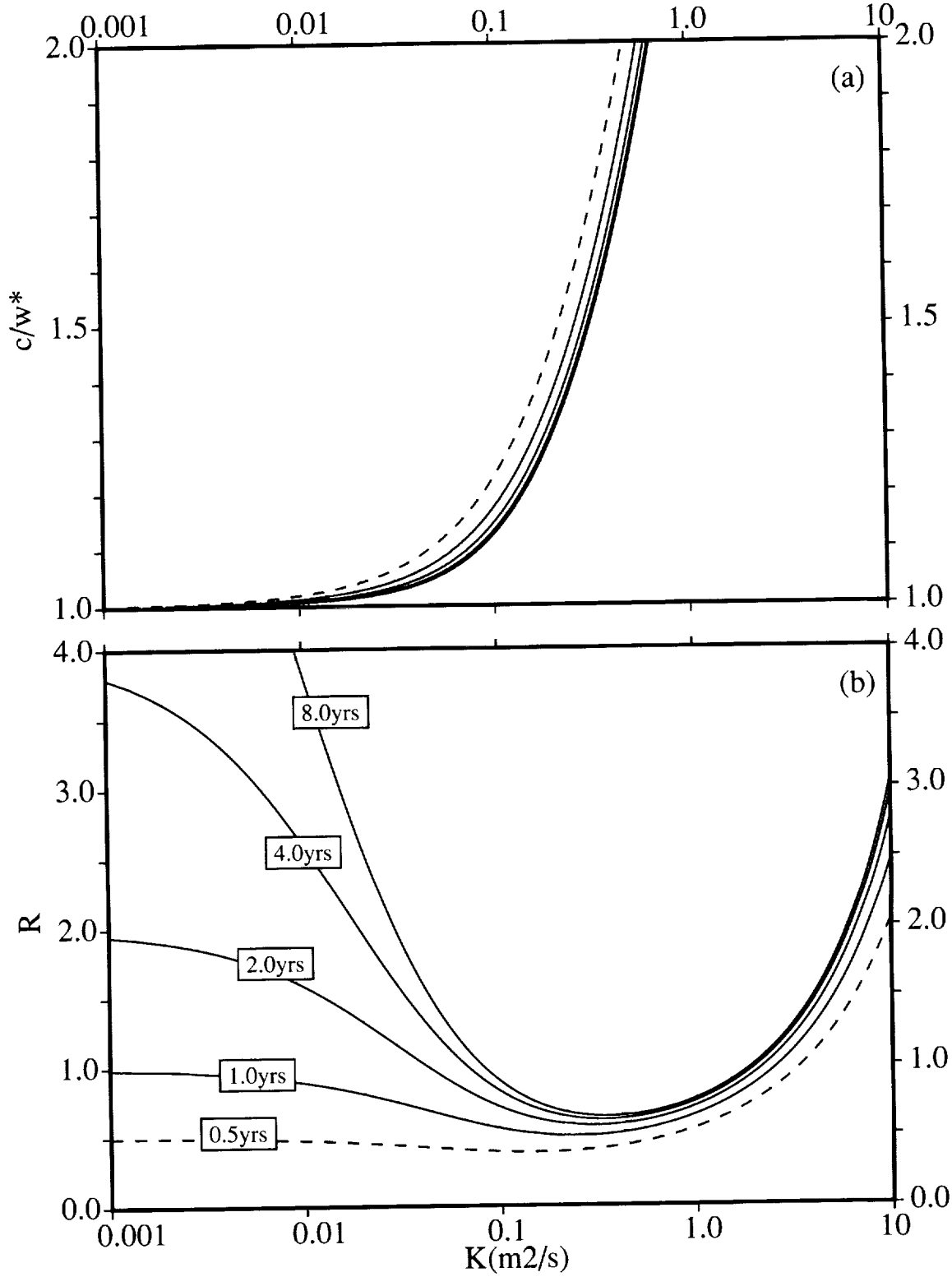

Figure 2.16. The dependence of (a) c/w and (b) R on K in the simple tropical leaky pipe model for $\tau = 0.5$, 1.0, 2.0, 4.0, and 8.0 years ($\tau = 0.5$ years is indicated by a long-dash). For these curves, $w = 0.3$ mm/s.

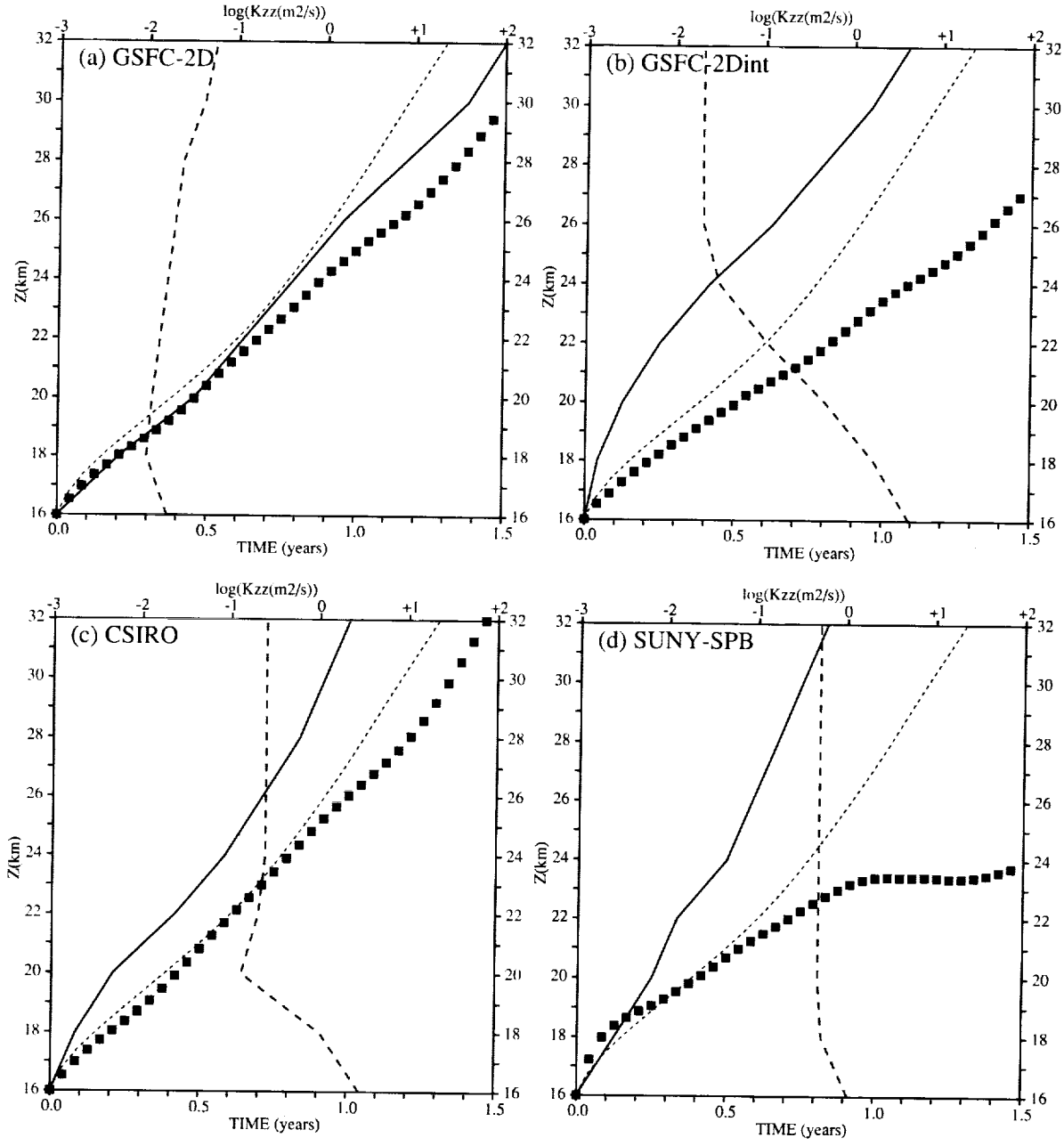

Figure 2.17. Tropical profiles of model annually-averaged K_{zz} (top log scale; dashed), model τ_ω (bottom scale; solid line), HALOE $\hat{H}$ τ_ω (bottom scale; dotted), and model advective time by $\bar{w}^*$ (bottom scale; symbols). The different panels correspond to different models: (a) GSFC-2D; (b) GSFC-2Dint; (c) CSIRO; and (d) SUNY-SPB.

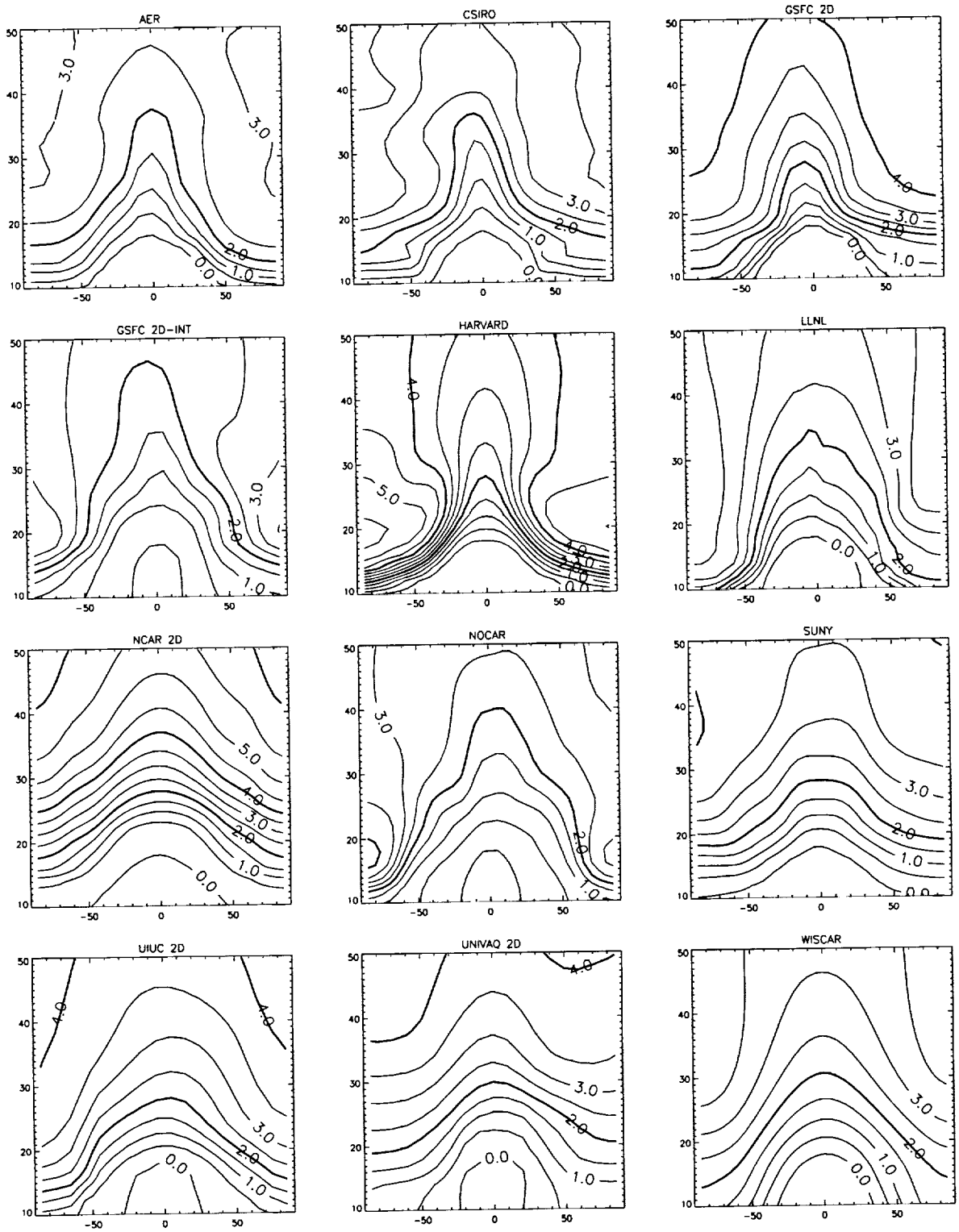

Figure 2.18. Modeled mean age distributions in the latitude-height plane as derived from the age spectrum. Each panel corresponds to an MM2 two-dimensional model, as labeled. Mean age is taken as zero at the equator and 18 km. Countour intervals are 0.5 years, and the heavy contours indicate 2 year intervals. Negative values are not shown.

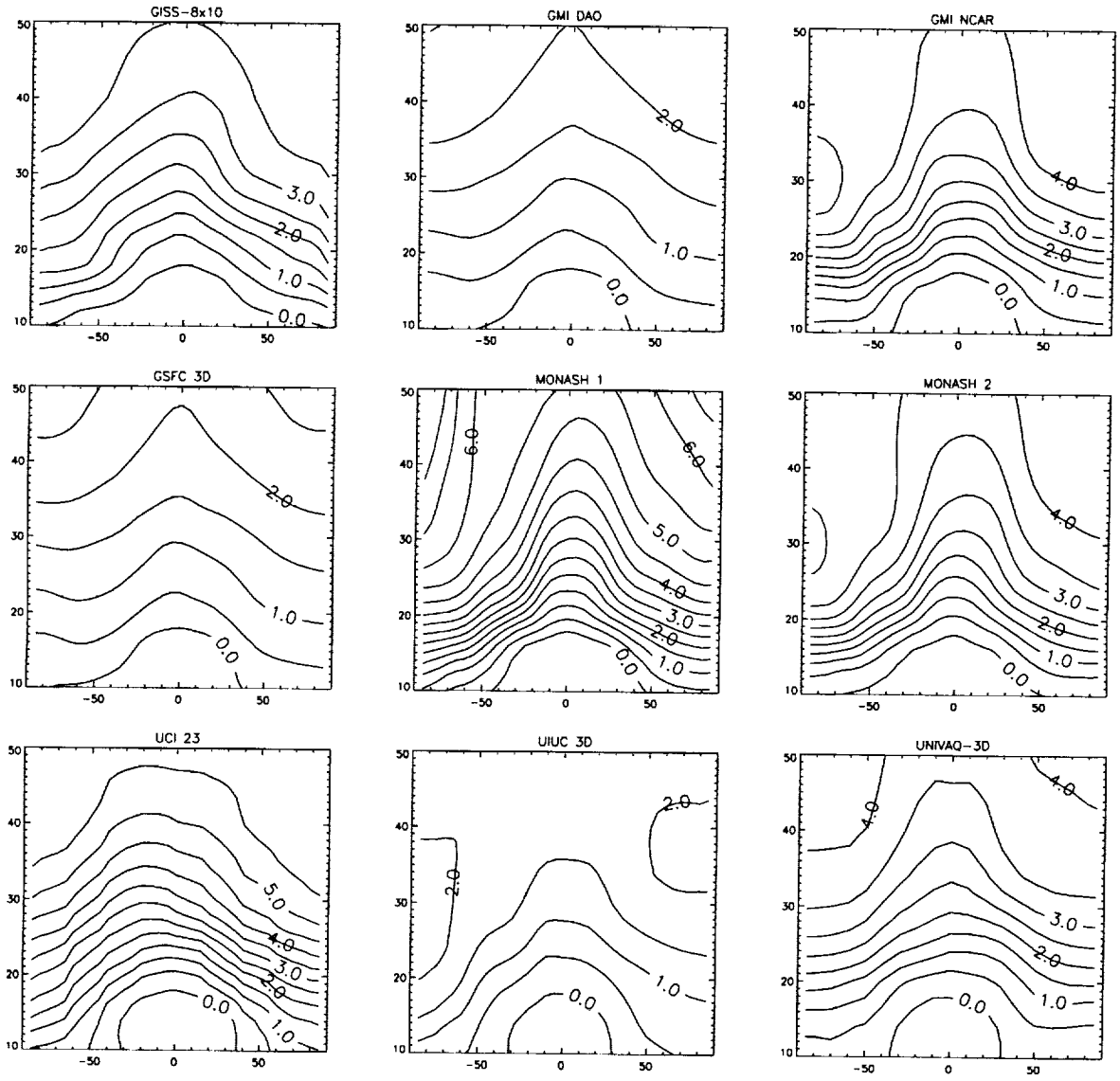

Figure 2.19. Modeled mean age distributions in the latitude-height plane as derived from the age spectrum. Each panel corresponds to an MM2 three-dimensional model, as labeled. Mean age is taken as zero at the equator and 18 km. Countour intervals are 0.5 years, and the heavy contours indicate 2 year intervals. Negative values are not shown.

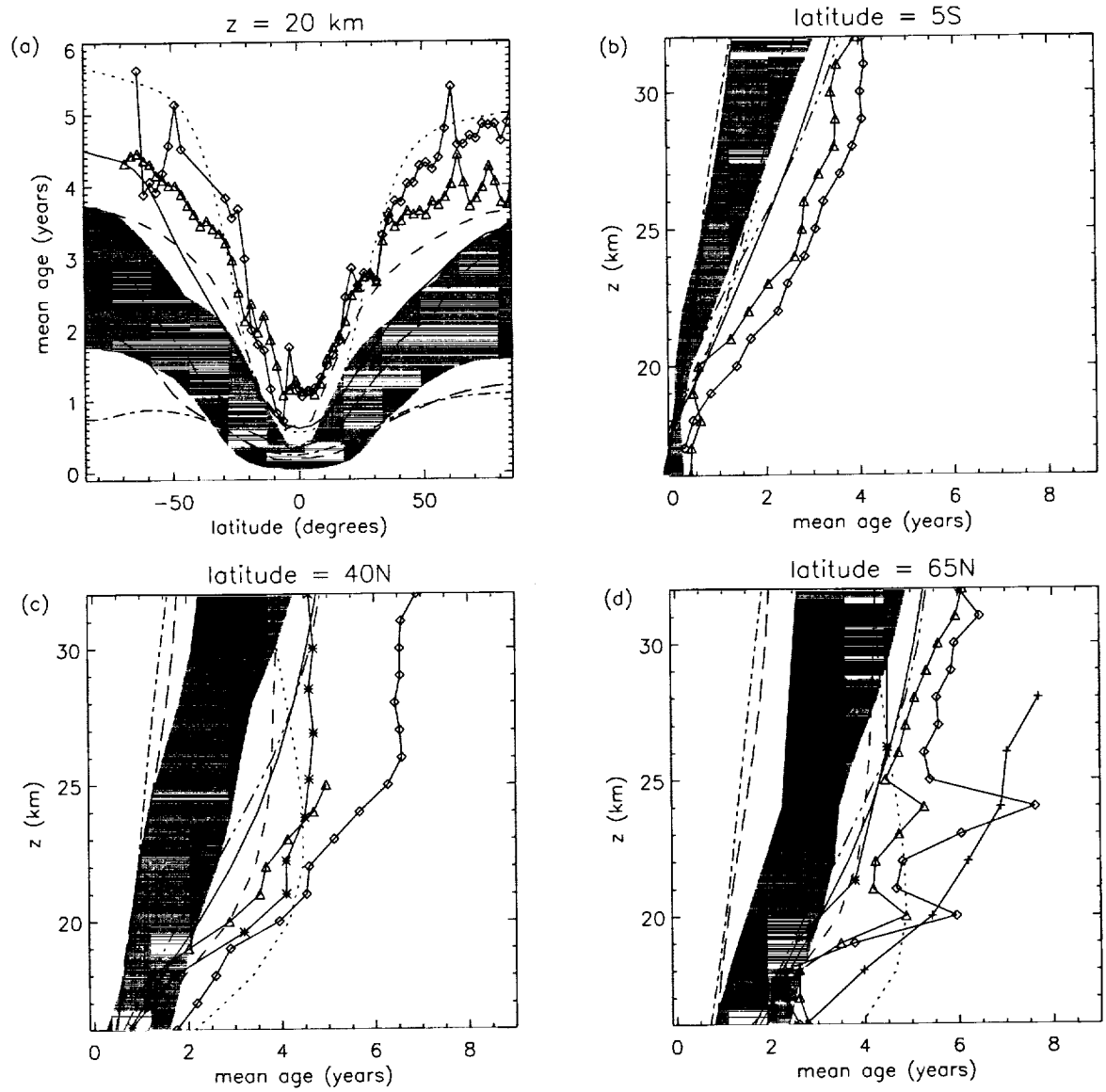

Figure 2.20. In all panels, the shaded region indicates the range of mean ages of models, with the exceptions of HARVARD (dot), MONASH1 (solid), GSFC-2D (dash), UCI23 (dash dot dot dot), GSFC-3D (dash dot), and UIUC (long dashes). The symbols represent observations: mean age from in situ CO_2 (triangles) and in situ SF_6 (diamonds). Observations are as follows: (a) Latitudinal profile of in situ aircraft measurements from SPADE, ASHOE/MAESA, STRAT, and POLARIS for CO_2 and from ASHOE/MAESA (one deployment only), STRAT, and POLARIS for SF_6. Data are averaged in 2.5 degree latitude bins (plotted at the midpoint) for both tracers, and in 19.5-21.5 km for CO_2 and 19-21 km for SF_6. (b) Vertical OMS balloon profiles at 5°N averaged in 1 km altitude bins over three flights for in situ CO_2 (one February, two November, 1997) and over two flights for in situ SF_6 (February, November, 1997). (c) In situ SF_6 and CO_2 mean ages from a single OMS balloon flight of September, 1996, from 35°N, binned in altitude as in 5b, and mean age from SF_6 whole air samples, September, 1993, from 44°N (asterisk) [Harnisch et al, 1996]. (d) In situ CO_2 and SF_6 mean age from the OMS balloon flight of June, 1997, 65°N, and whole air SF_6 samples at 68°N inside (asterisk; average of four flights) and outside (pluses; single flight) the winter polar vortex [Harnisch et al., 1996]. (OMS SF_6 data provided courtesy James W. Elkins and Fred. L. Moore.) See text for further details.

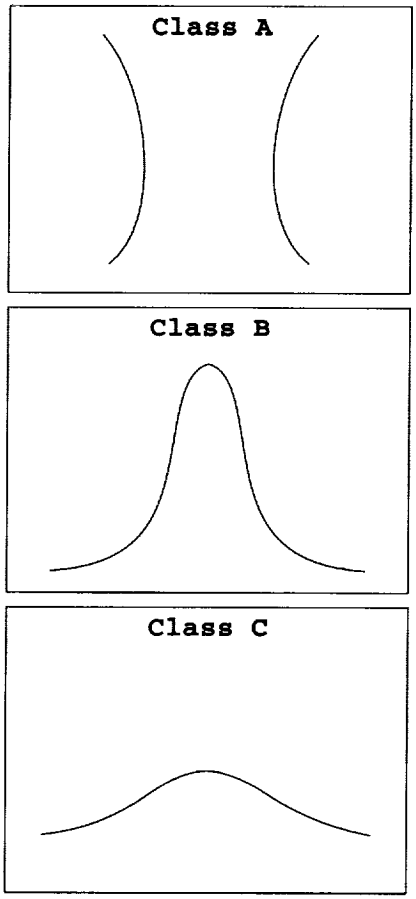

Figure 2.21. Schematic representation of the variation of model global Γ distribution, and its categorization into three classes.

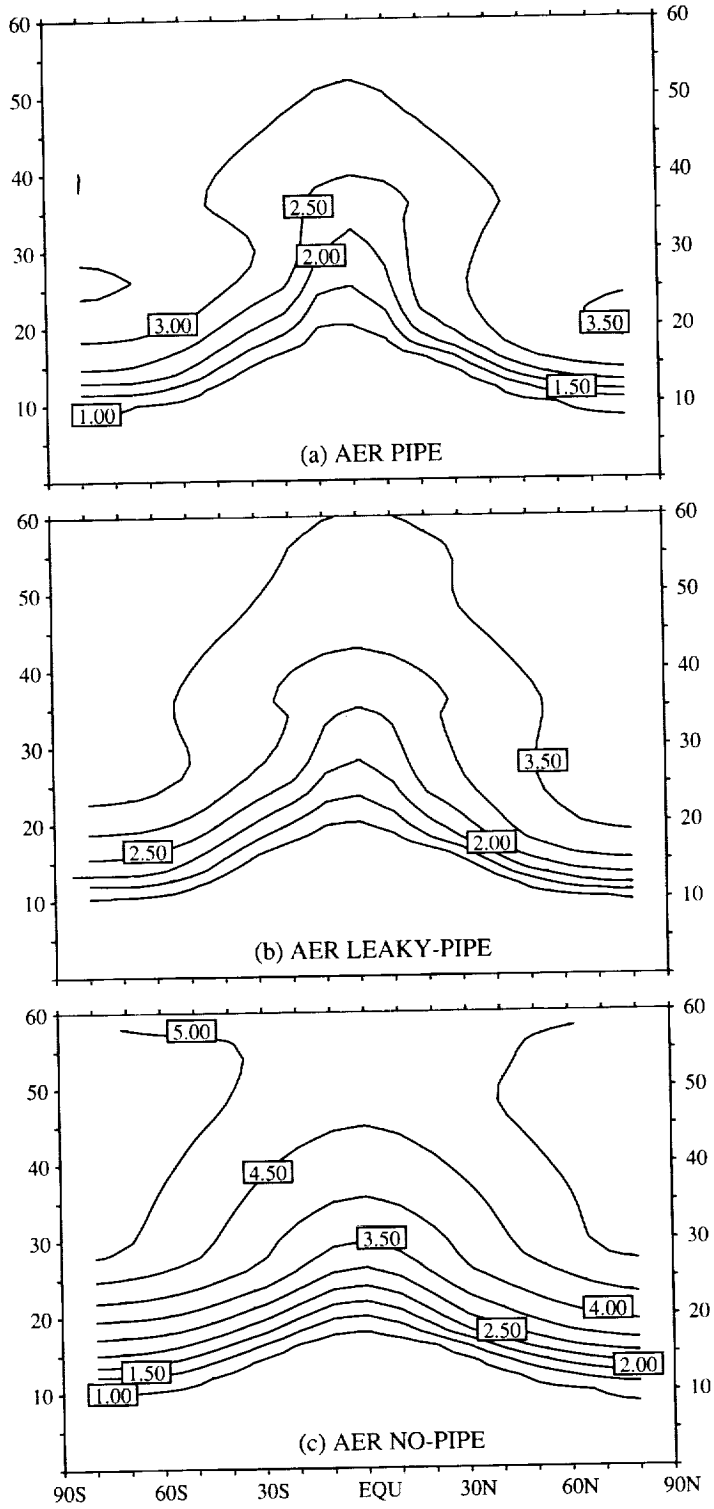

Figure 2.22. Mean age distributions for: (a) the AER "tropical pipe" model; (b) the AER "leaky pipe" model (the version submitted to MM2); and (c) the AER "no pipe" model.

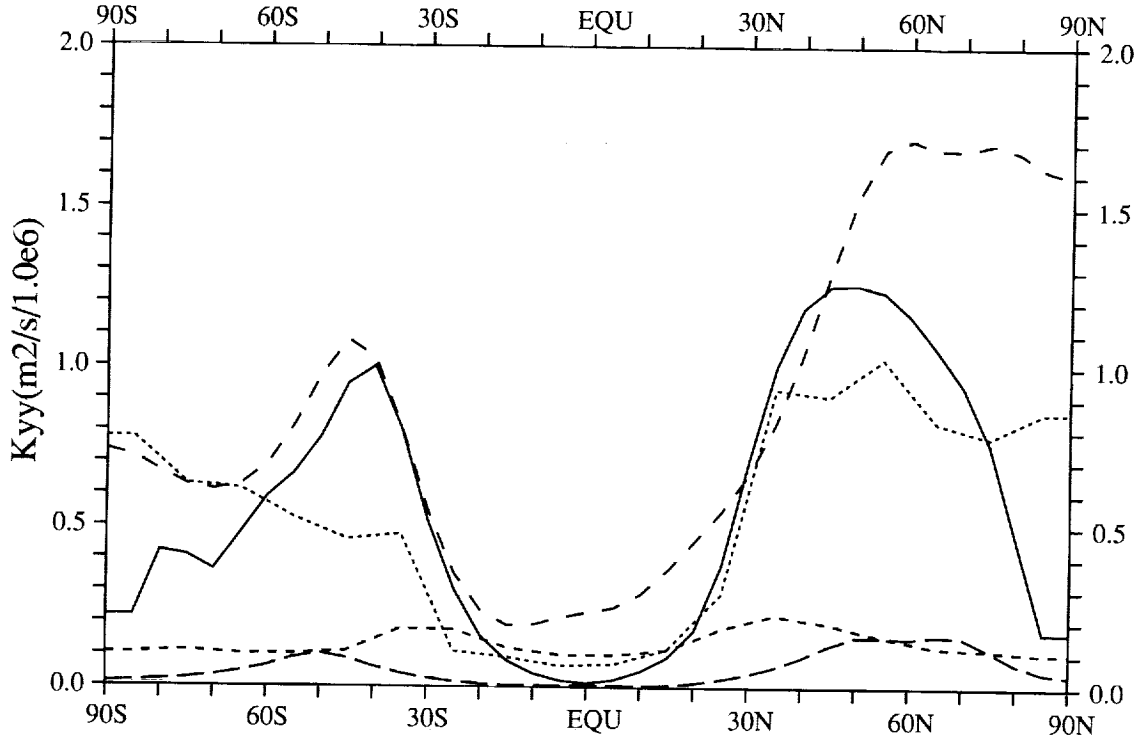

Figure 2.23. Latitudinal profiles of annual-mean K_{yy} averaged from 18 km to 24 km for 5 2D models: CSIRO (solid); GSFC-2D (dotted); GSFC-2Dint (short-dash); SUNY-SPB (medium-dash); and HARVARD (long-dash).

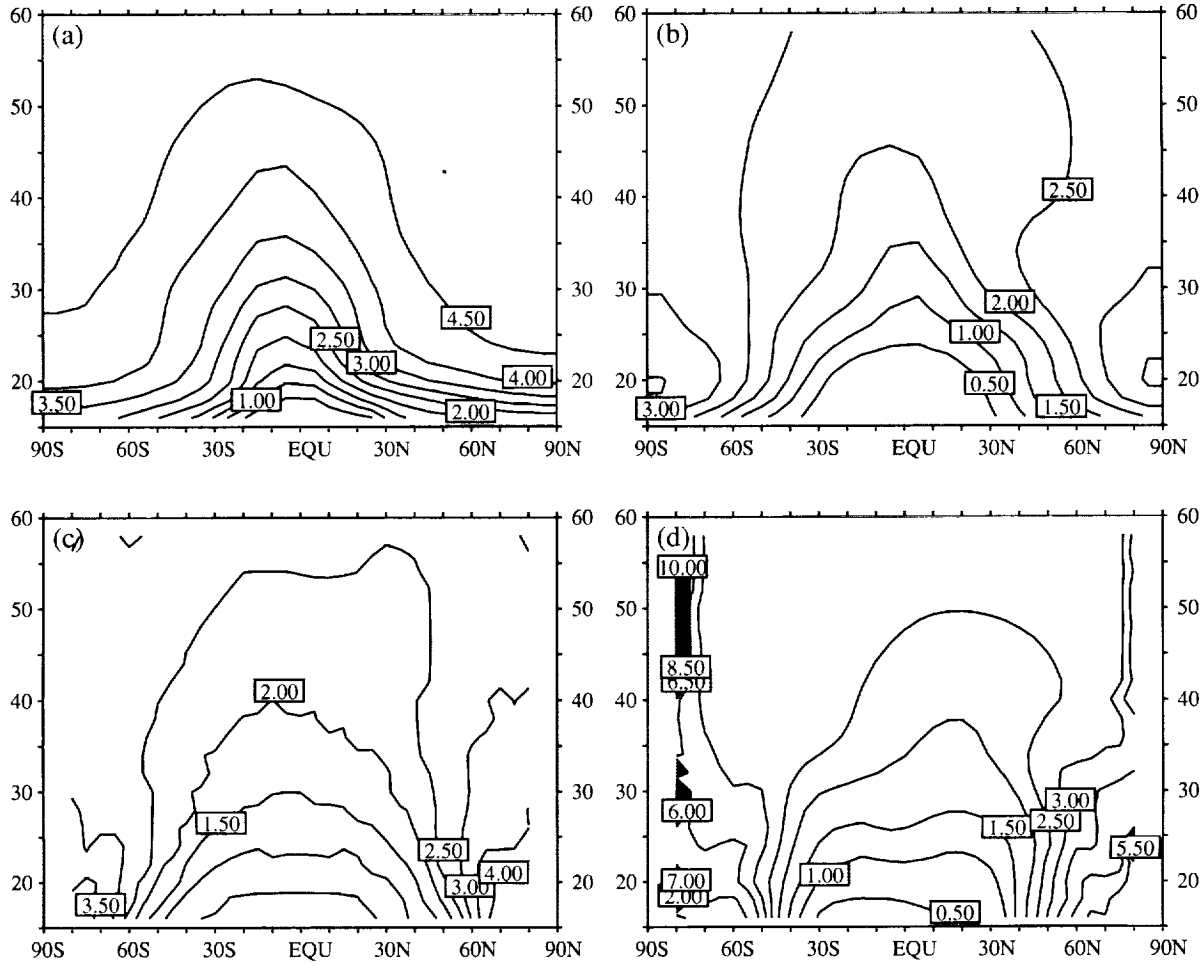

Figure 2.24. (A) The latitude-height mean age distribution for GSFC-2D; (B) The mean age distribution for GSFC-2Dint; (C) The transit time distribution, using only the GSFC-2D residual circulation for transport; (D) The transit time distribution, using only the residual circulation of GSFC-2Dint for transport.

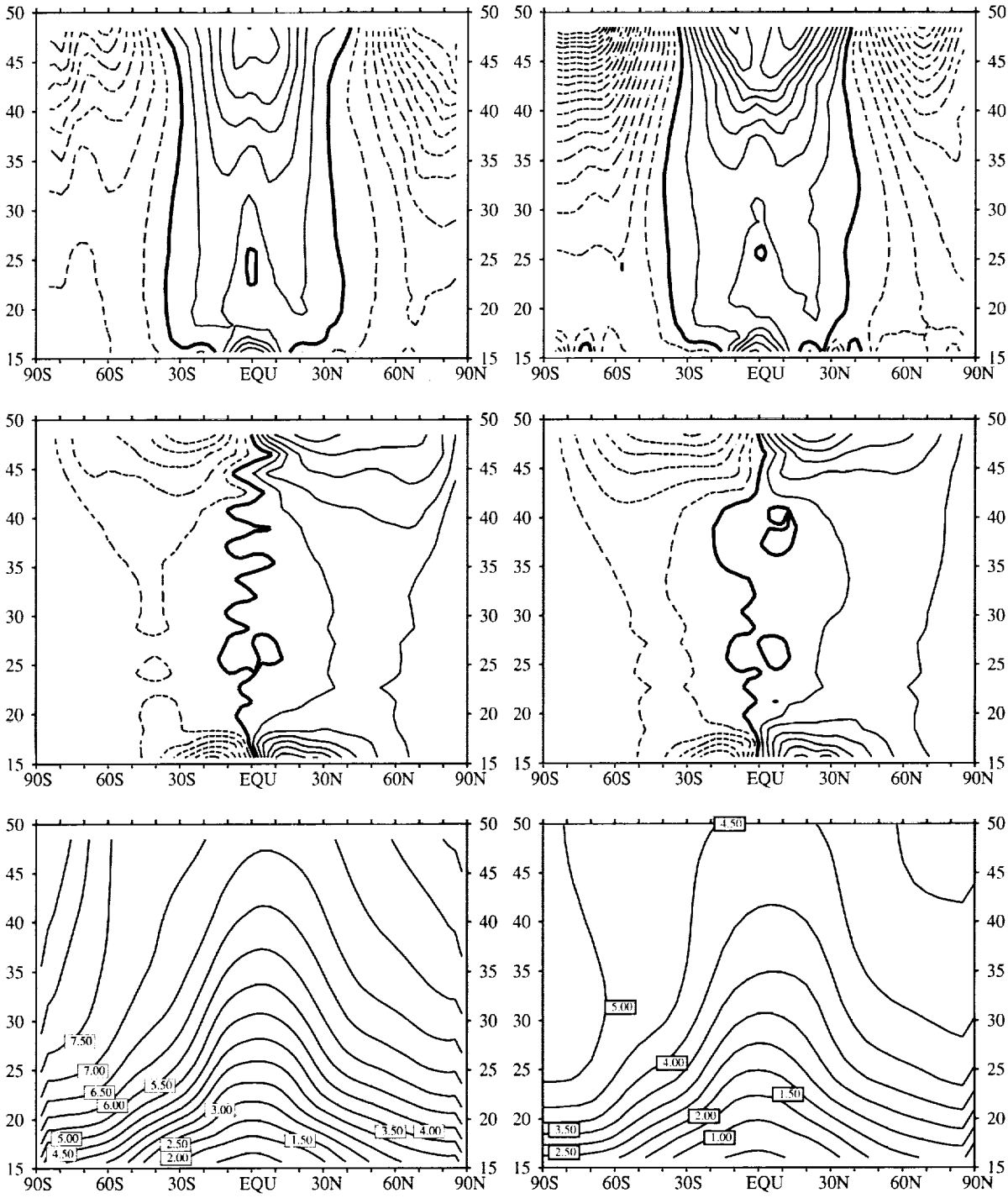

Figure 2.25. The residual circulation for the two versions of the MACCM2 GCM, used by MONASH1 and MONASH2, and the corresponding Γ distributions. The left column of panels is for MONASH1, and the right for MONASH2. The top row is annual mean $\bar{w}^*$ in 0.5 mm/s contours (solid positive, dashed negative), the middle row annual mean $\bar{v}^*$ in 0.5 m/s contours (solid positive, dashed negative), and the bottom row mean age, in 0.5 year contours.

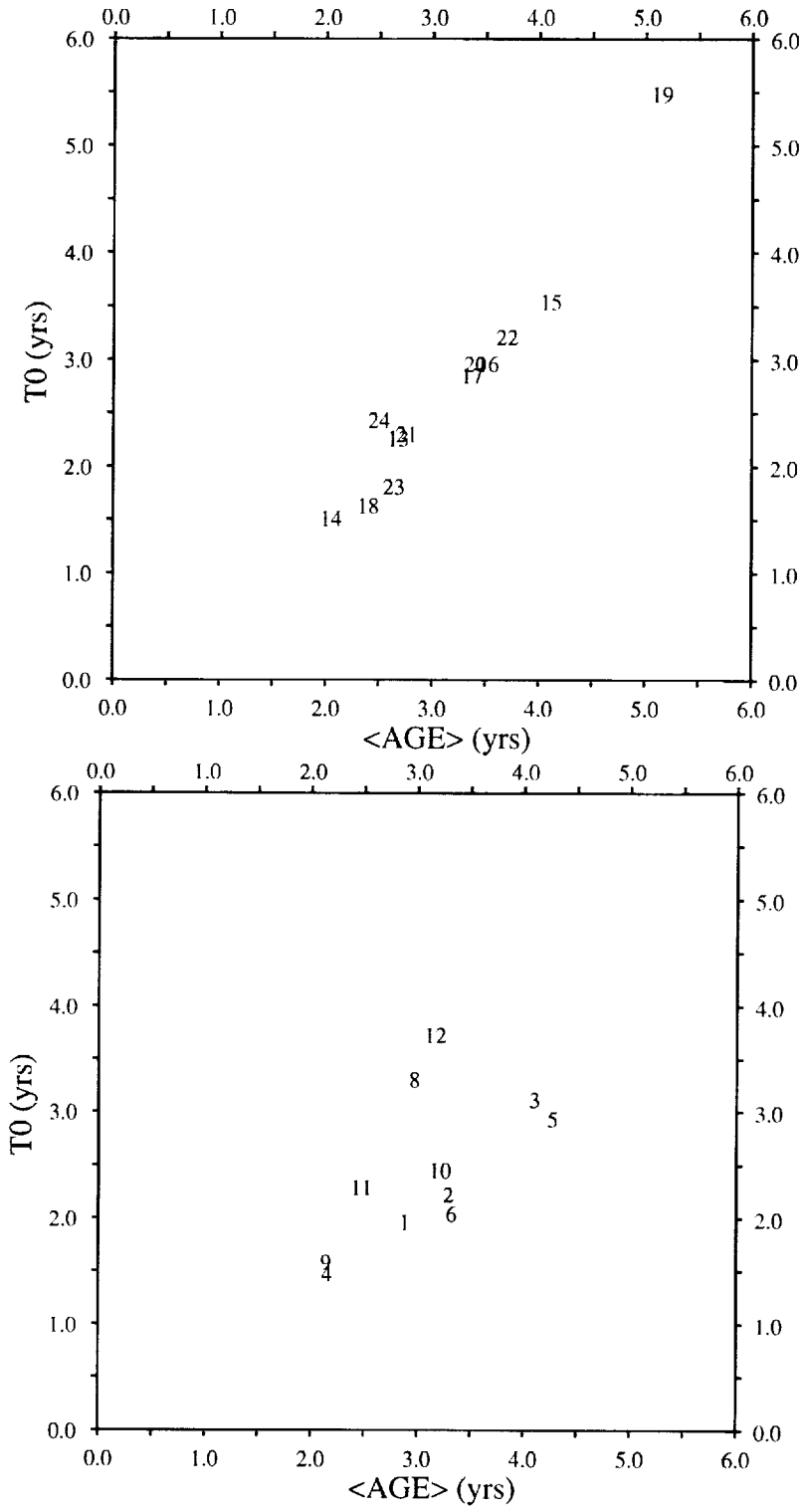

Figure 2.26. Scatter plot of $\bar{\Gamma}$ versus τ_0 for models listed in Table 2.2. $\bar{\Gamma}$ is the mass-weighted integral of $\Gamma(\mathbf{x})$, for $z > 20$ km.

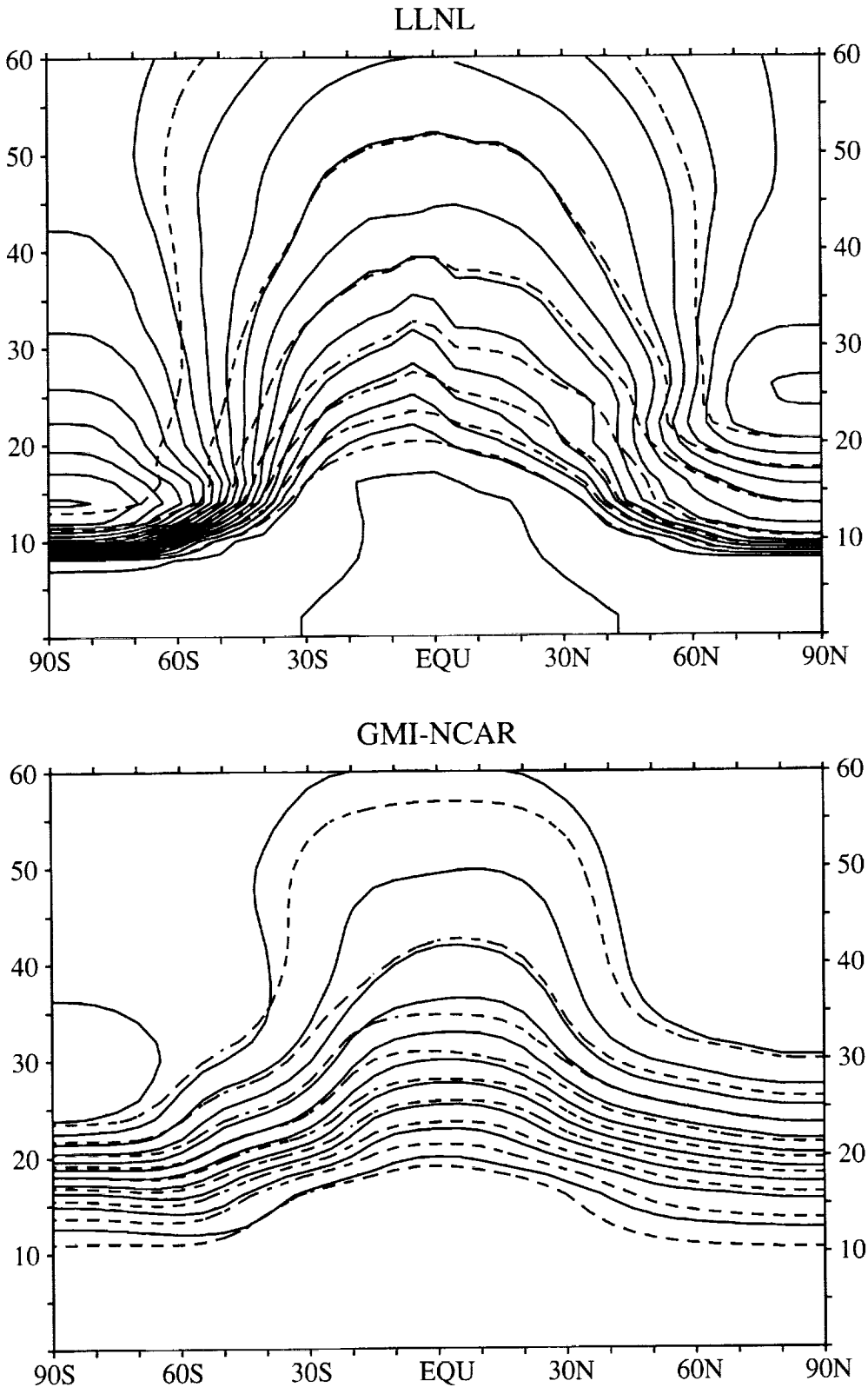

Figure 2.27. Contour plots of $\Gamma(\mathbf{x})$ (dashed) and $\psi_0(\mathbf{x})$ (solid) for LLNL (top panel) and GMI-NCAR (bottom panel). $\Gamma(\mathbf{x})$ is contoured in 0.5 year intervals. $\psi_0(\mathbf{x})$ is scaled to unity at the equator and 60 km. Its contours intervals are 0.1, decreasing toward the troposphere.

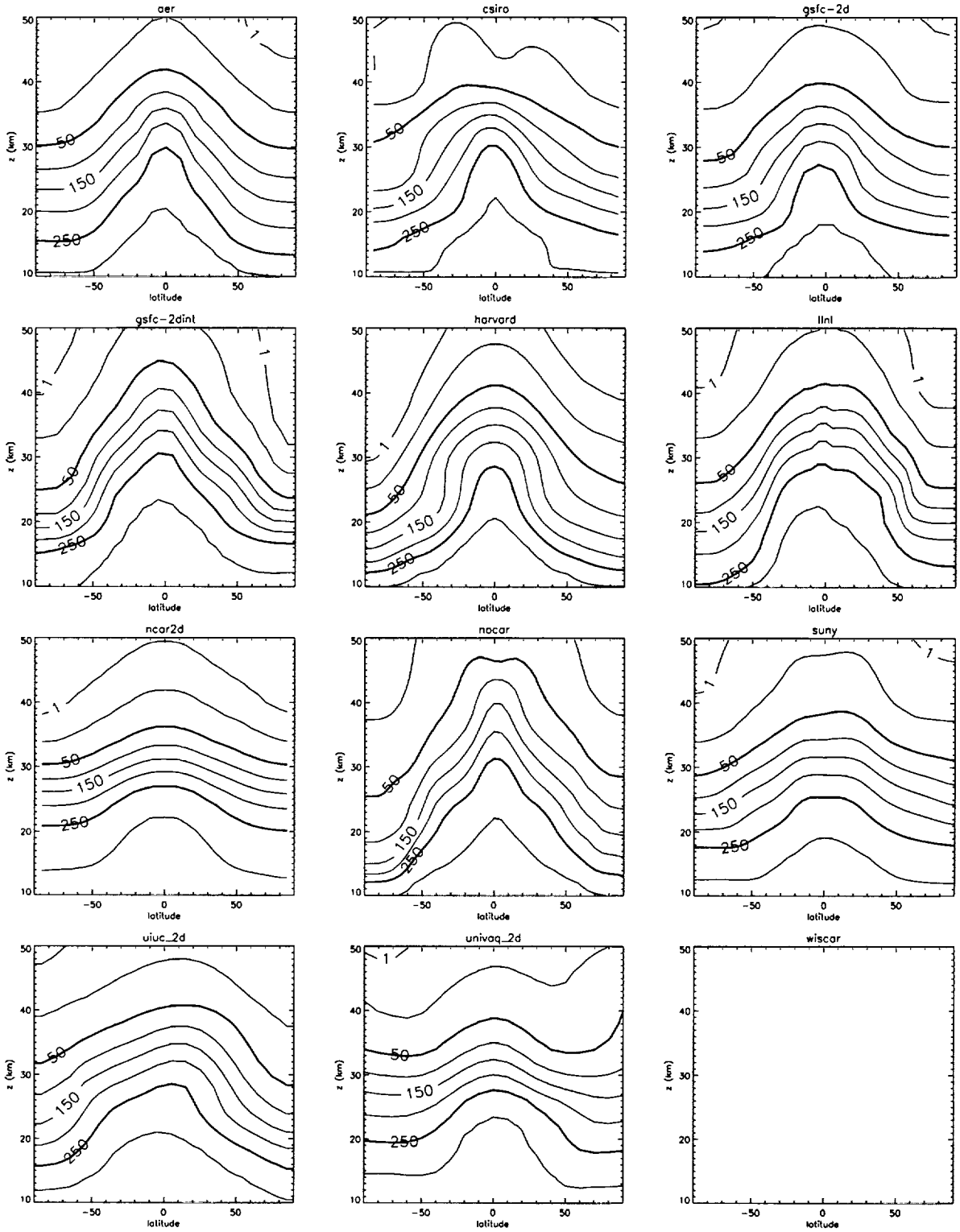

Figure 2.28. Annual-mean N_2O distributions in the latitude-height plane. Each panel corresponds to an MM2 2D model model, as labeled. Contour intervals are 50 ppb, and the 25 ppb and 1 ppb contour are also shown. Empty panels correspond to models for which data was not available and are included for ease of comparison to Figure 2.18.

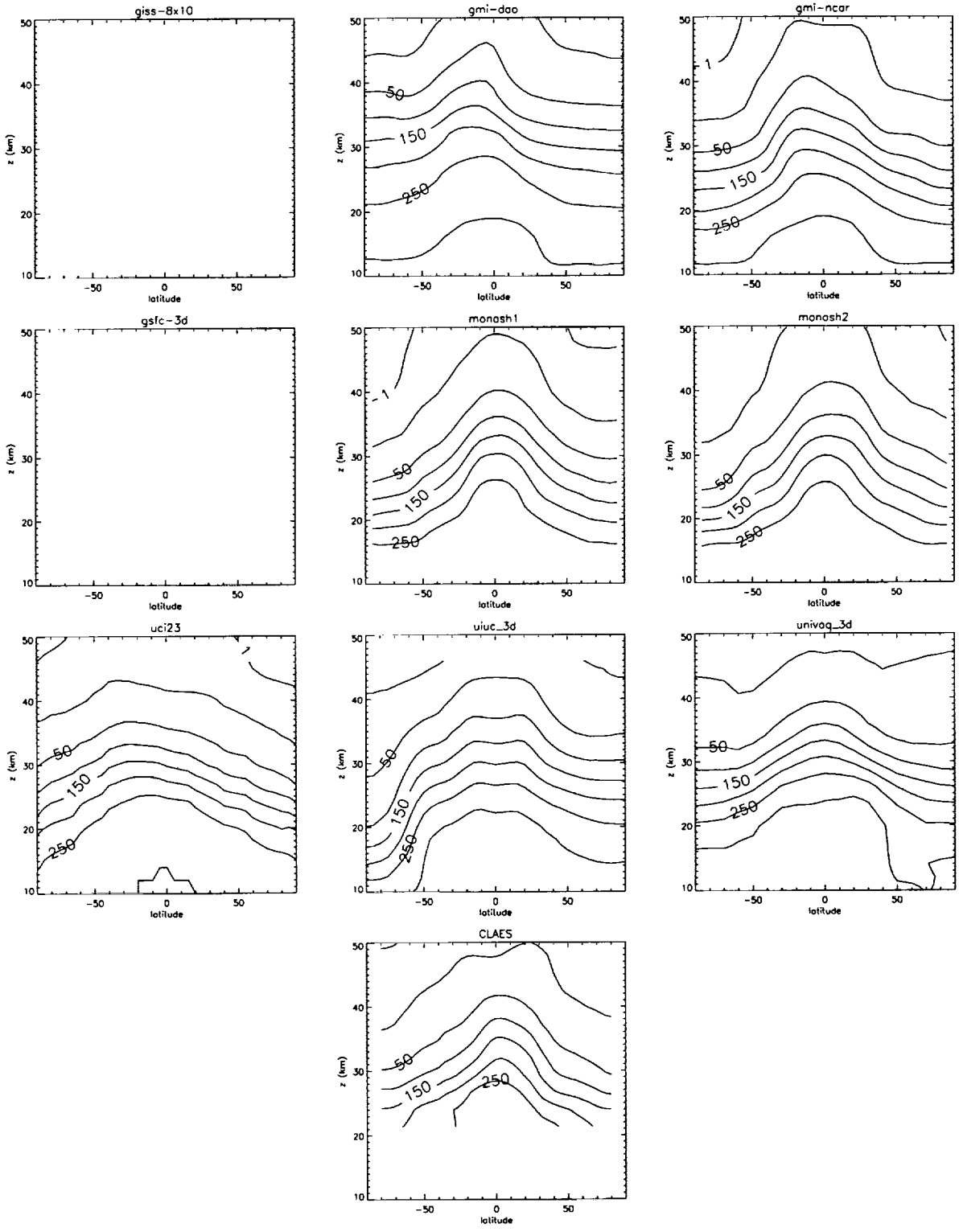

Figure 2.29. Same as Figure 2.28, but for 3D models. N_2O data from the CLAES instrument on HALOE are shown at bottom [Randel et al., 1994]. Empty panels correspond to models for which data was not available and are included for ease of comparison to Figure 2.19.

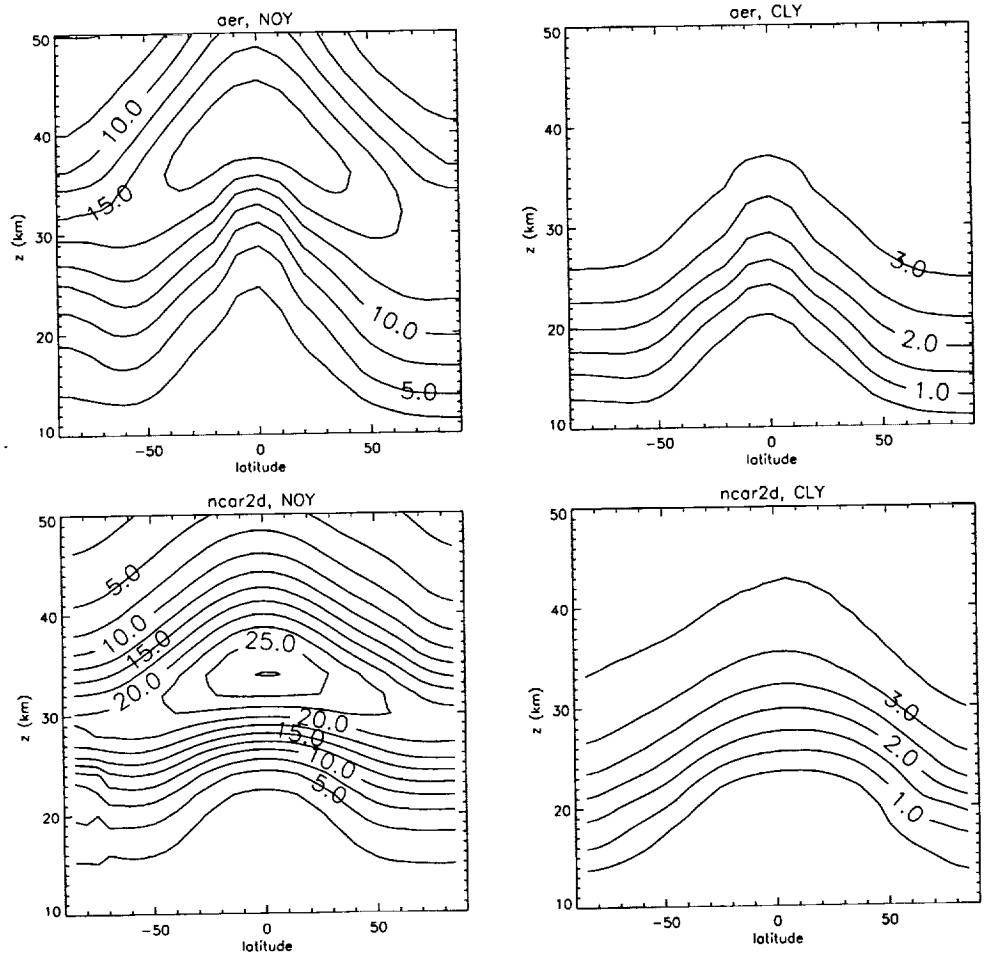

Figure 2.30. Annual-mean latitude-height distributions of NOy (left column) and Cly (right column) for the models AER and NCAR-2D, as labeled. These data are from the full chemistry runs of B4. Contour intervals are 2.5 ppb for NOy and 0.5 ppb for Cly.

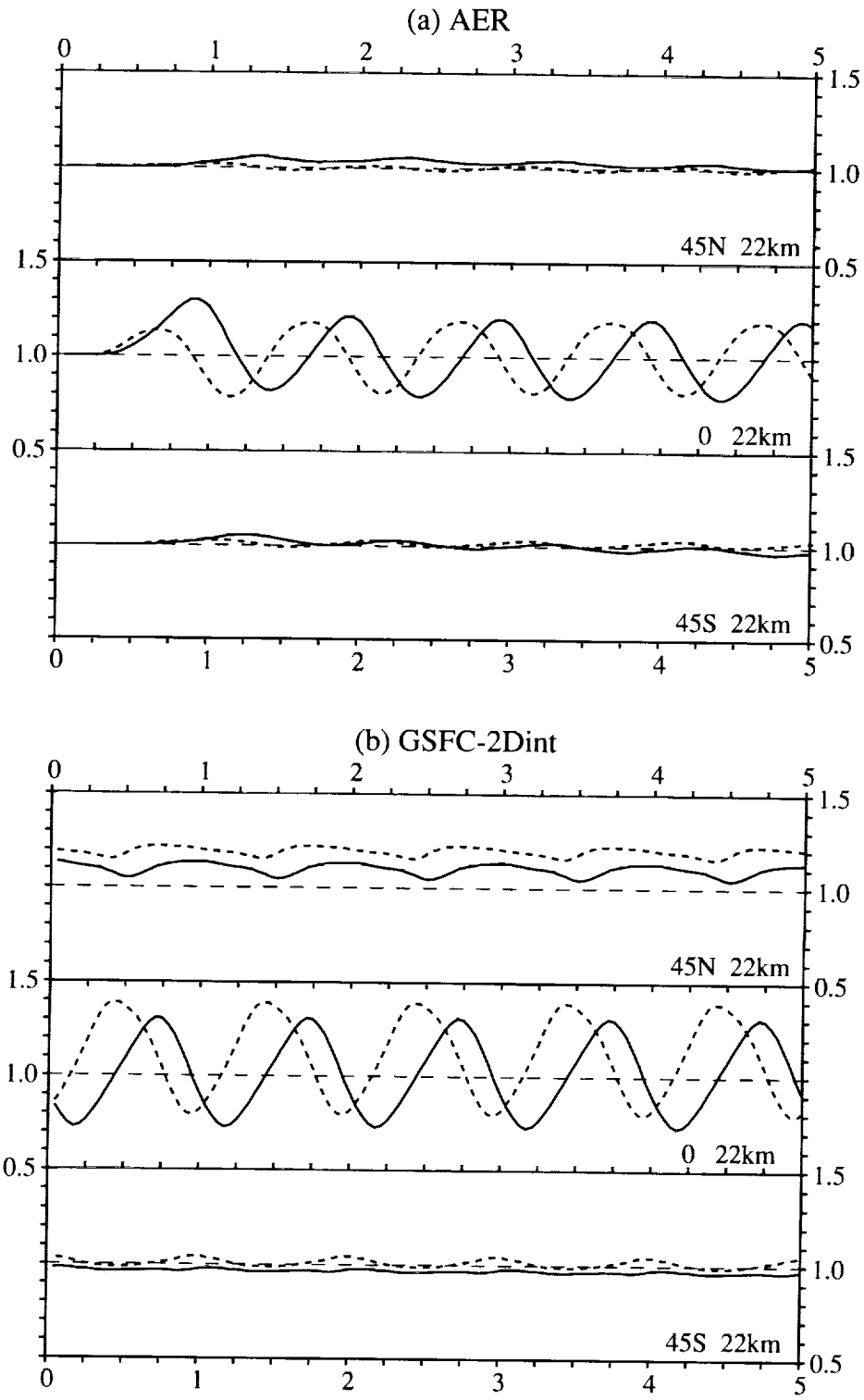

Figure 2.31. Time series of experiment A2a, the sine forcing (solid); and A2b, the cosine forcing (short dash), for two models: AER (top) and GSFC-2Dint (bottom). For each model, three latitudes are plotted at 22 km: 45°N (top time series), the equator (middle time series), and 45°S (bottom time series).

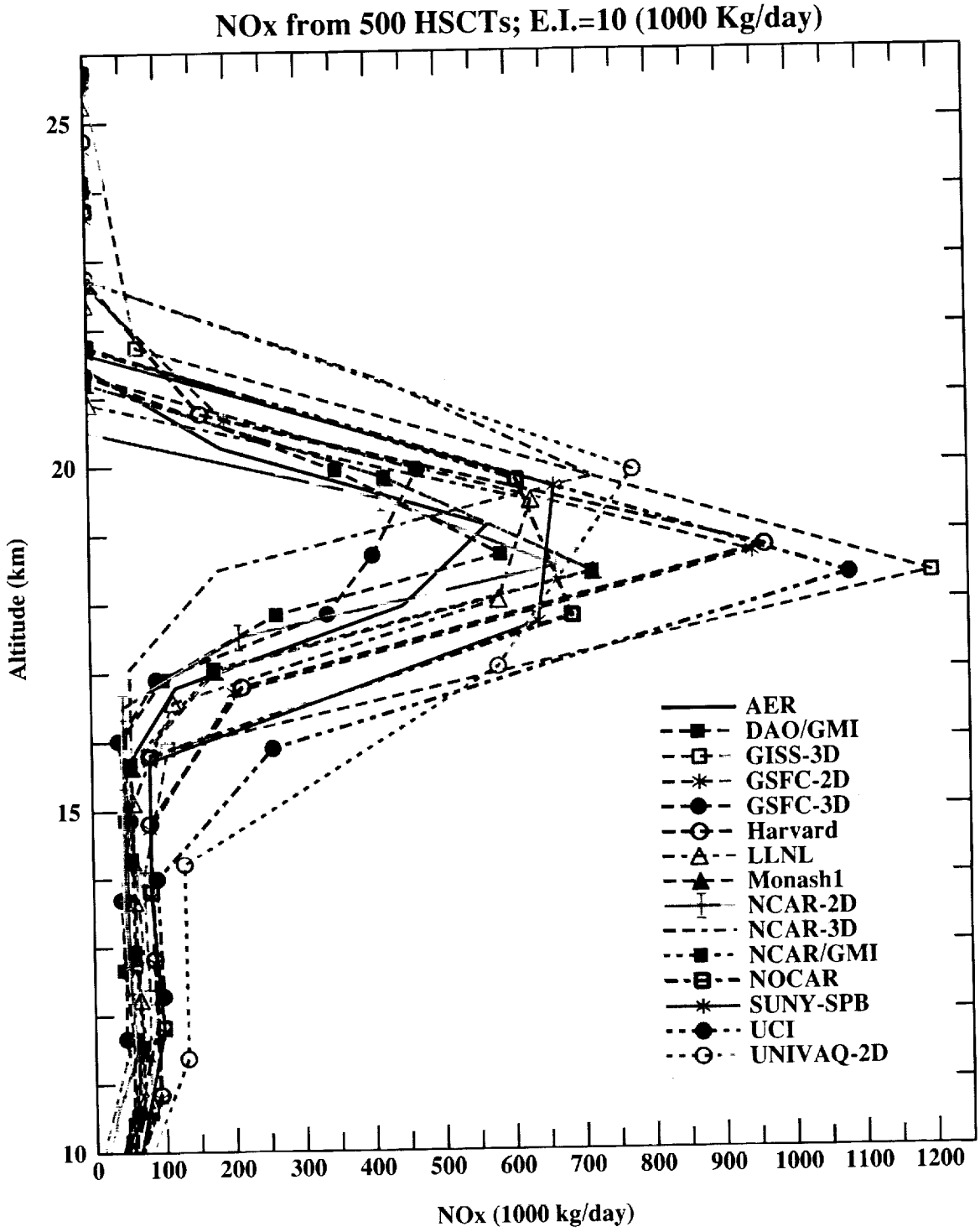

Figure 2.32. Vertical profile of integrated A3 input rates (kg/s) for various models.

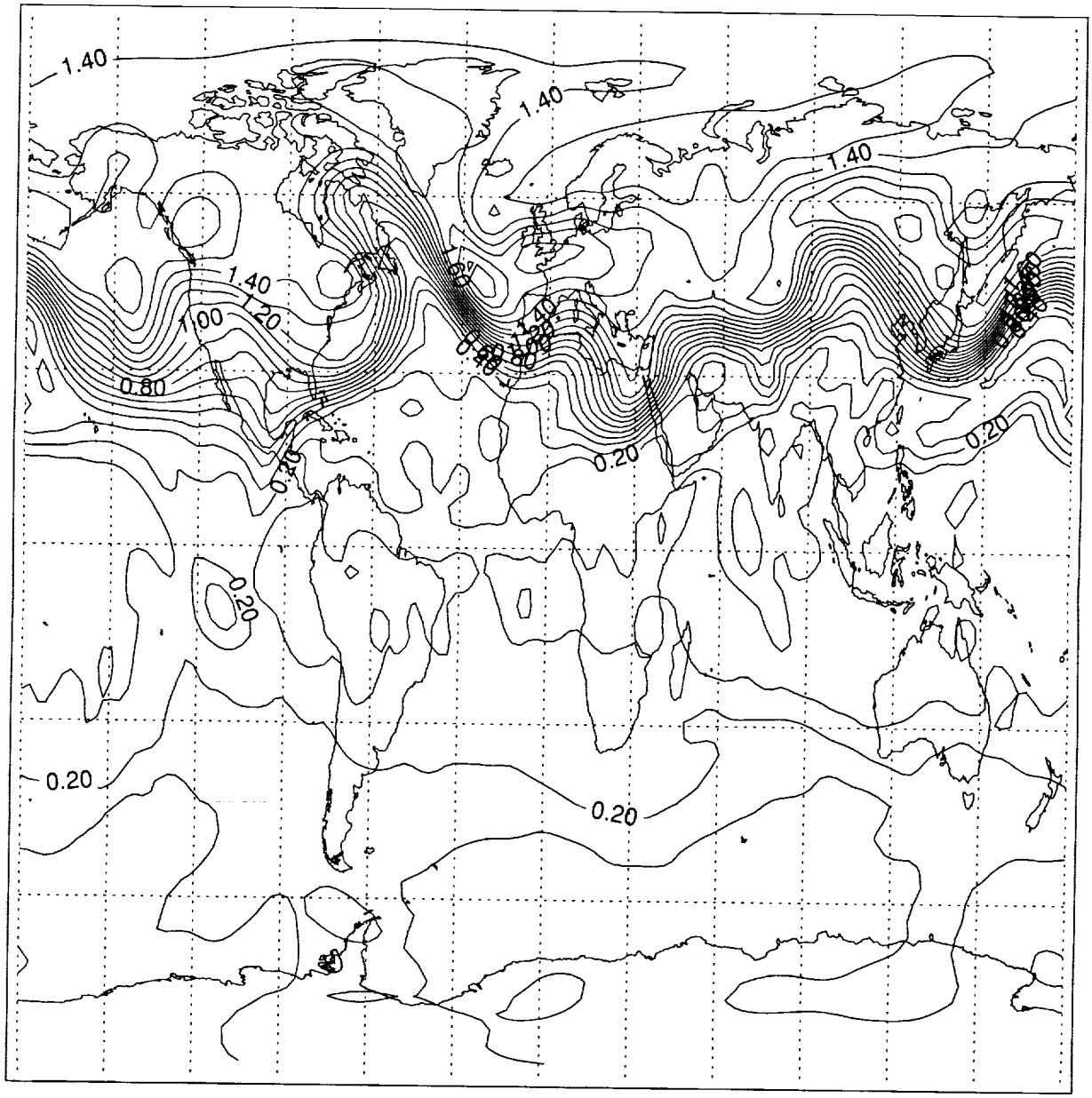

Figure 2.33. Contours of HSCT ΔNOy tracer mixing ratio (ppbv) at 69 mb for August 23 in the LARC T32 model.

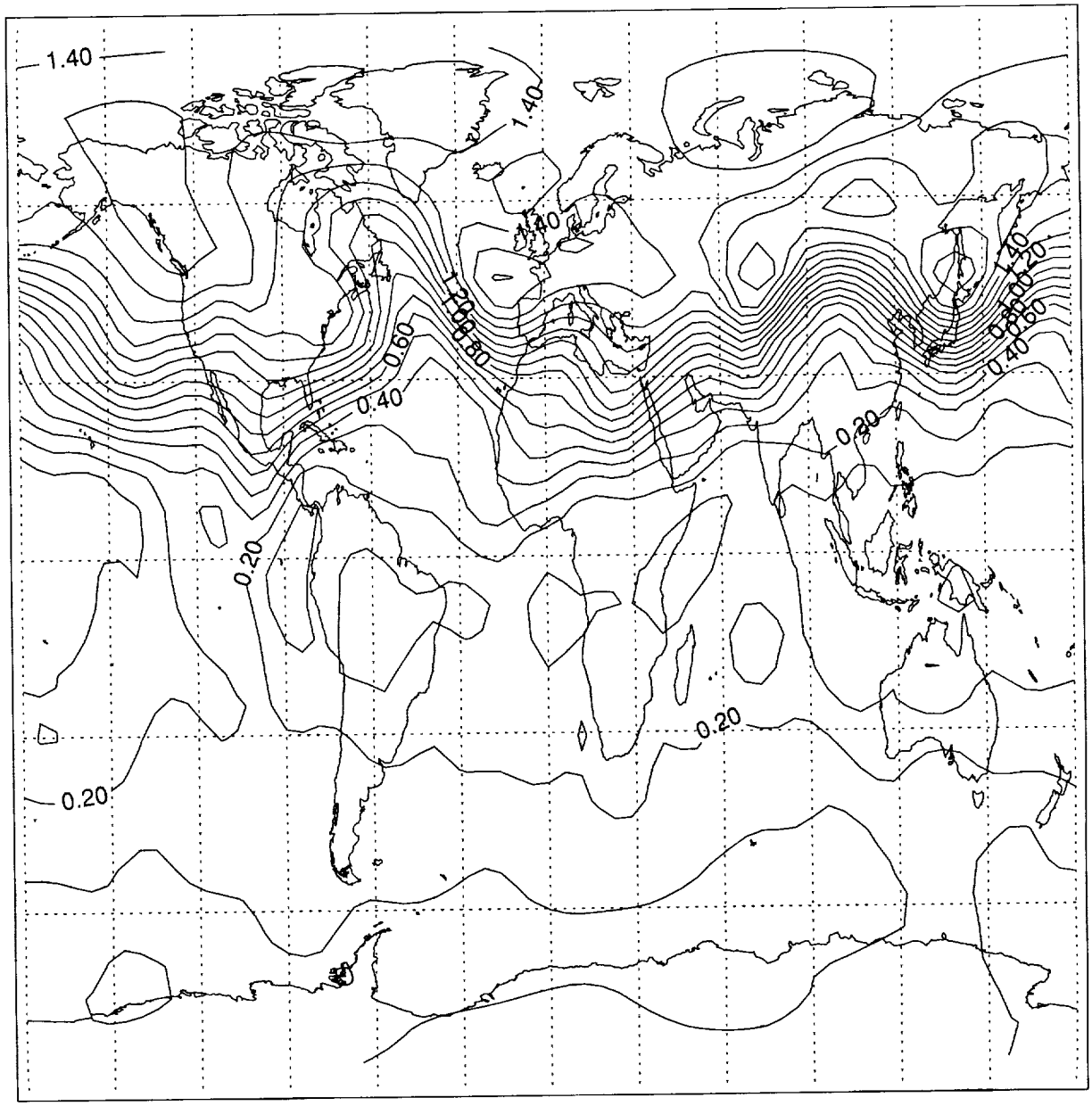

Figure 2.34. Contours of HSCT ΔNOy tracer mixing ratio (ppbv) at 69 mb for August 23 in the LARC T16 model.

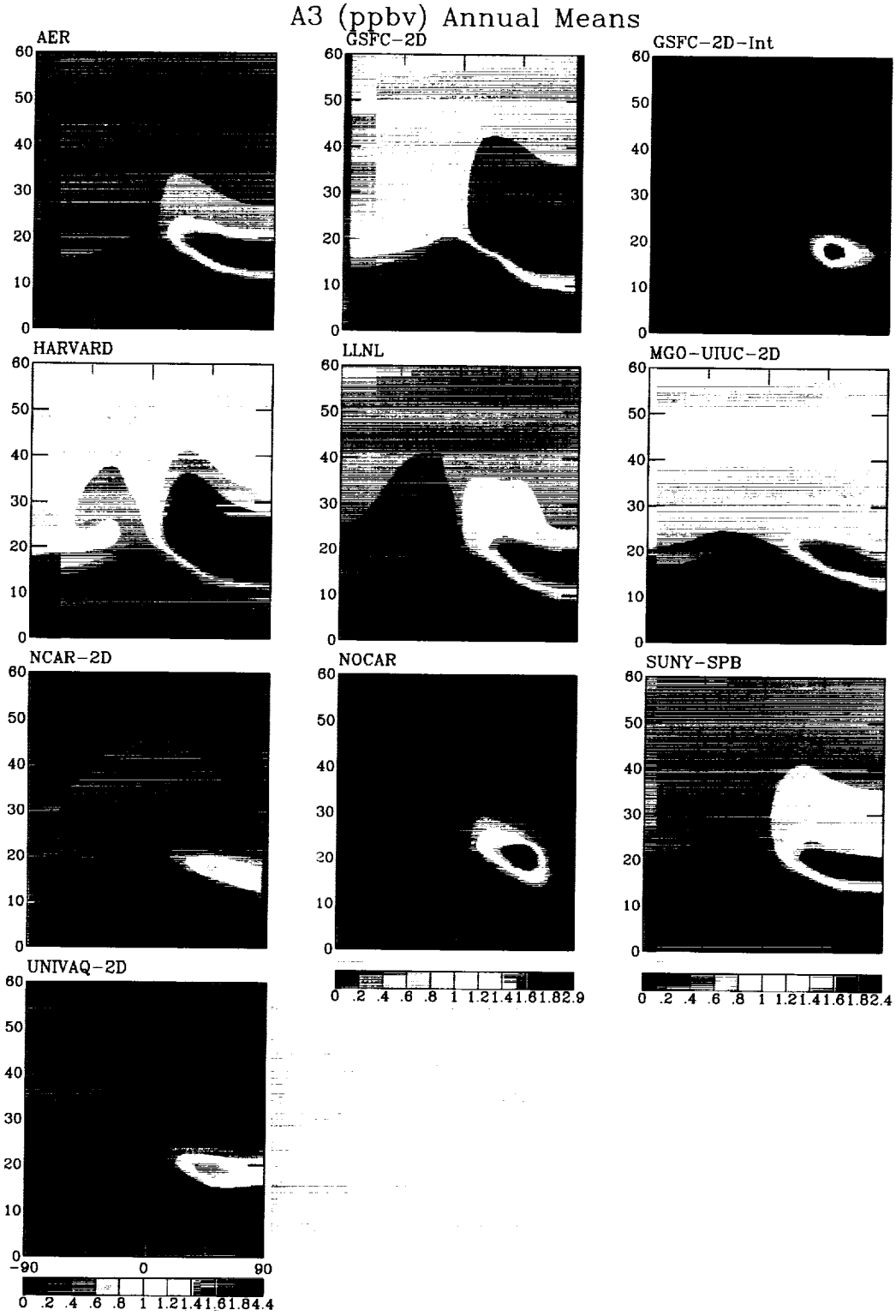

Figure 2.35. Contour plots of the A3 HSCT ΔNOy tracer annual mean mixing ratio for (a) 2D models; and (b) 3D models.

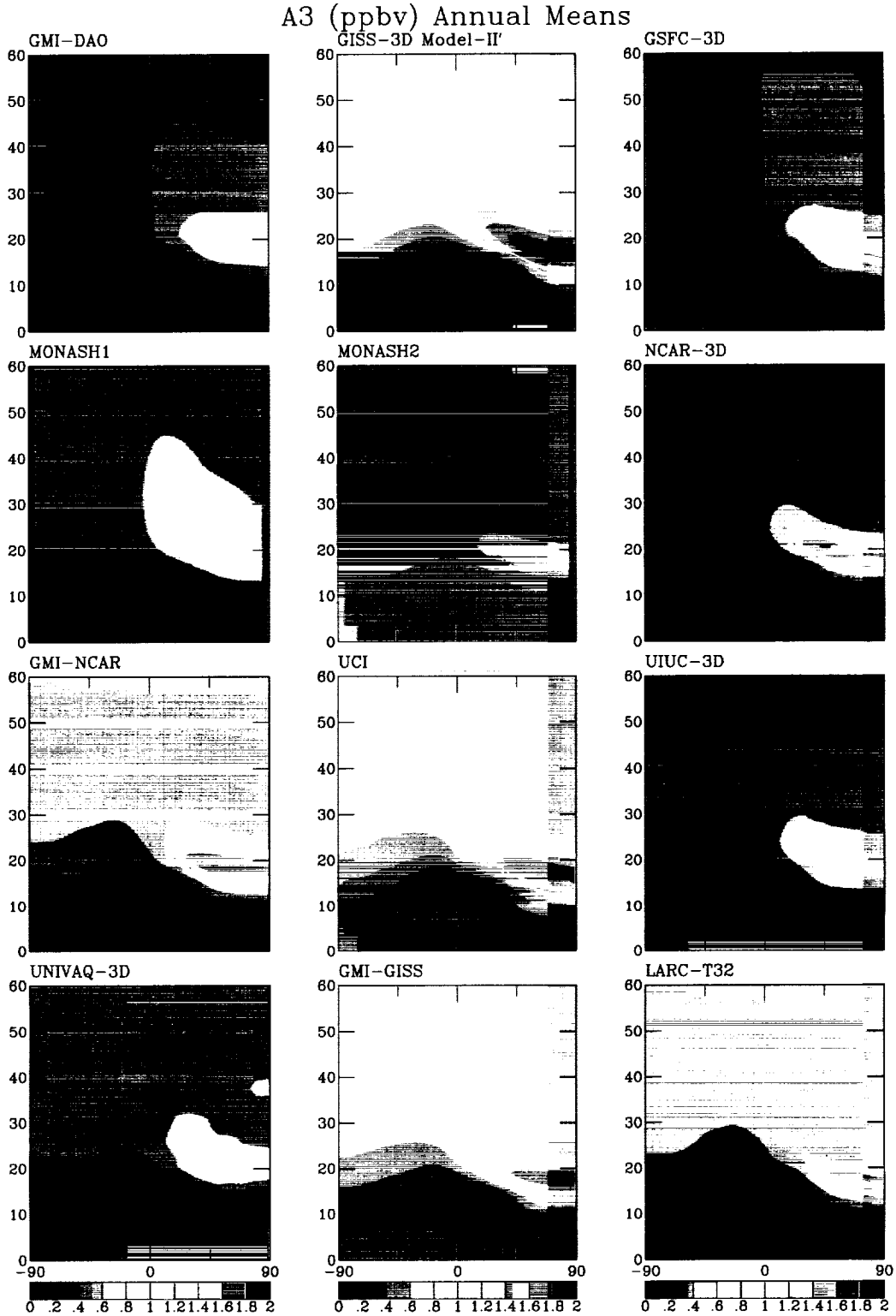

Figure 2.35. Concluded.

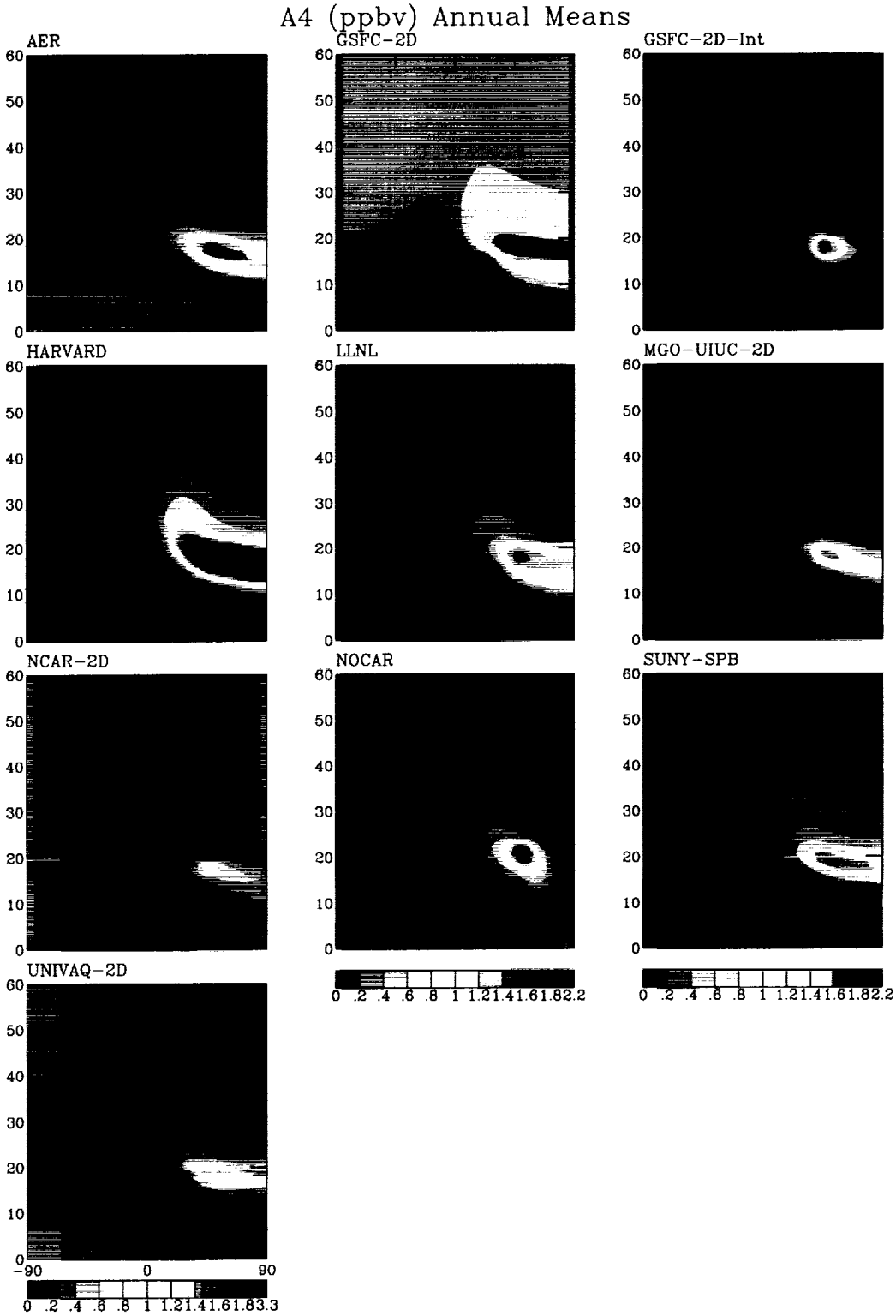

Figure 2.36. Contour plots of the A4 HSCT ΔNOy tracer annual mean mixing ratio for (a) 2D models; and (b) 3D models.

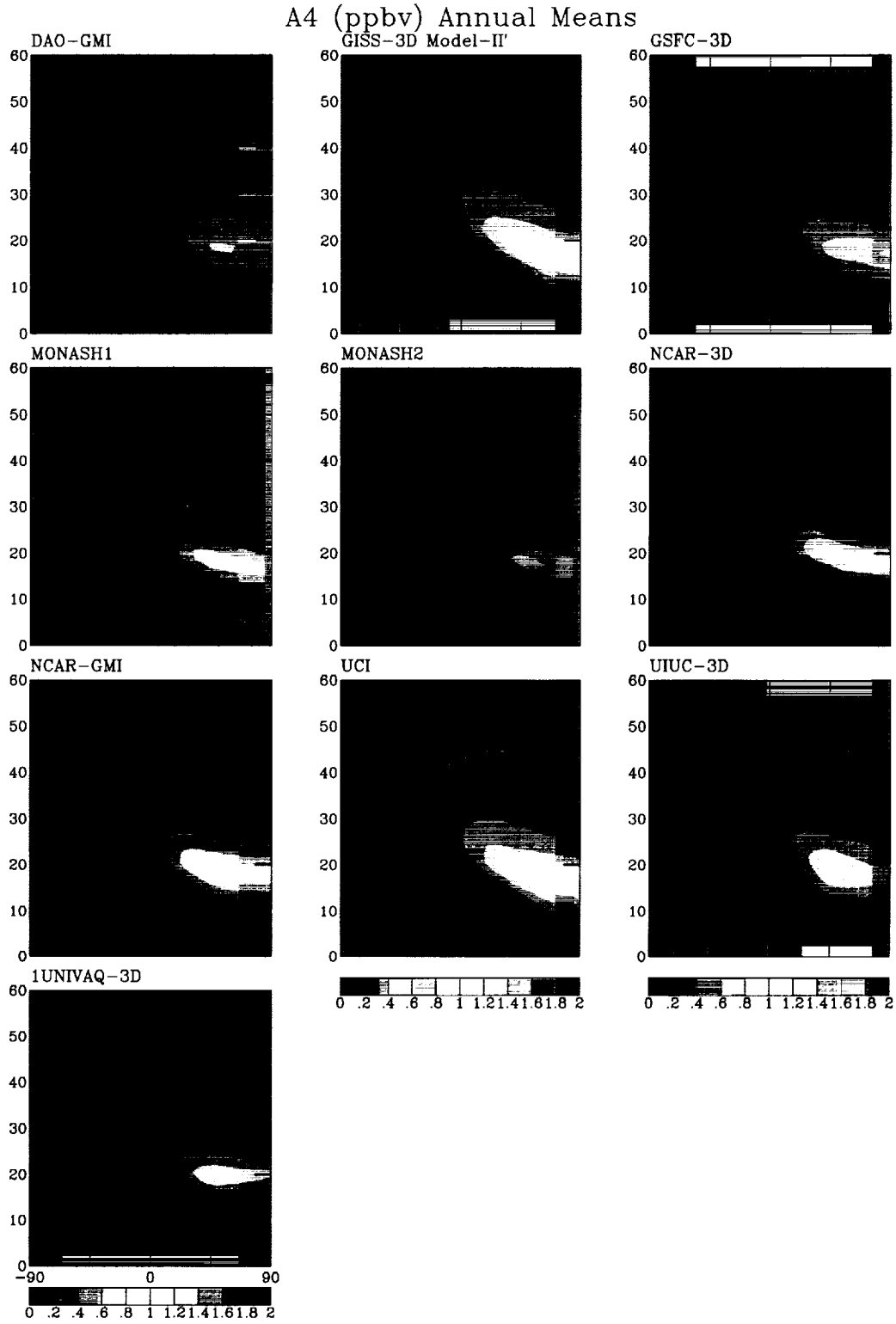

Figure 2.36. Concluded.

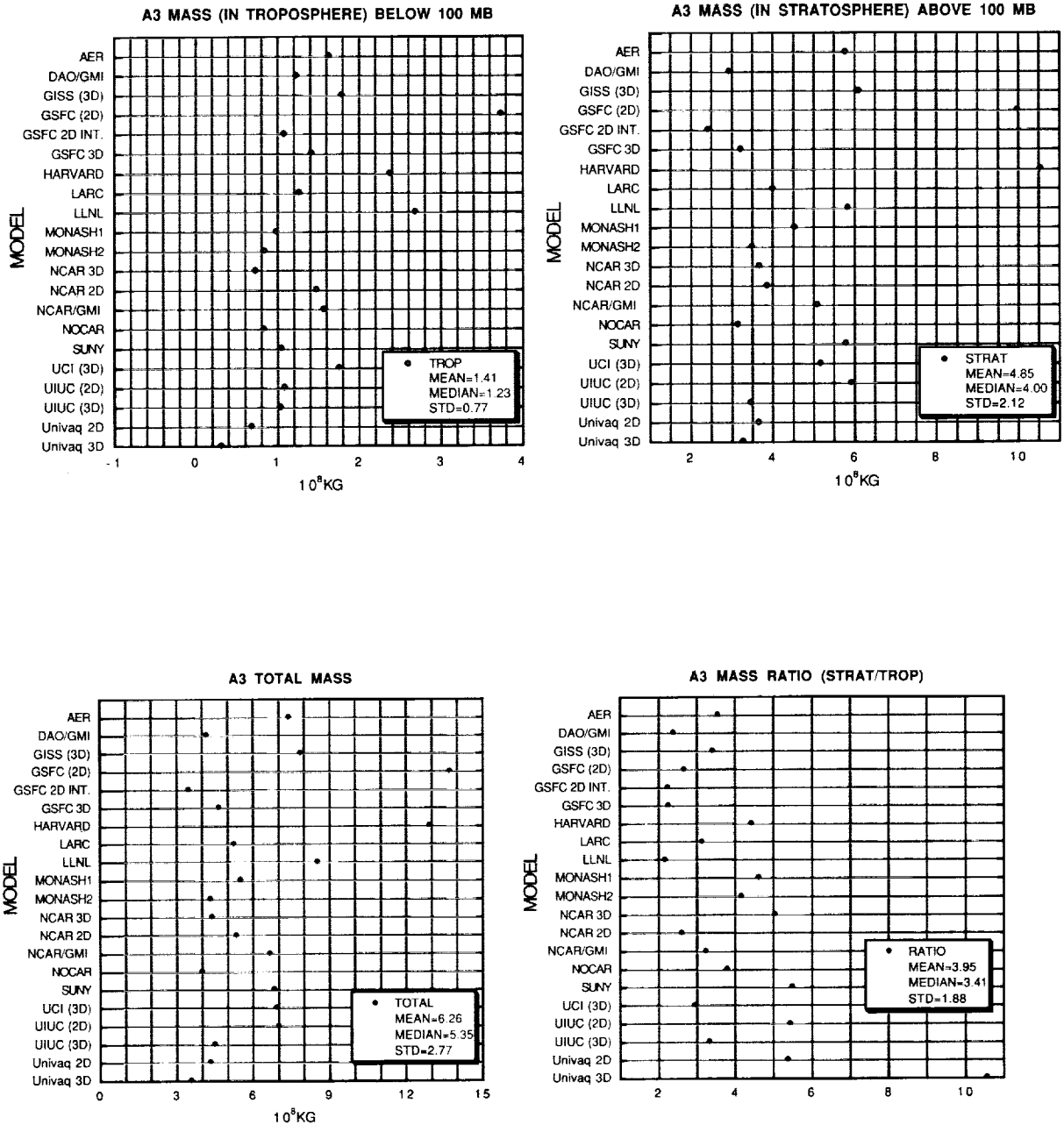

Figure 2.37. Histogram for the A3 experiment of total ΔNOy mass, troposphere mass, stratosphere mass, and strat/trop ratio as listed in Table 2.3. Masses in units 10^8 kg.

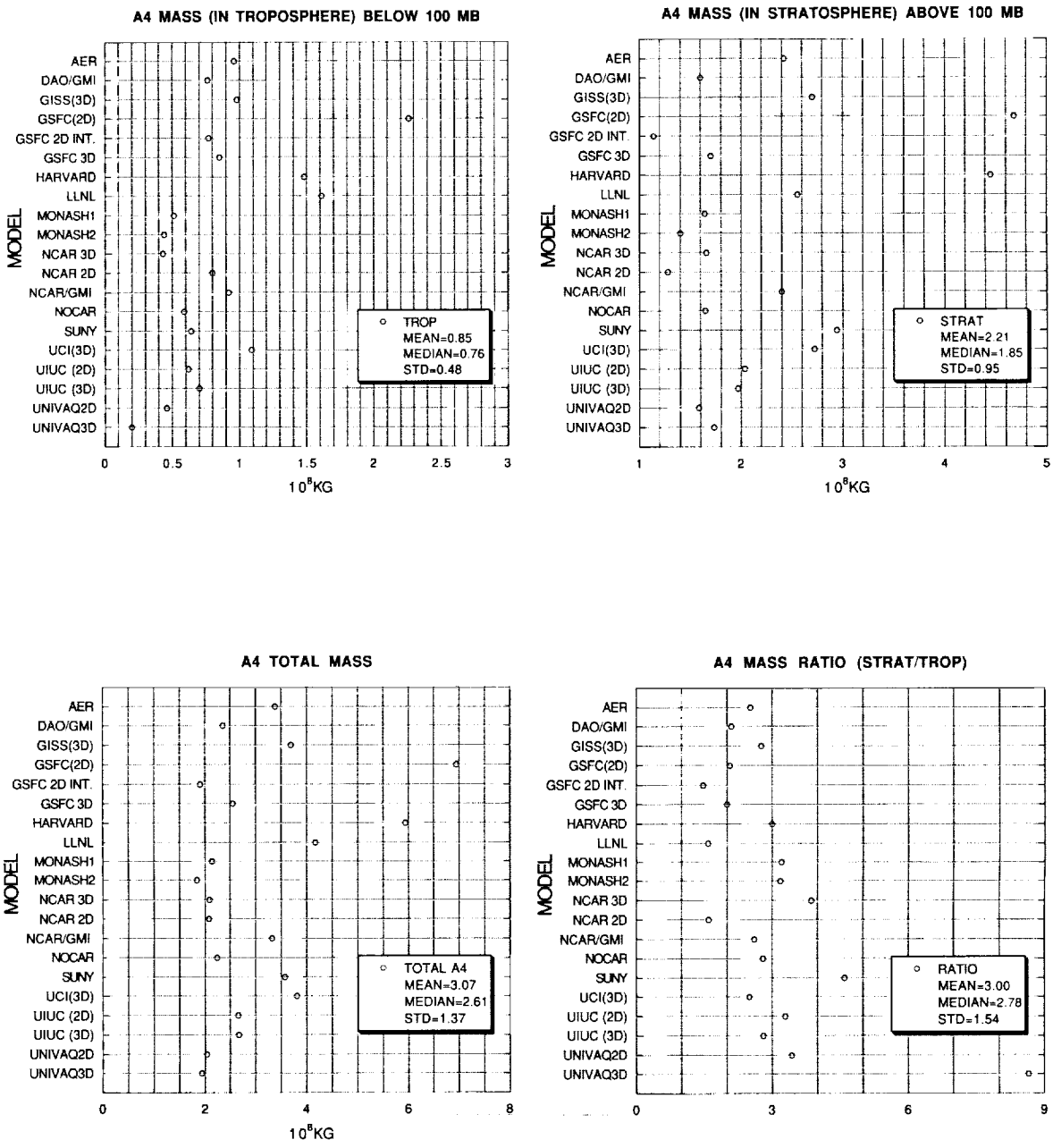

Figure 2.38. Histogram for the A4 experiment of total ΔNOy mass, troposphere mass, stratosphere mass, and strat/trop ratio as listed in Table 2.3. Masses in units 10^8 kg.

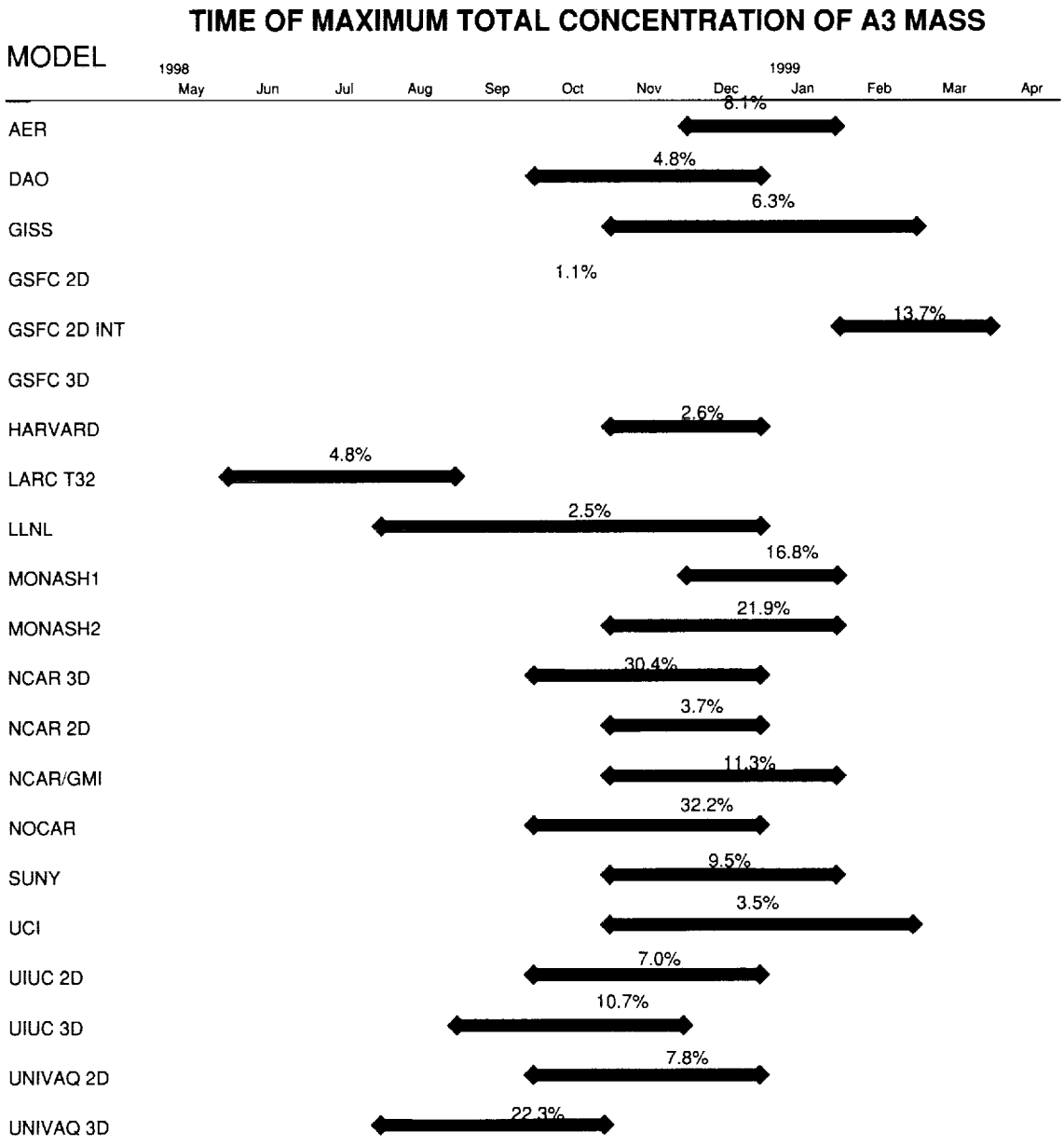

Figure 2.39. Seasonal distribution of the total atmospheric ΔNOy tracer mass for the A3 experiment. The numbers indicate the peak to peak amplitude over the year as a percentage of the annual mean for each model.

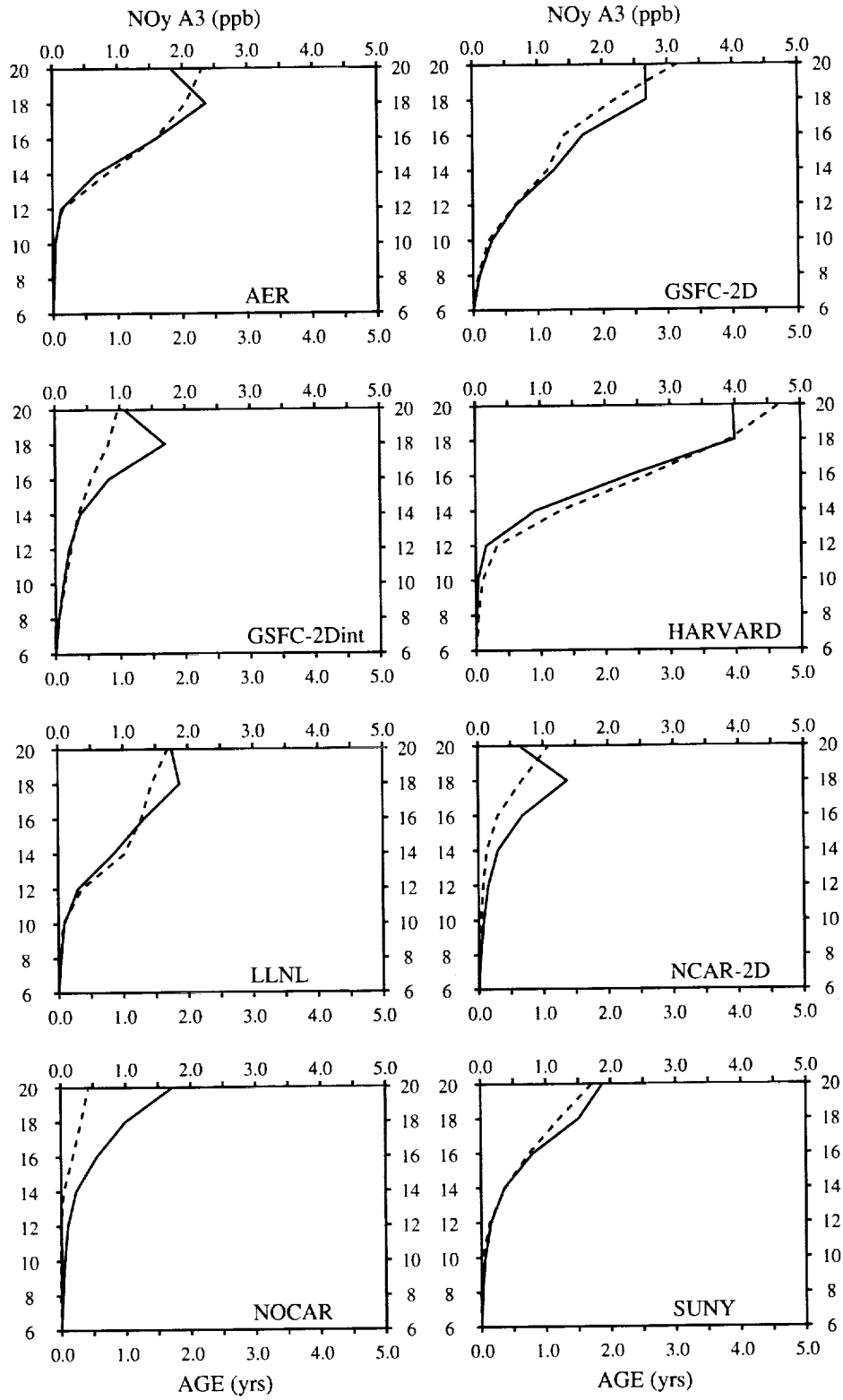

Figure 2.40. Profiles of Γ (dashed) and A3 ΔNOy (solid) for 2D models. The bottom axis is Γ in years, and the top ΔNOy in ppb. Values have been averaged annually and over the latitude range 35°N to 55°N. Γ is referenced to zero at 6 km. Panels correspond to models, as labeled.

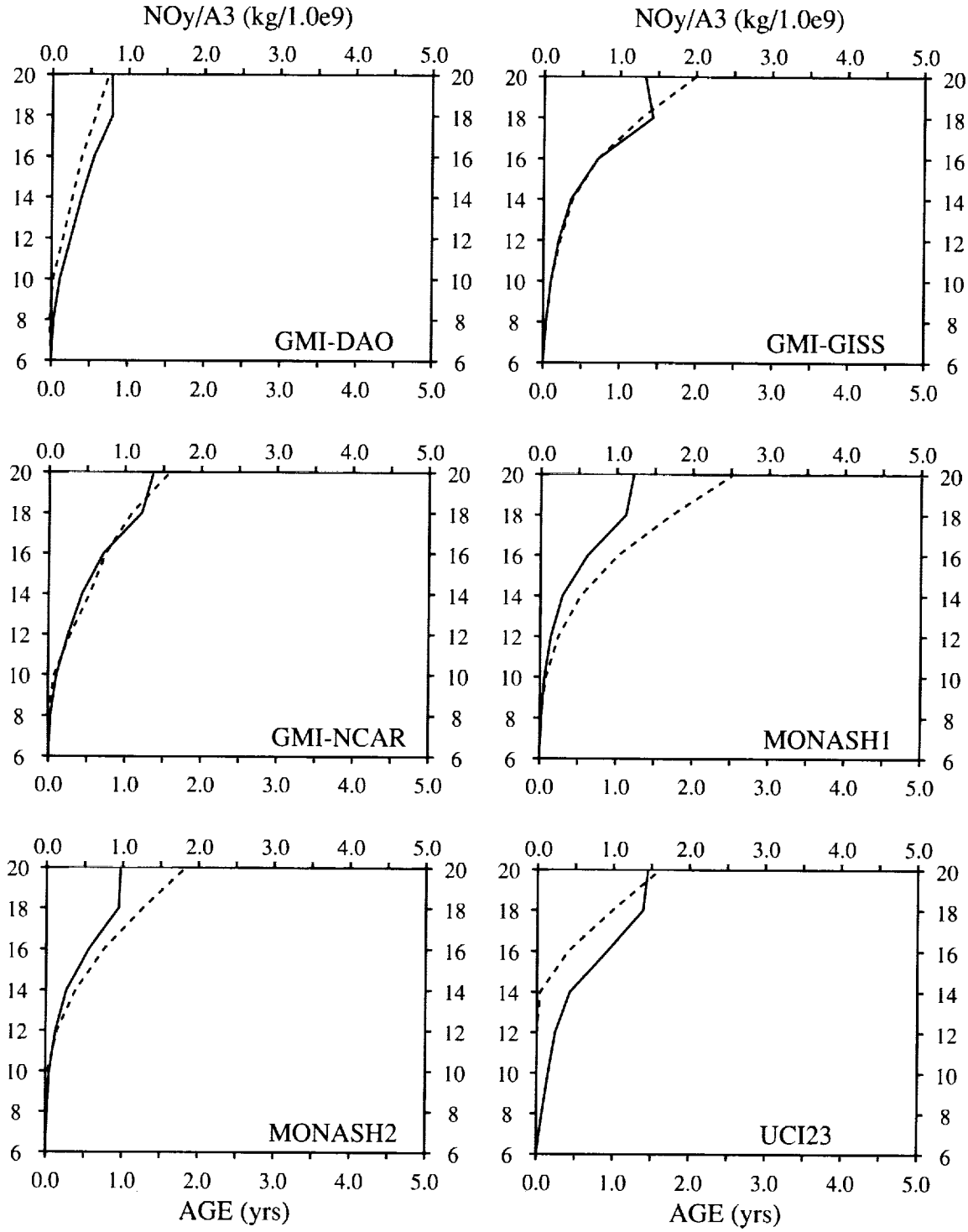

Figure 2.41. Same as Figure 2.42, but for 3D models.

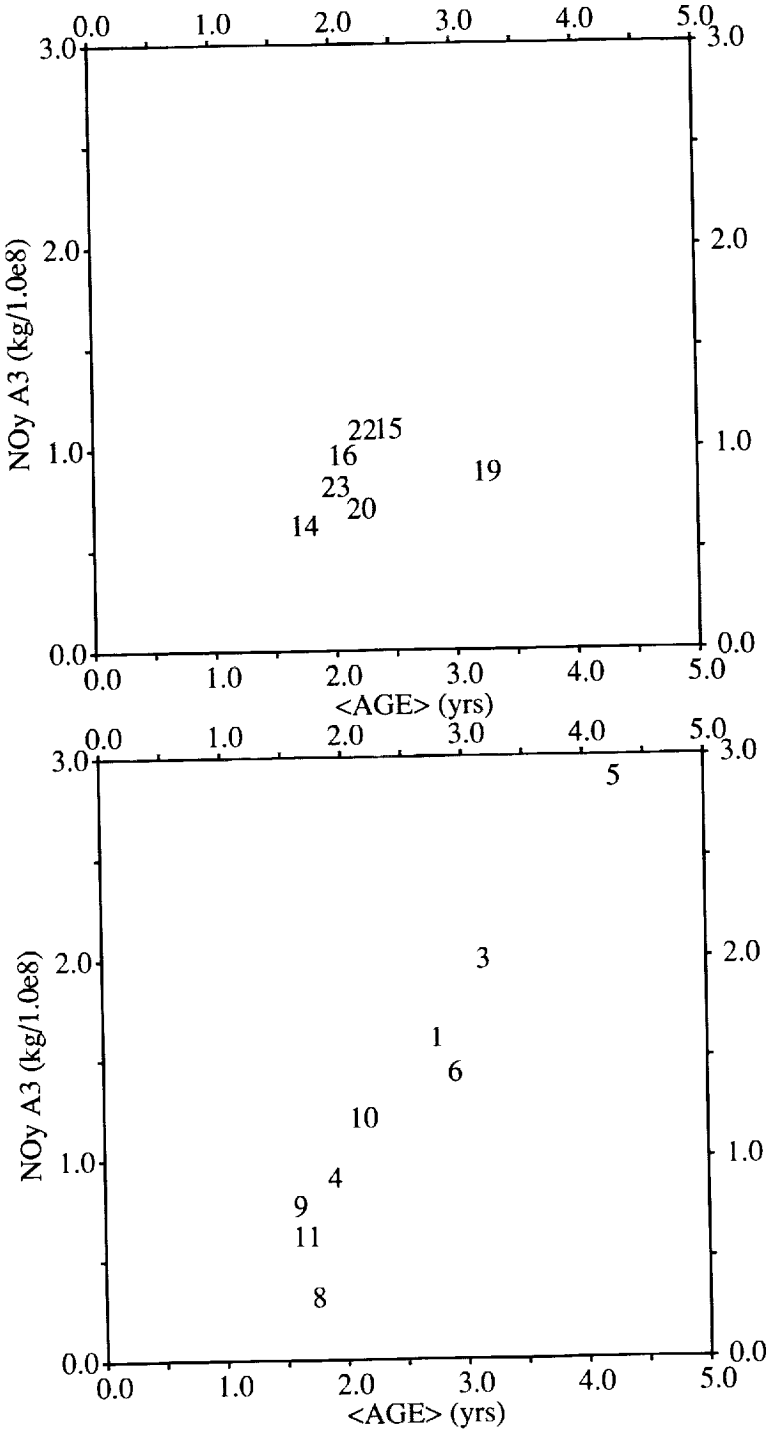

Figure 2.42. $\overline{\Delta NOy}$ versus $\bar{\Gamma}$, where $\overline{\Delta NOy}$ is the total ΔNOy tracer mass over the region 35°N to 55°N and 16 km to 22 km, and $\bar{\Gamma}$ is the mass weighted average of the mean age over the same region. The top panel shows 3D models, and the bottom panel 2D models, with numbers corresponding to models as listed in Table 2.2.

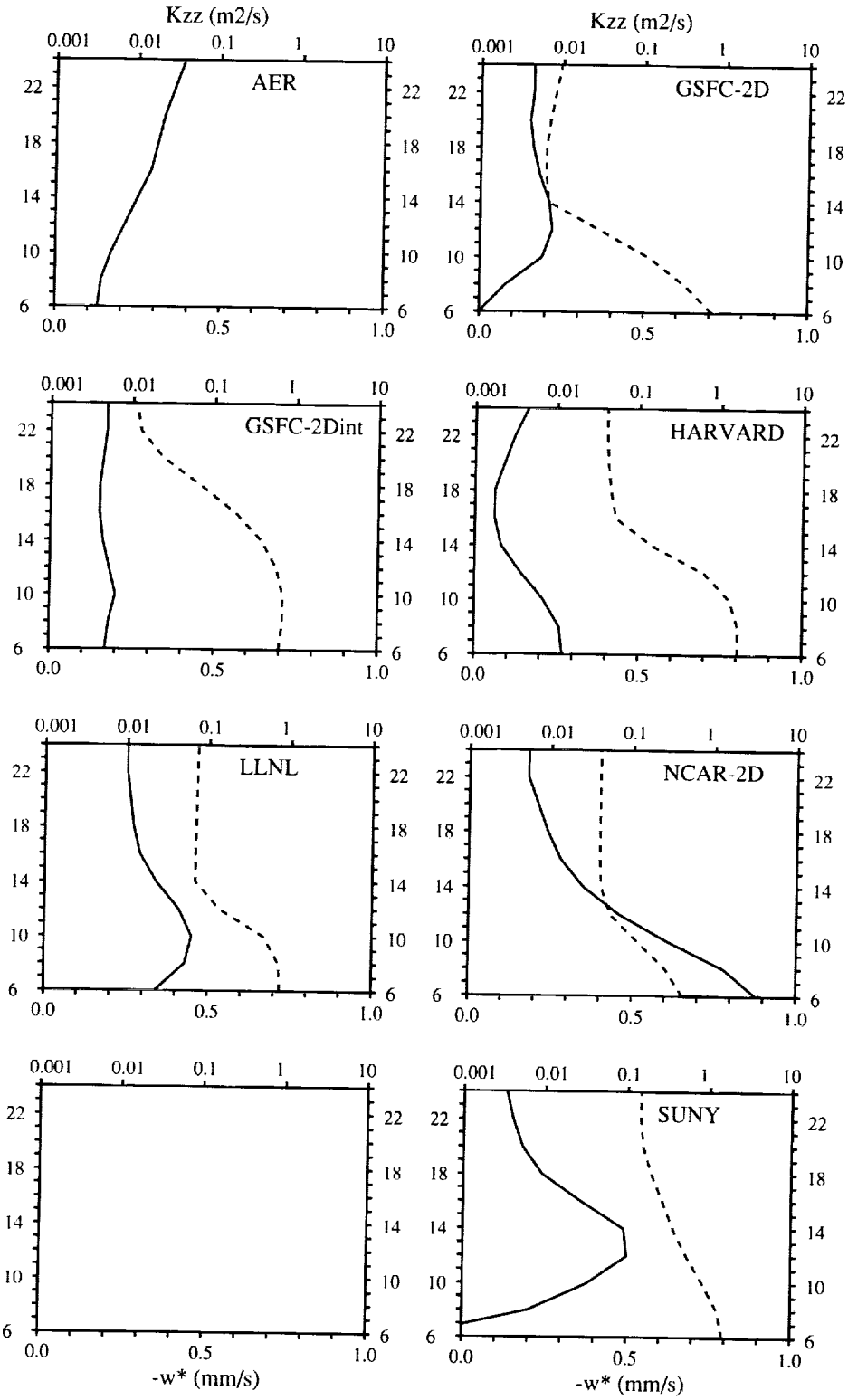

Figure 2.43. Profiles of 2D model $-\overline{w}^*$ (solid) and K_{zz} (dashed). The bottom axis is $-\overline{w}^*$ in mm/s, and the top K_{zz} in m^2/s. Values have been averaged annually and over the latitude range 35°N to 55°N. Panels correspond to models, as labeled. Empty panels indicate models for which data was not available and are included for ease of comparison to Figure 2.40.

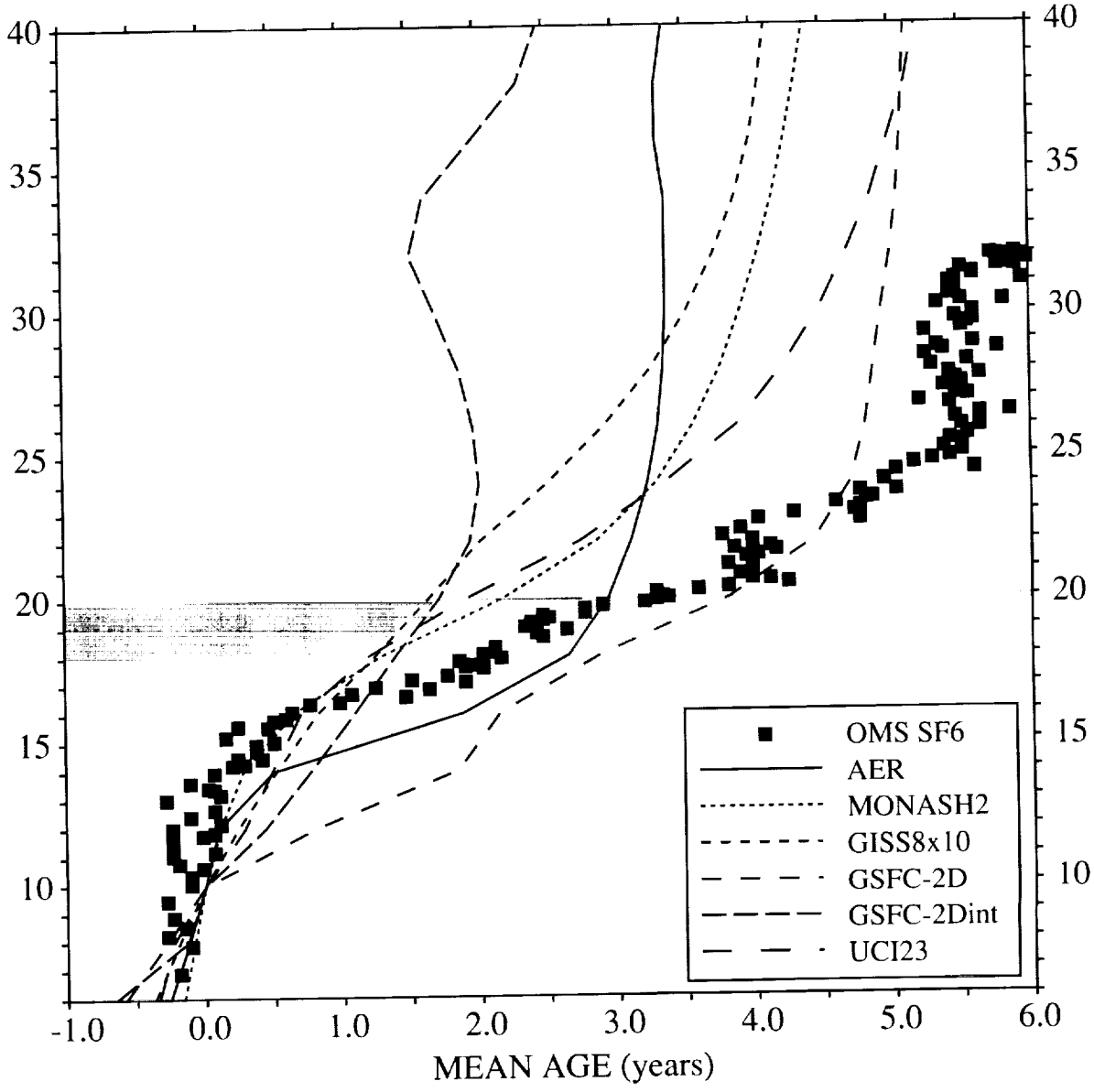

Figure 2.44. Profiles of $\Gamma(x)$ from several models (solid, dashed, and dotted lines, as indicated) at 35°N through the upper troposphere and lower stratosphere, and values inferred from SF_6 measured from an OMS balloon flight at similar latitude. Here, the model $\Gamma(x)$ are taken from the SF_6 simulations, so that the month corresponding to the balloon flight (September) may be plotted. $\Gamma(x)$ is referenced to zero at 6 km. The shaded region indicates the height of peak ΔNOy emissions for simulations A3 and A4.

Table 2.1. MM2 models that performed transport experiments

2D models	3D models
AER	GISS8 × 10
CSIRO	GISS4 × 5
GSFC-2D	GMI-DAO
GSFC-2Dint	GMI-GISS
HARVARD	GMI-NCAR
LLNL	GSFC-3D
MGO-UIUC-2D	LARC T32
NCAR-2D	MONASH1
NOCAR	MONASH2
SUNY-SPB	NCAR-3D
UNIVAQ-2D	UCI21
WISCAR	UCI23
	UIUC-3D
	UNIVAQ-3D

Table 2.2. Parameter values used by each model

		τ_0 (yrs)	H_a (km)	c (mm/s)	$dz/d\Gamma$ (mm/s)	R
1	AER	1.87	6.62	0.48	0.24	0.44
2	CSIRO	2.15	5.97	0.45	0.28	0.42
3	GSFC-2D	3.04	4.07	0.30	0.14	0.42
4	GSFC-2Dint	1.40	7.72	0.51	0.42	0.48
5	HARVARD	2.86	2.18	0.26	0.15	0.26
6	LLNL	1.97	3.78	0.42	0.23	0.28
7	MGO-UIUC-2D		3.83	0.36	0.18	0.33
8	NCAR-2D[a]	3.23	3.43	0.33	0.14	0.33
9	NOCAR	1.51	5.26	0.59	0.31	0.28
10	SUNY-SPB	2.38	3.76	0.54	0.17	0.22
11	UNIVAQ-2D	2.22	3.09	0.54	0.25	0.18
12	WISCAR	3.66	3.97	0.54	0.19	0.23
13	GISS8 × 10	2.19	4.43	0.48	0.22	0.30
14	GMI-DAO	1.44	8.73	0.95	0.38	0.29
15	GMI-GISS	3.47	2.31	0.40	0.12	0.18
16	GMI-NCAR	2.89	4.61	0.48	0.15	0.31
17	GMI-NCARcon	2.78	4.41	0.51	0.16	0.28
18	GSFC-3D	1.56	8.35	0.85	0.35	0.31
19	MONASH1	5.41	3.03	0.40	0.12	0.24
20	MONASH2	2.89	4.43	0.59	0.18	0.24
21	UCI21	2.23	5.74	0.63	0.22	0.29
22	UCI23	3.14	2.34	0.45	0.13	0.24
23	UIUC-3D	1.74	6.24	1.09	0.32	0.18
24	UNIVAQ-3D	2.36	3.55	0.59	0.20	0.19
	HALOE $\hat{H}$[b]		7.6	0.30		0.7
	OMS $\hat{H}$[c]		3.7	0.24		0.5
	OMS SF_6				0.11	

[a]Fits may be corrupted by a high tropopause.
[b]Derived from analysis of Mote et al. [1998]; note that a fit from 16 km to 20 km yields H_a = 5.4 km.
[c]Data range from 16 km to 20 km.

Table 2.3. Masses of the A3 and A4 tracer in the stratosphere and troposphere and the strat/trop ratio. All masses in units 10^8 kg. Stratosphere and troposphere defined as above and below 100 mb pressure surface

Model	A3 Trop	A3 Strat	A3 Total	A3 Ratio	A4 Trop	A4 Strat	A4 Total	A5 Ratio
2D Models								
AER	1.63	5.78	7.41	3.55	0.96	2.42	3.38	2.52
GSFC-2D	3.74	9.98	13.72	2.67	2.26	4.68	6.95	2.07
GSFC-2Dint	1.08	2.42	3.49	2.24	0.77	1.14	1.91	1.48
HARVARD	2.38	10.54	12.92	4.42	1.48	4.45	5.94	3.00
LLNL	2.69	5.84	8.54	2.17	1.61	2.56	4.17	1.59
MGO-UIUC-2D	1.09	5.93	7.02	5.44				
NCAR-2D	1.48	3.86	5.35	2.61	0.80	1.28	2.08	1.60
NOCAR	0.83	3.15	3.99	3.80	0.59	1.65	2.24	2.80
SUNY-SPB	1.05	5.79	6.84	5.51	0.64	2.94	3.58	4.59
UNIVAQ-2D	0.68	3.66	4.34	5.38	0.46	1.58	2.04	3.43
3D Models								
GISS4x5	1.79	6.10	7.89	3.41	0.98	2.70	3.68	2.76
GMI-DAO	1.23	2.94	4.17	2.39	0.76	1.60	2.36	2.10
GMI-GISS	1.84	5.08	6.93	2.76				
GMI-NCAR	1.57	5.09	6.66	3.24	0.92	2.40	3.32	2.61
GSFC-3D	1.42	3.23	4.65	2.27	0.85	1.70	2.55	2.00
LARC	1.27	4.00	5.27	3.15				
MONASH1	0.98	4.54	5.52	4.63	0.51	1.64	2.14	3.21
MONASH2	0.84	3.50	4.34	4.17	0.44	1.40	1.84	3.18
NCAR-3D	0.73	3.68	4.41	5.04	0.43	1.66	2.09	3.86
UCI23	1.76	5.17	6.93	2.94	1.09	2.72	3.81	2.50
UIUC-3D	1.04	3.46	4.50	3.33	0.70	1.97	2.67	2.81
UNIVAQ-3D	0.31	3.28	3.58	10.58	0.20	1.73	1.94	8.65

Table 2.4. Ratio of northern hemisphere to southern hemisphere annual mean of the tracers at 20 km. Also given is the northern hemisphere season of maximum ratio. "L" indicates "late."

Model	A3 NH/SH	Season	A4 NH/SH	Season
2D Models				
AER	2.81	LSUM/FA	9.83	LSUM/FA
GSFC-2D	2.33	FALL	5.09	NONE
GSFC-2Dint	3.79	SUMMER	120.15	SUMMER
HARVARD	3.51	SUMMER	94.58	SUMMER
LLNL	2.76	LSUM/FA	12.20	LSUM/FA
MGO-UIUC-2D	2.12	FALL	6.85	SUMMER
NCAR-2D	1.44	SUMMER	2.11	SUMMER
NOCAR	5.04	LSUM/FA	68.86	LWIN/SU
SUNY-SPB	2.67	NONE	7.06	FALL/SP
UNIVAQ-2D	2.62	LSUM/FA	29.17	FALL
3D Models				
GISS4x5	2.62	WINTER	7.30	WINTER
GMI-DAO	2.89	SPRING	7.18	SPRING
GMI-GISS	2.47	WINTER		
GMI-NCAR	2.28	SUMMER	5.84	SUMMER
GSFC-3D	2.72	NA	6.42	NA
LARC	2.60	WINTER		
MONASH1	2.00	NONE	6.58	FALL
MONASH2	2.02	FALL	6.04	FALL
NCAR-3D	3.20	FALL	11.77	FALL
UCI23	2.86	WINTER	7.65	WINTER
UIUC-3D	3.16	NONE	8.30	SPRING
UNIVAQ-3D	2.48	LSUM/FA	9.41	SPRING

Table 2.5. Ratios for A3 and A4 of northern hemisphere value at 30 km to absolute peak, 40 km to absolute peak and 50 km to absolute peak.

Model	A3 30/pk	A3 40/pk	A3 50/pk	A3 Season	A4 30/pk	A4 40/pk	A4 50/pk	A4 Season
2D Models								
AER	0.23	0.16	0.16	NONE	0.06	0.06	0.06	WINTER
GSFC-2D	0.48	0.42	0.42	FALL	0.32	0.23	0.23	NONE
GSFC-2Dint	0.10	0.10	0.07	SUM/FA	0.04	0.04	0.04	NONE
HARVARD	0.46	0.31	0.24	FALL	0.25	0.18	0.06	FALL
LLNL	0.40	0.36	0.28	FALL	0.25	0.19	0.06	FALL
MGO-UIUC-2D	0.39	0.39	0.39	NONE				
NCAR-2D	0.36	0.36	0.29	FALL	0.09	0.09	0.09	NONE
NOCAR	0.22	0.13	0.09	FALL	0.07	0.04	0.04	SUMMER
SUNY-SPB	0.48	0.40	0.38	FALL	0.36	0.25	0.19	SUMMER
UNIVAQ-2D	0.31	0.31	0.31	NONE	0.11	0.07	0.07	NONE
3D Models								
GISS4x5	0.52	0.43	0.43	NONE	0.37	0.22	0.22	NONE
GMI-DAO	0.77	0.55	0.44	FALL	0.66	0.38	0.22	FALL
GMI-GISS	0.50	0.41	0.41	SUM/FA				
GMI-NCAR	0.56	0.44	0.44	NONE	0.33	0.25	0.25	NONE
GSFC-3D	0.42	0.33	0.25	NA	0.41	0.29	0.23	NA
LARC	0.50	0.50	0.50	FALL				
MONASH1	0.64	0.64	0.60	FALL	0.33	0.11	0.11	FALL
MONASH2	0.42	0.42	0.42	NONE	0.22	0.11	0.11	NONE
NCAR-3D	0.33	0.28	0.22	FALL	0.21	0.12	0.07	FALL
UCI23	0.50	0.43	0.43	NONE	0.32	0.24	0.24	NONE
UIUC-3D	0.50	0.33		SUM/FA	0.40	0.20		SUM/FA
UNIVAQ-3D	0.50	0.33	0.33	SUMMER	0.30	0.30	0.25	NONE

3. Chemistry Experiments

3.1 Summary of the MMII Intercomparisons for Chemistry

Guy Brasseur[1] and Ellis Remsberg[2]

1. National Center for Atmospheric Research
2. NASA Langley Research Center

The purpose of the chemistry component of the model comparison is to assess to what extent differences in the formulation of chemical processes explain the variance between model results. Observed concentrations of chemical compounds are used to estimate to what degree the various models represent realistic situations.

For readability, the materials for the chemistry experiment are reported in three separate chapters. Chapter 3 discussed the data used to evaluate the models in their simulation of the source gases and the NOy and Cly species. Chapter 4 discussed the ozone climatoloty and comparison with the model results. Chapter 5 reported on a number of special diagnostics.

Several concerns were expressed during the MM I exercise in 1993, regarding specifically the modeling of photochemical processes between 20 and 40 km altitude, unsatisfactory simulations of photolysis rates and chemical cycles, and large differences in Clx and Brx partitioning. Since this earlier comparison, specific aspects of these model differences have been analyzed, and addressed. At the same time, more complex models, with a higher degree of interactivity between chemisry and dynamics have been devleoped, introducing new potential causes for disagreements between models. Overall, the new comparison (which also includes 3-D models) tends to show a better degree of similarity regarding species like ozone, NOx, HNO_3, HCl, etc., even when polar stratospheric clouds are included in the models. Model/data differences tend to be larger in the lower stratosphere, where transport of source and reservoir species tends to play a more important role. These deficencies represent potential problems for an accurate asessment of the impact of projected high altitude aircraft.

The major findings resulting from the Chemistry comparisons can be summarized as follows:

1. Source Gases

The comparison between calculated and measured source gas concentrations provides primarily a diagnostic for model transport, and should be related to the discussion presented in earlier sections of this report. However, the success in simulating the global distribution of long-lived species has a direct consequence for the simulation of fast-reactive gases that are produced by these long-lived source gases.

A general pattern is that the calculated lifetime of source gases differs among the participating models, and that models which tend to derive the smallest lifetimes also produce the steepest latitudinal gradients. This behavior is probably indicative of the strength of upwelling in the tropics and the permeability of the tropical barrier. In most cases, calculated species cross-sections for nitrous oxide and methane show larger meridional gradients across the tropical barrier than shown by UARS observations, while, conversely, calculated gradients are smaller than indicated by measurements of CFC-11 from the ATMOS and ER-2 observations. It is clear that the representation of transport in models remains inaccurate in many cases, and that obtaining a more realistic transport will not be trivial.

2. Nitrogen and Chlorine Compounds

The comparison of nitrogen species between the participating models suggests that calculated NOy concentrations differ by 30 percent among the models. This difference is even larger when N_2O is constrained. The calculated NO mixing ratios differ widely among models, and most models do not properly reproduce the seasonal variation of the NO maximum observed at 45 km by HALOE. The calculated seasonal variability of the NO_2 mixing ratio maximum at 34 km is in good agreement with HALOE observations. NO_2 concentrations in the mid-troposphere at mid-latitudes are more similar among models than is the case of NO, and are in good agreement with HALOE data. The seasonal variation in the HNO_3 mixing ratio maximum at 24 km at high latitudes is in relatively good agreement with CLAES data, but the calculated magnitude of this maximum shows a wide spread among models.

In the case of Cly concentrations, differences of approximately 10 percent are found when the different models are compared. This difference is larger when CFC distributions are constrained in the model. The ClO mixing ratios are characterized by a wide spread among models, both for the vertical profile and the seasonal variation. In most cases, the model simulated $ClONO_2$ agrees well with CLAES and ATMOS measurements at mid-latitudes. However, the seasonal behavior in $ClONO_2$ is not well reproduced by all models. The model estimates of HCl are generally lower that the observations by HALOE and ATMOS, with large differences in the concentrations between the participating models.

3. Ozone

The different models participating in the intercomparison usually provide similar results regarding ozone in the upper stratosphere (above 25 km), where the ozone budget is mostly controlled by gas-phase chemistry. Theoretical estimates at these heights are in good agreement with observations. The models start to diverge below 25 km, where transport and heterogeneous chemistry plays an increasingly important role. The largest differences are located between 20 km and the tropopause, and are as high as 50 percent in the models that show the best agreement with the observations. The ozone column calculated by the models is within 10-20 percent of the climatological values. Most models show the best agreement with observations in the tropics.

4. Chemical Partitioning

Partitioning of the radical species has been calculated by the Photo-Stationary-State model of Salawitch using long-lived species concentrations from the individual output of the participating models. In many cases and for most situations the calculated radical concentrations are in fair agreement with the measured concentrations, although in certain cases large differences were reported for specific models.

5. Representation of Polar Processes

Because both chemical and dynamical conditions play an important role in the evolution of ozone and other chemical compounds at high latitudes, polar processes are difficult to represent in 2-D and even 3-D models. The model comparison suggests that the observed structure of long-lived atmospheric tracers (such as N_2O) are not consistently well simulated by the participating 2-D and 3-D models. In particular, most models (with some exceptions) underestimate the strength of the meridional gradients in the vicinity of the polar votices. In addition, the seasonal cycle of species such as N_2O is not well simulated in most models. On the other hand, simulations of the seasonal evolution of nitric acid in the polar lower stratosphere are in reasonable agreement with observations from CLAES. However, the

models differ by several months in the timing of the onset of the HNO_3 decrease associated with PSC formation.

Comparisons of calculated polar (inorganic) Cly with estimates inferred from ER-2 observations suggest that several models underestimate Cly in the polar regions of both hemispheres, with large differences in the Cly profiles among models. In the southern hemisphere, the models also differ in the extent to which chlorine is released from HCl and $ClONO_2$. The comparison shows significant differences among the participating models regarding the vertical extent over which polar processes are important, the intensity of the chlorine activation, and the partitioning among chlorine species. For example, large variance is found in the partitioning between Cl_2O_2 and ClO. As a result the model ClO profiles (which determines the rate of ozone destruction in polar regions) also exhibit significant variance, and calculated polar ozone in the Southern hemisphere differs from observations for all models in significant ways.

In the northern hemisphere, all models show less chlorine activation than in the Antarctic region, but there are still significant differences among the models. Because the observations of ClO and ozone by MLS in the Arctic exhibit much more variability than in the Antarctic, the comparison between models and measurements is difficult in the Northern hemisphere. For example, the large interannual variability shown in the observations is not reproduced in climatological models. Models using assimilated meteorological data are probably more appropriate to reproduce Arctic proceses.

6. Ozone Production/Destruction

Several models involved in the MM II comparison also provided calculated ozone production and destruction rates. The losses due to the various chemical families, taking into account heterogeneous processes at a time (1992) where the aerosol load was high (due to the Pinatubo eruption in 1991) were analyzed and compared among the different models. All models suggest that the HOx loss dominates in the lower stratosphere (below 20 km) and in the upper stratosphere/mesosphere (above 45 km). The NOx family dominates the ozone destruction in the middle stratosphere (20-40 km), while the influence of the ClOx family is quite large (more than 30 percent) in the middle and upper stratosphere (35-50 km). The BrOx family contributes significantly (more than 30 percent) to the ozone destruction in the lower polar stratosphere. The relative contribution of these families varies with season, and with chlorine and aerosol loading. In all models, the ozone production rate is approximately equal to the total destruction rate in the upper stratosphere, suggesting that photochemical conditions apply to ozone in this region of the atmosphere.

Calculations of the ozone abundance for prescribed ozone production and loss rates show significant differences among the models both in the ozone meridional distribution and in the ozone column, suggesting that variance in transport formulation among models has a significant impact on calculated ozone. When ozone production and destruction are prescribed, the agreement between models and observations is usually worse than when production and destruction rates are self-consistently calculated in the model.

References

Hall, T.M., et al., Transport experiments, in MMII Report, pp. 110–189, 1999.

Mlynczak, M., C. J. Mertens, R. R. Garcia, and R. Portmann, A detailed evaluation of the stratospheric heat budget. II. Global radiation balance and diabatic circulations, accepted by J. Geophys. Res., 1998.

Scott, C.J. and M.K.W. Ko, Source gases comparisons, in MMII Report, pp. 226–239, 1999.

3.2 Data Quality

Ellis E. Remsberg
NASA Langley Research Center

Almost all the data sets that were used for the models and measurements (or MM) comparisons (Prather and Remsberg, 1993) have been revised or replaced with better and more complete compilations. UARS satellite data sets are the primary ones being used for the middle and upper stratosphere (Chapters 3.3, 3.4, 3.5, 5.4, and 5.5), although it was not possible to employ the observed atmosphere that has recently been compiled from UARS for the April 1992 to April 1993 period (see http://hyperion.gsfc.nasa.gov/Analysis/UARS/urap/home.html). One particular form of those data is the monthly zonal means of species in terms of pressure versus equivalent latitude coordinates—which would be most suitable for comparisons with 2-D models (see e.g., Randel et al., 1998). It is noted that this reference atmosphere of Randel et al. is not so specific for the 1992 year, but then neither are the transport circulations for many of the models.

It is important to note that new versions of the UARS data sets are still being developed and made available. Presently, HALOE comparisons are conducted using its Version 18 data. A Version 19 will be available in early 1999, but only minor changes from Version 18 are occurring for most species. The largest changes will be for water vapor and NO_2 below about the 50 mb level. These changes are due to improved estimates of the so-called solar lockdown position for sunrise and sunset scans. V19 sunrise NO_2 (and NOx) will be sharply lower at 100 mb and at higher latitudes, while the sunset values will be larger by at least 50 percent below the 50 mb level. Changes are within 10 percent between the 40 and 7 mb levels. V19 NO (and NOx) will be smaller in the upper stratosphere by about 10% in both the sunrise and sunset data during the 1997 period of the POLARIS field experiment because of the removal of a false trend that had been assumed in V18 for the NO gas cell content. The V18 results for NO during 1992 and 1993 did not change much.

The operative CLAES data are from either Version 7 or 8; T(p), CH_4, and CFC-12 are more accurate on Version 7, and N_2O_5 and CFC-11 are more accurate in Version 8. A Version 9 is being prepared but was not available for this MM2 exercise. In particular, temperature and NO_2 will be better in Version 9. The current ISAMS data are Version 10; an eventual Version 12 will have significant improvements in N_2O, N_2O_5, and CO. Finally, the MLS Version 3 data have been used for comparisons up to now. The recent MLS Version 4 contains improvements in O_3 and H_2O, plus new distributions of HNO_3. MLS Version 5 will contain further improvements and will have retrievals at all UARS levels, not only at every other level. As a result, the peak values of ClO in the winter high latitudes of the lower stratosphere will be reduced and smoothed somewhat, leading to lower and more accurate values of Cly. This result will impact the polar chemistry comparisons in Chapter 5.5. MLS Version 5 data will be available soon.

Estimates of stratospheric wave activity can be derived from daily analyses of both trace and minor species from CLAES, ISAMS, MLS and to a lesser extent HALOE data and from the temperatures and winds from the assimilated meteorological analyses (see Chapter 5.4). The standard deviation of this wave activity about the zonal mean value of a given parameter is an excellent diagnostic of large-scale atmospheric variations (and indirectly the fidelity of the transport) for the 3-d models, although it is expected that there will be some interannual variability in those data values. Similar diagnostics were developed from the Nimbus 7 LIMS data as part of a pre-UARS climatology.

A new ozone profile climatology has been prepared from Version 5.96 SAGE II data and from the representative, higher quality ozonesonde profiles in each 10 degree latitude zone (see chapter 4). The

Version 7 TOMS total ozone is used as a data reference in Chapter 5.3. However, neither of these climatologies is specific to the 1992 year of the baseline model run (B1) for MM2.

Satellite data are also used for model comparison in the lower stratosphere, but their accuracy is reduced for some species, especially early in the 1992 baseline year when the volcanic aerosols interfered with the measured signals. Thus, assessments of the models in the lower stratosphere for 1992 rely more critically on data and correlation diagrams from the ER-2 flights during AASE II and SPADE. Data from later aircraft campaigns have also been used for comparisons. The measured chemical radicals provide consistency checks on the specific proposed reaction mechanisms (Chapter 5.1). Data on CO_2 and SF_6 from the ER-2 and OMS platforms provide very good estimates of tracer transport and determinations of the age of air. In general, all the aircraft and balloon in situ data are both precise and accurate. The only concerns are with regard to how representative they are of a particular latitude or season, and whether enough measurements have been obtained for a good characterization of the enhanced effects of heterogeneous chemistry during 1992 and for determining the chemical processing due to PSCs for any given year.

One outstanding concern was reiterated in Chapter 3.3 regarding the NOx/NOy ratios in the mid and lower stratosphere and the fact that the observed NO_2 concentrations become progressively higher than model values below 30 km. It is interesting that when NOy and $J(NO_2)$ from the ER-2 are used to constrain model estimates of the NOx/NOy ratio, there is generally good agreement with the observed ratio (Gao et al., 1997). Model/data agreement is less satisfactory when the constraints are from remote measurements (Sen et al., 1998).

The largest component of NOy in the lower stratosphere is HNO_3. Thus, if the observations of HNO_3 have a bias, there will also be a bias in the model NOy and in the model/data comparisons for the components of NOy. Observations of HNO_3 from the remote sensors ATMOS, MkIV, and UARS have an accuracy of no better than 16 percent, but the systematic errors due to biases in the HNO_3 spectral line parameters are much smaller than that (Aaron Goldman, private communication, 1998). During the early period of UARS there was significant underlying absorption and/or emission from the volcanic aerosols that also had to be accounted for. In situ determinations of NOy on the ER-2 have an accuracy of 15 percent (Fahey et al., 1989). Therefore, it is unlikely that the estimates of NOy (or HNO_3) can explain all of the discrepancies between the observed and calculated NOx/NOy ratios. More profiles of the observed ratios of selected components of NOy would be very instructive.

Solar occultation measurements of NO and NO_2 occur at sunrise and sunset, when both species are varying rapidly. Corrections have been applied to the retrieved HALOE, ATMOS, and MkIV profiles to account for this diurnal variation. Those sunset corrections are small for NO_2, even in the lower stratosphere (Sen et al., 1998). The corrections are larger for NO, but Newchurch et al. (1996) report good agreement between diurnally corrected ATMOS NO and ER-2 measurements of NO in November 1994. HALOE V18 NO is much greater than from MkIV below the 40 mb level for their 1993 sunset comparisons, while V18 sunset NO_2 is much less than that from ATMOS or MkIV below the 40 mb level. The combined HALOE NO + NO_2 is also less than from MkIV at those altitudes.

Systematic errors for NOx for all three remote sensing data sets get large in the lower stratosphere. In particular, HALOE NO_2 is sensitive to uncertainties in line half-widths for H_2O—its primary interfering species in the lower stratosphere. Therefore, model comparisons with the more plentiful and more accurate in situ measurements of NO, NO_2, and NOx should be more instructive for the lower stratosphere.

A possible criticism of MM2 is that we did not re-evaluate the quality of the present models for duplicating a baseline atmosphere for a period (say, the mid 1990s) when the effects of heterogeneous chemistry are less important. For example, HALOE, TOMS/SBUV, SAGE II, and MLS data are available for comparison for the mid 1990s, and there are data from the aircraft and balloon campaigns in the mid 1990s, as well.

References

Fahey, D., et al., In situ measurements of total reactive nitrogen, total water, and aerosol in a polar stratospheric cloud in the Antarctic, J. Geophys. Res., vol. 94, 11299-11315, 1989.

Gao, R. S., et al., Partitioning of the reactive nitrogen reservoir in the lower stratosphere of the southern hemisphere: Observations and modeling, J. Geophys. Res., vol. 102, 3935-3949, 1997.

Newchurch, M. J., et al., Stratospheric NO and NO_2 abundances from ATMOS solar-occultation measurements, Geophys. Res. Lett., vol. 23, 2373-2376, 1996.

Prather, M. J., and E. E. Remsberg, Eds., The atmospheric effects of stratospheric aircraft: Report of the 1992 models and measurements workshop, NASA Ref. Publ. 1292, March 1993.

Randel, W. J., F. Wu, J. M. Russell III, A. Roche, and J. W. Waters, Seasonal cycles and QBO variations in stratospheric CH_4 and H_2O observed in UARS HALOE data, J. Atmos. Sciences, vol. 55, 163-185, 1998.

Sen, B., G. C. Toon, G. B. Osterman, J.-F. Blavier, J. J. Margitan, R. J. Salawitch, and G. K. Yue, Measurements of reactive nitrogen in the stratosphere, J. Geophys. Res., vol. 103, 3571-3585, 1998.

3.3 Comparison Overview

Ellis Remsberg,[1] Patrick Purcell,[2] Praful P. Bhatt,[2] Karen H. Sage,[2] and Donald E. Brown[2]

1. NASA Langley Research Center
2. Science Applications International Corporation

3.3.1 Introduction

The focus of this analysis is model comparisons with the UARS, CLAES and HALOE data. In general, the model results for the Present-day Atmosphere Comparisons (B1) are not specific to 1992, except for the tropospheric source gas boundary conditions and an enhanced SAGE II stratospheric aerosol surface area for the Pinatubo event. Because the transport in most of the models is more appropriate for a generic year, we expect some differences from that of early 1992, which had a stronger than normal residual circulation and meridional mixing. Exceptions are the SLIMCAT and GSFC-3D models, which use assimilated meteorological data for their transport.

We have elected to look closely at the March/April and September/October periods of the B1 simulation. A March/April period should reflect the wintertime accumulation of ozone in the northern hemisphere. September is an interesting but more dynamically active time at the end of southern hemisphere winter. One should see the effects of heterogeneous chemistry on surfaces of PSC aerosols at high southern latitudes in September. Comparisons are shown first for the source gases, N_2O, CH_4, and H_2O. Then we compare the results for the chemically-generated species, NOx, HNO_3, NOy, HCl, and O_3.

N_2O profiles were selected from March and September 1992 and HNO_3 profiles were selected from September 1992 and March 1993 from CLAES Version 8 data. In order to get the maximum latitude coverage we obtained data from two successive yaw cycles of the UARS spacecraft. Poleward of 34N the N_2O data cover the period March 1-21, 1992; poleward of 34S the data span is March 26 to April 1, 1992. The lower latitudes were sampled nearly each day in March. A similar approach was used for September - the southern hemisphere (SH) was sampled from Sept. 1-18 and the northern hemisphere (NH) from Sept. 24-30. The HNO_3 data from 1993 are from March 1-17 in the NH and March 22-31 in the SH.

The HALOE Version 18 CH_4 and H_2O data were considered from the sunrise sweep of March 10-April 26, 1992, (poleward of 30N from March 14-April 8 and poleward of 20S from April 20-26) and the sunset period of September 7-October 13, 1992, (the NH from Sept. 7-Oct. 5 and the SH from Oct. 5-13). HALOE data for NO + NO_2, HCl, and O_3 were considered for the same September-October period in 1992 and from the sunset period of March 6-April 2 (SH) and April 3-11 (NH) of 1993. The 1993 period was chosen for the more chemically reactive species because of the significant uncertainties in the CLAES and HALOE radiances of the lower stratosphere for early 1992 from just the emission/absorption from the Pinatubo aerosols. Due to interannual variability in transport, there are differences for all the species for March/April of 1992 versus 1993, but the differences for the tracers in the middle and upper stratosphere are generally small compared to the model-to-model differences for those species in a given year.

The HALOE sunset NO + NO_2 should be a good proxy for the daytime average NOx from the 2-d models, particularly if we include $2*N_2O_5$ with the model NO + NO_2. When combined with CLAES HNO_3, the observed total ought to be a very good estimate of NOy in the stratosphere, at least for regions outside of polar night. In an attempt to remove the effect of transport in the results, we also

show comparisons for the ratio NOx/NOy. HALOE sunrise NO + NO_2 is not as accurate in the lower stratosphere because of its larger diurnal correction (Gordley et al., 1996) and should also be somewhat smaller than the model daytime average NOx in the middle stratosphere (Morris et al., 1997). The HALOE NOx results for March 1992 are also less accurate in the lower stratosphere, because of uncertainties in the correction for the large amount of aerosol interference at that time. Therefore, we have avoided early 1992 in our comparisons of the chemically active species. Comparisons of HCl provide a first order validation for total chlorine in the upper stratosphere of the models. The daytime average O_3 comparisons are a measure of the net results of both chemistry and transport.

Although we evaluated the distributions of the more chemically active species for all of the models, we decided to focus on the results from four of the 2-d models which were involved in both the MM and MMII comparison studies and which are being involved in many of the stratospheric assessment studies. Those modeling groups are AER, GSFC-2D, LLNL, and UNIVAQ-2D. Several of the other groups did not report daytime average chemical distributions. These include the 3-d model groups which report zonal averages at a single Greenwich hour (12Z for the LARC-3D model), i.e., a 24-hour average result. The NOCAR group reported noontime chemistry. The HARVARD and CSIRO model runs did not include PSC chemistry. Otherwise, the results of the chemistry calculations were very similar for all the models, as demonstrated by their respective distributions for the NOx/NOy ratio.

3.3.2 Results

Source Gas Comparisons for March/April

The following comparisons are in terms of zonal average differences in percent, (model - data)/data. Results are shown as 4 panels per page. Models are grouped according to: (a) AER, GSFC-2D, LLNL, and UNIVAQ-2D; (b) SLIMCAT, GSFC-3D, LARC-3D, and NCAR-2D; and (c) NOCAR, SUNY-SPB, CSIRO, and HARVARD. The model output is for March 1992.

Figure 3.3.1a is the CLAES N_2O above 100 mb (a Z* of 16 km) for March 1992. Single profile random errors are 6 to 8% from 4.6 to 46 mb, and increasing to 39% at 1 mb. But the random errors are much smaller for a monthly zonal average, so it is presumed that the relative spatial variations have been measured well. Systematic errors are of order 15 to 20% from 1 to 46 mb (Roche et al., 1996), but Figure 3.3.1a shows minimum mixing ratios near 0.5 mb (about 55 km) with higher values above—an unrealistic prospect. Much larger systematic errors are likely there.

Figures 3.3.1(b-d) are plots of the model N_2O differences versus the CLAES data. Some striking features are characteristic of almost all the models: (1) only weak SAO transport occurs in the model upper tropical stratosphere, and (2) there is a lack of strong meridional gradients in N_2O at 30 km, 30N and at 40 km, 60S. It is perhaps unreasonable to expect the models to duplicate those specific characteristics of the 1992 transport, and, in fact, the March 1993 CLAES N_2O distribution shows evidence of a northward advection of N_2O at 35 km and midlatitudes compared with March 1992. Those models that have residual circulations and mixing transports that are specific to 1992 ought to agree best with the CLAES 1992 field. Accordingly with the exception of the northern extratropics of the upper stratosphere, the model/data difference patterns are in good agreement for the two chemical/transport models (CTMs), SLIMCAT and GSFC-3D that use 1992 assimilated data. The reason for the notable differences in the northern extratropics is unclear, although the GSFC-3D model circulation is obtained with Data Assimilation Office (DAO) analyses and SLIMCAT uses UKMO analyses. But because the CLAES N_2O values are less than 25 ppbv in that region, it is more likely that even small differences in

the model net transport are the problem. The difference patterns for those two models are more consistent between 20 and 40 km (see discussion below for CH_4, too).

The CLAES data in Figure 3.3.1a indicate large asymmetries in the amount of poleward mixing and descent for the two hemispheres of the high latitude upper stratosphere. Yet, it is clear that there are larger differences in net transport of N_2O among the models—i.e., the amount of poleward and downward transport. There is a lot a similarity between the the model/data differences of the CSIRO and SLIMCAT models. In general though, the significant differences among the set of model simulations of N_2O agree with the findings from the more specific model transport exercises of the "A" runs of MMII. If we avoid those regions of high vertical and meridional N_2O gradients, we expect agreement with CLAES to within +/-20%, and generally that is what we find for the lower stratosphere, at least outside the polar vortex regions.

Several models seem to have deficiencies in their chemistry and/or photolysis of N_2O, as well. For example, there is an excess of N_2O in the upper stratospheric results (above 35 km) for the NOCAR model. Alternatively, K_{yy} may be too weak. In about half of the models there are significant deficits of N_2O in the upper stratosphere. Without other guidance it is hard to know whether any model is correct in that region, since the CLAES N_2O data also have large errors near the stratopause.

Model comparisons with the HALOE CH_4 distribution of March 1992 are shown in Figure 3.3.2(a-d). Precision of the HALOE CH_4 in Figure 3.3.2a is very high and its accuracy varies from 6% to 11% from 0.4 to 10 mb and then 15% at 40 mb (Park et al., 1996). First, it is noted that the HALOE CH_4 data have a similar pattern to that for CLAES N_2O, except HALOE CH_4 has a much weaker vertical gradient in the upper stratosphere. That difference in gradient is expected to some extent because the chemical loss rate is much greater for N_2O than for CH_4. However, because the HALOE CH_4 decreases smoothly at the stratopause, as expected, this is indirect evidence that the CLAES N_2O data have systematic errors at that level. Once again, the lack of a clear SAO in the model CH_4 causes enhanced differences in the upper tropical stratosphere. If we consider the region between about 20 and 40 km, the difference patterns for N_2O and for CH_4 are more similar for a given model. The results for CH_4 from SLIMCAT and GSFC-3D are very similar in the northern hemisphere upper stratosphere, unlike the findings for N_2O. Those two models differ near 45 km and 30S for CH_4. Still, based on the CH_4 comparisons, there seems to be no common transport defficiency among the set of models.

The accuracy of the methane oxidation mechanism must also be considered for those models that include it. Many of the models have an excess of CH_4 throughout the lower stratosphere, possibly because some model CH_4 fields are not calculated but are prescribed from the Nimbus 7 SAMS data which are biased high below about 28 km. Conversely, the LARC-3D model has a prescribed CH_4 field obtained from an early version of the NOCAR model. Comparisons with HALOE CH_4 for March/April 1993 are similar to those for 1992 below 40 km. The data differences between those 2 years are generally much smaller than the model-to-model variations for March of a single year.

Middle atmosphere water vapor is calculated in some models and prescribed in others. The comparisons with HALOE water vapor in Figure 3.3.3 generally reveal differences of less than +/-20% throughout the stratosphere. Two models (UNIVAQ-2D, NCAR-2D) show differences of order +30 to +50% at about 40 km; one model (SUNY-SPB) has 30% less H_2O near the stratopause, where the HOx chemical cycle is becoming more important for ozone. At 20 km there is more variability among the models but generally no worse than 25%, which is also the uncertainty in the HALOE values in the lower stratosphere (Harries et al., 1996). However, the precision and relative variations in the HALOE H_2O are known to better than 25%. Because the H_2O differences for many models tend to vary with

latitude at 20 km, those results can provide an important check of the degree of meridional mixing and transport in a given model.

Chemically-Reactive and Reservoir Species for March/April

Results for NOx show better uniformity among the models. The model daytime average results from March/April 1992 (not shown) are much greater then the observed sunrise values in the mid stratosphere, in part because N_2O_5 is present at sunrise but was not included in our observed sum for NOx. But N_2O_5 is not so important in the lower stratosphere, where model NOx is still much higher than observed for early 1992. At least part of that NOx difference may be due to an underestimate of the conversion of NOx to HNO_3 for the models in the presence of the early 1992 aerosol levels, but it is more likely that the March 1992 HALOE NOx is not so reliable below about 30 km due to its large and uncertain aerosol correction. Therefore, we make our comparisons with the sunset NOx data for March/April 1993.

The observed distribution of NOx for March 1993 is in Fig 3.3.4a, and the measurements are considered very good in the middle and upper stratosphere. The HALOE NOx data are still not highly accurate below 20 mb (or about 27 km), and we note that there is an unrealistic minimum near 20 km, due most likely to not accounting properly for interfering cloud and H_2O absorption near the tropopause. HALOE comparisons with correlative measurements do show large percentage differences in the lower stratosphere, even though any correlative occultation data should be subject to similar sources of error as HALOE (Gordley et al., 1996).

Sunset comparisons with model daytime average NO + NO_2 + 2*N_2O_5 from the four 2-d models are shown in Figure 3.3.4b. Again the effect of a reduced SAO signature is apparent in the model upper tropical stratosphere. Otherwise there is a general excess of NOx for most models near the stratopause and a slight deficit of NOx in the middle stratosphere. Outliers from that pattern are the HARVARD and NCAR-2D models, which have deficits of NOx in the extratropical upper stratosphere. In addition, the NCAR-2D model has an excess of NOx at 35 km that is consistent with its deficit in N_2O in the upper stratosphere but which is not seen in the other models. HALOE NO + NO_2 errors are smaller than 30% between 27 and 40 km (Gordley et al., 1996), but the differences for some models slightly exceed that uncertainty from 27 to 30 km. This lack of agreement is likely because more of the atmospheric NOy is in the form of NOx in 1993, whereas the NOy partitioning in the models is based on the heterogeneous chemistry on the larger volcanic aerosol amounts of spring 1992. The models generally show less NOx below 30 km when compared with March/April 1993 HALOE data—a clear difference from the 1992 HALOE comparisons. Because the NOy partitioning is critically time-dependent on the true aerosol surface area for several years after the Pinatubo eruption, the model/data differences in Figure 3.3.4b are not surprising for the lower stratosphere. The model/data agreement for NOx for most models is much better between 30 and 40 km, where the NOx family has a primary effect on the ozone chemical cycle.

Figure 3.3.5 is the comparison with CLAES HNO_3 for 1993, and there is general consistency among the models. (The CLAES differences for HNO_3 between 1992 and 1993 are not large.) Model HNO_3 is in excess above about 25 km, even though the CLAES systematic errors are estimated at about 10% (Kumer et al., 1996). However, comparisons of CLAES HNO_3 with correlative measurement profiles indicate that the CLAES results are too low in the middle stratosphere. Thus, it is likely that the models are performing better at those altitudes than indicated in Figure 3.3.5b. The differences for March 1993 at 25 to 30 km may be explained by a preferred partitioning of NOy into HNO_3 in the models for their elevated aerosol surface areas of 1992, which is consistent with the model deficits of NOx in Figure 3.3.4b at those same altitudes. At 20 km the CLAES HNO_3 is not as accurate (14%), and the model results diverge sharply from one another (c.f., GSFC-2D and UNIVAQ-2D). A better diagnosis

of the model differences at 20 km must come from comparisons with the aircraft data on NOy and NOx and from the simulations of the tracer lifetimes in the lower stratosphere.

A more meaningful result is obtained by generating the sum of HALOE sunset NO and NO_2 plus the HNO_3 from CLAES and then comparing that total with the NOy from the models. That distribution for the March 1993 data is given in Figure 3.3.6a, and the differences with the model NOy are given in Figure 3.3.6b. It is easier to compare with model NOy than NOx, because the NOy should not be sensitive to the time-of-day for its reported average or affected by a partitioning. As expected though, there is not a lot of similarity among the model distributions of NOy because of the model transport differences and whether a given model NOy calculation has achieved near equilibrium.

When the NOx is referenced to NOy from the models (Figure 3.3.7), the results are very similar from model-to-model and somewhat similar to that from the satellite data (Figure 3.3.7a). This is an indication that the model partitioning of NOy is reasonable. The 0.2 and 0.4 contours occur near 23 and 26 km in the data of Figure 3.3.7a, whereas those ratios in Figure 3.3.7b from the models occur closer to 26 and 28 km. The differences at 30N are shown more clearly in Figure 3.3.7c. This discrepancy is in line with the preferred conversion of NOx to HNO_3 for the models for March 1992 versus 1993, and the fact that peak values of HNO_3 were 48% higher in 1992 than in 1993 (Kumer et al., 1996). Obviously, during a period when volcanic aerosols are a major contributor to the surface area estimates, the model/measurement comparisons of NOx/NOy must be conducted for similar conditions. The observed monthly estimates of the NOx and NOy from the UARS data represent new and accurate estimates of the stratospheric distributions of those chemical families, at least in the middle stratosphere. In this way they are similar to the estimates of NOx and NOy obtained from the nighttime LIMS data on NO_2 and HNO_3. Although retrievals of NOx in the lower stratosphere from HALOE are more certain for the middle than the early 1990s, the mid 1990s data should be compared with a baseline atmosphere run from the models for the condition of low or background aerosol surface area.

About 80 to 90% of total chlorine is in the form of HCl in the upper stratosphere, and Figure 3.3.8 indicates good similarity among the model results where the gas-phase, chlorine catalytic cycle affects the ozone chemistry. HALOE HCl has uncertainties of order 14% in the middle and upper stratosphere (Russell et al., 1996). Almost all of the models are within that uncertainty in the upper stratosphere. Model HCl deficits in the middle stratosphere may be due to their daytime partitioning of Cly and, in part, due to their overall Cly amounts. In the lower stratosphere, where the HCl mixing ratios are small, the HALOE uncertainties are closer to 20%. Once again the model results at those altitudes are dissimilar from one another and often by much more than the estimate of HALOE bias. Part of the model differences may be due to a preferred partitioning of total chlorine in the presence of aerosol surfaces from its reservoir HCl and into reactive forms of chlorine. Overall best agreement was obtained with the CSIRO model.

Because reasonably good model/data agreement was found for those altitude regions where the respective chemical families affect ozone, there ought to be similarly good agreement for March ozone. Figure 3.3.9 shows the well-documented model deficit of ozone in the upper stratosphere of order 10 to 30%. HALOE ozone is believed to be accurate to better than 12% in that region (Bruhl et al., 1996). At about 30 km there tends to be model/data agreement. Between 20 and 30 km many models have ozone values that are too large at middle latitudes, indicating that the accumulation of ozone from above is too great. At tropical latitudes at 25 km many models have an ozone deficit, indicating ascent that is too rapid and/or meridional mixing that is too weak. Model O_3 at 20 km is greater than observed at low latitudes for most models, indicating rapid meridional mixing of the accumulated ozone from higher latitudes. Exceptions are the UNIVAQ-2D and NOCAR models, which have ozone deficits that extend to extratropical latitudes of the lower stratosphere, an indication of strong diabatic ascent at tropical

latitudes followed by efficient poleward transport at 20 to 25 km. HALOE ozone is not very accurate below 15 km, and most models give higher values. Finally, in the mesosphere the SLIMCAT and LARC-3D models have high ozone values, perhaps due to their reported 24-hour averages.

The stratospheric results shown here are very similar to the model ozone comparisons with the April ozone climatology for 1988 to 1996 (Logan and McPeters, 1999), indicating that the HALOE data of 1993 are representative of that multiyear average. However, the differences with HALOE become pronounced at about 15 km where the HALOE ozone is systematically lower than the ozonesonde climatology, most likely because the HALOE data have not been corrected and/or screened properly for cloud contamination effects near the tropopause.

Comparisons for September/October 1992

The comparison results for September/October 1992 (not shown) were similar to those for March/April 1993, except in the Antarctic lower stratosphere where heterogeneous chemistry on PSC aerosols is a factor. But the interpretation of any success of the polar chemistry in the models is critically dependent on the exact timing of the comparisons. For the region poleward of 60S the sunset HALOE data were actually obtained from October 9-13, while the CLAES data were measured during September 1-18. The amount of polar N_2O_5 must also be included in a comparison of data with model NOx and NOy, and we have not added the N_2O_5 from CLAES. Nevertheless, the models are generally consistent with one another, and show considerably less NOx, more HNO_3, and less HCl than the data between 20 and 25 km at those high southern latitudes. The two models without PSC chemistry (HARVARD and CSIRO), have the smallest differences for NOx and HCl, perhaps because there was an atmospheric recovery to a more nearly gas phase partitioning of the Cly and NOy by mid October 1992. Interestingly, those two models are in general agreement with the other models in that they show more HNO_3 than was observed in early to mid September from CLAES, perhaps because of differences in the amount of HNO_3 in the particle phase. Although we have not made a comparison here with the MLS ClO measurement, most models do show relatively large amounts of reactive chlorine in the vortex region at that time. Many models give less O_3 than observed above 25 km, in agreement with their differences for the other reactants. But below 23 km most models have more O_3 as well as more CH_4 than observed for the vortex, indicating that the effect of descent from higher altitudes in the models is not extending to the lowest parts of the polar stratosphere. The polar descent in the HARVARD model seems to be the exception; its CH_4 is less than observed in the Antarctic vortex region.

3.3.3 Summary

In general, the CLAES and HALOE data sets that were used for the model comparisons of the baseline atmosphere (experiment B1) are of good quality by mid 1992. Due to the large aerosol corrections in the satellite data in early 1992, it is best to rely on the balloon and aircraft data for the model verification in the lower stratosphere at that time. The CLAES N_2O and HNO_3 data are not as accurate at the low mixing ratios of the upper stratosphere, and the accuracy of HALOE NO + NO_2 also degrades in the lower stratosphere.

Model/data differences for both the source and reservoir gases are due more to model differences in transport than chemistry. Even so, the model chemical partitioning of NOy and Cly for early 1992 is hard to verify with the satellite data because of their inaccuracies in the lower stratosphere. By 1993 the measured data are more reliable but the aerosol surface area distribution used in the models is not representative of 1993. The aircraft measurements from the lower stratosphere are a better comparison data set for 1992.

References

Bruhl, C., et al., Halogen Occultation Experiment ozone channel validation, J. Geophys. Res., vol. 101, pp. 10217-10240, 1996.

Gordley, L. L., et al., Validation of nitric oxide and nitrogen dioxide measurements made by the Halogen Occultation Experiment for UARS platform, J. Geophys. Res., vol. 101, pp. 10241-10266, 1996.

Harries, J. E., et al., Validation of measurements of water vapor from the Halogen Occultation Experiment (HALOE), J. Geophys. Res., vol. 101, pp. 10205-10216, 1996.

Kumer, J. B., et al., Comparison of correlative data with HNO_3 version 7 from the CLAES instrument deployed on the NASA Upper Atmosphere Research Satellite, J. Geophys. Res., vol. 101, pp. 9621-9656, 1996.

Logan, J., and R. McPeters, Ozone climatology, in MMII Report, Chapter 4, 1999.

Morris, G. A., D. B. Considine, A. E. Dessler, S. R. Kawa, J. Kumer, J. Mergenthaler, A. Roche, and J. M. Russell III, Nitrogen partitioning in the middle stratosphere as observed by the Upper Atmosphere Research Satellite, J. Geophys. Res., vol. 102, pp. 8955-8965, 1997.

Park, J. H., et al., Validation of Halogen Occultation Experiment CH_4 measurements from the UARS, J. Geophys. Res., vol. 101, pp. 10183-10203, 1996.

Roche, A. E., et al., Validation of CH_4 and N_2O measurements by the cryogenic limb array etalon spectrometer instrument on the Upper Atmosphere Research Satellite, J. Geophys. Res., vol. 101, pp. 9679-9710, 1996.

Russell, J. M., III, et al., Validation of hydrogen chloride measurements made by the Halogen Occultation Experiment from the UARS platform, J. Geophys. Res., vol. 101, pp. 10151-10162, 1996.

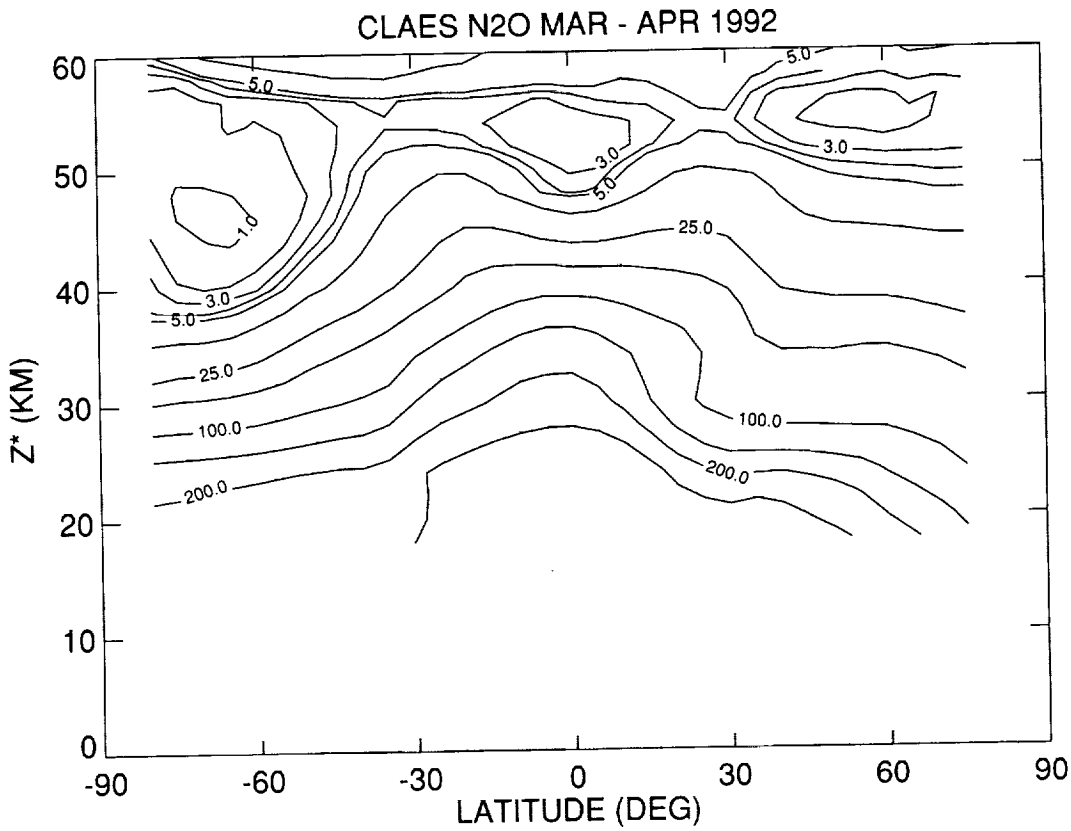

Figure 3.3.1. Comparisons for N_2O for March 1992. (a) zonal mean field from March, 1992, CLAES data—contour increments are not uniform; (b) (Model-data)/data differences in percent for AER, GSFC-2D, LLNL, UNIVAQ-2D; (c) as in (b) but for SLIMCAT, GSFC-3D, LARC-3D, NCAR-2D; (d) as in (b) but for NOCAR, SUNY-SPB, CSIRO, HARVARD. In (b-d) the contour increments are 10% from 0 to 100 and 50% above that.

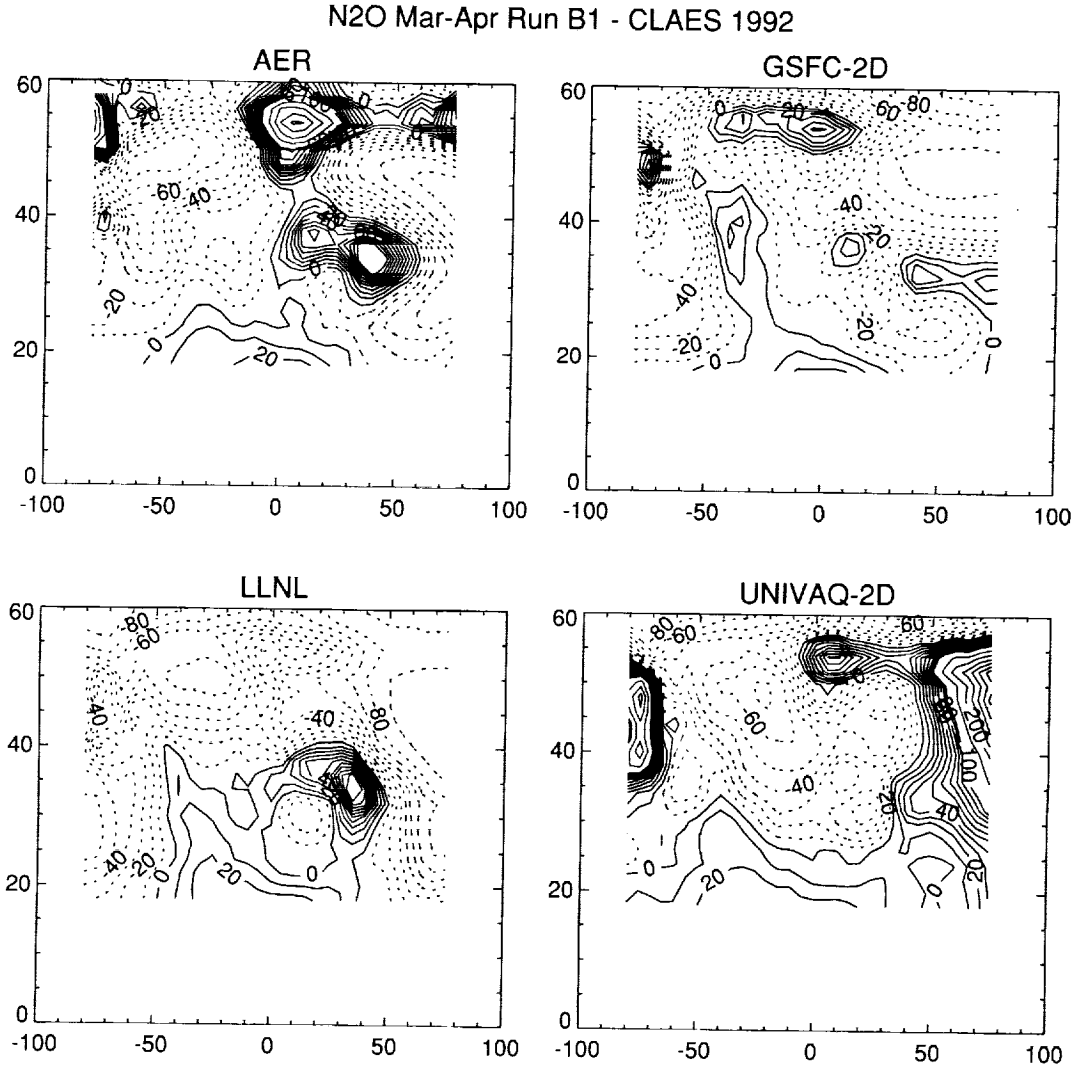

Figure 3.3.1. Continued.

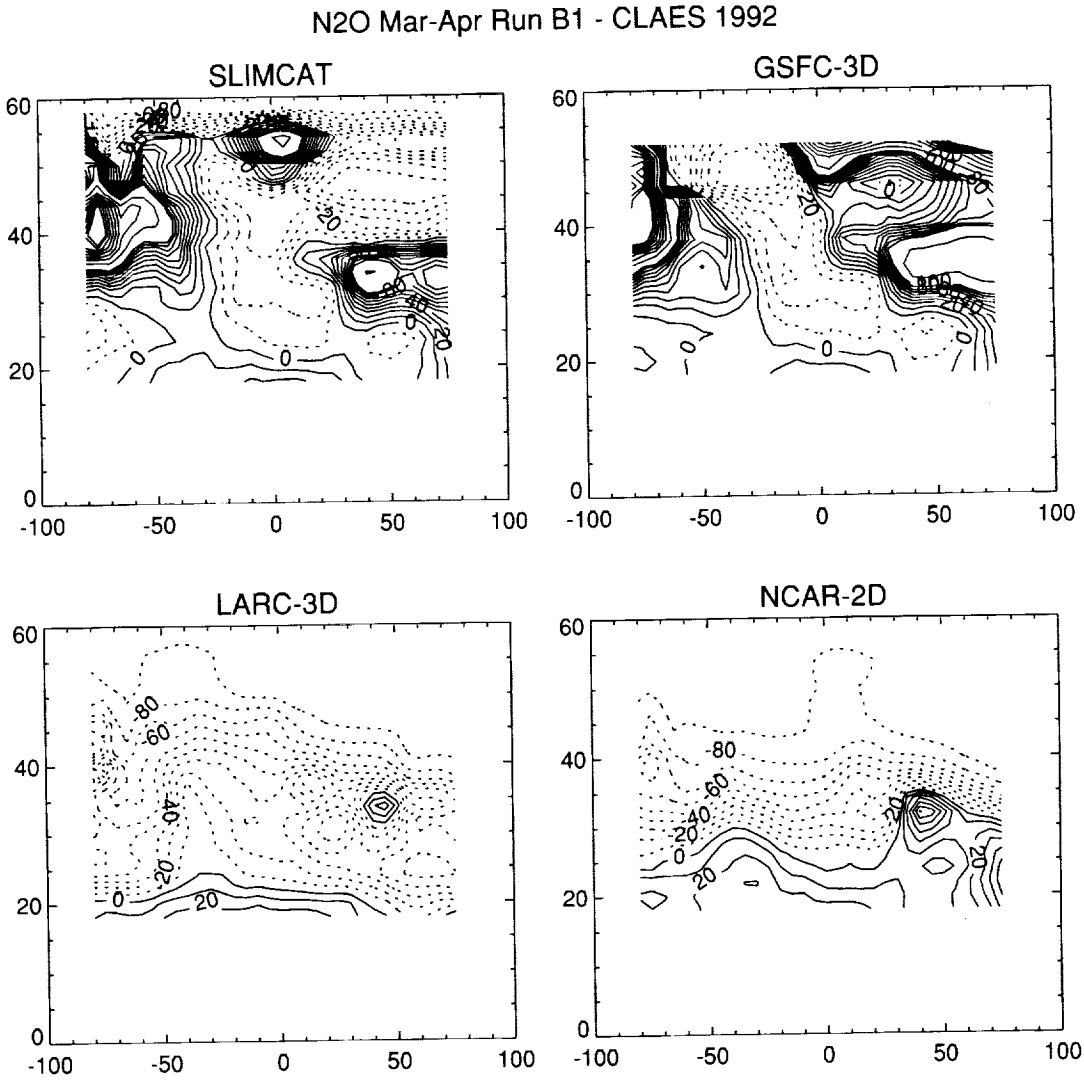

Figure 3.3.1. Continued.

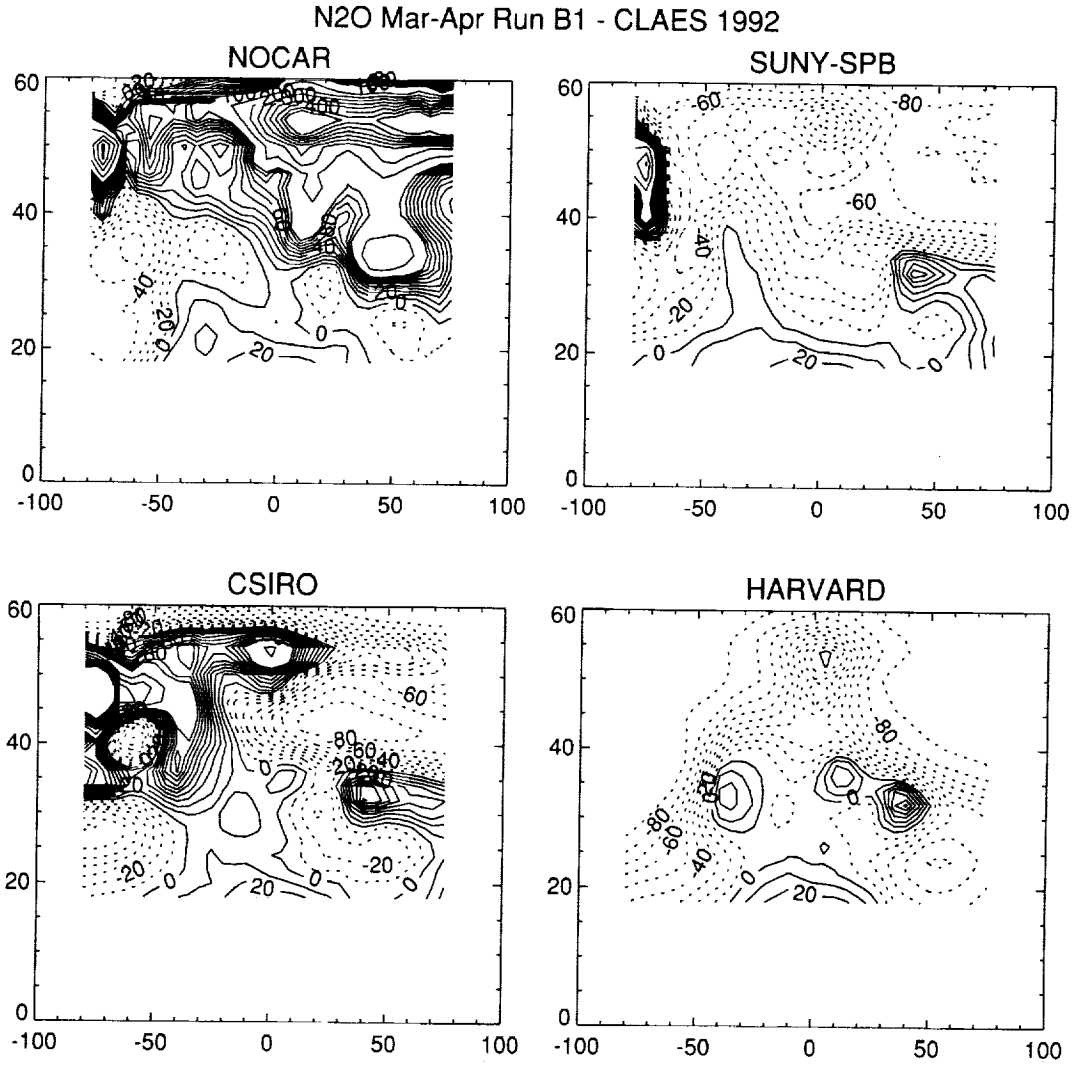

Figure 3.3.1. Concluded.

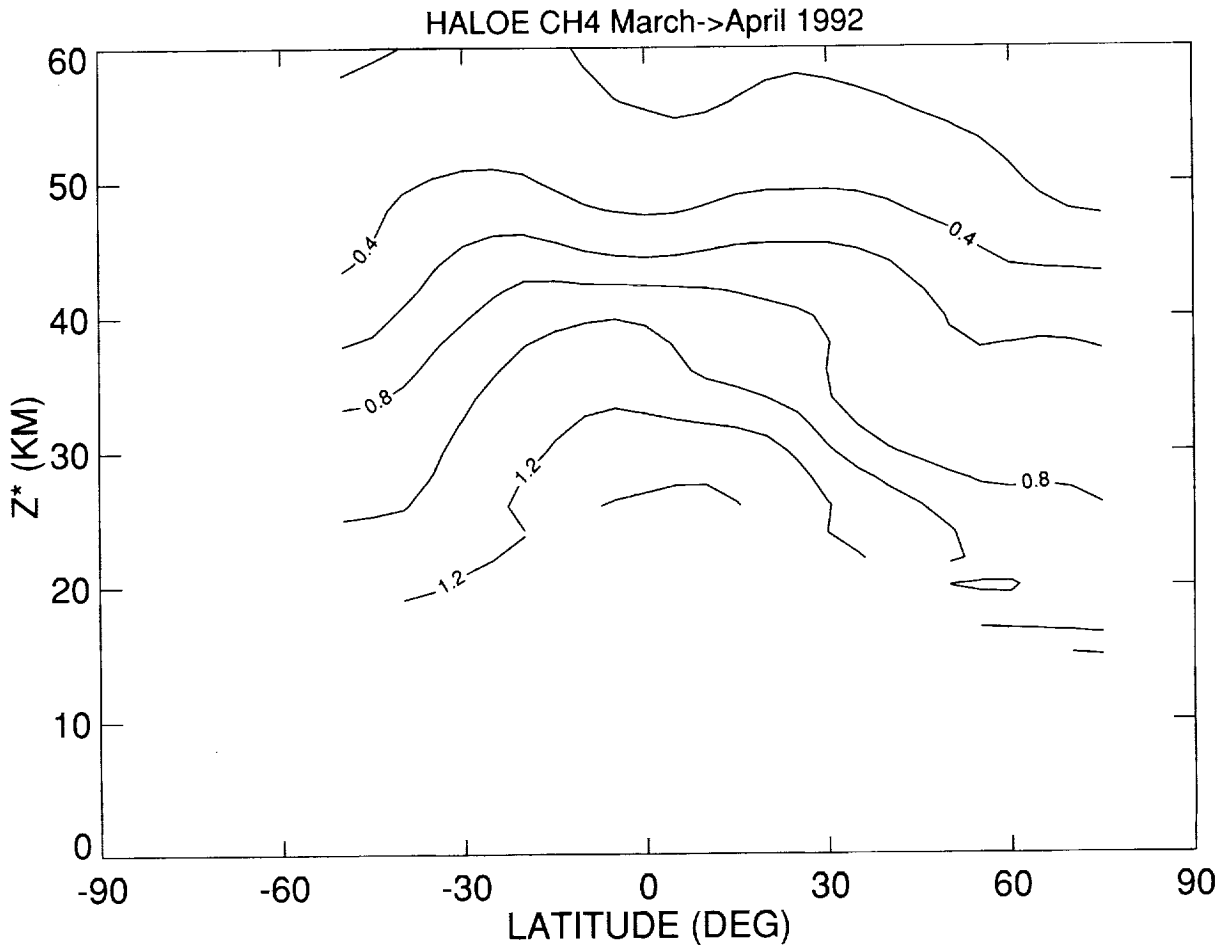

Figure 3.3.2. As in Figure 3.3.1(a-d), but for HALOE CH_4 for March 10-April 26, 1992. CH_4 increments in (a) are 0.2 ppmv.

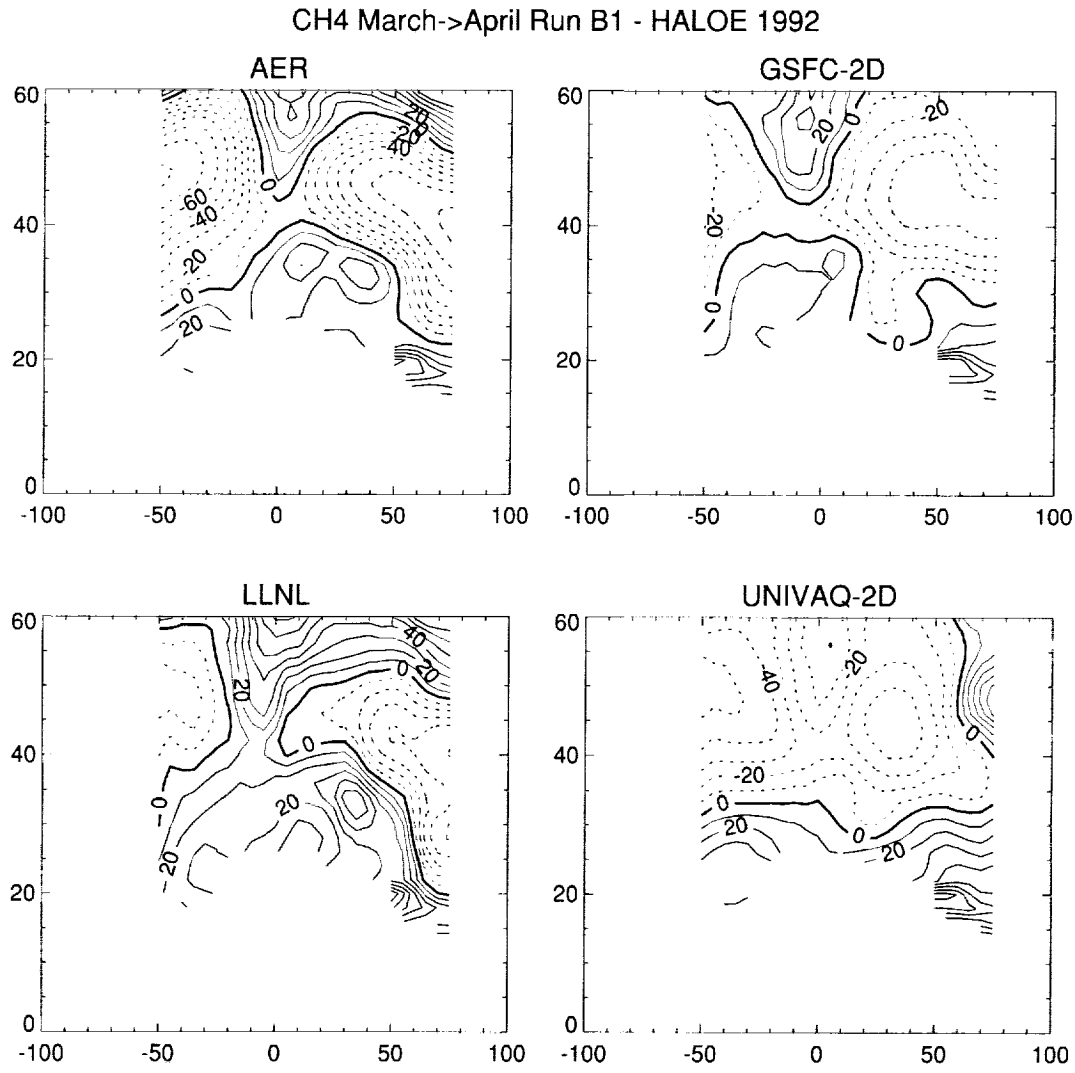

Figure 3.3.2. Continued.

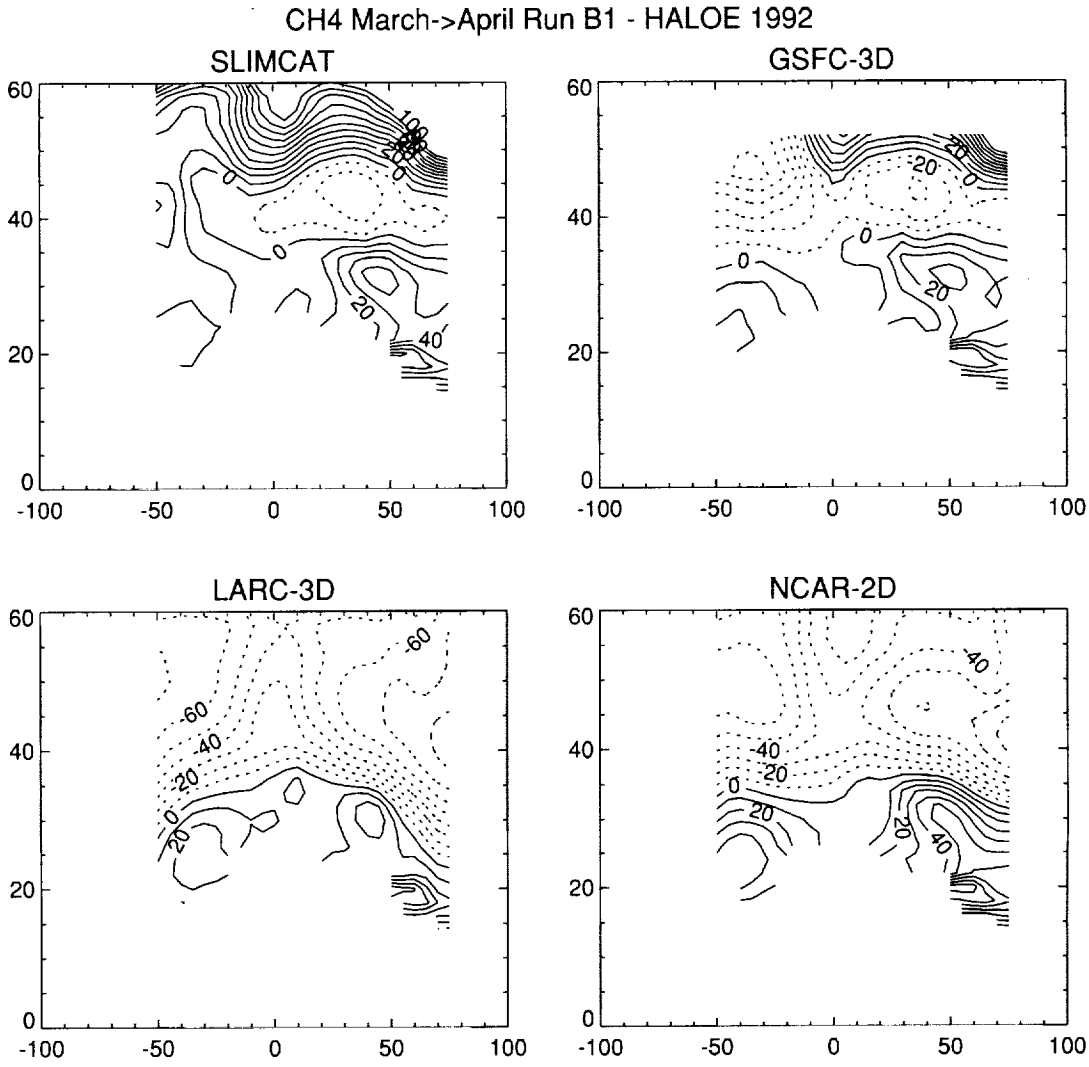

Figure 3.3.2. Continued.

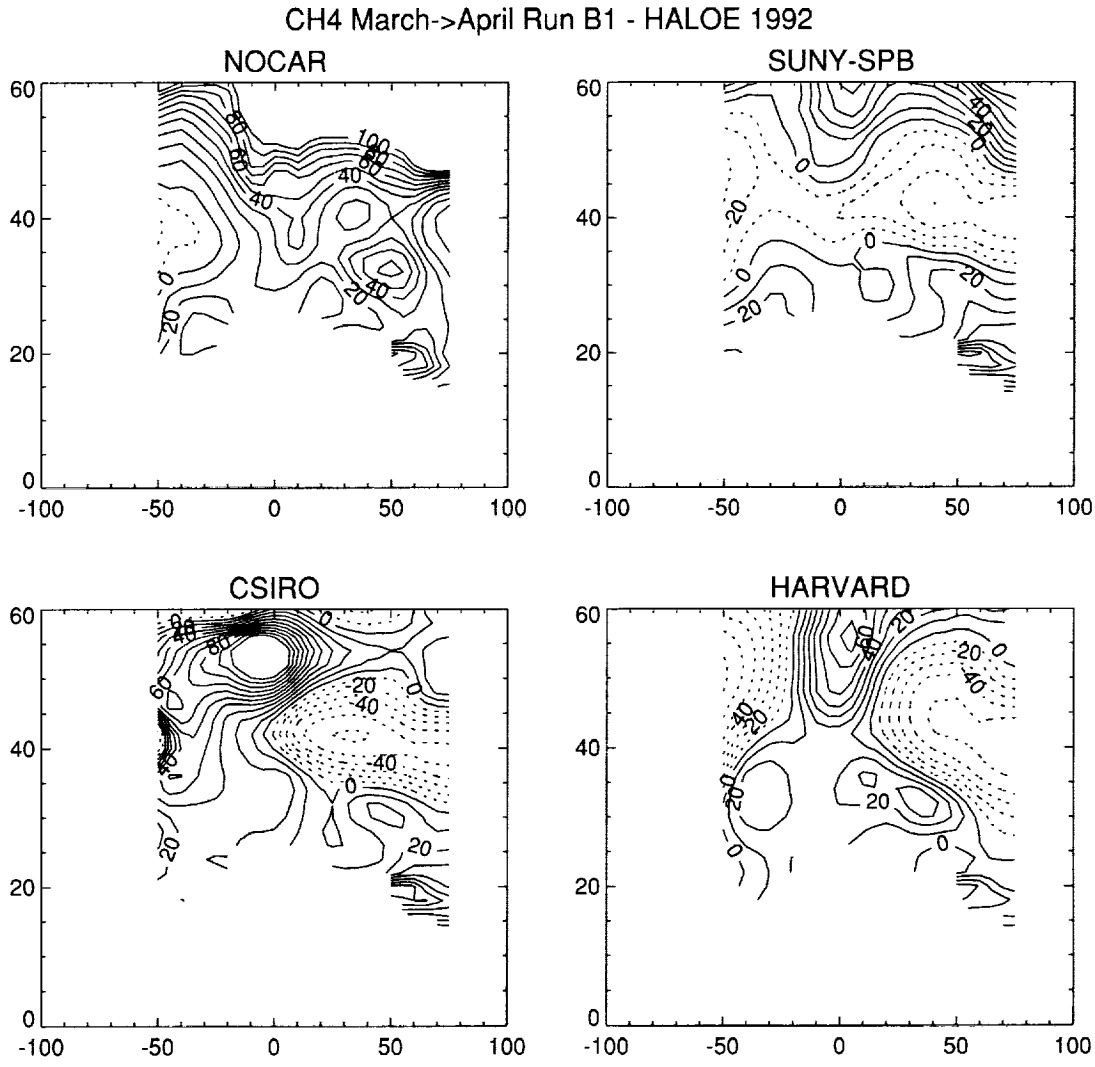

Figure 3.3.2. Concluded.

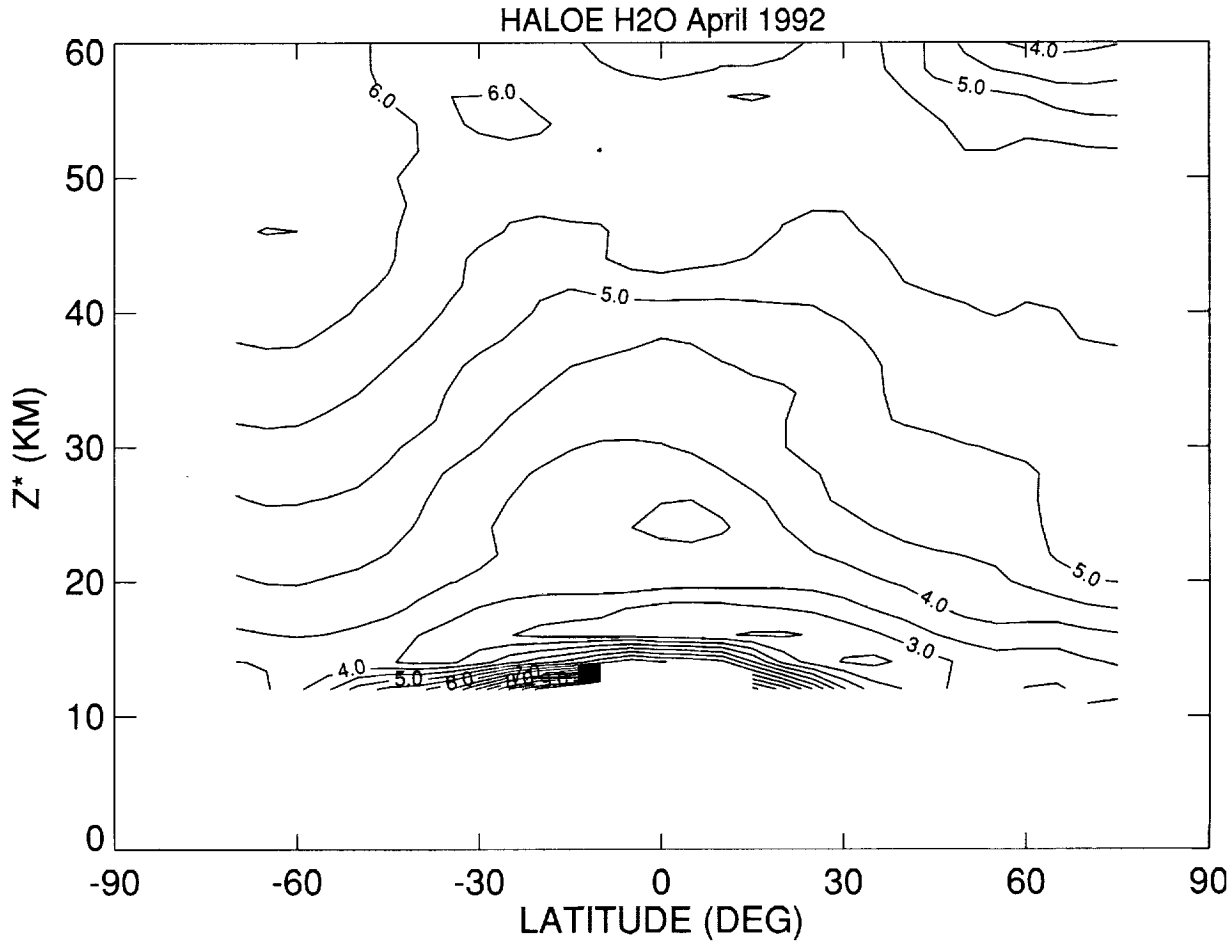

Figure 3.3.3. Comparisons for H_2O. (a) zonal mean field from HALOE for March 10-April 26, 1992, contour increment is 0.5 ppmv; (b) model comparisons for AER, GSFC-2D, LLNL, and UNIVAQ-2D and contour increment is 5%.

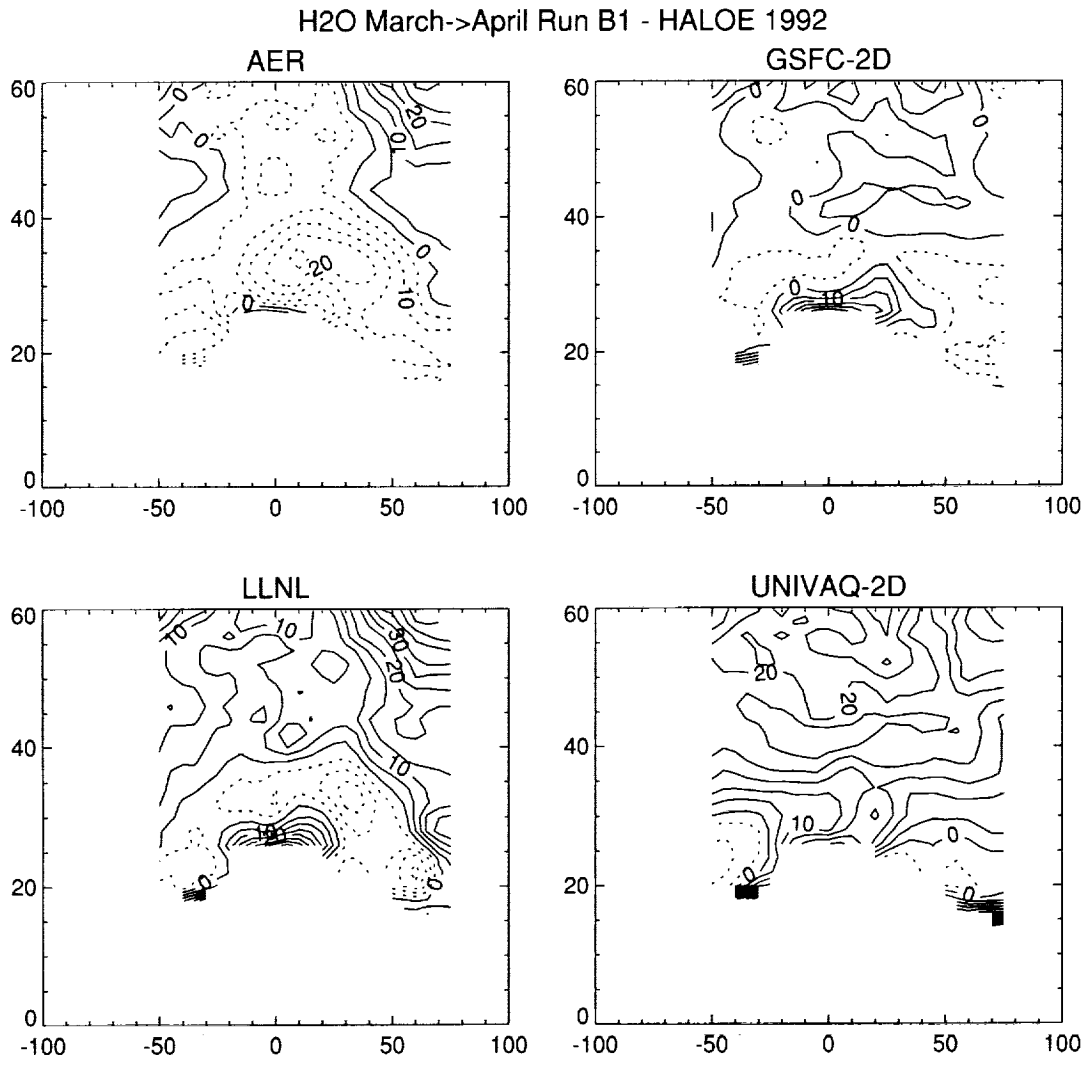

Figure 3.3.3. Concluded.

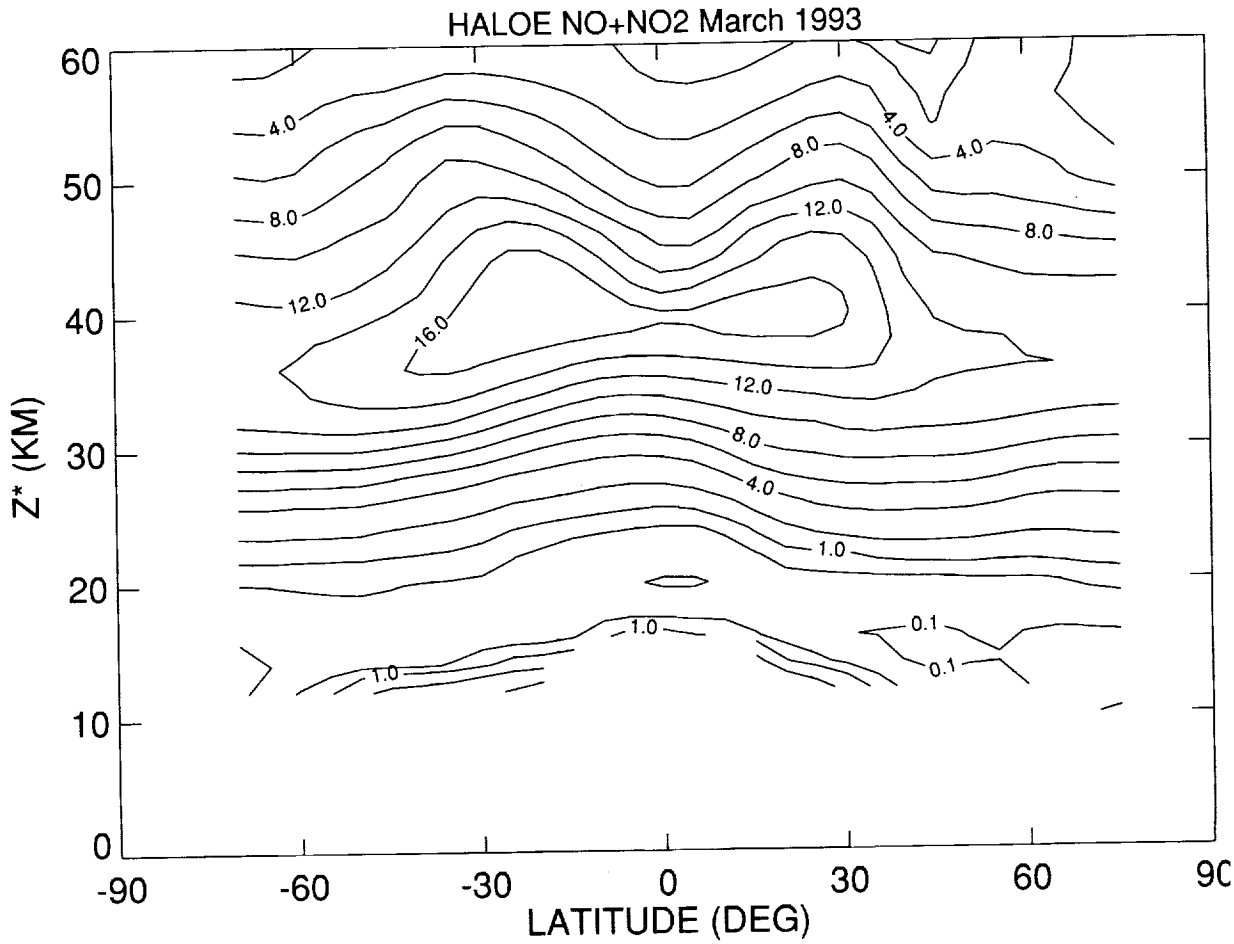

Figure 3.3.4. As in Figure 3.3.3, but for HALOE sunset NO + NO_2 from March 6-April 11, 1993. Contour increment for (a) is 2 ppbv above the 2 ppbv value. In (b) the increment is 10%.

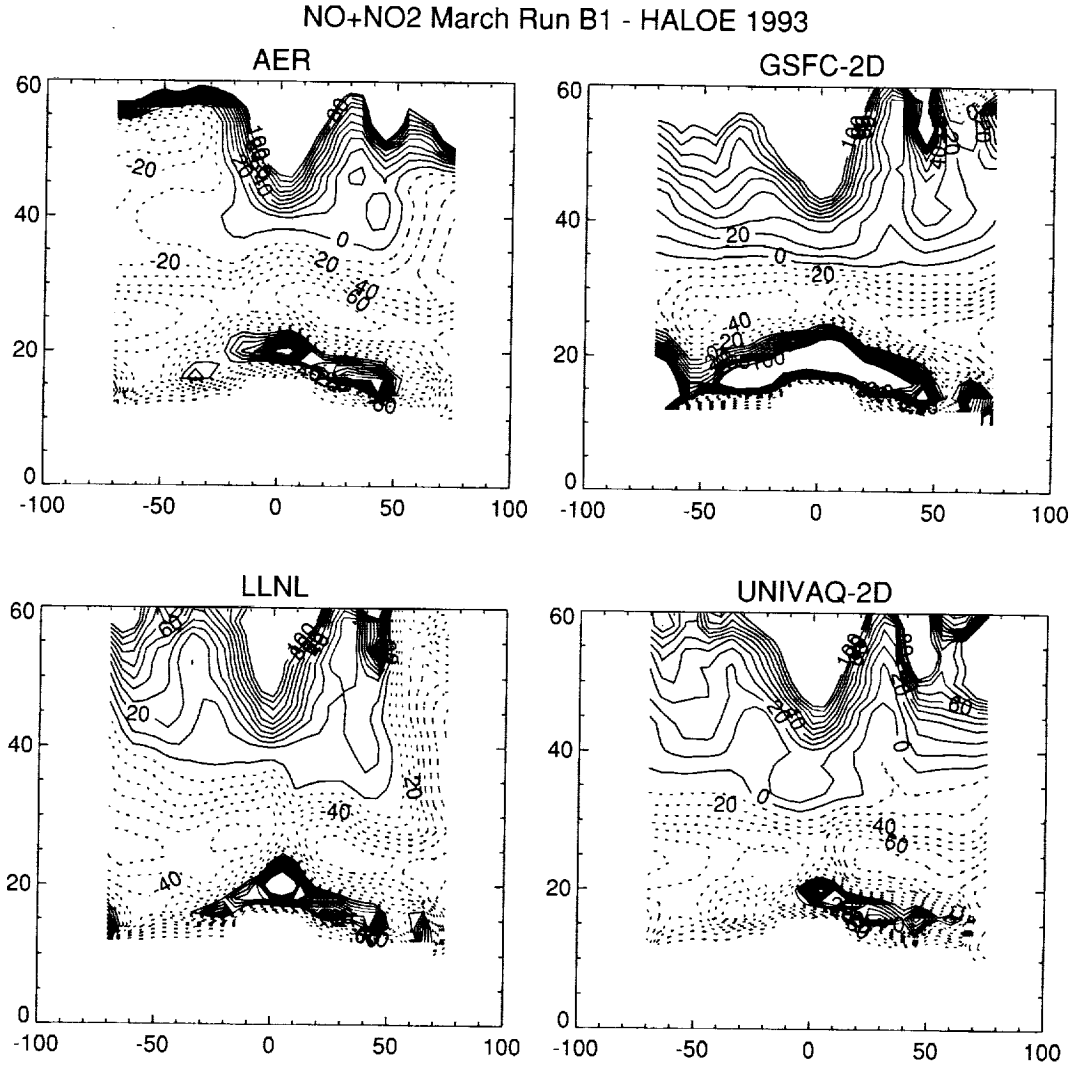

Figure 3.3.4. Concluded.

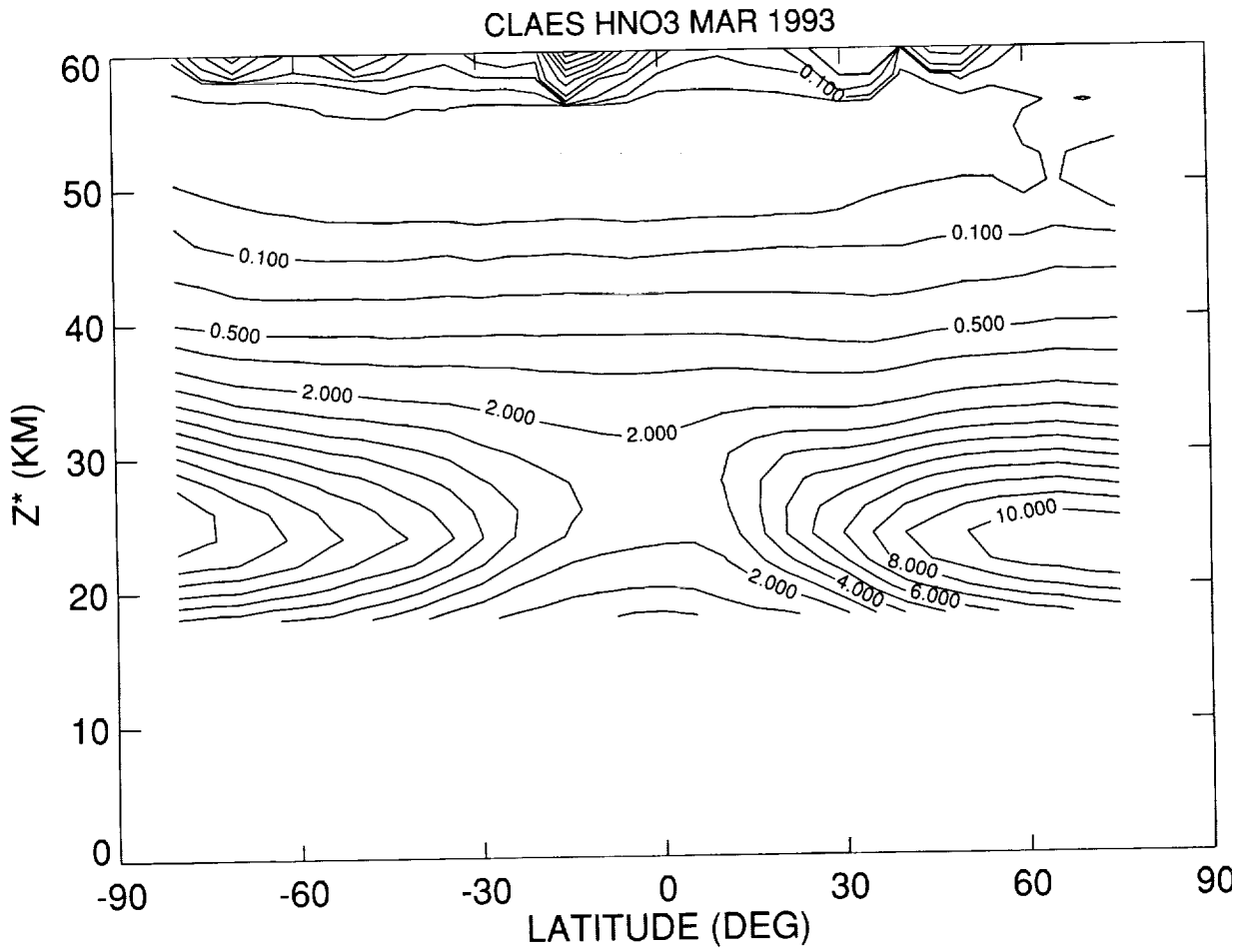

Figure 3.3.5. Comparisons for HNO_3. (a) zonal mean field from CLAES for March 1993—contour increment is 1 ppbv except for values less than 1 ppbv; (b) model comparisons for AER, GSFC-2D, LLNL, and UNIVAQ-2D—contour increment is 10%.

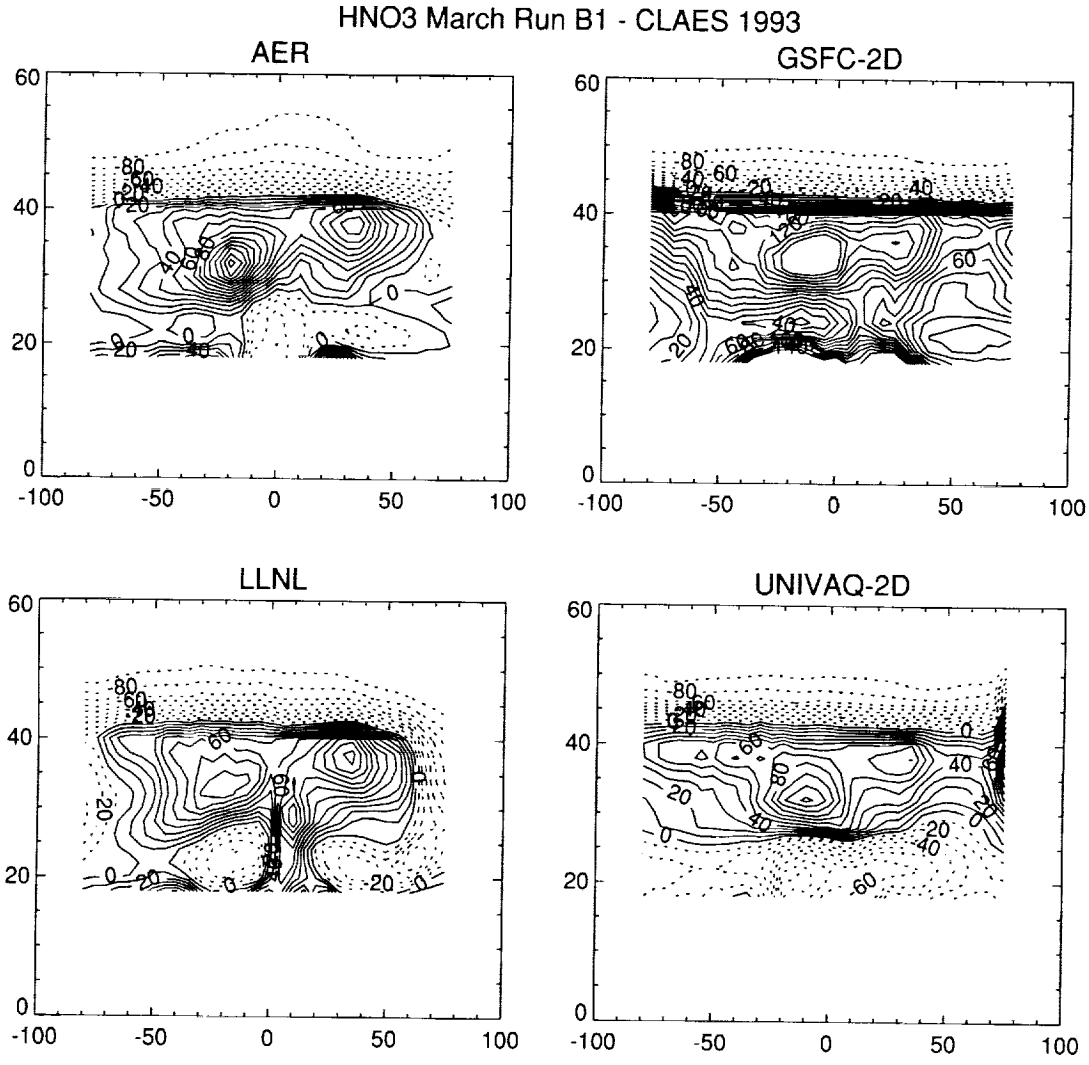

Figure 3.3.5. Concluded.

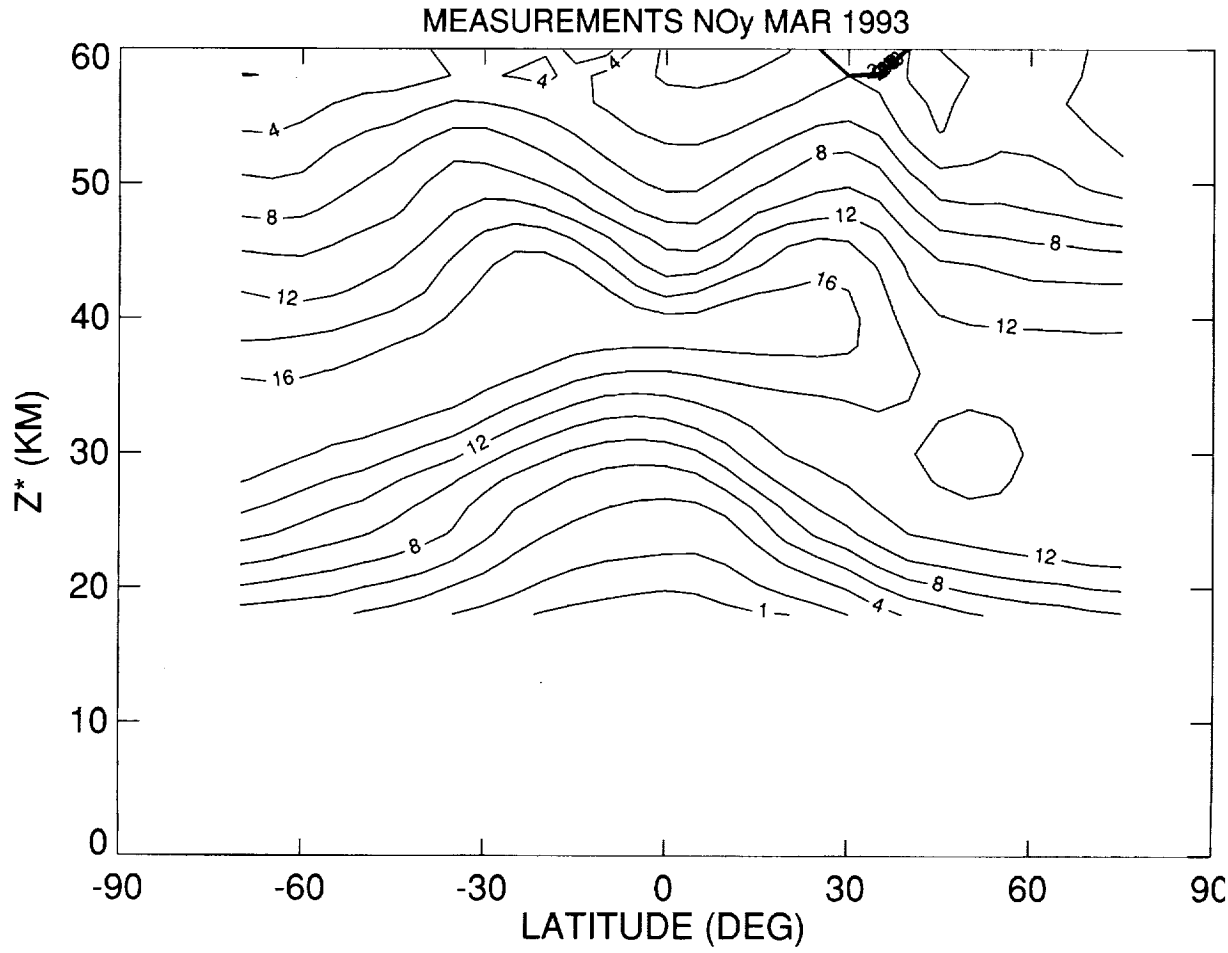

Figure 3.3.6. As in figures 3.3.4 and 3.3.5, but for NOy. Contour increment in 3.3.6a is 2 ppbv and in 3.3.6b it is 10% up to 100% and 50% above that.

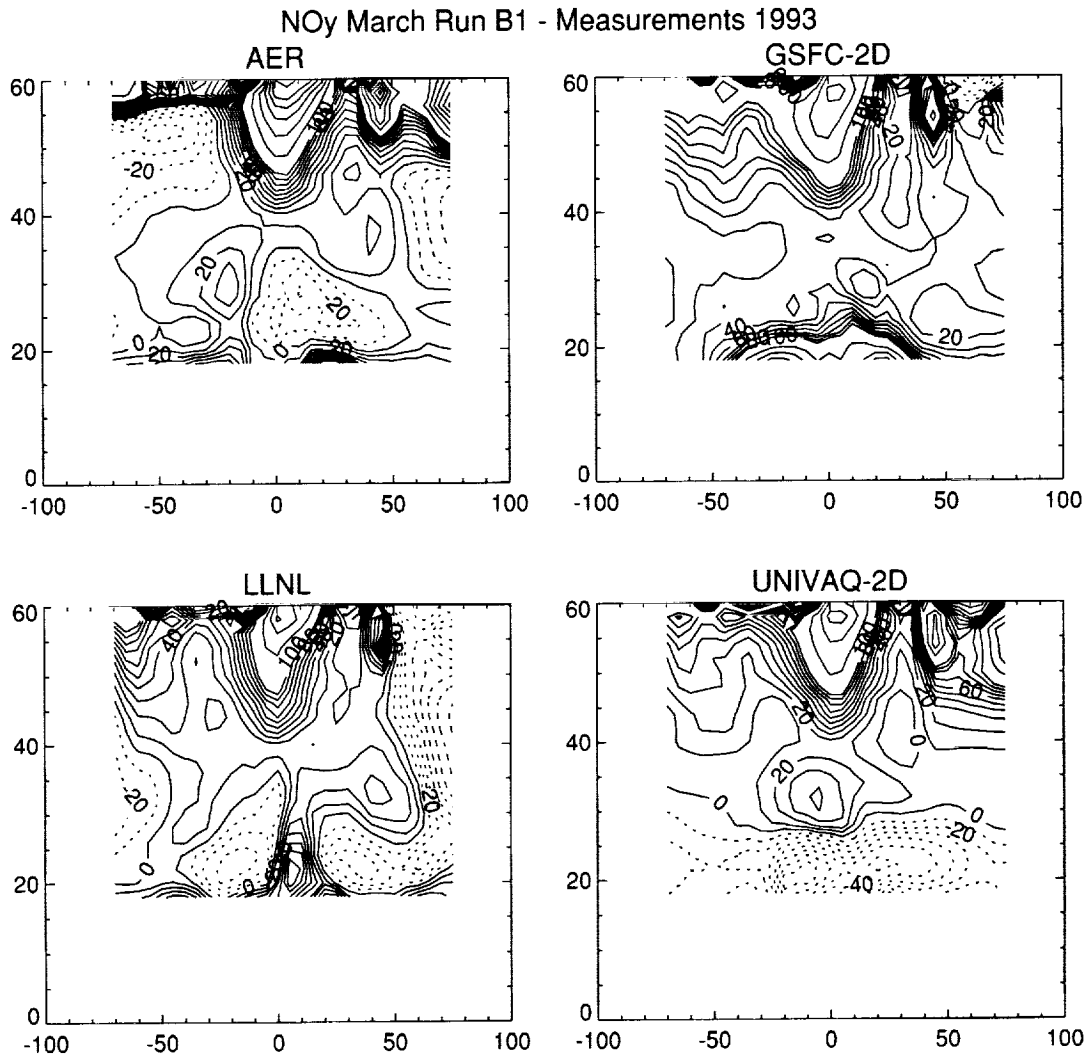

Figure 3.3.6. Concluded.

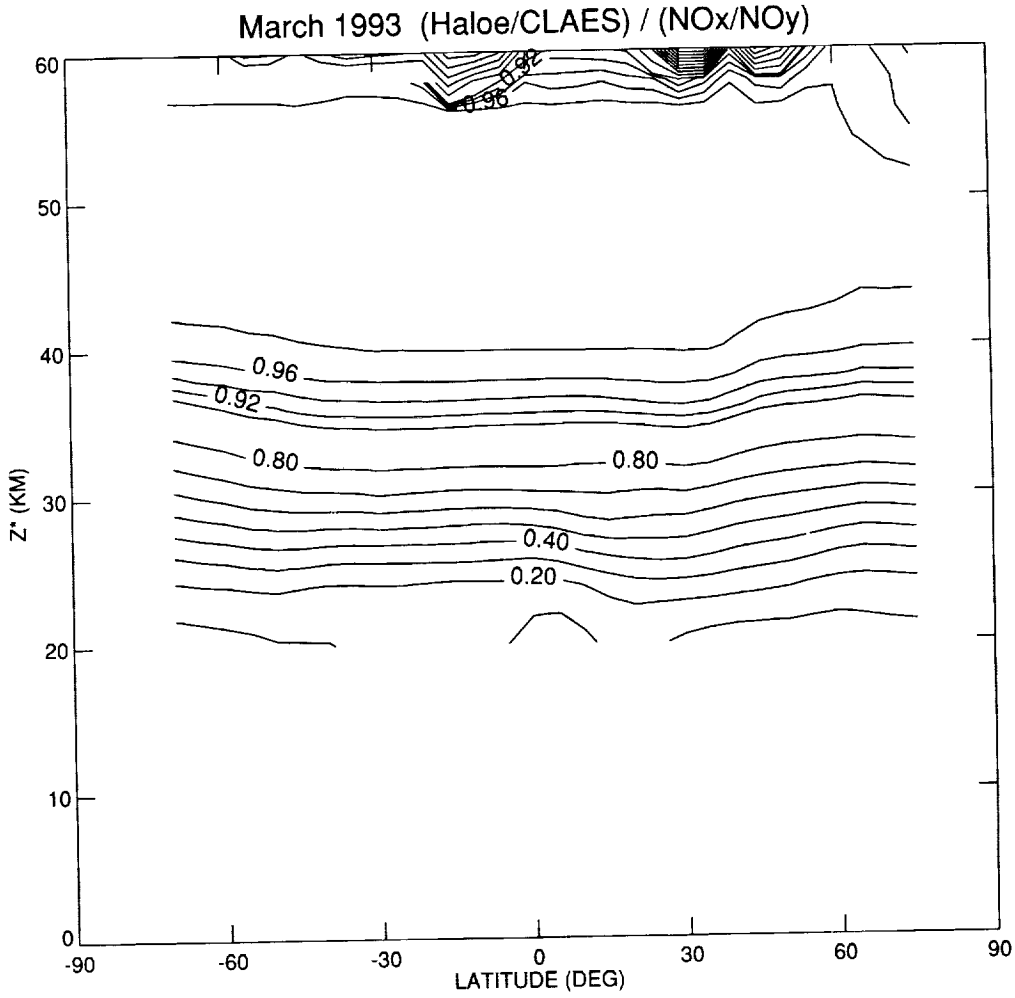

Figure 3.3.7. (a and b) As in figure 3.3.6, but for the ratio NOx/NOy; Contour increment is 0.1 up to 0.9 and 0.02 above that. (c) NOx/NOy ratios at 30N.

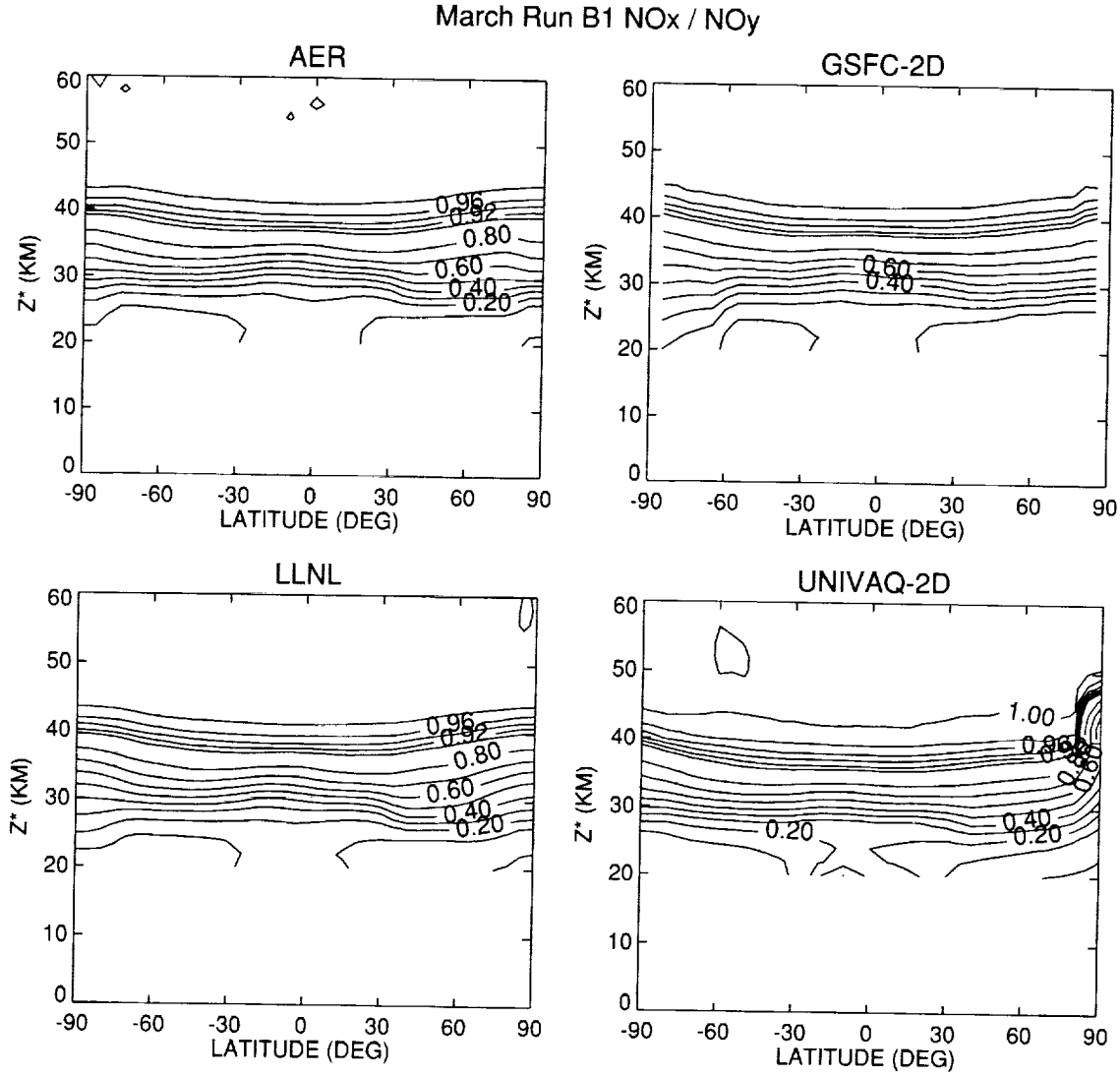

Figure 3.3.7. Continued.

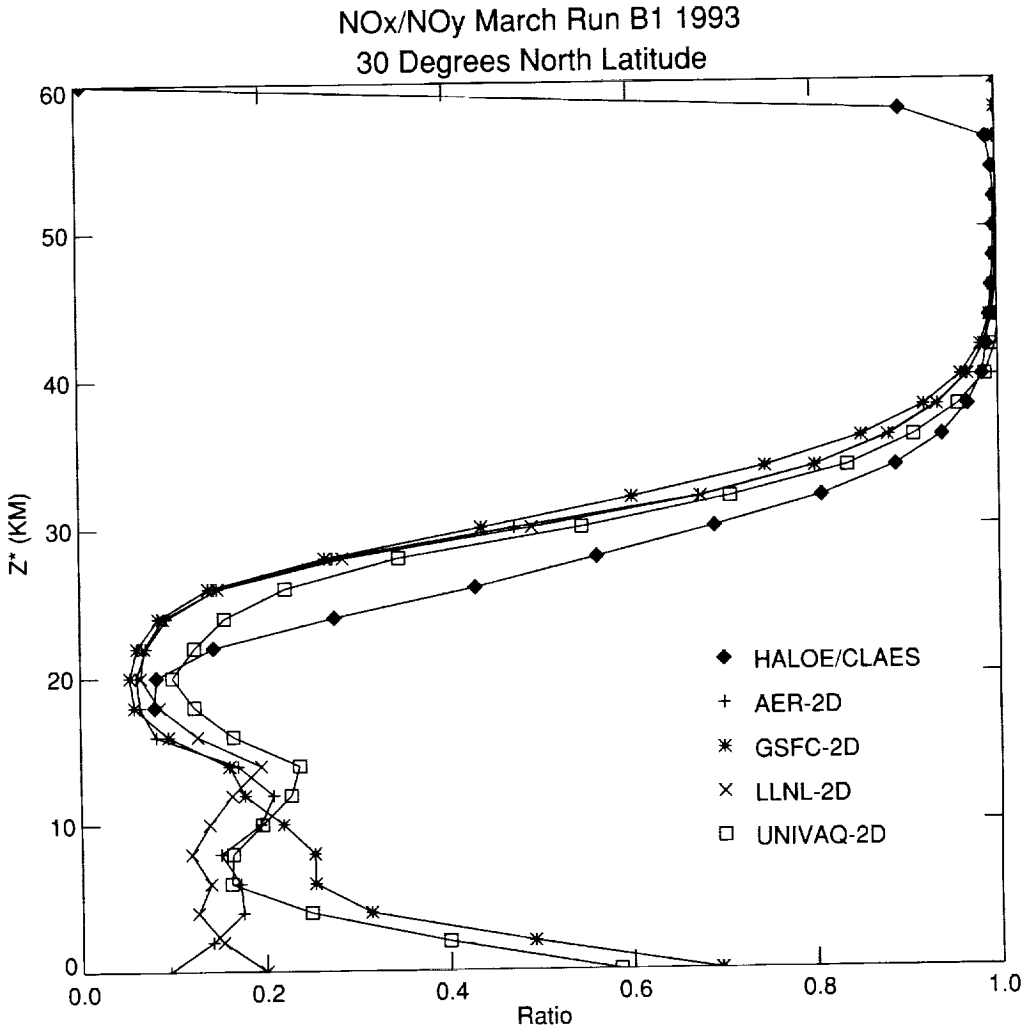

Figure 3.3.7. Concluded.

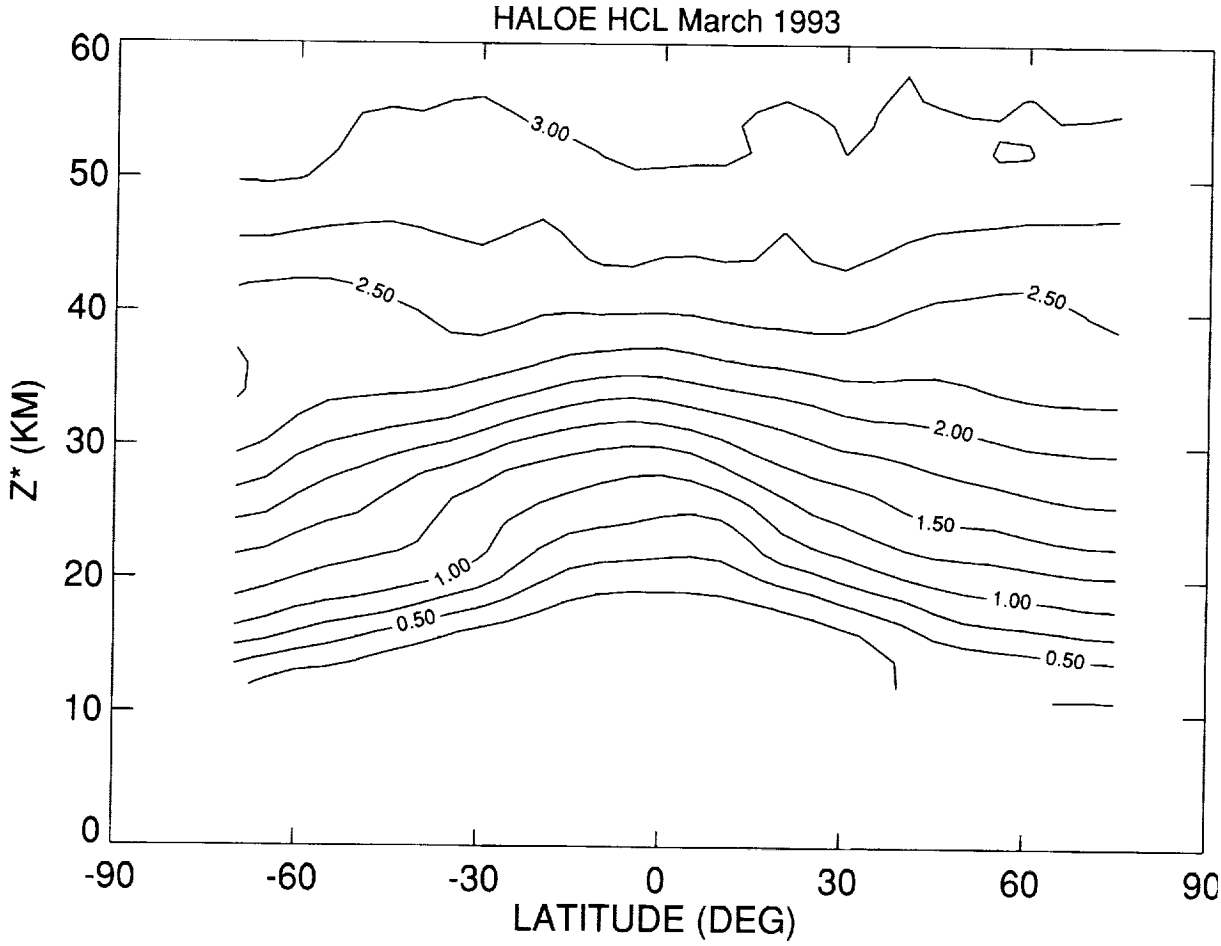

Figure 3.3.8. As in Figure 3.3.4, but for HALOE HCl. Contour increment for (a) is 0.25 ppbv and for (b) it is 5%.

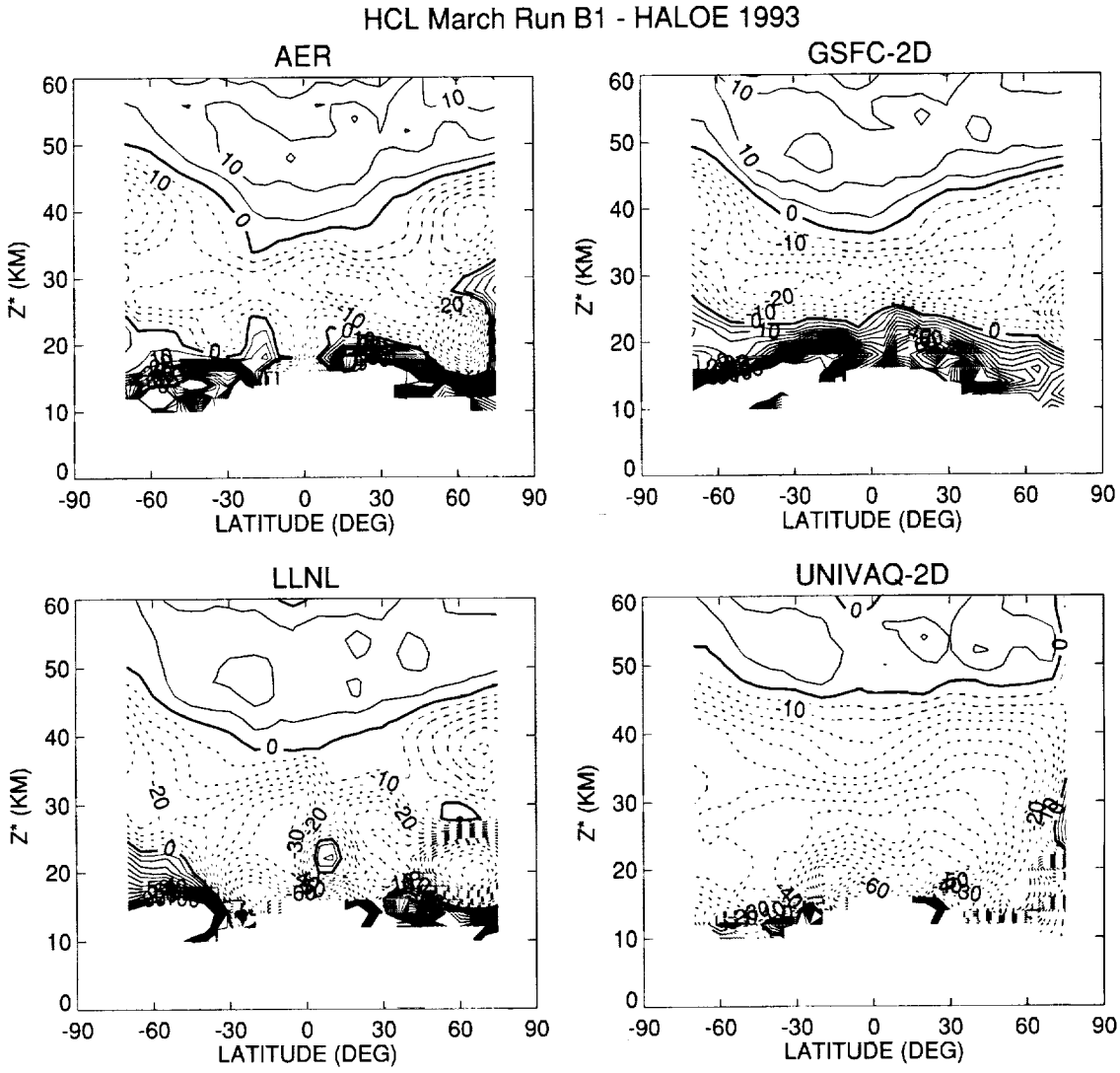

Figure 3.3.8. Concluded.

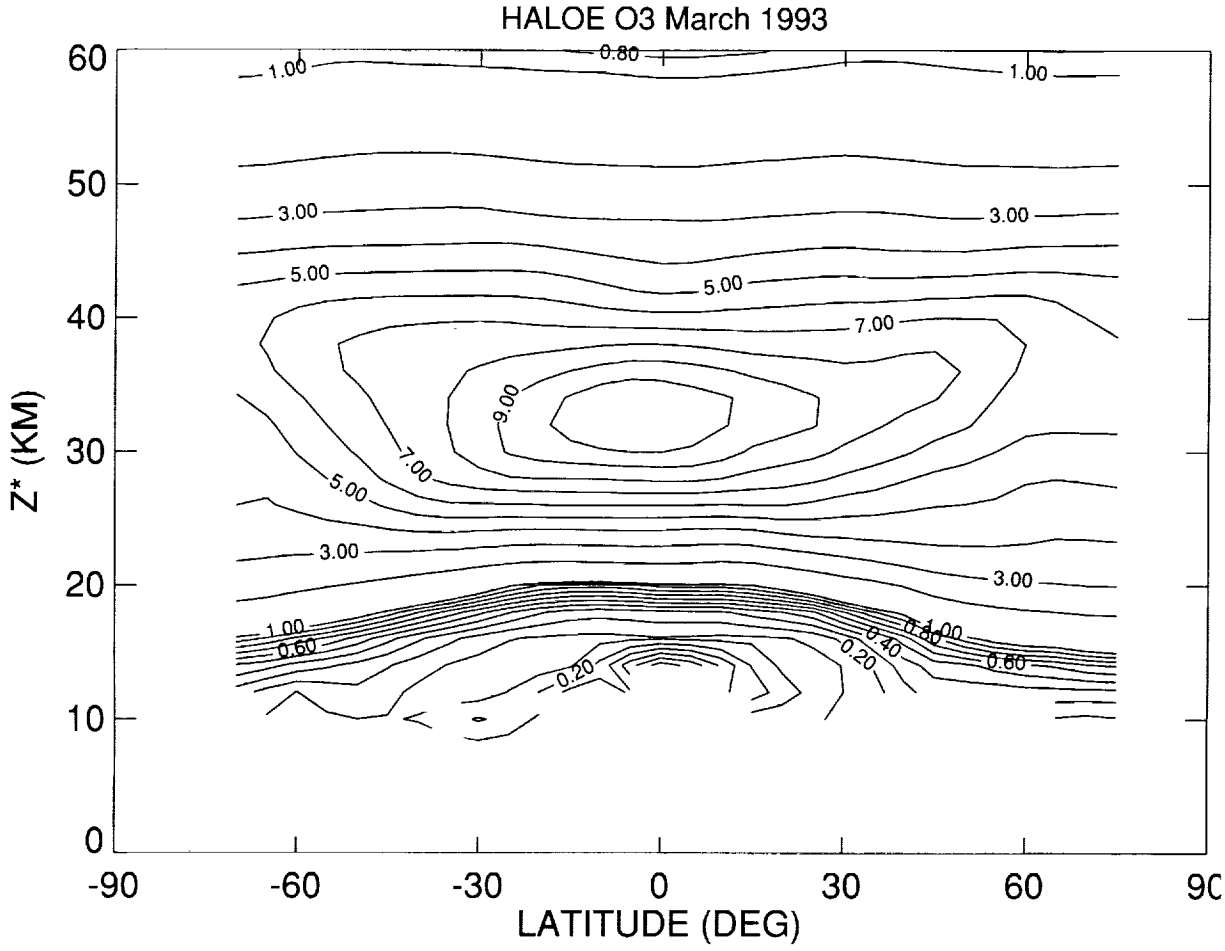

Figure 3.3.9. As in Figure 3.3.4, but for HALOE O_3. Contour increment for (a) is 1 ppmv, but below 1 ppmv it is 0.1 ppmv. Contour increment for (b) is 5%.

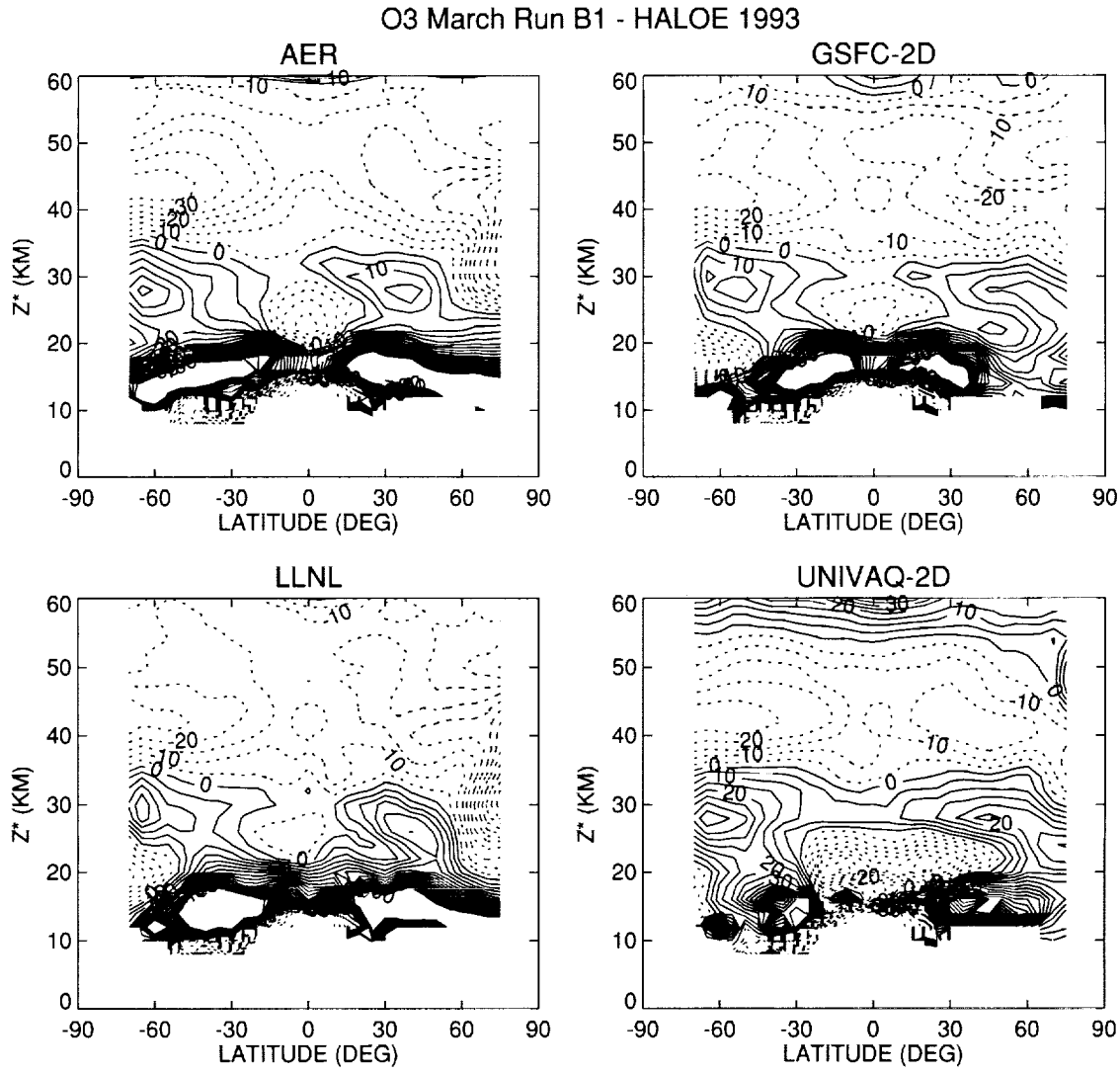

Figure 3.3.9. Concluded.

3.4 Source Gases Comparisons

Courtney J. Scott and Malcolm K. W. Ko

Atmospheric and Environmental Research, Inc.

3.4.1 Introduction

Comparisons of measured and model calculated distributions and stratospheric lifetimes of long-lived source gases emitted from the surface of the earth provide a useful diagnostic for model transport and chemistry in the lower stratosphere. These long-lived species play an important role in the ozone budget, affecting the concentrations of Cly and NOy, which influence ozone production and loss. Source gases from the present day atmosphere were examined using calculations from participating models and selected measurements. These gases, unlike many of the tracers discussed in Part A, are dependent on chemistry as well as transport. Differences in chemical treatment among the models, such as photolysis rate calculations and diurnal averaging, could create substantial differences in source gas concentrations. A previous intercomparison of photolysis rates helped to remove much of the inter-model difference in this quantity, so we will assume that transport differences are responsible for the bulk of the inter-model differences in source gases. If this is true, then a consistent picture of model transport should emerge based both on source gases and the inert tracer experiments in Part A.

Observed source gas concentrations, which are compared with model results, are from the version 7.0 CLAES data from the UARS satellite, zonally averaged ATMOS data from the November 1994 ATLAS3 mission (Gunson et. al., 1996), and data from numerous aircraft campaigns that obtained *in-situ* measurements in the lower stratosphere between 1992 and 1997. Comparisons between measurements and model calculations can be difficult. Aerosols emitted during the Mt. Pinatubo eruption may have compromised CLAES data from 1991 and 1992. Aircraft campaigns do not always capture data representative of the zonal and climatological mean and do not take samples at many altitudes. Nevertheless, the measurements do provide a yardstick for model comparison.

Model results for source gases were obtained from Scenario B1, the 1992 atmosphere calculation. In this scenario, modelers were asked to calculate their best 1992 atmosphere. The models were initialized with a 1990 steady state calculation and then continued for an additional 2 years. Sulfate surface areas for 1991 and 1992 from SAGE II were provided, along with 1992 temperatures from NCEP. Models were required to use the JPL-97 reaction and photolysis rates (DeMore et. al, 1997). Models participating in this study were: AER, GSFC-2D, LLNL, CSIRO, SUNY-SPB, UNIVAQ-2D, LARC-3D, HARVARD, GSFC-3D, ECHAM3/CHEM and NOCAR. Eight of the eleven models provided both global and stratospheric calculated lifetimes for 10 source gas species, ranging from stratospheric lifetimes of 35 years for CH_3Br to around 200 years for $CHClF_2$. Close examination of mixing ratios, both in altitude and latitude, for CH_4, N_2O and $CFCl_3$ was also made. These particular species were selected based on the availability of measured data and their stratospheric lifetimes.

3.4.2 Global and Stratospheric Lifetimes

The atmospheric residence time, or lifetime, of a species defines the mixing ratio expected due to a given steady state emission rate. In our analysis, we examine the global lifetime, the total atmospheric burden divided by the total atmospheric loss, and the stratospheric lifetime, the total atmospheric burden divided by the stratospheric loss. Given the assumptions stated above, the global and stratospheric lifetimes of long-lived source gases may be useful in determining transport signatures within models.

Global and stratospheric lifetimes for 10 species and eight models are shown in Table 3.4.1. For comparison, global lifetimes recommended in Scientific Assessment of Ozone Depletion (WMO, 1995) and stratospheric lifetimes derived from the ASHOE/MAESA (A/M) campaign (Volk et. al., 1997) are also shown. Note that for CF_2Cl_2, $CFCl_3$, and CCl_4, the derived mean stratospheric lifetime is smaller than the recommended global lifetime though the upper limit of the error range is comparable to the global lifetime. This may reflect the limited data used to derive the stratospheric lifetimes or uncertainty in the WMO global lifetimes.

The LARC-3D model, the only 3D CTM to submit lifetimes, calculates stratospheric lifetimes for N_2O, CF_2Cl_2, and CH_3Cl that are substantially longer than the other models and 40% longer than the derived stratospheric lifetimes from A/M. Comparison of LARC-3D with the WMO global lifetimes also indicate the 3D CTM is calculating lifetimes that are 40% longer for N_2O and CF_2Cl_2. It should be noted that the unusually large lifetimes calculated by the LARC-3D model may be due to a non-converged 1990 data set.

Comparison of the global lifetimes with the WMO lifetimes for the longer lived species, N_2O, CF_2Cl_2 and $C_2Cl_3F_3$, indicate the remaining seven models calculate lifetimes in good agreement with the documented values, calculating mean global lifetimes that are within +/-5% of the WMO values. The calculated global lifetimes of the shorter lived species show model means, with the exception of the HARVARD model which calculates much longer OH reactive lifetimes than any of the other models, to be within +/-10% of the WMO values for the OH reactive species and within +/-25% for the photolytically reactive species.

Comparison of the calculated stratospheric lifetimes for the long-lived species, N_2O, CF_2Cl_2 and $C_2Cl_3F_3$, show most of the models to be in good agreement with the A/M lifetimes, calculating mean lifetimes within the error bars noted. For N_2O and CF_2Cl_2, the LARC-3D value is close to a factor of 2 larger than the A/M value. While the rest of the models are within +/- 10% of each other, around 100 years. Among the seven models, AER and LLNL calculate the shortest lifetimes while GSFC-2D calculates the longest. All of the models calculate much longer lifetimes for CH_4 than the A/M values indicate. The calculated lifetimes of the short-lived species do not represent the derived values as well as the long-lived species. For $CFCl_3$, GSFC-2D, HARVARD and LARC-3D calculate lifetimes around 60 years, about 50% larger than the A/M value. The remaining five models calculate a mean lifetime within +/-10% of each other around 47 years, well within the error bars noted. HARVARD and GSFC-2D calculate lifetimes larger than 55 years for CCl_4, about 70% larger than the A/M values. Values from the remaining six models calculate a mean of 44 years, very close to the A/M calculated values. In this group, the UNIVAQ-2D calculates the shortest lifetimes closest to the A/M lifetimes.

The 10 species studied can be separated into two groups, those with stratospheric lifetimes less than 60 years and those with stratospheric lifetimes over 120 years. Species with shorter lifetimes such as CCl_4 and $CFCl_3$ are more sensitive to the transport characteristics at 75 mb while those with longer lifetimes (such as N_2O and CF_2Cl_2) are more sensitive to the model transport around 10 mb. The 2D CTMs are in relatively good agreement with each other. Figure 3.4.1 gives a graphical representation of the calculated stratospheric lifetimes for selected species. In Figure 3.4.1, patterns can be noted with certain models. The HARVARD model tends to calculate lifetimes that are shorter for the longer lived species, while they calculate large lifetimes for the shorter lived species we examined. The UNIVAQ-2D model shows an opposite pattern, where the shorter lived species have lifetimes below the mean of all models. The remaining models tend to be in the middle and show no obvious patterns. These behaviors apply to species whose removals are both driven by photolysis and by OH chemistry and is interpreted as indicative of the transport differences in the models. A general pattern is noted that models that tend to calculate shorter lifetimes for a given species have steeper latitudinal gradients for that species. This behavior may be indicative of the strength of the tropical upwelling and/or the tropical barrier. Comparison of the model calculated stratospheric lifetimes shows AER and LLNL tend to calculate similar lifetimes.

Based on these correlations, AER and LLNL may have similar upwelling and/or have similiar tropical barriers at the 75 and 10 mb surfaces. HARVARD and UNIVAQ-2D may have smaller upwelling rates at their 75 mb surface. The differences in model calculated lifetimes seem to be related to the age of air from the SF_6 and the tracer experiments, see pertinent sections. Models that are calculating longer lifetimes tend to have older air, giving model calculated ages that are closer to the age of air derived from measurements of SF_6 (Volk et. al., 1997) and CO_2 from the ER-2 aircraft. The longer source gas lifetimes in the models could suggest that the upwelling in the lower tropical stratosphere for the models is too weak but this is inconsistent with the findings from the CO_2 study, which deduces that the model calculated seasonal signal for CO_2 is advected up in the tropics too fast when compared to observations. This seemingly contradictory situation, that the model ages are too young from the SF_6 experiment, but the model calculated lifetimes are too long compared to observations, could be an indication that the meridional flux across the tropical barrier is too weak.

3.4.3 Source Gas Concentrations

In order to discern dynamical signatures of upwelling verses horizontal mixing in the lower stratosphere, results from the AER 2-D CTM using three different mixing rates ranging from a weak tropical barrier to a strong tropical barrier were examined. The models are: the Global Diffuser (NO PIPE) (Kotamarthi et al., 1994; Weisenstein, et al., 1993); the Partial Barrier (LEAKY PIPE) (Shia et. al., 1998); and the Tropical Barrier (PIPE) (Weisenstein et. al., 1996). The three models have identical chemistry and advection and differ only in the horizontal diffusion coefficients in the lower and middle stratosphere. Three different properties of the source gases were examined: lifetimes, latitudinal cross sections at specified altitudes, and profiles at specified latitudes. Table 3.4.2 illustrates calculated stratospheric lifetimes for the three AER models. In all species examined, the PIPE model calculates the shortest lifetimes while the NOPIPE model calculates the largest lifetimes. This is true not only for the photolytically driven species, but also for the OH reactive species, such as CH_4. Clearly, the strength of the tropical barrier effects the lifetimes of the species, as the highest concentrations are found in the tropical regions where chemical processing is most intense. Thus, the highest concentrations are seen with the strongest tropical barriers, leading to greater overall loss and shorter lifetimes. Differences in advective transport may also impact the permeability of the tropical barrier. If this is truly a transport signature, the calculated species concentrations in the tropics should be correlated with lifetimes. Specifically, models which calculate longer lifetimes should also calculate smaller concentrations in the lower tropical stratosphere. Additionally, one expects the gradients of the source gas isopleths to be steeper across the tropical barrier if the model is calculating shorter lifetimes. To test this hypothesis, three source gas species were examined: CH_4 and N_2O at 10 mb and $CFCl_3$ at 75 mb. Figure 3.4.2 shows the latitudinal cross sections at 10 mb of CH_4 calculated for spring for all models. In Figure 3.4.2, GSFC-2D, UNIVAQ-2D, SUNY, LARC and GSFC-3D are all grouped together peaking 20% below the zonal mean UARS CH_4 in the tropics. The remaining models, AER, HARVARD, LLNL, NOCAR and CSIRO, all fall within 10% of the UARS zonal mean CH_4 in the tropics. Spring and fall equatorial profiles of CH_4 for all models, UARS and ATMOS are shown in Figure 3.4.3. In the lower stratosphere all model calculated CH_4 falls below the measured UARS data. Note that the ATMOS data is lower in magnitude and the models are higher than ATMOS data for the same altitude range. A large spread is seen in calculated CH_4 concentrations in the middle and upper stratosphere.

Figure 3.4.4 shows the latitudinal cross section of spring N_2O at 10 mb. As in Figure 3.4.2, UARS zonal mean data are shown for 1992 and 1993. Much larger variation is seen in the UARS N_2O data than in the CH_4 data. This may be due to a small contamination by the Mt. Pinatubo aerosols effecting the data retrieval. Again, the models fall into two separate groups. The first group, containing the models SUNY-SPB, LARC, UNIVAQ-2D and GSFC-3D, are approximately 10% below the UARS tropical concentrations. The second group, consisting of the models AER, HARVARD, LLNL, NOCAR and

CSIRO are 15 to 40% too high in the tropics. The GSFC-2D model falls the closest to the UARS data. Figure 3.4.5 shows spring and fall equatorial profiles for N_2O. In contrast to the CH_4, the calculated N_2O values more closely represent the UARS and ATMOS measured N_2O in the lower stratosphere, falling within +/-30%. The spread in the middle and upper stratosphere is as large for the N_2O as the CH_4.

Figures 3.4.6 and 3.4.7 show fall $CFCl_3$ calculated and measured data, with a latitudinal cross section at 75 mb and an equatorial profile, respectively. Examination of Figure 3.4.6 does not show the same pattern that both the N_2O and CH_4 at 10 mb did. This is indicative of a different pattern of mixing that drives the concentrations at 75 mb. All model calculated tropical $CFCl_3$ mixing ratios are grouped together closely and fall within the error bars of the ER-2 flight data examined. Zonal mean ATMOS measurements are also shown in Figure 3.4.6. These data show larger tropical air concentrations than the ER-2 data. Most of the calculated tropical $CFCl_3$ data falls well below the ATMOS data. UARS $CFCl_3$ was not used due to a retrieval contamination by Mt. Pinatubo aerosols. It is worth noting that GSFC-2D shows one of the flatter distributions and also calculates the longest lifetime for $CFCl_3$. Additionally, the spread of calculated lifetimes for $CFCl_3$ is smaller than the lifetimes seen from N_2O. The calculated $CFCl_3$ from most of the models have flatter distributions across the tropical barrier than the measured data examined. This may be indicative of too much meridional flux across the tropical barrier at the 75 mb level. This would substantiate a younger age of air calculation seen in the SF_6 calculations. At mid and high latitudes, the measured data, ATMOS, A/M and STRAT show a large spread. These values are probably indicative of polar vortex air, which most of the models do not represent well. Figure 3.4.7 illustrates the same behavior seen in the N_2O and CH_4, where a small spread in calculated concentrations is seen in the lower stratosphere with the spread increasing at higher altitudes.

In all species examined, a large spread of calculated concentrations is seen at high latitudes. This may be indicative of different polar process or high latitude dynamics. LARC-3D is consistently calculating much smaller mixing ratios than other models in the tropical lower stratosphere and tends to have one of the flatter distributions for N_2O, CH_4 and $CFCl_3$. This is consistent with the longer calculated lifetimes for the source gases. Additionally, GSFC-3D, GSFC-2D, UNIVAQ-2D, SUNY-SPB, and LARC-3D seem to group together for the longer lived species, showing flatter distributions at the 10 mb surface than the other models. Examination of the calculated source gases from the LLNL and AER models show mixing ratios in the tropical stratosphere that are higher than the UARS data and the other models. This also seems to substantiate the shorter calculated lifetimes seen in Figure 3.4.1. Deviations from these systematic dynamical signatures in the profiles and cross sections could be due to differences in the photolysis rates and/or the chemistry.

3.4.4 Conclusions

We attempt to use calculated and measured source gas concentrations and lifetimes as a diagnostic for model transport. Based on our examination of the AER NO PIPE, PIPE and LEAKY PIPE models, we found evidence that a stronger tropical barrier will mean younger stratospheric lifetimes, higher source gas mixing ratios in the equatorial region and lower source gas mixing ratios in the mid-latitudes (all in the lower stratosphere). Examination of stratospheric lifetimes of 10 species and mixing ratios of CH_4, N_2O and $CFCl_3$ indicate that there are systematic dynamical signatures that may be seen in these parameters. A general pattern is noted that models that tend to calculate shorter lifetimes have steeper latitudinal gradients. This behavior may be indicative of the strength of the tropical upwelling and the permeability of the tropical barrier. Comparison of the model calculated stratospheric lifetimes show AER and LLNL tend to calculate similar lifetimes. Based on these correlations, AER and LLNL may have similar upwelling on the 75 and 10 mb surfaces. HARVARD and UNIVAQ-2D may have smaller upwelling rates at their 75 mb surface.

The differences in model calculated lifetimes seem to be related to the age of air from the SF_6 and the tracer experiments. Models that are calculating longer lifetimes tend to have older air, giving model calculated ages that are closer to the age of air derived from measurements of SF_6 and CO_2 from the ER-2 aircraft. The longer source gas lifetimes in the models would suggest that the upwelling in the lower tropical stratosphere for the models is too weak. This is inconsistent with the conclusion from the CO_2 study, which shows that the model calculated seasonal signal for CO_2 is advected up in the tropics faster than observations. Thus, we have the seemingly contradictory situation that the model ages are too young from the SF_6 experiment, but the model calculated lifetimes are too long compared to observations.

Two groups of models tend to be seen in the 10 mb analysis. SUNY-SPB, LARC-3D, UNIVAQ-2D and GSFC-3D form the first group, which are consistently calculating the longest lifetimes and have the lowest tropical concentrations at 10 mb. The second group, AER, LLNL, HARVARD, NOCAR and CSIRO, are consistently calculating shorter lifetimes and have the highest concentrations in the tropics at 10 mb. Evidence of these groupings in the 75 mb analysis is not seen. This may be attributed to a smaller range of calculated species concentrations at 75 mb or an indication that transport across the tropical barrier at 75 mb is inconsistent among the models. Overall, almost all models examined show calculated mixing ratios of CH_4, N_2O and $CFCl_3$ at the equator and 50°N that are smaller than those measured by the UARS version 7.0 CLAES.

Calculated species cross sections of N_2O and CH_4 show larger gradients across the tropical barrier than the UARS data would indicate. This also substantiates mixing ratios that are too high and ages of air that is to young. Conversely, measured data from the ATMOS and ER-2 flights for $CFCl_3$ indicate a larger gradient at the 75 mb region than the models are exhibiting. This indicates the models may have too much meridional mixing at the 75 mb level. Clearly, the transport in the models differs for each altitude examined and obtaining more realistic transport will not be trivial. Additionally, a large spread of calculated mixing ratio values is seen for all species examined at high latitudes. This may be indicative of different polar process or differences in high latitude dynamics. These differences should be considered when interpreting results concerning the HSCT impact on ozone.

References

DeMore, W.B, et al., Chemical Kinetics and Photochemical Data for Use in Stratospheric Modeling, JPL Publication 97-4, 1997.

M. R. Gunson et al. "The atmospheric trace molecule spectroscopy (ATMOS) experiment: Deployment on the ATLAS Space Shuttle missions" *Geophys. Res. Lett. 23*, 2333-2336 (1996).

Kotamarthi, V.R., M.K.W. Ko, D.K. Weisenstein, J.M. Rodriguez, and N.D.Sze, Effect of Lightning on the concentration of odd nitrogen species in the lower stratosphere: An update, *J. Geophys. Res., 99*, 8167-8173, 1994.

Volk, C.M, Elkins, J.W., Fahey, D.W., Dutton, G.S., Gilligan, J.M., Loewenstein, M., Podolske, J.R., Chan, K.R., Gunson, M.R., Evaluation of source gas lifetimes from stratospheric observations, *J. Geophys. Res., 102*, 25,543-25,564, 1997.

Shia, R.-L., M. K. W. Ko, D. K. Weisenstein, C. Scott and J. Rodriguez, Transport between the tropical and mid-latitude lower stratosphere: Implications for ozone response to HSCT emissions, *J. Geophys. Res.*, 1998.

Weisenstein, D.K., Ko, M.K.W., Sze, N.D. and Rodriguez, J.M., Potential impact of SO_2 emissions from stratospheric aircraft on ozone, *Geophys. Res. Lett., 23*, 161-164, 1996.

Weisenstein, D.K., M.K.W.Ko, J.M. Rodriguez, and N.D. Sze, Effects on statospheric ozone from high-speed civil transport: Sensitivity to stratospheric aerosol loading, *J. Geophys. Res., 98*, 23,133-23,140, 1993

World Meteorological Organization (WMO), Scientific assessment of ozone depletion:1994, Rep. 37, Global Ozone Res. and Monit. Project., Geneva, 1995.

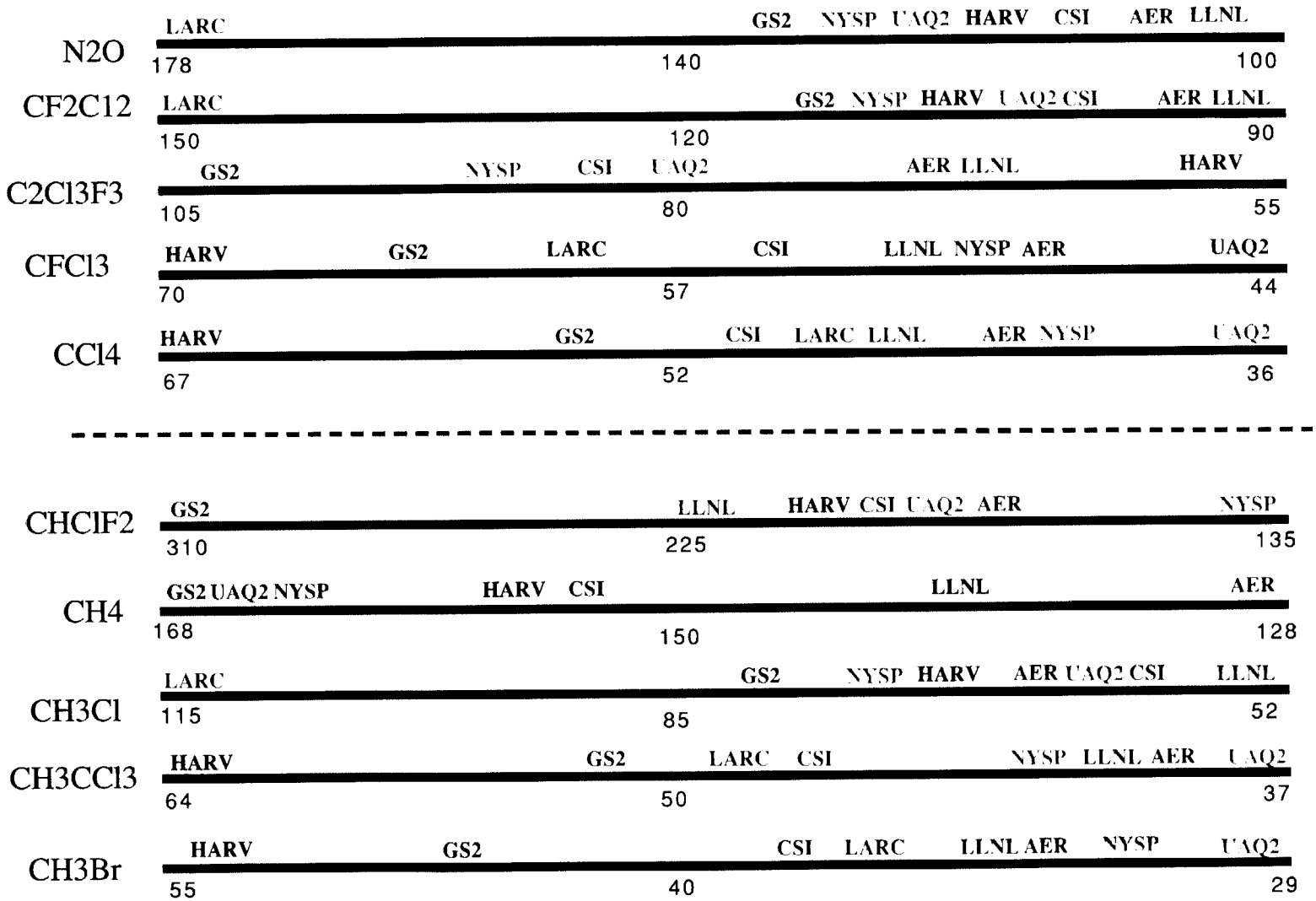

Figure 3.4.1. Graphical representation of the Model calculated stratospheric lifetimes (years) shown in Table 3.4.2. Species in the upper half of the figure are primarily driven by photolytic reactions while species below the dotted line are driven primarily by OH reactions. All scales are linear.

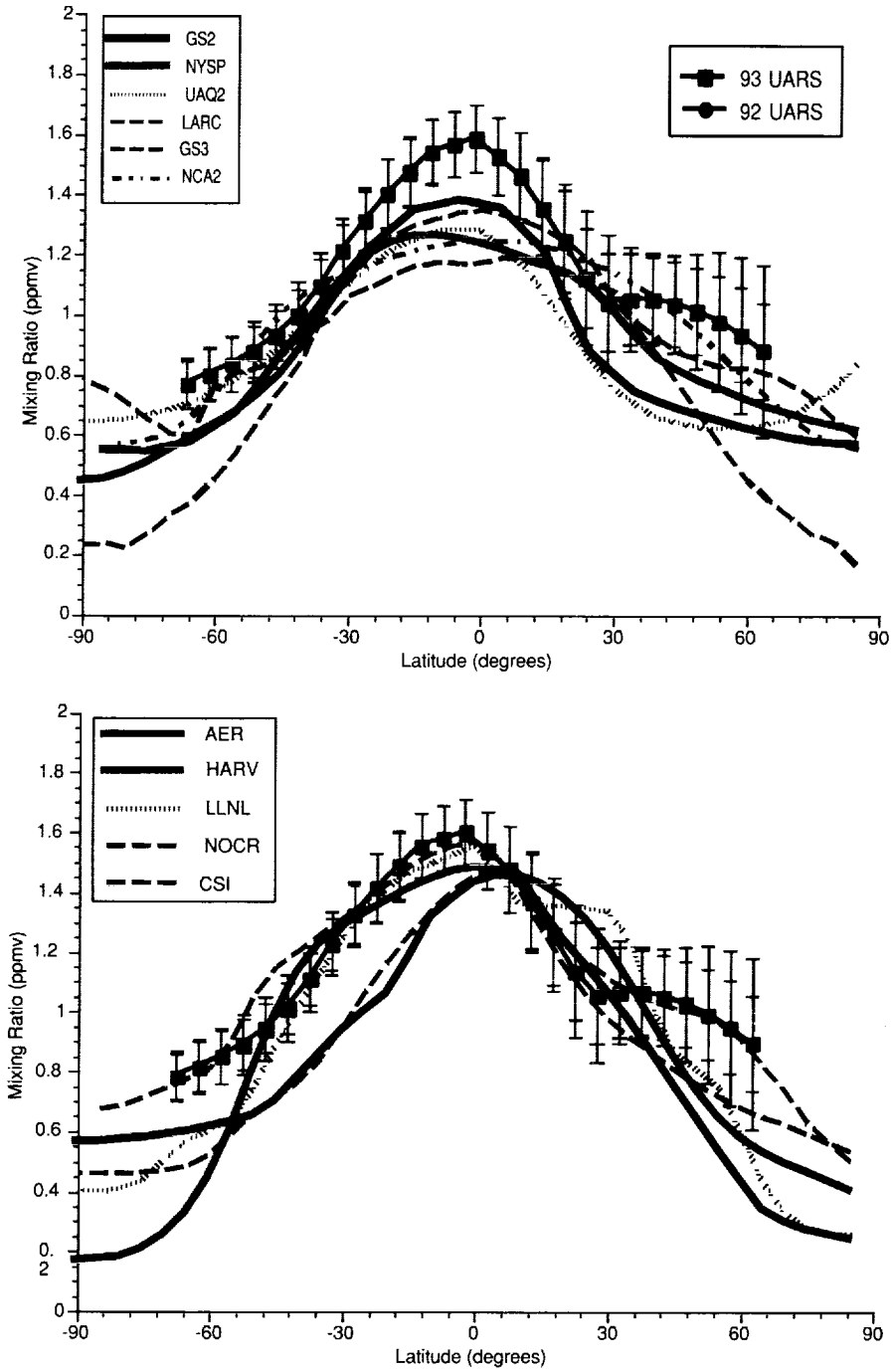

Figure 3.4.2. Calculated CH_4 for spring at 10 mb. Symbols denote the spring 10 mb UARS version 7.0 CLAES data. Error bars represented the meridional variations of the CH_4.

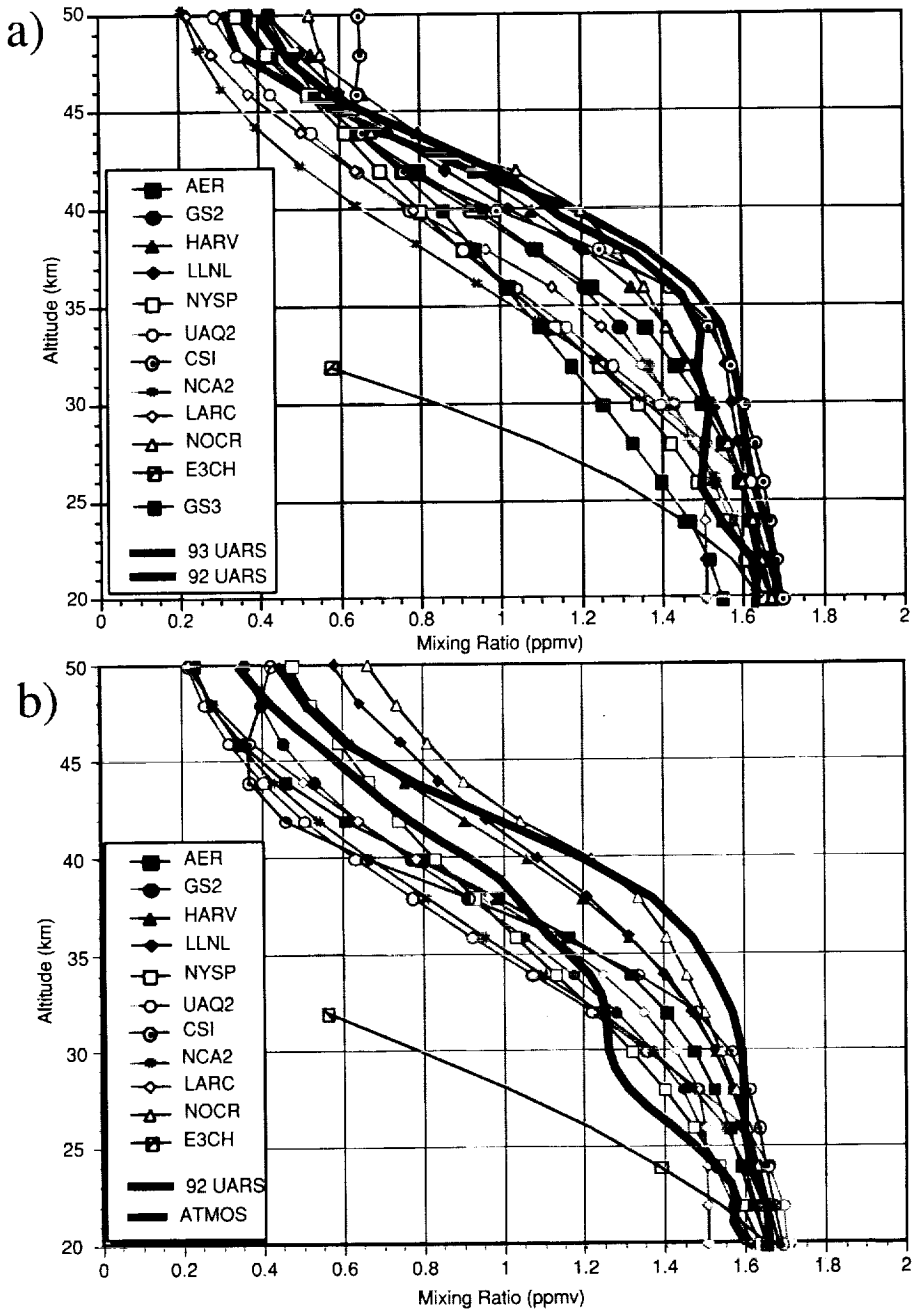

Figure 3.4.3. Calculated CH_4 at the equator between 20 and 50 km. Spring data is in the upper panel (a) while fall values are given in the lower panel (b). Solid lines denote UARS and ATMOS data. The E3CH calculated points represent the model's resolution. Values are shown at 20, 24 and 32 km. The 32 km value represents the top layer of the model, from 0 hPa to 20 hPa and centered at 10 hPa.

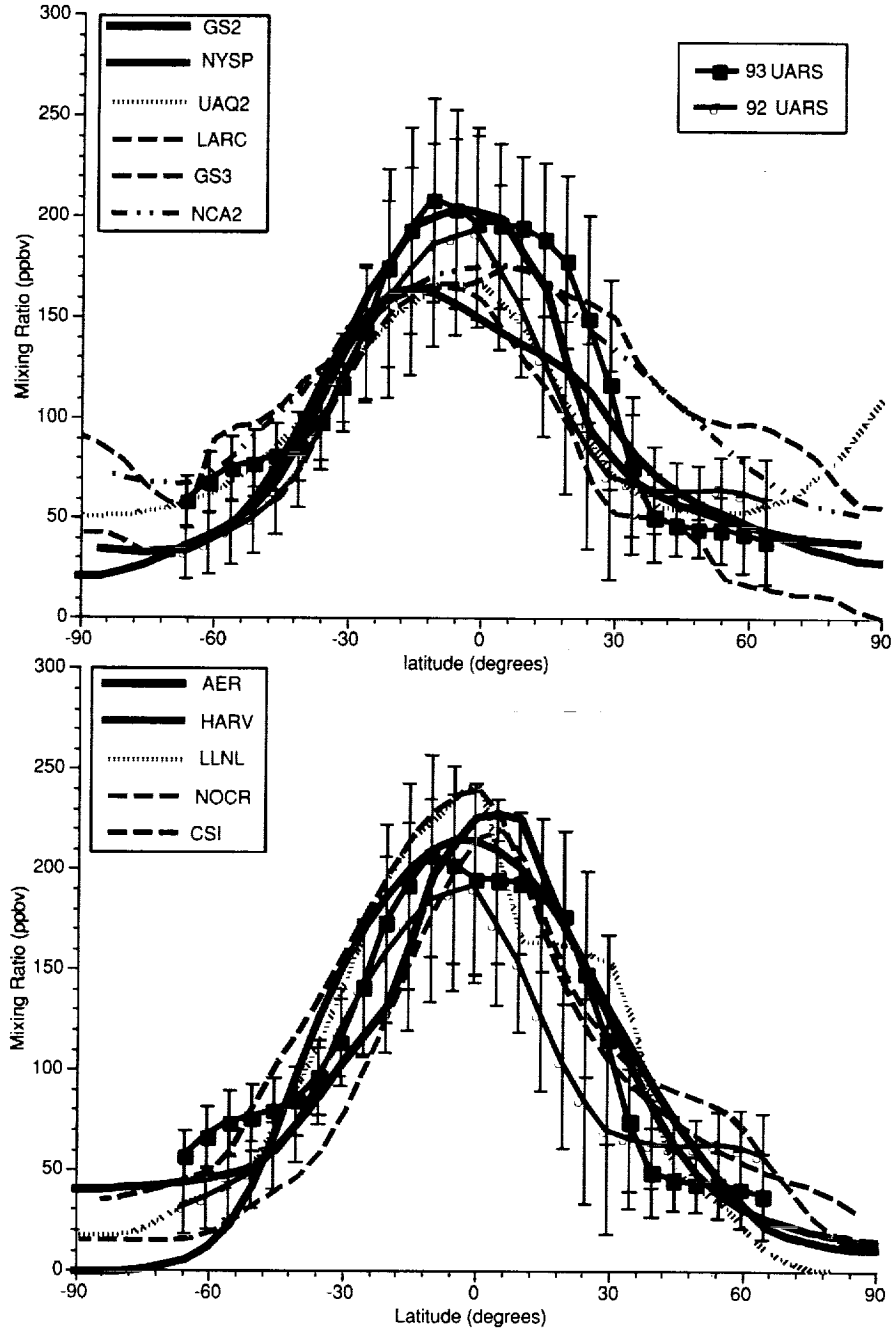

Figure 3.4.4. Calculated N_2O for spring at 10 mb. Symbols denote the spring 10 mb UARS version 7.0 CLAES data. Error bars represent the meridional variations of the N_2O.

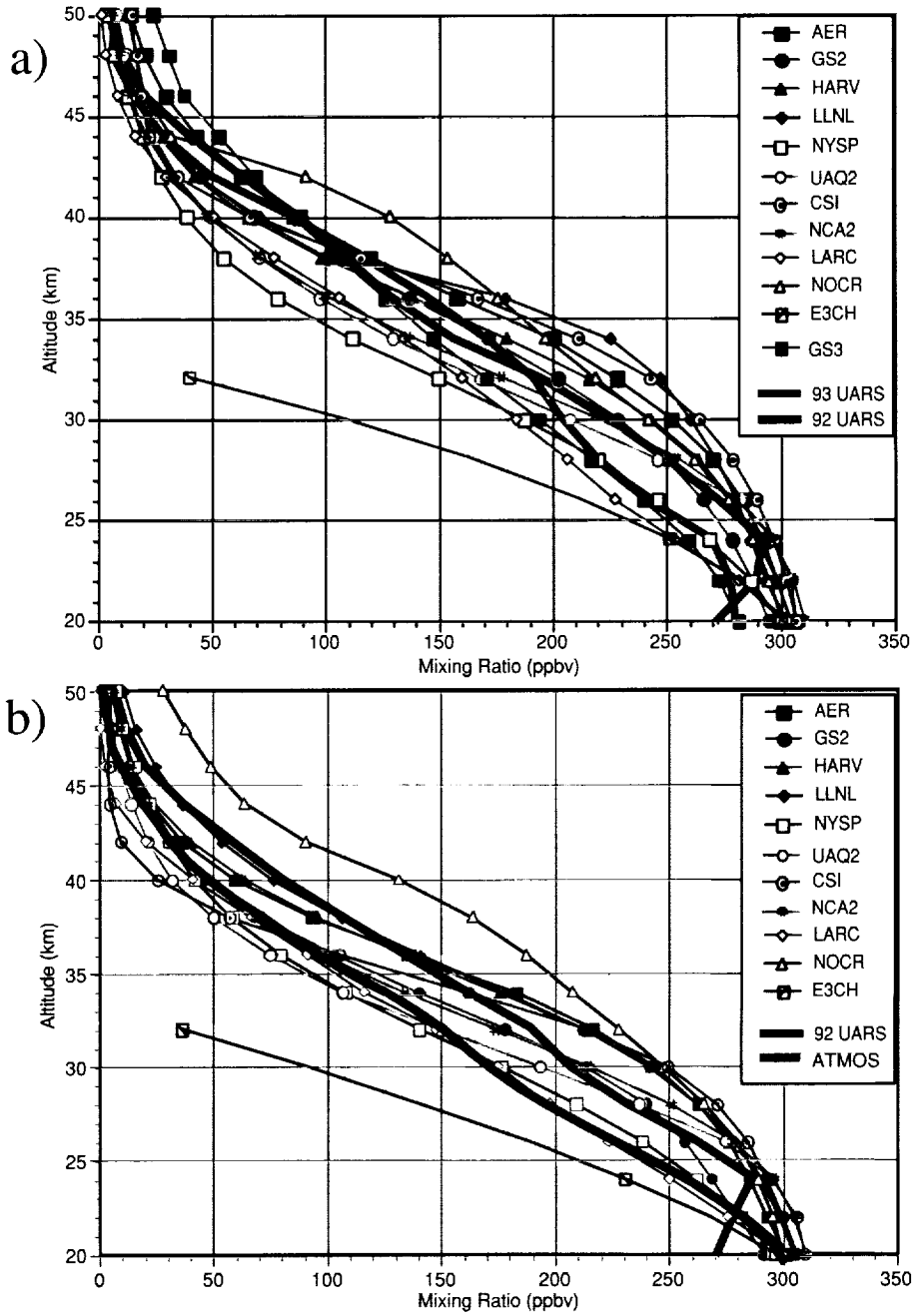

Figure 3.4.5. Calculated N_2O at the equator between 20 and 50 km. Spring data is in the upper panel (a) while fall values are given in the lower panel (b). Solild lines denote UARS and ATMOS data. The E3CH calculated points represent the model's resolution. Values are shown at 20, 24 and 32 km. The 32 km value represents the top layer of the model, from 0 hPa to 20 hPa and centered at 10 hPa.

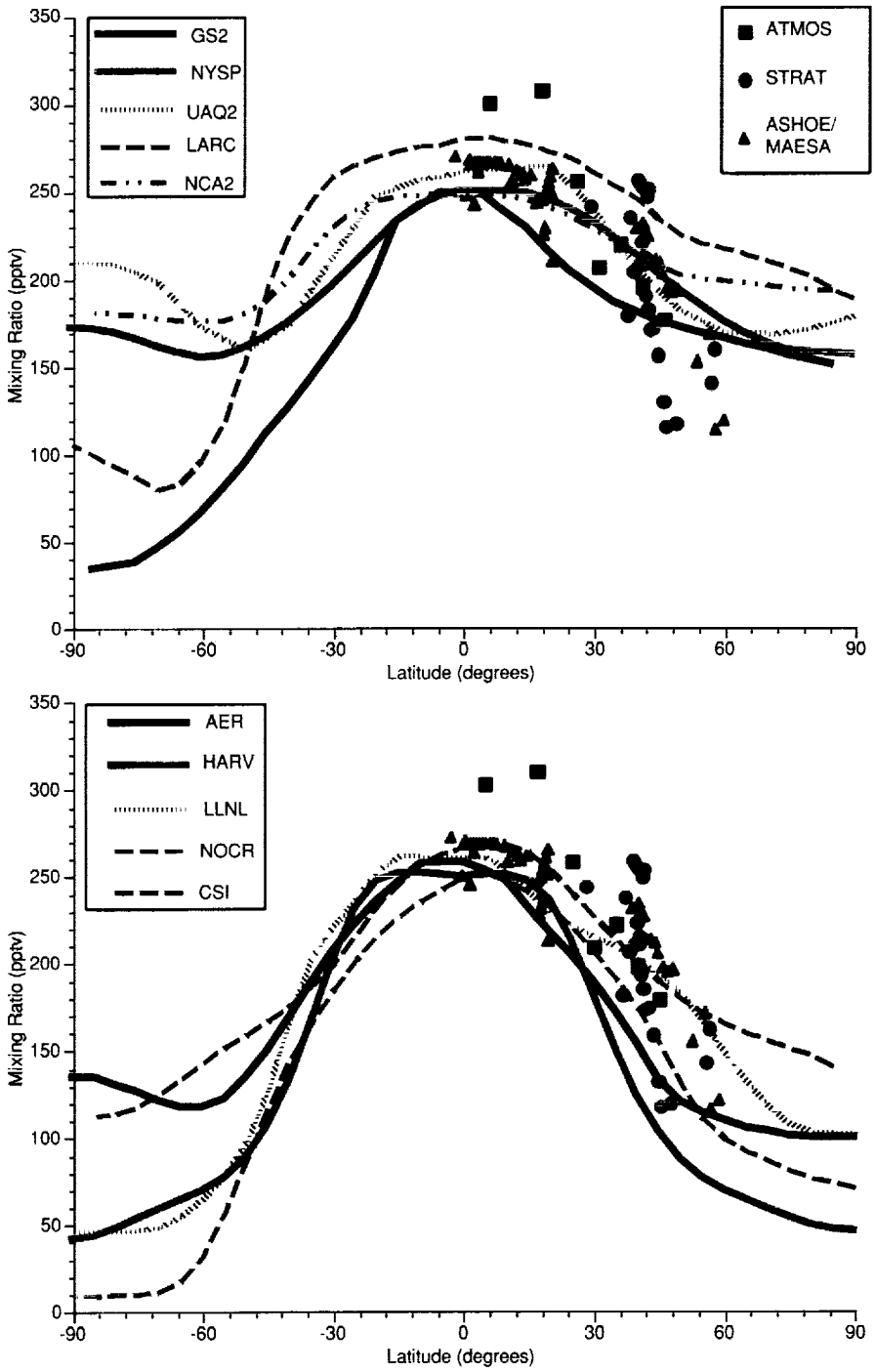

Figure 3.4.6. Calculated $CFCl_3$ for fall at 75 mb. Symbols denote the fall ATMOS and flight data from the STRAT and A/M data sets.

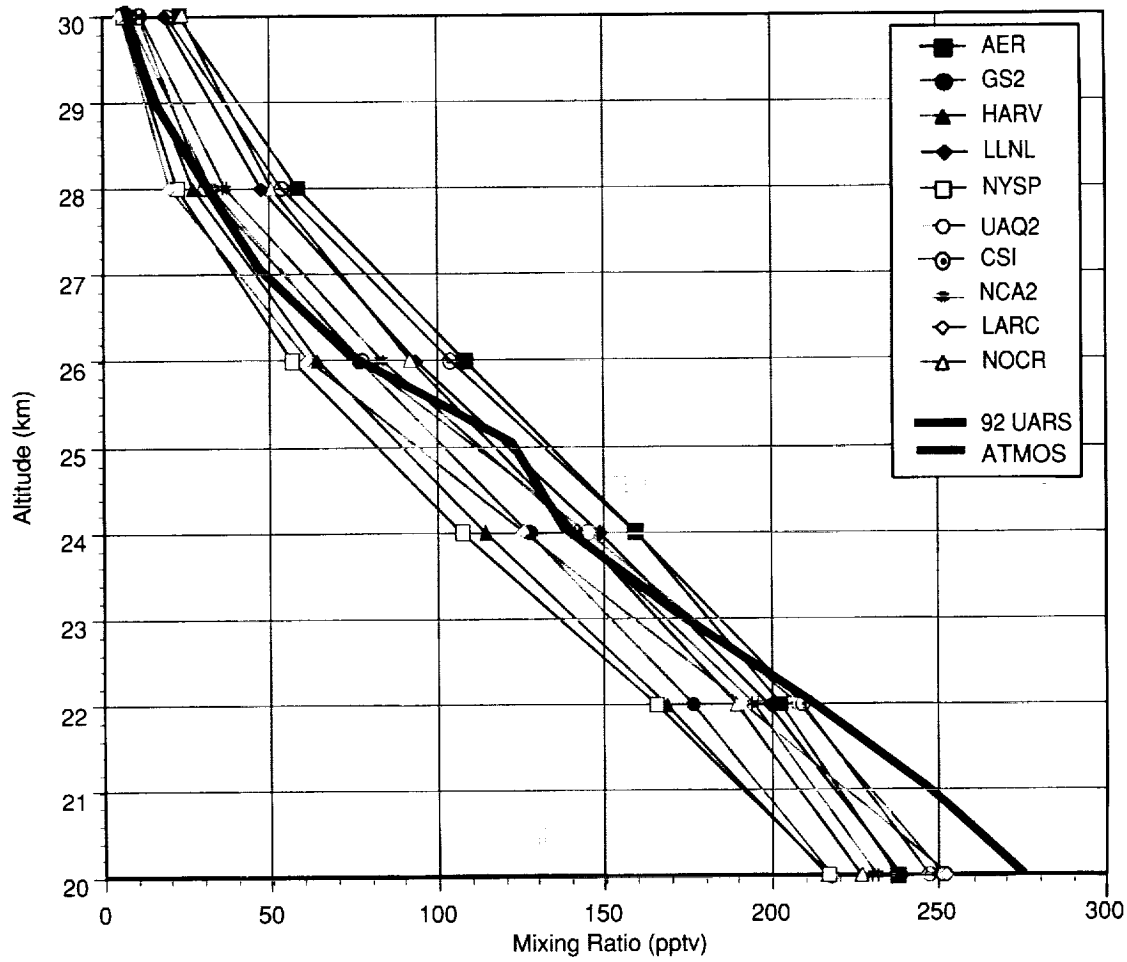

Figure 3.4.7. Calculated $CFCl_3$ for fall at the equator between 20 and 30 km. Solid line denotes ATMOS data.

Table 3.4.1. Calculated global and stratospheric lifetimes in years for participating models and measurements. The global lifetime is the upper value.

	LARC	HARV	GS2	NYSP	UAQ2	CSI	LLNL	AER	@
SPECIES									
N_2O	175 178	122 122	130 132	125 126	122 123	117 118	106 107	109 110	120 124 +/-49
CF_2Cl_2	149 151	92 106	111 112	106 107	105 105	100 101	92 93	92 93	102 77 +/- 26
$C_2Cl_3F_3$	- -	55 59	101 103	87 87	81 82	82 83	81 81	77 77	85 89 +/- 35
$CFCl_3$	57 59	68 70	61 63	49 50	44 44	53 55	49 51	47 48	50 41 +/- 12
CCl_4	44 45	64 67	53 55	39 40	36 36	46 47	42 44	41 42	42 32 +/- 11
CH_4	- -	26.5 157	8.7 168	12.7 164	11.0 166	11.0 155	12.2 140	11.9 128	14.5 84 +/- 35
CH_3Cl	1.4 115	4.4 65	1.4 77	2.0 65	1.8 58	1.8 57	1.9 52	2.0 59	- -
CH_3CCl_3	5.0 49	14.0 64	4.9 56	6.6 42	5.9 37	2.1 47	6.4 43	6.4 42	5.4 30 +/- 9
CH_3Br	1.7 38	5.9 54	1.7 48	2.4 34	2.1 29	6.0 38	2.3 37	2.4 35	1.7* -
$CHClF_2$	- -	34.9 210	11.8 309	16.5 135	14.6 206	14.6 206	16.0 223	15.9 197	13.3 -

@ upper values denote the global lifetimes from the WMO 1995 report, Table 13-1, lower values denote stratospheric lifetimes as given by Volk et. al. 1997 calculations based on ASHOE/MAESA measurements.

* denotes the global lifetime from the WMO 1995 report, Chapter 10.

Table 3.4.2. Calculated stratospheric lifetimes in years of the AER-2-D CTM with different mixing rates in the tropical and sub-tropical region

	NOPIPE	**LEAKY PIPE**	**PIPE**
SPECIES			
N_2O	132	110	103
$C_2Cl_3F_3$	95	78	72
$CHClF_2$	224	205	201
$CFCl_3$	58	49	46
CF_2Cl_2	114	93	87
CCl_4	49	42	40
CH_3Cl	73	63	62
CH_3Br	41	36	35
CH_3CCl_3	49	42	40
CH_4	151	133	128

3.5 NOy and Cly Intercomparisons

XueXi Tie, Guy P. Brasseur, and Theresa Huang

National Center for Atmospheric Research

3.5.1 Nitrogen Compounds

In this section, we compare model calculations of nitrogen compounds (specifically NO, NO_2, NOx, and HNO_3) with available data. NO, NO_2, and NOx are measured by the HALOE instrument (version 18) on board UARS, while HNO_3 are provided by the UARS CLAES instrument (version 7). Vertical profiles of nitrogen compounds at selected latitudes were also measured by the ATMOS instruments which flew at several occasions on the space shuttle as part of the ATLAS program. The information of participating models is presented in Table 3.5.1. Note that the results submitted by 3-D models are 24-hour average, while most of the results submitted by 2-D models are day-time average. As a results, the NO and NO_2 can not be compared directly.

Total Nitrogen (NOy)

Two case runs of NOy results are available for comparison. Case B1 calculates NOy from model dependent N_2O simulations, and case B2 specifies N_2O concentrations. Figure 3.5.1 shows the calculated NOy vertical profiles at various latitudes in July, for cases B1 (Fig. 3.5.1a,b) and B2 (Fig. 3.5.1c). The large increase in NOy concentrations at polar region in winter shown in NCAR and NOCAR models are due to the effect of downward transport of NOy from the mesosphere and the lower thermosphere, as both these models have their upper boundary in the lower thermosphere. Comparison of NOy results of B1 and B2 indicate that the deviation of the NOy results among different models does not improve with the constraint in N_2O concentrations (B2). In fact, the spread of NOy among models are even larger in B2 runs than in B1 runs, especially in the tropics. In the following inter-comparisons, only the B1 results will be used to compare with measurements.

In the tropics and mid-latitudes, the calculated NOy mixing ratios are more similar among models than at higher latitudes. The maximum mixing ratio located near 32 km in the mid-latitudes range from 15 to 20 ppbv; while in the tropics, the NOy maximum is near 40 km, with values ranging from 17 to 25 ppbv. The deviation among models are larger at high latitudes than at lower latitudes. For example, the mixing ratios of NOy at 85N and 30 km varies from 10 to 30 ppbv from model to model.

Nitric Oxide (NO)

Figure 3.5.2 shows the sunset (2a) and sunrise (2b) concentrations of NO measured by HALOE for four different seasons as a function of latitude and height. The NO concentrations between sunset and sunrise are similar, expect that the sunset concentrations are slightly larger than the sunrise concentrations. In all seasons, NO mixing ratio increases with height above the tropopause (typically 2 ppbv at 30 km, 6 ppbv at 35 km, and 10 ppbv at 40 km in the tropics). In the tropics, it reaches a maximum of about 15 ppbv at approximately 45 km. The location of this maximum varies slightly with season (30S in March, 20N in June, 30N in September, 5S in December). Above 45 km, the mixing ratio decreases to about 3 ppbv at 58 km.

For comparison with the HALOE measurement, Figure 3.5.3 shows the model calculated daytime NO latitude-height cross section in March and September. In general, the model NO results exhibit similar features to the HALOE data. All models shows an increase in NO concentration from the tropopause to a maximum at around 45 km in the tropics. However, the NO maximum concentration are quite different among different models. For example, during March at 45 km, NO mixing ratios range from 12 ppbv (HARVARD) to 20 ppbv (GSFC-2D, NOCAR, and CSIRO). In addition, the observed seasonal variabilities of the shift in latitude location of the maximum at 45 km (15S in March and 20N in September) are not simulated in the models.

To compare the seasonal variation of the NO maximum, Figure 3.5.4 shows the NO mixing ratio (ppbv) at 40 km, 50N. Measurements of NO by HALOE indicates that it has a very small seasonal variation with a maximum concentration in November (9 ppbv), and a minimum concentration in August (8 ppbv). The majority of the model results of NO do not exhibit this type of seasonal variation. In addition, large deviations in NO concentrations exhibit among models.

The NO vertical profiles at 50N are compared between models and HALOE and ATMOS measurement in November (Fig. 3.5.5). The vertical profile of NO was measured at 49N by ATMOS and corrected for the diurnal effects by Newchurch et al. (1996). The measured profiles indicate a daytime mixing ratios of 0.10 ppbv at 15 km, 0.07 ppbv at 20 km, 1 ppbv at 25 km, and a maximum of around 7.5 ppbv at 44 km. The model results of NO exhibit a large deviation from model to model. In particular, at 44 km, the NO values range from 5 ppbv to 15 ppbv. It is worth noting, that the NO from the UNIVAQ-2D model show a closet comparison to measurements at this latitude location. Note that 3-D models (LARC-3D and SLIMCAT) tend to underestimate NO concentrations. Since the 3-D model results of NO represent diurnally averaged value instead of the daytime averaged value from the 2-D model and the MLS measurements, their values tend to be lower. This is due to fact that the concentration of NO is smaller during the night.

Nitrogen Dioxide (NO_2)

Sunset NO_2 abundances derived from HALOE observations (Fig. 3.5.6a) as a function of latitude and height in the stratosphere are characterized by mixing ratios of typically 1 ppbv at 20 km, 6 ppbv at 30 km, and a maximum of 8-9 ppbv at 35 km. The mixing ratio decreases with altitude to less than 1 ppbv above 48 km. The NO_2 concentration exhibit a pronounced diurnal cycle as a result of the effect of NO_2 photolysis during the daytime; therefore, sunrise NO_2 abundances are smaller than sunset abundances. A seasonal cycle is visible, which tends to shift the mixing ratio maximum towards the summer high latitudes. The model simulated NO_2 daytime-averaged mixing ratios in June and December are shown in Figure 3.5.7. The model results have similar maximum locations (around 35 km) compared to the HALOE measurements. However, the magnitude of the NO_2 maximum at 35 km is quite different among different models, ranging from 5 ppbv (HARVARD) to 8 ppbv (NCAR-2D and NOCAR) in June.

The seasonal variation of the maximum concentration of NO_2 at 40 km and 50N is compared between the models and HALOE measurements (Figure 3.5.8). The comparison show that some models (such as CSIRO, LLNL, GSFC-2D, and SUNT_SPB) produce a similar seasonal variation of NO_2 compared to HALOE measurements, exhibiting a very small seasonal variation. However, 3-D models are the exceptions which produce a large seasonal variation compared to HALOE measurement.

Figure 3.5.9 shows the vertical profiles of NO_2 mixing ratio at 50N in November for the model results and HALOE measurements. It indicates that most models produce NO_2 profiles that are in good agreement with that of HALOE measurements. The 3-D model NO_2 results presented here is probably

higher since the results submitted are diurnal averaged value instead of the daytime averaged value submitted by the 2-D models. Because the concentration of NO_2 is higher during the night, the 3-D model results tend to be higher than the 2-D model results and the observation.

NOx ($NO+NO_2$)

Sunset NOx abundances derived from HALOE observations (Fig. 3.5.10) as a function of latitude and height in the stratosphere are characterized by mixing ratios of typically 6 ppbv at 20 km, 10 ppbv at 30 km, and a maximum of 16 ppbv at 40 km. Unfortunately, there are no data at polar region in winter to check the downward transport from the mesosphere. The model simulated NOx daytime-averaged mixing ratios in June and December are shown in Figure 3.5.11. The model results show that the location and the magnitude of the NOx maximum are quite different among different models, e.g. the magnitude of NOx ranges from 14 ppbv (GSFC-3D) to 24 ppbv (CSIRO) in March.

To compare the seasonal variation of the NOx concentration, Figure 3.5.12 shows the NOx mixing ratio (ppbv) at 40 km, 50N. Measurements of NOx by HALOE indicates that it has a very small seasonal variation. However, some models a large seasonal variability. The deviation of modeled NOx concentrations is very large, indicating that the differences among the modeled NO and NO_2 concentrations mentioned above are not only due to the defences in the partitioning of NO and NO_2, but also are due to the differences in the calculation of NOx. Note that the NOx mixing ratio of 3-D models (SLIMCAT and LARC-3D) is much consistent with measurements, which further explains that the underestimation of NO and overestimation of NO_2 in the 3-D models are due to fact that the results submitted are diurnal averaged value.

Figure 3.5.13 shows the vertical profiles of NOx mixing ratio at 50N in November for the model results and HALOE measurements. The model results of NOx exhibit large deviations from model to model, which is similar to NO results shown in Figure 3.5.5. This indicates that the large diversities of NO among the models are the major contributor to the NOx differences.

Nitric Acid (HNO_3)

Figure 3.5.14 shows the meridional distribution of HNO_3 as observed by CLAES during four seasons. In this case, the maximum mixing ratio is found at high latitudes (near 25 km), and is most pronounced during winter, when HNO_3 photolysis is weak. During winter and early spring, in the lower stratosphere, there is an indication of HNO_3 removal as a result of PSC formation and sedimentation. Figure 3.5.15 shows the calculated HNO_3 meridional distributions in June and December. In general, the meridional distributions between models and CLAES measurements are quite similar. For example, both models and measurements shows two maxima at high latitudes and a minimum in the tropics in the lower stratosphere. The high latitude maximum is larger in winter than in summer. In the Antarctic winter, some models (AER, GSFC-2D, and UNIVAQ-2D) simulates a decease in HNO_3 concentrations as a result of PSC formation.

Figure 3.5.16 shows the seasonal variation of HNO_3 mixing ratio at 60S and 24 km for model calculations and measurements provided by CLAES. The model results of HNO_3 have a similar seasonal variations as the measurements (higher in winter and lower in summer). However, the concentrations among the models are very different, which range from 7 to 20 ppbv in winter, and 6 to 15 ppbv in summer.

Figure 3.5.17 shows the vertical profiles of HNO_3 at 60N in November for the model results and CLAES measurements. Both model results and CLAES measurements are characterized by a maximum centered at around 25 km. The CLAES maximum at this altitude is about 11 ppbv, while the model results have a wide spread in values, ranging from 7 ppbv to 16 ppbv.

NOx /NOy

Finally, the ratio of NOx/NOy is compared among models. Figure 3.5.18a shows the seasonal variation of NOx/NOy at 34 km, 60S. The result indicates that the seasonal variations among models are very similar, which exit a maximum in January and a minimum in July. The deviation of modeled NOx/NOy is relatively small in January (from 0.7 to 0.8), and relatively large in July (from 0.25 to 0.55). Figure 3.5.18b shows the vertical profiles of NOx/NOy at 40N in November for the model results. The model results of NOx/NOy exhibit large deviations in the troposphere, the ratio of NOx/NOy is relatively high from the model results of UNIVAQ-2D, NCAR-2D, and GSFC-2D, and relatively low from the model result of CSIRO. In the stratosphere, the model results are similar, except that in the lower stratosphere the SUNY-SPB result is slightly higher than the other models.

3.5.2 Chlorine Compounds

Satellite observations of the most abundant inorganic chlorine compounds HCl, $ClONO_2$, and ClO, are available from UARS (ClO from MLS of version 3, HCl from HALOE of version 18, and $ClONO_2$ from CLAES of version 7). Vertical profiles of the same three compounds were also measured by ATMOS at selected locations. Note that the results submitted by 3-D models are 24-hour average, while the results submitted by 2-D models are day-time average. As a results, the ClO and $ClONO_2$ can not be compared directly.

Total Inorganic Chlorine (Cly)

The model simulated Cly for two case runs B1 and B2 are compared. Case B1 calculated Cly according to the model simulated CFCs concentrations, and case B2 uses a specified CFCs concentrations. Figure 3.5.19 shows the calculated Cly vertical profiles at 85S, 45S, equator, and 85N in July for cases B1 (Fig. 3.5.19a,b) and B2 (Fig. 3.5.19c). Similar to the comparisons of NOy, the comparison of NOy from B1 and B2 indicates that a constraint of CFCs on the model does not produce a better comparison of Cly between different models. The spread of values among models are actually greater for B2 than the B1 runs. In the following inter-comparisons, only the B1 results will be used to compared with measurements.

Chlorine Monoxide (ClO)

The MLS observations of ClO for the months of March, June, September and December is shown in Figure 3.5.20. In March, the ClO maximum at 40 to 45 km reaches approximately 0.6 to 0.7 ppbv at higher latitudes. In the tropics, the maximum mixing ratio of ClO is on the order of 0.2 ppbv. Figure 3.5.21 shows the calculated ClO meridional distribution in March (Fig. 3.5.21a,b) and in September (Fig. 3.5.20c,d). In general, the meridional distribution of the model ClO results compares well with MLS measurements, which indicates two maxima in high latitudes at 45 km and a minimum in the tropics at 40 km. In September, large ClO concentrations are produced in the southern polar latitudes between 15 and 30 km as a results of the formation of PSCs in most of the models. The large ClO concentration in the polar region is consistent with MLS measurements.

In Figure 3.5.22 the seasonal variation of ClO is compared between the models and MLS measurements at 44km and 45S. The seasonal change exhibit in the MLS data implies a higher concentration in winter (0.7 ppbv in August) and a lower concentration in summer (0.55 ppbv in January). Model results indicates a somewhat similar seasonal variation compared to the MLS observations, except for the LARC-3D model which shows a ClO seasonal variation that is very uniform in time. Some models also show large discrepancies from the observed values. In August, the calculated ClO mixing ratios range from 0.4 to 1.1 ppbv, and in January, ClO range from 0.3 to 0.75 ppbv. Note that 3-D models (LARC-3D and SLIMCAT) tend to underestimate ClO concentrations. Since the 3-D model results of ClO represent diurnally averaged value instead of the daytime averaged value from the 2-D model and the MLS measurements, their values tend to be lower. This is due to fact that the concentration of ClO is smaller during the night. The SLIMCAT model has included ClO+OH -> $HCl+O_2$ as a 5% channel. This reaction tends to reduce ClO concentration in the upper stratosphere.

Figure 3.5.23 shows the vertical profile of ClO at 40N in November by model calculations and by measurements from MLS and ATMOS. Mixing ratio of ClO derived by Zander et al. (1996) for the 1994 November ATMOS flight at 39-49N is approximately 0.2 ppbv at 30 km, 0.5 ppbv at 37 km (maximum value), and less than 0.1 ppbv at 50 km. Mixing ratio provided by MLS at 40N is of similar values below 35 km. However, above 35 km, the MLS ClO mixing ratios are slightly higher than the ATMOS measurements. Both the model ClO results and the measurements have maximum mixing ratio located between 37 and 40 km, except for the SLIMCAT model that has the maximum located at 45 km. The magnitudes of the maxima are widely spread, from to 0.3 ppbv (LARC-3D) to 1.3 ppbv (UNIVAQ-2D). This in contrast to the values of 0.55 to 0.6 ppbv as measured by ATMOS and MLS.

Chlorine Nitrate ($ClONO_2$)

Figure 3.5.24 shows the ClONO2 mixing ratio measured by CLAES. It shows a $ClONO_2$ maximum at high latitudes between 25 and 30 km. This maximum is most pronounced in winter, where it reaches a value between 1.4 and 1.6 ppbv, when the photolysis of $ClONO_2$ is at its weakest. On the other hand, a typical mixing ratio in the tropics is 0.1 ppbv at 20 km, 0.6 ppbv at 30 km, and 0.2 ppbv at 40 km. Lower $ClONO_2$ mixing ratio (less than 0.2 ppbv) is seen below 20 km in the southern hemisphere polar region from June to September when heterogeneous chemistry converts chlorine reservoirs into reactive chlorine radicals. Figure 3.5.25 shows the calculated $ClONO_2$ meridional distributions in June (24a) and December (24b). The meridional distribution of the model results and the CLAES measurement compares well, in particular the two maxima in high latitudes and a minimum in the tropics in the lower stratosphere. However, the observed seasonal variations of $ClONO_2$ is not reproduced well in models, particularly the maximum concentrations in high latitudes that is higher in winter than in summer. In winter Antarctic, most of the model simulate a depletion of $ClONO_2$ as a result of heterogeneous reactions on the surface of PSC, but with large differences in the depletion magnitude. In particular, the SUNY_SPB model simulates a very small heterogeneous depletion of $ClONO_2$, while the AER and LLNL models simulate the strongest heterogeneous depletion.

The seasonal variation of $ClONO_2$ at 60S and 30km is shown in Figure 3.5.26 from model calculations and CLAES observation. The measured seasonal variability provided by CLAES is rather pronounced. It is highest in July (12 ppbv) and lowest in January (0.5ppbv). None of the model can reproduce this seasonal variability. In general, all the models overestimate its concentration in summer. For example, in January, the calculated $ClONO_2$ mixing ratio range from 0.8 to 1.3 ppbv compared to the observed 0.5 ppbv by CLAES. In winter, the observed value falls within the range of calculated $ClONO_2$ concentrations, but the spread of $ClONO_2$ value among the models is great, with values ranging from 0.5 ppbv to 1.5 ppbv.

The vertical profiles of $ClONO_2$ at 40N in December is shown in Figure 3.5.27 for the model calculations and the profile measured at 35-49N by Zander et al. (1996) during the ATMOS/ATLAS mission, and by CLAES. The ATMOS profile is characterized by mixing ratios of 0.4 ppbv at 20 km, 0.9 ppbv at 27 km (maximum value), 0.1 ppbv at 40 km. Mixing ratio provided by CLAES at 40N is very similar to ATMOS below 25 km. However, above 25 km, the CLAES $ClONO_2$ mixing ratio is slightly higher than the ATMOS measurements. Both the model results and the measurements have maximum mixing ratio located between 22 and 30 km. The magnitudes of maxima are widely spread among the models, ranging from 0.8 ppbv (LLNL) to 1.6 ppbv (NCAR-2D). Compared with the measured maxima (0.9 ppbv by the ATMOS and 1.0 ppbv by the CLAES), most models simulate $ClONO_2$ value that are consistent with the observed values, especially the LLNL, CSIRO, NOCAR, HARVARD, UNIVAQ-2D, and SUNY_SPB models.

Hydrogen Chloride (HCl)

Shown in Figure 3.5.28 is the mixing ratio of HCl as measured by HALOE. The HCl mixing ratio is relatively uniform in latitude above 30 km, and its value reaches around 2.8 ppbv at 45 km. Its mixing ratio increase with altitude, with value of typically 0.2 ppbv at the tropopause, 1.6 ppbv at 30 km, and 2.5 ppbv at 40 km. In the lower stratosphere, the HCl mixing ratio increases with latitude. At 20 km, its value ranges from 0.4 ppbv at the equator to about 1.4 ppbv at 60 N. In Figure 3.5.29, the calculated HCl mixing ratio of June (29a,b) and December (29c,d) is shown. In general, the calculated mixing ratios of HCl in the tropics and in mid-latitudes decrease with altitude between the tropopause and 50 km. However, at high latitudes, the disparity among models are more complex. In particular, some model results (AER, GSFC-2D, NOCAR, LLNL, and SLIMCAT) suggest the depletion of HCl as a result of the formation of PSCs. Note that SUNY_SPB model submits day-time mean data everywhere except polar night regions, so that polar night results are included in the figures.

Figure 3.5.30 shows the seasonal variation of HCl for models and from HALOE measurements at 60S and 34 km. The HALOE measurement of HCl shows a weak seasonal variation. For most of the model, the calculated seasonal variation of HCl is also very uniformed in time, except the HARVARD model in which a strong seasonal variation is produced. The magnitude of HCl mixing ratio from models is in general smaller then that measured by HALOE.

Figure 3.5.31 shows the vertical profile of HCl mixing ratio from model estimates and that measured during the ATMOS/ATLAS mission in November, 1994 (35-49 N) by Zander et al. (1996). The measured HCl is 1.2 ppbv at 20 km, 2 ppbv at 27 km, 2.9 ppbv at 40 km, and 3.4 ppbv at 48 km. At 48 km, nearly all the chlorine loading is in the form of HCl. Compared to these observation values, model results also show a decrease with latitude for the mixing ratio of HCl (see Fig. 3.5.30), but overall the calculated mixing ratios of HCl are lower than the ATMOS results. The calculated HCl concentrations are widely spread among the models. For instance, at 35 km, the calculated highest value of HCl is about 2.8 ppbv which is close to the measured value, while the calculated lowest value of HCl is about 1.5 ppbv which is about half of the measured value.

3.5.3 Brief Summary

Following is the conclusion drawn from the comparison of NOy and Cly between models and measurements by UARS and ATMOS: (1) The calculated NOy differ by 30% among different models. The difference among the models are even larger with constrained N_2O distributions. (2) The calculated NO mixing ratios differ widely among models, while most of the models fail to reproduce the HALOE seasonal variabilities of NO maximum at 45 km. (3) The calculated seasonal variability of NO_2 maximum

at 34 km in mid-latitudes agrees well with HALOE measurements. The model NO_2 concentrations is more similar among models than the NO concentrations. At 50N in November, the calculated vertical profiles agree well with the HALOE measurement. (4) The model simulated seasonal variability of the HNO_3 maximum at 24 km in high latitudes agree well with CLAES measurements, but the calculated magnitude in HNO3 shows a wide spread in values among models. (5) The calculated Cly differ by 10% among different models. The difference is even greater with constrained CFCs distributions. (6) The ClO mixing ratio shows a wide spread in values among different models in both the profile and the seasonal variation. (7) The model simulated $ClONO_2$ agrees well with CLAES and ATMOS measurements in mid-latitudes. However, the seasonal variation of CLAES measurement cannot be reproduced by all models. (8) The HCl mixing ratio varies widely among models. The model estimates are generally lower than HALOE and ATMOS measurements.

Acknowledgements

We thank K. Sage for making all plots for this analysis. The UARS data are analyzed by W. Randel and F. Wu at NCAR Atmospheric Chemistry Division. We also thank all modelers for providing their model results.

References

Zander, R, et al., The 1994 northern midlatitude budget of stratospheric chlorine derived from ATMOS/ATLAS-3 observations, *Geophys. Res. Lett.*, *23*, 2357-2360, 1996.

Michelsen et al., Stratospheric chlorine partitioning: Constraints from shuttle-borne measurements of HCl, $ClNO_3$, and ClO, *Geophys. Res. Lett.*, *23*, 2361-2364, 1996.

Newchurch, M., et al., Stratospheric NO and NO_2 abundances from ATMOS solar-occulation measurements, *Geophys. Res. Lett.*, *23*, 2373-2376, 1996.

Aelig, C.P., et al., Latitudinal distribution of upper stratospheric ClO as derived from space bound microwave spectroscopy, *Geophys. Res. Lett.*, *23*, 2321-2334, 1996.

Table 3.5.1. Participating models

AER	2-D
CSIRO	2-D
ECHAM3	3-D
GSFC-2D	2-D
GSFC-3D	3-D
HARVARD	2-D
LARC-3D	3-D
LLNL	2-D
NCAR-2D	2-D
NOCAR	2-D
SLIMCAT	3-D
SUNY_SPB	2-D
UNIVAQ-2D	2-D

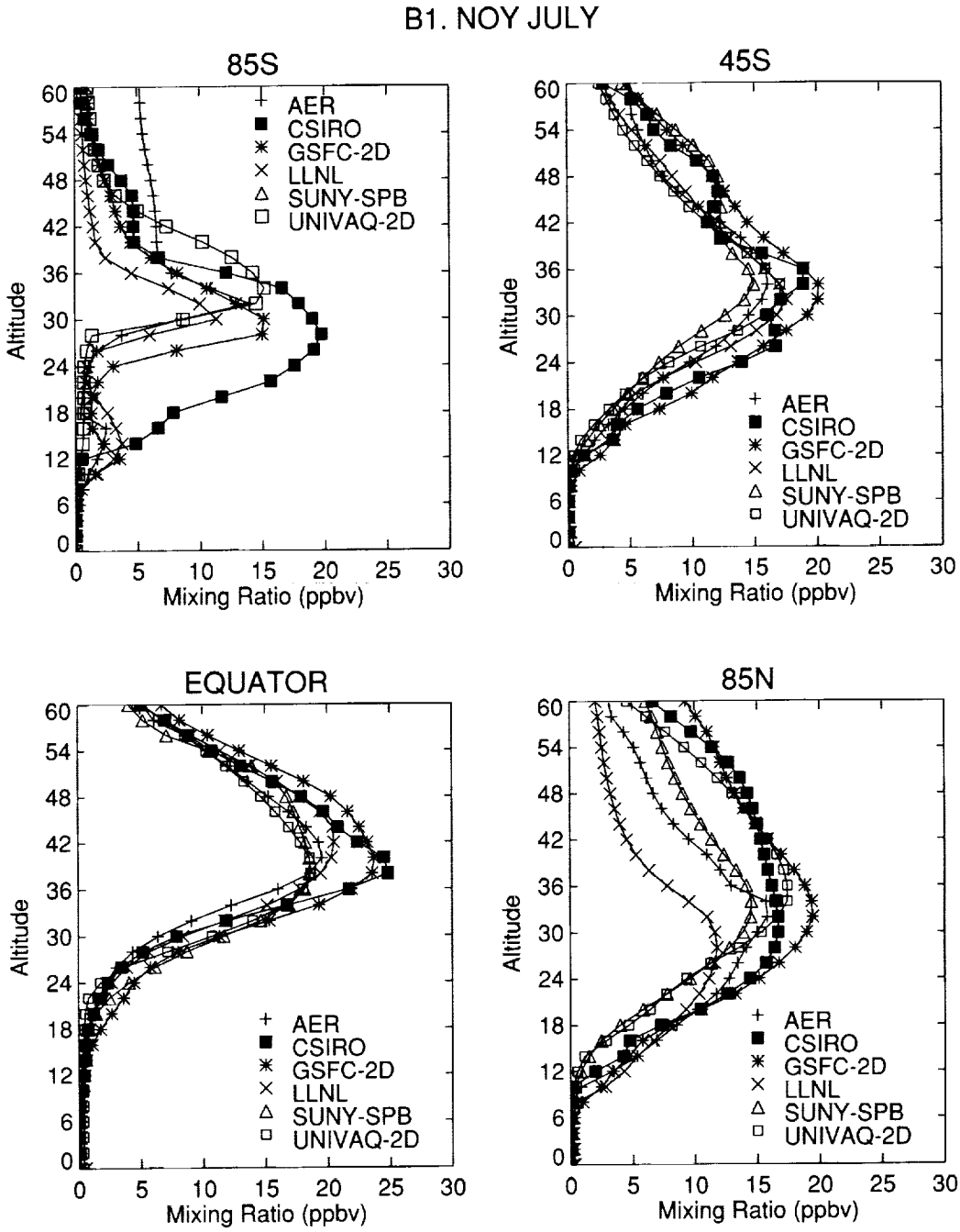

Figure 3.5.1a. Vertical profiles of model calculated NOy at 85S, 45S, equator, and 85N in July for case (a-b) B1 and (c) B2.

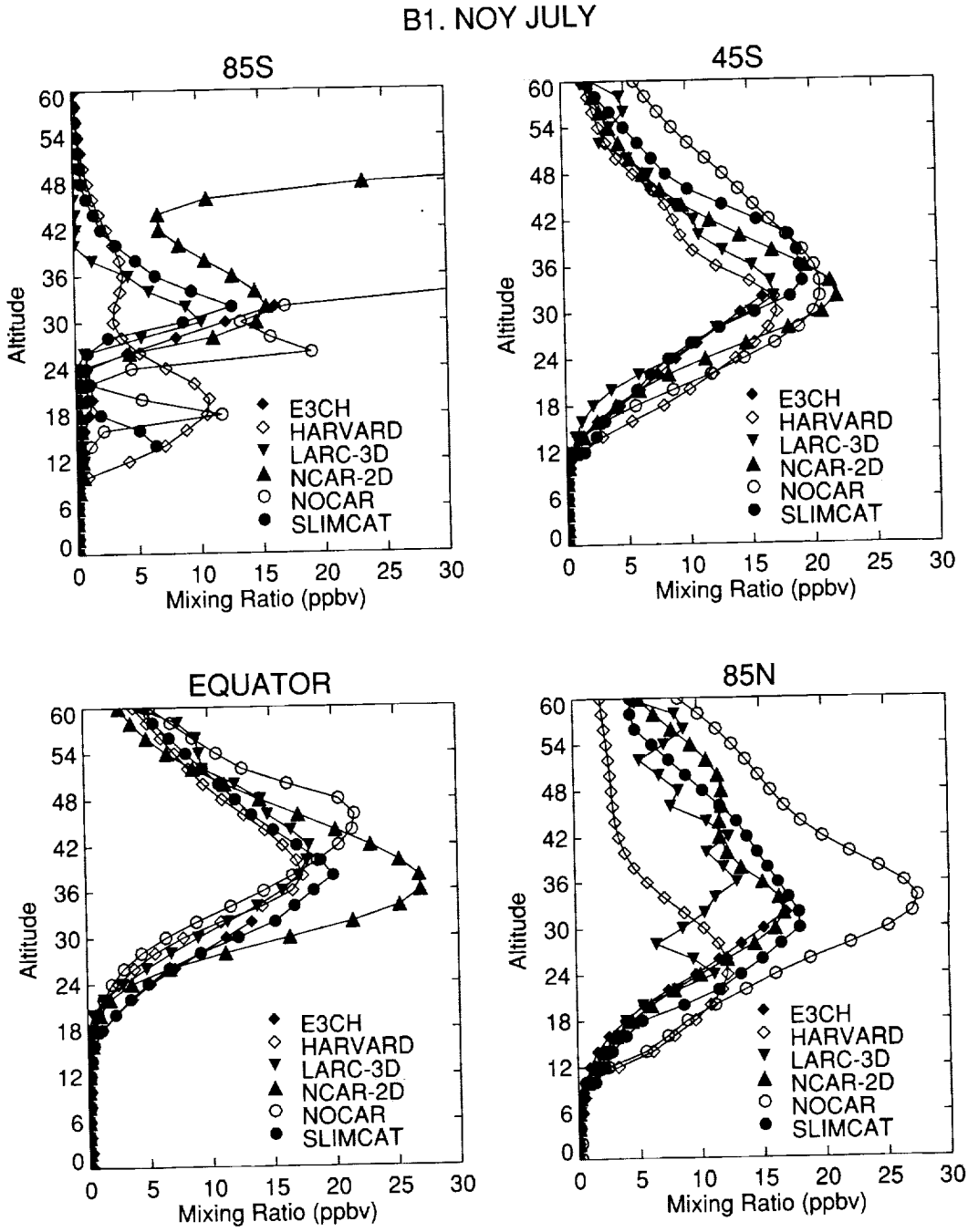

Figure 3.5.1b. Continued.

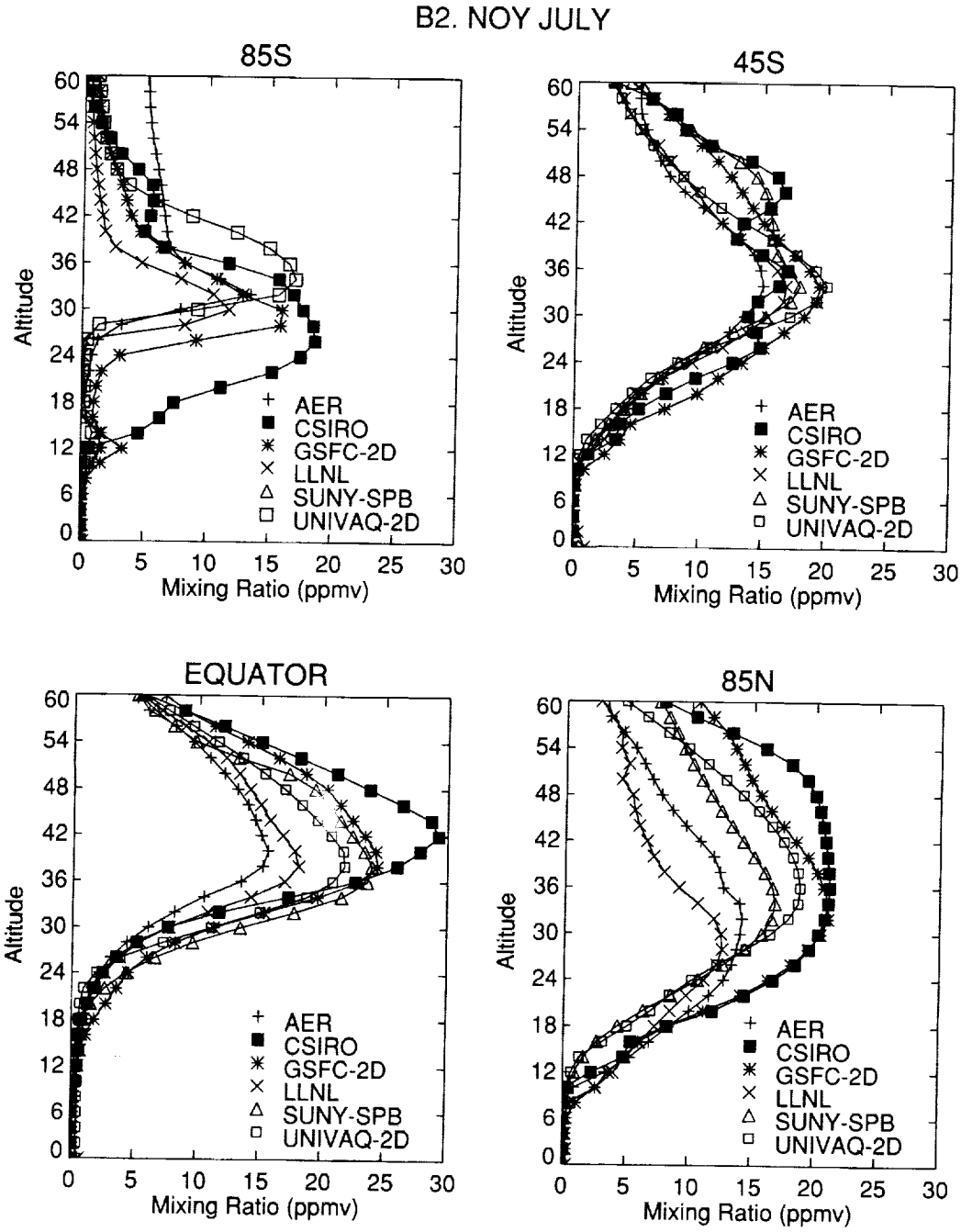

Figure 3.5.1c. Concluded.

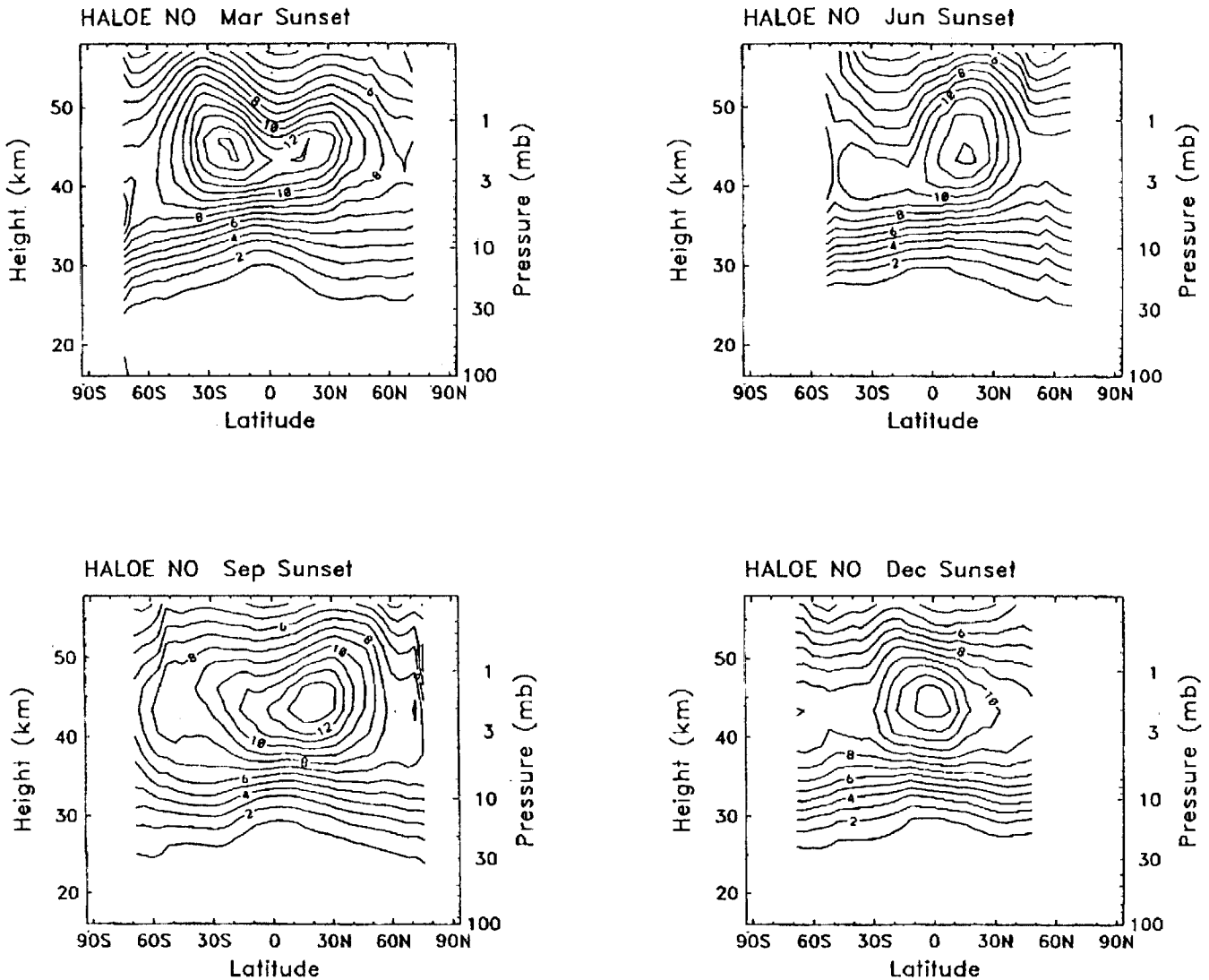

Figure 3.5.2. HALOE measured NO latitude-height cross section for March, June, September and December from (a) sunset measurements and (b) sunrise measurements.

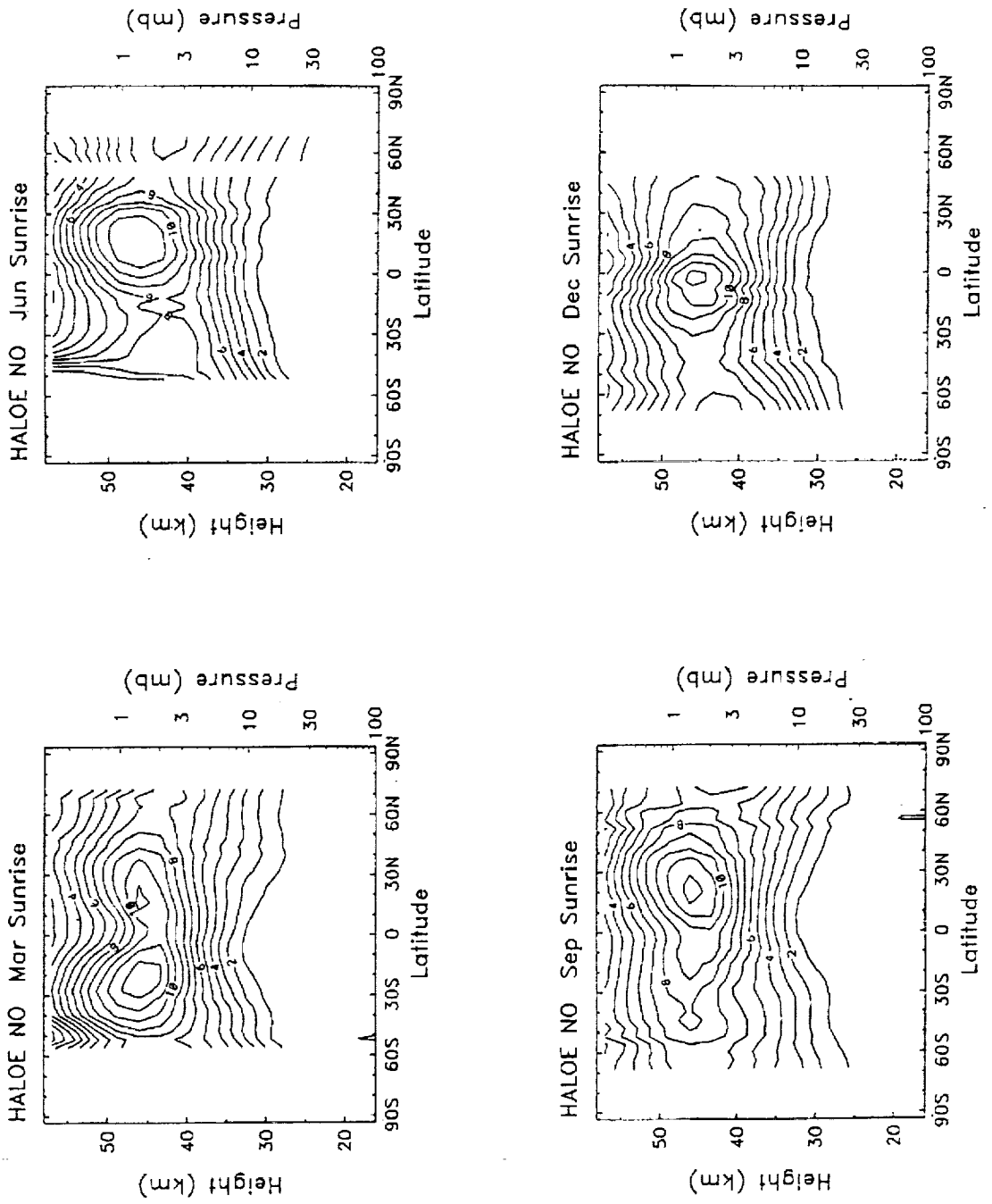

Figure 3.5.2. Concluded.

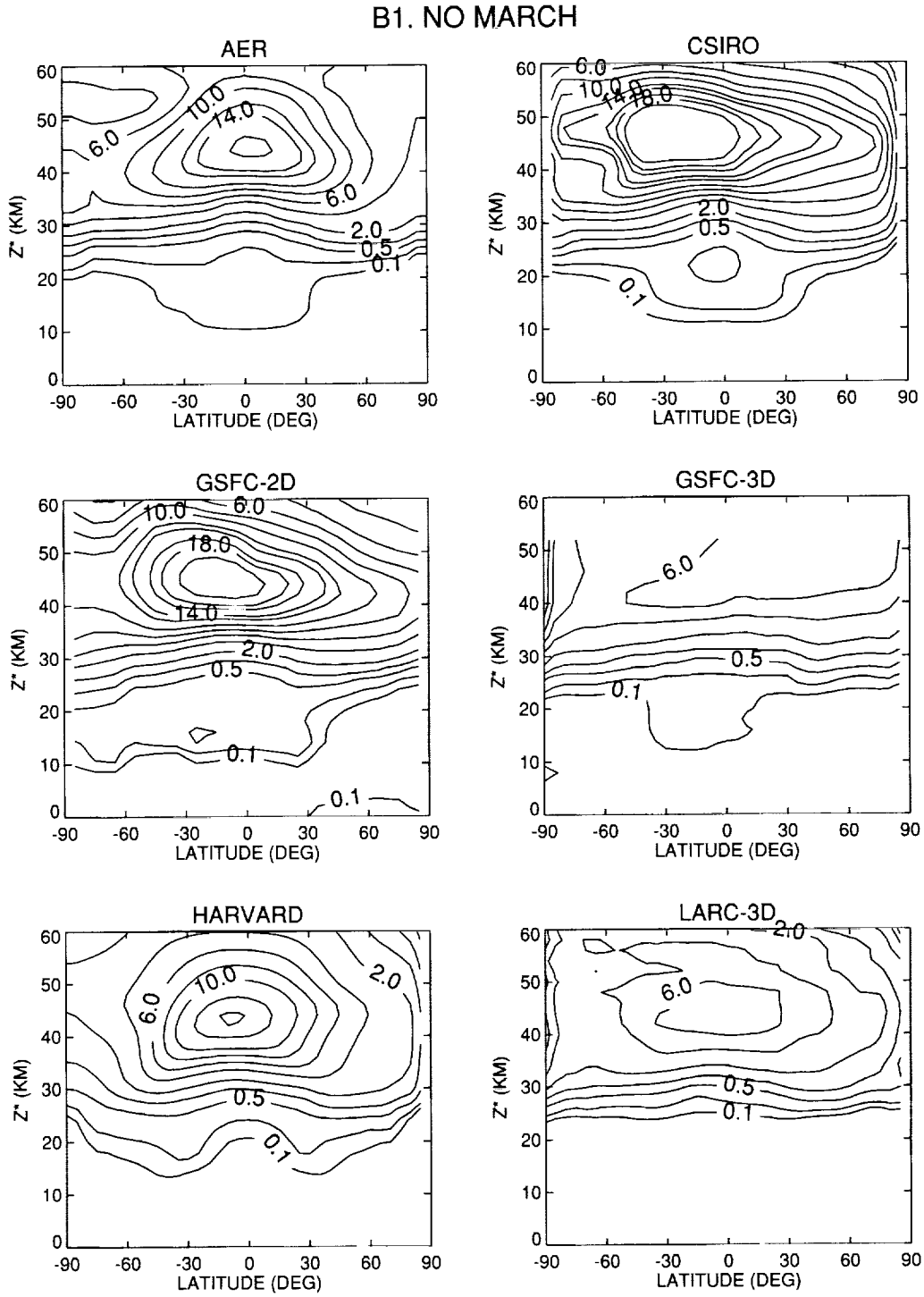

Figure 3.5.3. Model simulated daytime averaged NO latitude-height cross section for (a-b) March and (c-d) September.

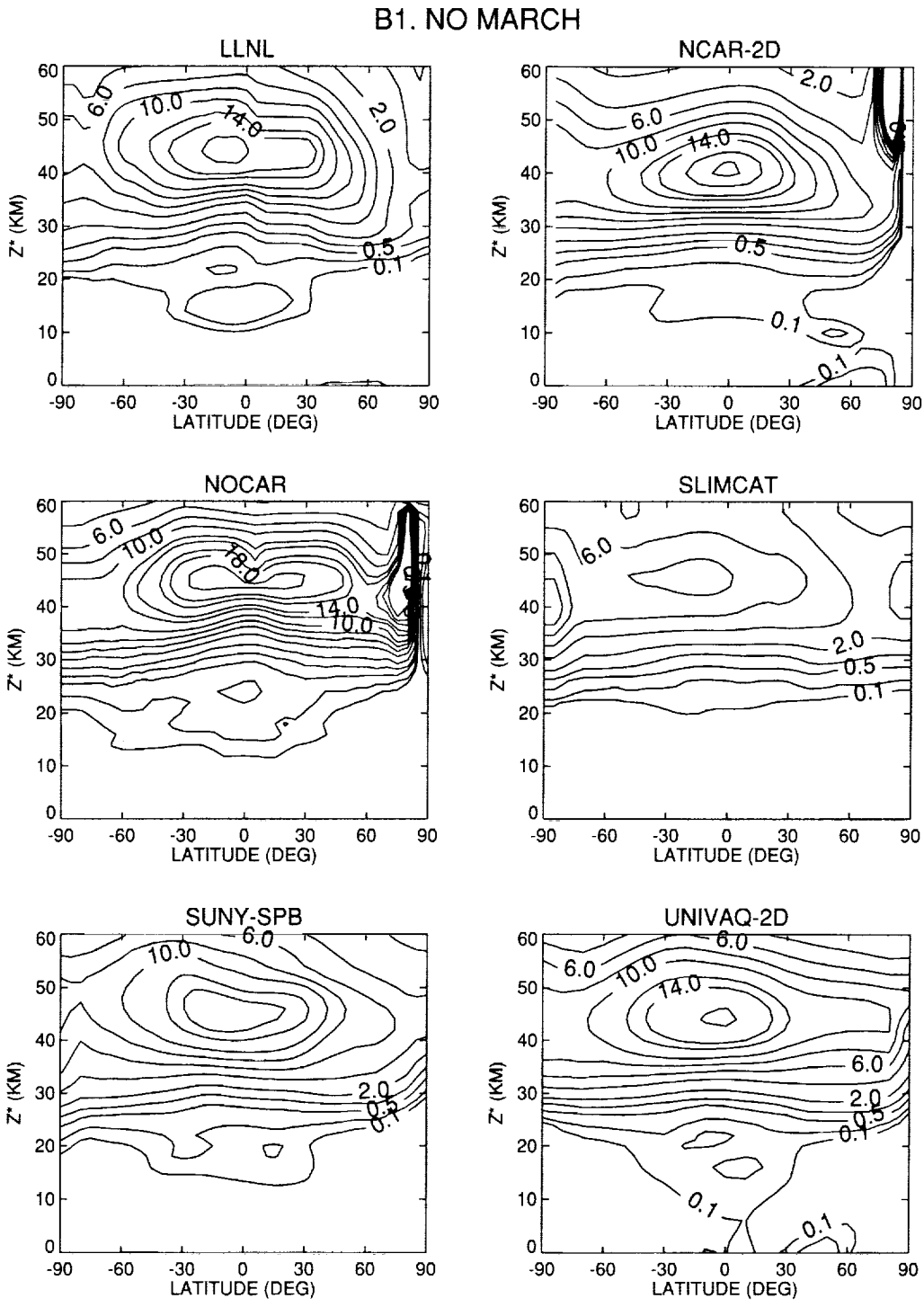

Figure 3.5.3. Continued.

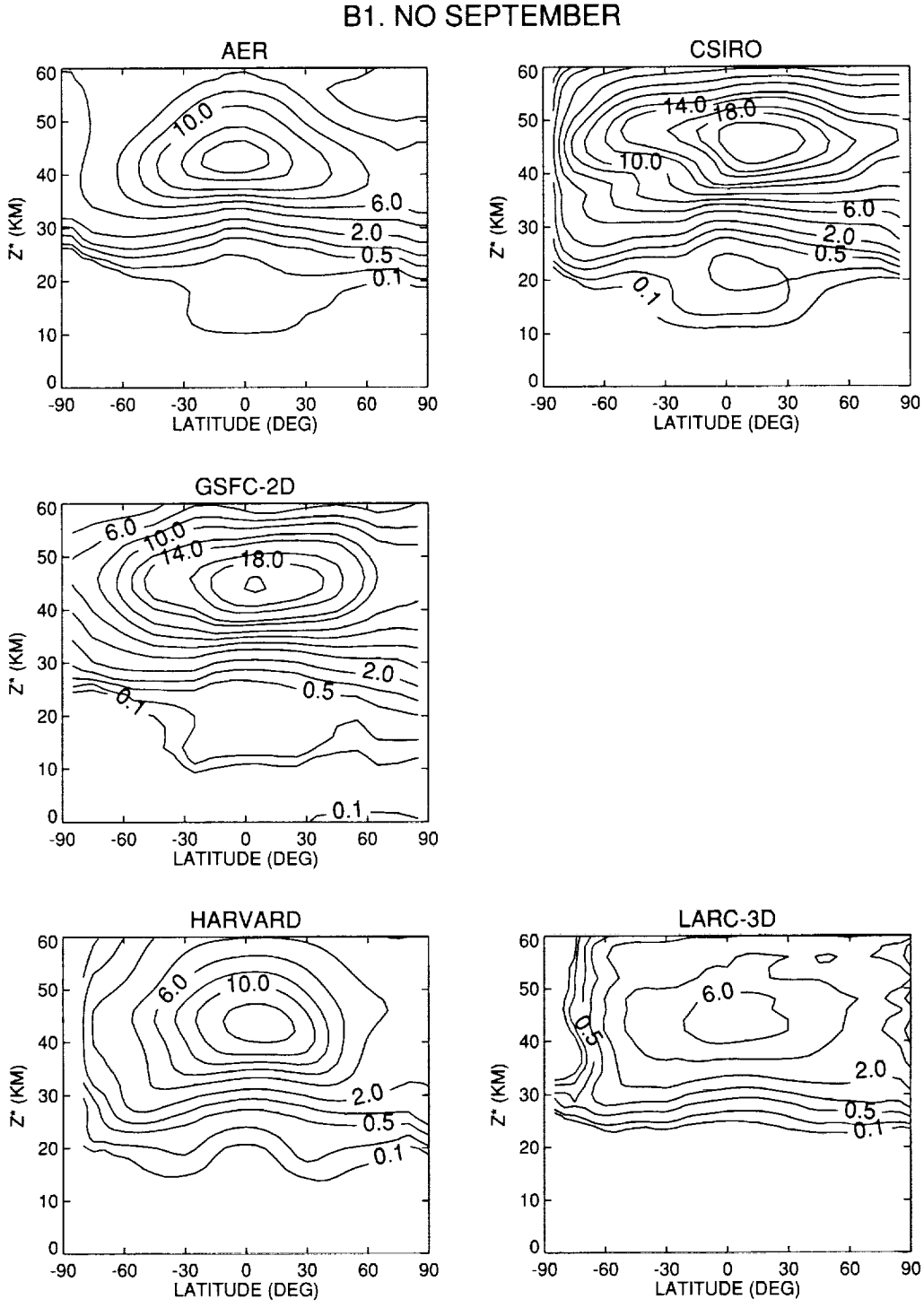

Figure 3.5.3. Continued.

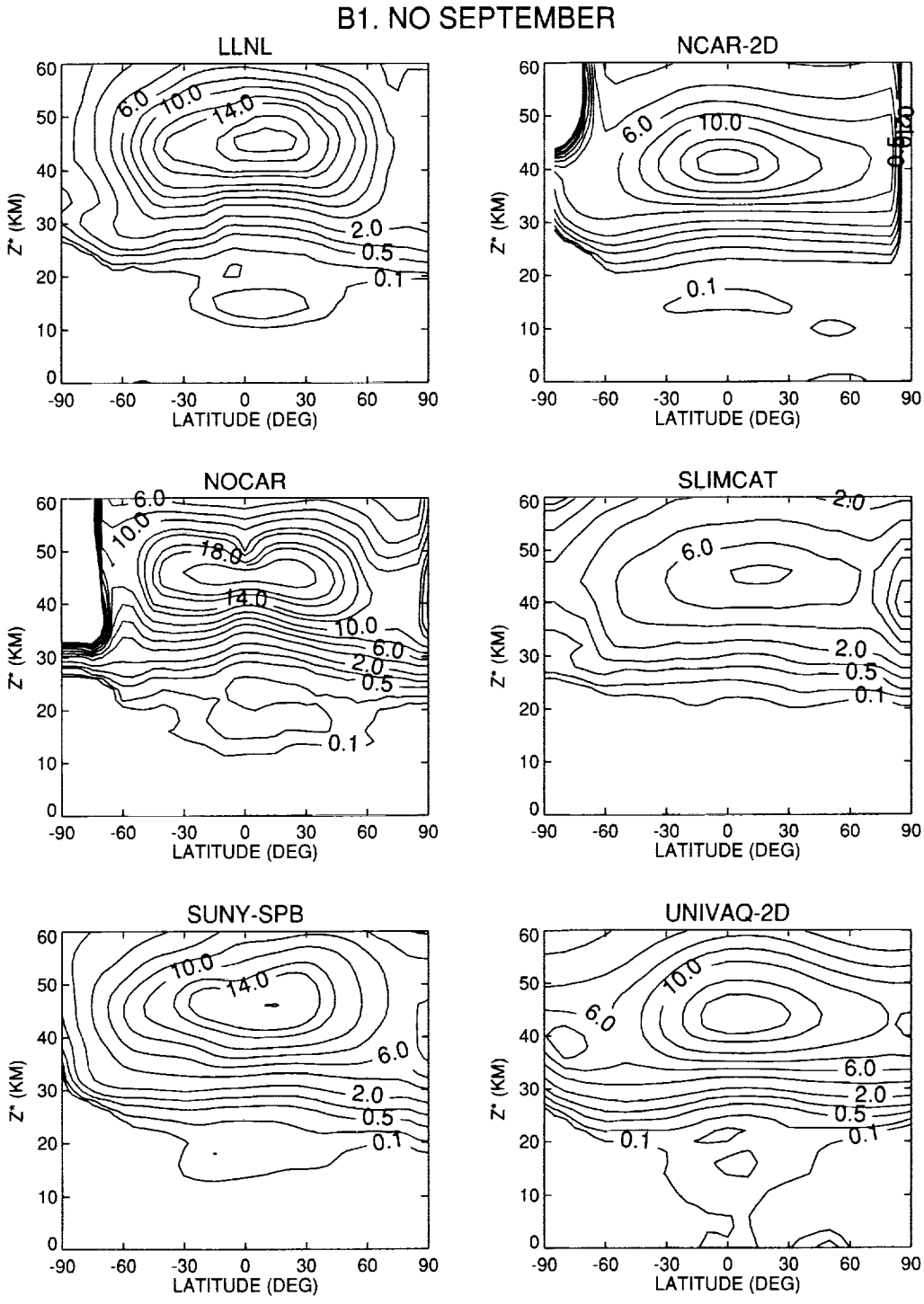

Figure 3.5.3. Concluded.

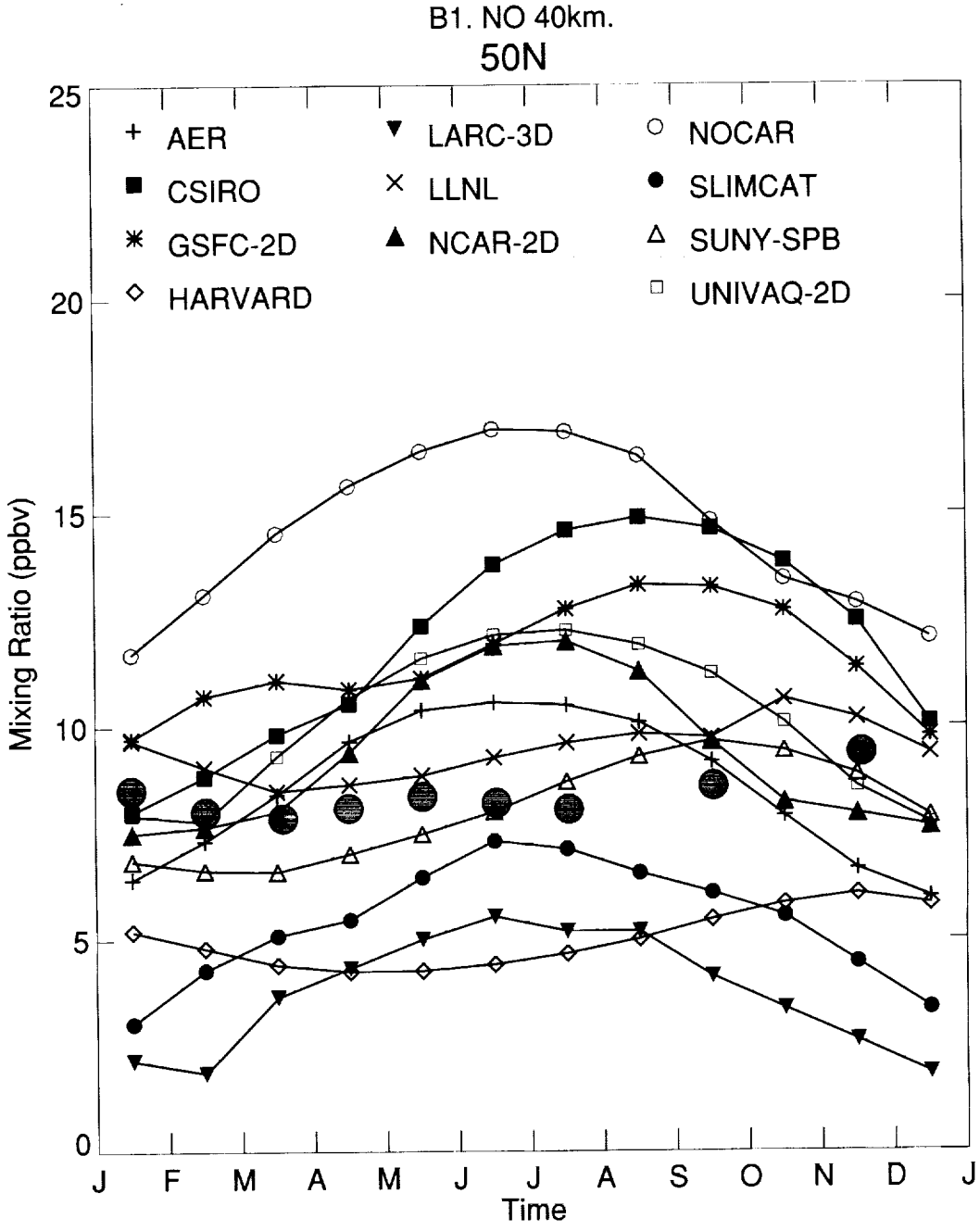

Figure 3.5.4. Seasonal variation of NO at 40 km and 50N for model simulations and HALOE measurement. (Filled circle: HALOE)

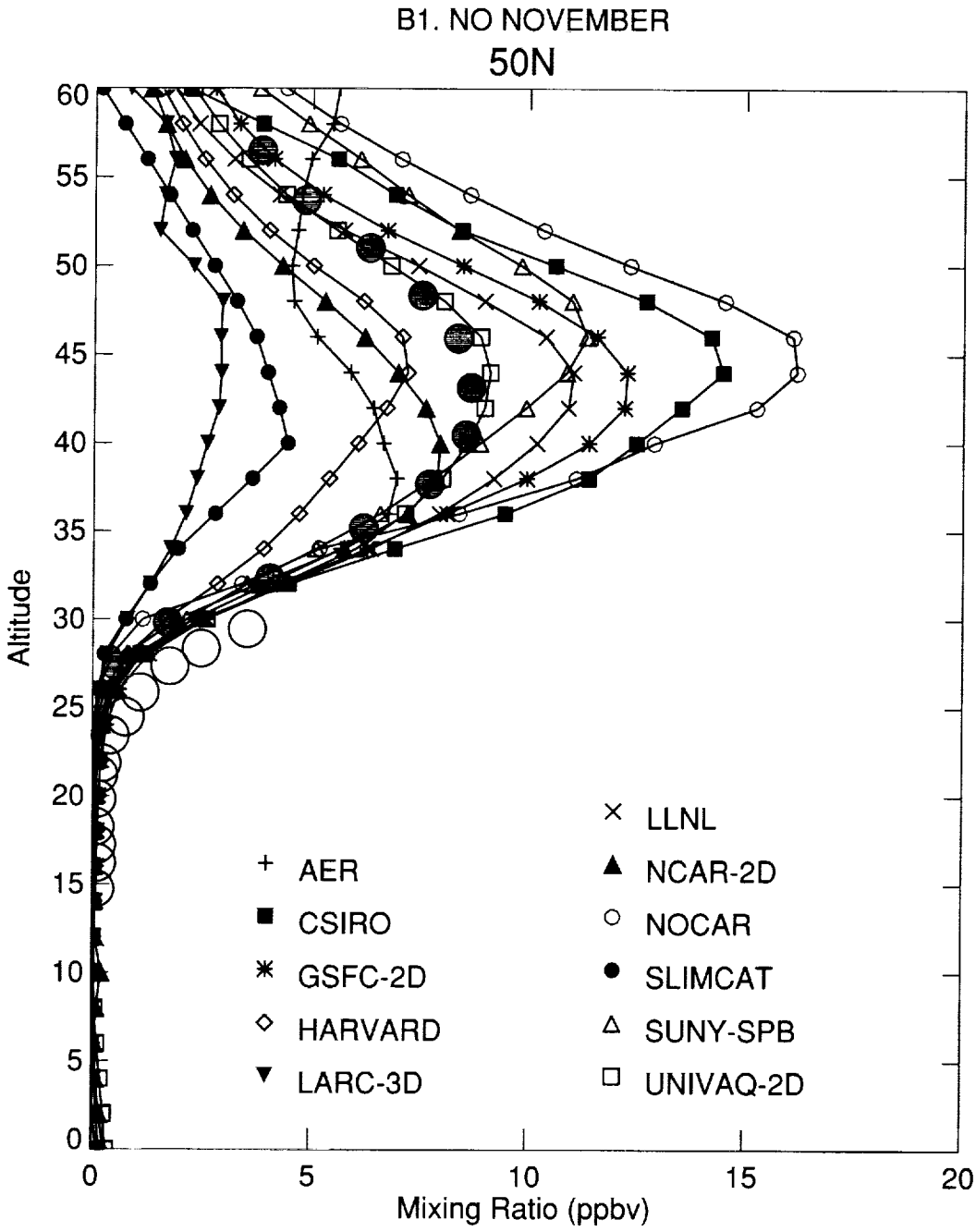

Figure 3.5.5. Vertical profiles of model calculated and measured NO at 50N in November. (Filled circle: HALOE, white circle: ATMOS)

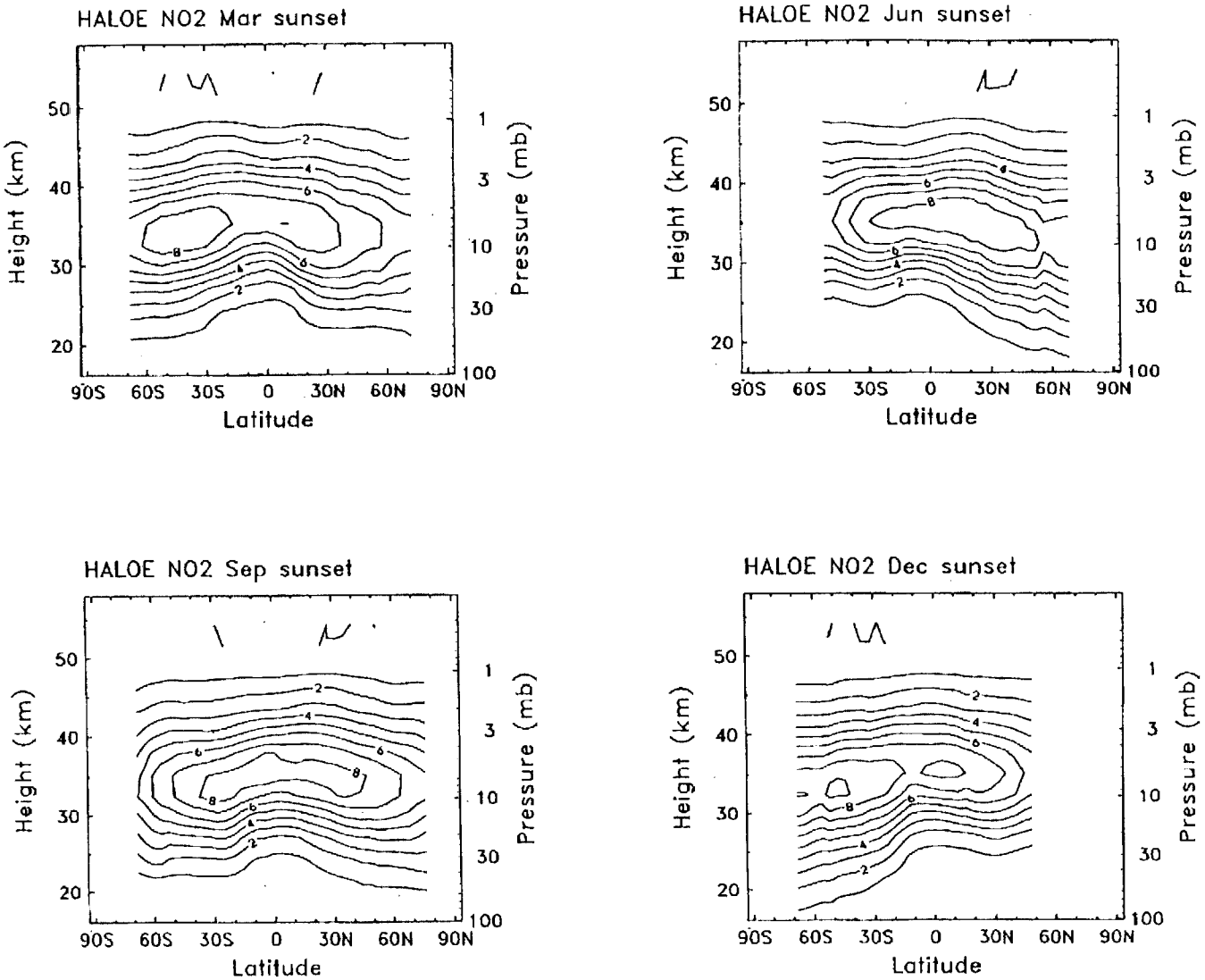

Figure 3.5.6. HALOE measured NO_2 latitude-height cross section for March, June, September and December from (a) sunset measurements and (b) sunrise measurements.

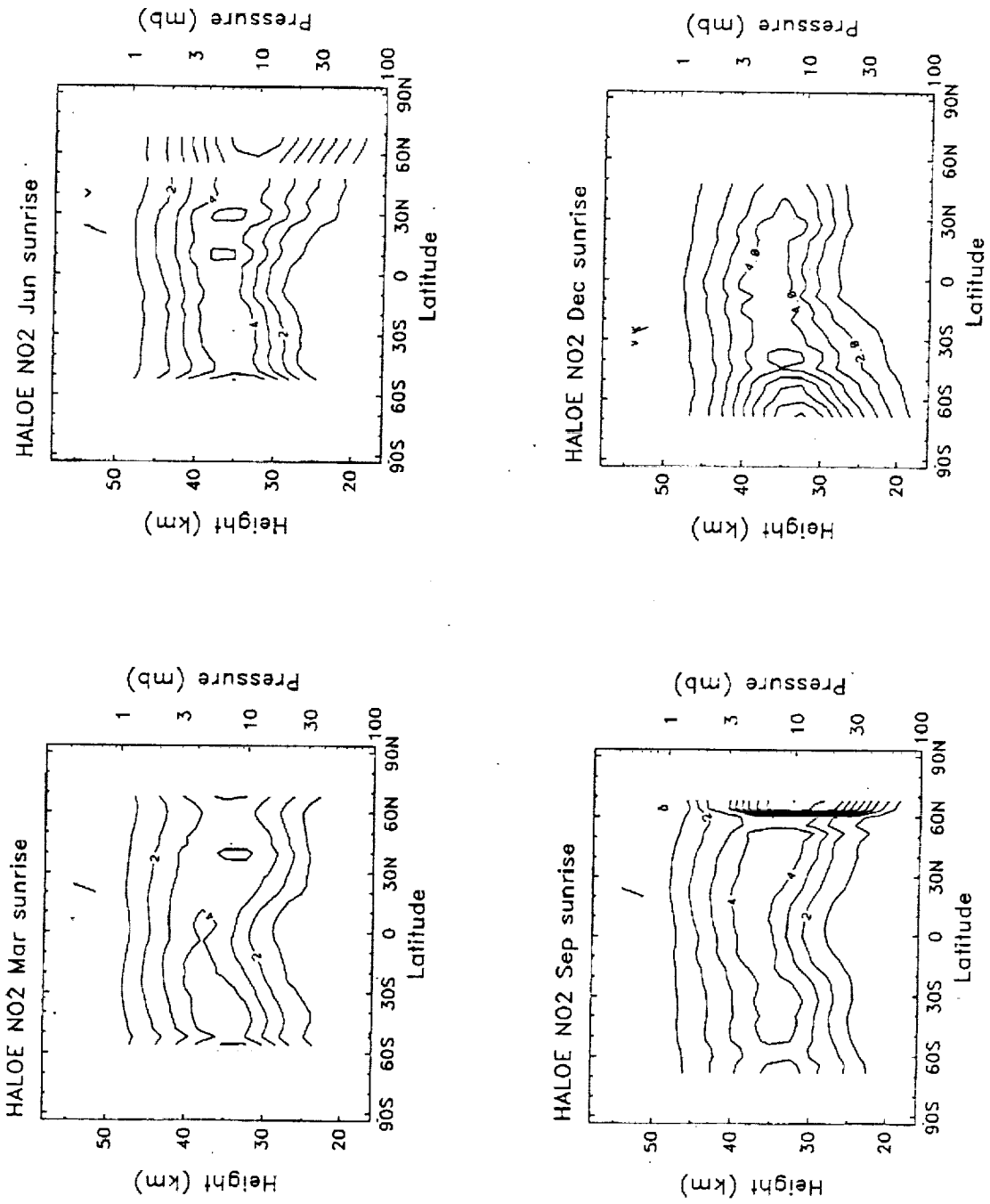

Figure 3.5.6. Concluded.

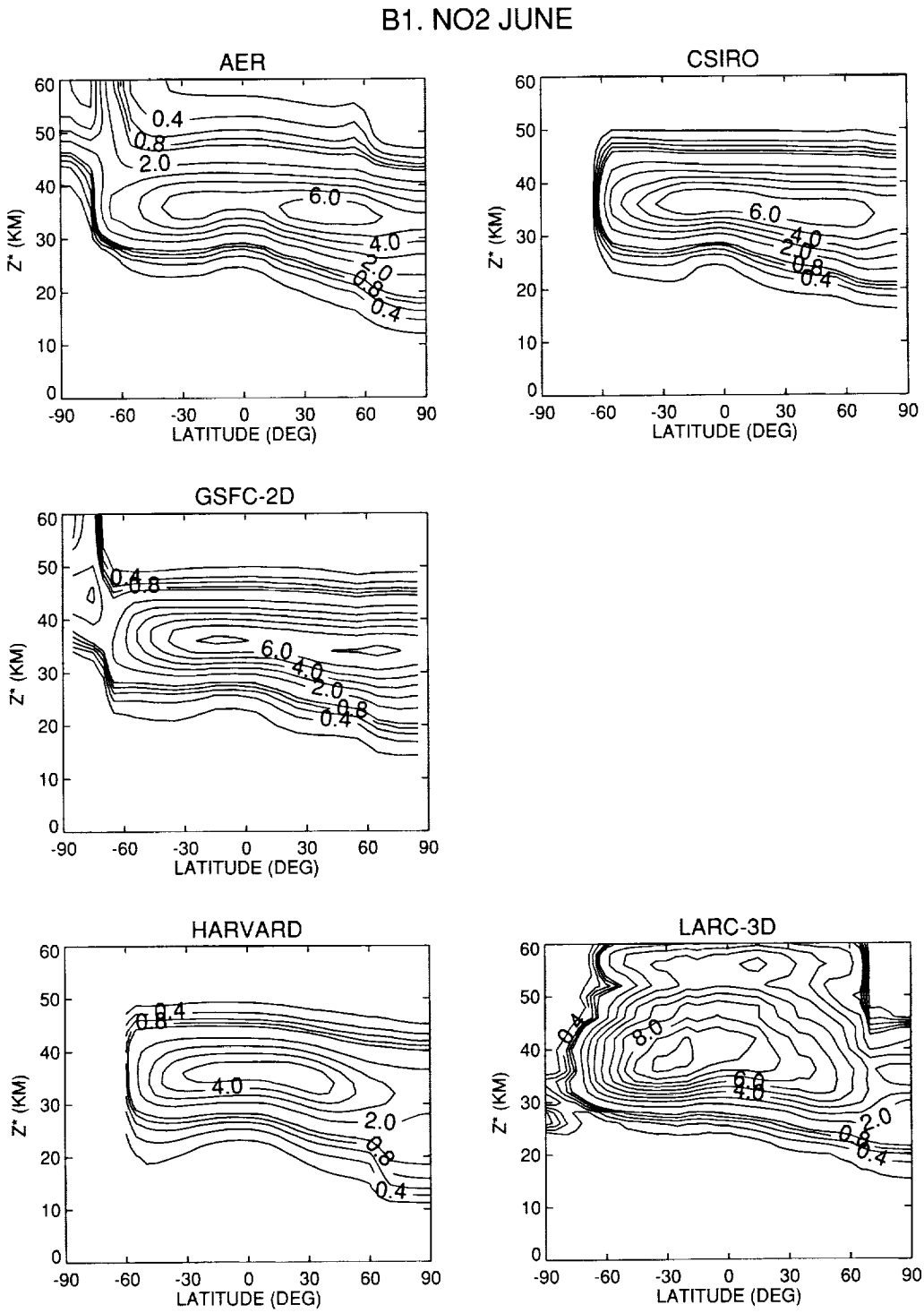

Figure 3.5.7. Model simulated daytime averaged NO_2 latitude-height cross section for (a-b) June and (c-d) December.

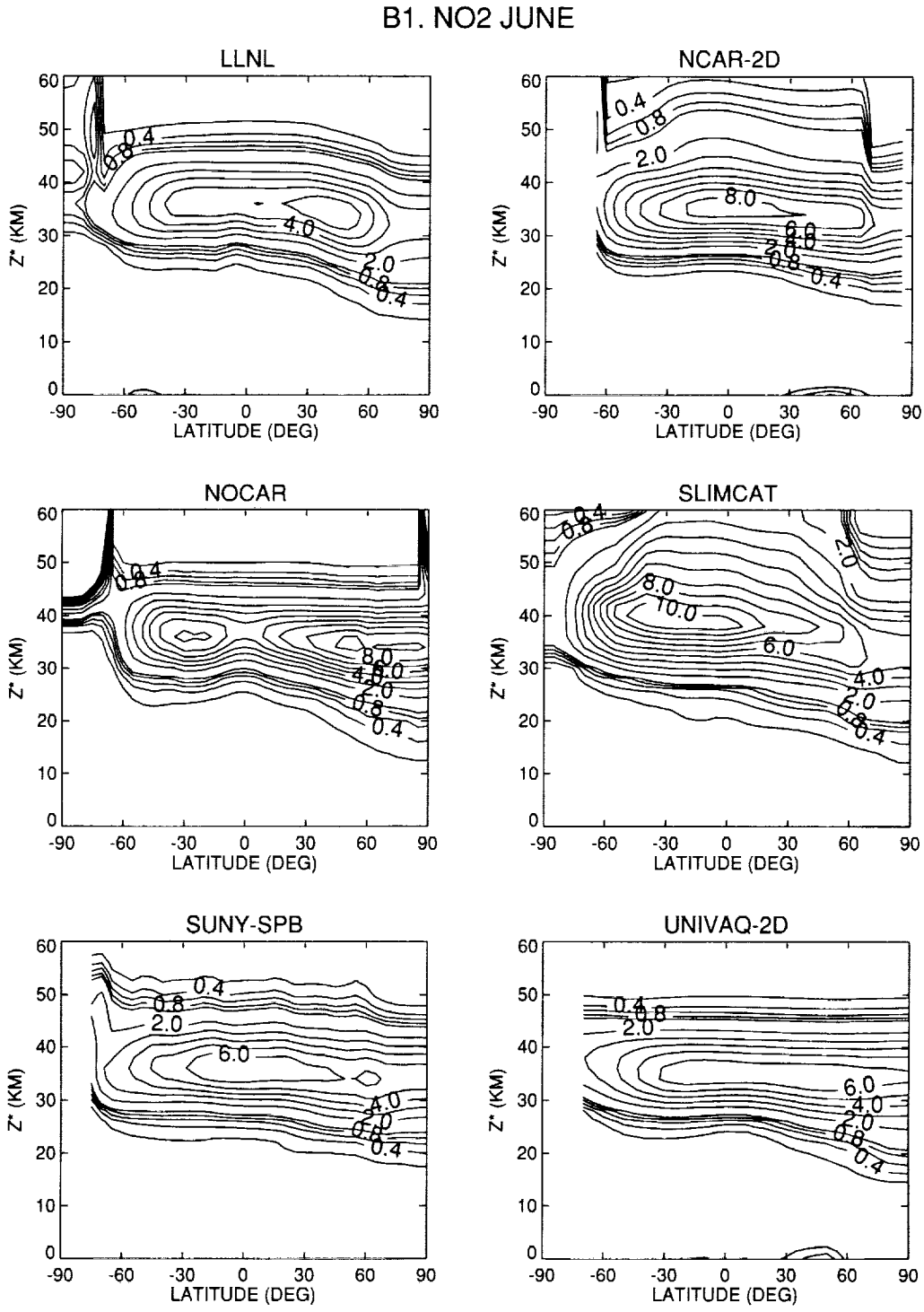

Figure 3.5.7. Continued.

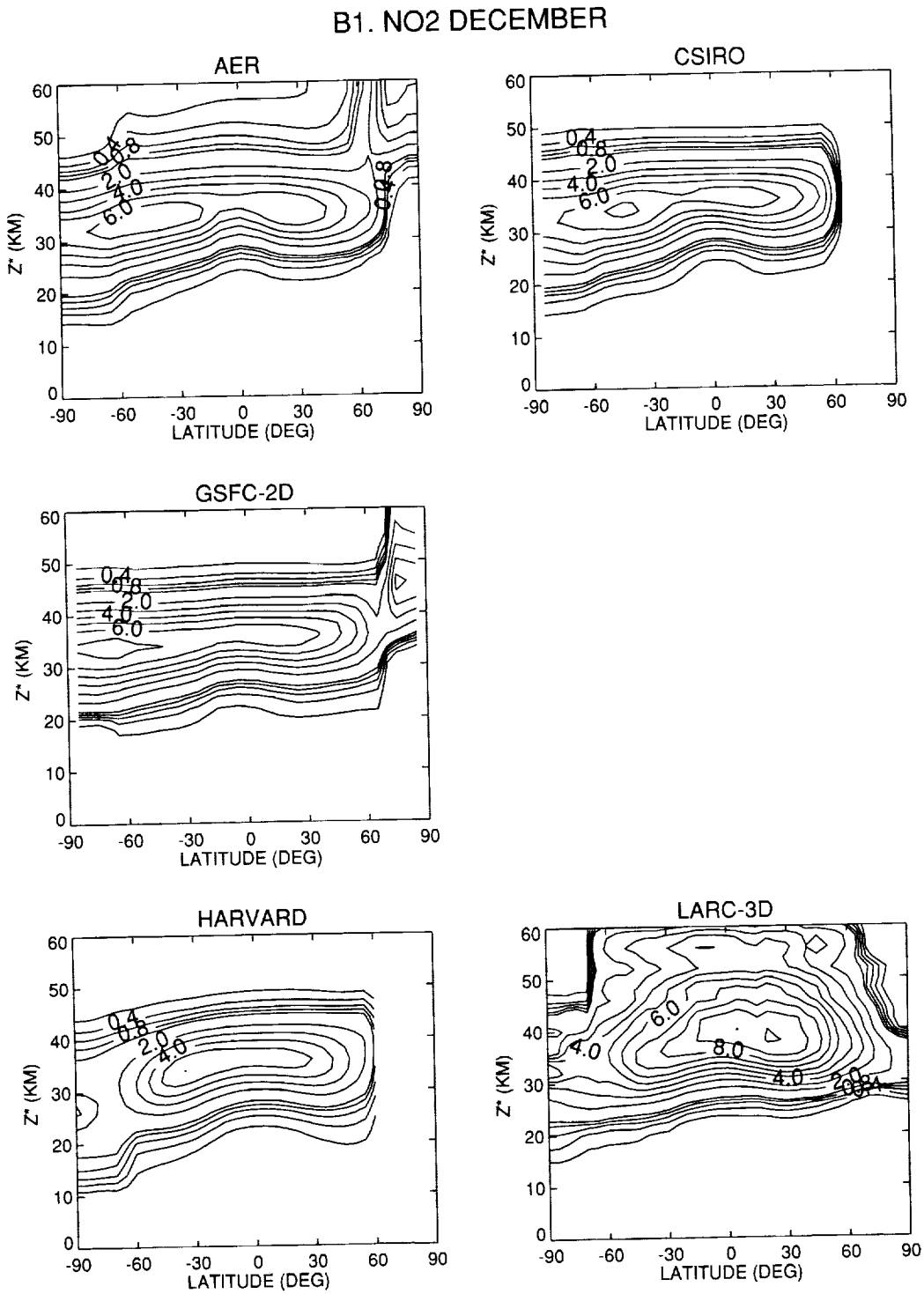

Figure 3.5.7. Continued.

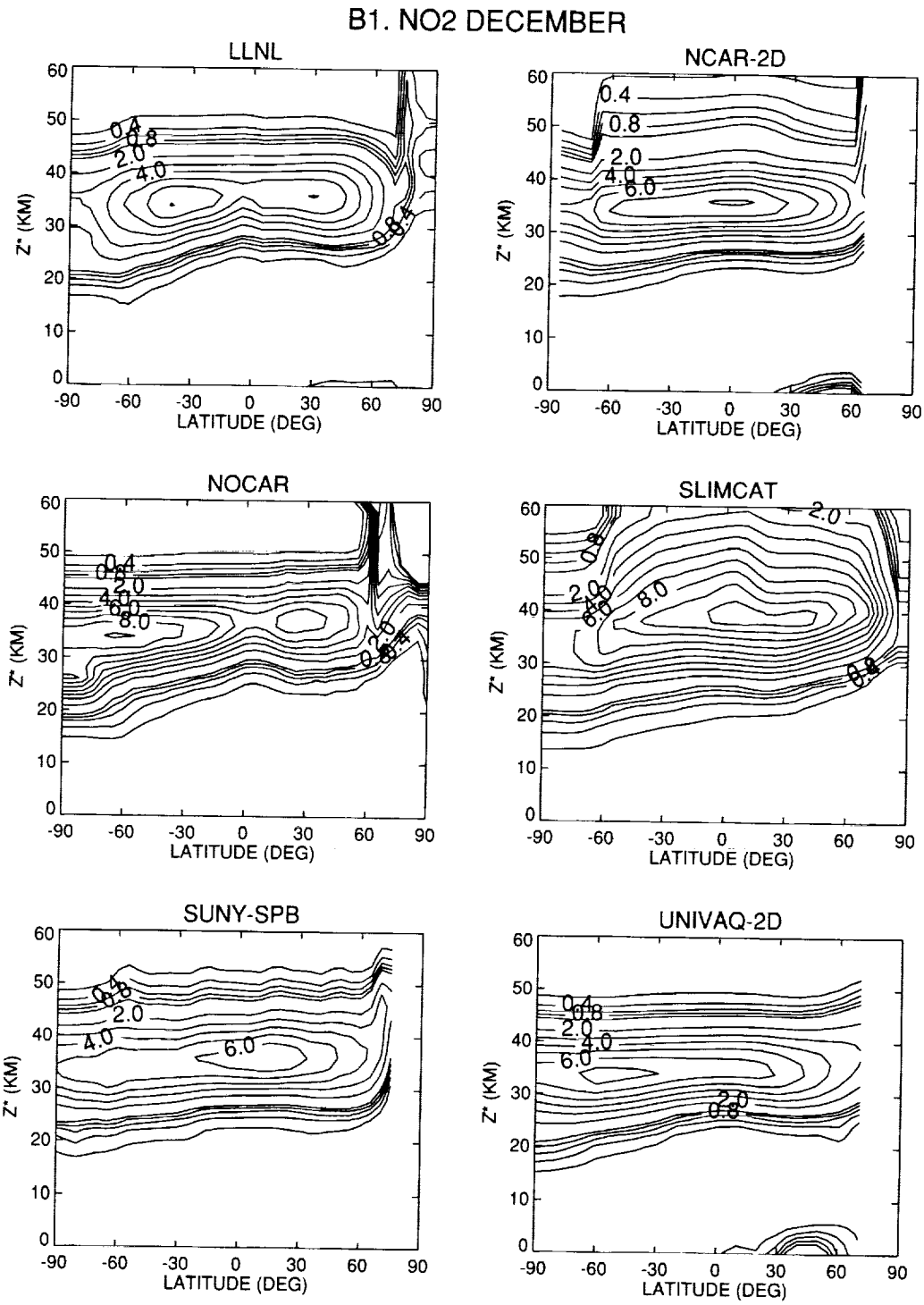

Figure 3.5.7. Concluded.

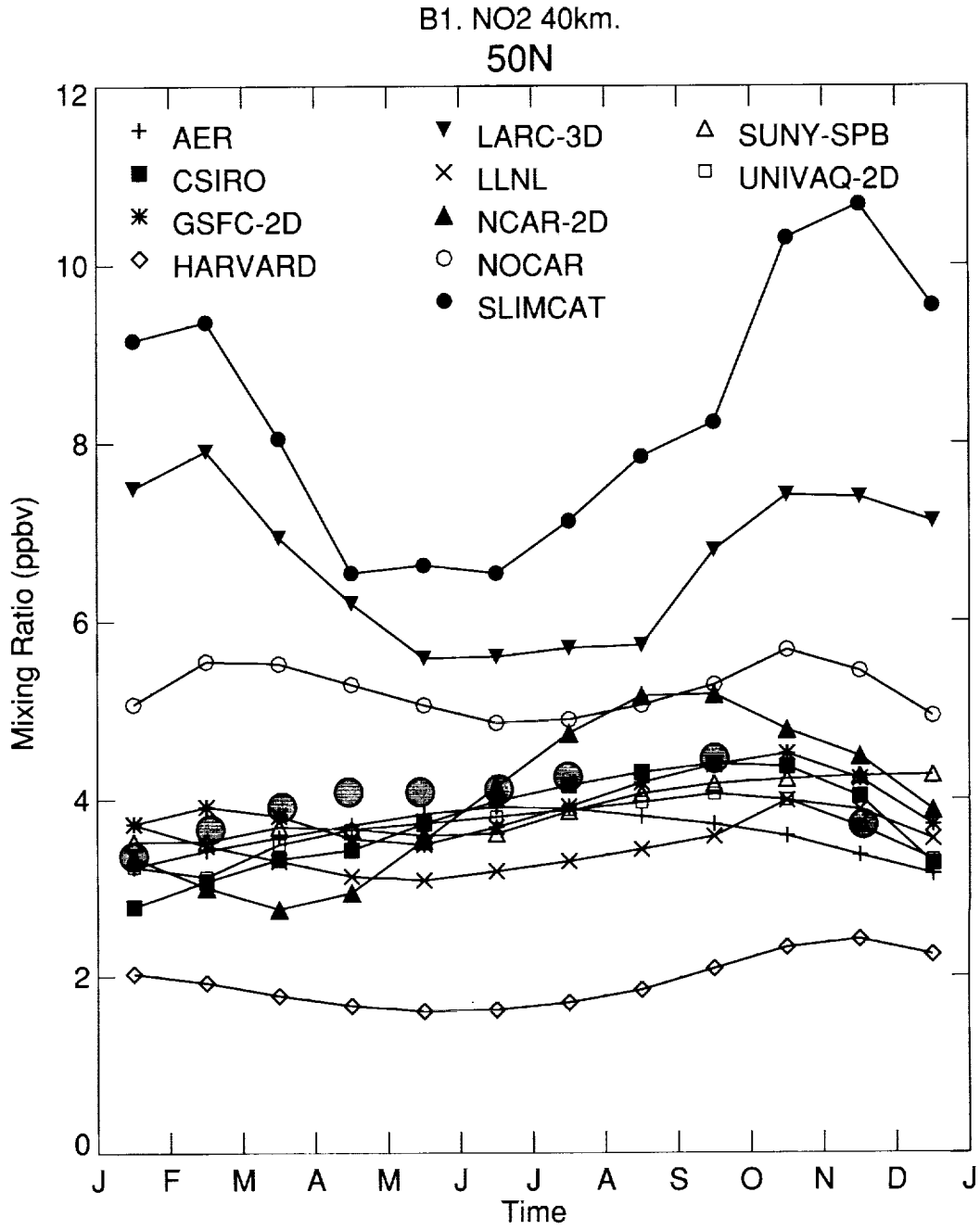

Figure 3.5.8. Seasonal variation of NO_2 at 40 km and 50N for model simulations and HALOE measurement. (Filled circle: HALOE)

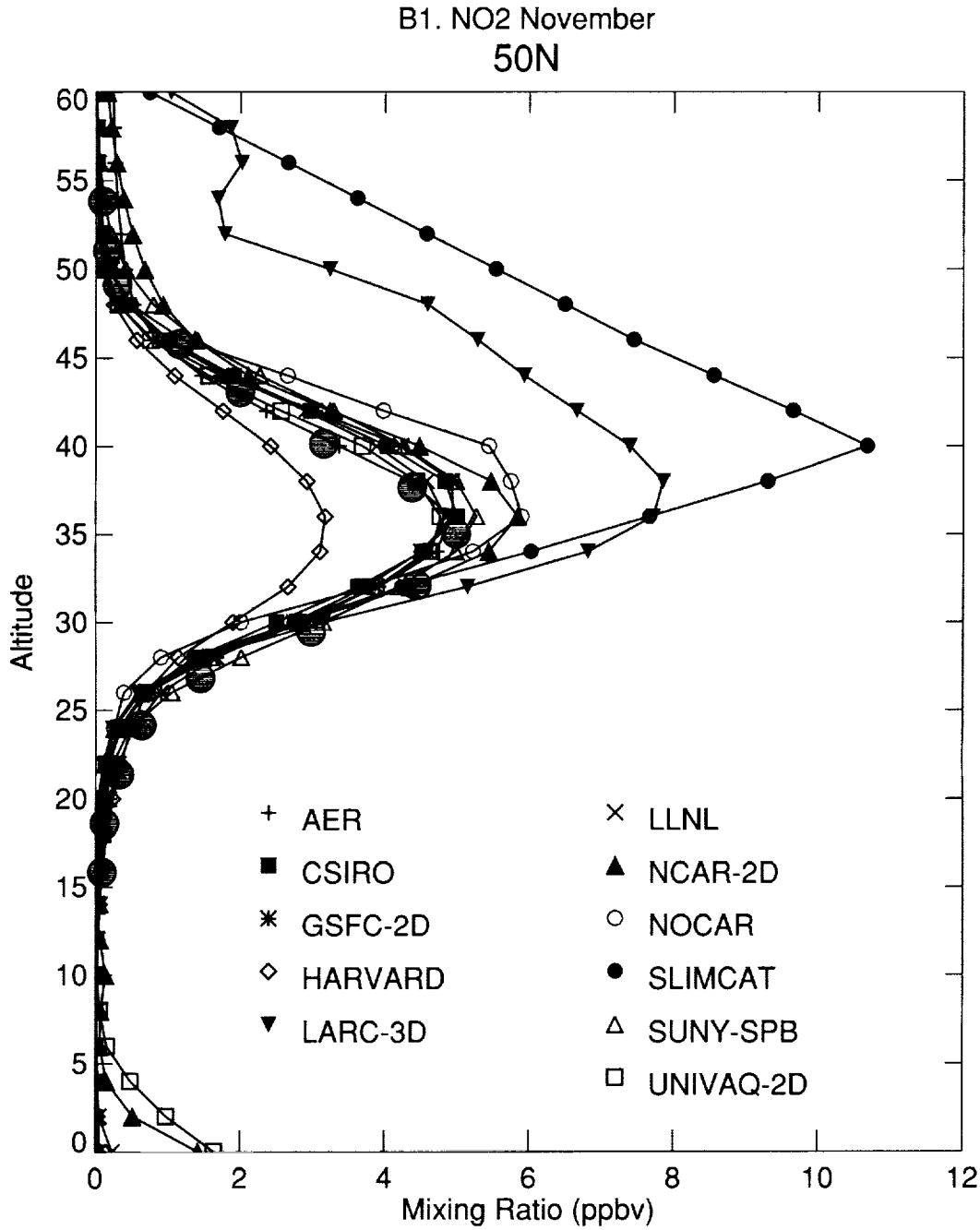

Figure 3.5.9. Vertical profiles of model calculated and measured NO_2 at 50N in November. (Filled circle: HALOE)

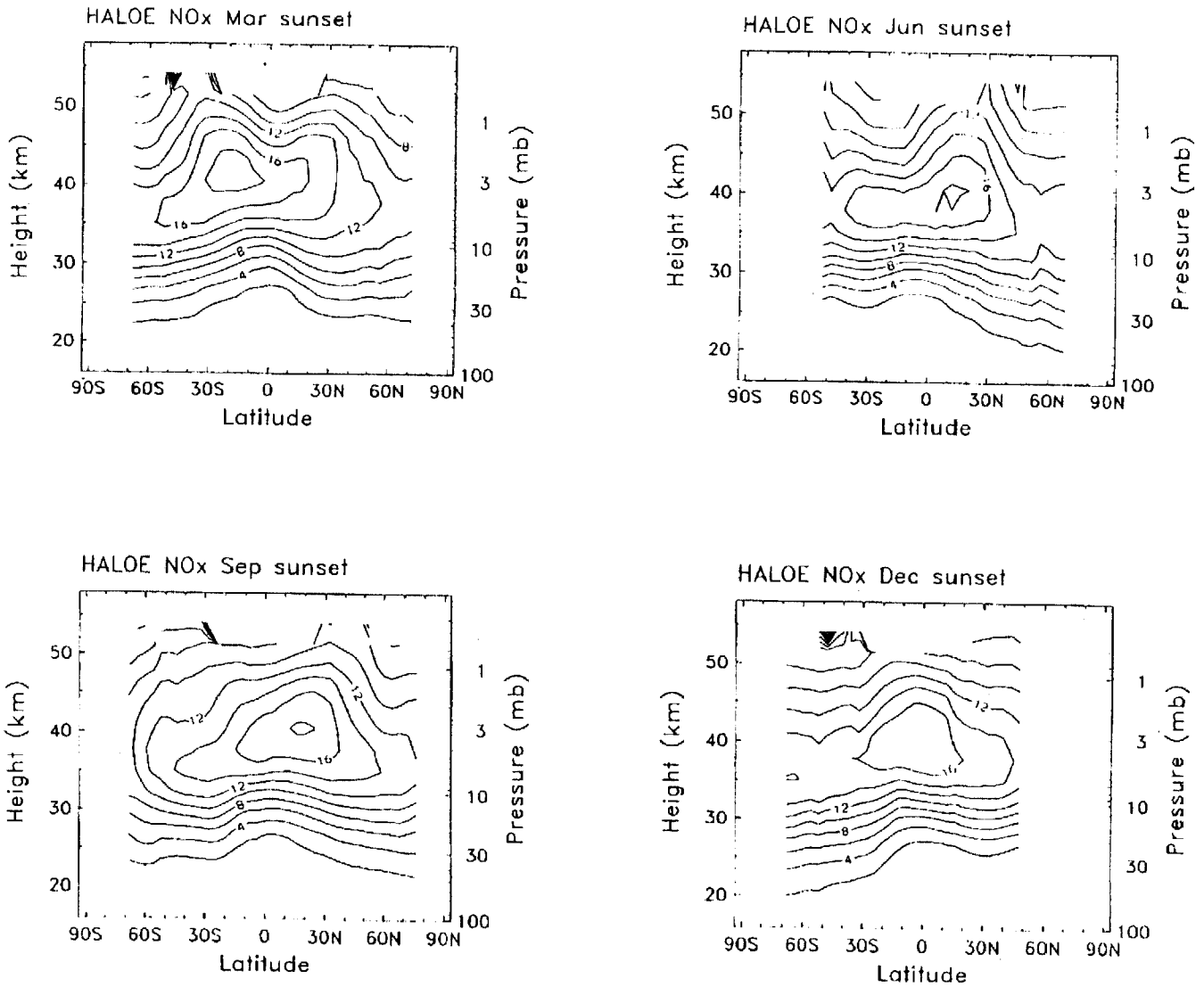

Figure 3.5.10. HALOE measured NOx ($NO+NO_2$) latitude-height cross section for March, June, September and December from sunset measurements.

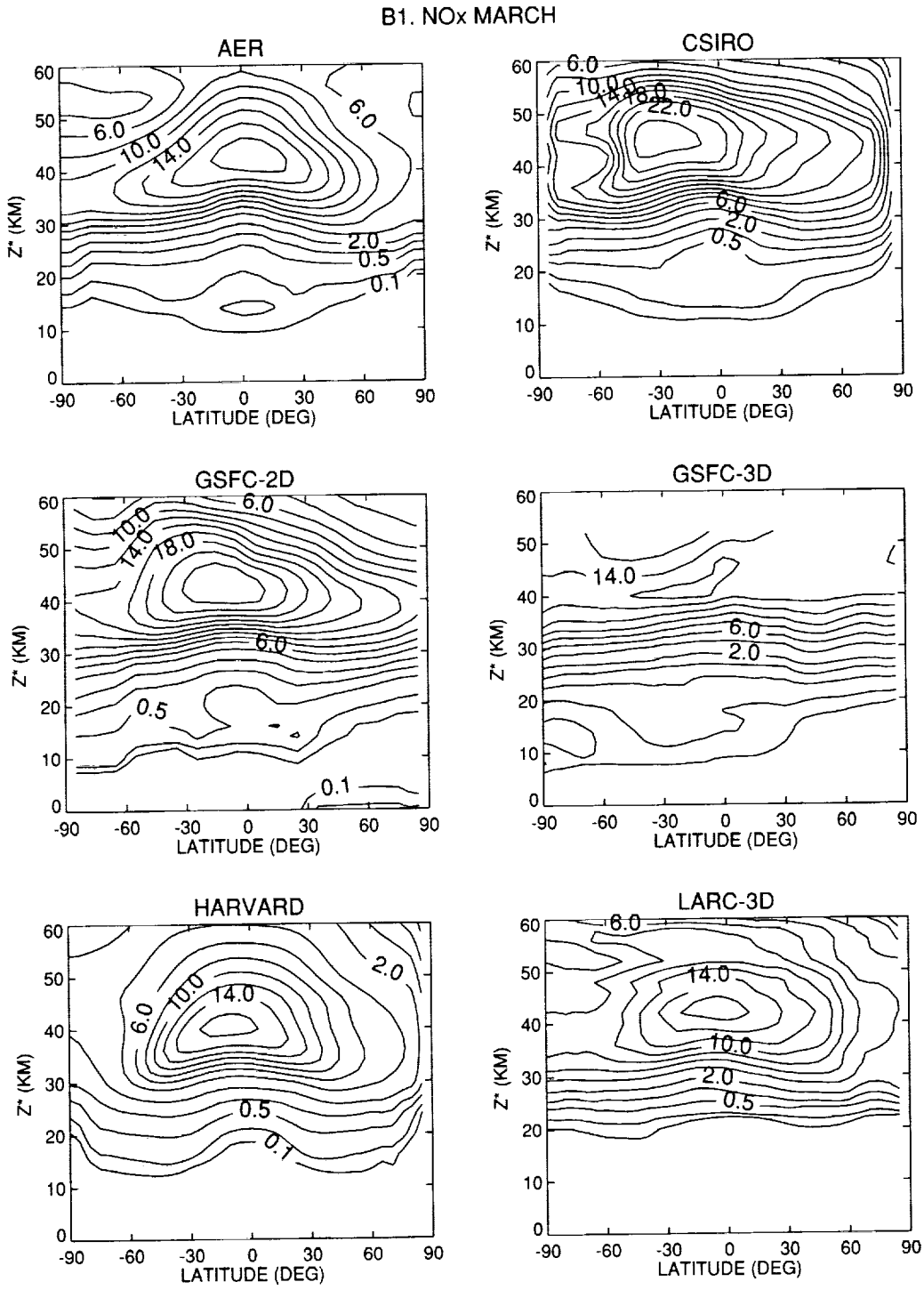

Figure 3.5.11. Model simulated daytime averaged NOx latitude-height cross section for (a-b) March and (c-d) September.

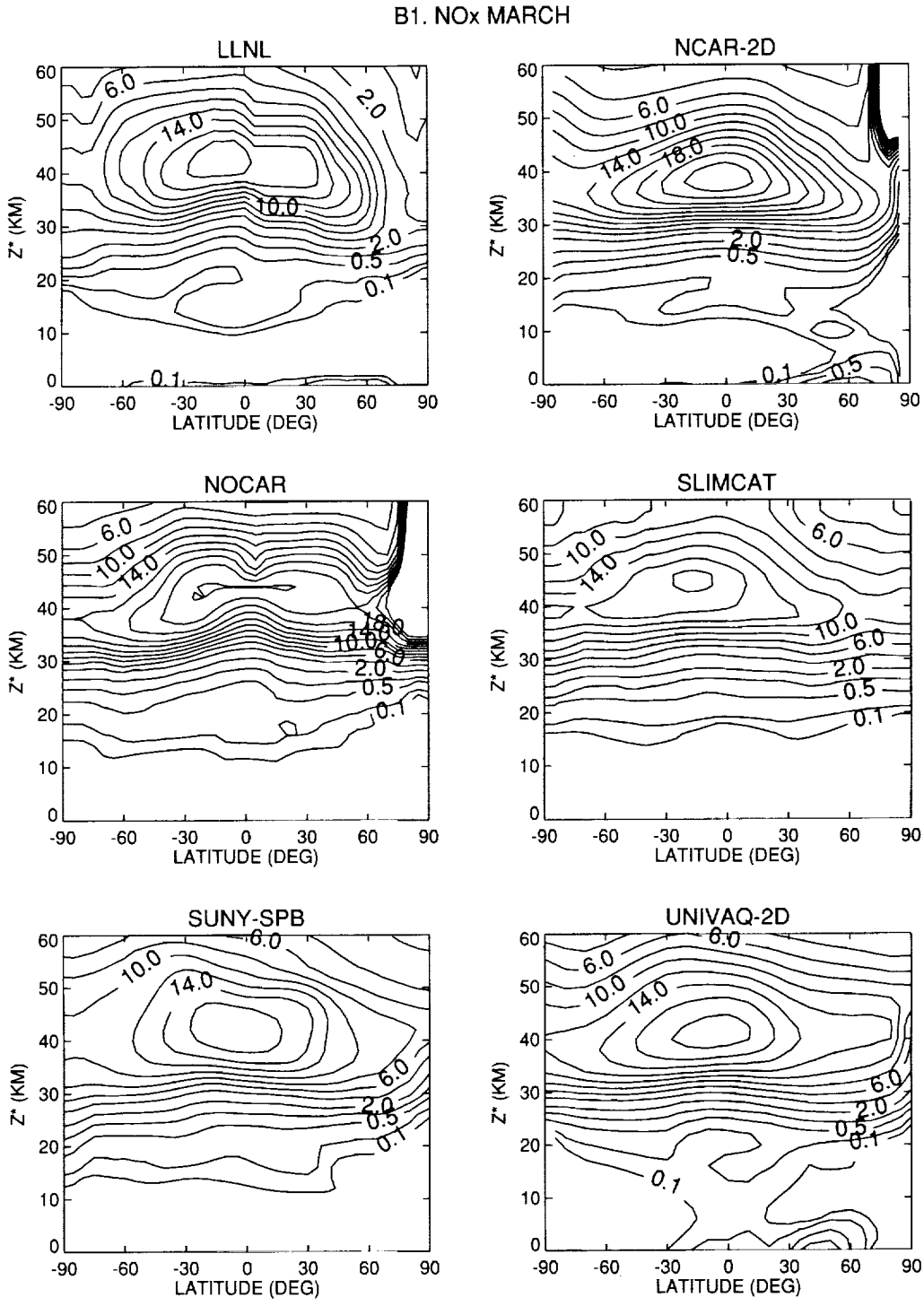

Figure 3.5.11. Continued.

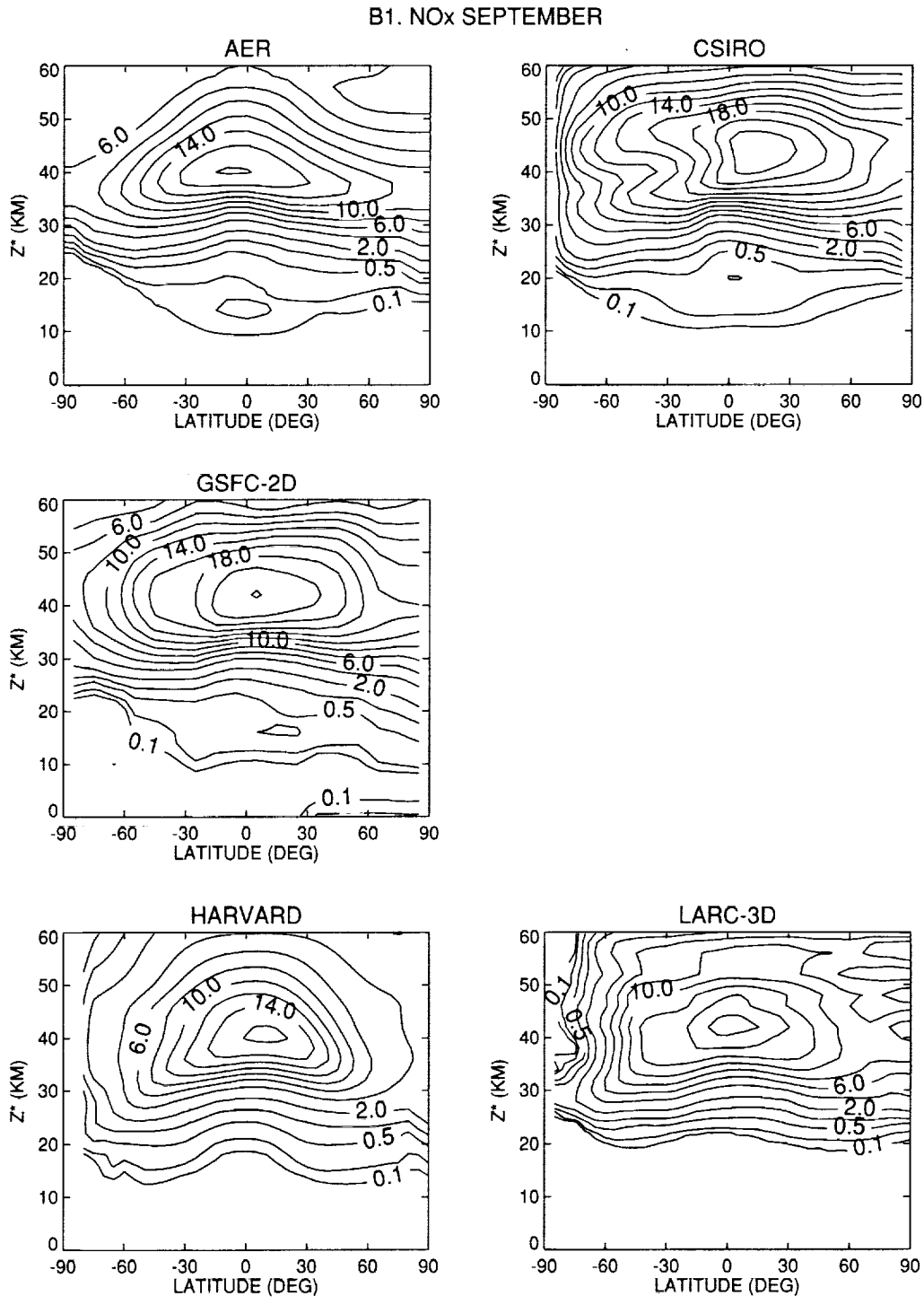

Figure 3.5.11. Continued.

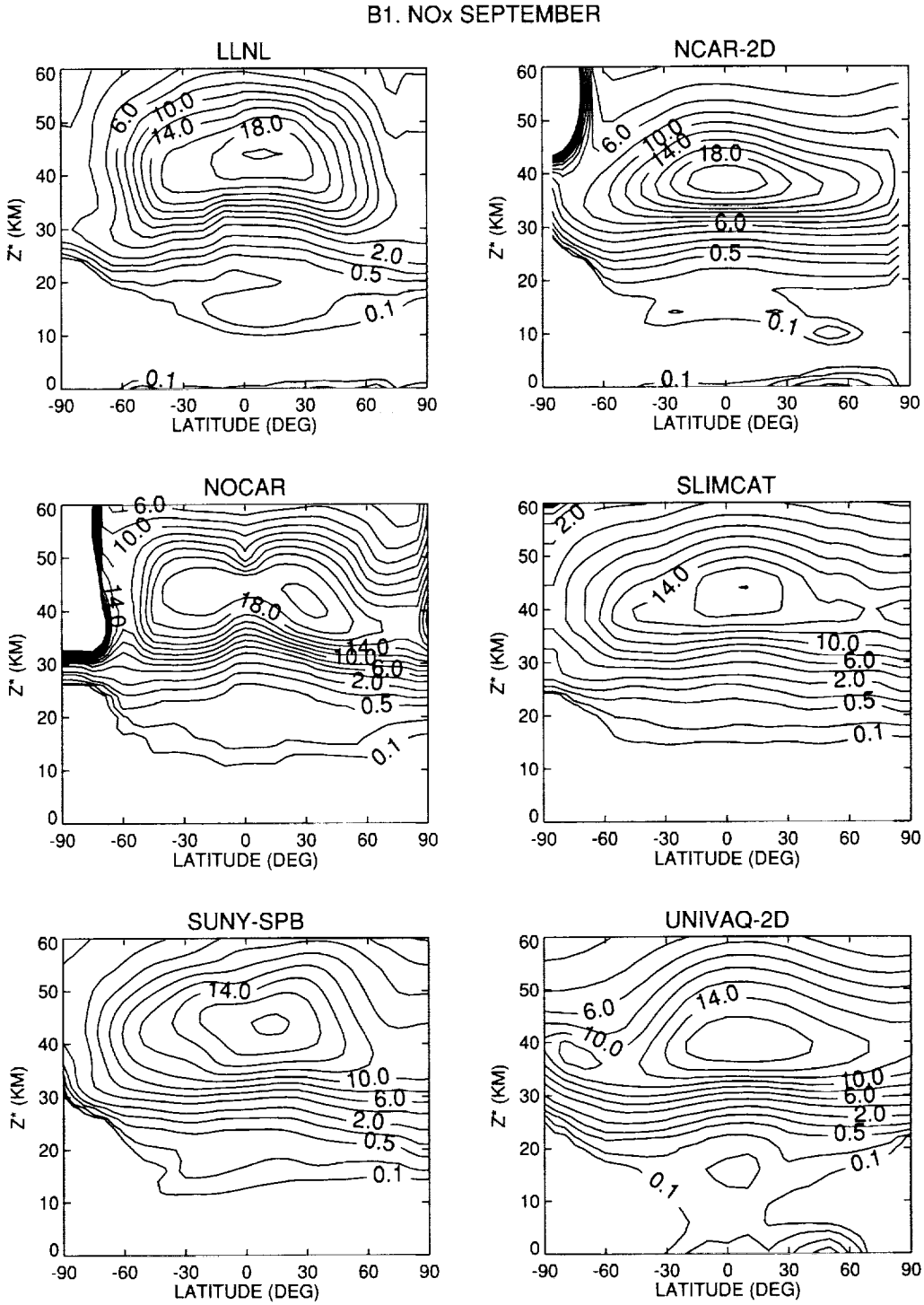

Figure 3.5.11. Concluded.

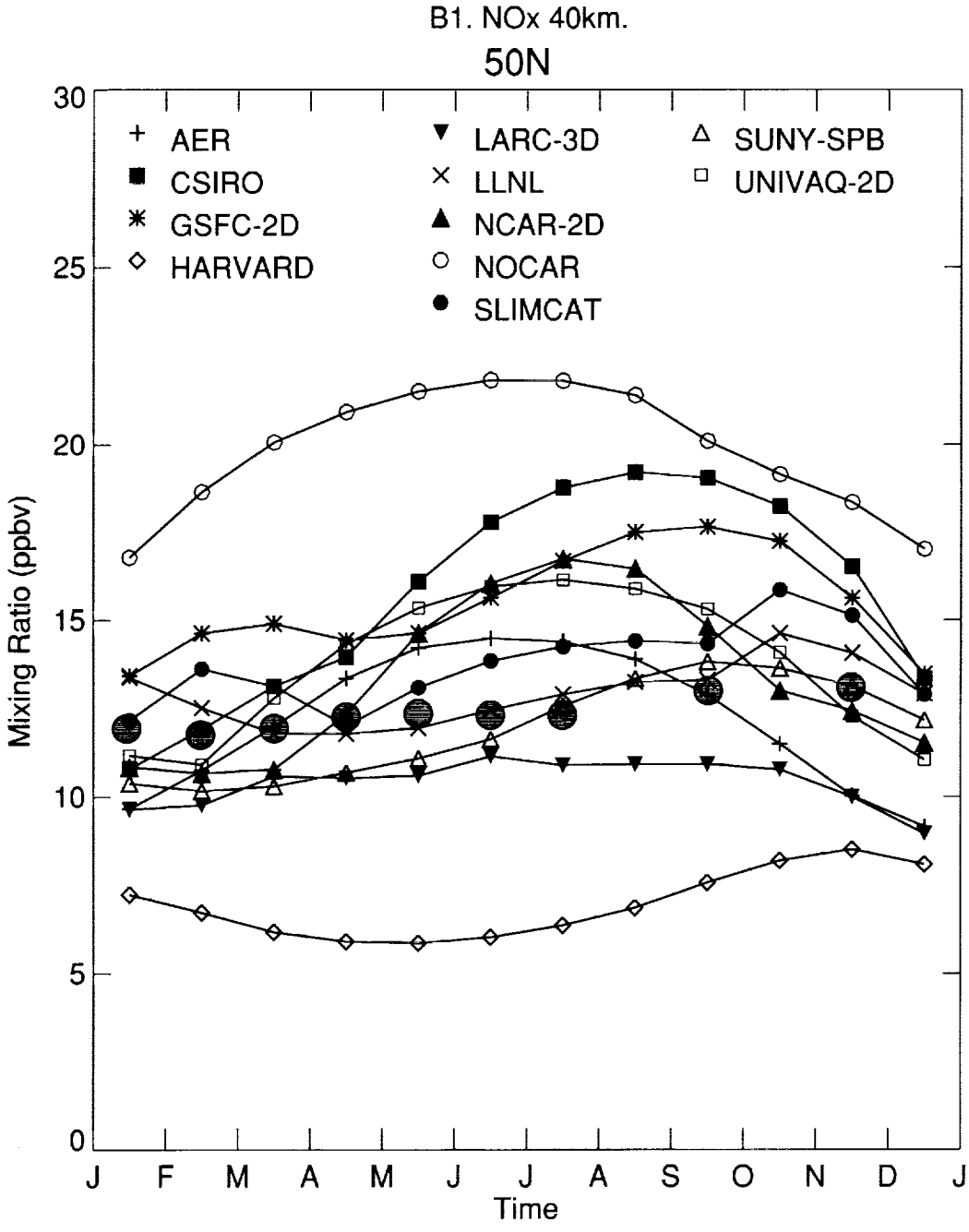

Figure 3.5.12. Seasonal variation of NOx at 40 km and 50N for model simulations and HALOE measurement. (Filled circle: HALOE)

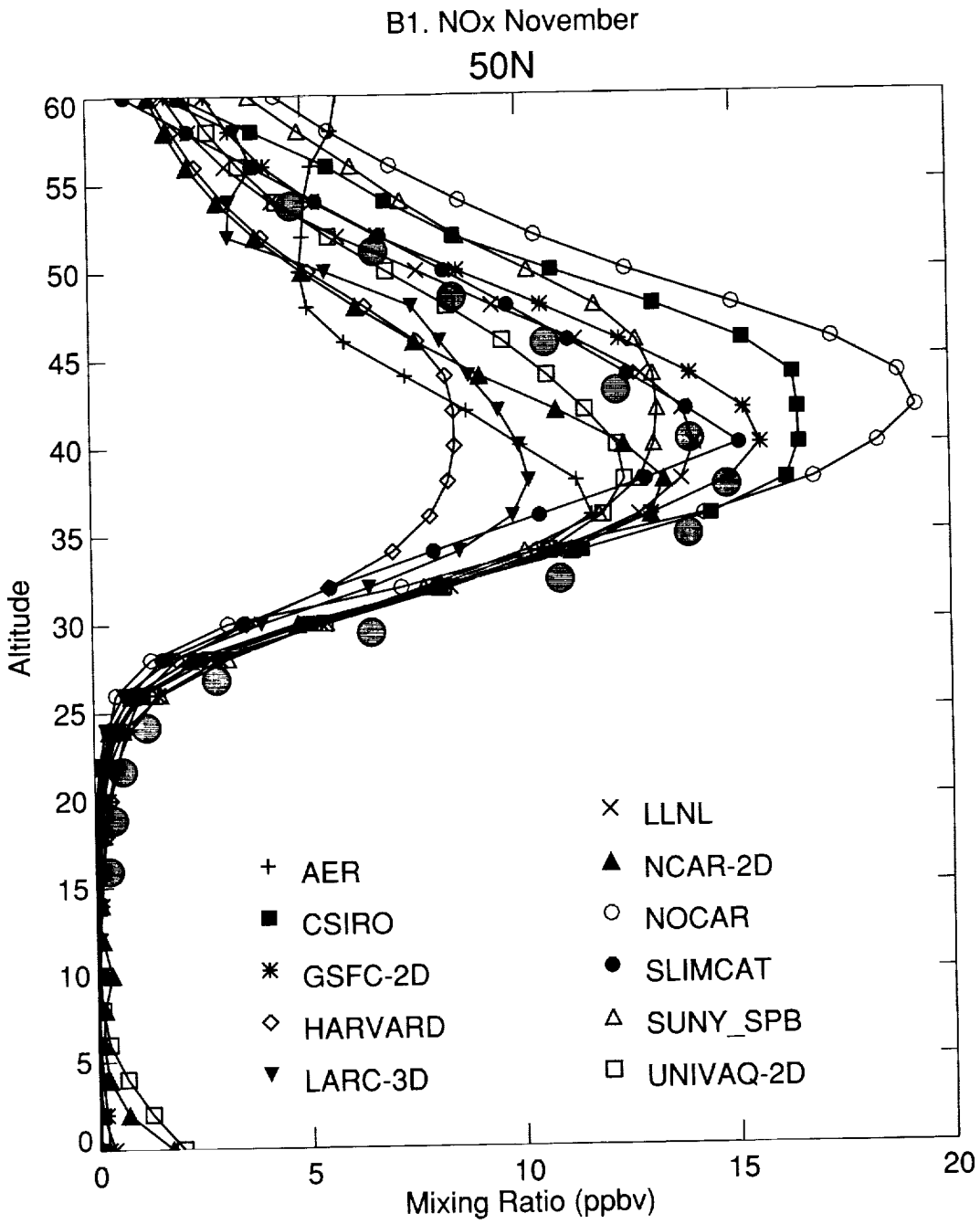

Figure 3.5.13. Vertical profiles of model calculated and measured NOx at 50N in November. (Filled circle: HALOE).

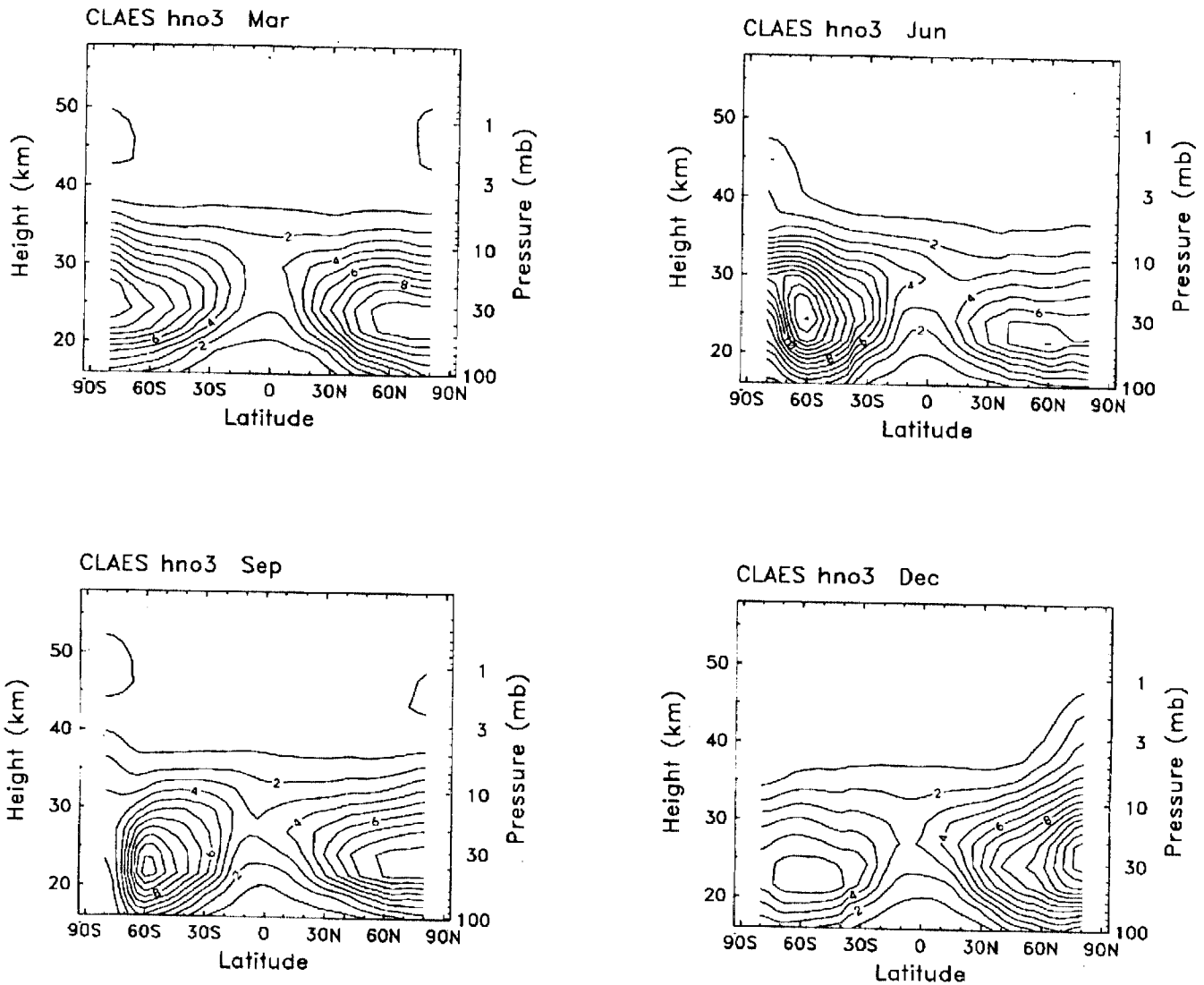

Figure 3.5.14. CLAES measured zonally-averaged HNO_3 latitude-height cross section for March, June, September and December.

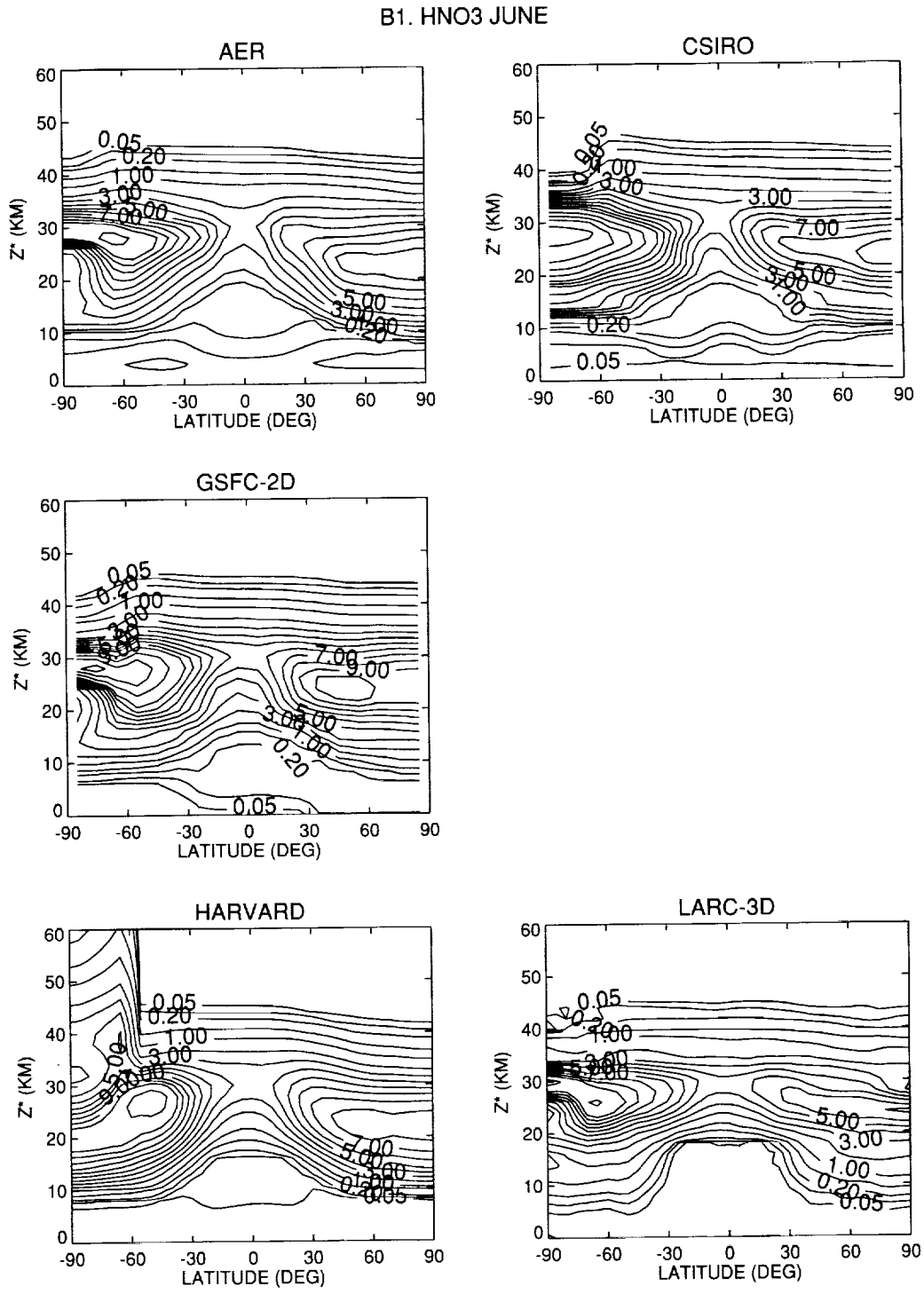

Figure 3.5.15. Model simulated zonally-averaged HNO_3 latitude-height cross section for (a-b) June and (c-d) December.

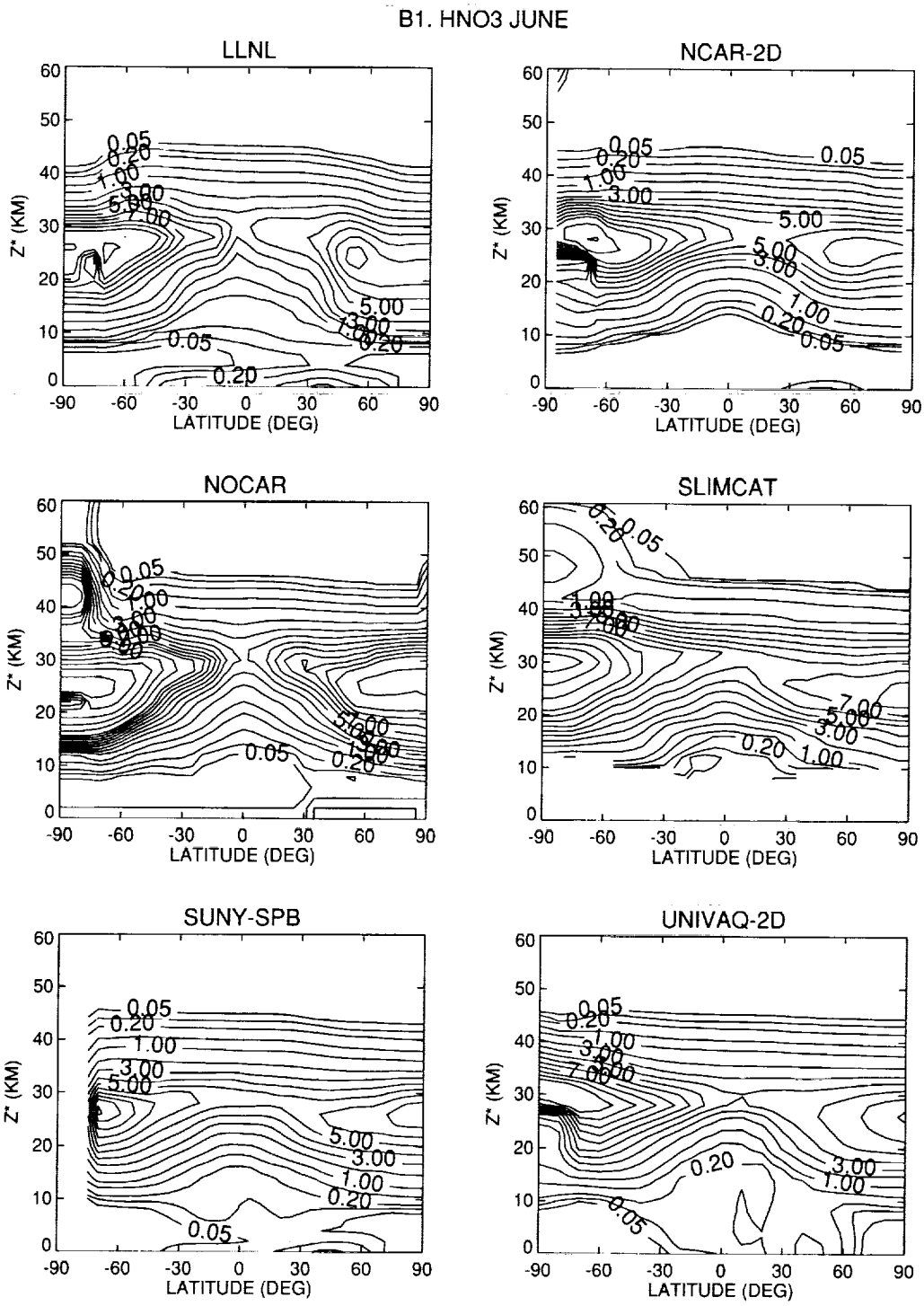

Figure 3.5.15. Continued.

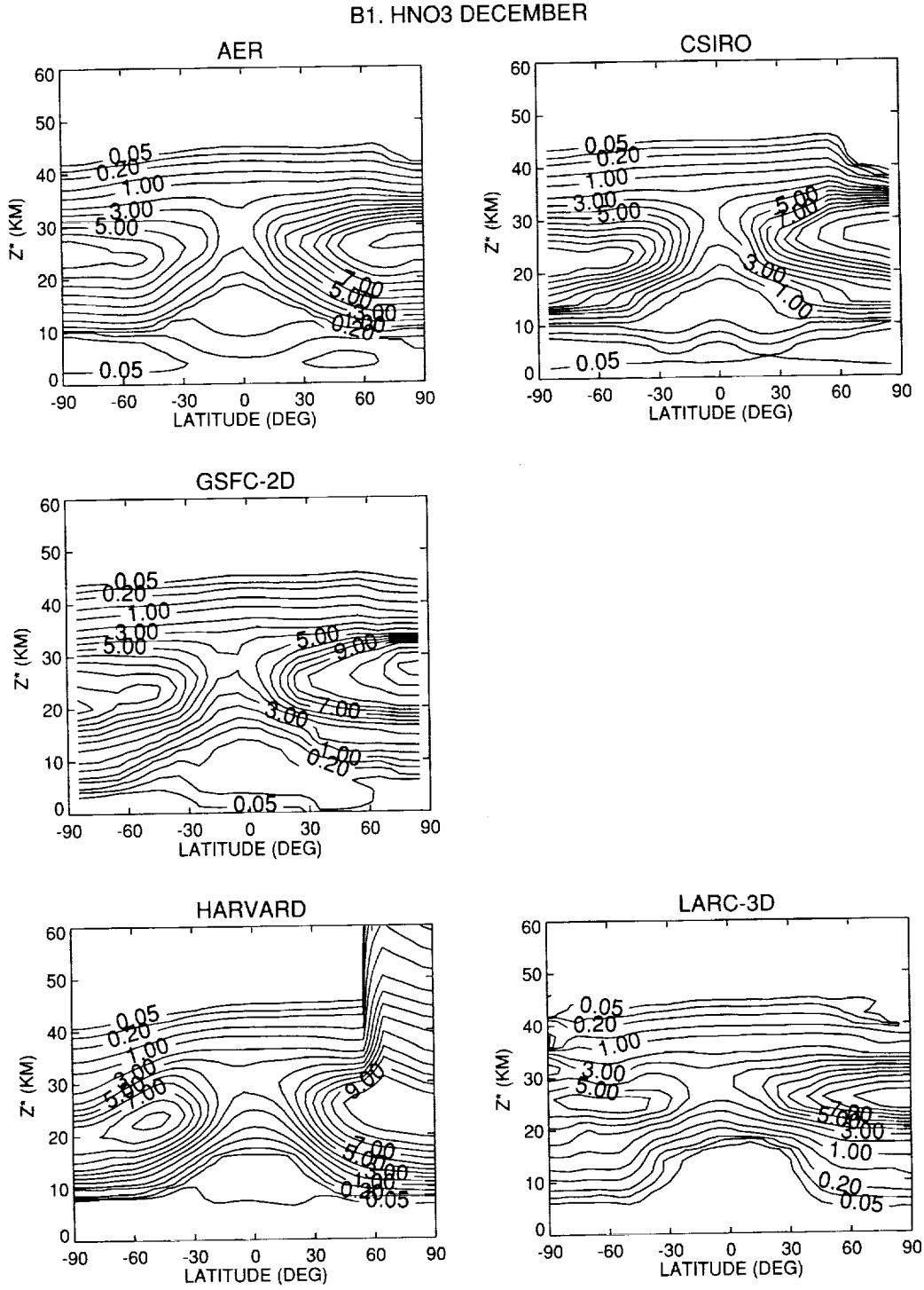

Figure 3.5.15. Continued.

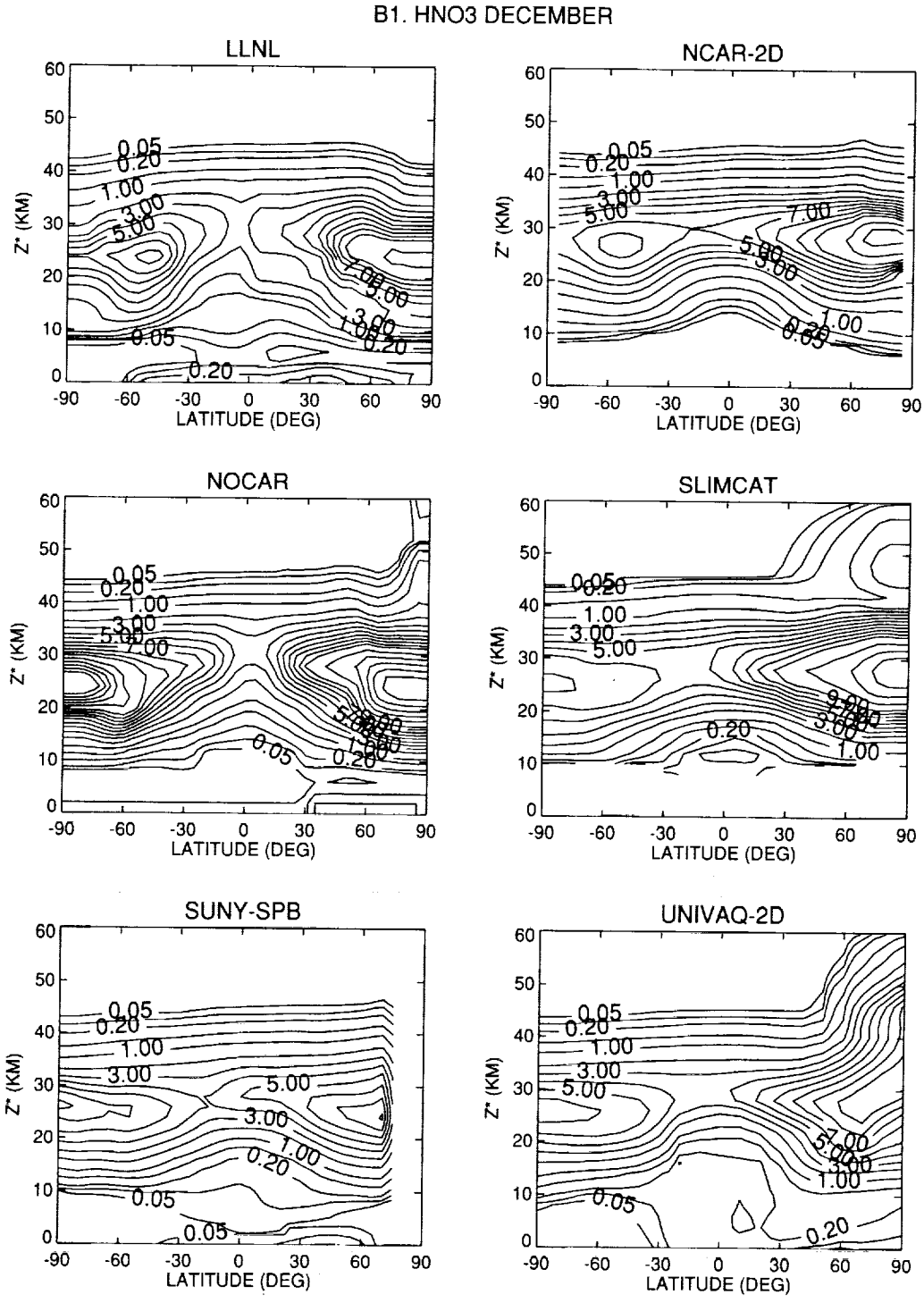

Figure 3.5.15. Concluded.

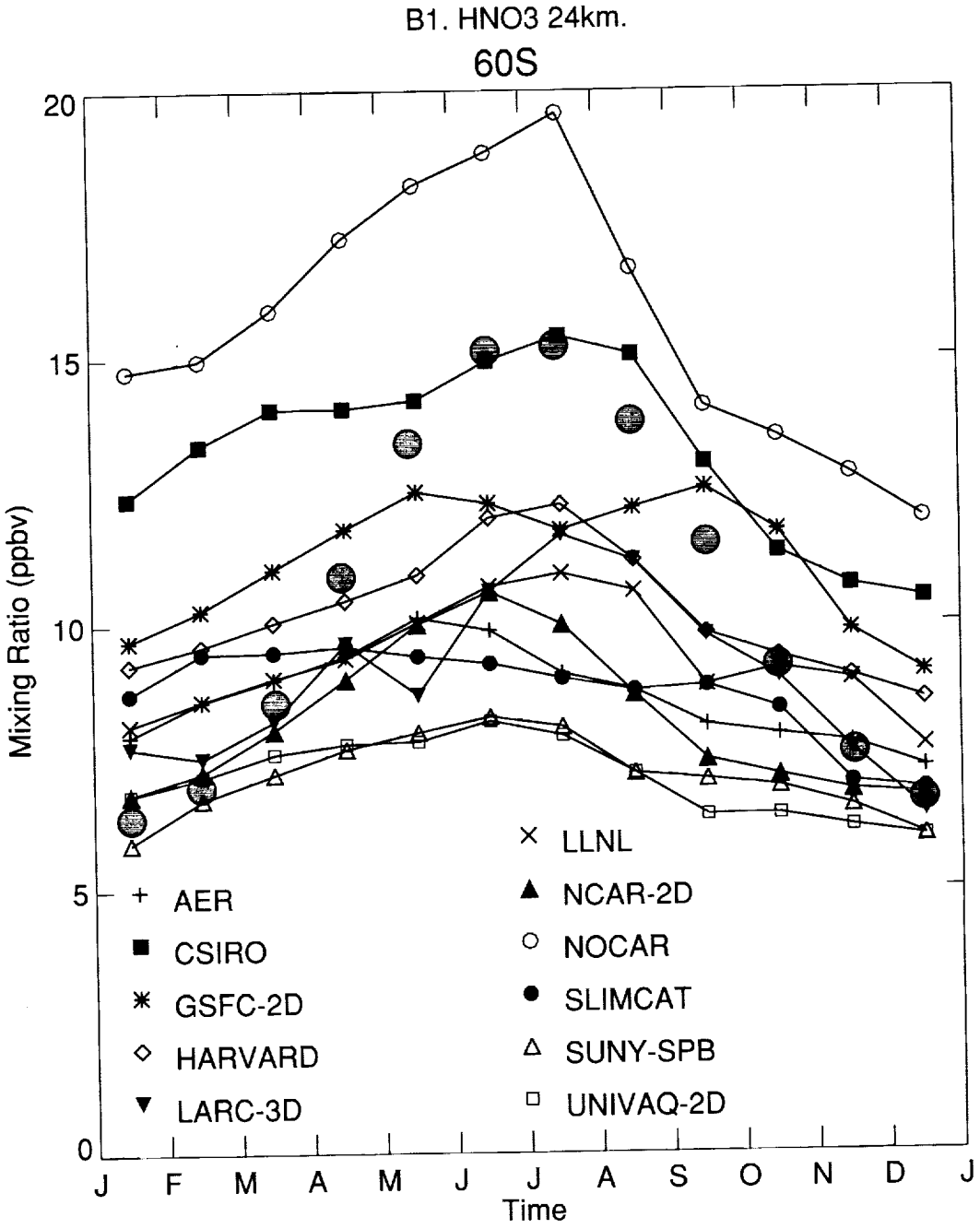

Figure 3.5.16. Seasonal variation of HNO_3 at 24 km and 60S for model simulations, and CLAES, MLS measurements. (Filled circle: CLAES).

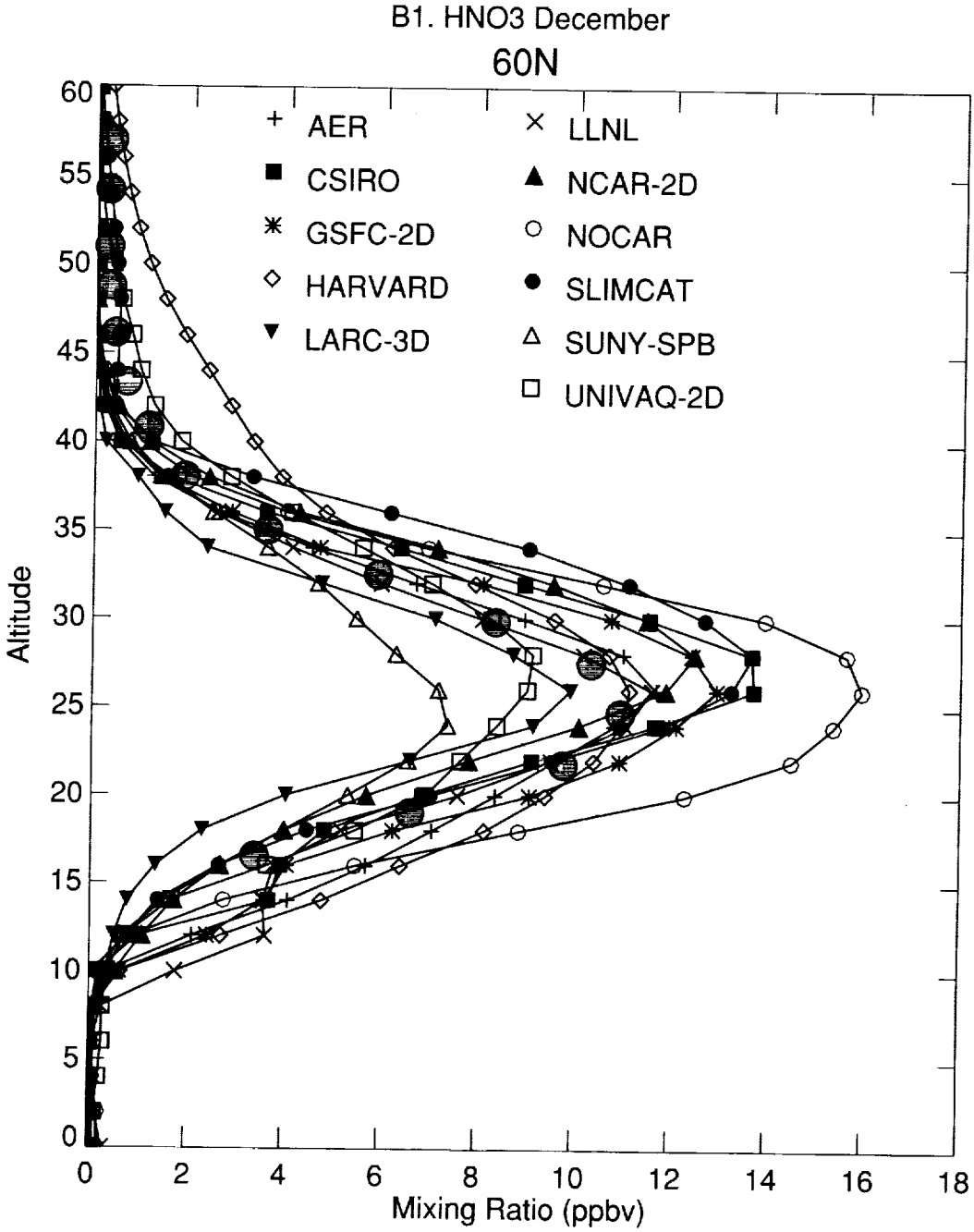

Figure 3.5.17. Vertical profiles of model calculated and measured HNO_3 at 60N in December. (Filled circle: CLAES)

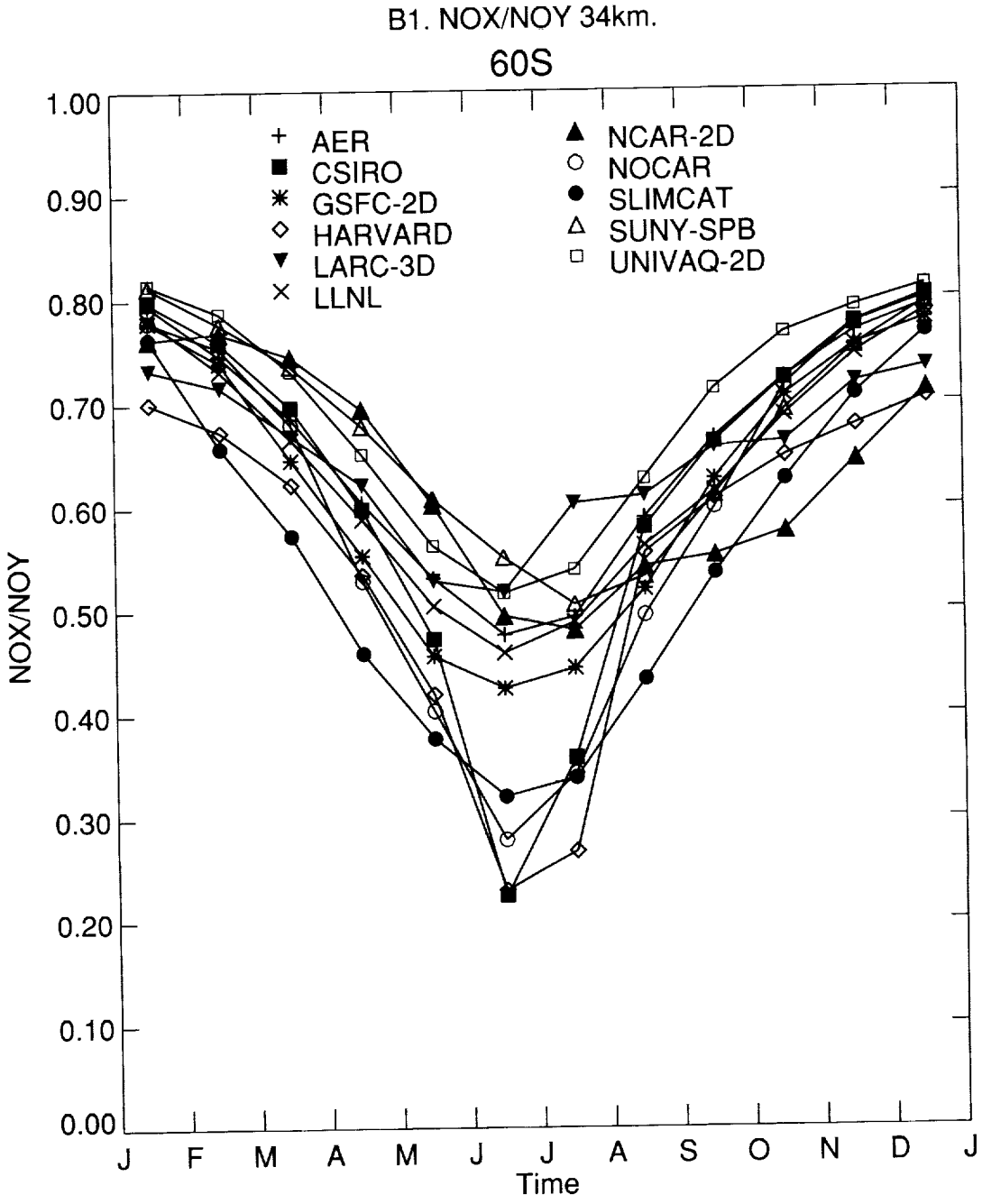

Figure 3.5.18. Model simulated NOx/NOy (a) Seasonal variation at 34 km and 60S, and (b) vertical profiles of model calculated at 40N in November.

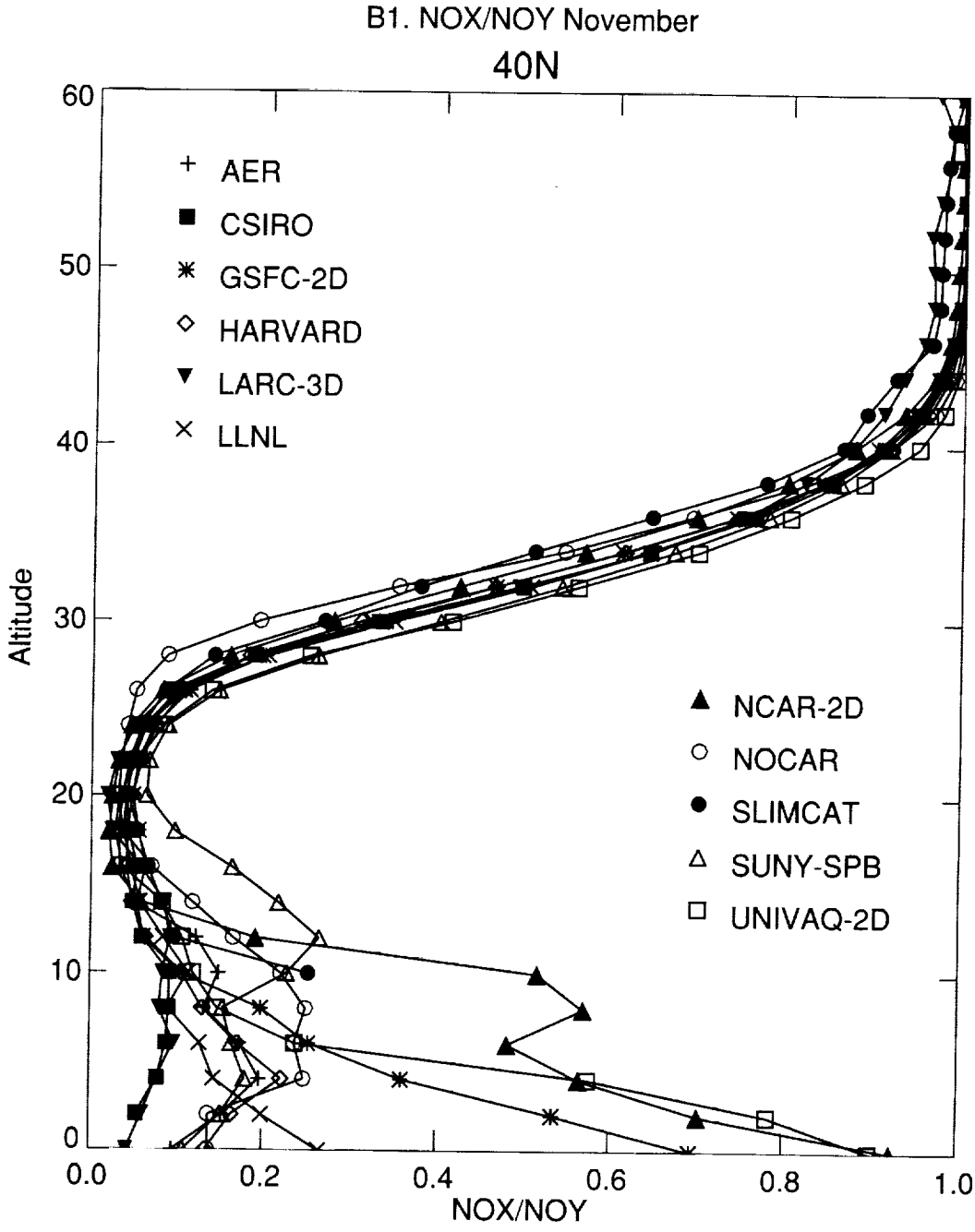

Figure 3.5.18. Concluded.

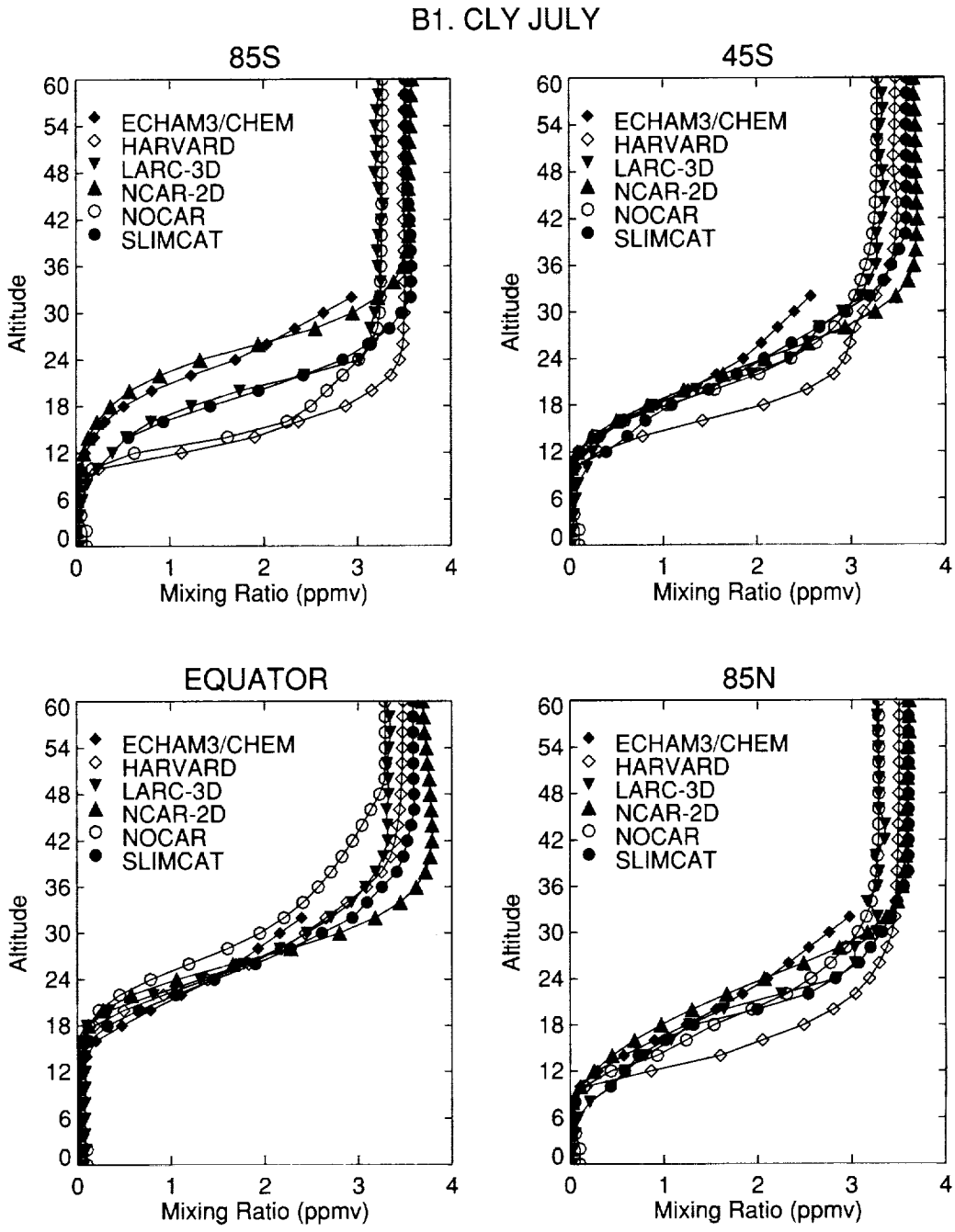

Figure 3.5.19. Vertical profiles of model calculated Cly at 85S, 45S, equator, and 85N in July for (a-b) case B1 and (c) case B2.

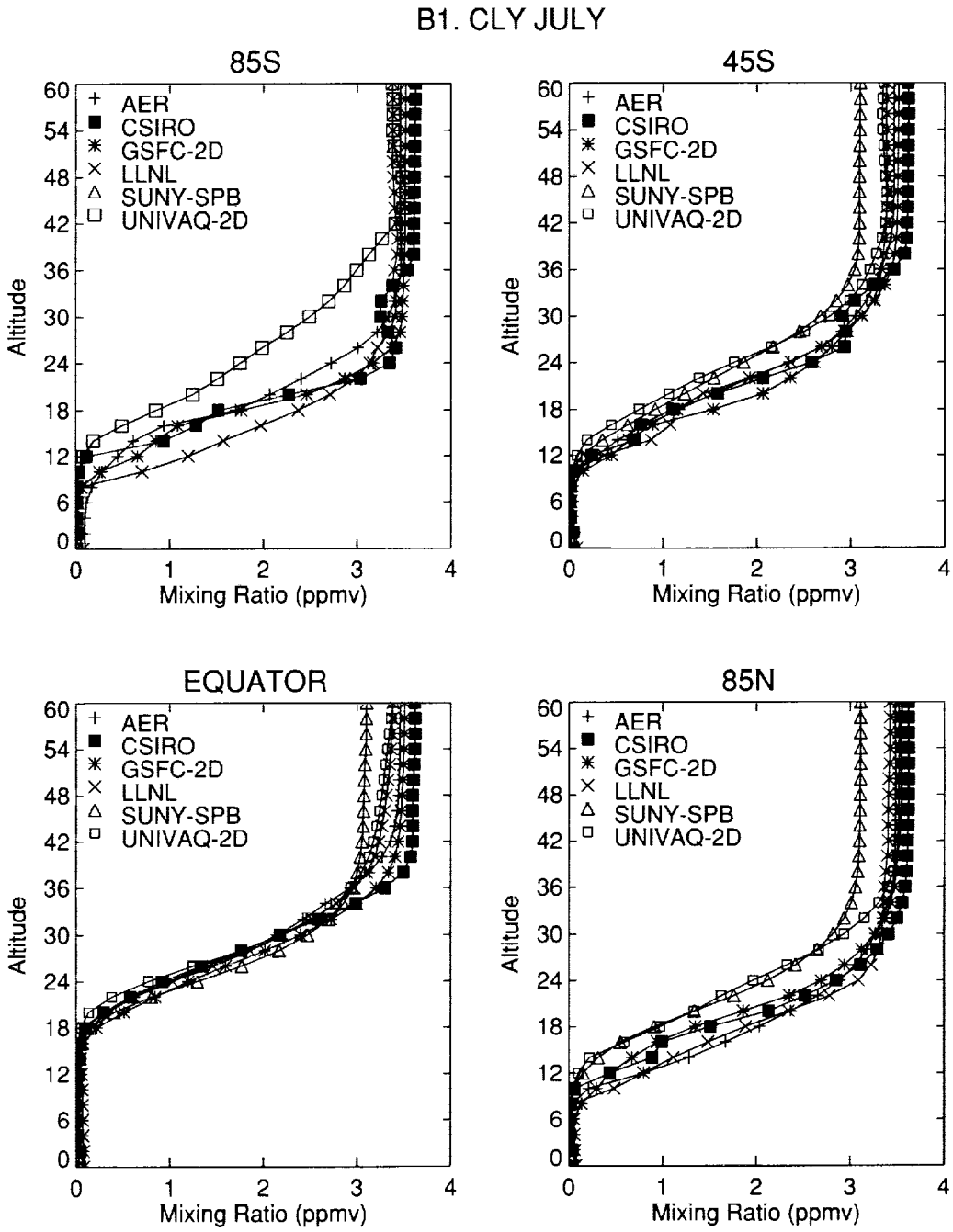

Figure 3.5.19. Continued.

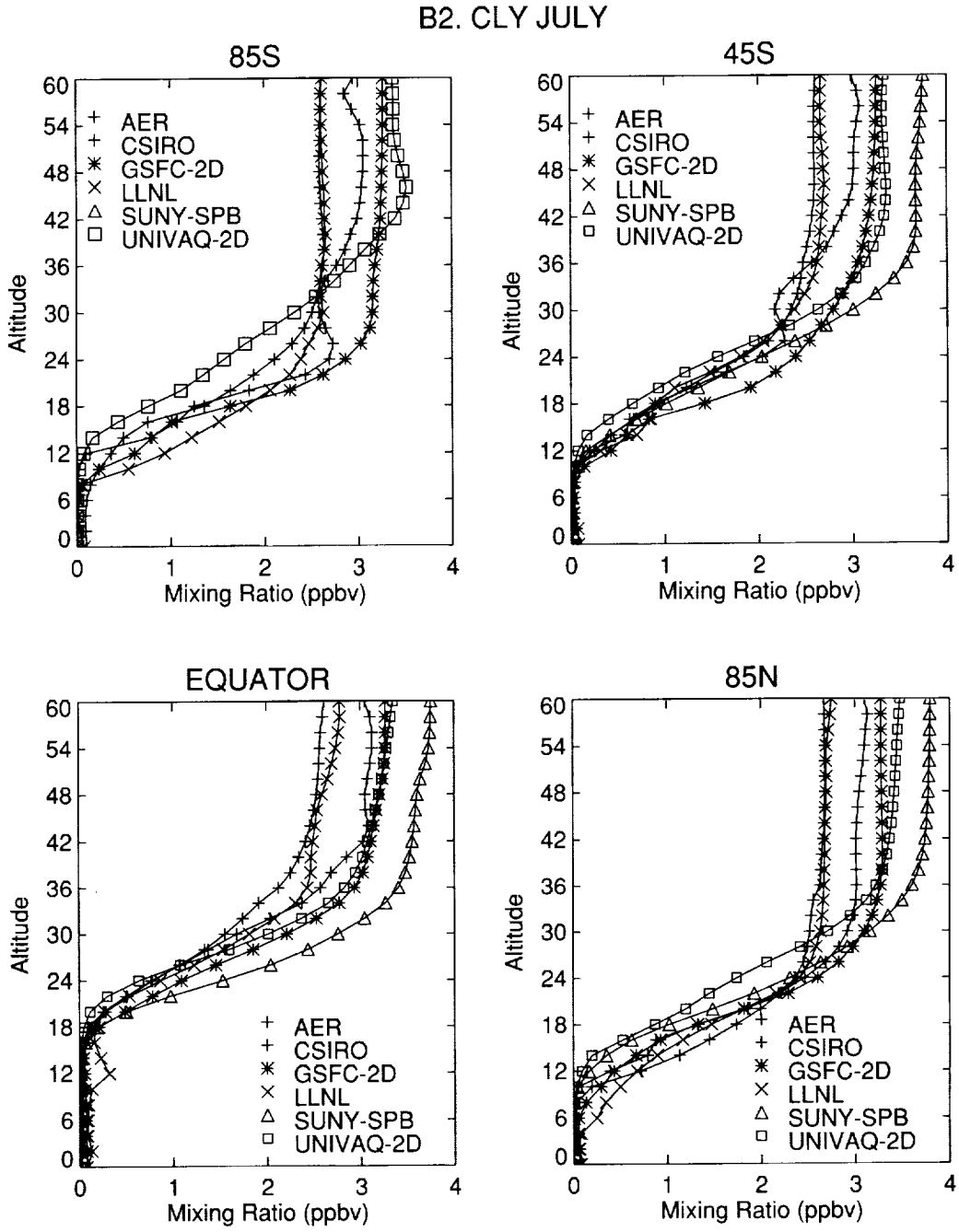

Figure 3.5.19. Concluded.

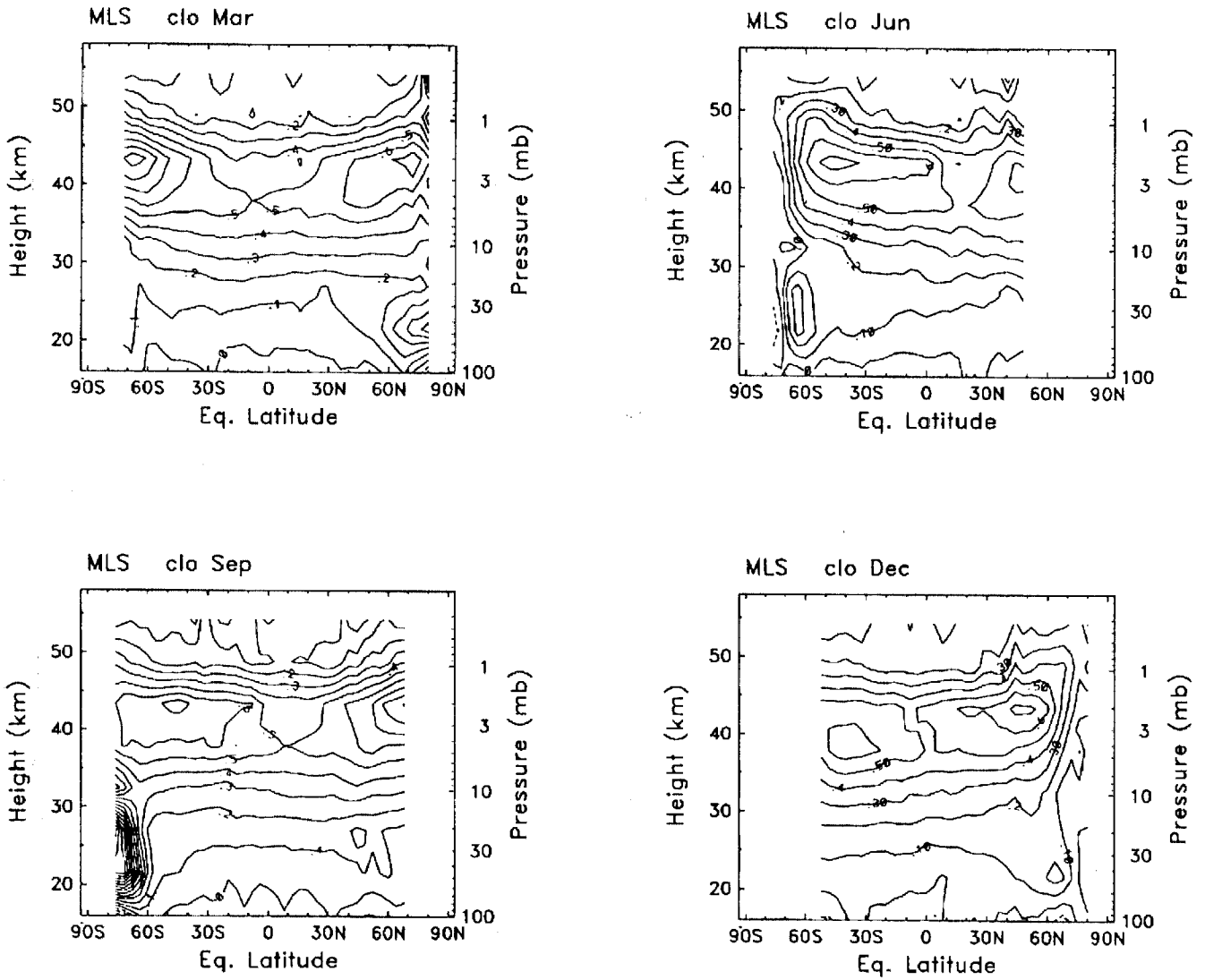

Figure 3.5.20. MLS measured ClO latitude-height cross section for March, June, September and December.

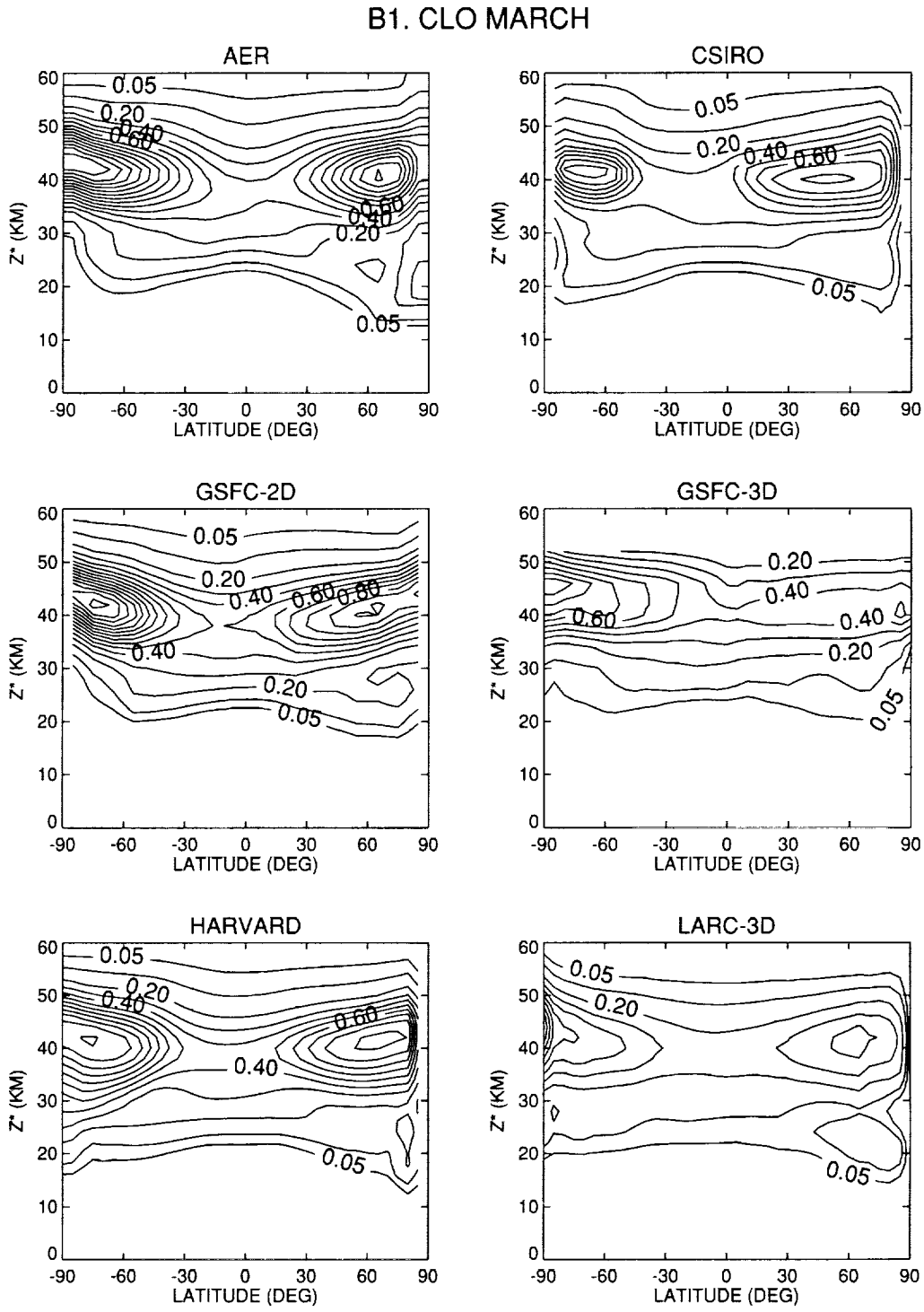

Figure 3.5.21. Model simulated daytime averaged ClO latitude-height cross section for (a-b) March and (c-d) September.

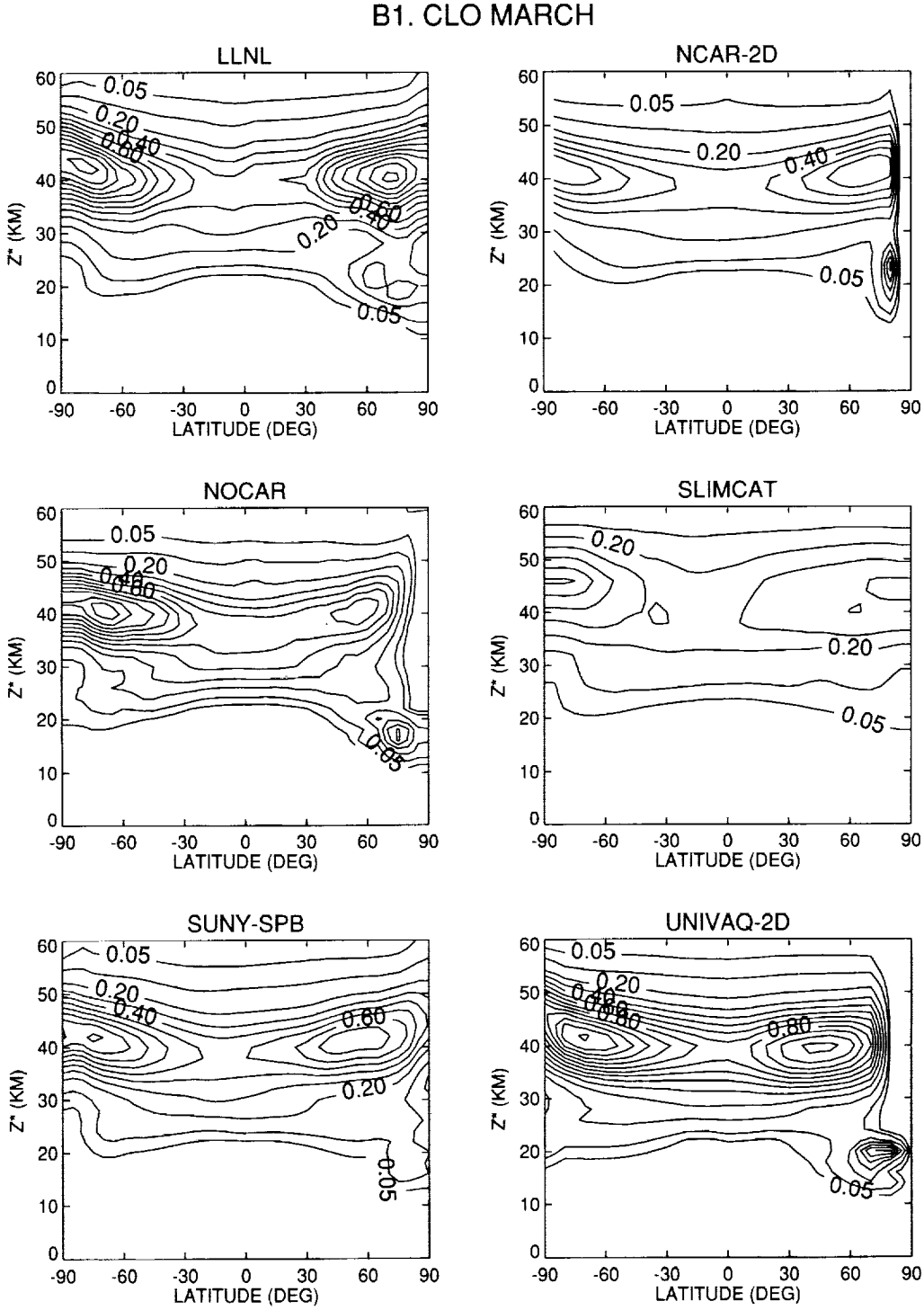

Figure 3.5.21. Continued.

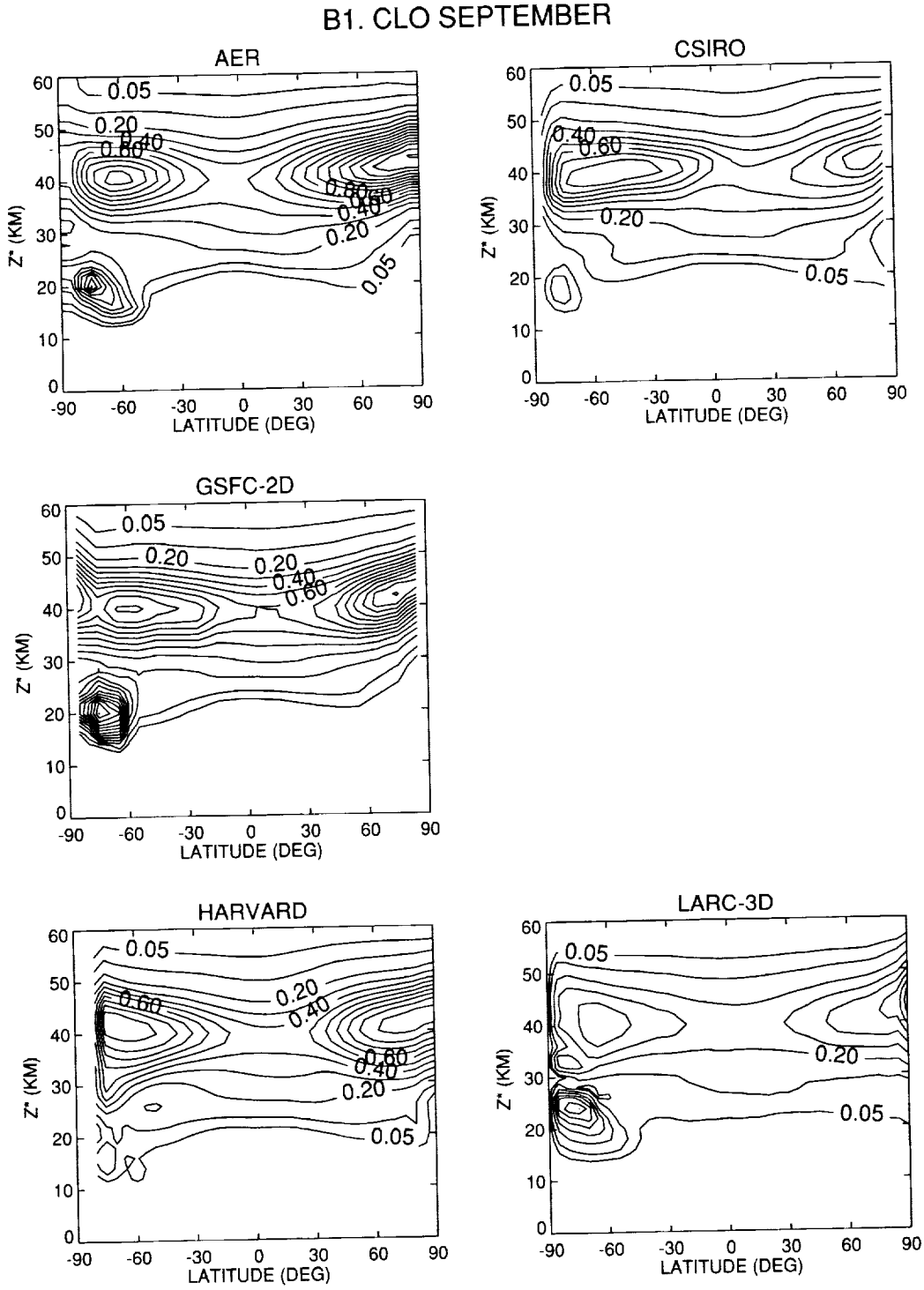

Figure 3.5.21. Continued.

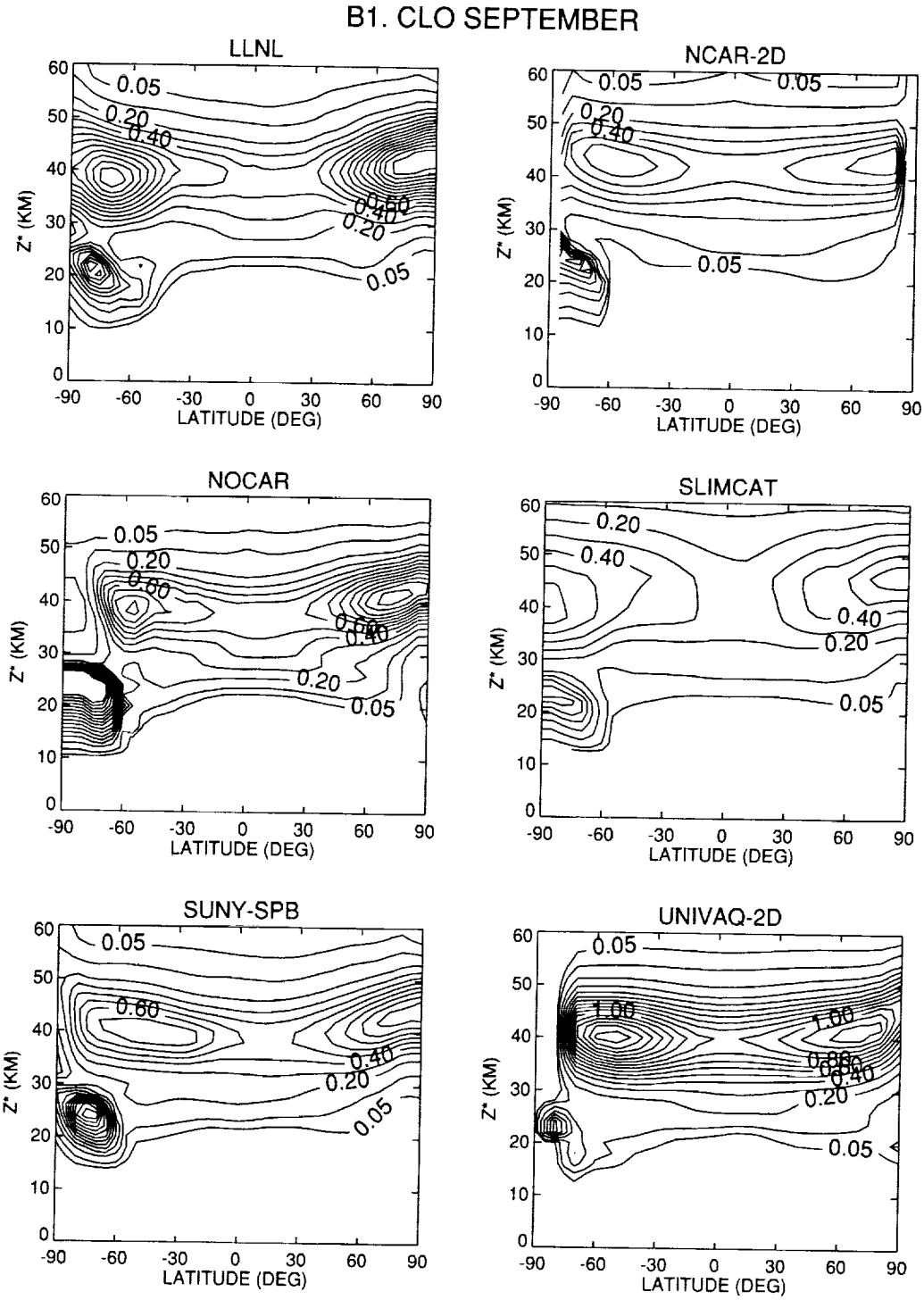

Figure 3.5.21. Concluded.

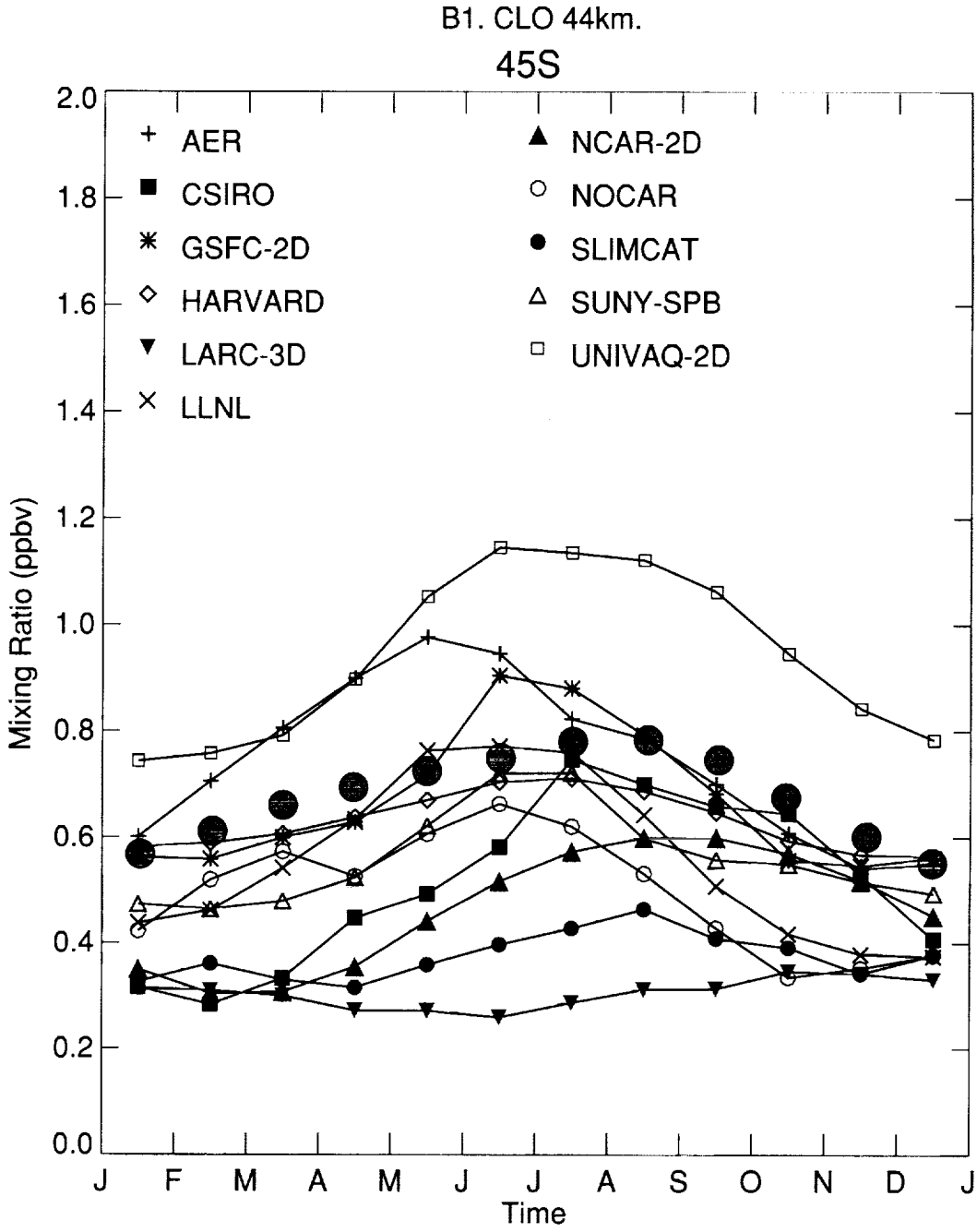

Figure 3.5.22. Seasonal variation of ClO at 44 km and 45S for model simulations and MLS measurement (Filled circle: MLS).

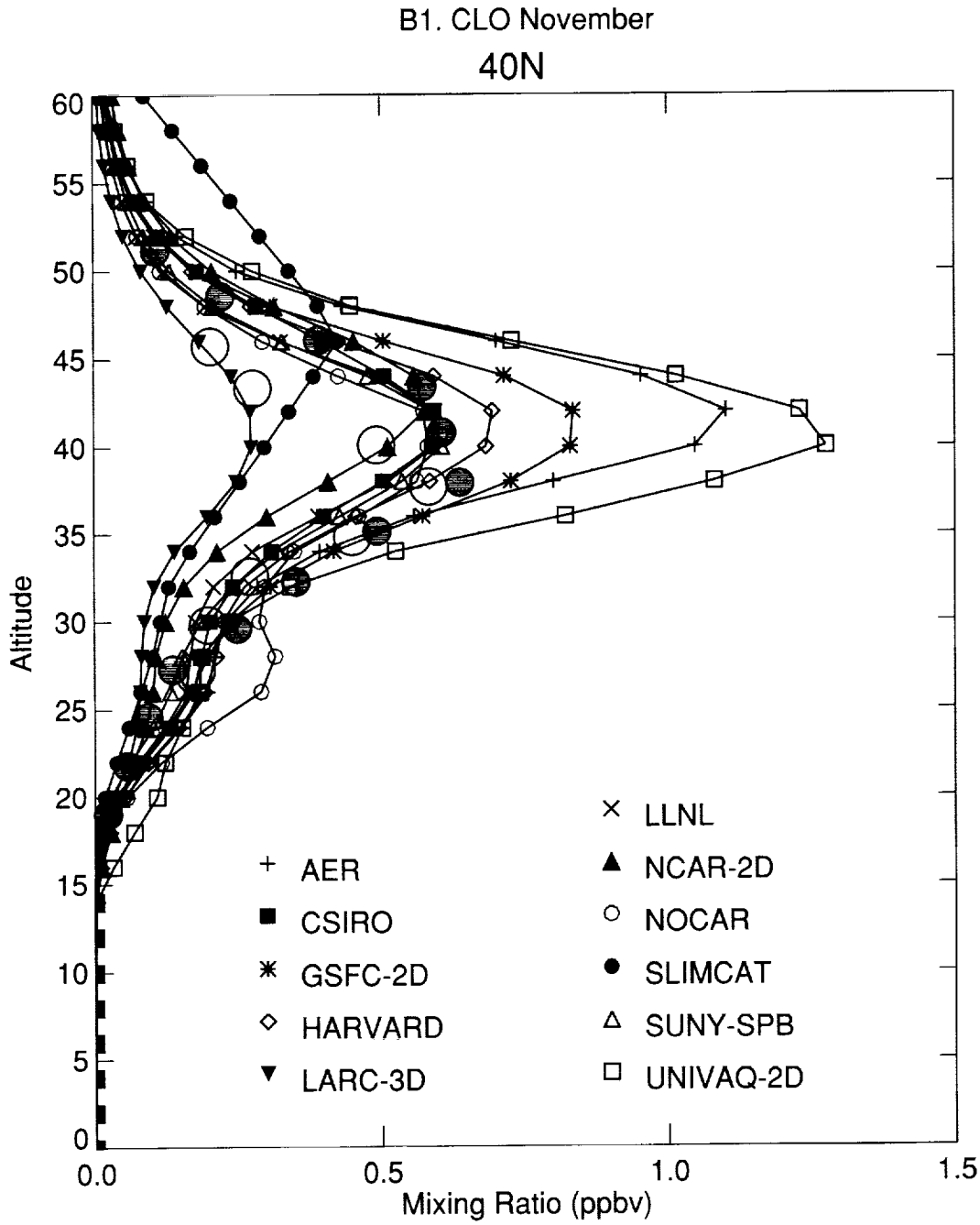

Figure 3.5.23. Vertical profiles of model calculated and measured ClO at 50N in November (Filled circle: MLS, white circle: ATMOS/MAS).

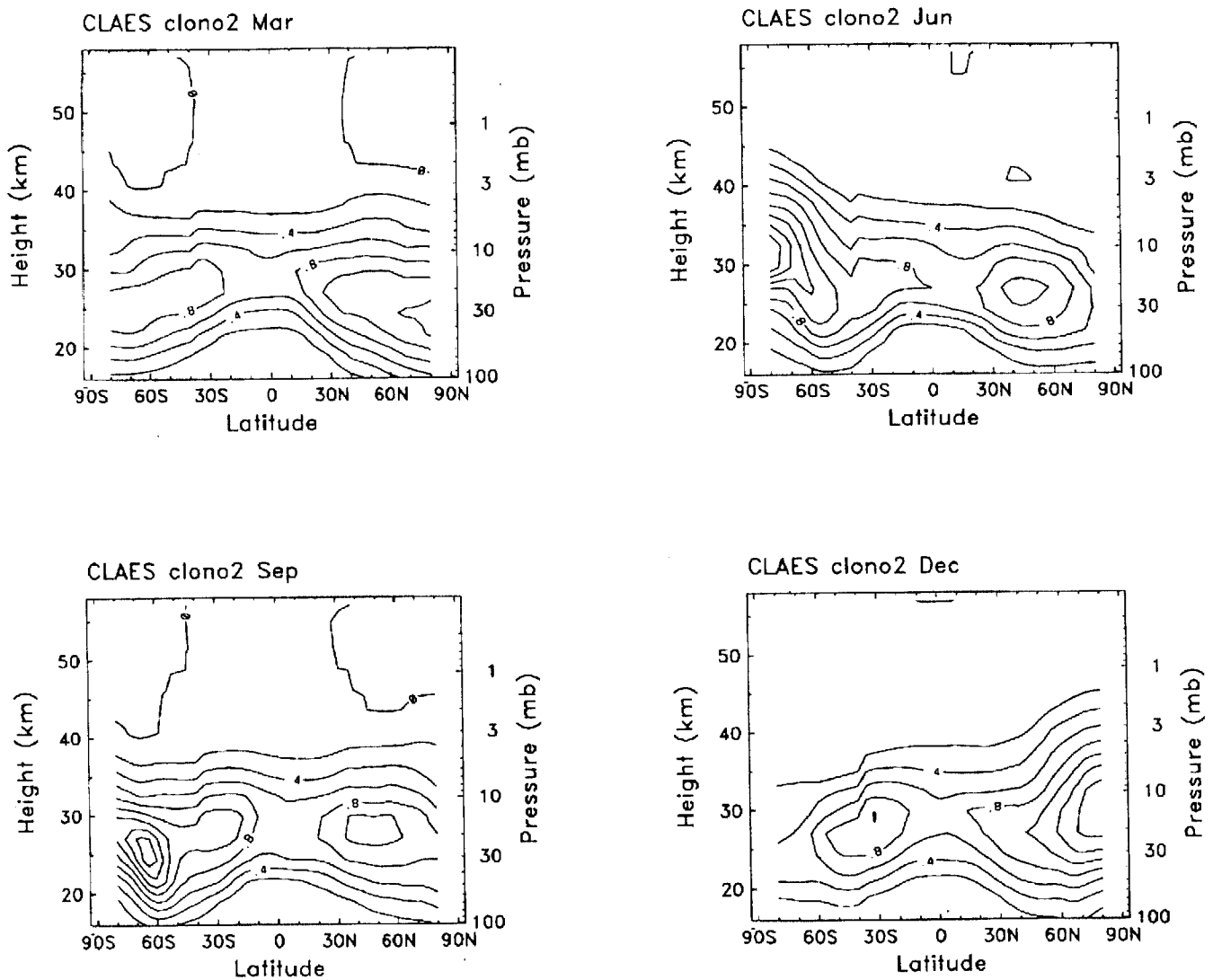

Figure 3.5.24. CLAES measured $ClONO_2$ latitude-height cross section for March, June, September and December.

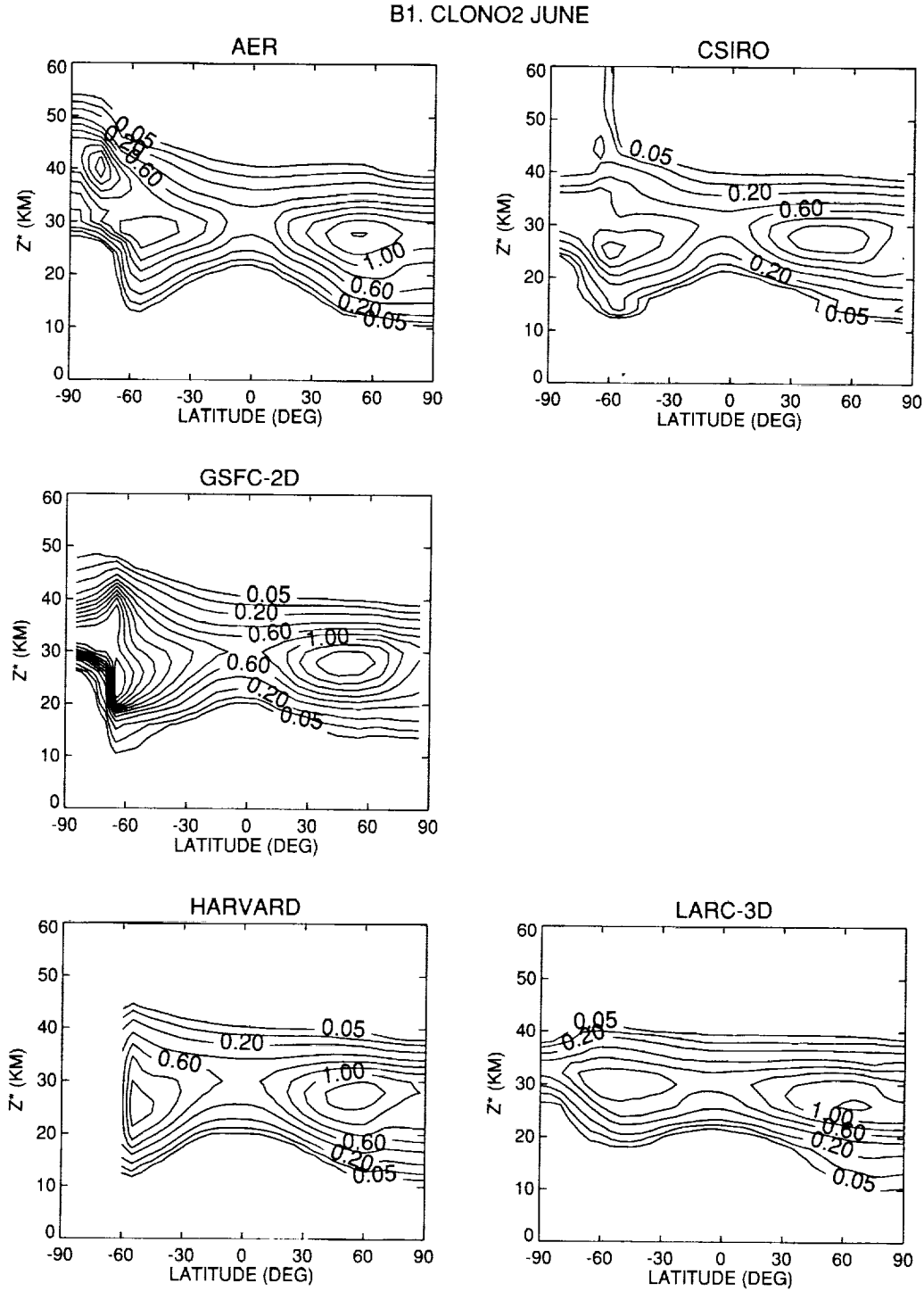

Figure 3.5.25. Model simulated $ClONO_2$ latitude-height cross section for (a-b) June and (c-d) December.

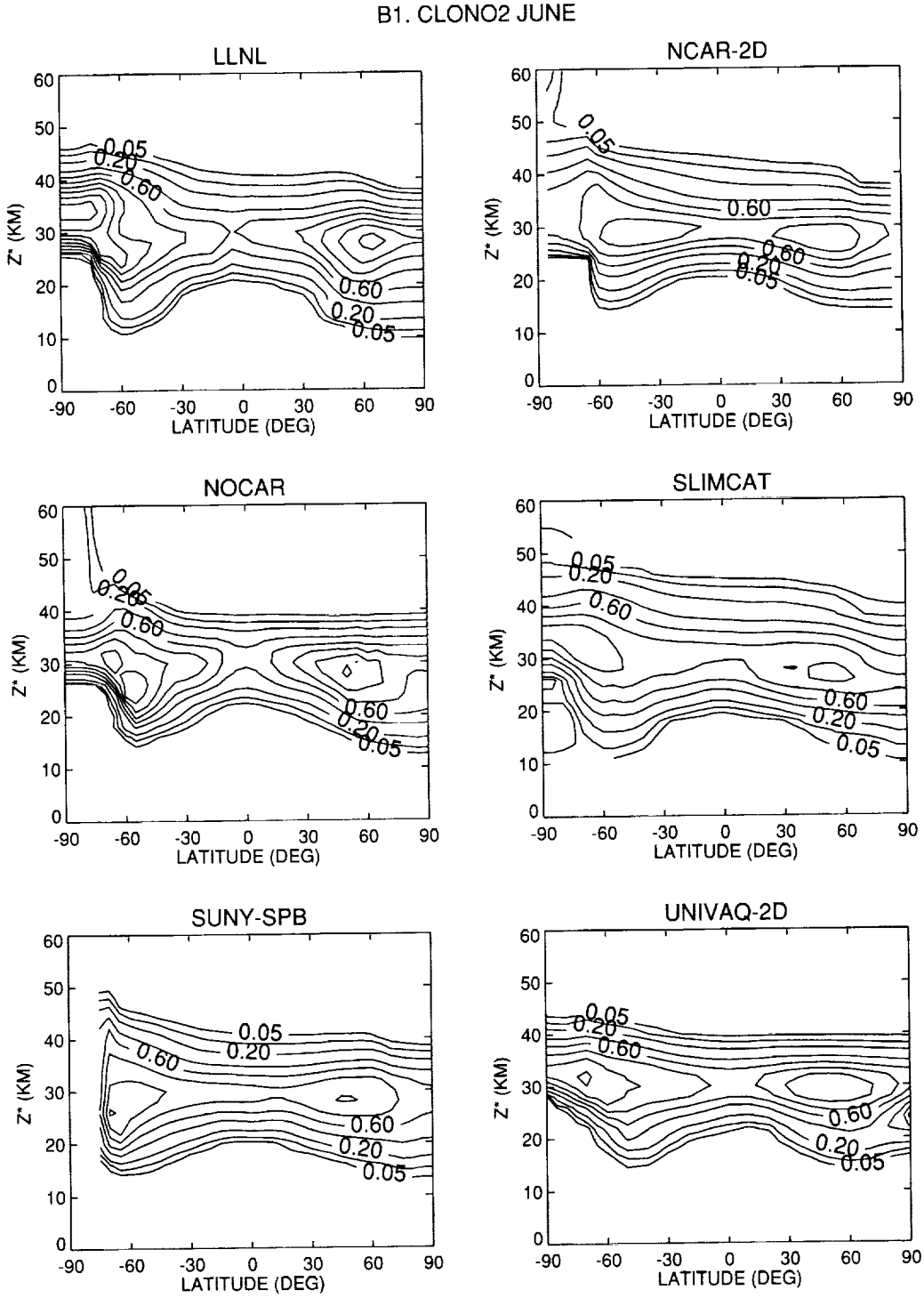

Figure 3.5.25. Continued.

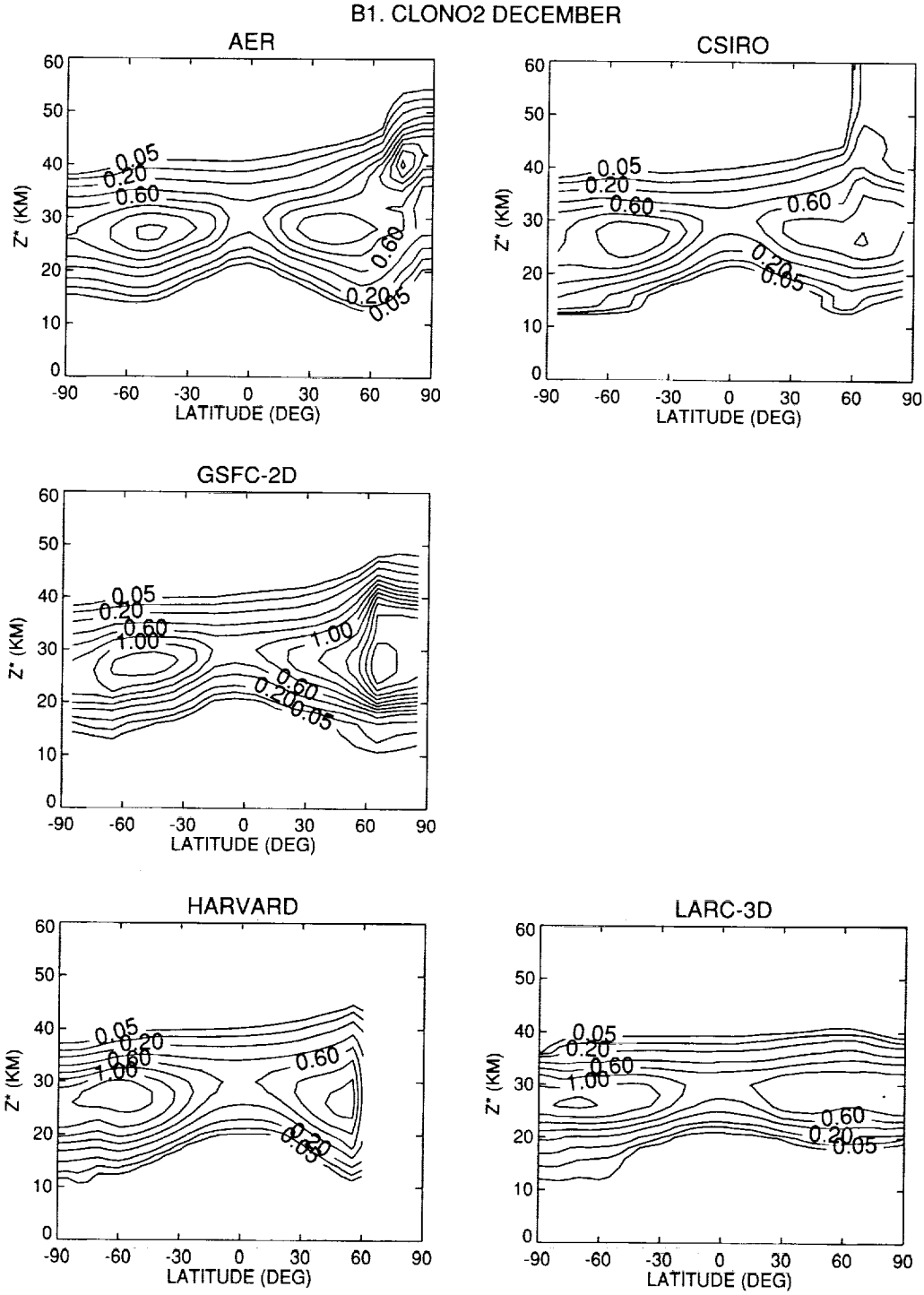

Figure 3.5.25. Continued.

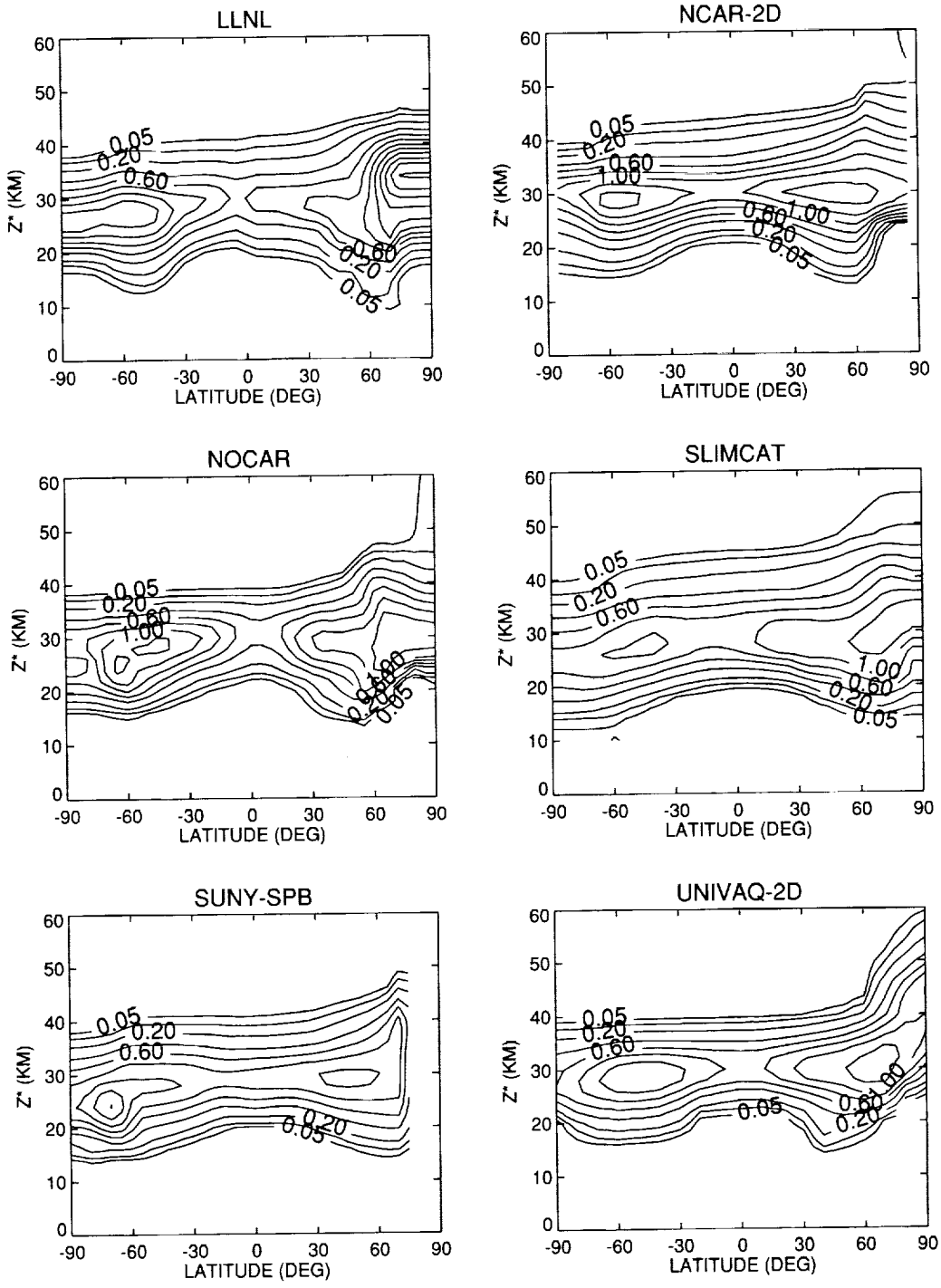

Figure 3.5.25. Concluded.

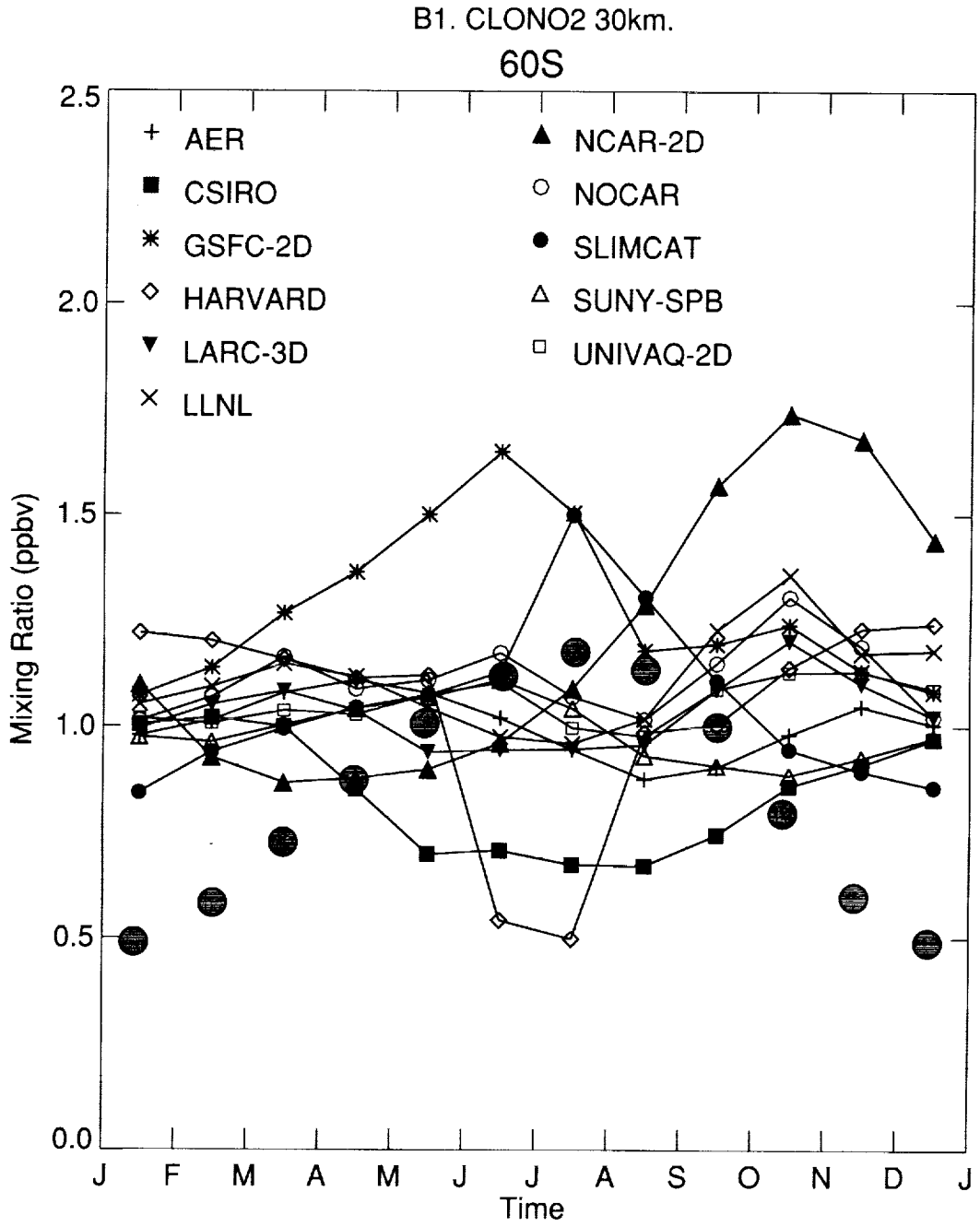

Figure 3.5.26. Seasonal variation of $ClONO_2$ at 30 km and 60S for model simulations and CLAES measurement (Filled circle: CLAES).

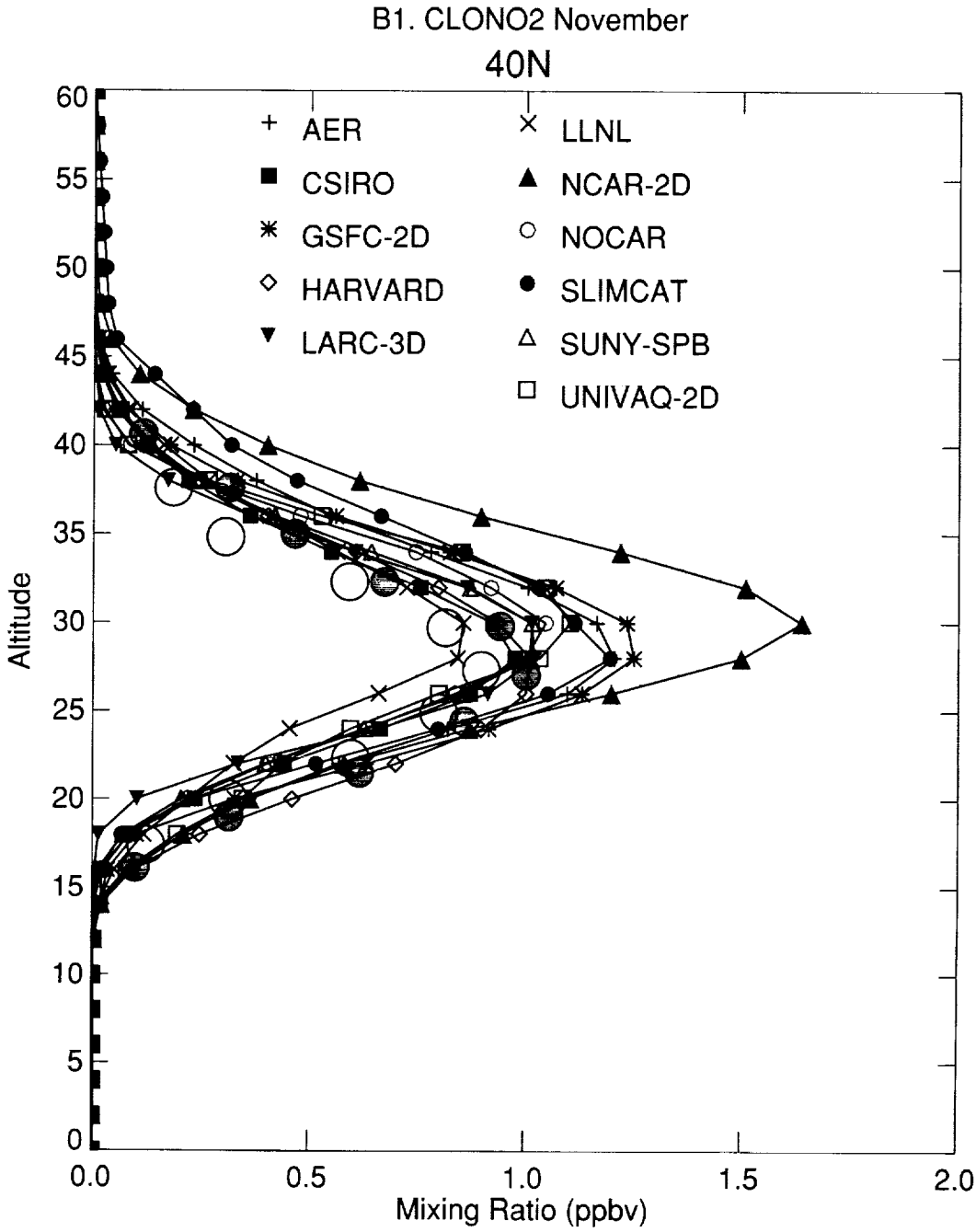

Figure 3.5.27. Vertical profiles of model calculated and measured $ClONO_2$ at 40N in November (Filled circle: CLAES, white circle: ATMOS/ATLAS)

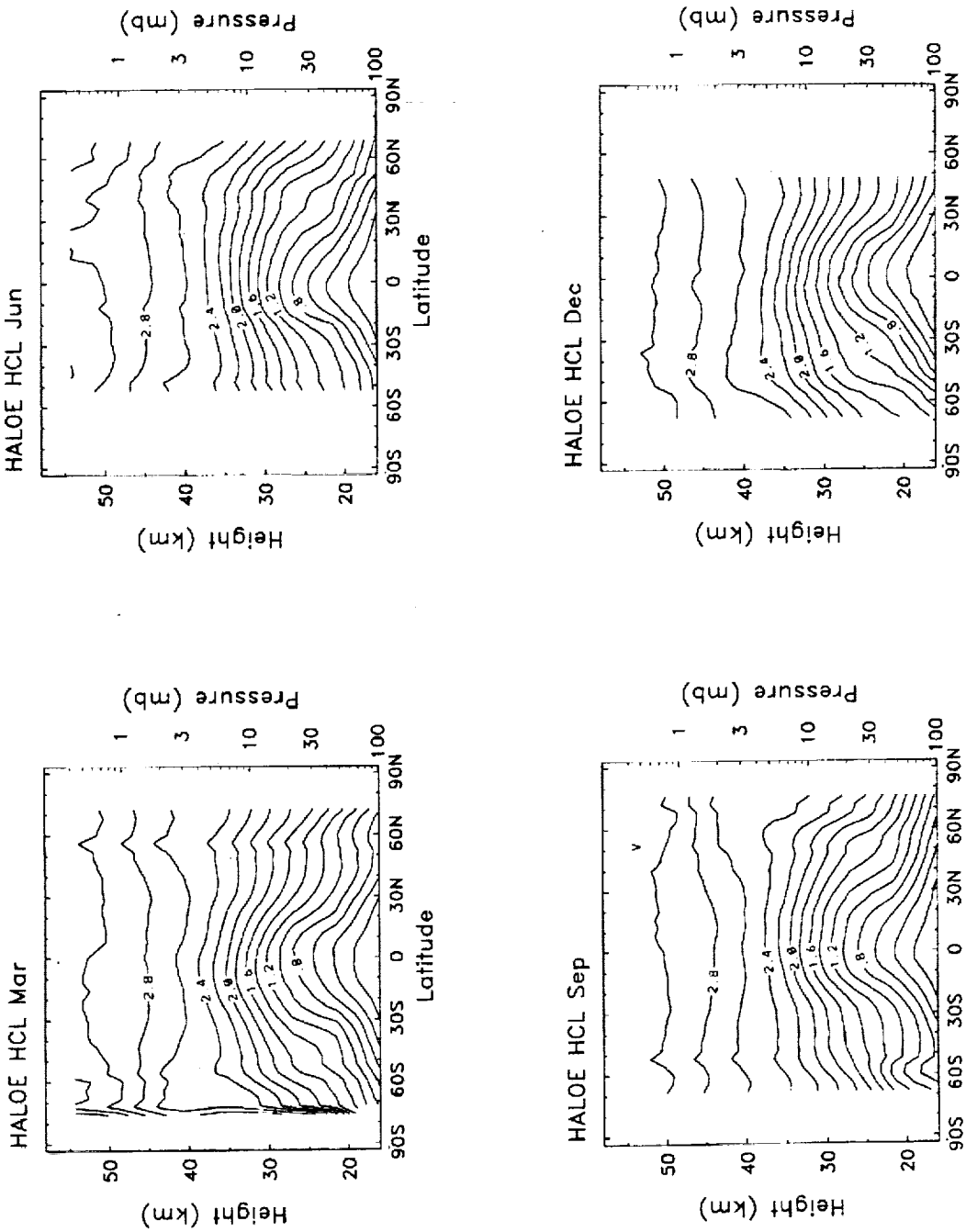

Figure 3.5.28. HALOE measured HCl latitude-height cross section for March, June, September and December.

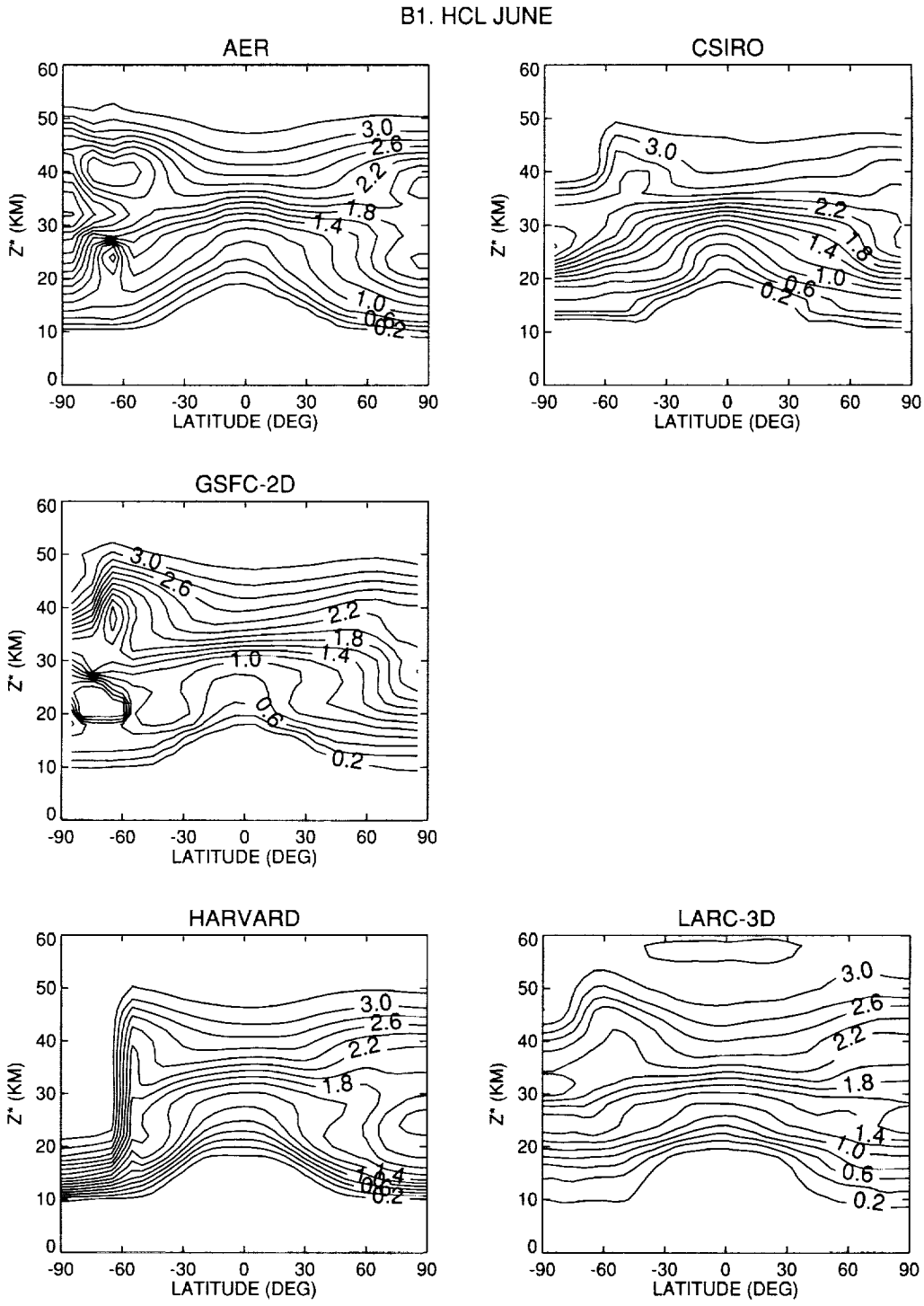

Figure 3.5.29. Model simulated HCl latitude-height cross section for (a-b) June and (c-d) December.

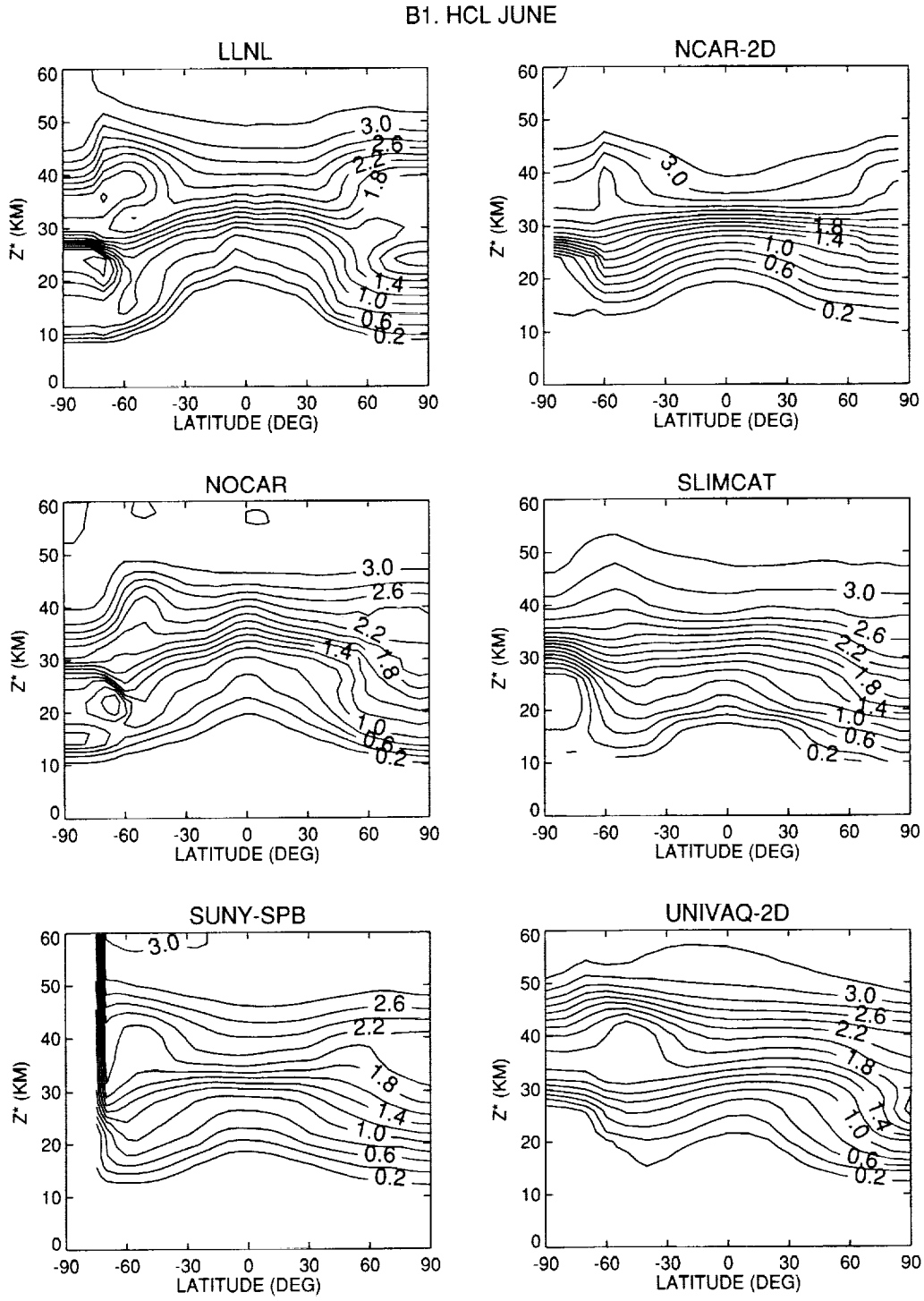

Figure 3.5.29. Continued.

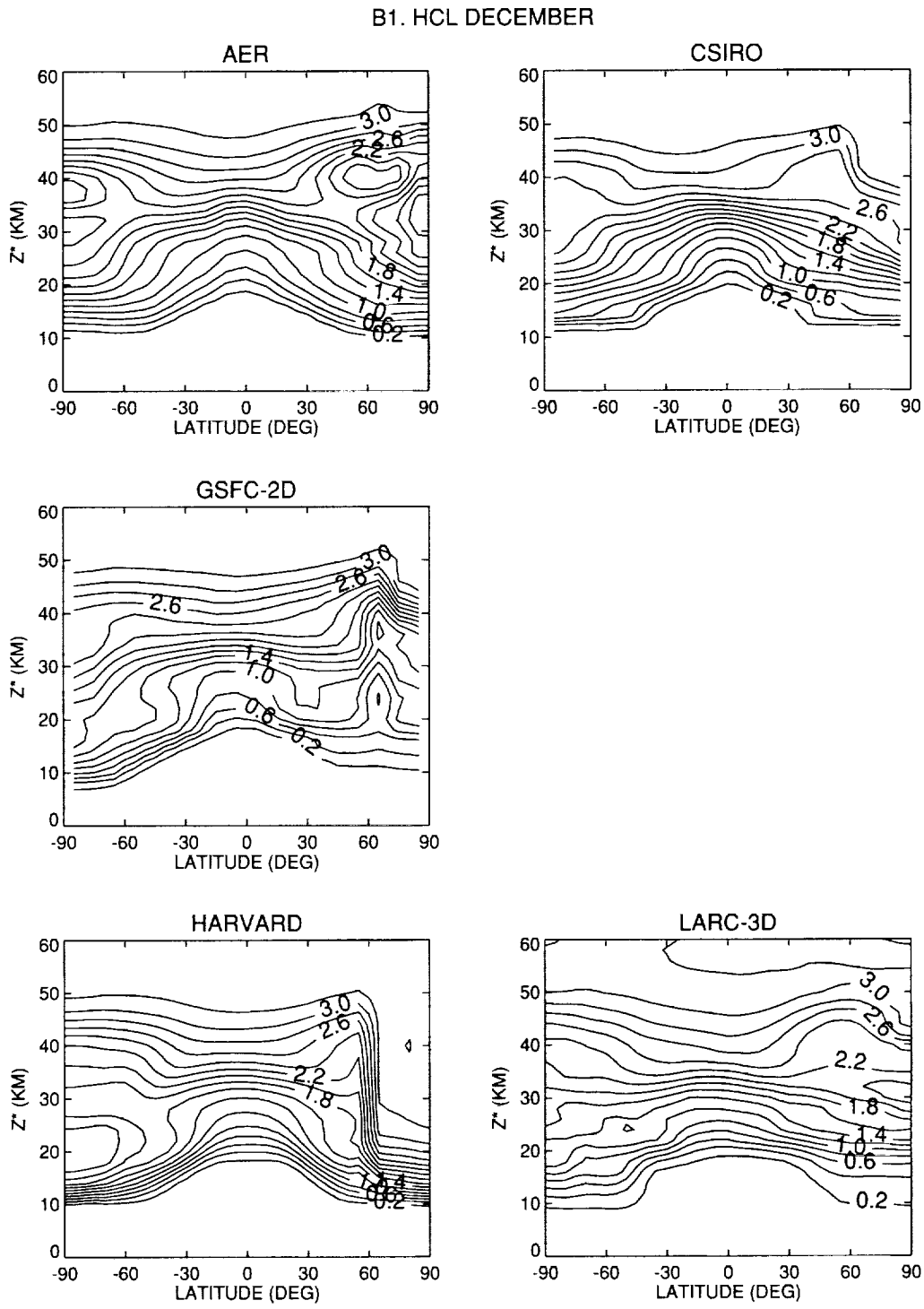

Figure 3.5.29. Continued.

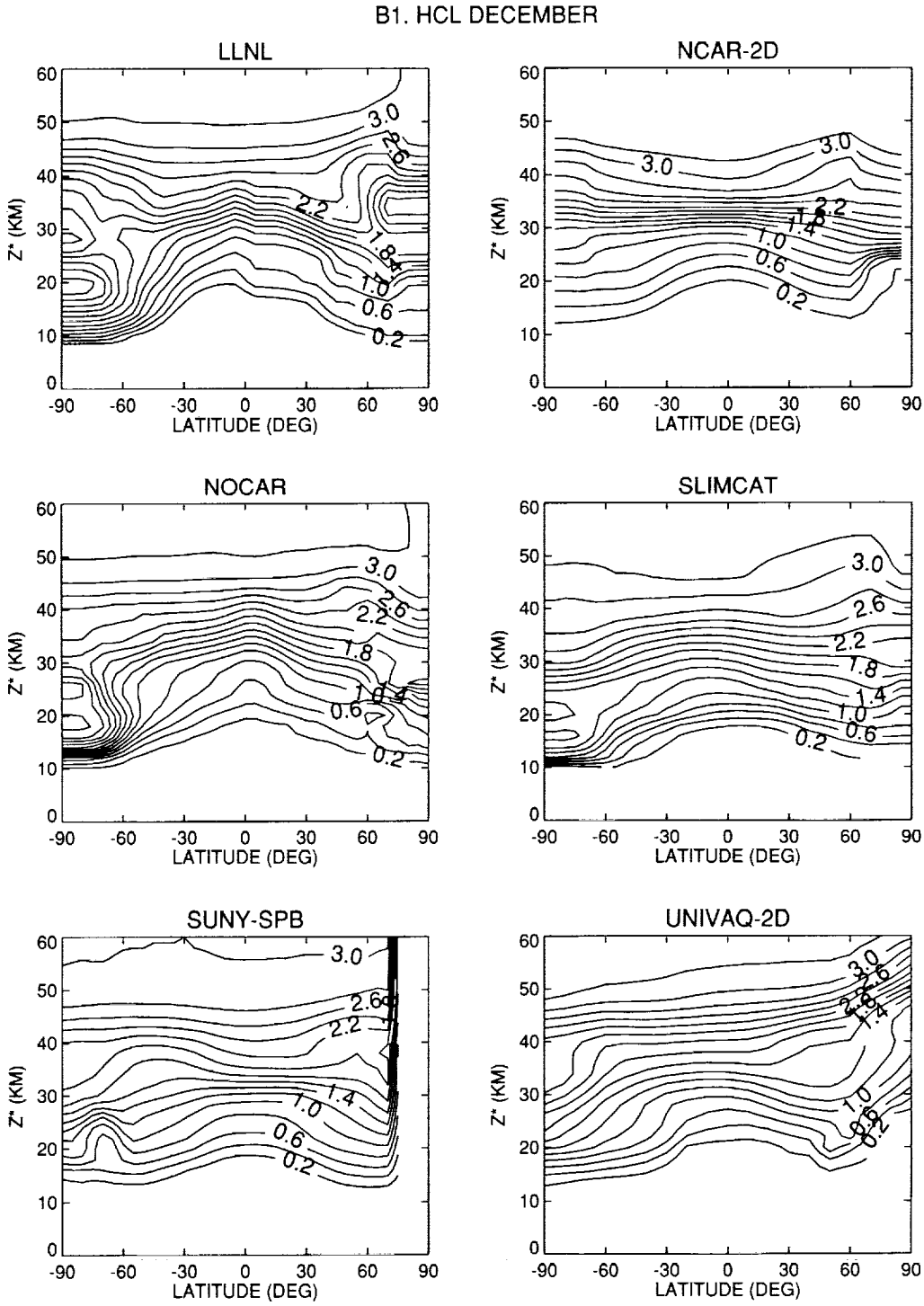

Figure 3.5.29. Concluded.

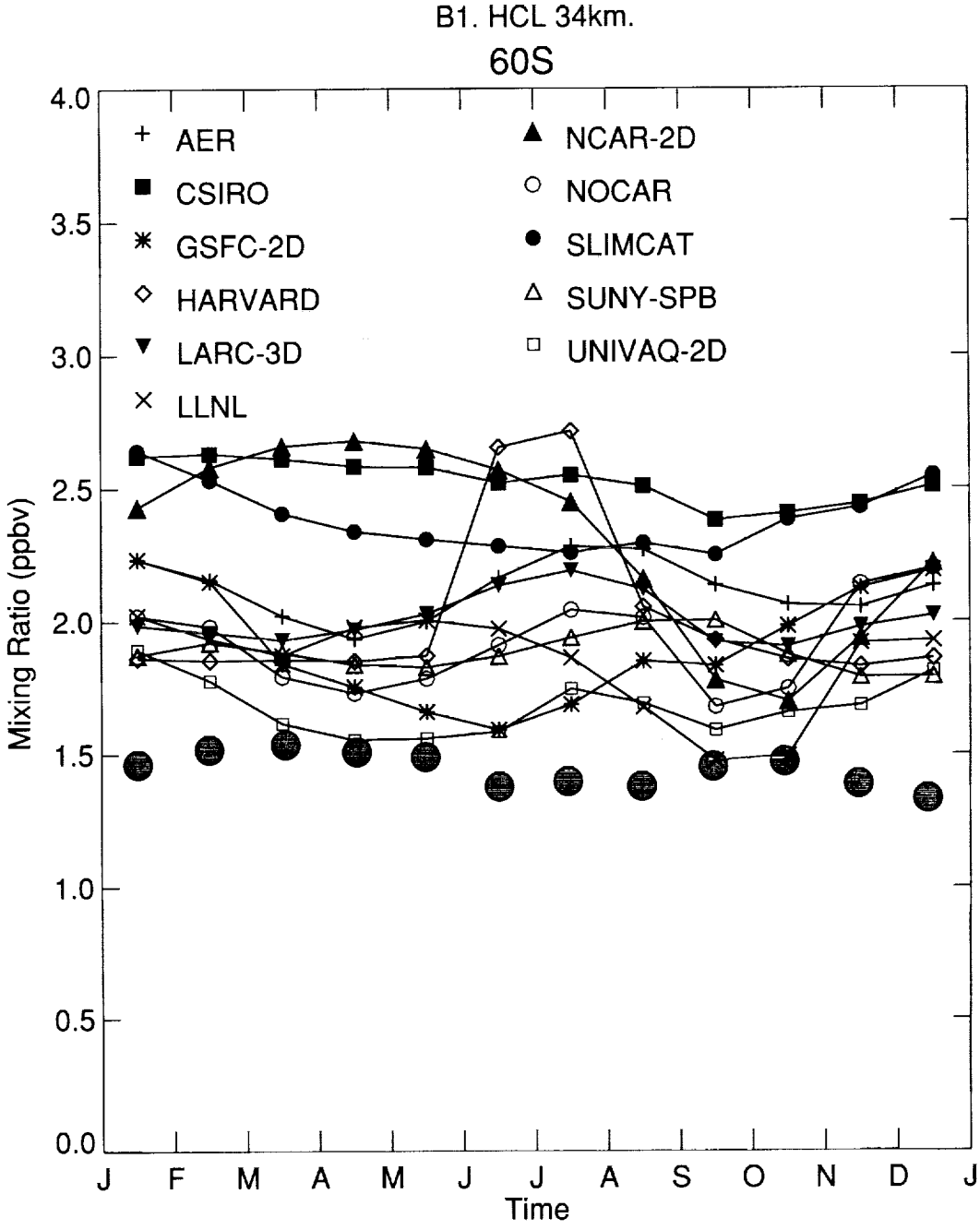

Figure 3.5.30. Seasonal variation of HCl at 34 km and 60 S for model simulations and HALOE measurement. (Filled circle: HALOE).

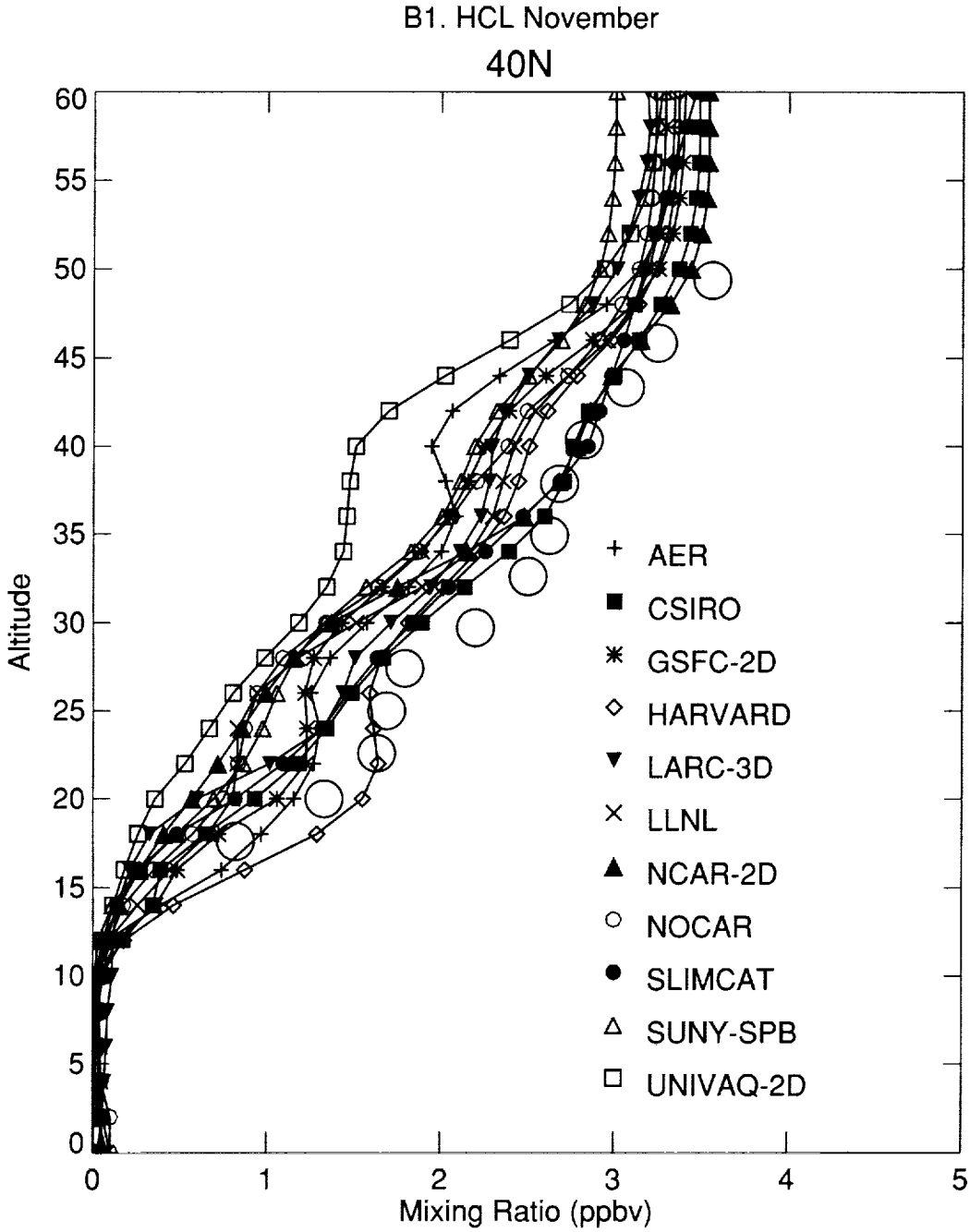

Figure 3.5.31. Vertical profiles of model calculated and measured HCl at 40N in November (white circle: HALOE)

4. Ozone Climatology

Jennifer A. Logan[1] and Richard D. McPeters[2]

1. Harvard University
2. NASA/Goddard Space Flight Center

4.1 Introduction

The primary role of models in the assessment process is to predict changes to ozone. It is crucial therefore that the ability of the models to reproduce the actual distribution of ozone be tested. Historically, maps of the ozone column (latitude by month) have been used for this purpose. In MM I a climatology was developed for the vertical distribution of ozone for 15-60 km, based on SBUV data for 1979-80. SBUV profiles are reported with vertical resolution of ~5 km, but the true resolution is lower, ~8 km above the ozone maximum and ~15 km for 10-25 km. The climatology was considered valid to about 20-30% at 20 km and to 50% at 15 km. Comparisons were made with models in mixing ratio (ppm), which emphasizes the middle and upper stratosphere.

A new ozone climatology was developed for the vertical distribution of ozone for MM II. Our goal was to develop a product that could be used to evaluate models in the lower stratosphere, the region where most of the ozone column resides and where most of the ozone loss is occurring, as well as the middle and upper stratosphere.

The data used for the climatology are from ozone sonde stations and from SAGE II. We derived the climatology for 1988-96. This period was centered on 1992, the base year for the B1 model runs. Several years of sonde data are required to develop a climatology, since many stations make measurements weekly. Also, the SAGE data could not be used for all altitudes for up to 2 years after the Pinatubo eruption in 1991. A several year average is thus needed to obtain a realistic climatology. Using the period 1988-96 dampens biases caused for example by anomalously low values at northern high latitudes in recent years in late winter and starting the period as late as 1988 allows the inclusion of several sonde stations that started in the late 1980s. The modeling groups were asked to provide their best simulation for 1992 in terms of both the tropospheric trace gas boundary conditions and the aerosol distribution (see Chapter 1). We used sonde data for 40-60 N, where there are stations that make measurements three times per week, to evaluate any bias between the 9 year average for ozone and data for 1992 exclusively. For these latitudes, ozone in 1992 was lower than the 9-year mean by 10-20% from about 30 to 200 mbar in January and December (40-50 N only); by less than 5% to 15% in February, May, June, August, September and November: and by less than 5% in March, April, July and October. For most months and altitudes, the 9-year climatology is within 10% (or less) of the values observed in the lower stratosphere at northern mid-latitudes in 1992. There may be similar small differences between 1992 and the mean for 1988-96 at higher latitudes, but the weekly soundings at the few high latitude stations are inadequate to define monthly anomalies for 1992.

4.2 Observational Data

The climatology using SAGE II and sonde data can be developed with some confidence, based on the results of the SPARC Ozone Trends Assessment (WMO, 1998). As part of that activity, SAGE II ozone profiles (Version 5.96) were compared with MLS, HALOE, SBUV, lidar, sonde, and Umkehr

data. The comparison with MLS data showed clearly when the SAGE II data were corrupted by aerosols following the Pinatubo eruption, and allowed the development of time filtering criteria (as a function of altitude and latitude) for SAGE II data. It was recommended that data be omitted for 6 months at 30 km, up to 1.5 years at 24 km, and up to 2.5 years at 19 km. One problem identified with SAGE II data (v5.96) is that there is a difference of ~10% between sunrise and sunset measurements above 45 km; it was recommended that these measurements be combined, as there is no reason to prefer one over the other. Comparison of SAGE II overpasses with sonde profiles showed agreement to within 10% for 20-30 km (with SAGE larger), but differences increased with decreasing altitudes and latitudes, to as much as 30% at 15 km. Lidar data also agree with SAGE II profiles to within about 5% for 22-35 km, with SAGE larger; SAGE II and HALOE agree to within 5% for 25-50 km; MLS concentrations are a few percent larger than SAGE II from about 26-42 km, and a few percent smaller than SAGE II at 48 km. Evaluation of the sonde data indicated that all three sonde types in use today provide consistent results between the tropopause and ~28 km. Comparison of sonde and lidar data in the stratosphere showed agreement to within ±3-5%.

Based on results of the SPARC data evaluation, we chose to use sonde data for 0-28 km, and SAGE II data for 22-60 km. Monthly means were formed for each type of data in 10° latitude bins for 80°N to 80°S, and with resolution of 2 km in pressure altitude. The SAGE data were converted from altitude to pressure using NCEP temperatures. Data from 2-4 sonde stations are available for each latitude band from 10° to 70°N, but there are only 1-2 stations in most southern hemisphere latitude bands, and none for 0°-10°N and 50°-60°S. Monthly means for all stations in a given latitude band were weighted equally. Data from 0°-10°S were used for 0°-10°N, and values for 50°-60°S were derived from neighboring latitude bands. The mean sonde and SAGE II profiles were compared (see Figure 4.1) and agreement between the two found to be excellent, except at 60°-70°S in September to December. The disagreement appears to be caused by a bias in the location of the sonde stations with respect to the position of the ozone hole, compared to the zonal mean measured by SAGE II. The method used here to form the climatology leads to a major problem in the depiction of tropospheric ozone - the longitudinal gradient in the southern tropics (Samoa, 14°S, 170°W, versus Natal, 6°S, 35°W) is translated into an unrealistic latitudinal gradient. The tropospheric part of the climatology in the tropics will be improved in future work.

The climatology was formed as follows: sonde data were used exclusively for 0-20 km, SAGE II data exclusively for 30-60 km, and weighted averages for 22-28 km (80% sonde and 20% SAGE at 22 km, 60% sonde and 40% SAGE at 24 km etc). An error analysis of the climatology was not made because of time constraints, but will be part of future work. We emphasize however the agreement between sonde and SAGE II for 20 to 30 km, generally better than 5-10%. Another important point to note is that the spread of monthly mean ozone profiles for each station in a given latitude band in the lower stratosphere (e.g., stations in the North America, Europe, and Japan) is much smaller than the spread among model results for the same altitude (Figure 4.2). The ozone climatology is shown for mid-season months in partial pressure and mixing ratio in Figures 4.3 and 4.4.

Ozone column data for 1988-96 were also compiled into a climatology, using TOMS measurements from Nimbus-7, Meteor 3 and Earth Probe (Figure 4.5a). This was compared to the integrated ozone profile climatology. Differences are generally less than 5% except for small regions in the northern tropics, southern subtropics, and near 60°S in October-November (Figure 4.5b). The reasons for these differences are understood.

4.3 Comparison of Models with Observations

Model results were available from 13 models for the 1992 baseline atmosphere run, B1 of MM II. These included six 2-d models that participated in MM I, AER, GSFC-2D, LLNL, NCAR-2D, NOCAR, and UNIVAQ-2D, as well as 3 other 2-D models, CSIRO, HARVARD and SUNY-SPB. In addition, four 3-d models provided results, GSFC-3D (January-May only), LARC-3D, SLIMCAT, and ECHAM3/CHEM. Comparisons were made with model results in mixing ratio (ppm) and partial pressure (nbars). A variety of formats were used to compare model and observation. These included:

(1) Plots of the ozone column (latitude x month), and difference plots for January, April, July and October.

(2) Altitude by latitude plots of ozone for the same months in ppm and nbars, and difference plots.

(3) Vertical profiles of ozone for the same months at selected latitudes in ppm and nbars.

(4) The annual cycle of ozone at 12, 16, 20, 26, 32, and 40 km.

The comparisons were made with 13 models in three arbitrary groups:

1. GSFC-3D, LARC-3D, SLIMCAT, ECHAM3/CHEM

2. GSFC-2D, HARVARD, LLNL, NOCAR, SUNY-SPB

3. AER, CSIRO, NCAR-2D, UNIVAQ-2D

Only a selection of these plots are shown here; the complete set may be found at the anonymous ftp site, uadp1.larc.nasa.gov in the directory "logan".

It was apparent on first inspection of the profiles in nbars that the models differed widely in the lowermost stratosphere. It was unclear if some of these differences were due to different tropopause heights, so a test of the tropopause height was devised based on the ozone gradient. This test was based on a prior analysis of the ozone gradient at the thermal tropopause (using sonde data) by Logan. The ozone tropopause is the first pressure altitude above 6 km at which the ozone gradient exceeds a threshold of 60 ppb/km for February to August and 45 ppb/km for September to January. This definition is specific to the northern hemisphere, and was applied there to both the climatology and to the model results. Limited sonde data for the southern hemisphere suggests the thresholds are somewhat different in southern mid-latitudes. Figures of the monthly tropopause heights at selected latitudes are also on the ftp site.

Ozone Column

Differences between model ozone columns and the climatology for 1988-96 are shown in Figure 4.6. Excluding the region affected by the Antarctic ozone hole (not all models include PSC chemistry), the agreement between models and the data is generally better than 10% for GSFC-2D, HARVARD, LLNL, SUNY-SPB and UNIVAQ-2D; better than 15% for AER and GSFC-3D; and better than 20% for CSIRO. Differences exceed 20% for some regions for ECHAM3/CHEM, LARC-3D, NCAR-2D, and SLIMCAT. The SLIMCAT model has no troposphere, which means the column amounts are actually biased low by about 10%. Column results were not available for NOCAR. Most

models overestimate the ozone column, particularly at middle and high latitudes; exceptions are GSFC-2D and HARVARD which show regions of over and underestimate at these latitudes. Most models show best agreement with the column in the tropics. Even for models that include PSCs there are large discrepancies between model and observations at high southern latitudes. The columns plots can be misleading about how well a model reproduces ozone, because of cancellation of errors, as discussed below.

Height-latitude Cross Sections

Differences between observations and all models are shown in Figure 4.7 as height-latitude cross sections for January, April, July , and October. Note that contours are given every 10% from -50 to 50, then at 75, 100, 150, and 200%. These figures show clearly that all models except HARVARD and SLIMCAT underestimate ozone from about 35 km to 55 km by 10-30%. This is an improvement over MM I, where discrepancies were about 20-40%. The HARVARD and SLIMCAT models inadvertently included the reaction path OH + ClO -> HCl + O_2 with a 5% yield, which increases ozone values. The SLIMCAT model uses meteorology for 1992 from the UKMO analysis, and 1992 was a cold year; the model also uses isentropic levels, and errors in the approximate conversion from pressure to altitude could lead to apparently higher ozone values in the region of strong vertical gradients (Chipperfield, pers. comm).

Several of the models agree with the observations within ±10% between 25 km and 35 km for all latitudes, with a tendency for the models to be high by about 10% near 25-30 km (CSIRO, ECHAM3/CHEM, GSFC-2D, GSFC-3D, LLNL). About half of the models agree within 10% except at higher latitudes, where there are differences of 20-30% or more (AER, HARVARD, LARC-3D, NCAR-2D, SLIMCAT, SUNY-SPB, UNIVAQ-2D). The NOCAR model is unusual in underestimating ozone by up to 30% at 25 km in the tropics; it is within 10% of the observations at high latitudes.

Differences between model and observations start to increase rapidly below 25 km, and are largest between 20 km and the tropopause. The group of models with the best agreement with the ozone column (within 10%) tend to show the best agreement with observations in the lowest part of the stratosphere, but even for these models there are differences up to (and in small regions exceeding) 50% in the ozone profile (GSFC-2D, LLNL, HARVARD, SUNY-SPB and UNIVAQ-2D). For the AER and GSFC-3D models, for which the columns agree within 15%, there are regions between about 12 and 18 km where the models exceed the observations by 50-100%. There are differences exceeding 100% in this altitude region for CSIRO, SLIMCAT, ECHAM3/CHEM, NCAR-2D and LARC-3D. The LARC-3D, NOCAR, and UNIVAQ-2D models are unusual in having large regions in both the tropics and mid-latitudes where the models are too low between the tropopause and 25 km, by as much as 30-40%.

For many of the models concentrations of tropospheric ozone are more than a factor of 2 too low, which can contribute to an underestimate of over 5% in the ozone column, compensating in part for the general overestimate of stratospheric ozone. The LARC-3D, NCAR-2D, and UNIVAQ-2D models have regions where tropospheric ozone is too high.

Vertical Profiles of Ozone

Comparisons between models and observations are shown in partial pressure for selected latitudes in Figure 4.8. The vertical profiles reveal features of the models that are difficult to discern from the difference plots discussed above.

These figures emphasize again that the variation among models tends to be largest and the lack of agreement with data tends to be worst in the lowermost stratosphere (12-18 km) and at the higher latitudes. The range of model values near 16 km is as large as a factor of 4 at middle and high latitudes, while the range is smaller, at most 30-50%, near the partial pressure maximum (22-24 km). The models tend to be larger than observations at these altitudes. For mid-latitudes, the models agree best with the observations and with each other above the partial pressure maximum.

Figure 4.8 shows that the shape of the vertical profile below the partial pressure maximum is often different from the observations at middle and high latitudes, while the shape is about the same as the observations in the tropics. One prominent feature in the northern hemisphere is the accumulation of ozone in the lowermost stratosphere in winter and early spring, and the appearance of a secondary maximum below 100 mbar (17 km); this maximum is apparent until about July and disappears by fall (see Figure 4.2). Many of the models have no such structure, perhaps because the vertical resolution is too coarse. LARC-3D and SLIMCAT have a secondary maximum with about the right phase, while GSFC-2D, LLNL-2D and CSIRO have a secondary maximum that persists too long.

The ECHAM3/CHEM model is prominent in having vastly too much ozone, with too low a peak, at most latitudes. The AER model has too broad an ozone peak at too low an altitude in summer at the higher northern latitudes. The SUNY model has unusually low ozone in the mid-winter months at 70°-80°, but nowhere else.

The ozone profiles for 20°-30°N are tropical in nature, with a tropopause near 16 km, and most models capture this feature. Both GSFC-3D and ECHAM3/CHEM have too low a tropopause (as defined by ozone) by 2-4 km in January to April, and the ozone profiles are much too high at 16 km. It might be expected that models using assimilated winds would have the tropopause in the correct location. The only two models with too high a tropopause in the tropics, NOCAR and LARC-3D, have less ozone than observed in the tropical lower troposphere.

A number of the models either have a seasonally invariant tropopause at mid-latitudes (AER, GSFC-2D, LLNL, NCAR-2D), or a model that does not have the correct seasonal variation (HARVARD, NOCAR, SLIMCAT). In some cases, the tropopause being too low by 4 km (e.g., GSFC-2D and LLNL in October at 50°-60°N) may be contributing to the large overestimate of the model in the lowermost stratosphere, but in other cases the model is too high in this region, even if the model tropopause is 2 km too high (e.g., AER at 40°-60°N in spring). In most cases, the model tropopause is within 2 km of that defined by the observed ozone gradient.

Vertical profiles are shown as mixing ratio in Figure 4.9. The disagreements at 16 km are hidden in the lower left, while the middle and upper stratosphere are highlighted. The two most obvious features of these figures are the small, but consistent, underestimate of ozone above about 35 km, and the fact that the position of the mixing ratio maximum is too low in altitude at middle and high latitudes, by 4-10 km in the winter half of the year and by 2-4 km in the summer half of the year. The maximum is at about the correct altitude for 30 N to 50 S.

Annual Cycle in Ozone

The annual cycle of ozone is compared to observations in Figure 4.10. Most models have the correct phase of the annual cycle at high latitudes, with a spring maximum below 30 km; most capture the change of phase at middle latitudes, from a spring maximum below about 24 km, to a flat distribution, then a summer maximum by about 30 km, and maxima in spring and fall near 40 km. Some models

have a summer maximum in ozone at mid-latitudes at lower altitudes than in the observations. Ozone has almost no annual cycle below about 26 km in the tropics, and the models generally reproduce this feature. At high southern latitudes, there is a winter minimum in ozone at 26 km which most models do not reproduce. At lower altitudes, ozone is lowest in spring (the ozone hole), and there is a large range in model behavior, partly because not all models include PSC chemistry.

4.4 Conclusions

Agreement between models and ozone observations (and among models themselves) is best above 25 km, where chemistry plays the largest role in controlling the ozone distribution. The models start to diverge below 25 km, and have the largest differences with observations primarily below 20 km at middle and high latitudes. Tests of model chemistry (e.g. Chapter 5.1) indicate that most models have similar gas-phase chemistry. The simplest interpretation is that these differences are due in large part to differences in model transport, although differences in chemistry may also contribute, particularly in the treatment of heterogeneous processes. Other studies in MM II (age of air, CO_2, SF_6, source gases) also revealed large differences in model transport.

Acknowledgements

We thank Gordon Labow his assistance with the ozone climatology and Karen Sage for generating the plots.

References

World Meteorological Association, Assessment of Trends in the Vertical Distribution of Ozone, SPARC Report No. 1, WMO-Ozone Research and Monitoring Project Report No. 43, 1998.

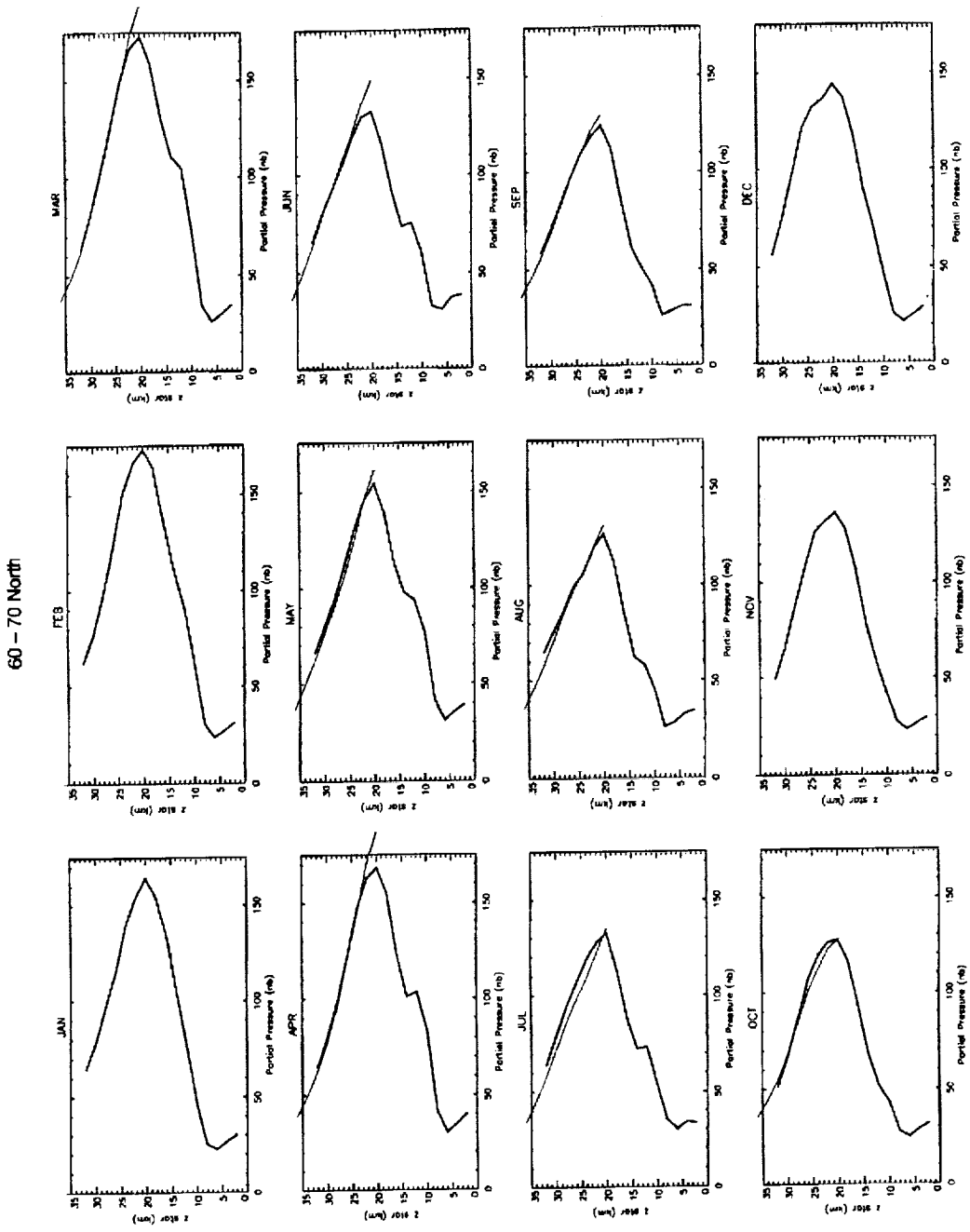

Figure 4.1. Comparison of vertical profiles for sonde and SAGE II. The heavy lines show the sonde profiles and the light lines show the SAGE II profiles.

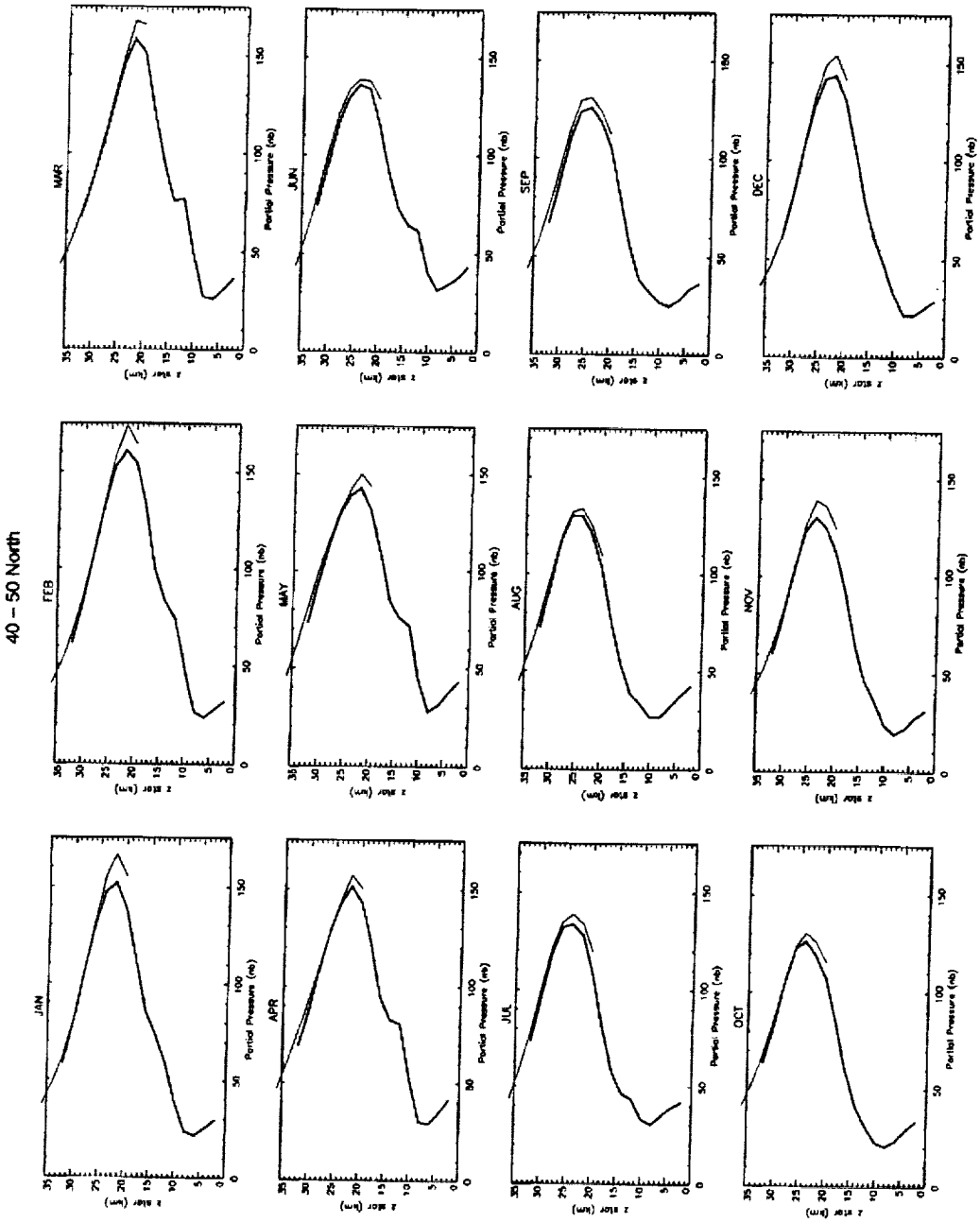

Figure 4.1. Continued.

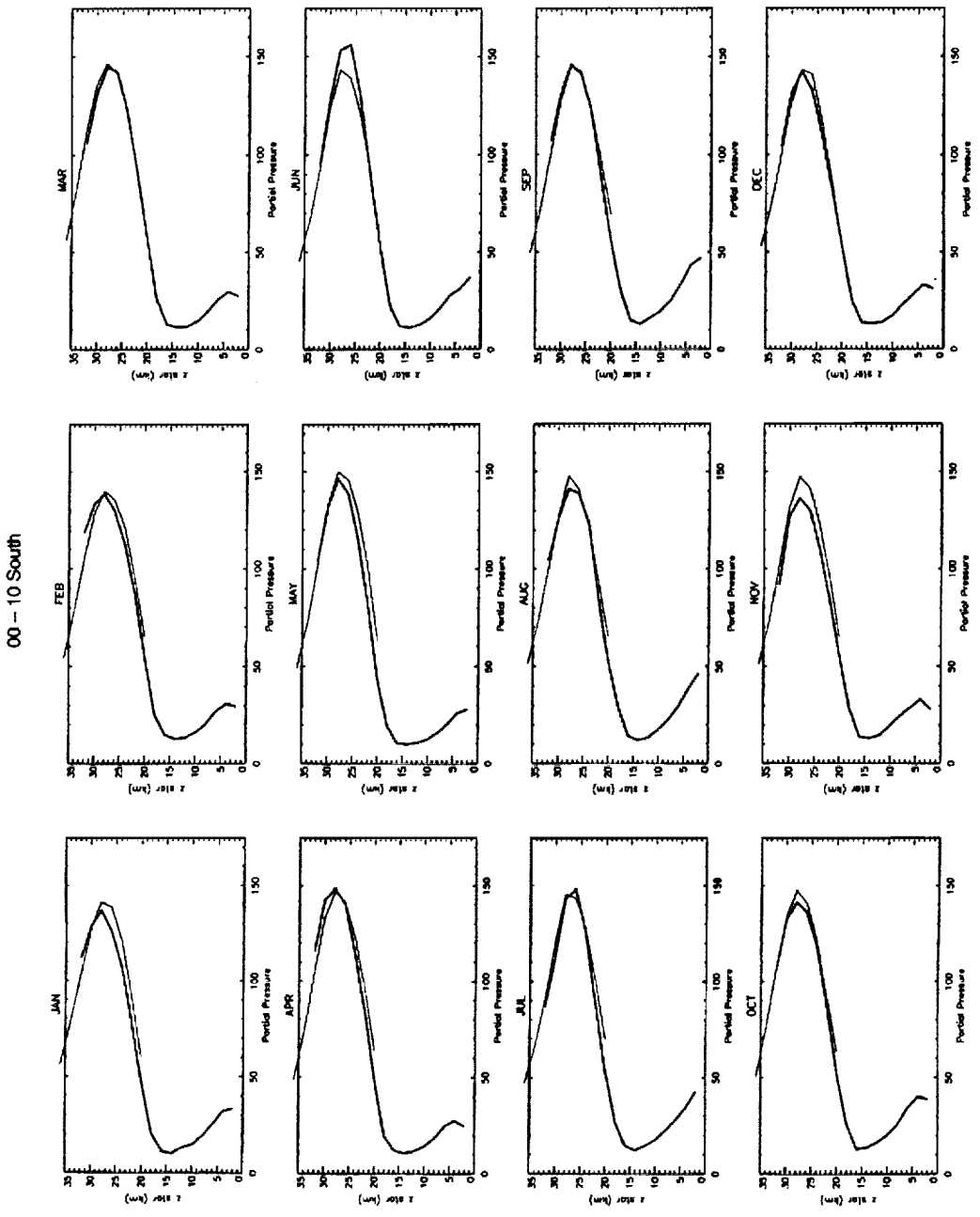

Figure 4.1. Continued.

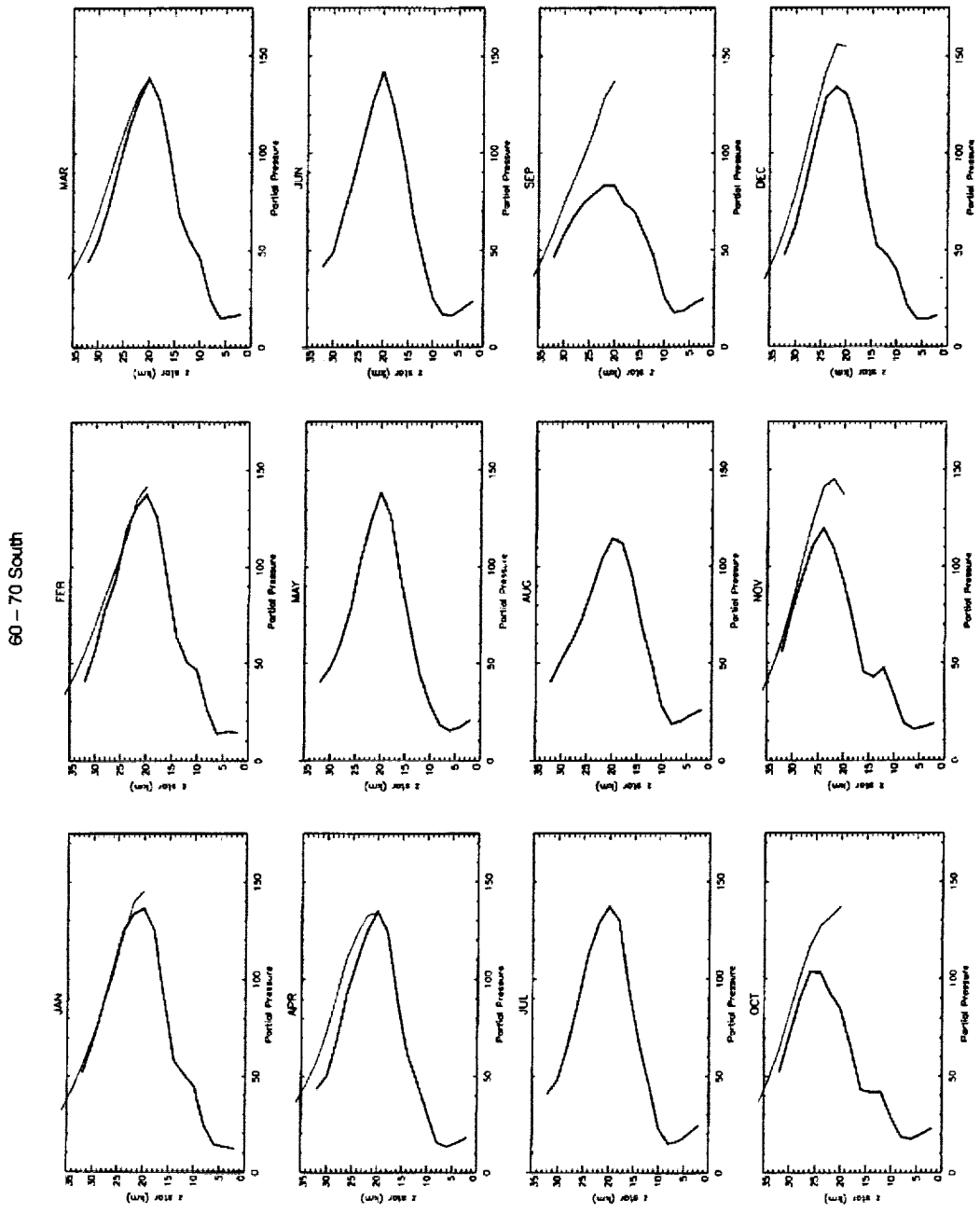

Figure 4.1. Concluded.

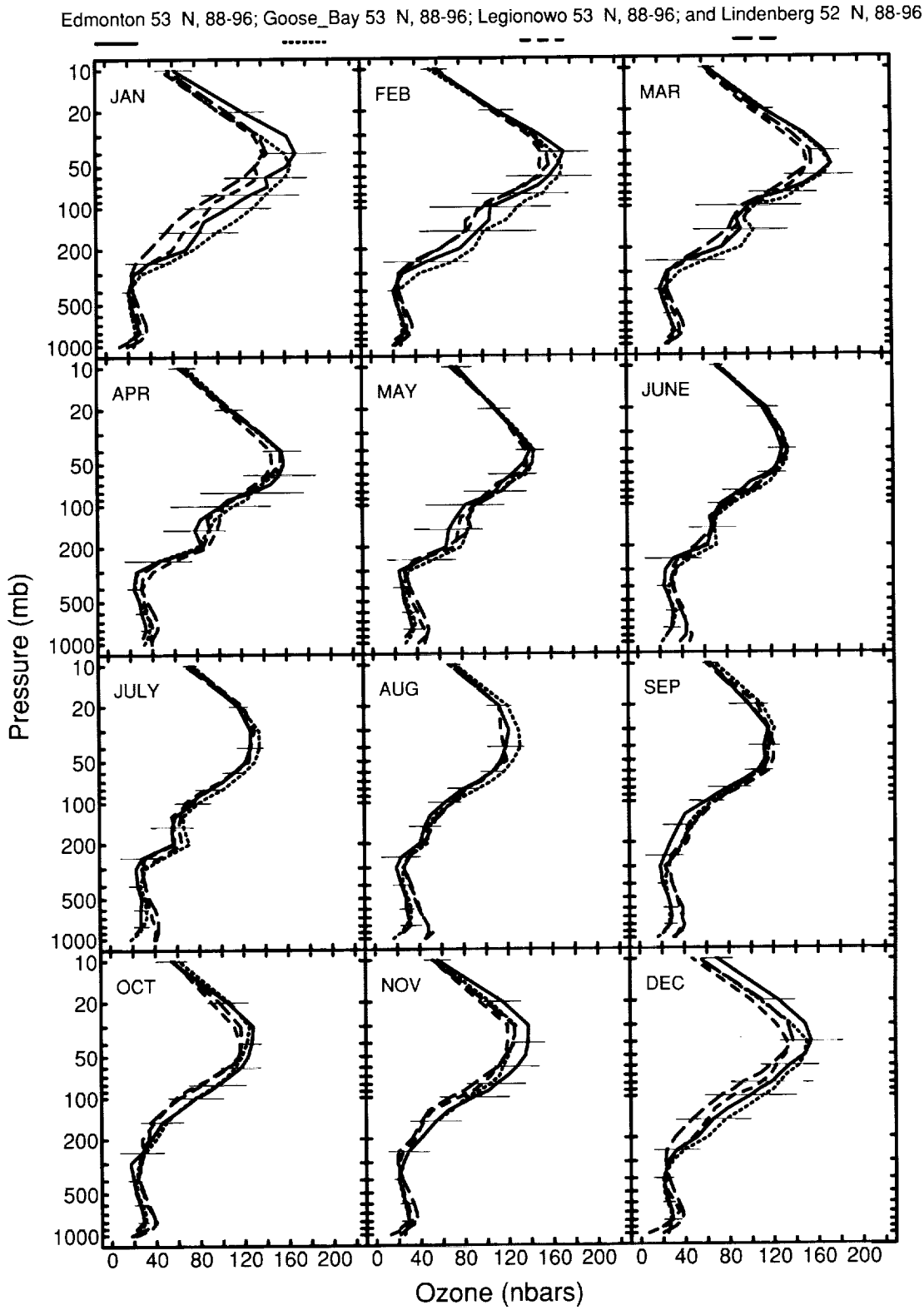

Figure 4.2. Vertical profile of ozone at Edmonton and Goose Bay in Canada, and at Lindenberg and Legionowo in Europe. All stations are near 53°N.

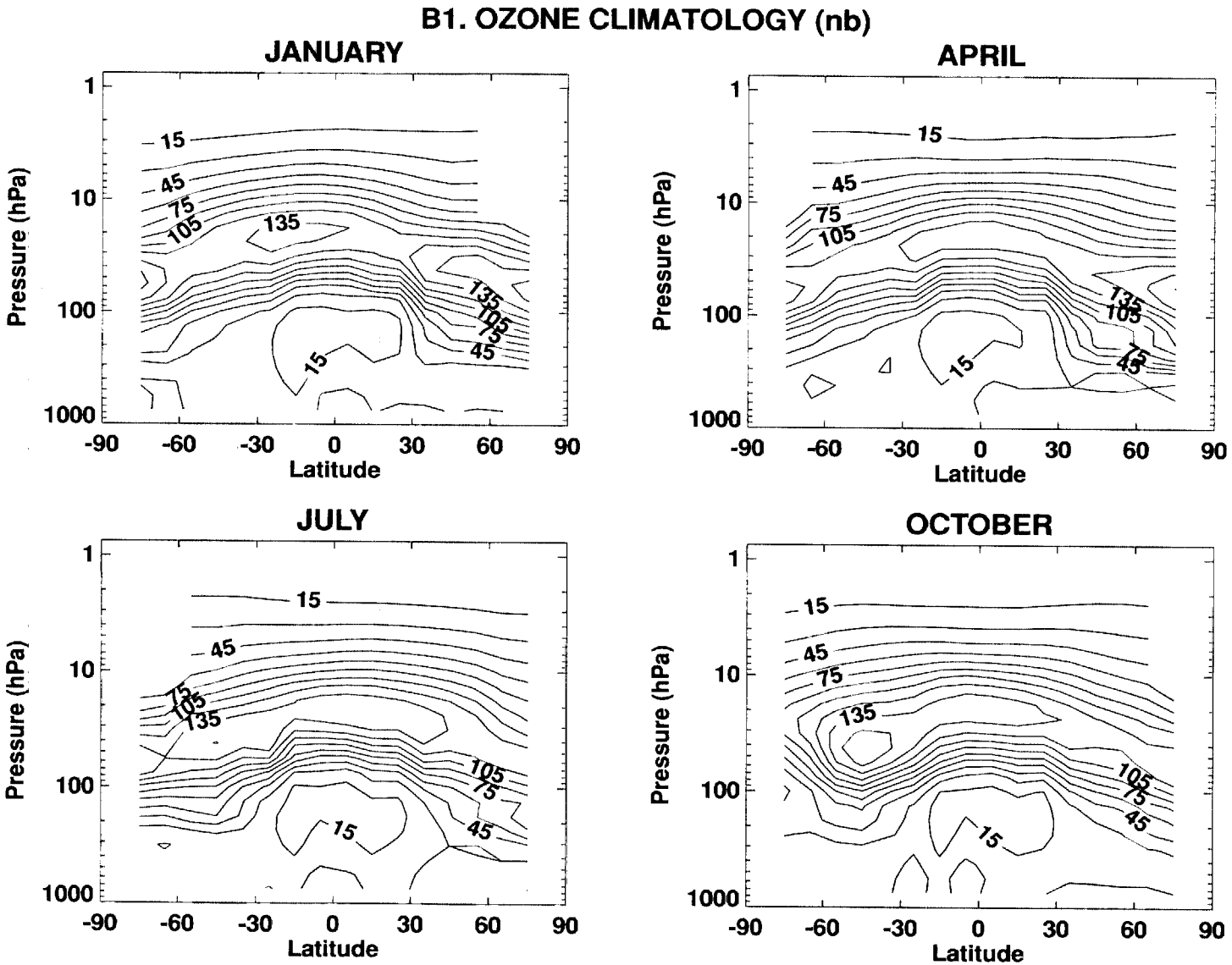

Figure 4.3. Ozone climatology in partial pressure (nbars) for 1988-1996 derived from ozonesondes and SAGE II.

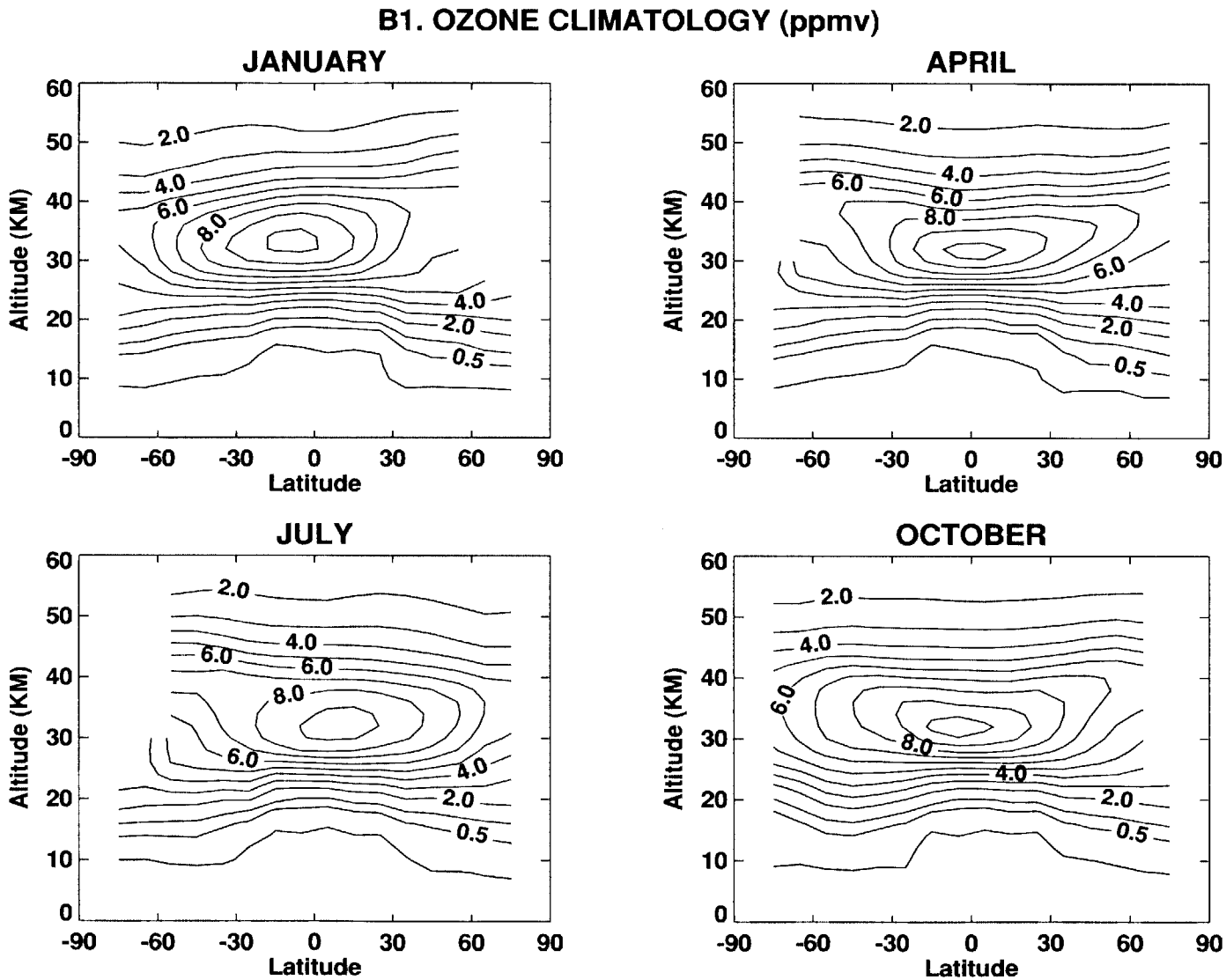

Figure 4.4. Ozone climatology in mixing ratio (ppm) for 1988-1996 derived from ozonesondes and SAGE II.

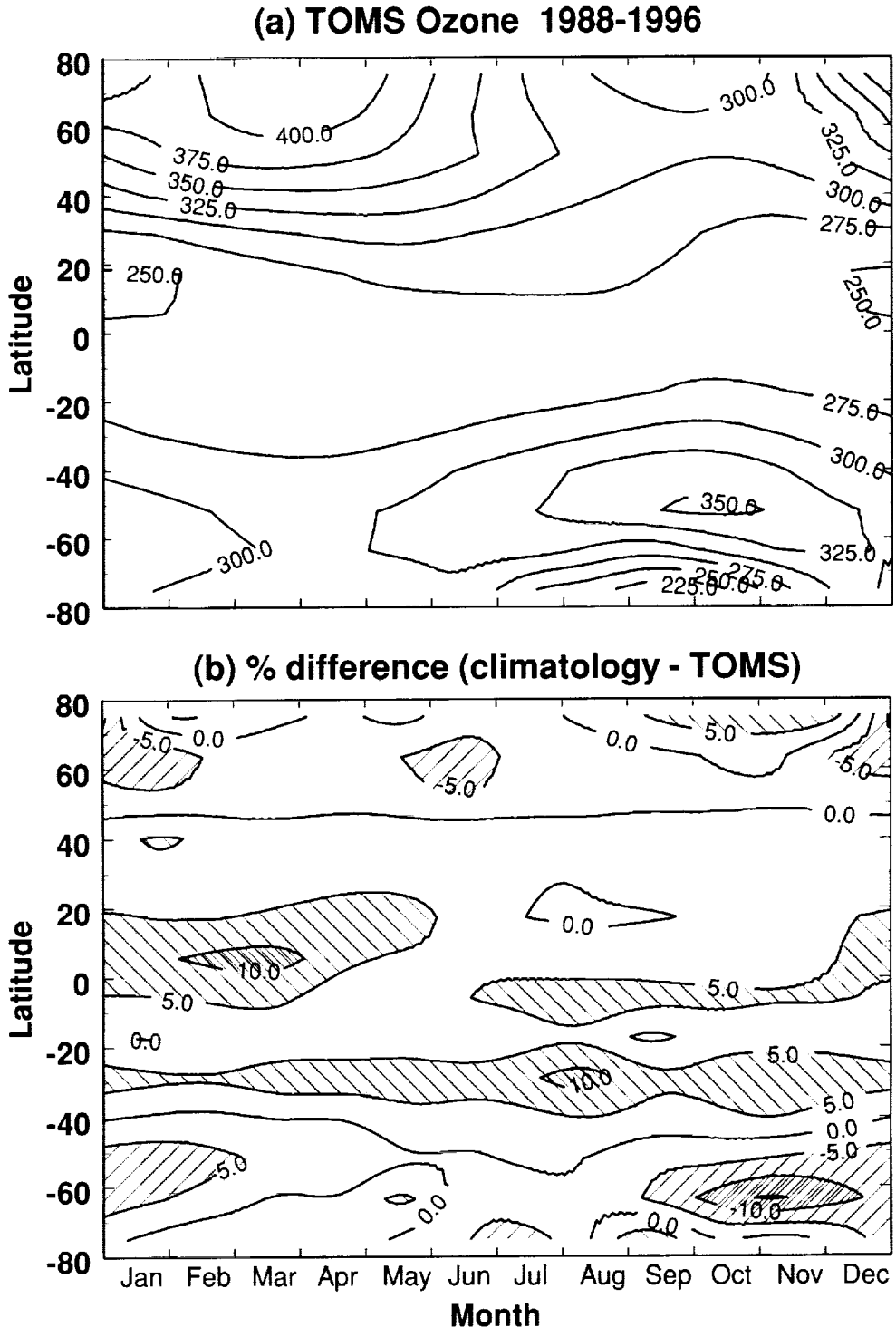

Figure 4.5. Ozone column for 1988-1996 derived from TOMS measurements on Nimbus-7, Meteor 3, and Earth Probe (top panel). The lower panel shows the difference in the ozone column derived from the TOMS data and that derived by integrating the sonde/SAGE II profile climatology.

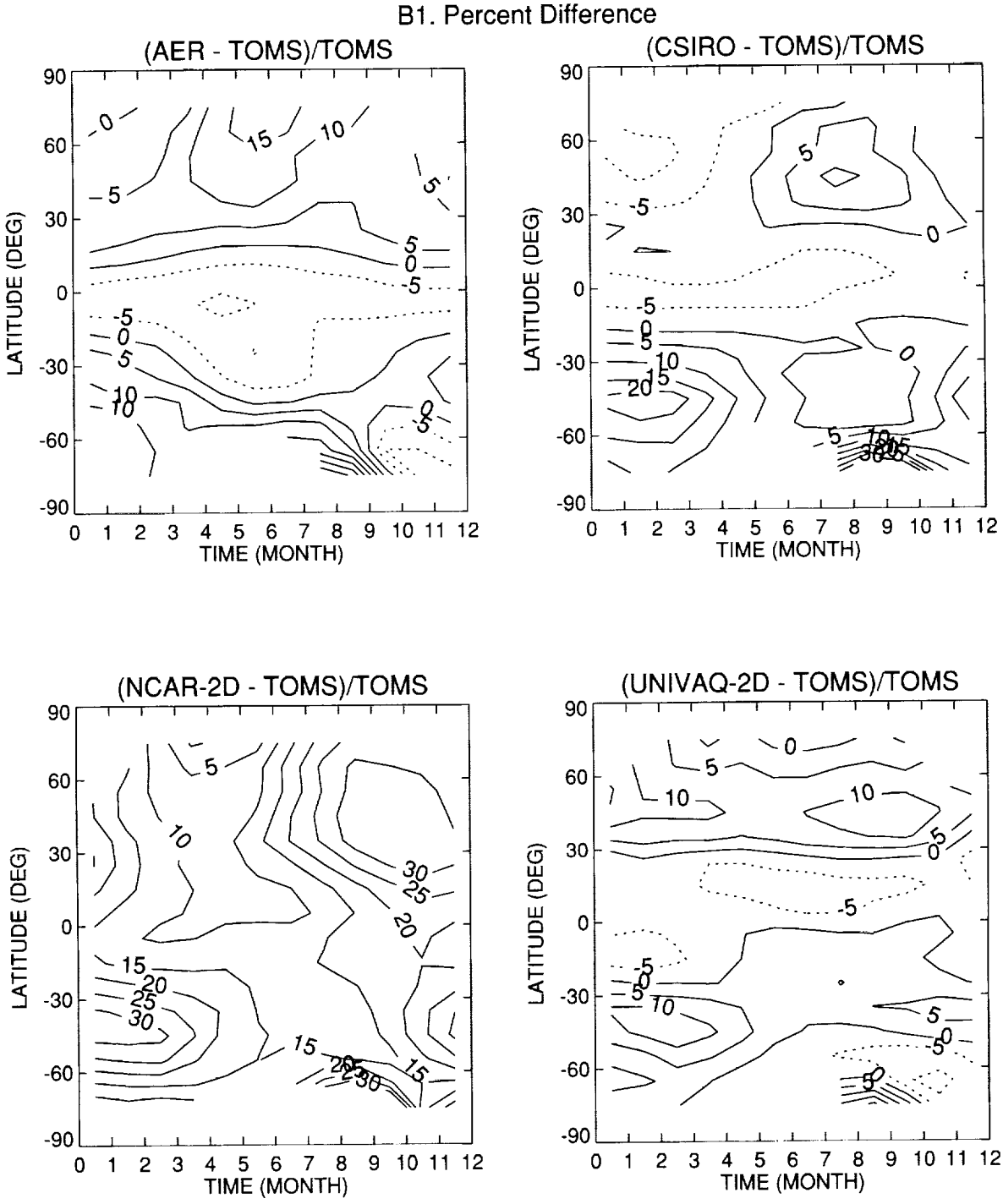

Figure 4.6. Percentage differences between models results and the ozone column shown in Figure 4.4.

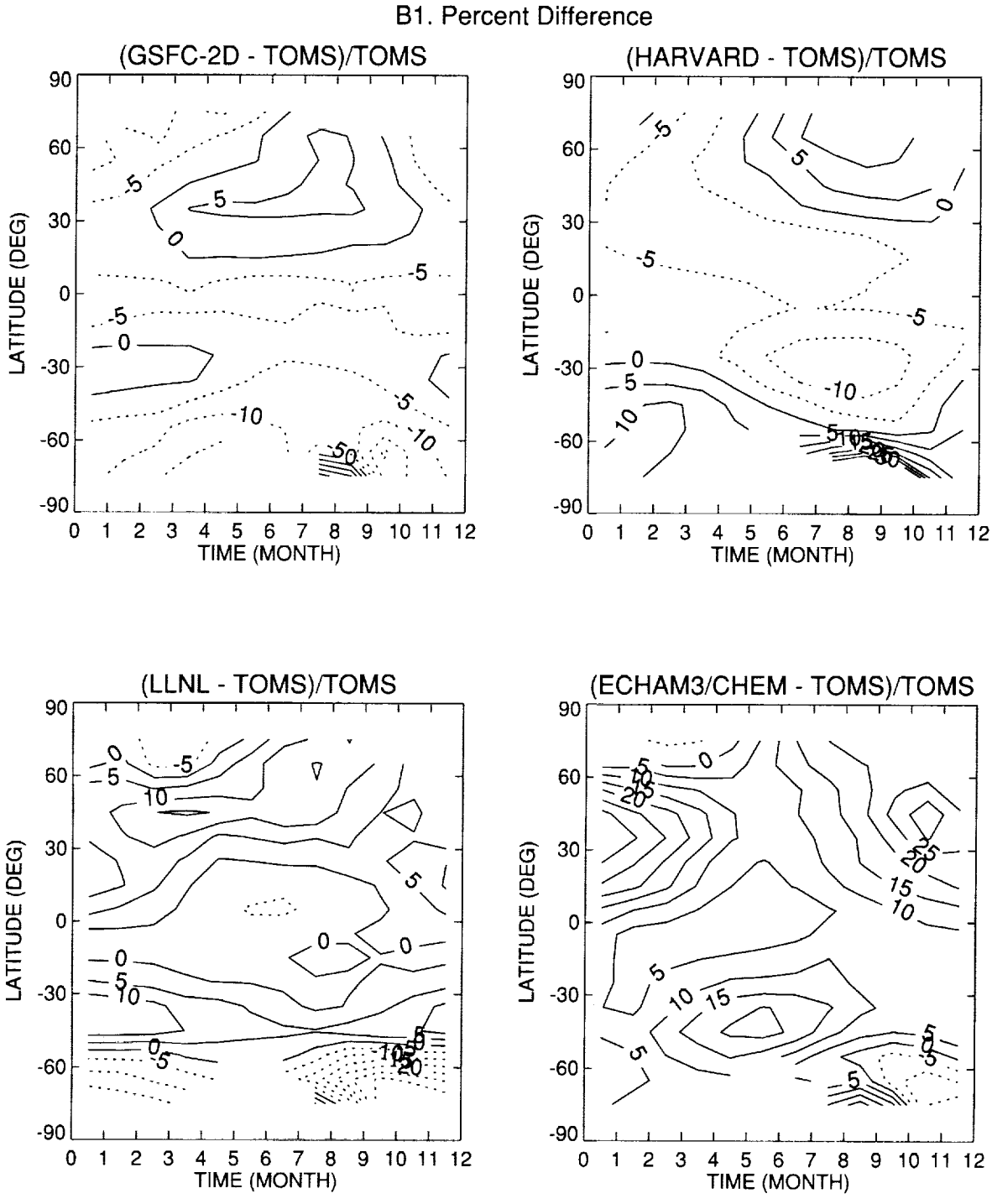

Figure 4.6. Continued.

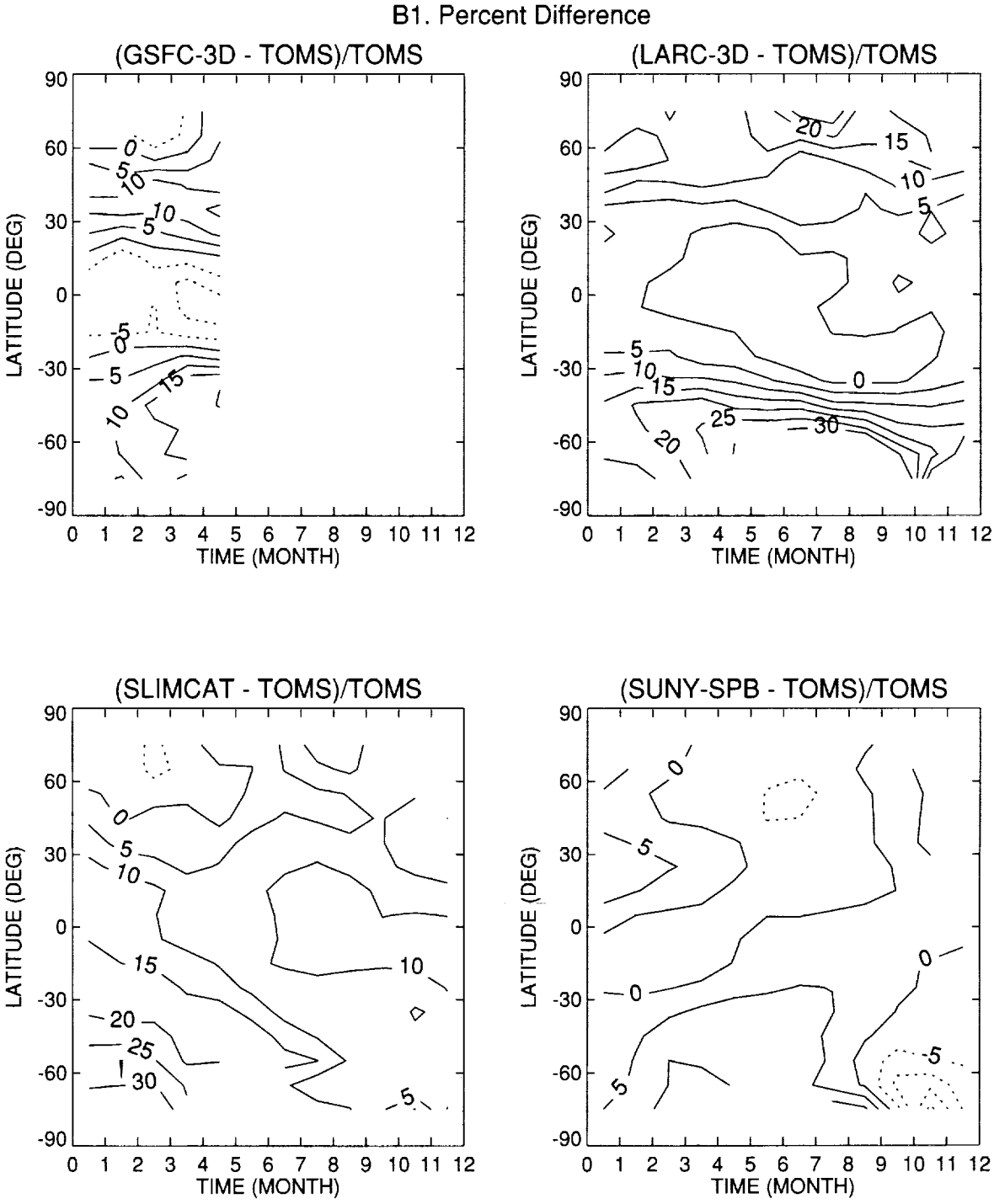

Figure 4.6. Concluded.

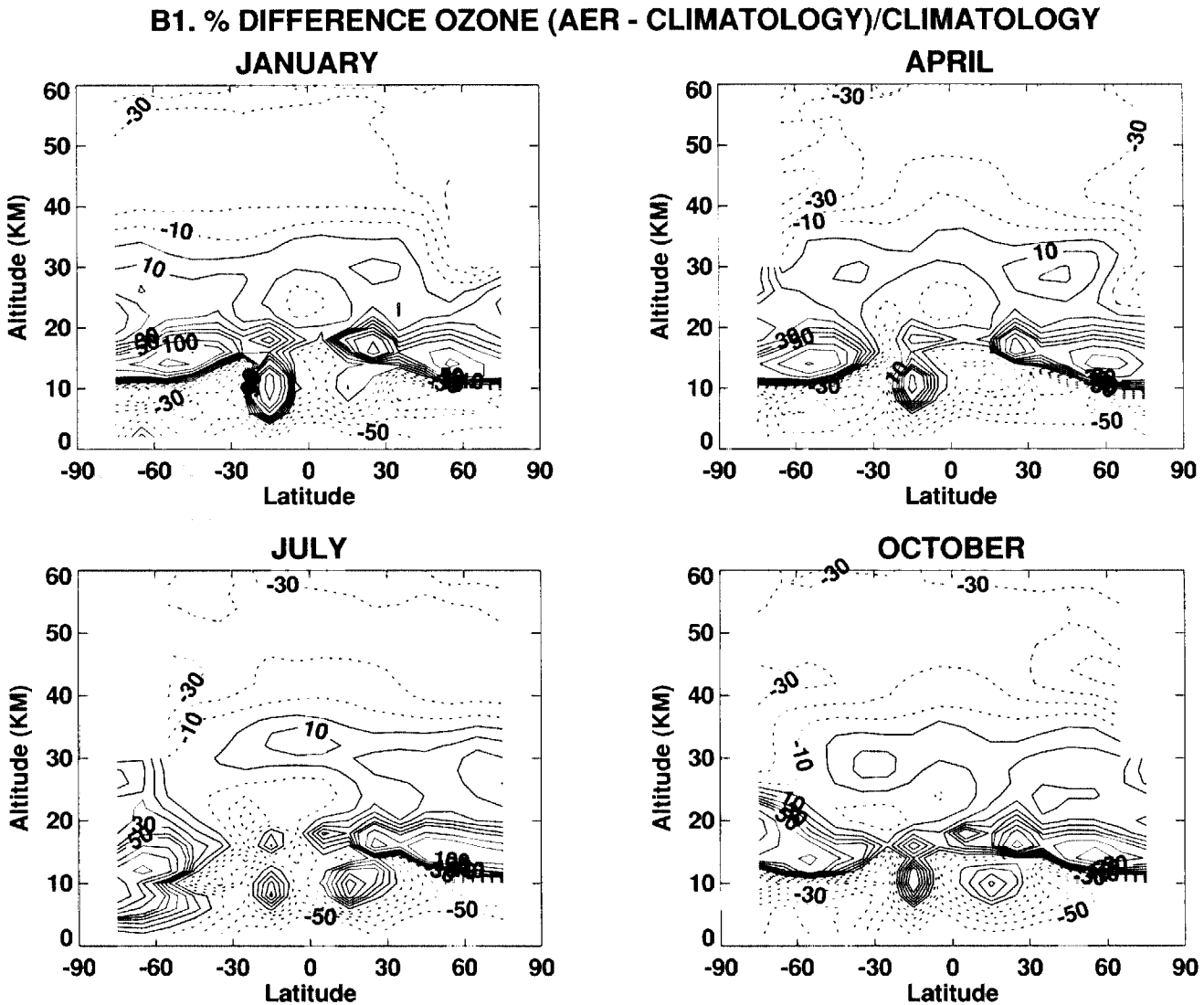

Figure 4.7. Percentage difference between the model ozone distribution (altitude x latitude) and the ozone climatology shown in Figure 4.3 and 4.4.

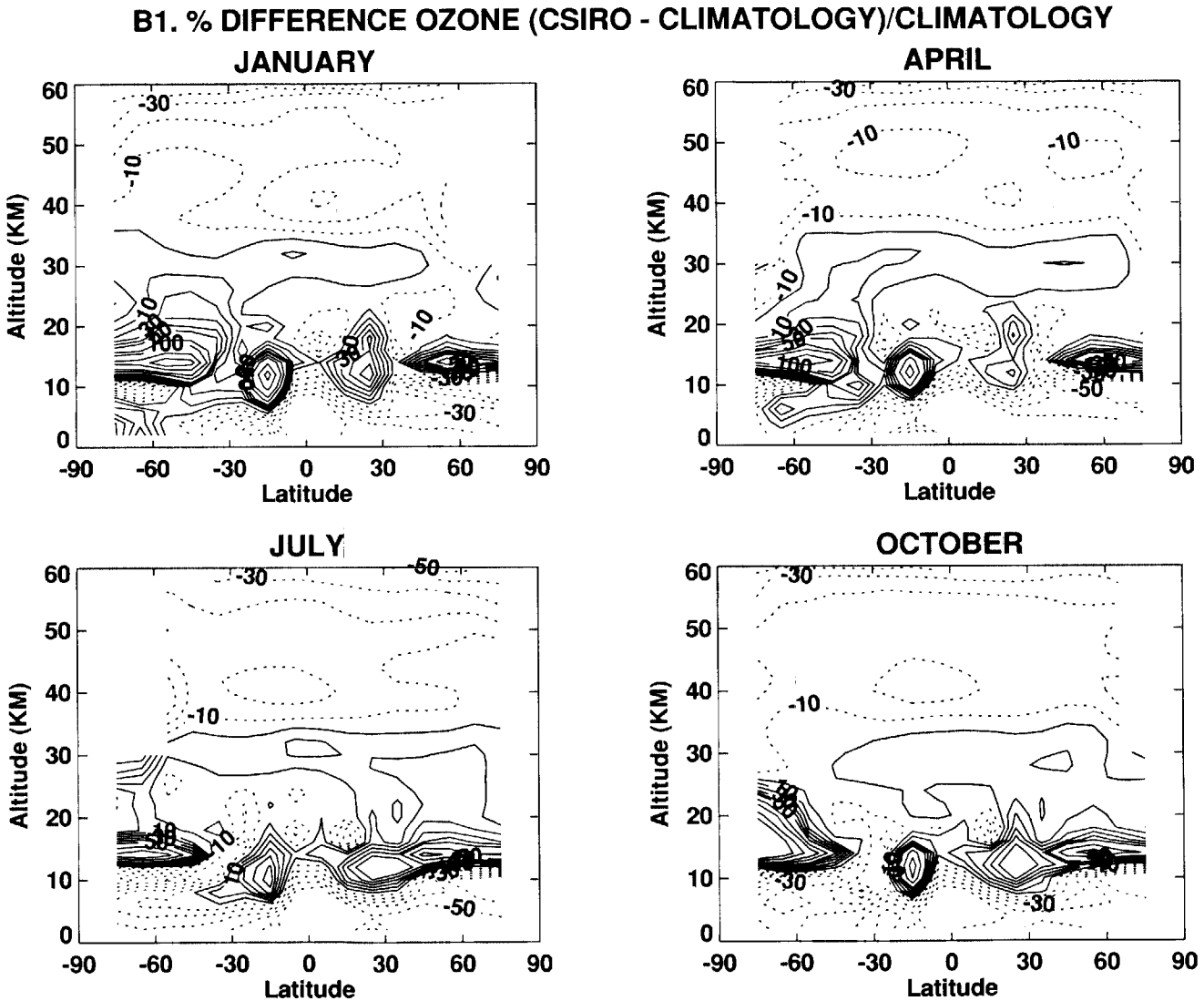

Figure 4.7. Continued.

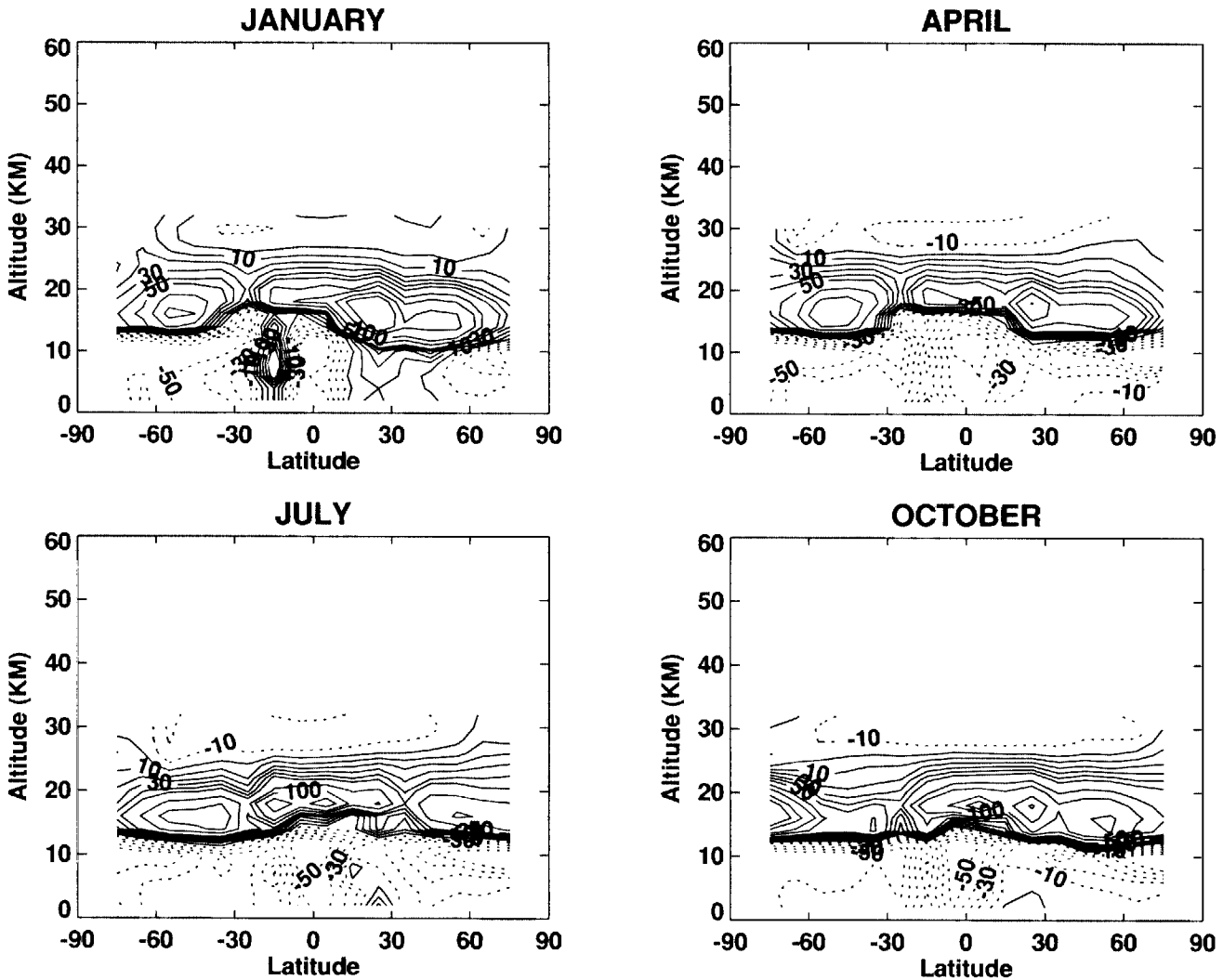

Figure 4.7. Continued.

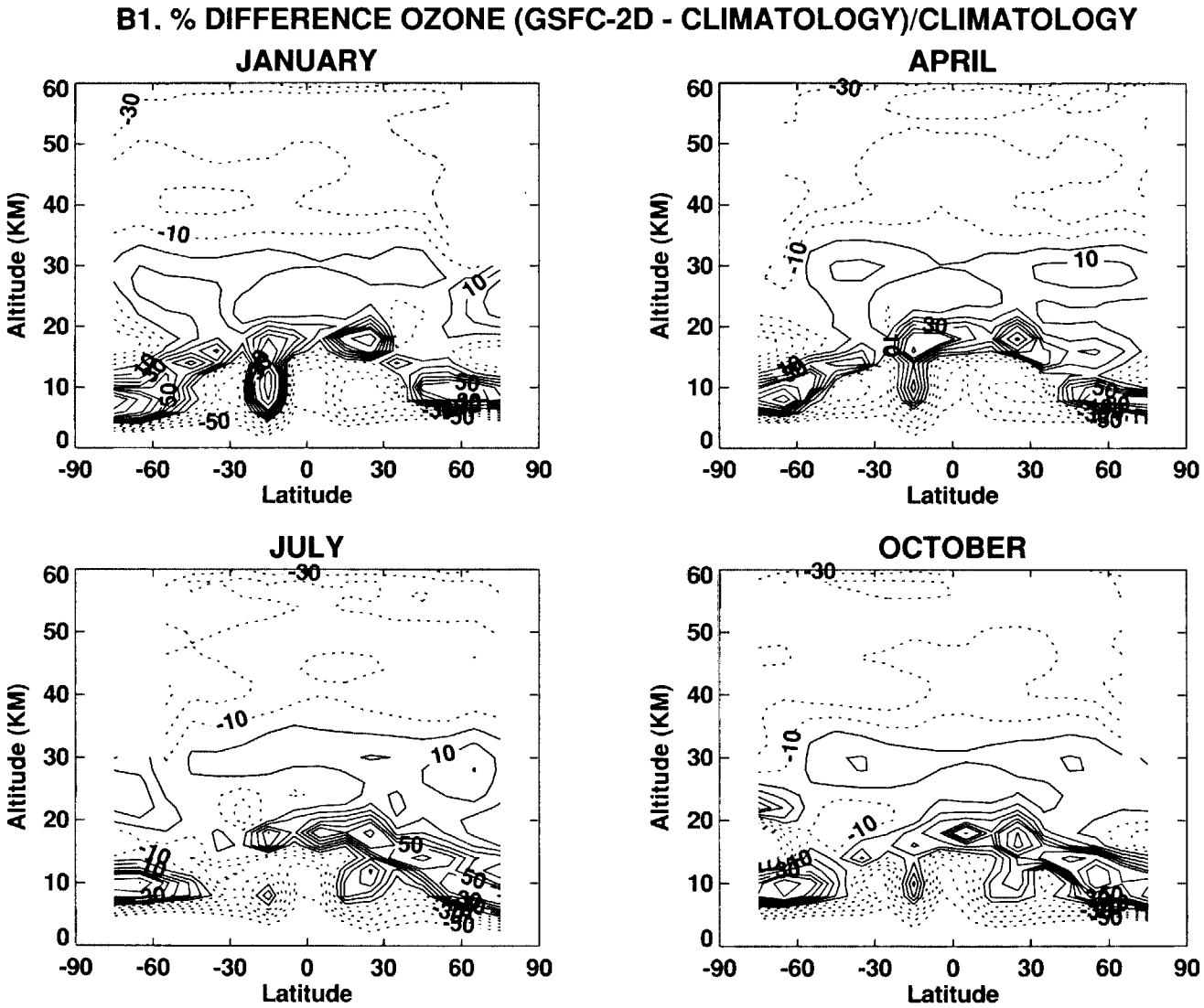

Figure 4.7. Continued.

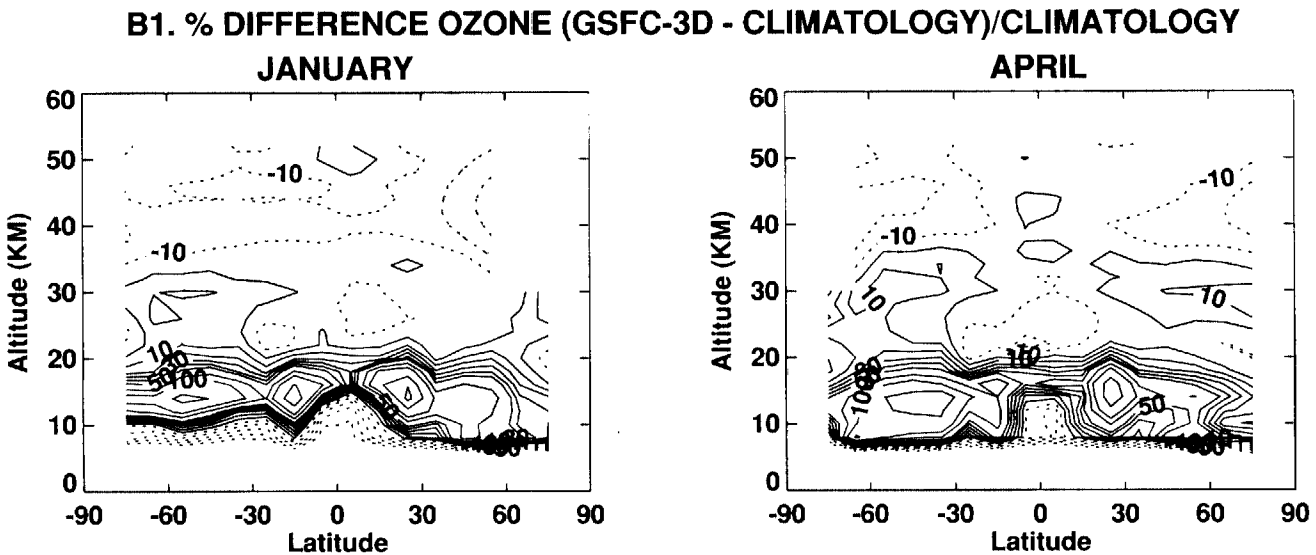

Fiogure 4.7. Continued.

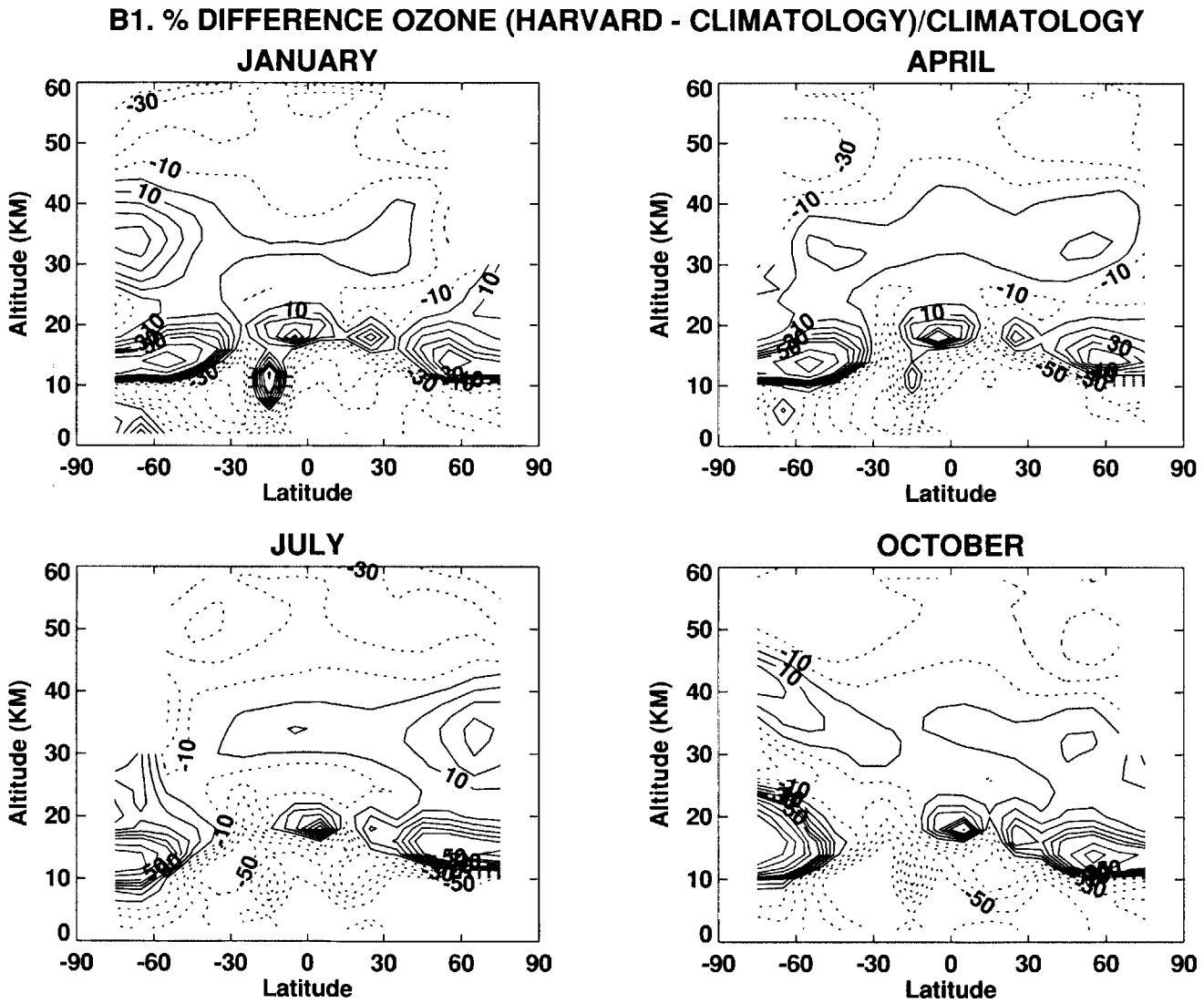

Figure 4.7. Continued.

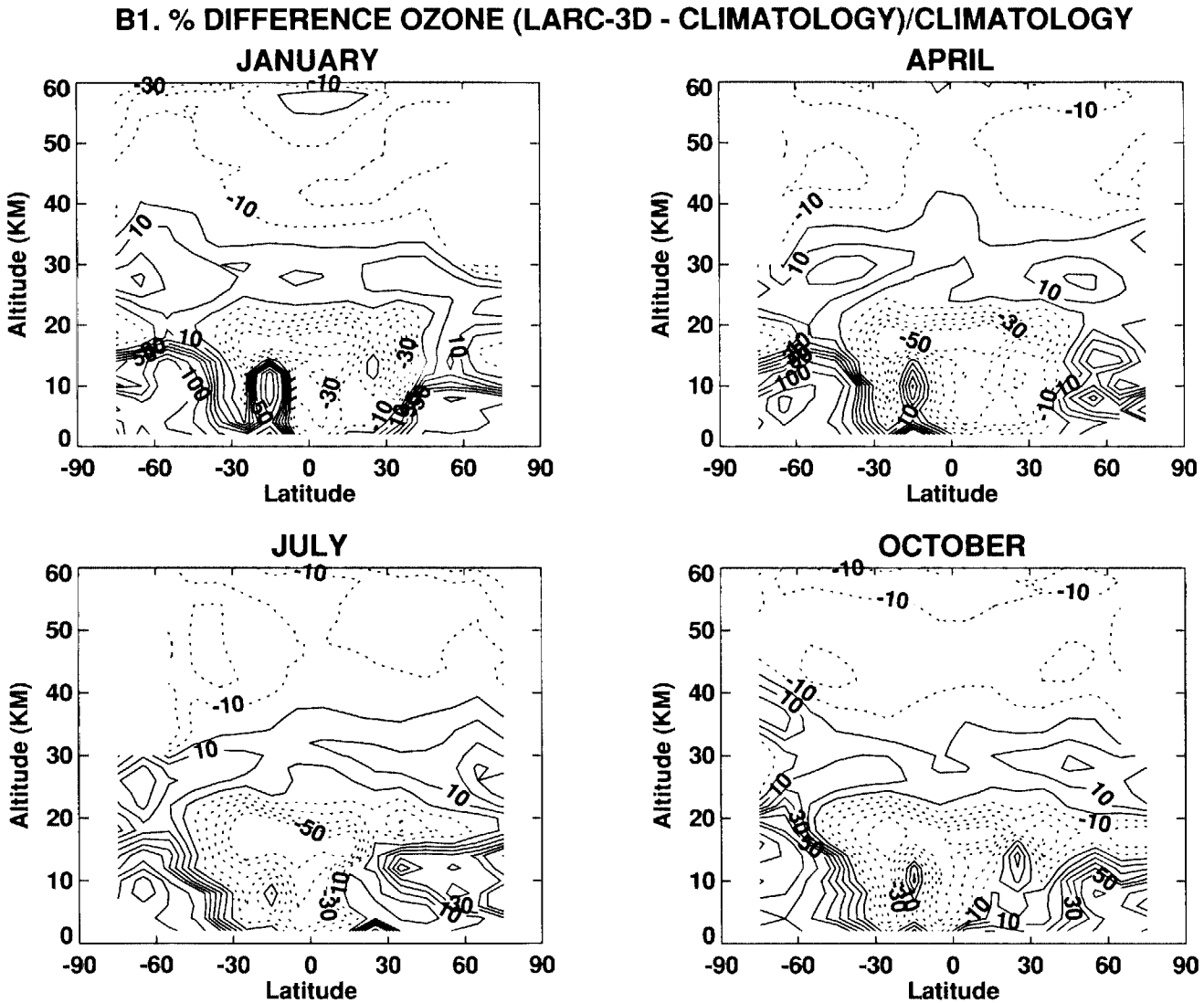

Figure 4.7. Continued.

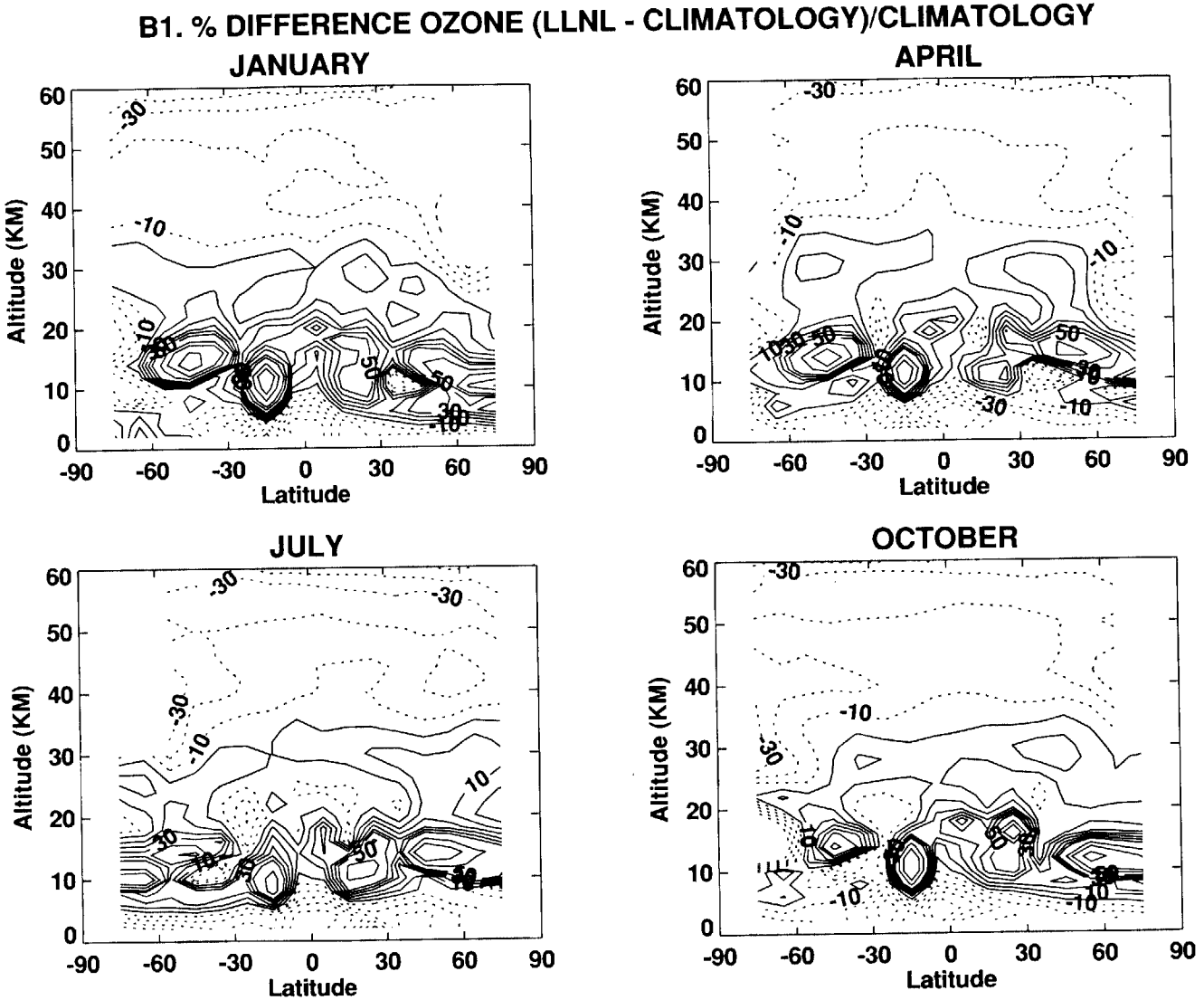

Figure 4.7. Continued.

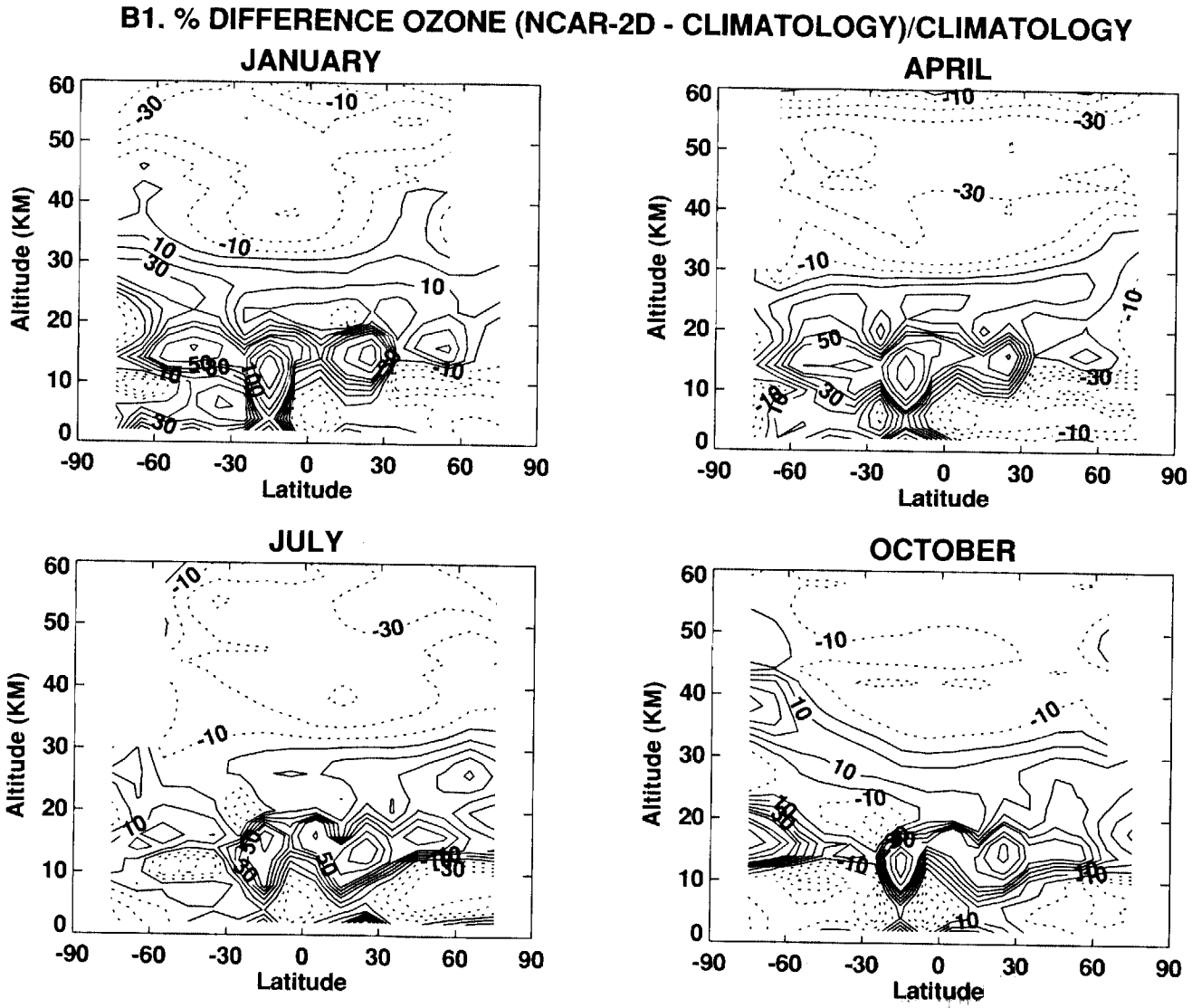

Figure 4.7. Continued.

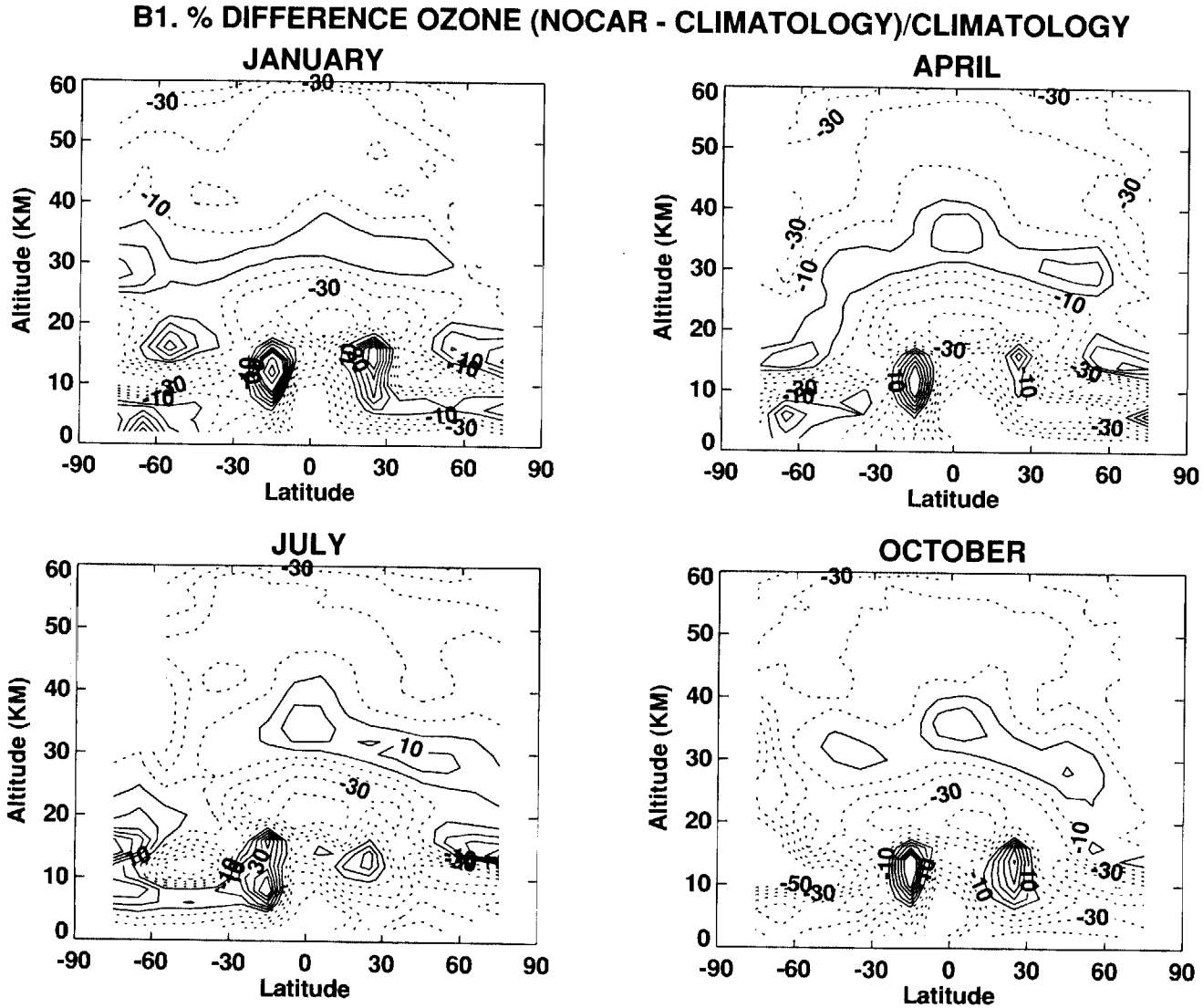

Figure 4.7. Continued.

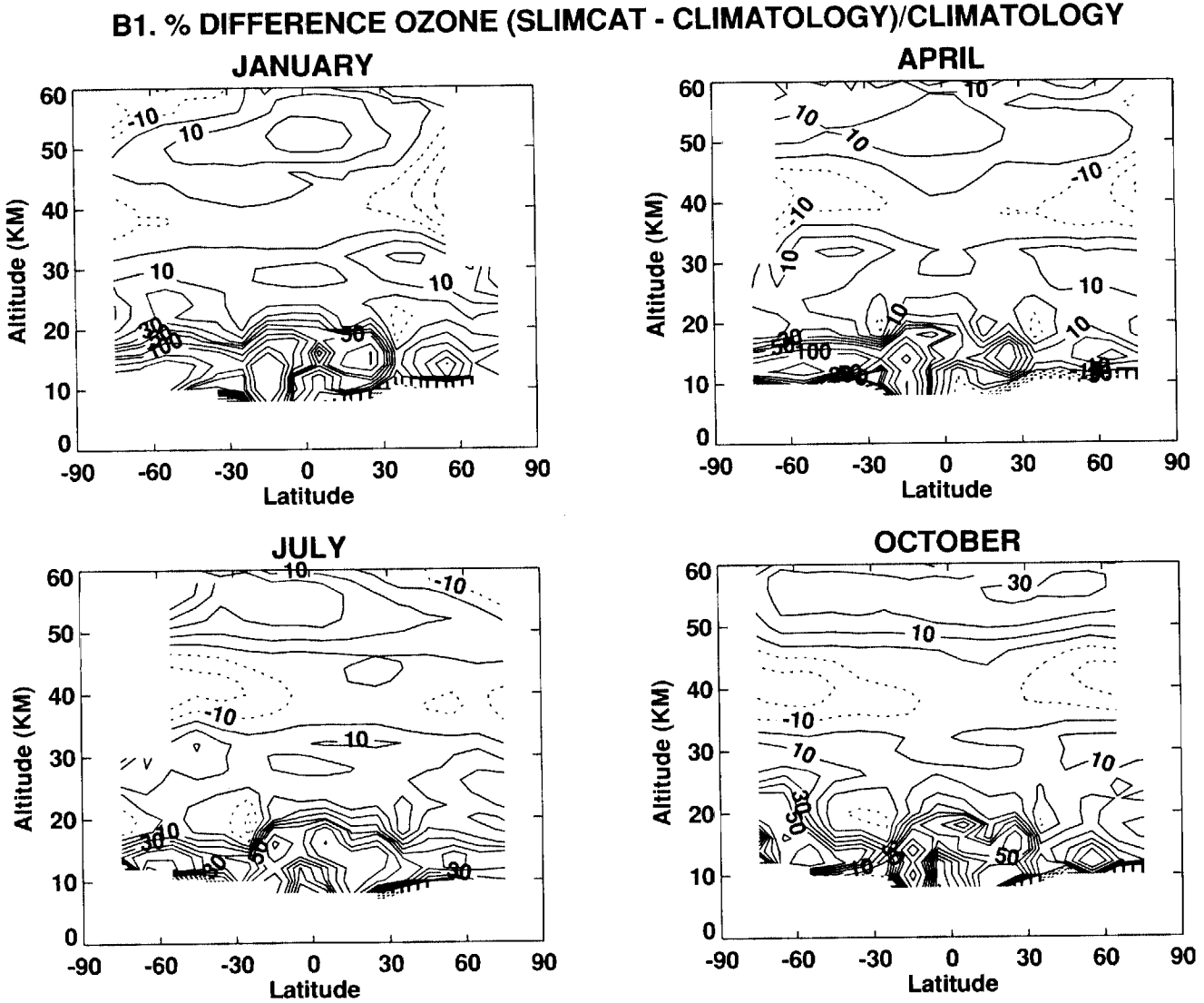

Figure 4.7. Continued.

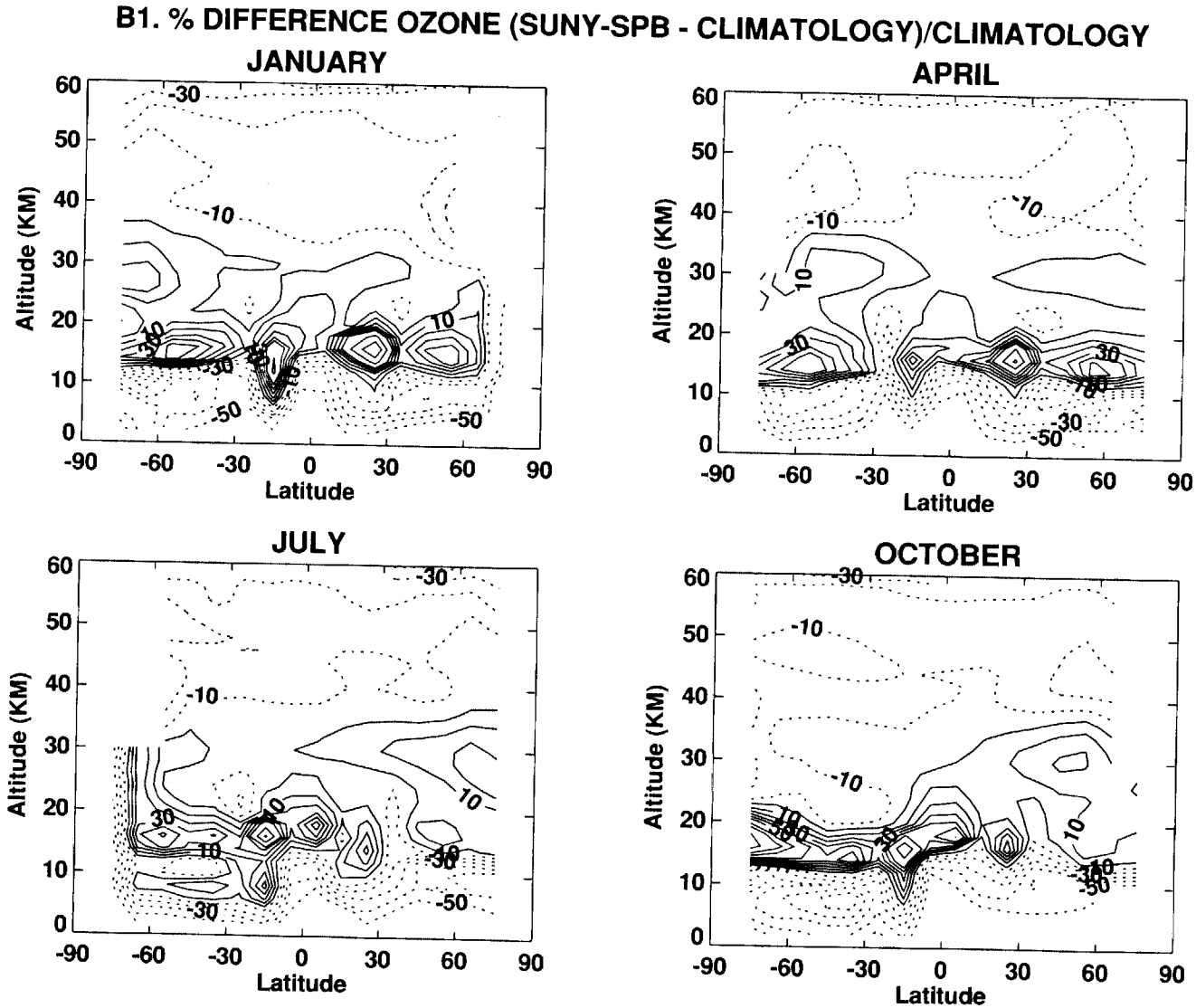

Figure 4.7. Continued.

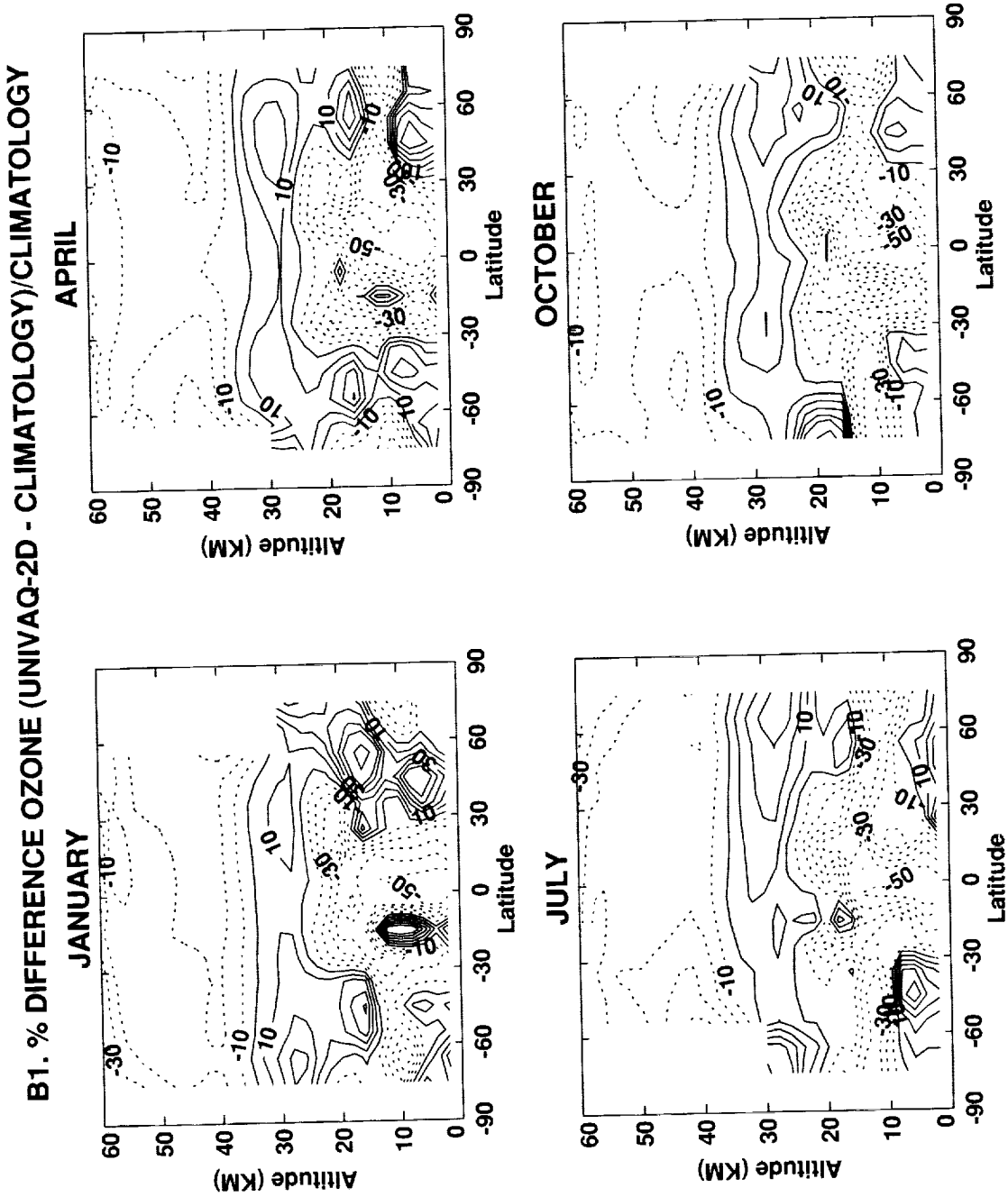

Figure 4.7. Concluded.

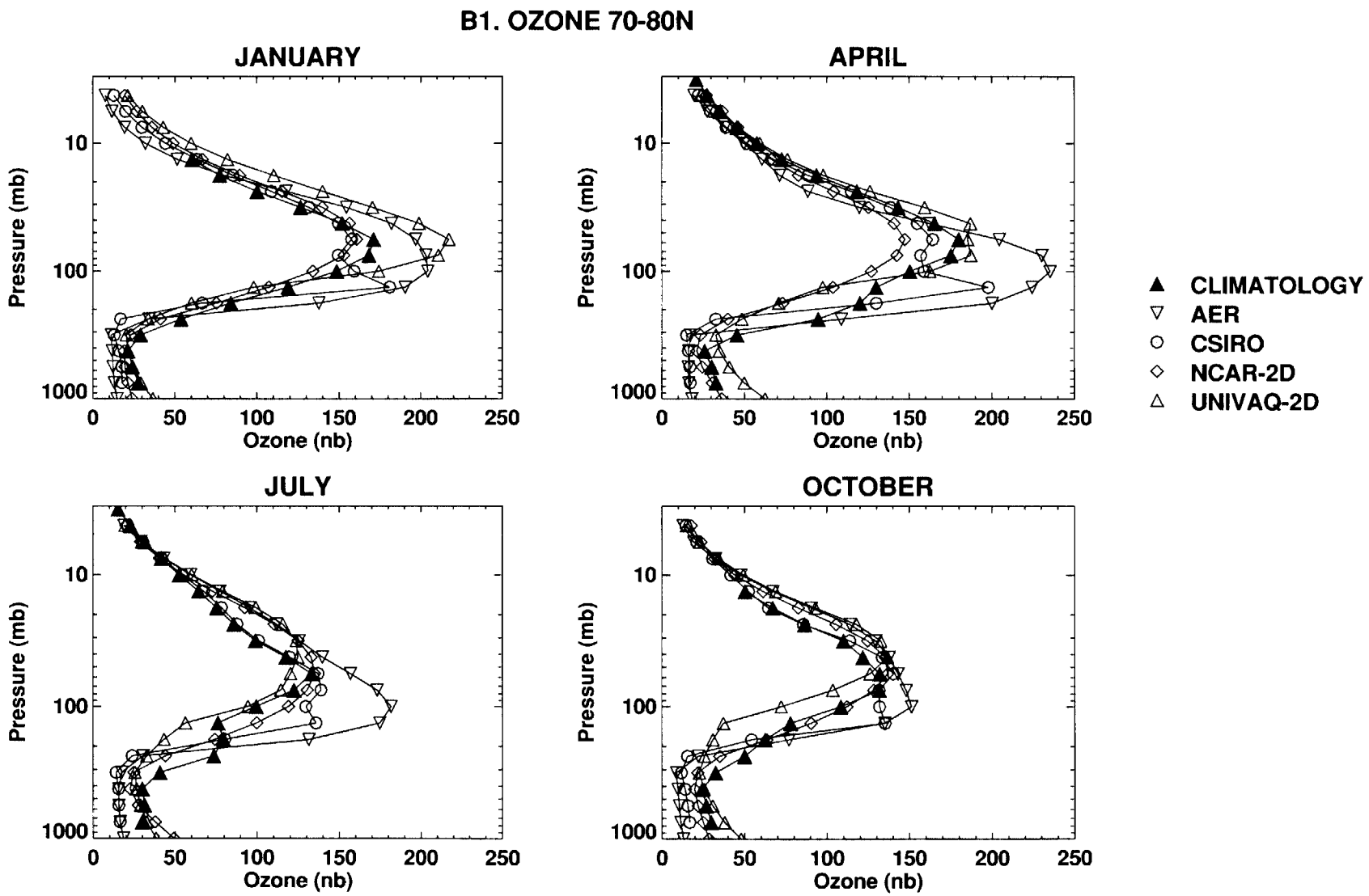

Figure 4.8. Vertical profiles of ozone partial pressure compared to observations for all models, for selected latitudes.

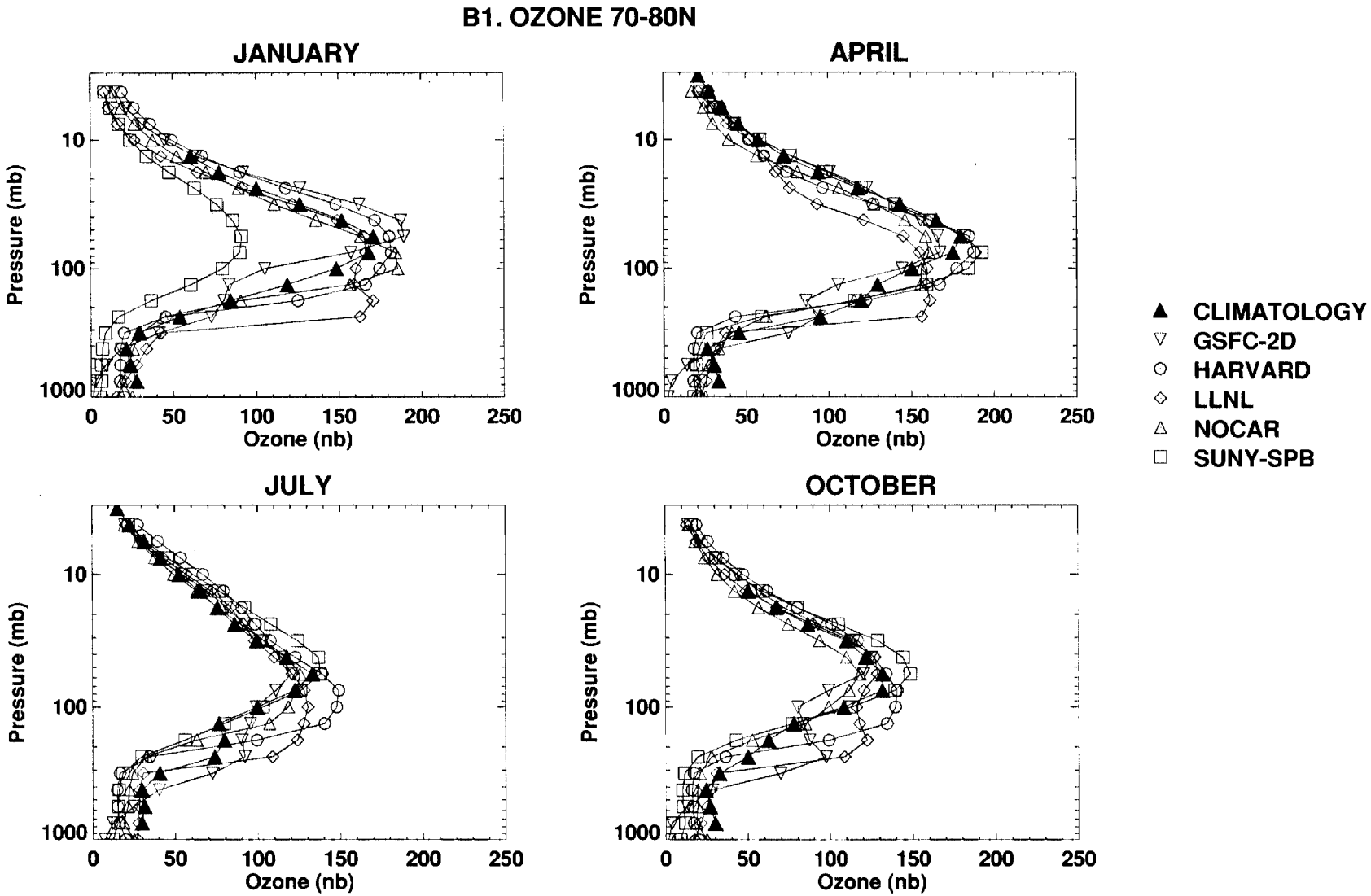

Figure 4.8. Continued.

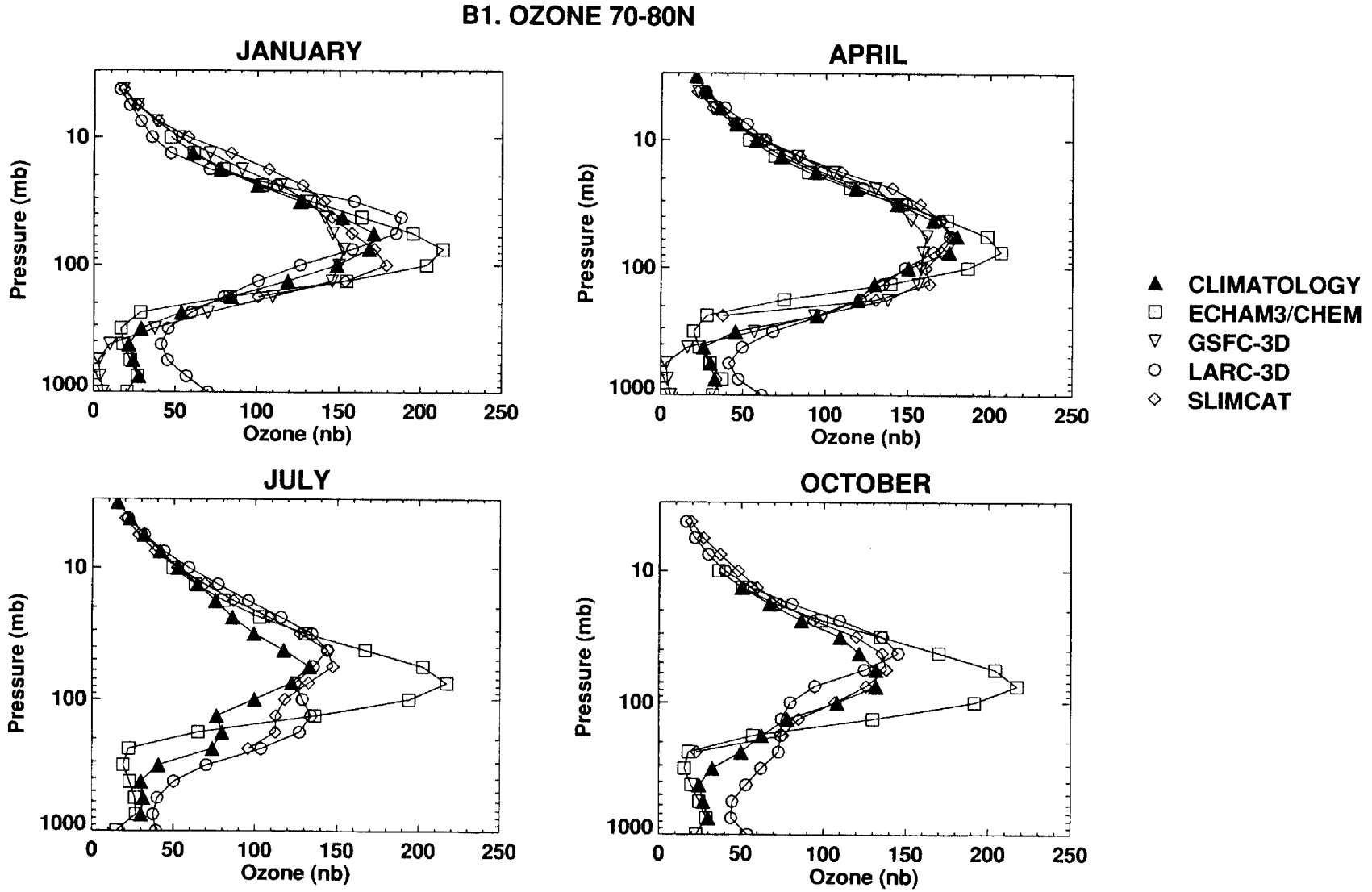

Figure 4.8. Continued.

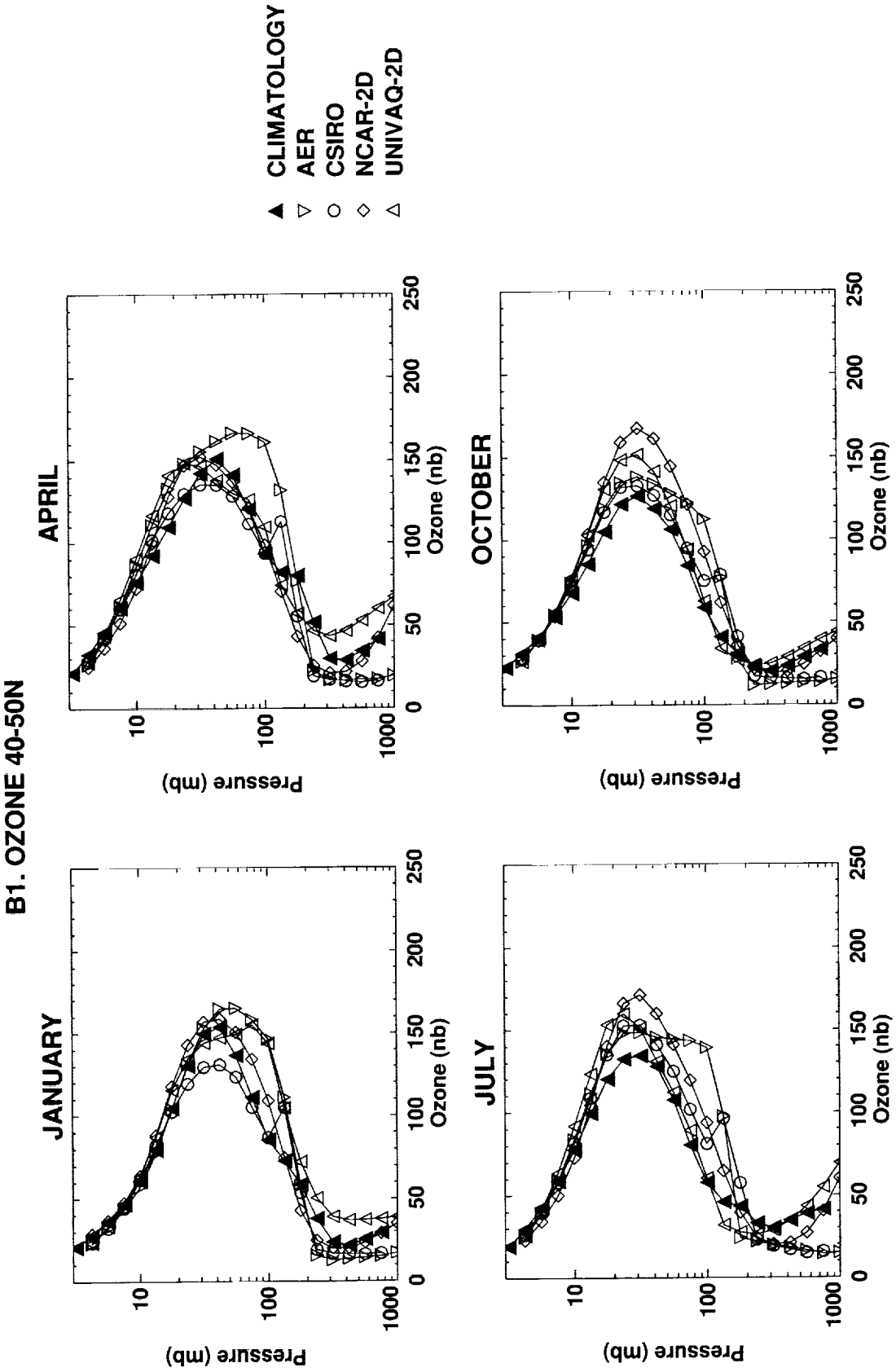

Figure 4.8. Continued.

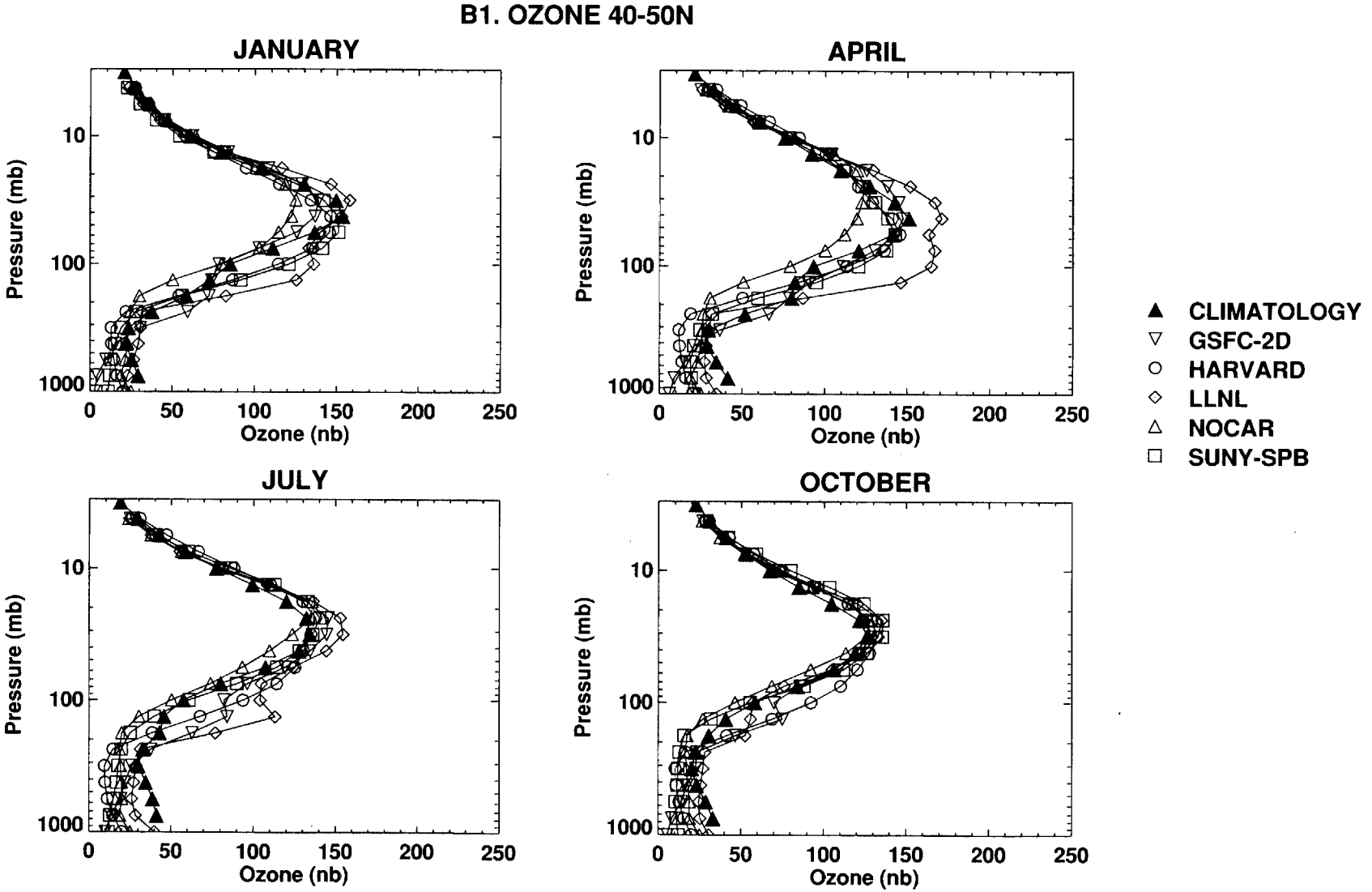

Figure 4.8. Continued.

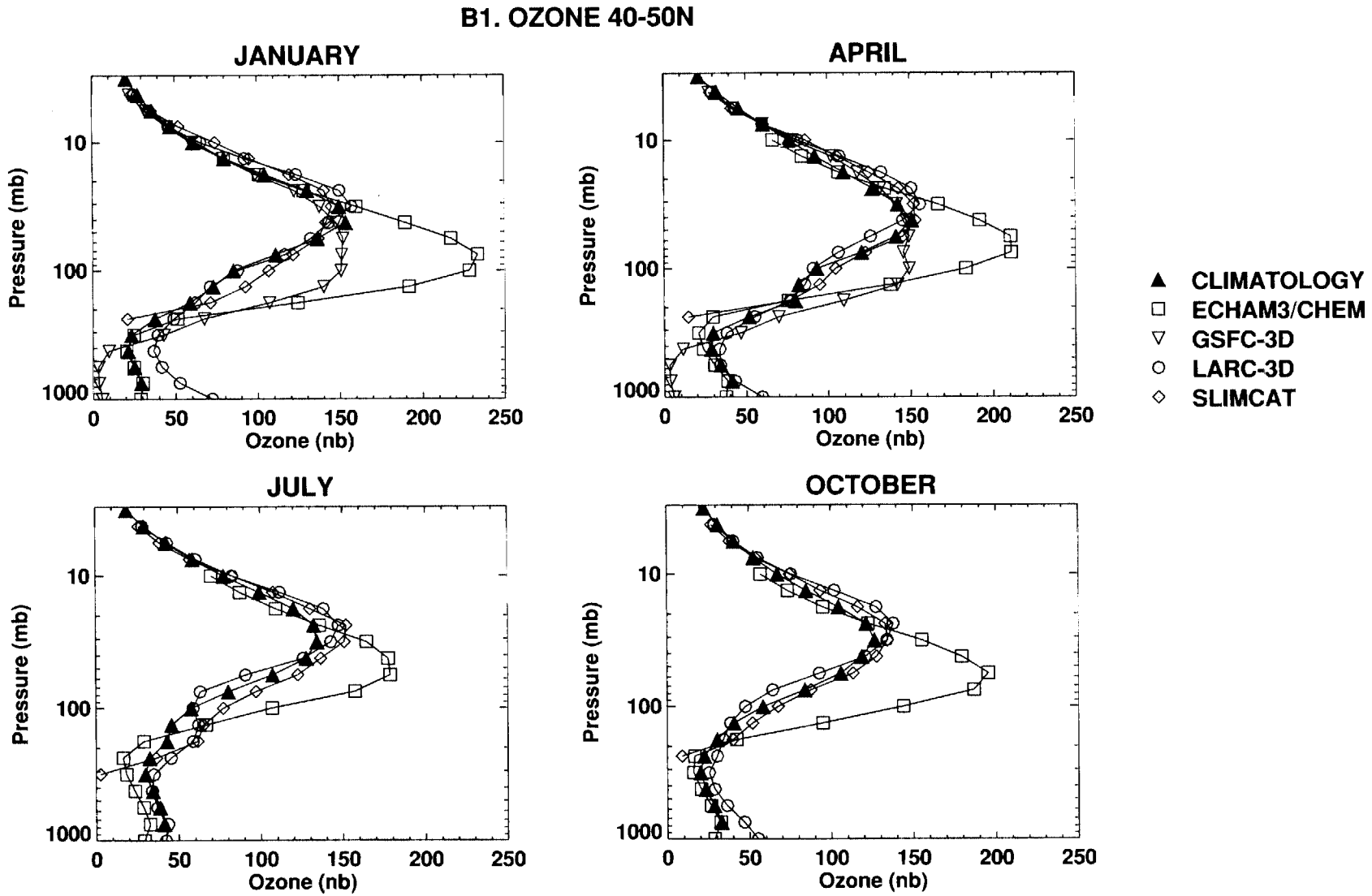

Figure 4.8. Continued.

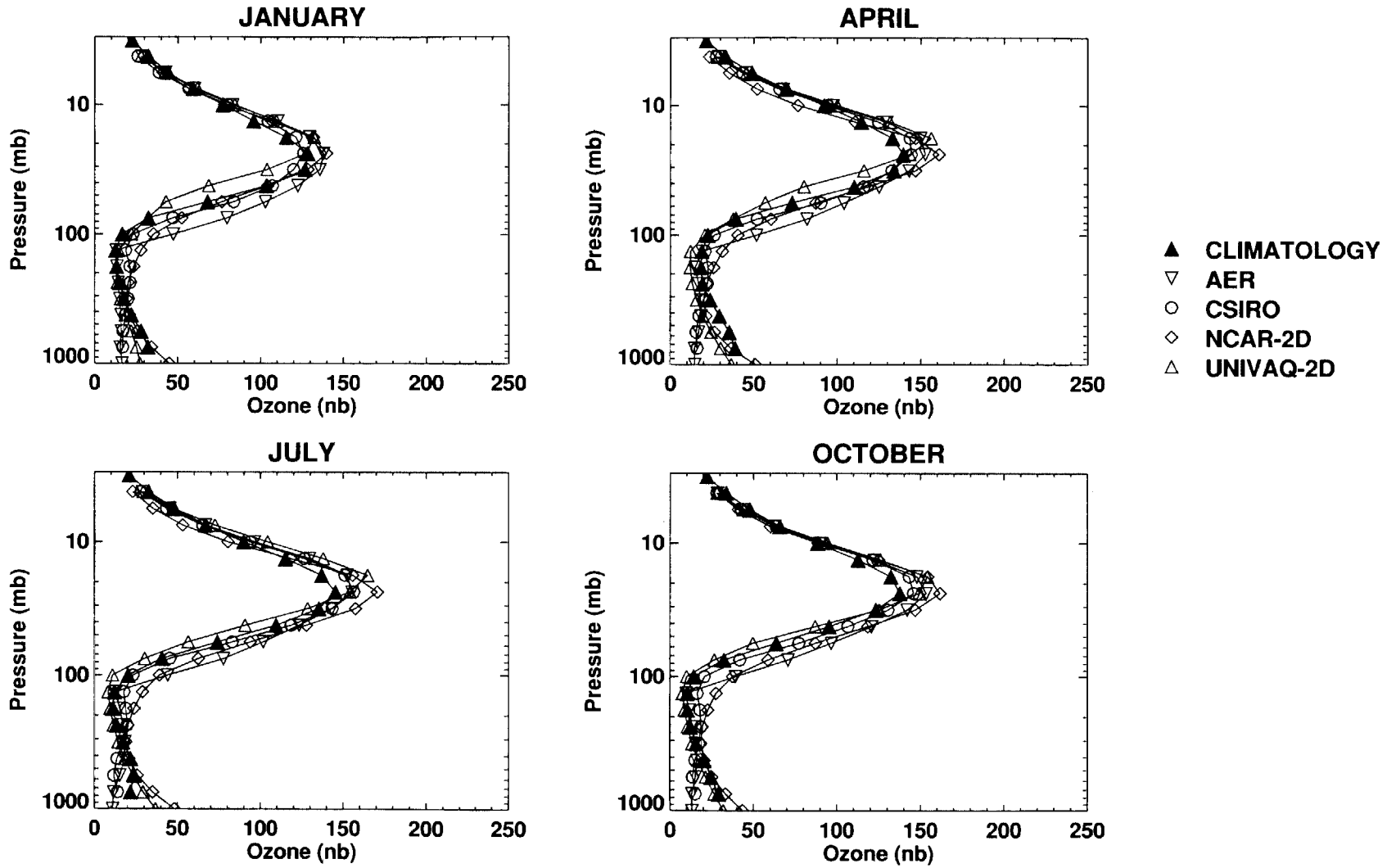

Figure 4.8. Continued.

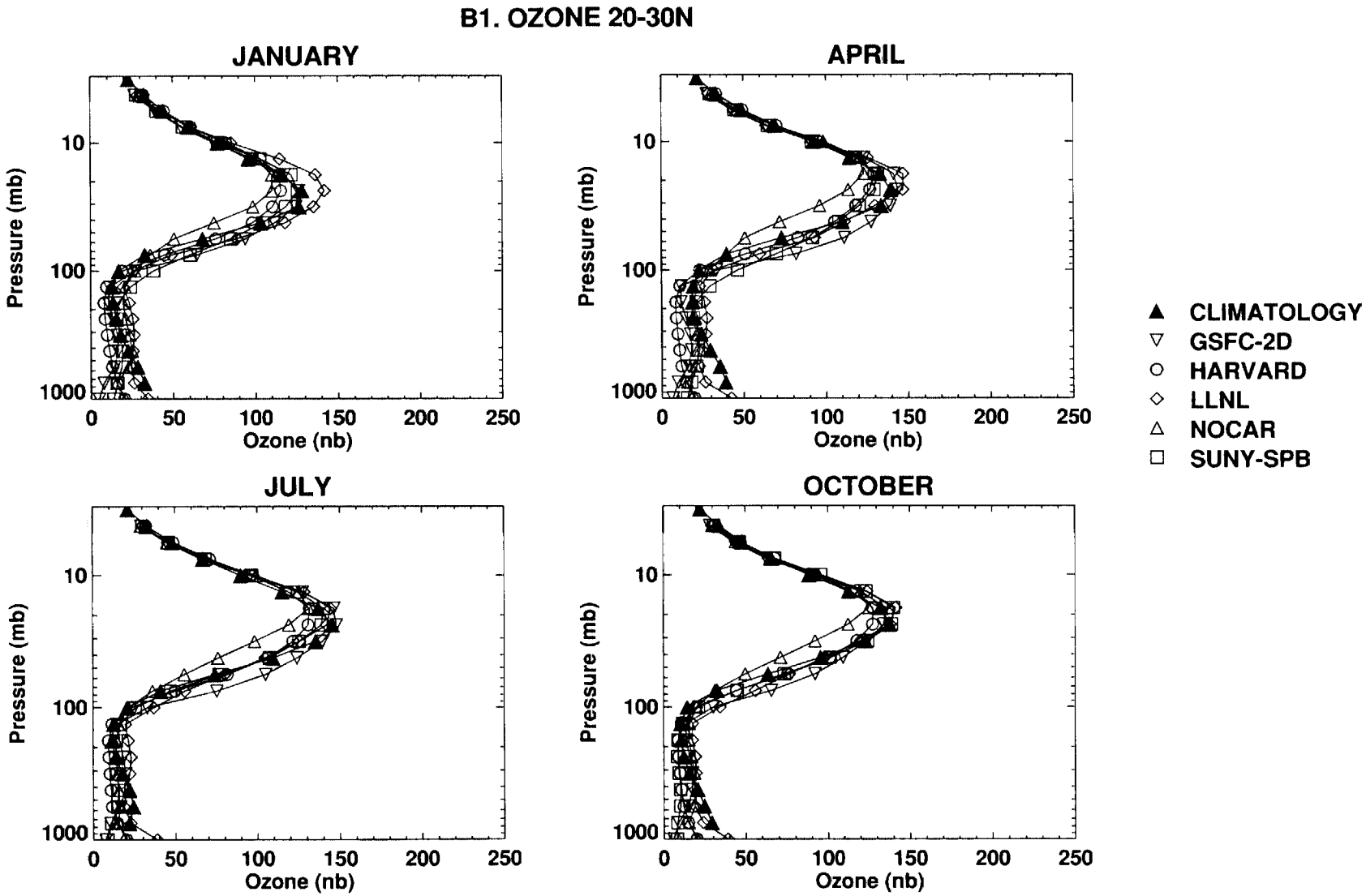

Figure 4.8. Continued.

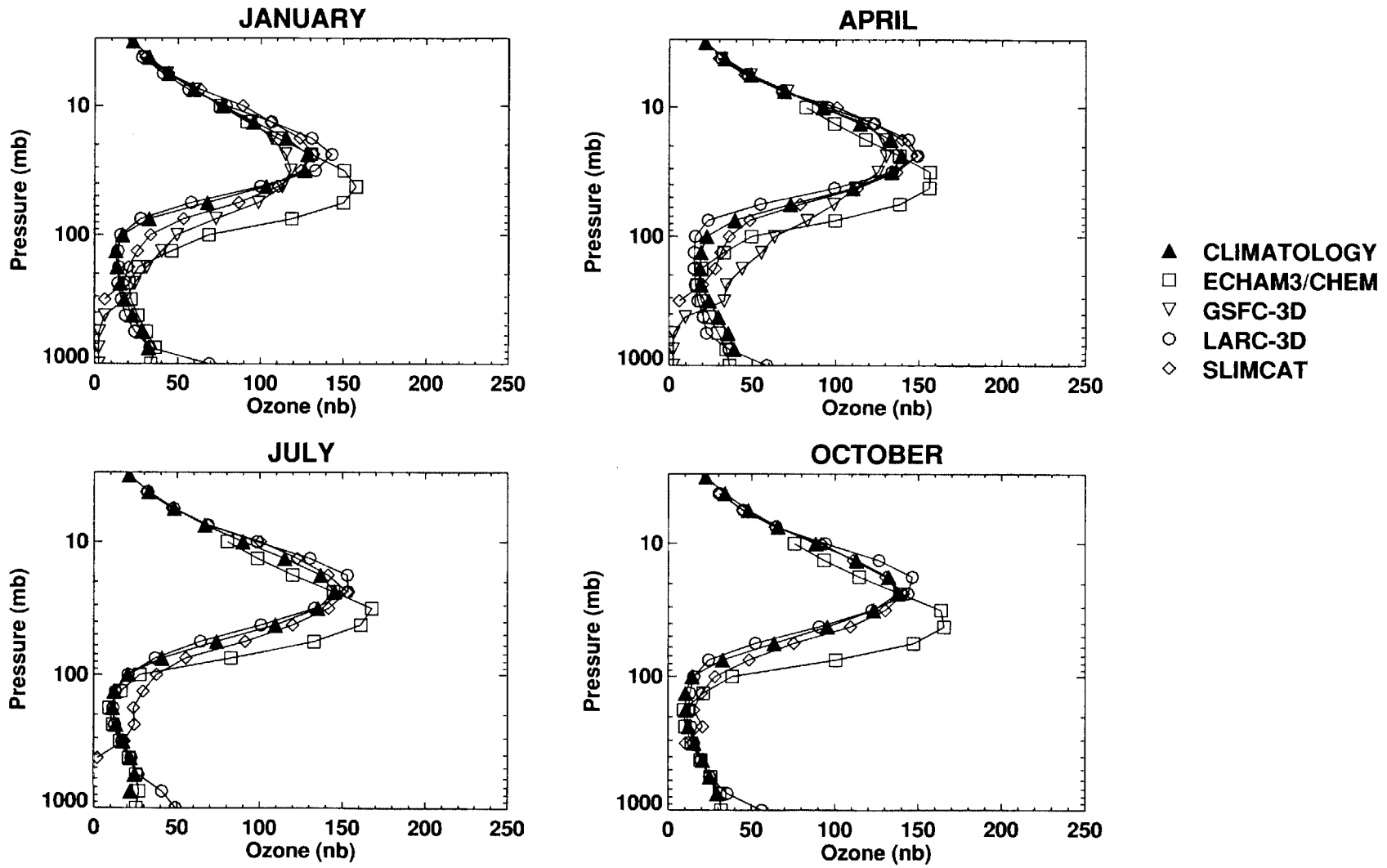

Figure 4.8. Continued.

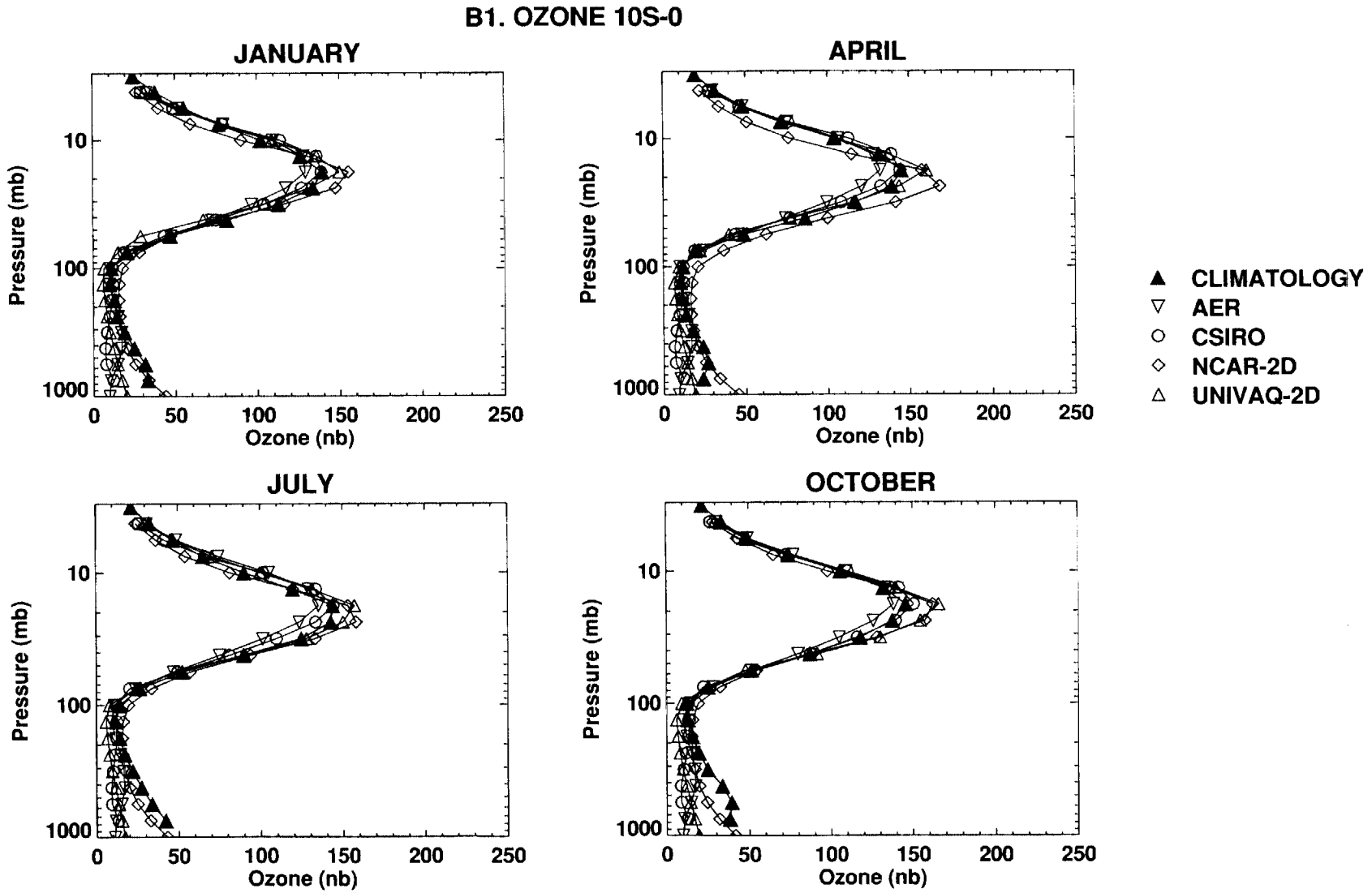

Figure 4.8. Continued.

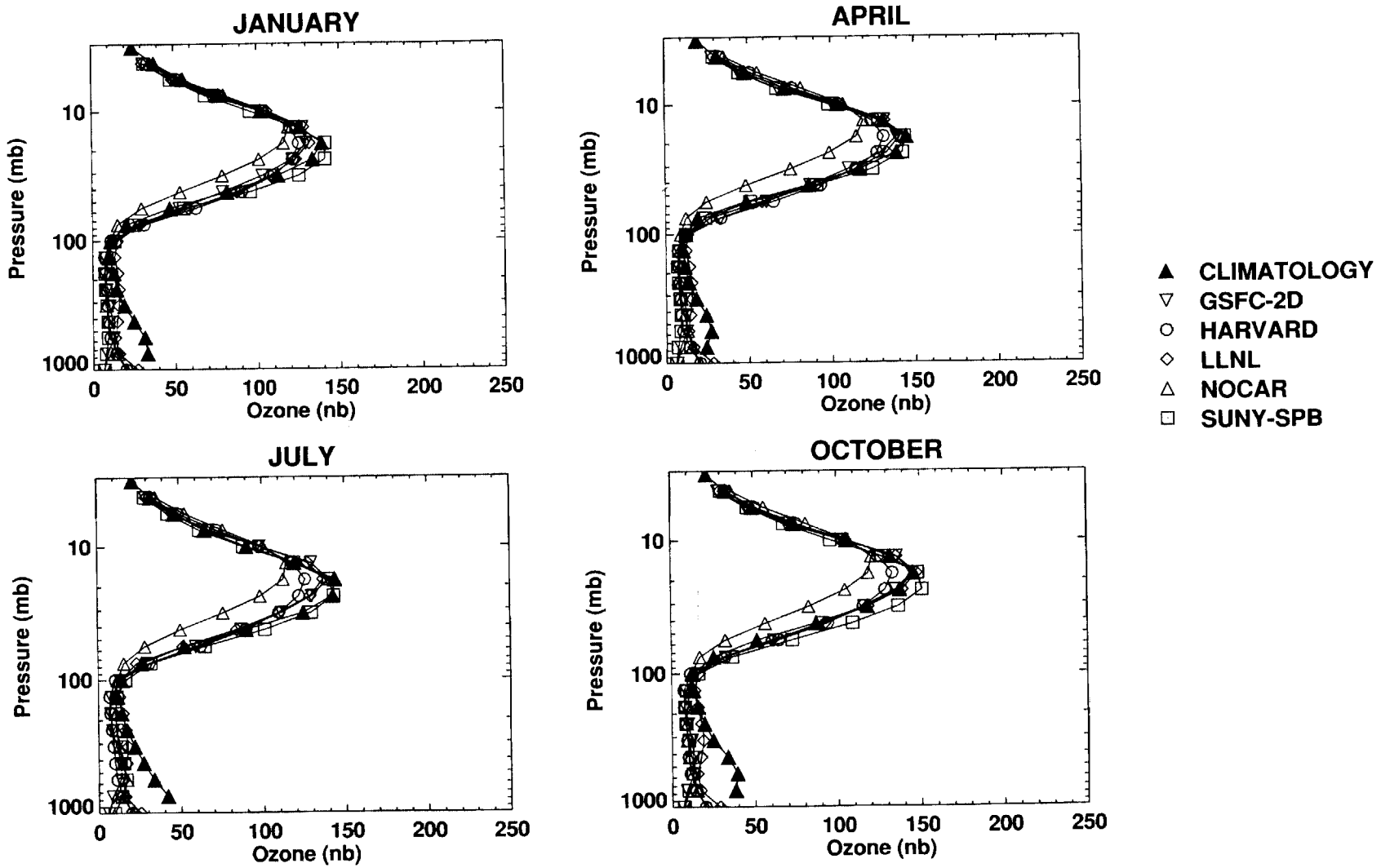

Figure 4.8. Continued.

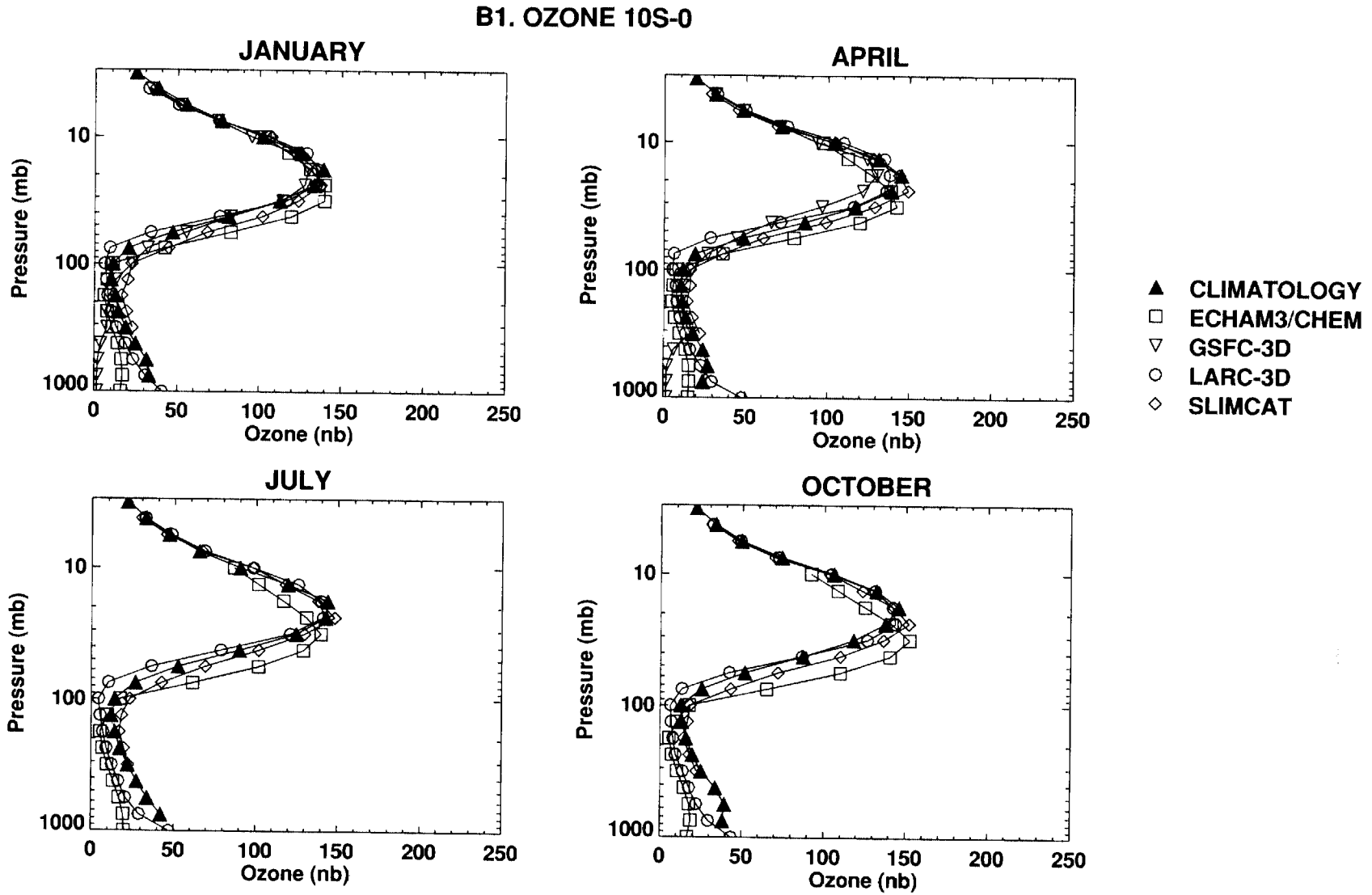

Figure 4.8. Continued.

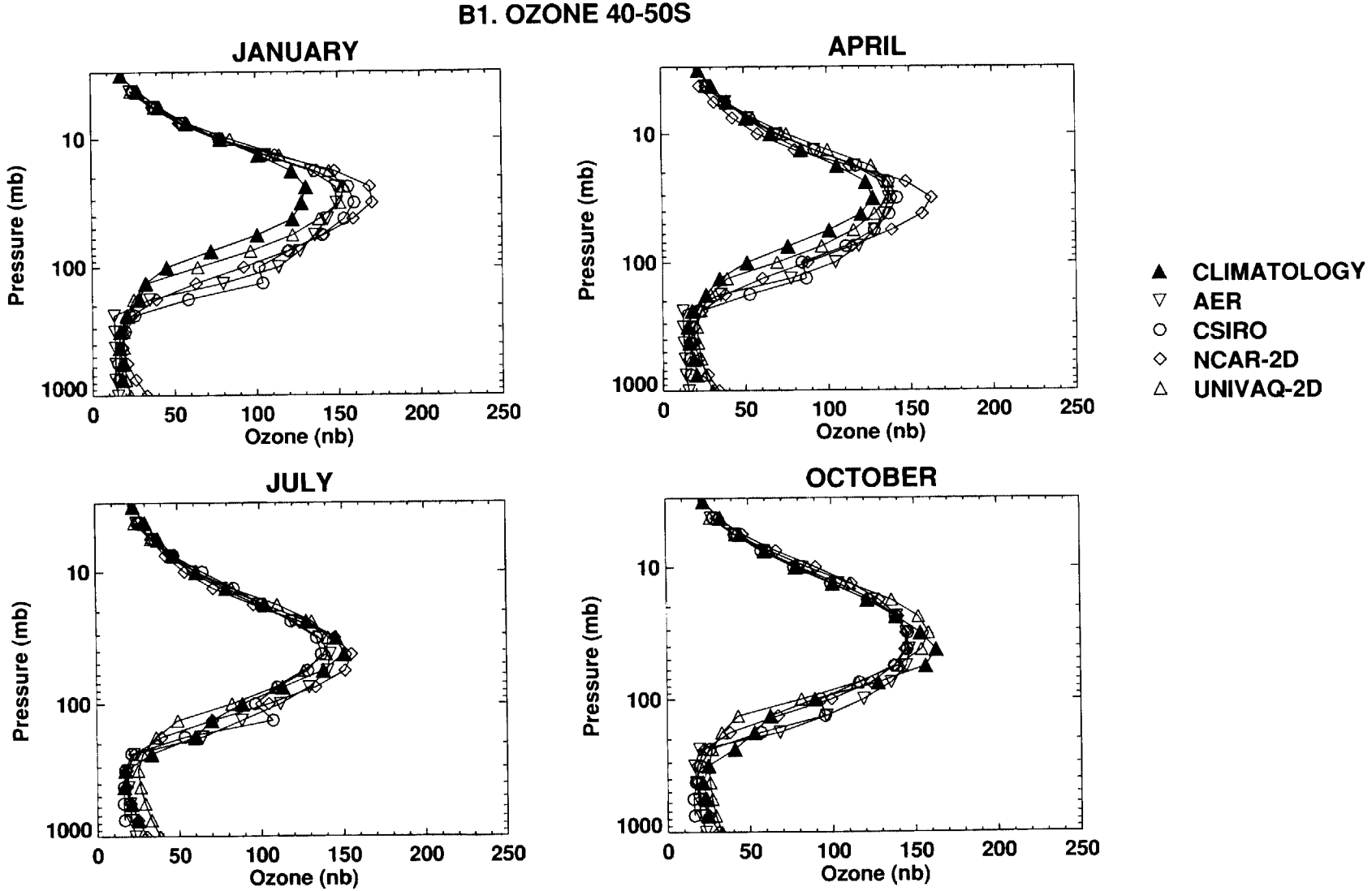

Figure 4.8. Continued.

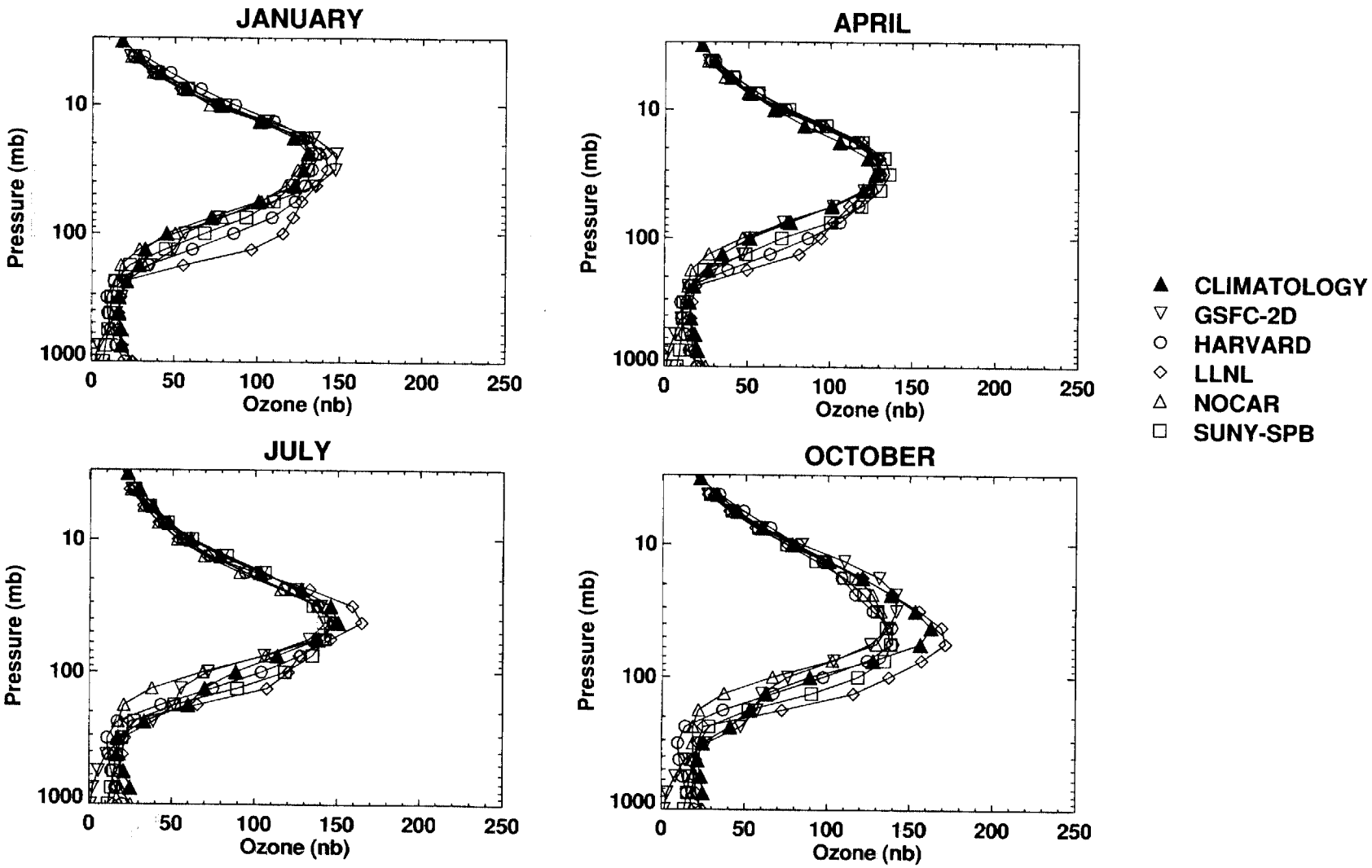

Figure 4.8. Continued.

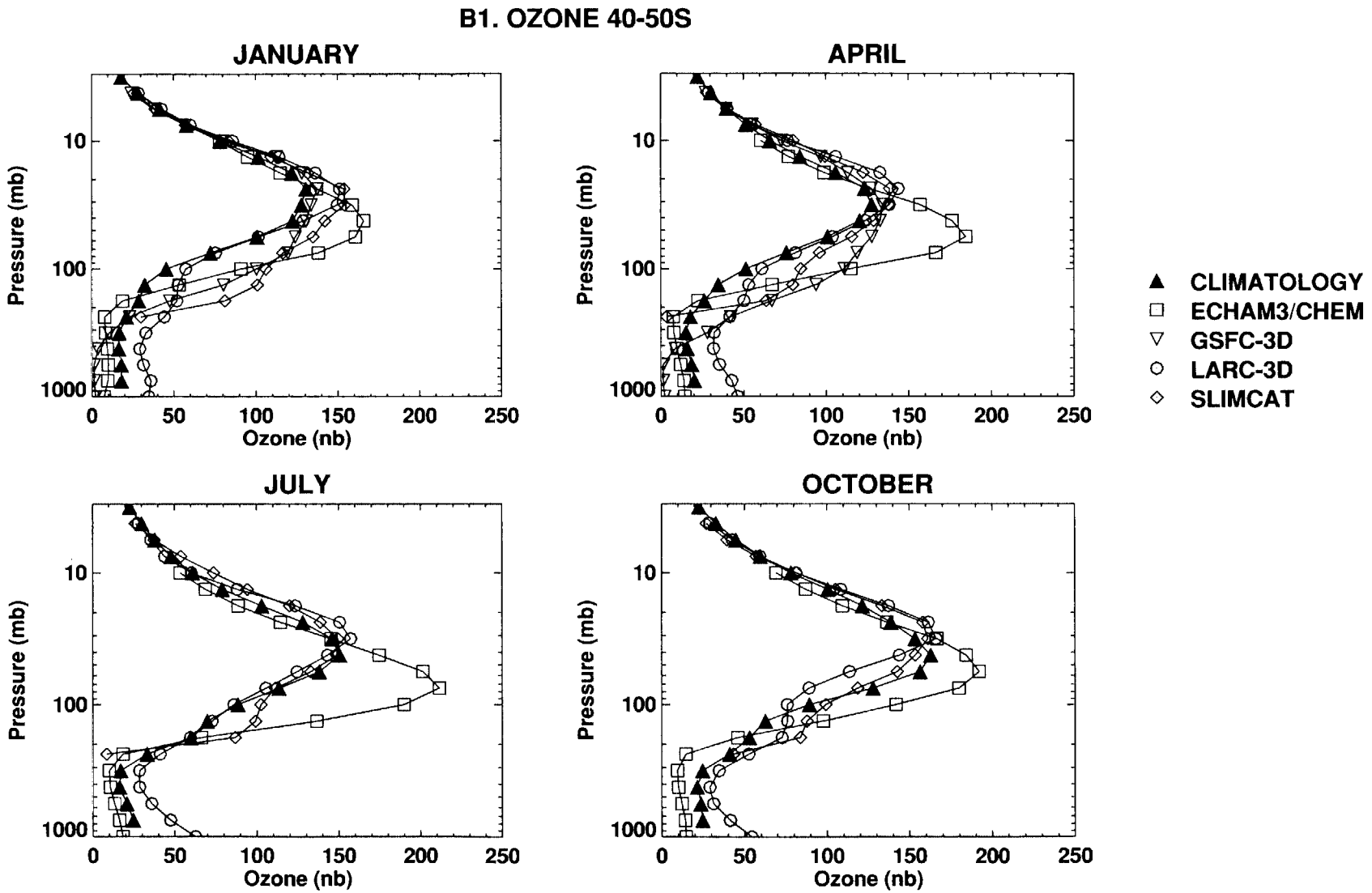

Figure 4.8. Continued.

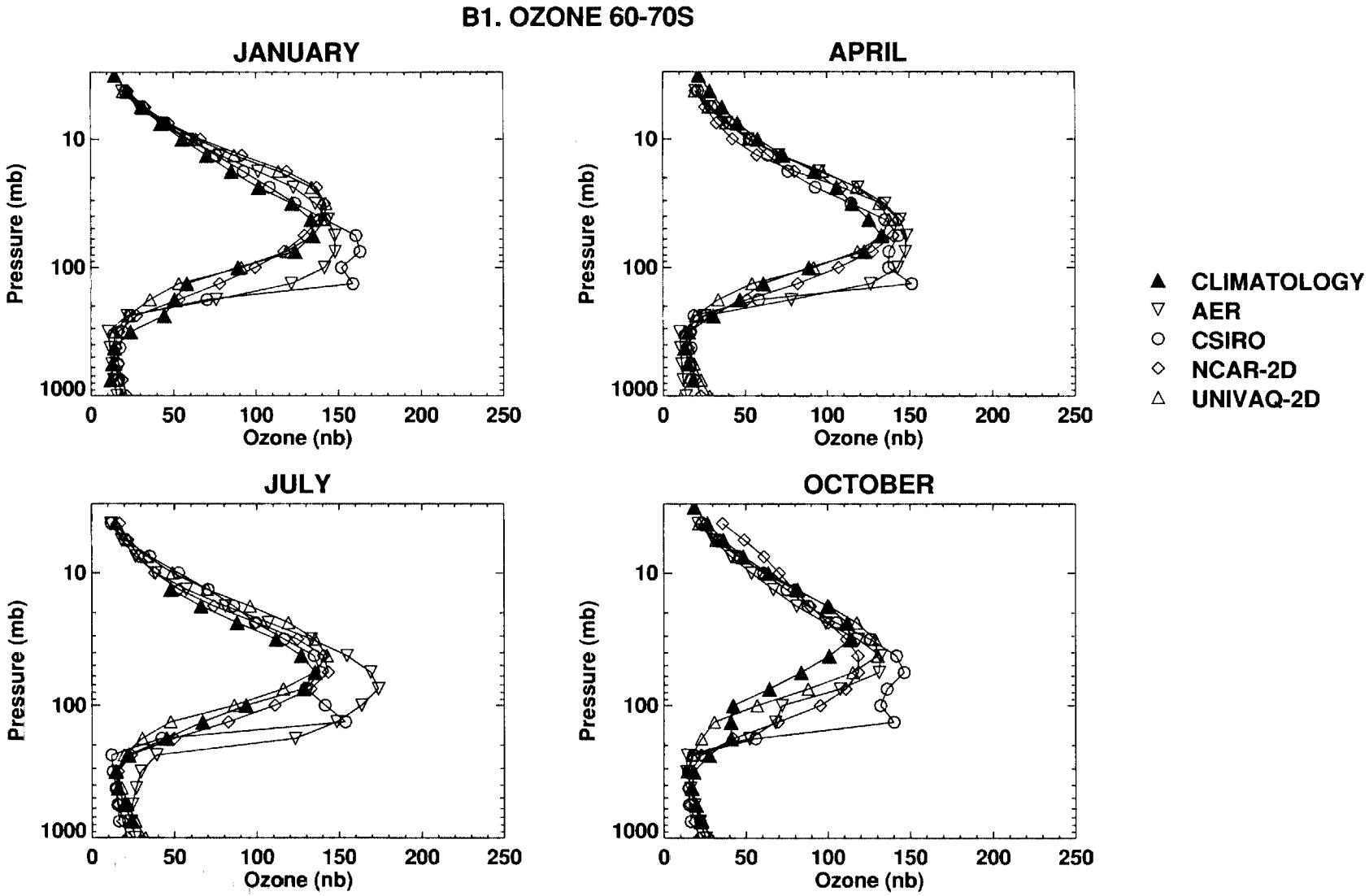

Figure 4.8. Continued.

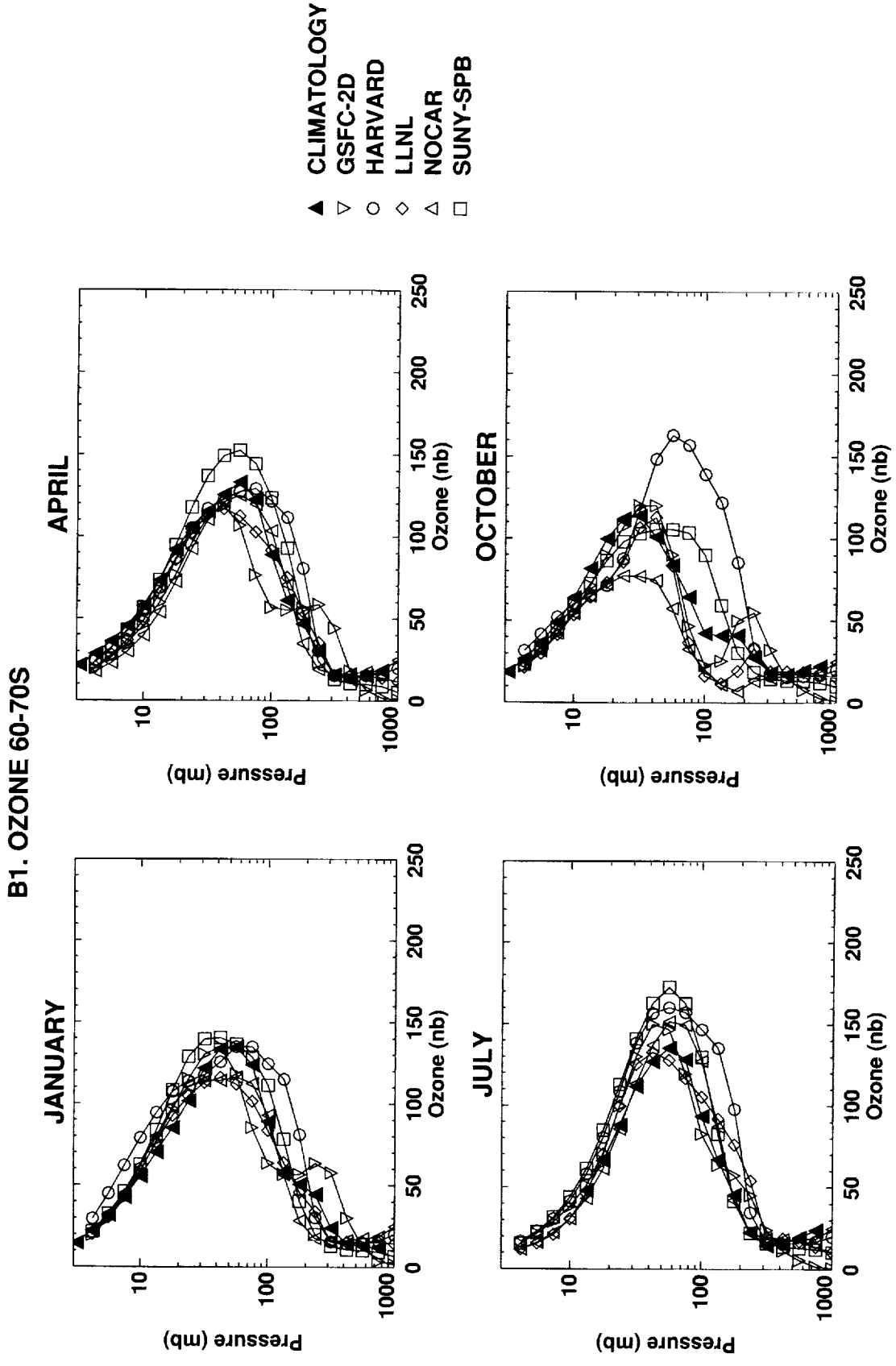

Figure 4.8. Continued.

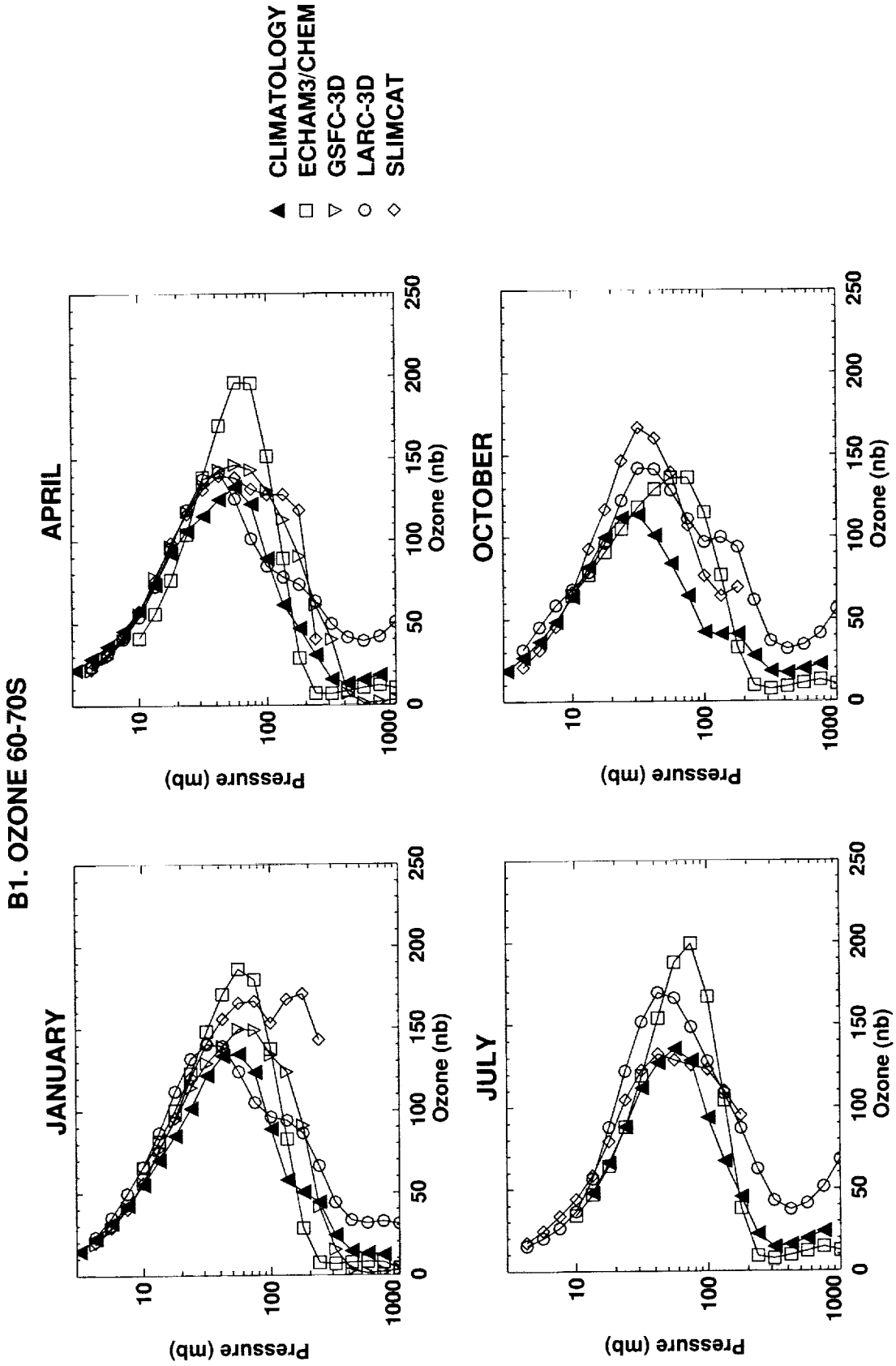

Figure 4.8. Concluded.

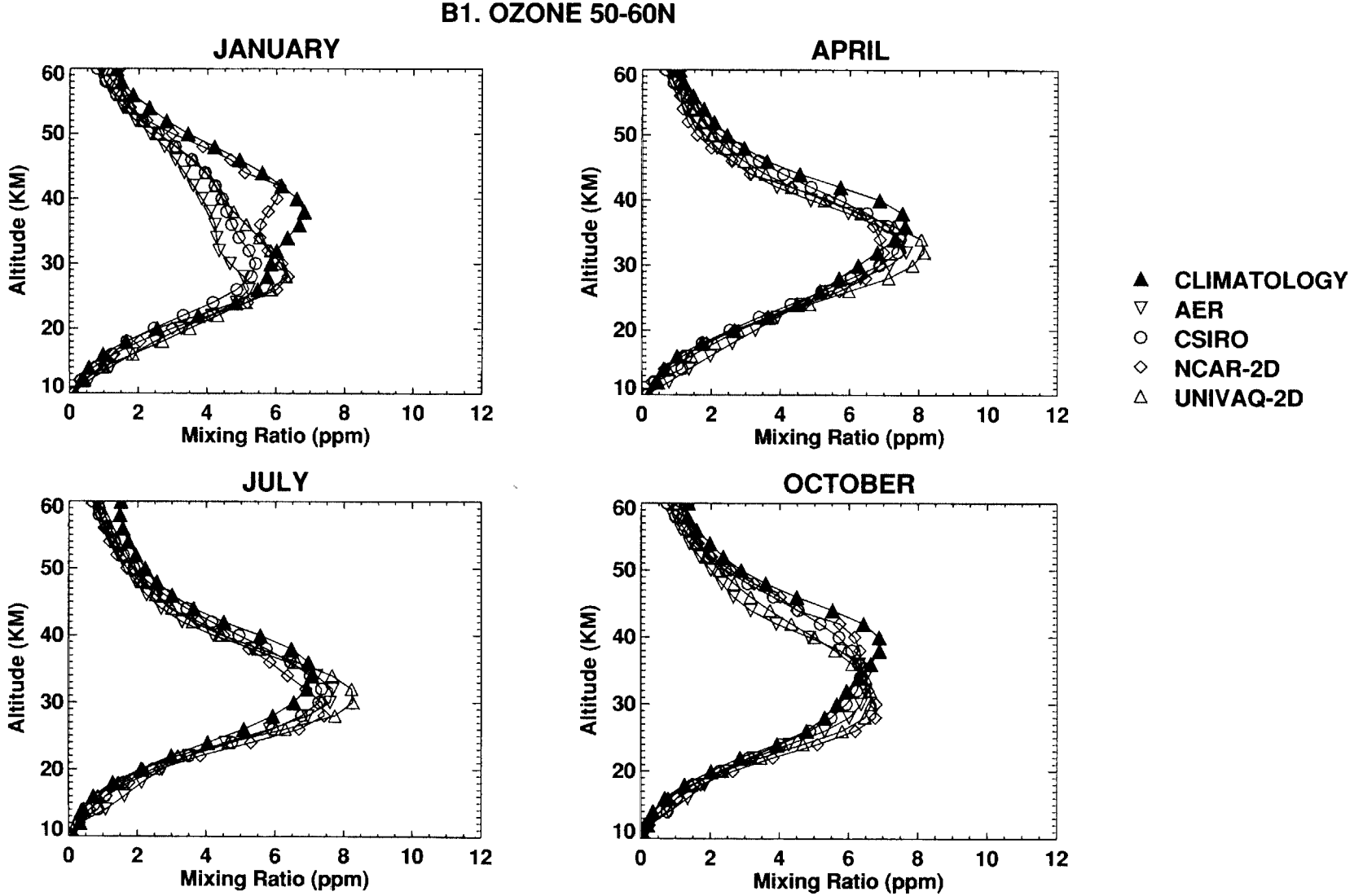

Figure 4.9. Vertical profiles of ozone mixing ratio compared to observations for selected models and latitudes.

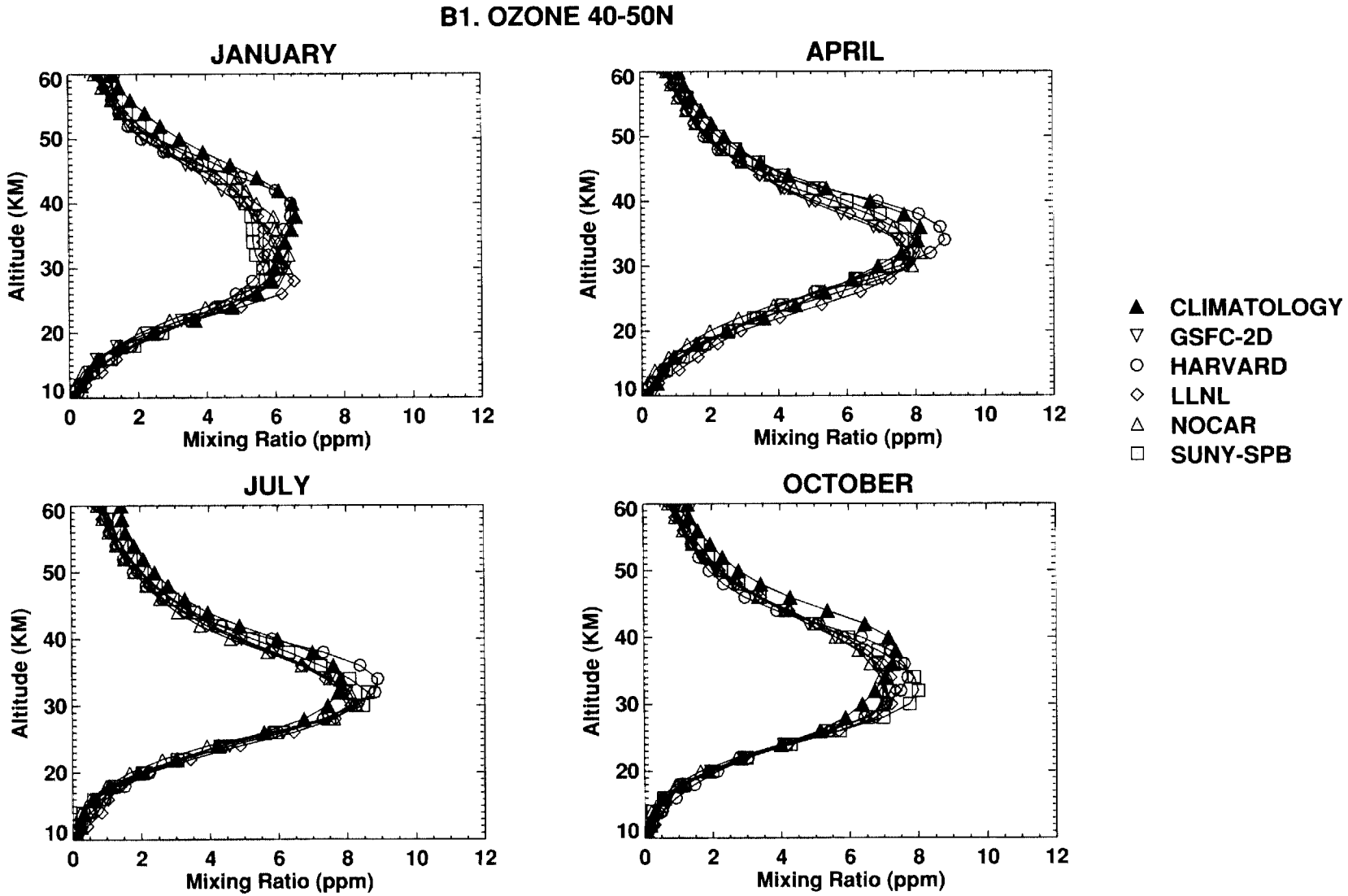

Figure 4.9. Continued.

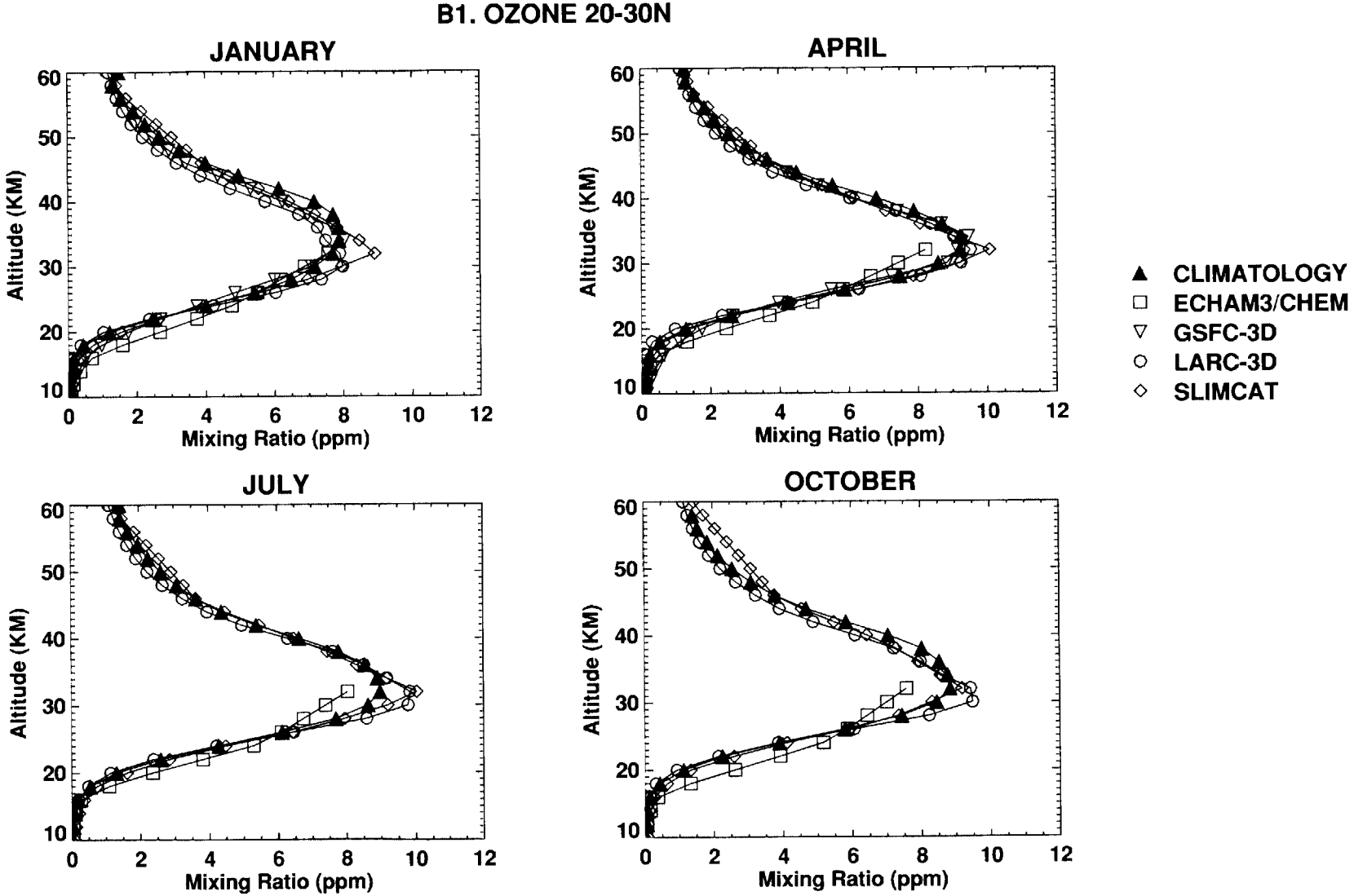

Figure 4.9. Continued.

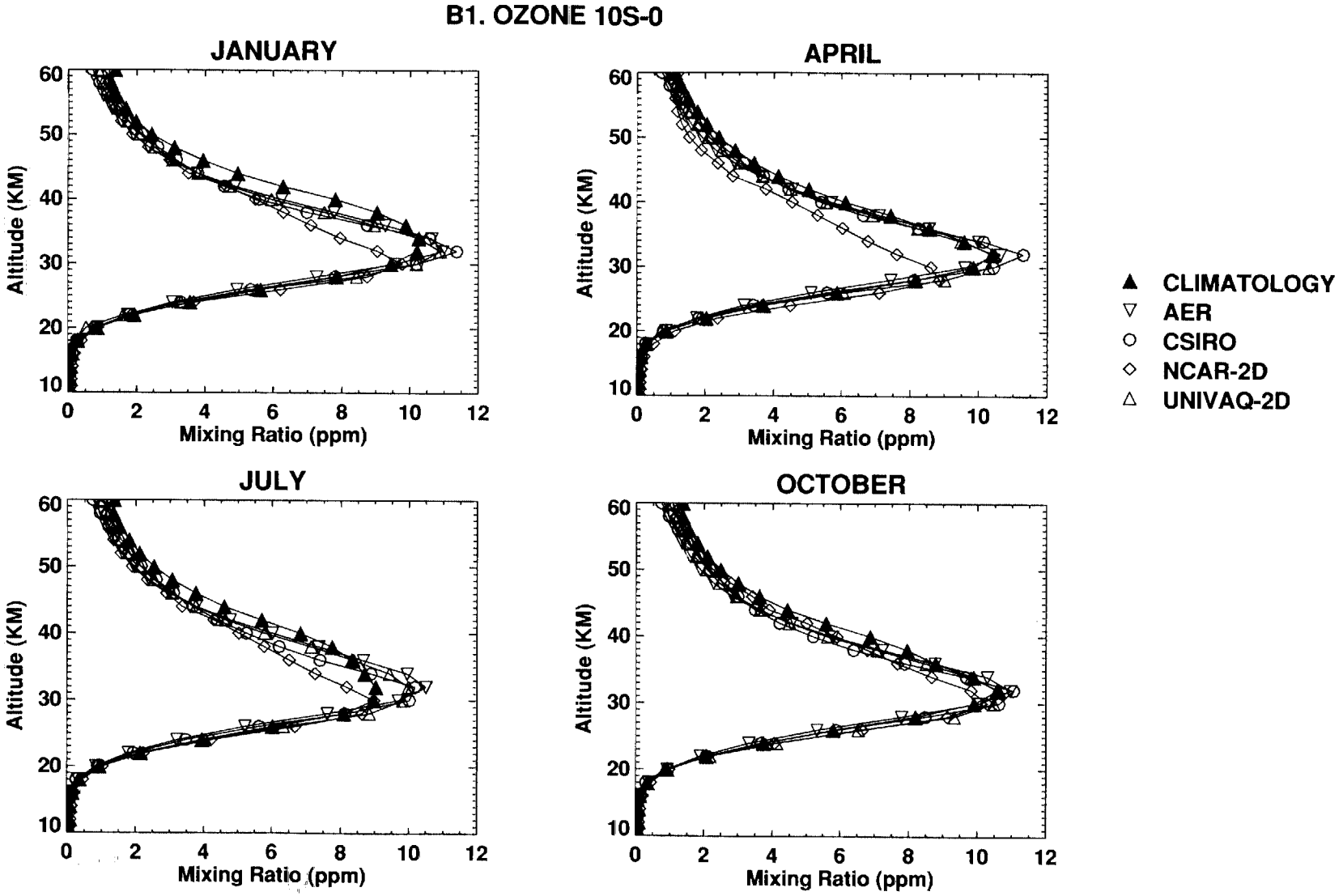

Figure 4.9. Concluded.

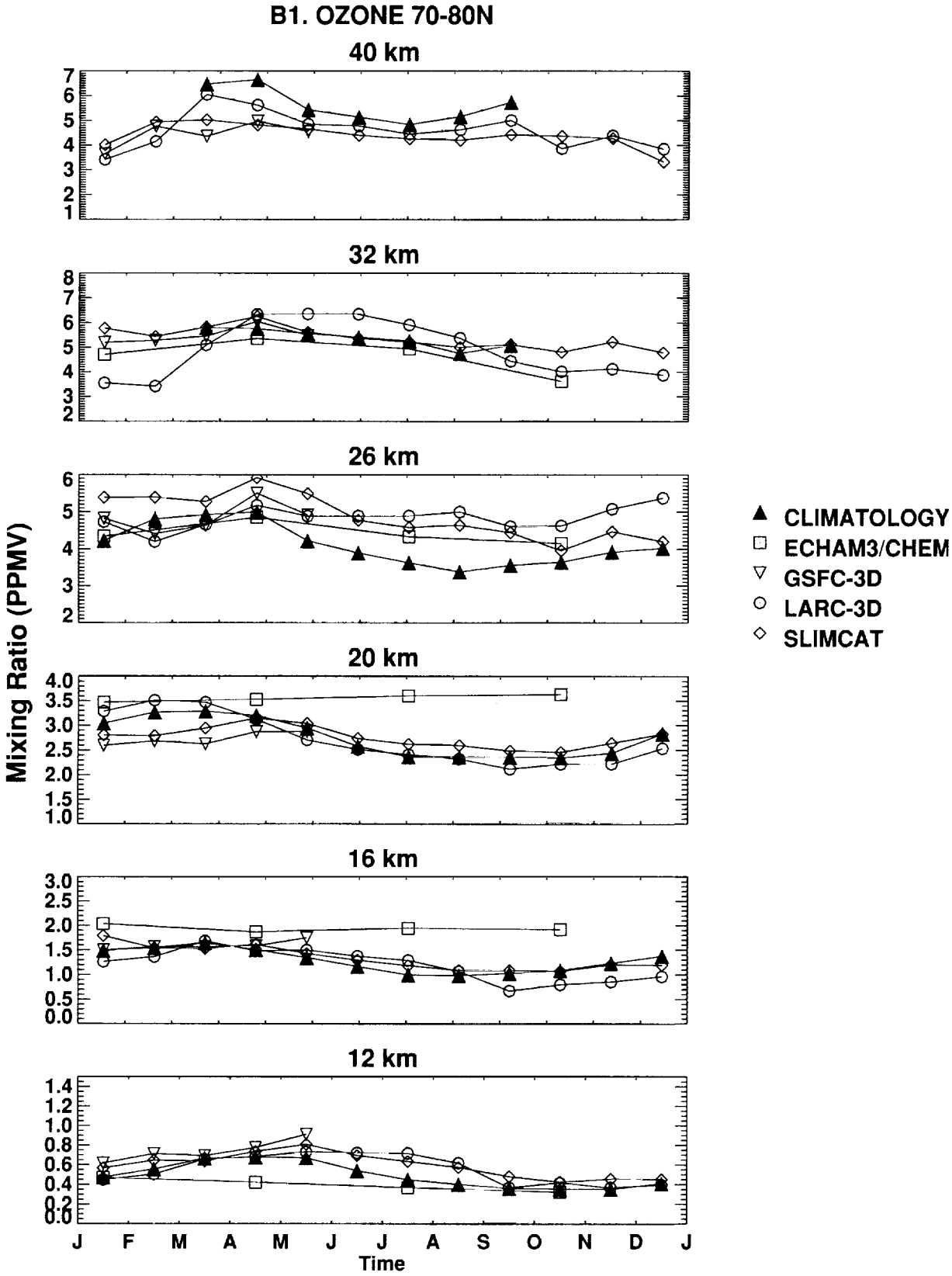

Figure 4.10. Annual cycle of ozone at various altitudes.

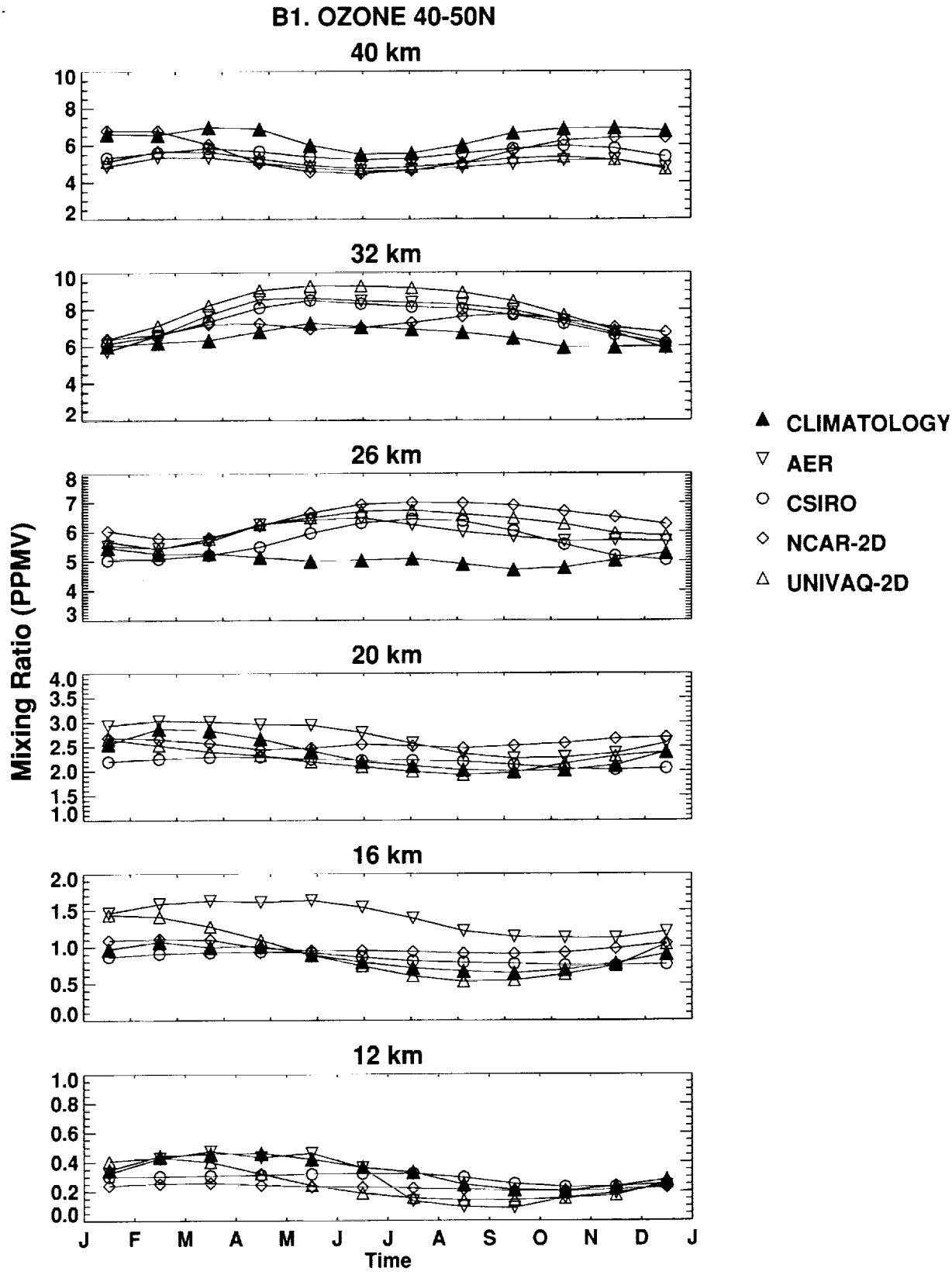

Figure 4.10. Continued.

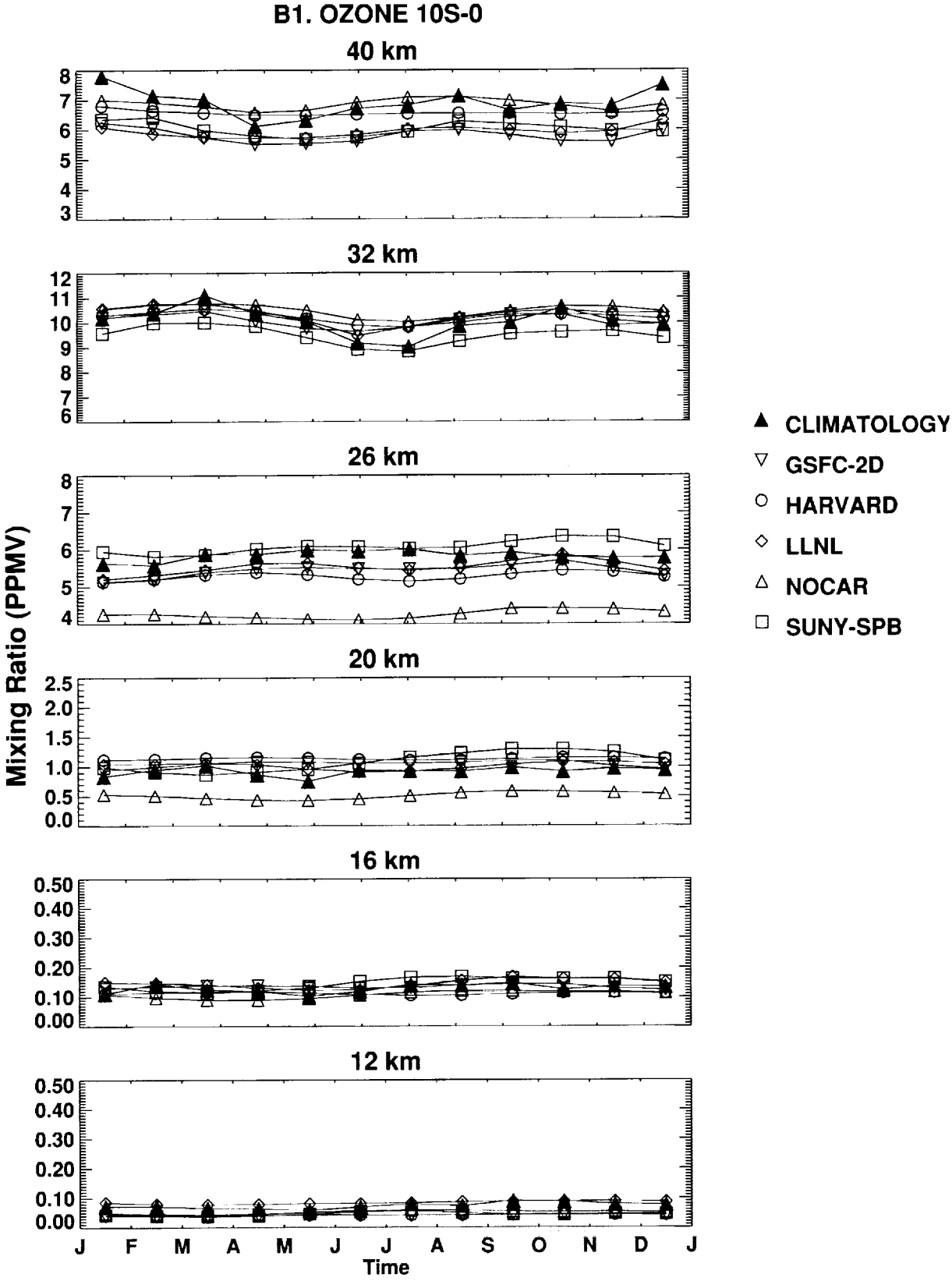

Figure 4.10. Continued.

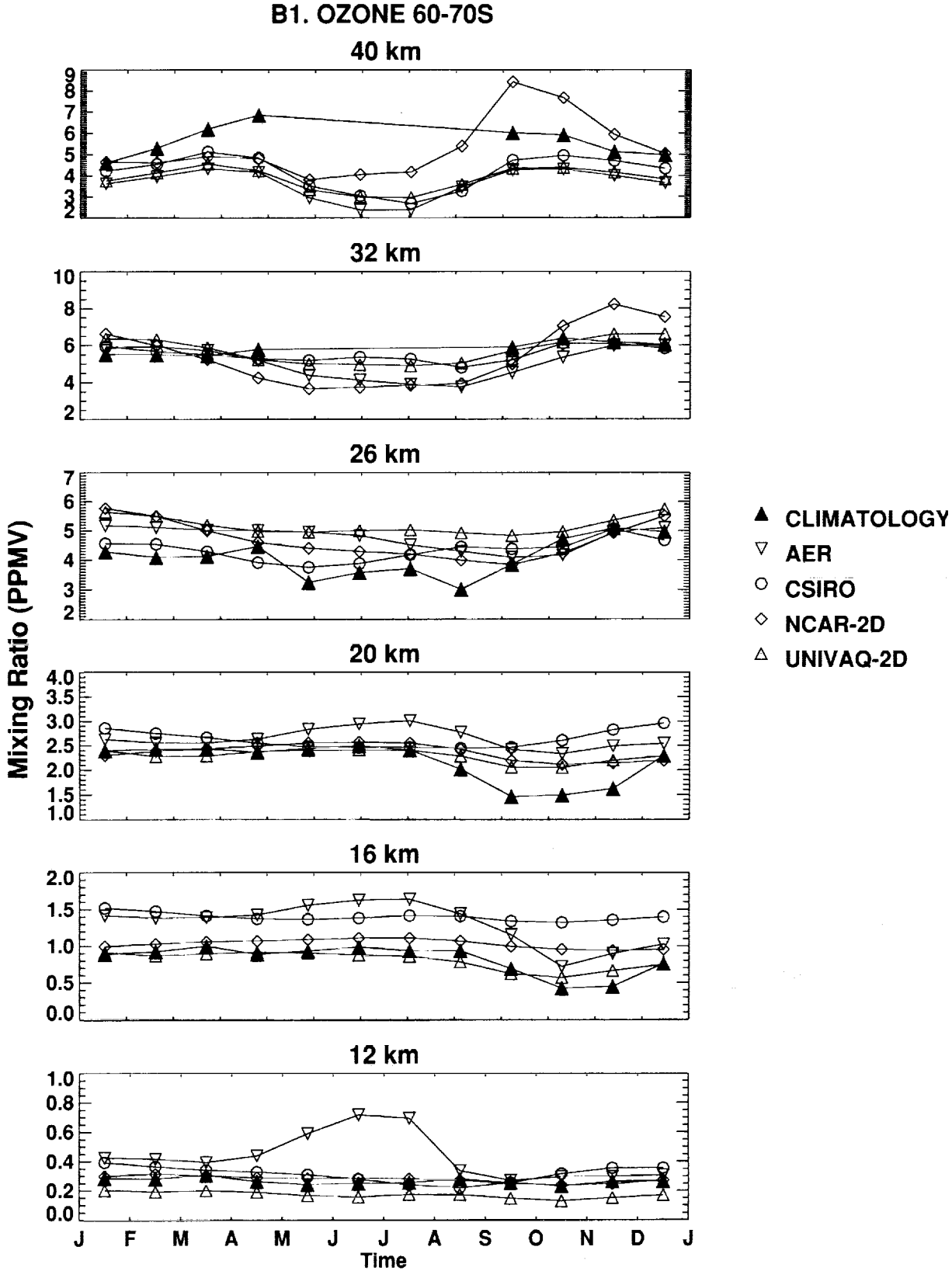

Figure 4.10. Concluded.

5. Special Diagnostics

5.1 Introduction

This section contains a number of special diagnostics that are designed to examine certain mechanisms. Section 5.2 reports on the method used to test the photochemical partitioning in the models. Sections 5.3 and 5.4 represent efforts to examine the model calculated production and removal rates for ozone and how the values are combined with transport rates in the models to produce the simulated ozone distributions. Sections 5.5 and 5.6 concentrate on polar processes including the dynamics aspect of vortex confinement and the chemical aspects of chlorine activation.

5.2 Partitioning of the Radical Species

Malcolm K. W. Ko[1] and Ross J. Salawitch[2]

[1]Atmospheric and Environmental Research, Inc.
[2]Jet Propulsion Laboratory

Assessment models are primarily designed to simulate ozone and its responses to perturbations. Although the assessment models also compute radical species concentrations needed to calculate the production and removal rates of the long-lived species, the models are not routinely used to simulate radical species concentrations for comparison with observations. It is possible to compare model results discussed in Chapter 3 with some longer time average radical measurements (several days to a month), however, it is usually inappropriate to compare model results with observations on shorter time scales (less than a few days). Models generally have difficulties simulating the short-term variabilities of the long-lived species that would affect the radical species concentrations. Since it is desirable to find a way to test whether the models are calculating the radical species correctly so that there is confidence in the model calculated production and removal rates, one methodology of model comparison is described in this section.

The results in chapter 3 clearly show that there are significant differences in the concentrations of the radical species simulated by the different models. The model calculated concentrations of the radical species at a particular location are influenced by both transport and photochemistry. For the purpose of testing models, it is necessary to separate the transport effect from the photochemical effect. Since the time scales for photochemical conversions among the radical species are shorter than the transport time scales, one can make use of the notion of the family approach, i.e., the radical species are transported together as a family while they are partitioned among themselves depending on changes in the local photochemical environment. The effects from transport and chemistry can then be partially separated by looking at ratios such as $[NO_2]/[NOy]$, and $[ClO]/[Cly]$. However, such ratios still depend on the local ozone concentration and the concentrations of NOy and Cly that are calculated by the models and are affected by transport.

One method used in previous studies to isolate the effect of the photochemical calculation was to isolate the photochemical code in the assessment model. The photochemical code of the more comprehensive model was employed as a box model to simulate the phtotostationery state of an air parcel that was held at the fixed latitude, longitude and altitude. The temperature and the concentrations of the long-lived species such as ozone, H_2O, CH_4, HNO_3, NOy and Cly were kept fixed in these calculations, while the solar insolation was allowed to follow the diurnal variation. The models using these constraints computed the partitioning of the radical species. These calculations were performed for situations where there was no Polar Stratospheric Cloud (PSC). Since the model used the same reaction rate constants, any differences were attributed to approximations inherent to the model code. A drawback to such approach was that the box model was off-line and may not be identical to the code used in the full model.

An alternative method is the use of the Photo-Stationary-State (PSS) model [Salawitch, 1994] which was developed originally to compute concentrations of the radical species using observed temperature and local concentrations of the long-lived species. The assumption was that the photochemical conversion times of the radical species were sufficiently short that their concentrations were in photochemical equilibrium. The model has been used to compute radical concentrations from long-lived species concentrations measured by the ER-2. The results of these studies suggest that for most situations where heterogeneous chemistry is relatively slow and metrics are largely zonal, the calculated radical concentrations were in good agreement with the measured concentrations. In preparing this report, the

PSS model was used to calculate the radical species concentrations using long-lived and reservoir species from the individual models' output. The model calculated radical species' concentrations were compared to the concentrations calculated by the constrained PSS model. To the extent that the PSS model has been used to analyze data from the ER-2 and found to perform in a satisfactory manner under many conditions, verification of the model results by the PSS model provides an indirect test of the photochemistry codes in the models.

At the same time, the results must be interpreted with care. Under certain conditions, (e.g. low sun and polar regions) the radical concentrations in the atmosphere may not be in photostationary state. Models that take this into account would disagree with the results from the PSS model. Some models use an average sun condition to compute averaged radical concentrations, which were then used with adjustment factors to compute the production and removal rates for the reservoir species. In those cases, disagreement with the PSS model at a given time does not necessarily mean that the model calculated production and removal rates were incorrect over the large time scales for which this approach is designed.

For models that use explicit diurnal time marching to compute the radical species' concentrations, there is good agreement with the PSS model. It was reasonable to assume in those cases that the radical concentrations were correctly calculated. We tried to concentrate on low latitudes and away from regions where PSCs were present to avoid regions where the comparisons may not be appropriate. Thus, the effect of PSC chemistry on radical partitioning has not been thoroughly tested.

5.3 Ozone Production and Loss from B-1 Runs

Charles H. Jackman

NASA Goddard Space Flight Center

Stratospheric ozone amounts are determined through the interaction of dynamical, radiative, and photochemical processes. We focus on the photochemical processes that influence the ozone amounts in this section. Although other photochemical sources of stratospheric ozone are important in various regions of the stratosphere, the primary production of stratospheric ozone is through the photolysis of molecular oxygen. Ozone is lost through a large number of reactions which are generally grouped according to families. The five families contributing to ozone loss are nitrogen [L(NOx)], hydrogen [L(HOx)], chlorine [L(ClOx)], bromine [L(BrOx)], and oxygen [L(Ox)].

The losses due to the various families have been analyzed before in models [see, e.g., Jackman et al. 1986; Stolarski et al. 1995] and measurements [Wennberg et al. 1994]. The model used in Jackman et al. [1986] included only gas-phase reactions, thus computed a huge dominance of L(NOx) in the middle to lower stratosphere. A snapshot of the losses in the various families was presented for March from the LLNL model in Stolarski et al. [1995]. The computations in Stolarski et al. [1995] were for a relatively clean atmosphere with a low background sulfate aerosol condition. The Wennberg et al. [1994] results showed computations of the ozone losses from measurements during May 1993, a moderately elevated sulfate aerosol condition.

Modellers were supposed to simulate year 1992 in model experiment B-1, which is a very enhanced sulfate aerosol condition because of the huge volcanic eruption of Mt. Pinatubo in June 1991. The ozone loss terms for B-1 are not easily compared with any others discussed in the literature due to large differences in the model or measurement conditions. Therefore, in this analysis we only compare the modelled production and loss terms for O_3 from B-1 with other models participating in these exercises.

Seven models (AER, GSFC-2D, HARVARD, LARC-3D, LLNL, SUNY_SPB, and UNIVAQ-2D) submitted model output for run B-1. Since some models submitted "daytime average" values and others submitted "24-hour average" results, it was not really productive to compare absolute numbers. The percentage losses in the various families were compared for run B-1 in Figure 5.3.1(a-g) for March 1992 and in Figure 5.3.2(a-g) for June 1992. In general, there were many similarities among the models even though the actual methodology for including the losses in each of the families differ from model to model, especially for L(ClOx), L(BrOx), and L(HOx).

The L(HOx) dominates in the lower stratosphere (<20 km) and upper stratosphere (>45 km). The L(NOx) dominates in the middle stratosphere (20-40 km). The L(ClOx) can be quite large (>30%) in the middle and upper stratosphere (35-50 km) whereas L(BrOx) can be large (>30%) in the lower polar stratosphere.

There are some significant differences between the percentage ozone loss rates for the two months compared. Values for the losses in the various families for latitudes poleward of about 67S in June should be ignored as the ozone catalytic loss cycles do not destroy ozone in the polar night. The percentage of ozone loss rate by the halogen families [L(ClOx) and L(BrOx)] and hydrogen family [L(HOx)] is larger at polar northern latitudes in March than in June, whereas the percentage of ozone loss rate by the nitrogen family [L(NOx)] is larger at polar northern latitudes in June than in March.

The ratio of total ozone loss [L(tot)] to total ozone production [P(tot)] was also investigated. These L(tot)/P(tot) values are given in Figure 5.3.3 for March 1992 and Figure 5.3.4 for June 1992. Again, there are many similarities among the models. All models showed the tropical lower to middle stratosphere region (tropopause to 30 km) with P(tot) greater than L(tot). The middle to upper stratosphere showed that P(tot) was about equal to L(tot). L(tot)/P(tot) should be near 1 in the upper stratosphere as the photochemical lifetime for ozone is less than a day and ozone should be approximately in photochemical equilibrium.

L(tot) was greater than P(tot) in the middle to polar latitudes and lower to middle stratosphere. L(tot) depends very critically on the amount of atomic oxygen, O, which is produced by photolysis of O_3 for wavelengths up to about 1140 nm. P(tot), on the other hand, depends on the very shortest of wavelengths (< 242 nm). These very high energy photons are absorbed quite efficiently at the very large column densities of O_2 and O_3 at low altitudes and high latitudes. Thus atomic oxygen is created at low altitudes and high latitudes resulting in ozone loss whereas the ozone production is being curtailed in the same region. For further discussion of L(tot)/P(tot) see Jackman et al. [1986].

References

Jackman, C. H., R. S. Stolarski, and J. A. Kaye, Two-dimensional monthly average ozone balance from limb infrared monitor of the stratosphere and stratospheric and mesospheric sounder data, J. Geophys. Res., 91, 1103-1116, 1986.

Stolarski, R. S., et al., 1995 Scientific Assessment of the Atmospheric Effects of Stratospheric Aircraft, NASA Reference Publication 1381, November 1995.

Wennberg, P. O., et al., Removal of stratospheric O_3 by radicals: In situ measurements of OH, HO_2, NO, NO_2, ClO, and BrO, Science, 266, 398-404, 1994.

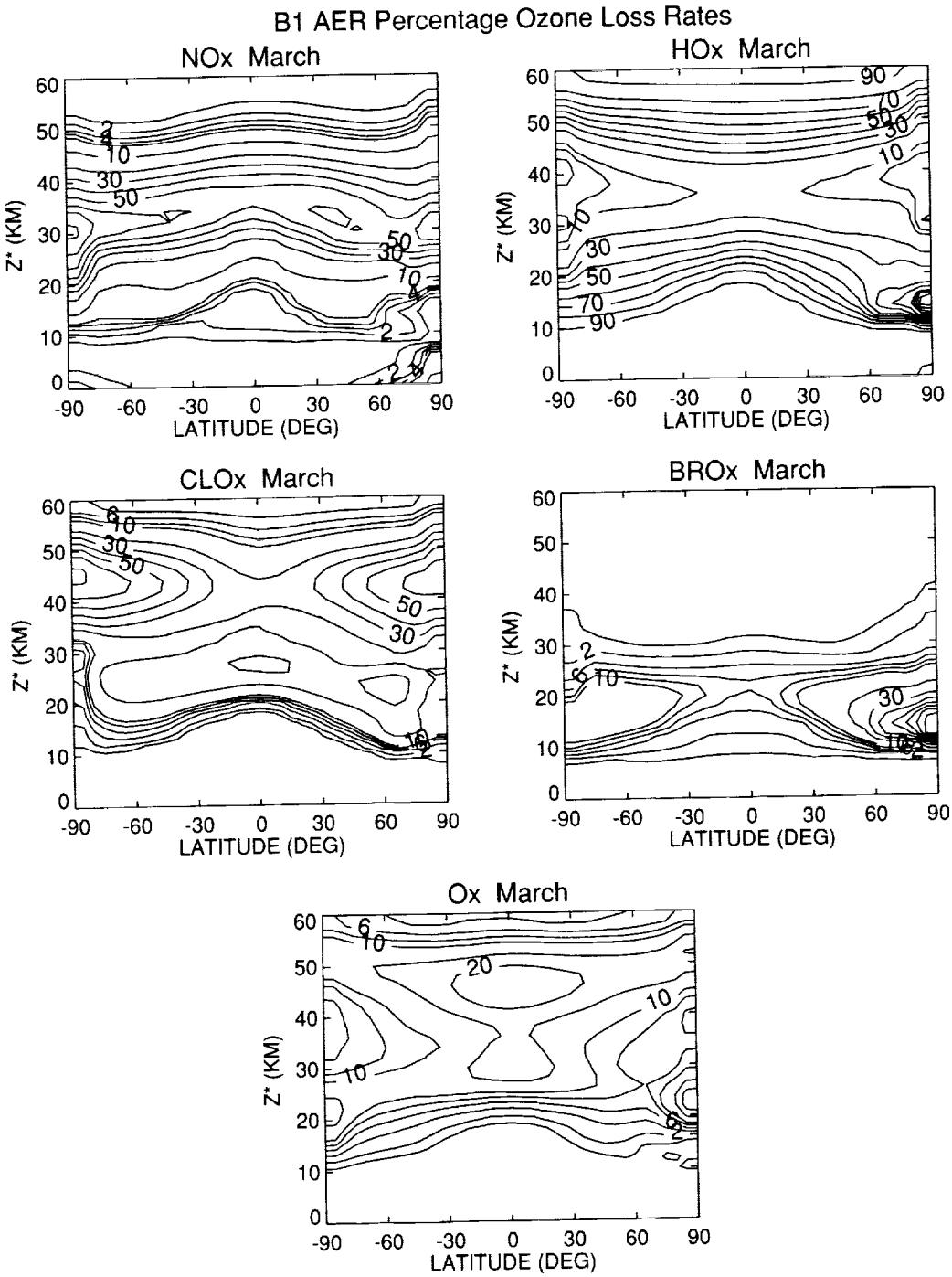

Figure 5.3.1a Ozone losses (in percent) due to the five families, L(NOx), L(HOx), L(ClOx), L(BrOx), and L(Ox) computed for March 1992 from the AER, GSFC-2D, HARVARD, LARC-3D, LLNL, SUNY_SPB, and UNIVAQ-2D models.

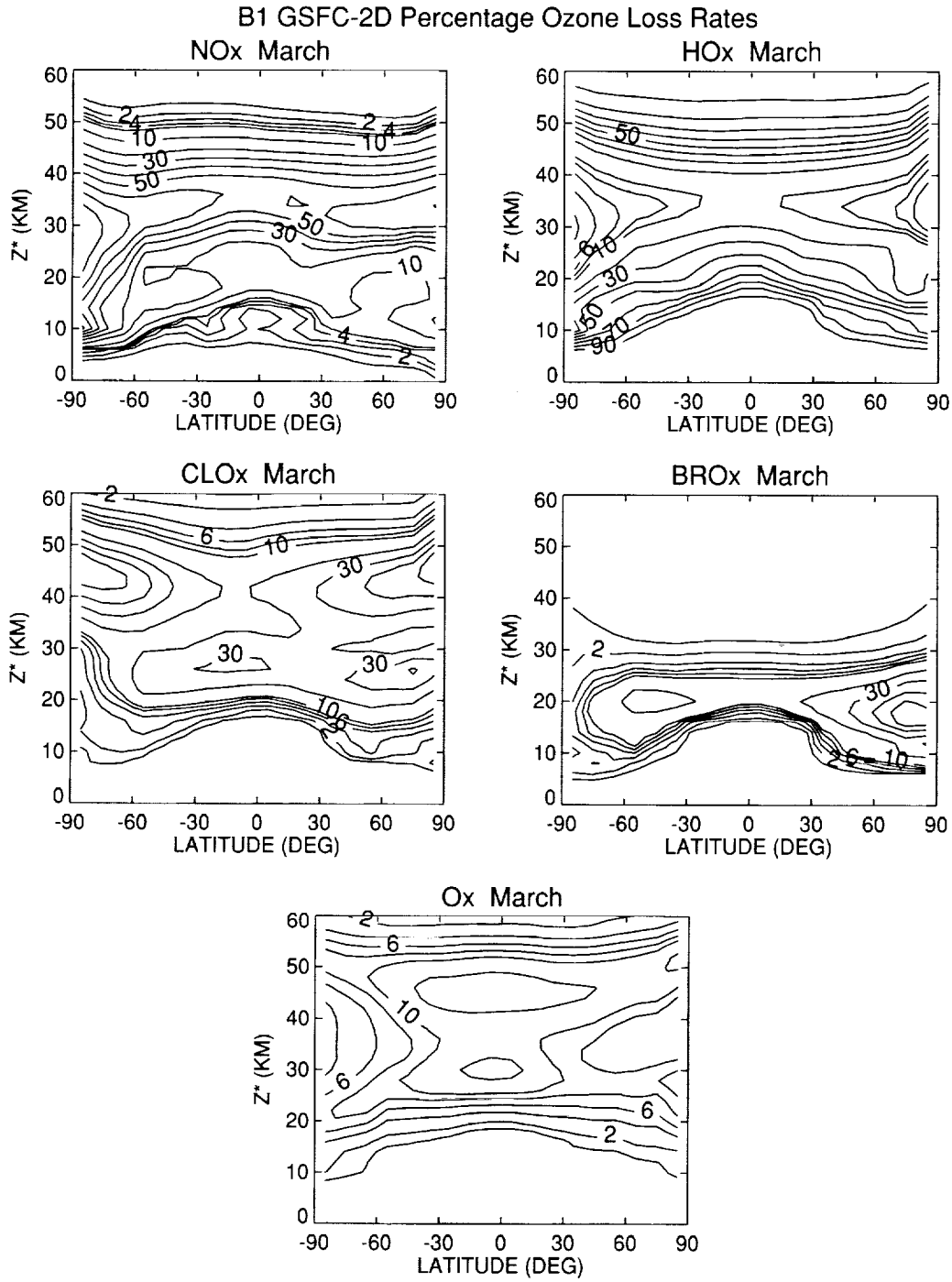

Figure 5.3.1b Continued.

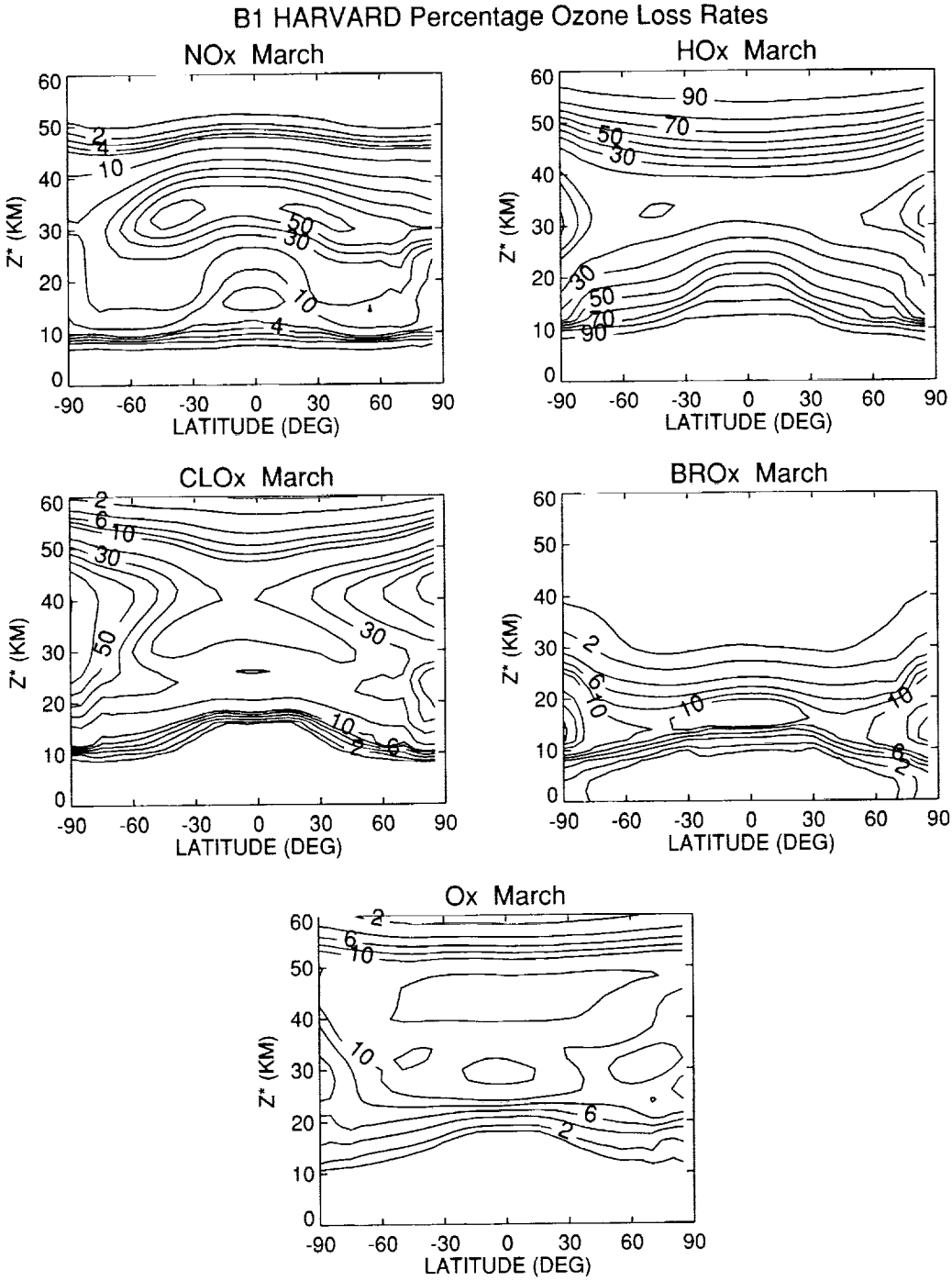

Figure 5.3.1c Continued.

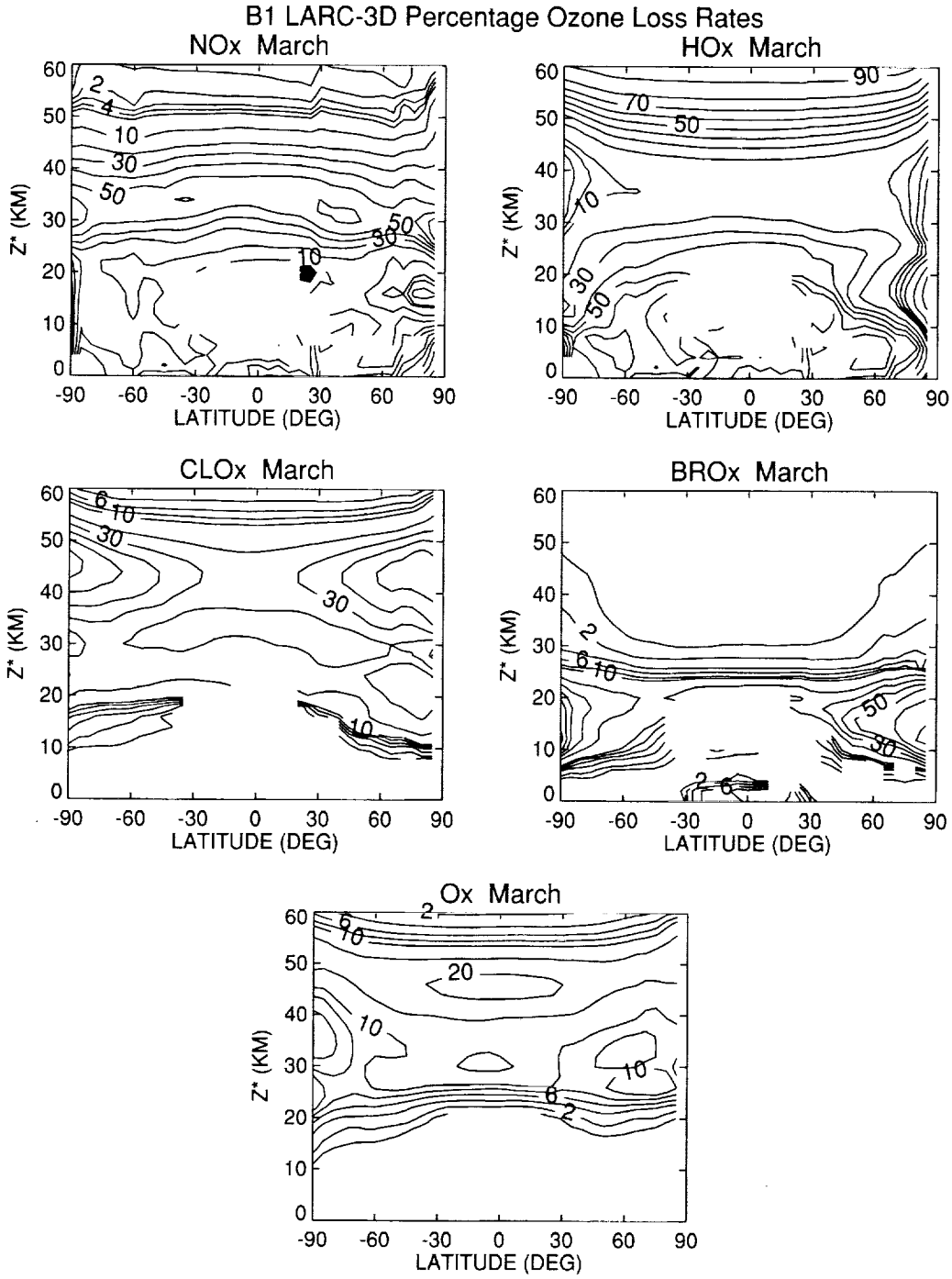

Figure 5.3.1d Continued.

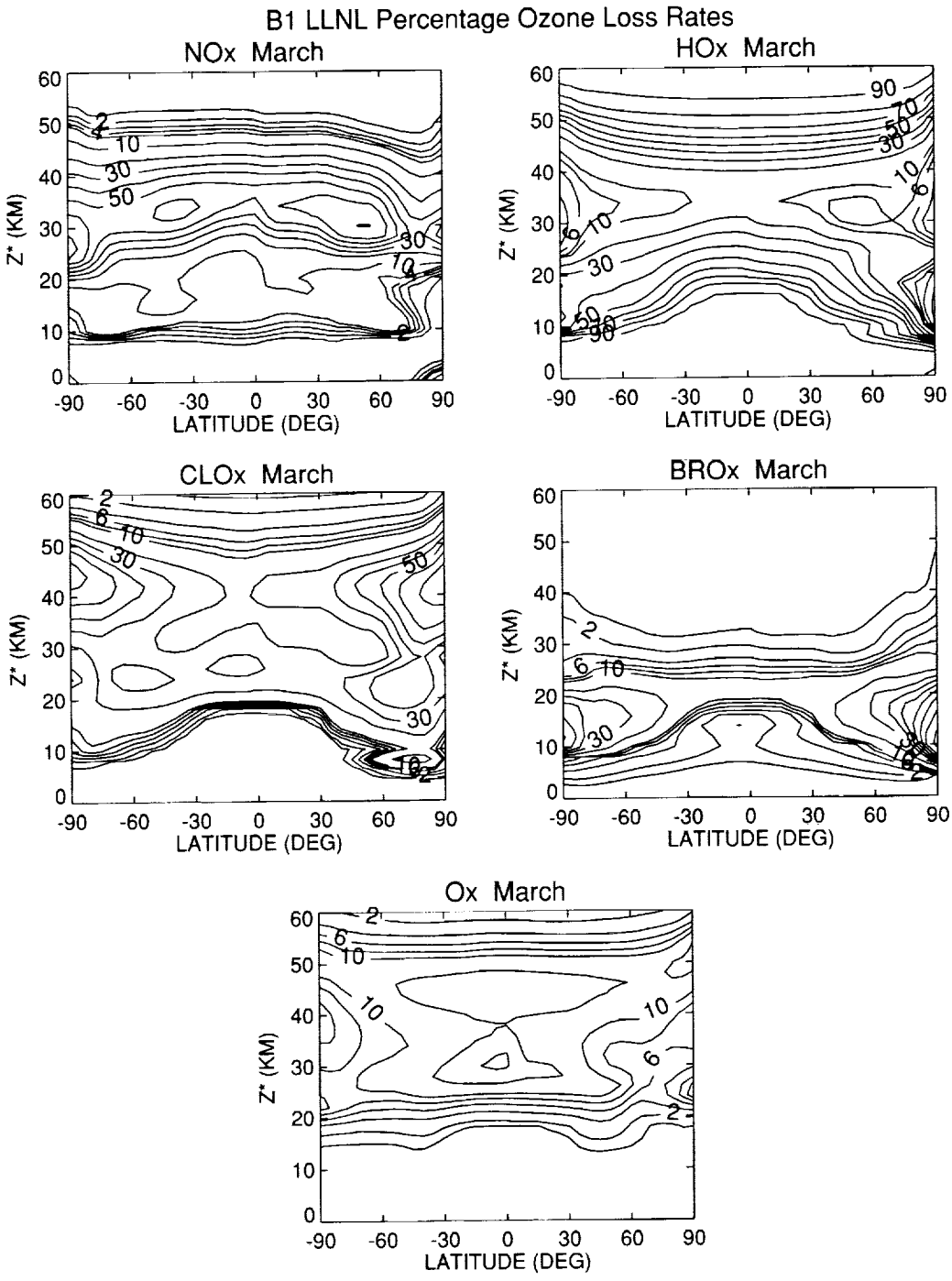

Figure 5.3.1e Continued.

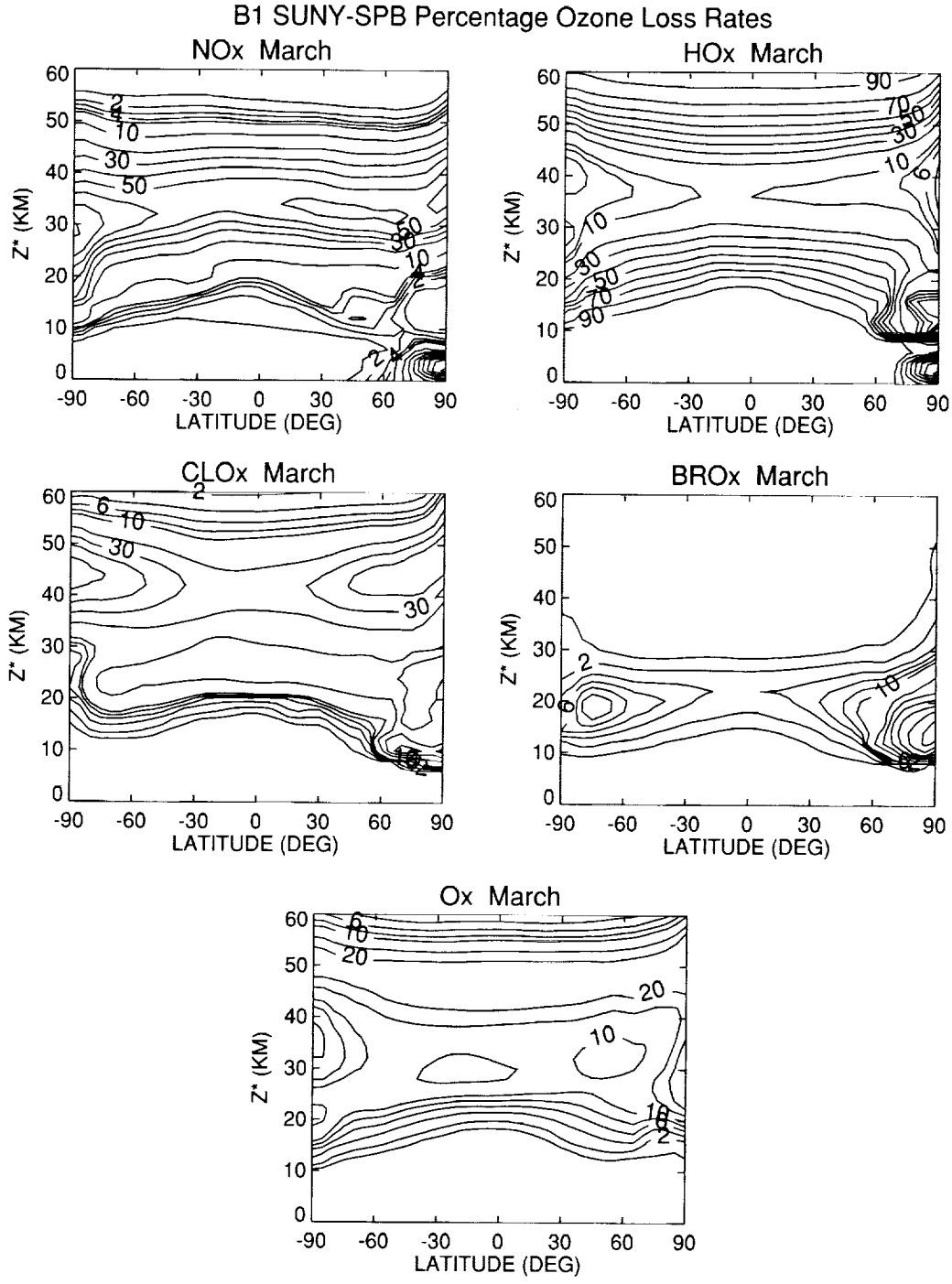

Figure 5.3.1g Continued.

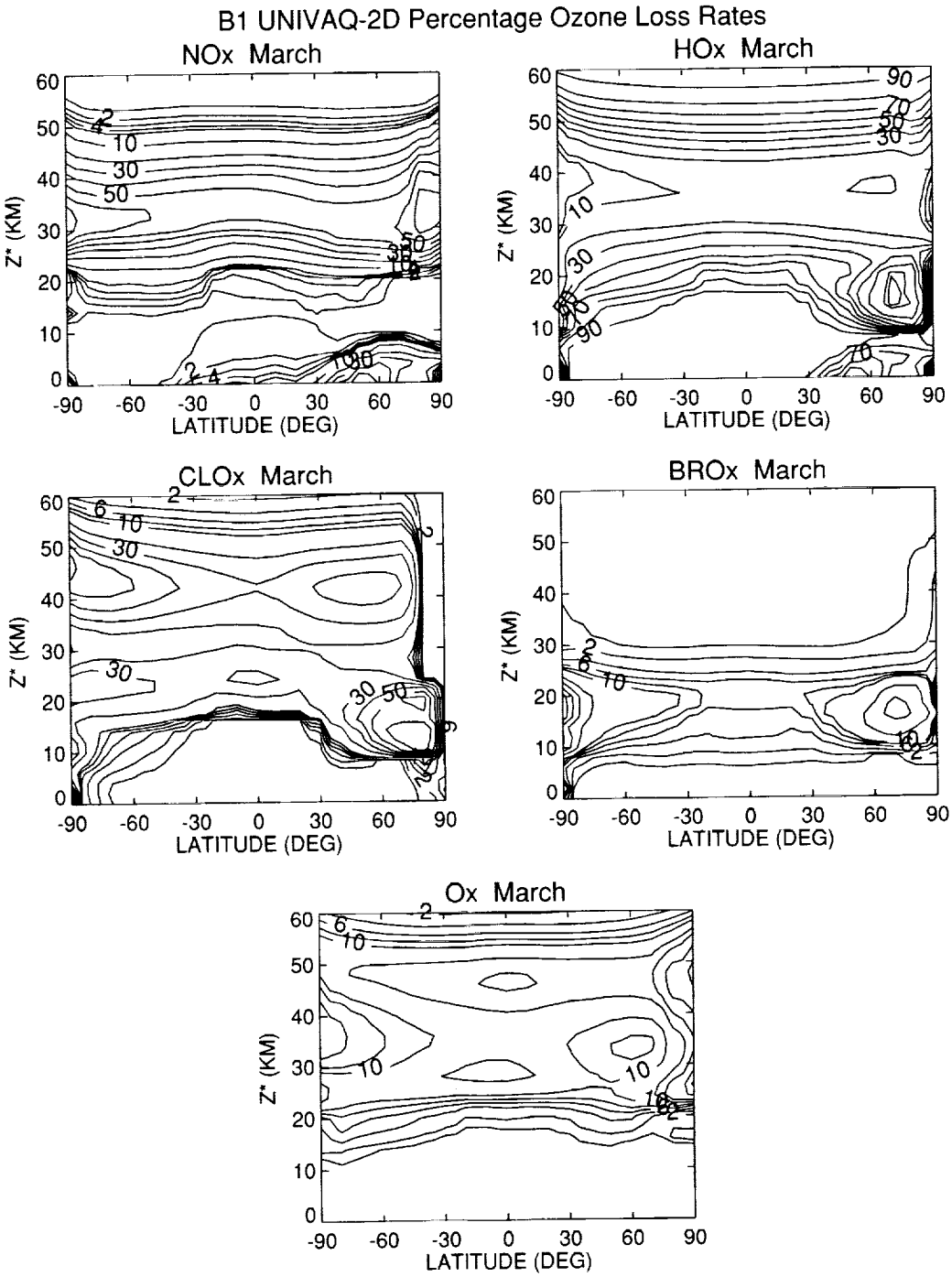

Figure 5.3.1g Concluded.

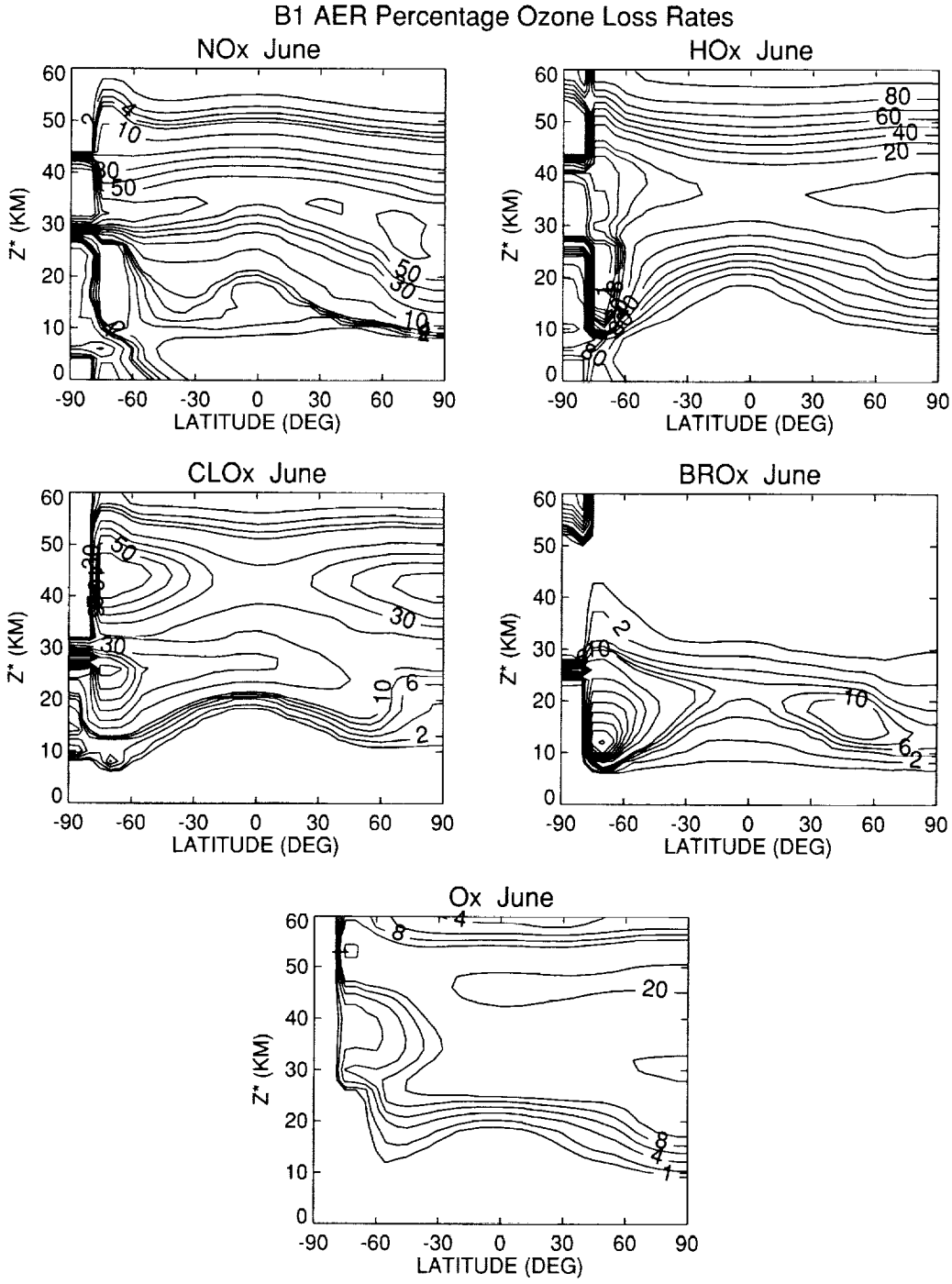

Figure 5.3.2a Ozone losses (in percent) due to the five families, L(NOx), L(HOx), L(ClOx), L(BrOx), and L(Ox) computed for June 1992 from the AER, GSFC-2D, HARVARD, LARC-3D, LLNL, SUNY_SPB, and UNIVAQ-2D models.

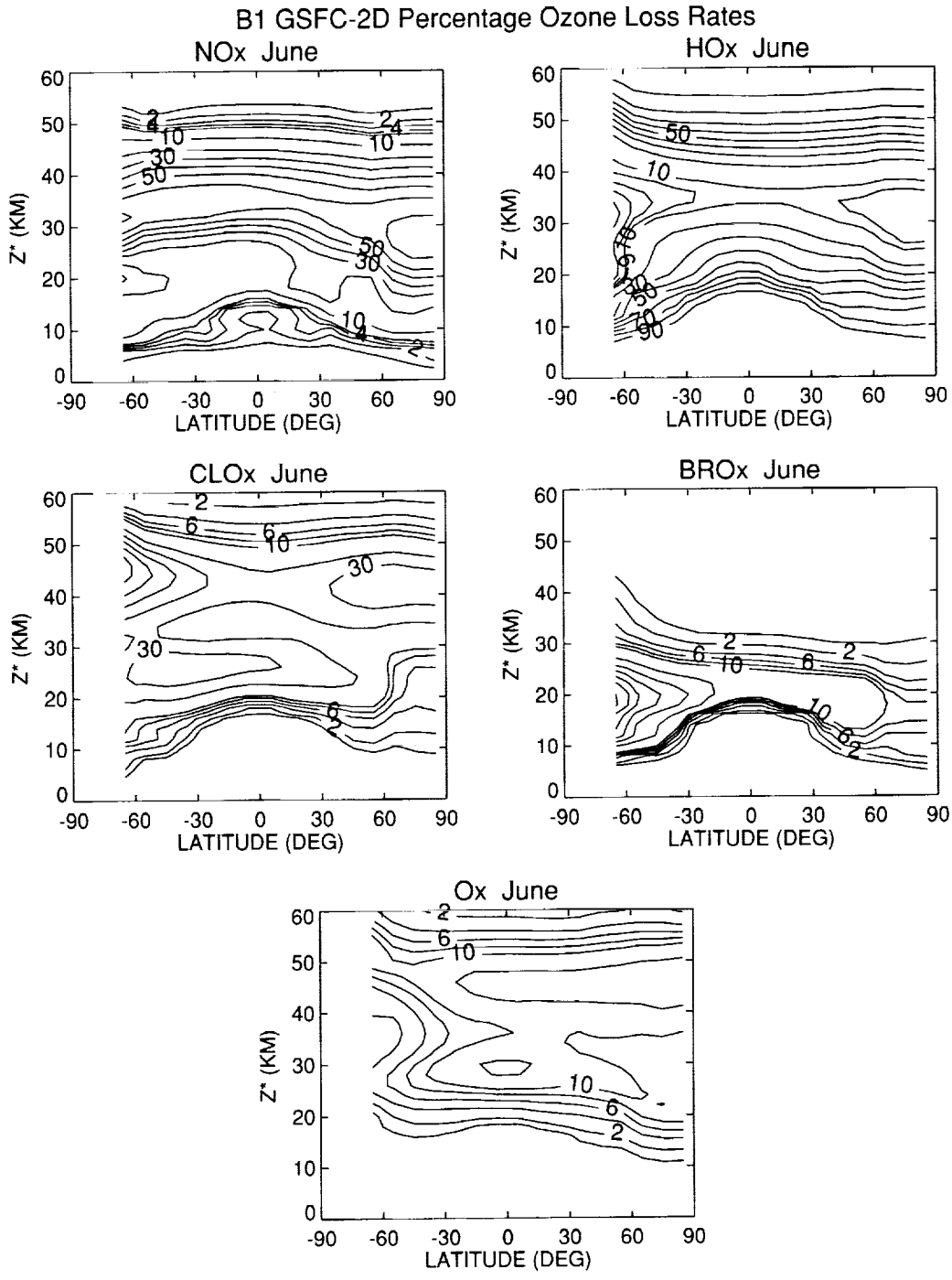

Figure 5.3.2b Continued.

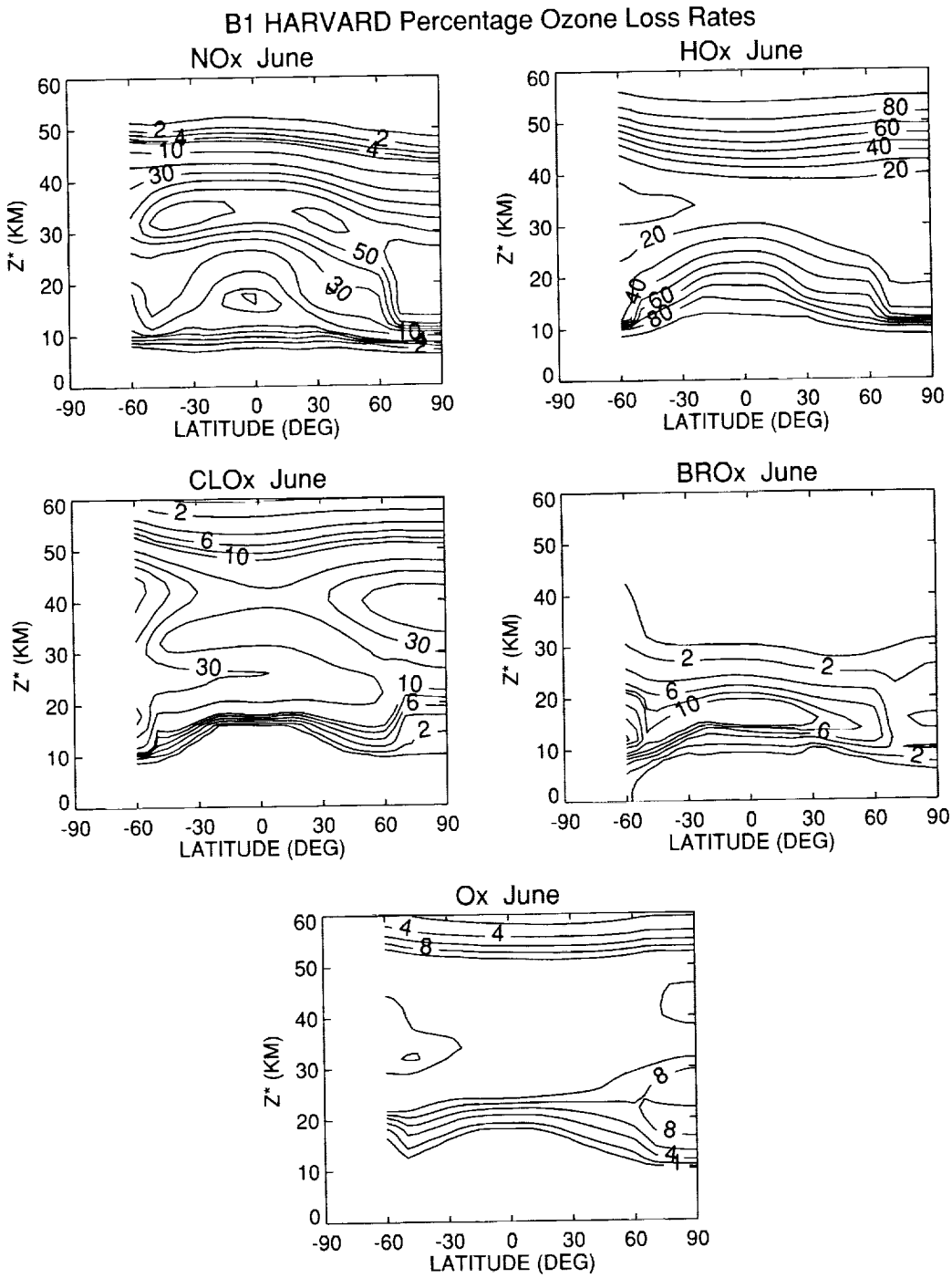

Figure 5.3.2c Continued.

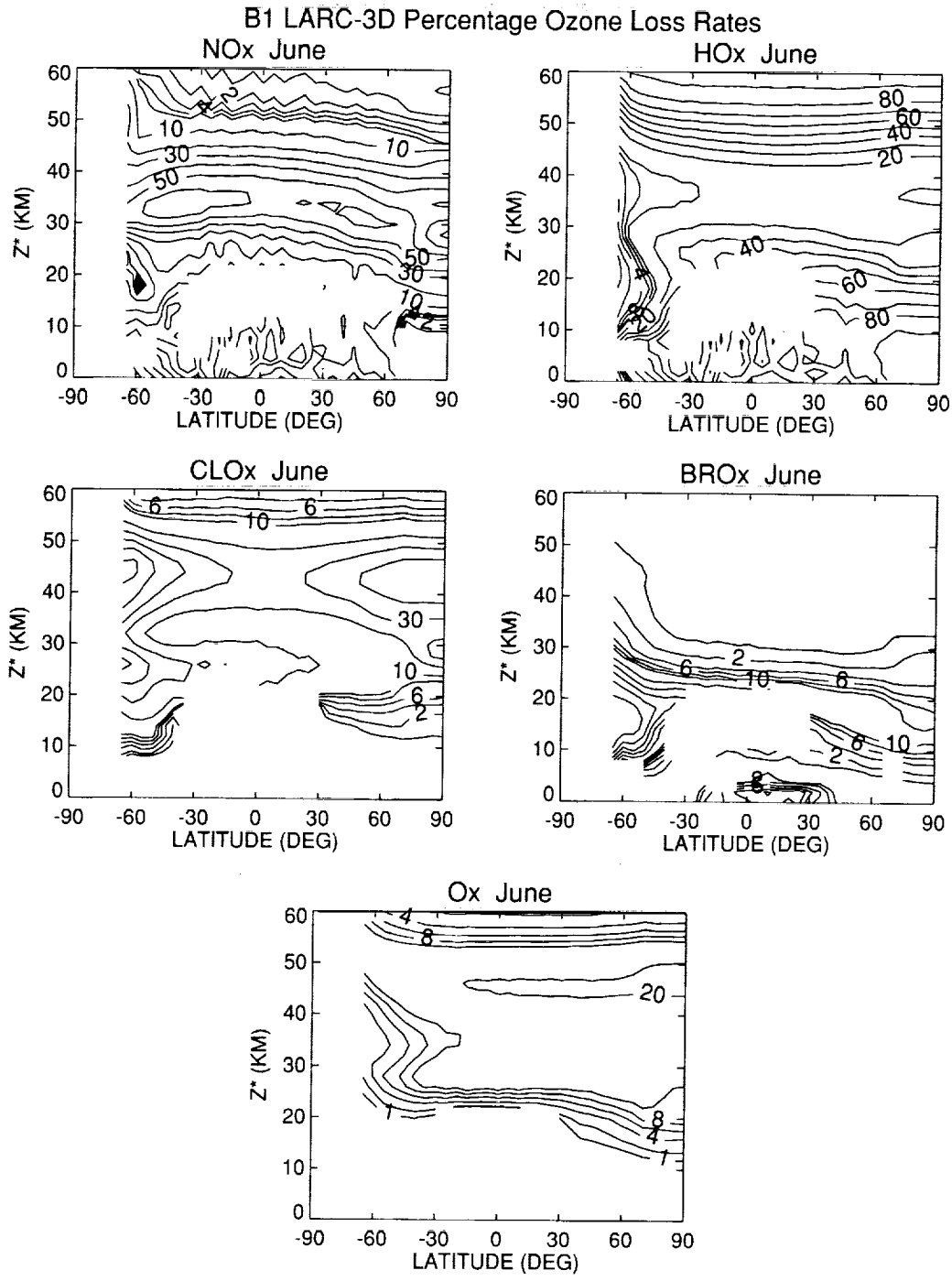

Figure 5.3.2d Continued.

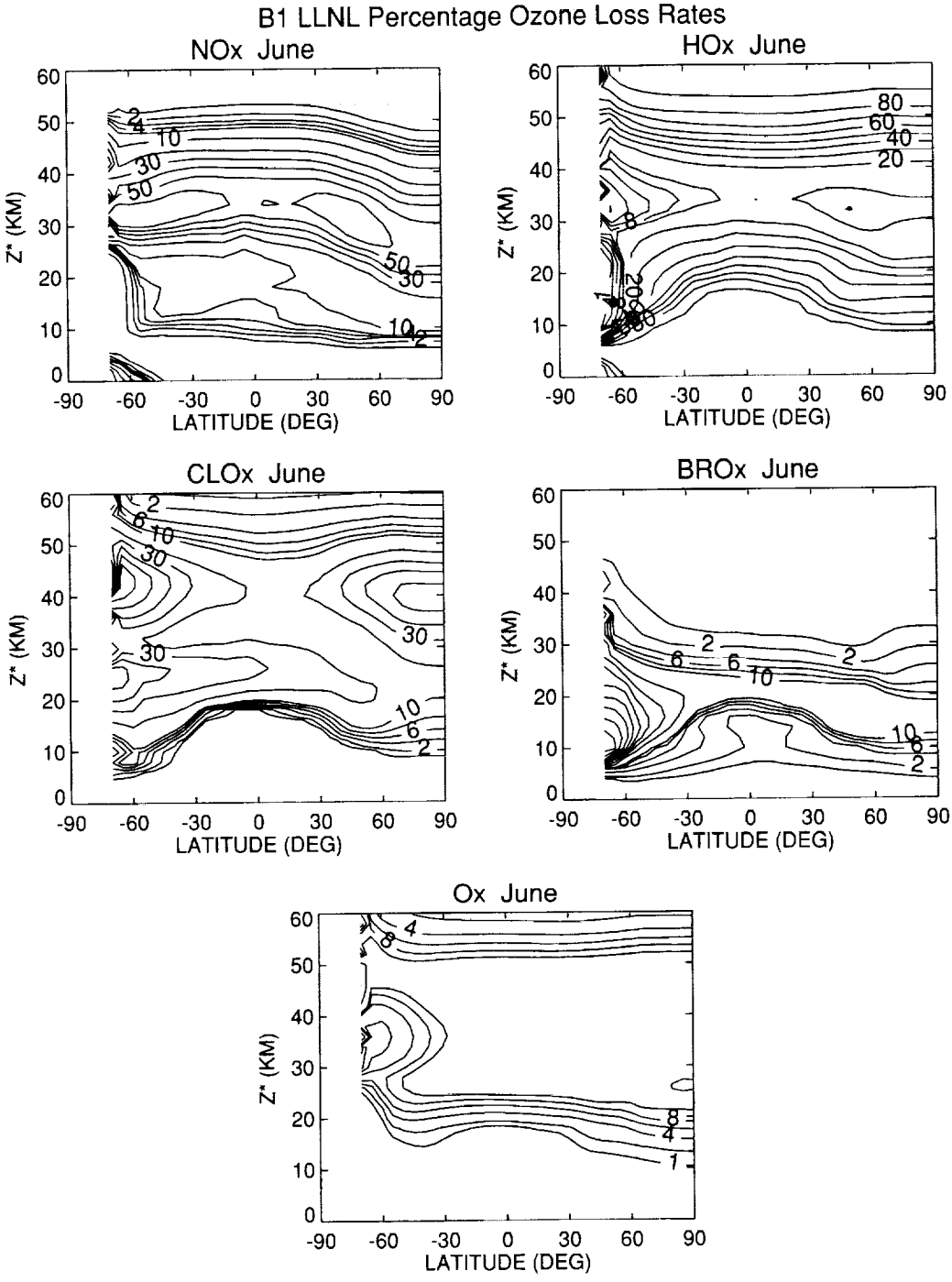

Figure 5.3.2e Continued.

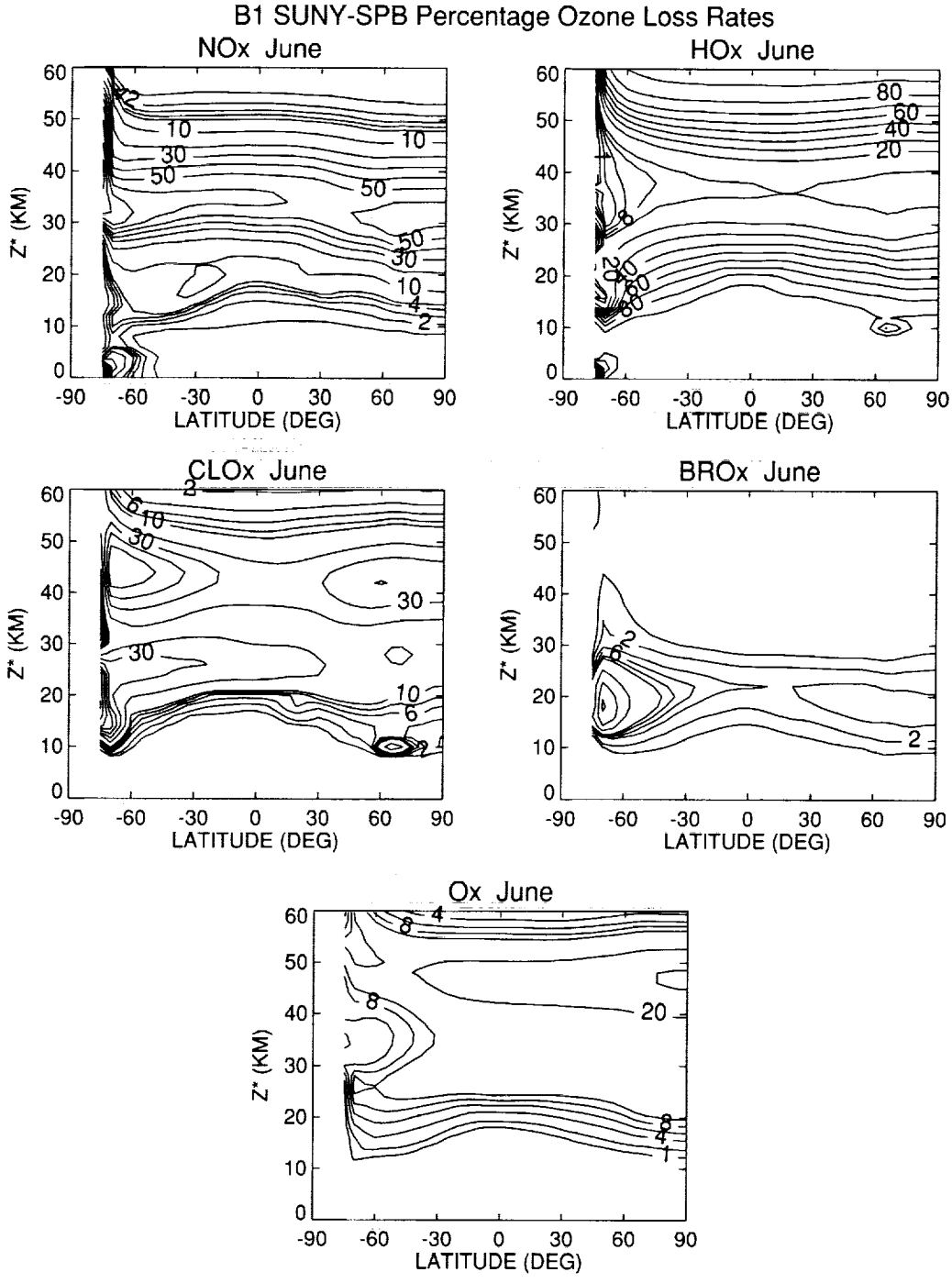

Figure 5.3.2f Continued.

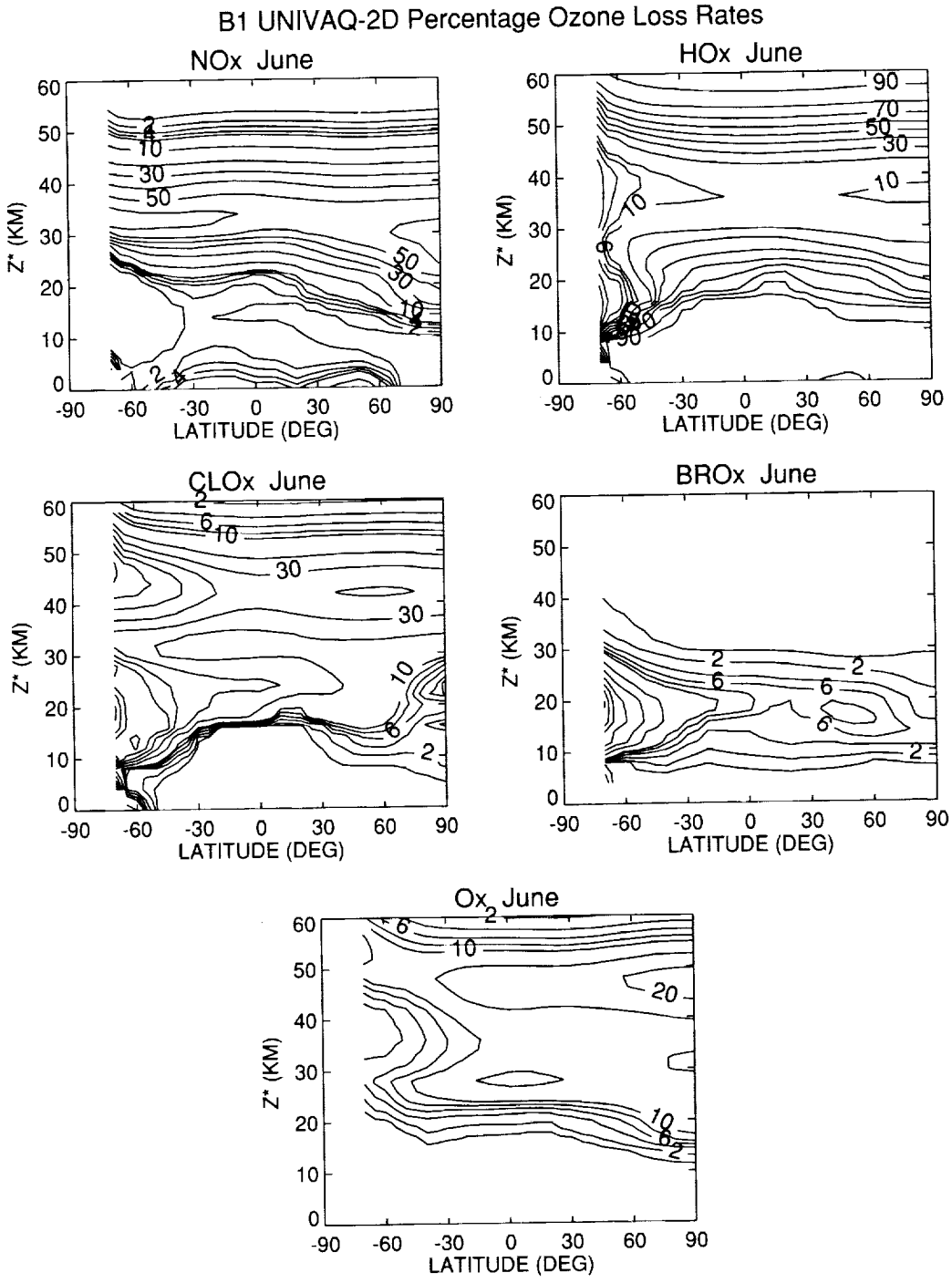

Figure 5.3.2g Concluded.

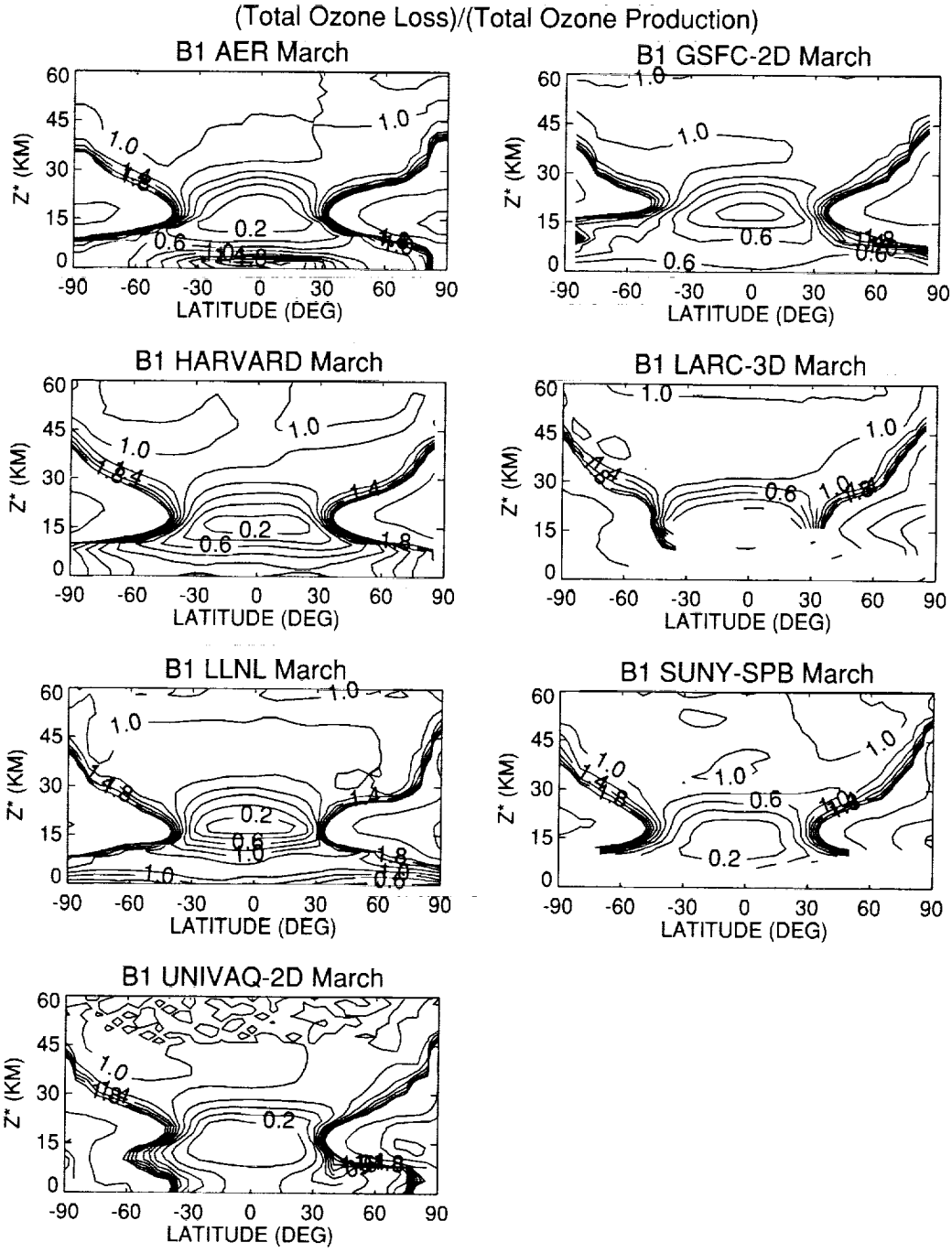

Figure 5.3.3. The ratio of total ozone loss [L(tot)] to total ozone production [P(tot)] computed for March 1992 from the AER, GSFC-2D, HARVARD, LARC-3D, LLNL, SUNY_SPB, and UNIVAQ-2D models.

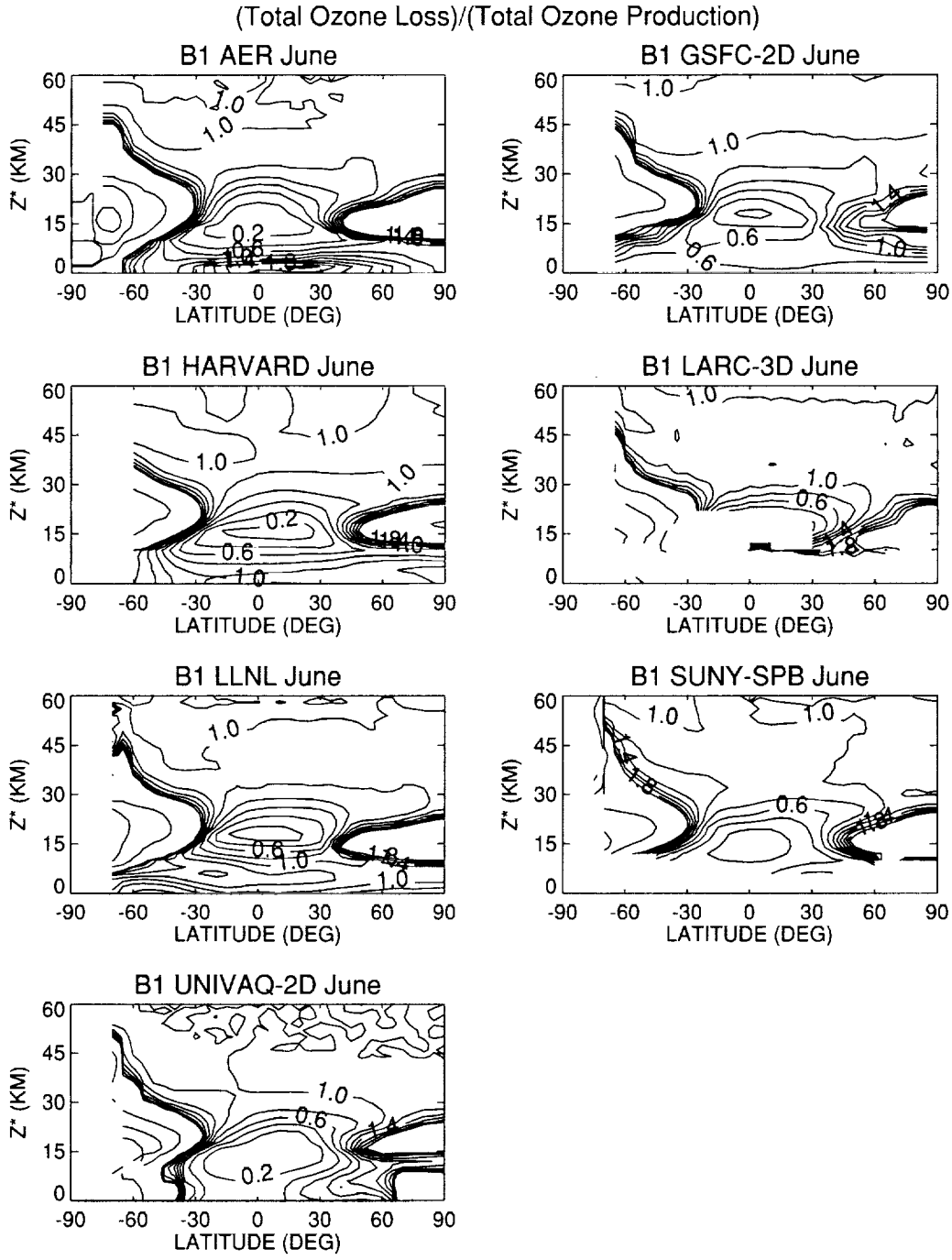

Figure 5.3.4. The ratio of total ozone loss [L(tot)] to total ozone production [P(tot)] computed for June 1992 from the AER, GSFC-2D, HARVARD, LARC-3D, LLNL, SUNY_SPB, and UNIVAQ-2D models.

5.4 Fixed Ozone Production and Loss

Charles H. Jackman,[1] Eric L. Fleming,[1] and Malcolm K. W. Ko[2]

1. NASA Goddard Space Flight Center
2. Atmospheric and Environmental Research, Inc.

The total photochemical production and loss terms for ozone were provided to the modellers for B-3 from the AER model. The only output for this model experiment was ozone. Since the chemistry for ozone was prescribed, this experiment highlighted the transport differences among the models. Seven models (AER, GSFC-2D, HARVARD, LLNL, SUNY_SPB, UNIVAQ-2D, UNIVAQ-3D) submitted model output for run B-3.

If each model had the same winds, diffusion, and numerical transport scheme as AER, then each model's ozone prediction would be the same. It was no surprise that there were large differences in predictions of total ozone among the models for this experiment. The total ozone predicted for runs B-3 and B-1 are presented in Figure 5.4.1(a-c) for all models. The TOMS (1988-92) average values are also shown for comparison.

The total ozone from each model for run B-3 was generally more similar to that particular model's total ozone prediction for run B-1 than the AER total ozone prediction for run B-3. For example, the LLNL total ozone predictions for runs B-1 and B-3 (see Figure 5.4.1b) were more similar than the LLNL and AER total ozone predictions for run B-3 (see Figures 5.4.1a and 5.4.1b). There were, however, differences between the total ozone predicted in runs B-1 and B-3 for a particular model, especially in the southern polar latitudes. As an example, the LLNL predicts much more total ozone in the southern polar latitudes for the spring period in run B-3 than in run B-1 (about 340 DU versus 160 DU). The LLNL photochemical ozone loss in this time period must be much larger than that predicted from the AER model. A similar difference is noted for the GSFC-2D model.

The total ozone from the various models for March and June is presented in Figure 5.4.2(a-b) for runs B-3 and B-1. The amount of ozone predicted in the tropics for run B-3 is related to the speed of transport through the lower stratosphere. The HARVARD model predicts a relatively large amount of ozone in the tropics, the SUNY_SPB and GSFC-2D models predict a lesser amount of tropical ozone than the HARVARD model, and the other models (AER, LLNL, UNIVAQ-2D, and UNIVAQ-3D) predict even less ozone in the tropics. The HARVARD model most likely has a much slower tropical upward advection than the other models. The SUNY_SPB and GSFC-2D models likely have a slower advection than all the other models except the HARVARD model.

A check on the conclusion about the HARVARD model having the slowest tropical upward advection of all the models can be made by looking at Figure 5.3.3. This figure shows the L/P values for March from a full chemistry run. The production of ozone (P) is probably very similar among all models as it depends only on the photodissociation of O_2 (as defined for the C-4 analysis). The primary difference among the models for L/P should be related to the total loss of ozone (L). A very slow tropical circulation would promote a larger ozone loss rate in the lower stratosphere as the radicals prominent in ozone loss would build up to larger amounts in this region than in a model with a stronger ciculation. Thus tropical lower stratosphere L/P values for the HARVARD model should be smaller than L/P values in other models and they generally are (see Figure 5.3.3).

The changes in total ozone from one month to the next also point out certain details of model differences. Figure 5.4.3(a-c) shows model changes for three of these periods (March-February; July-June;

and September-August) for runs B-3 and B-1. The GSFC-2D model shows a large negative difference in the south polar region for run B-3 (March-February) that is not present for run B-1. Such a structure in B-3 probably means that a) the AER model provided ozone loss is larger compared with the production than in the GSFC-2D model, and/or b) the GSFC-2D model has some ozone loss in that region due to transport.

The AER model shows a larger negative ozone change in the northern middle latitudes for both runs B-3 and B-1 (July-June) compared to all other models. The UNIVAQ-2D model shows the largest negative ozone change in the northern polar latitudes for both runs B-3 and B-1. The SUNY_SPB model indicates a negative change in ozone in the southern polar region for this time period in both runs B-3 and B-1, whereas all the other models (except LLNL over the 60S to 70S region) show positive changes in ozone.

The differences in the spring southern polar latitudes for the LLNL and GSFC-2D models noted above in Figure 5.4.1(a-c) are very apparent in this Figure 5.4.3(a-c). Both models show only modest negative changes in run B-3 (September-August), whereas they show huge negative changes in run B-1. Since the AER model shows about the largest negative changes in run B-3, it appears that the AER model transport is a major cause of this ozone decrease. The LLNL model shows an interesting latitudinal structure in the northern middle to polar latitudes, being a negative ozone change between about 30N and 60N and being a positive ozone change from about 60N to the pole in both runs B-3 and B-1.

Figure 5.4.4(a-c) shows a comparison of the models for their ozone column rates of change (in Dobson Units per day) for all latitudes over the months of the year. The TOMS (1988-92) average values are also shown for comparison. The models, at least for run B-1, should show a similar structure to that observed in the TOMS measurements. The AER model does a reasonable job in the northern hemisphere, however, the recovery of ozone after the "Antarctic ozone hole" goes on longer than measured. The HARVARD model has problems in representing the depth of the "Antarctic ozone hole," both in runs B-3 and B-1. The HARVARD model does not have polar stratospheric cloud chemistry, thus is not expected to predict an "Antarctic ozone hole" in run B-1. The LLNL model for run B-1 shows more structure in the negative and postive ozone "rate of change" fields than indicated in the measurements. The LLNL, SUNY_SPB, and UNIVAQ-2D models (like the AER model) all show the recovery of ozone after the "Antarctic ozone hole" going on longer than measured. The SUNY_SPB, UNIVAQ-2D, and UNIVAQ-3D models show differences compared to the measurements in the tropical latitudes.

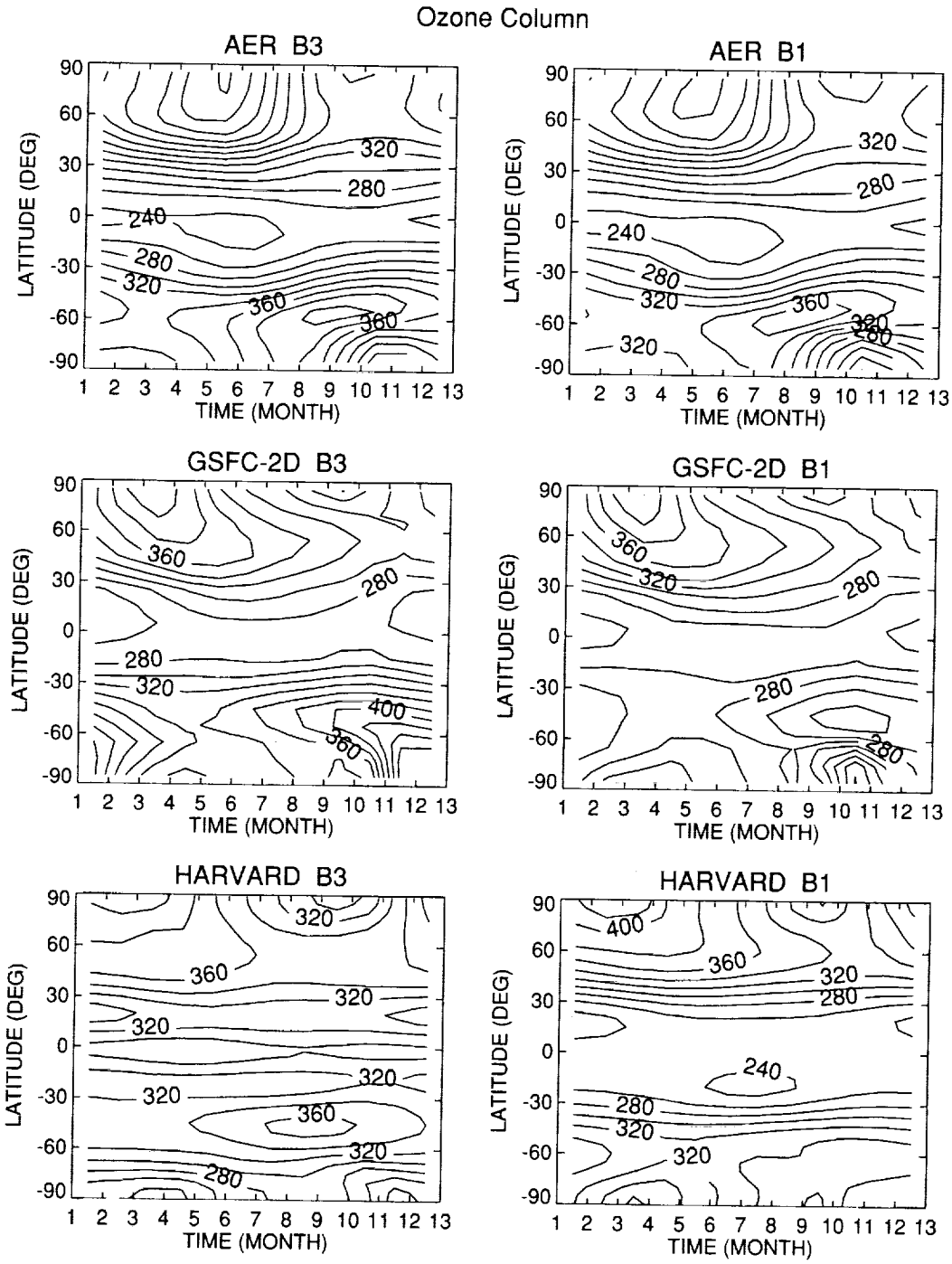

Figure 5.4.1a Ozone column (in Dobson Units) for runs B-3 and B-1 as a function of latitude and time for year 1992 from the AER, GSFC-2D, HARVARD, LLNL, SUNY_SPB, UNIVAQ-2D, and UNIVAQ-3D models. The TOMS (1988-92) average values are also shown for comparison.

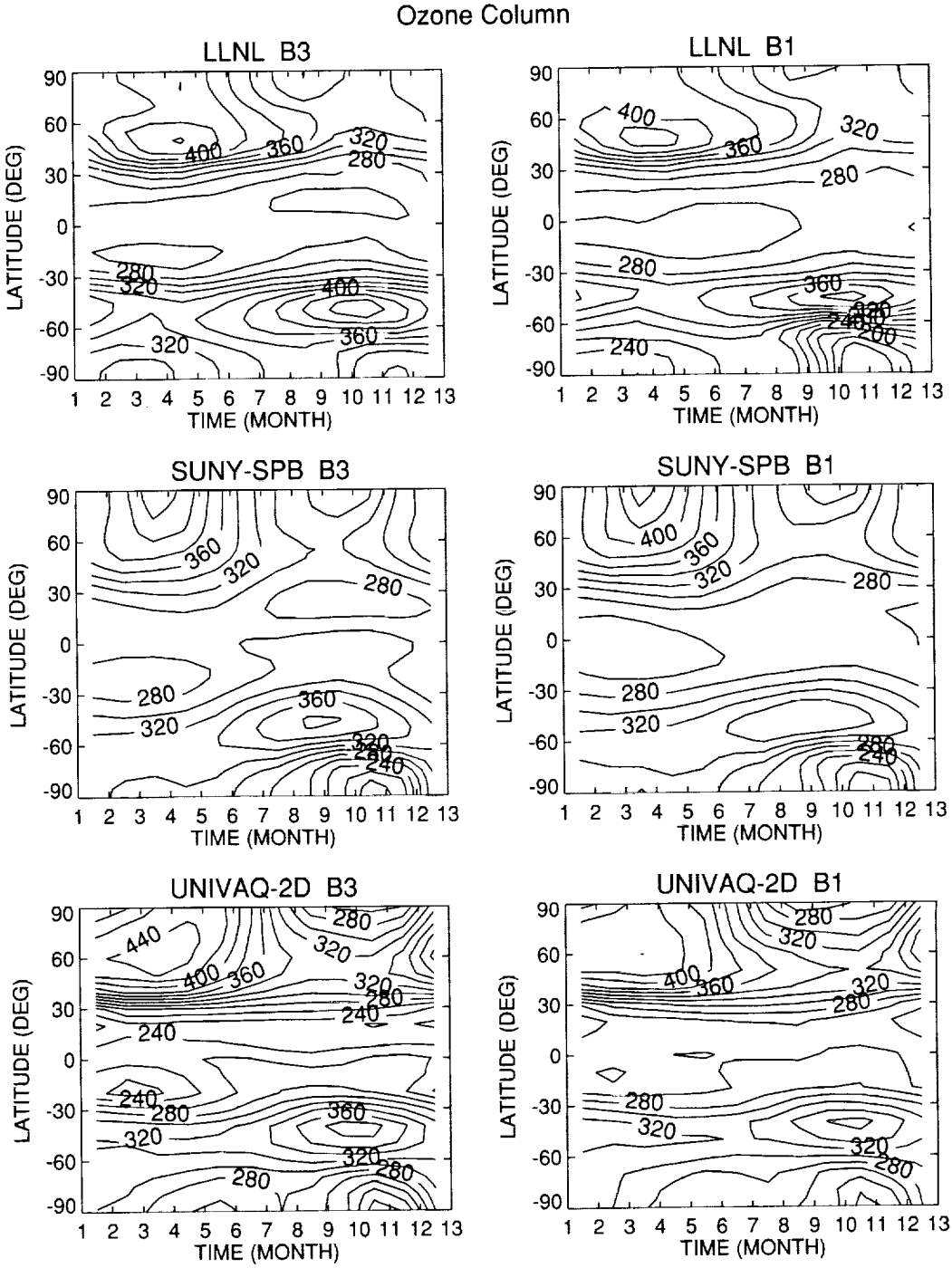

Figure 5.4.1b Continued.

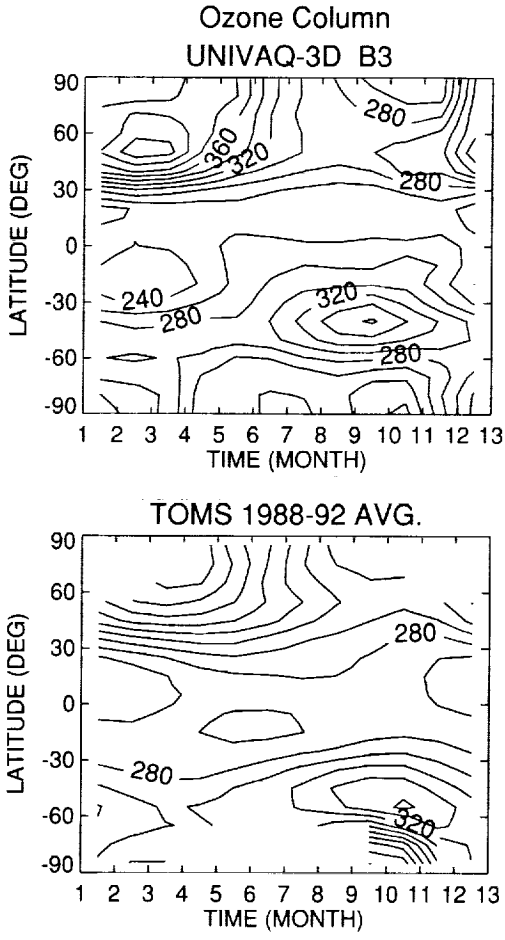

Figure 5.4.1c Concluded.

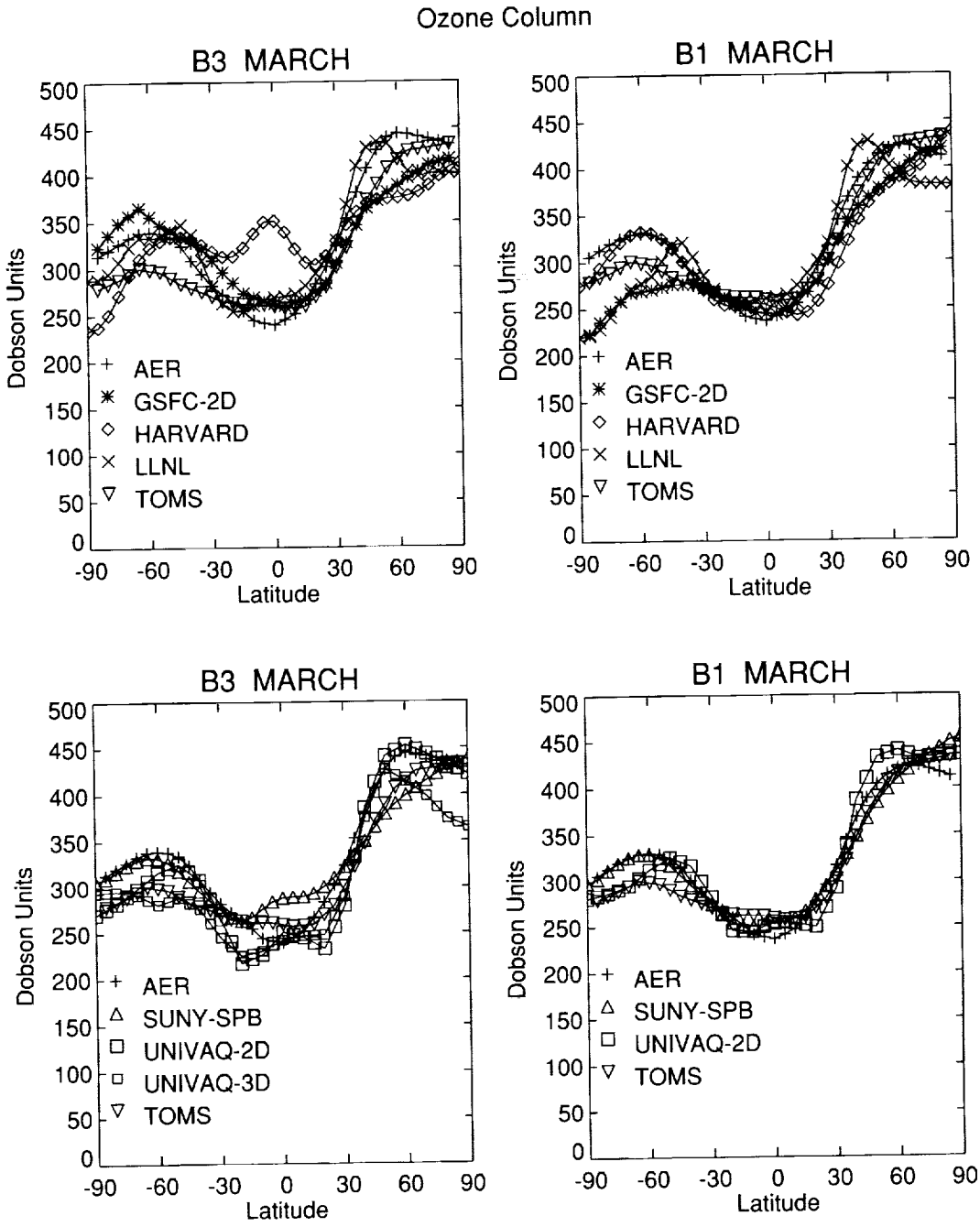

Figure 5.4.2a Ozone column (in Dobson Units) for runs B-3 and B-1 for March and June of 1992 as a function of latitude from the AER, GSFC-2D, HARVARD, LLNL, SUNY_SPB, UNIVAQ-2D, and UNIVAQ-3D models. The TOMS (1988-92) average values are also shown for comparison.

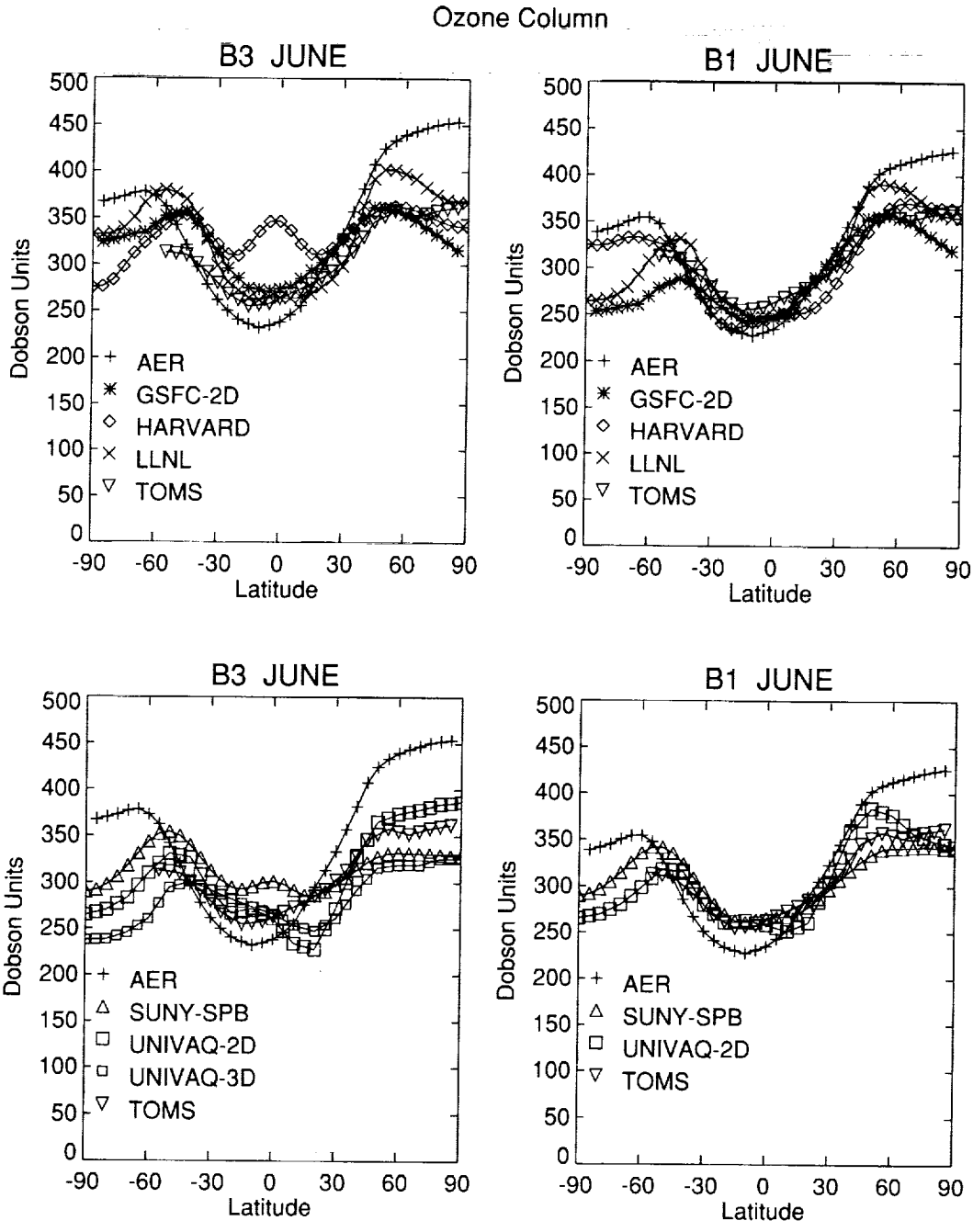

Figure 5.4.2b Concluded.

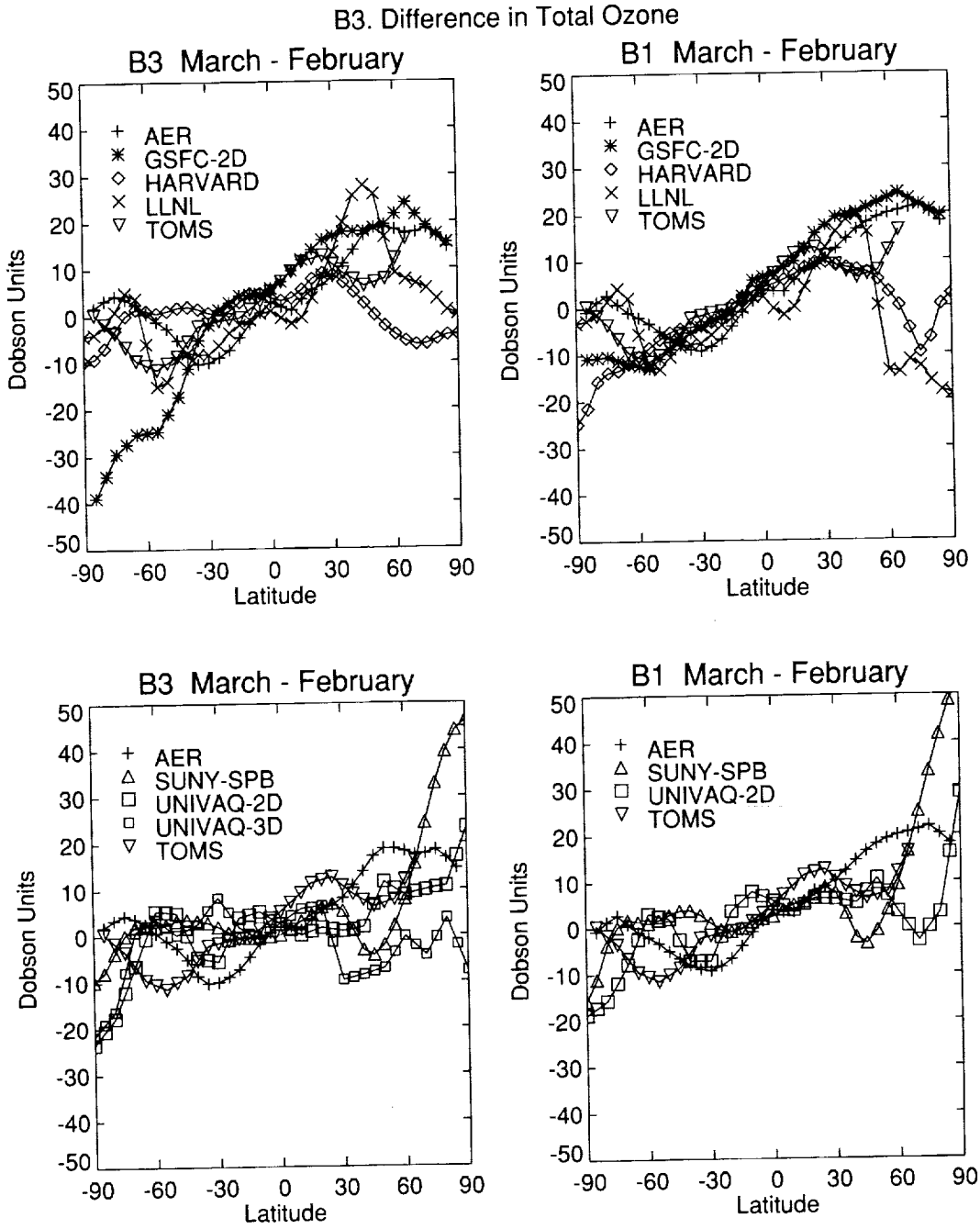

Figure 5.4.3a Difference in total ozone (in Dobson Units) for runs B-3 and B-1 for three periods (March-February; July-June; and September-August) in 1992 as a function of latitude from the AER, GSFC-2D, HARVARD, LLNL, SUNY_SPB, UNIVAQ-2D, and UNIVAQ-3D models. The TOMS (1988-92) average values are also shown for comparison.

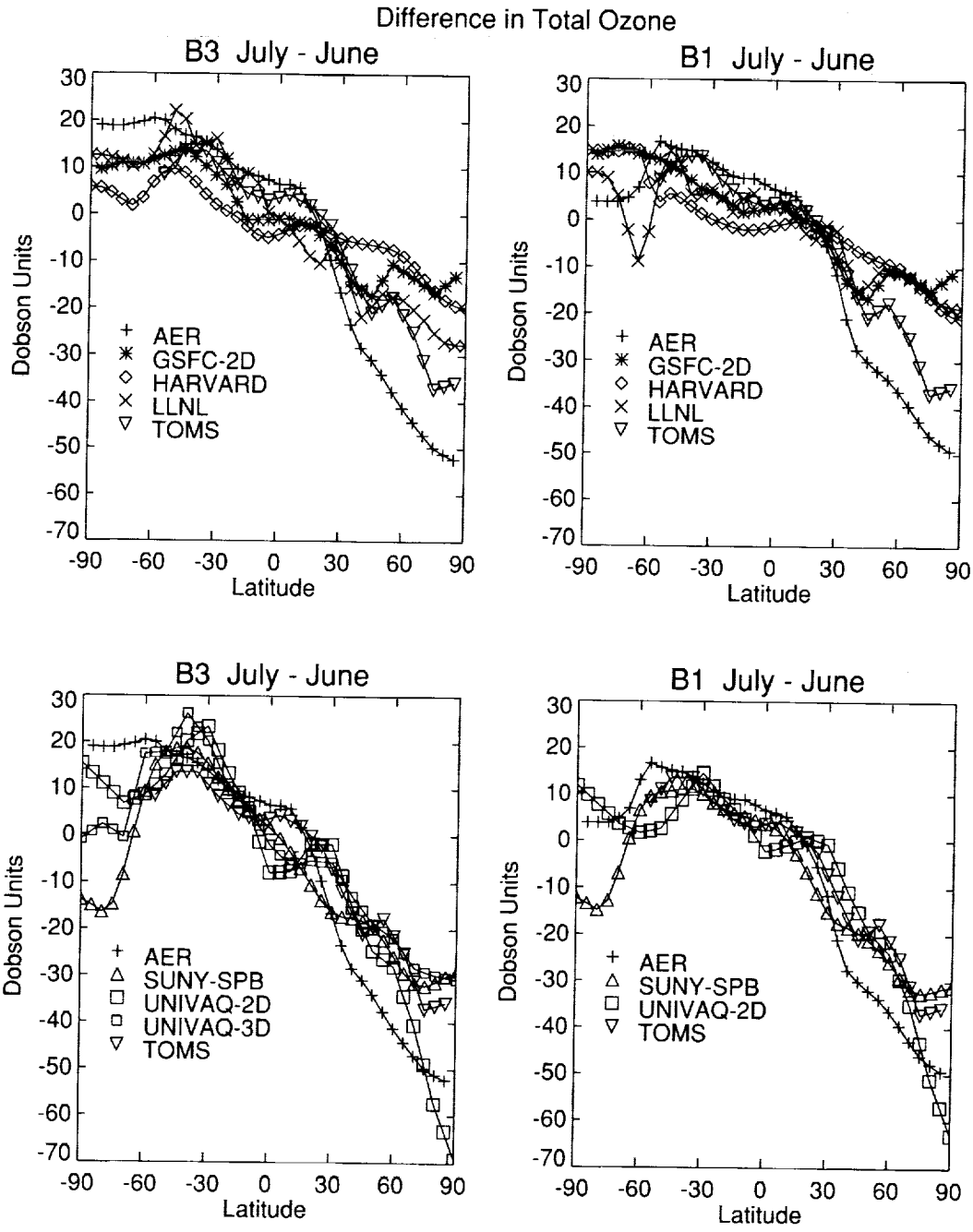

Figure 5.4.3b Continued.

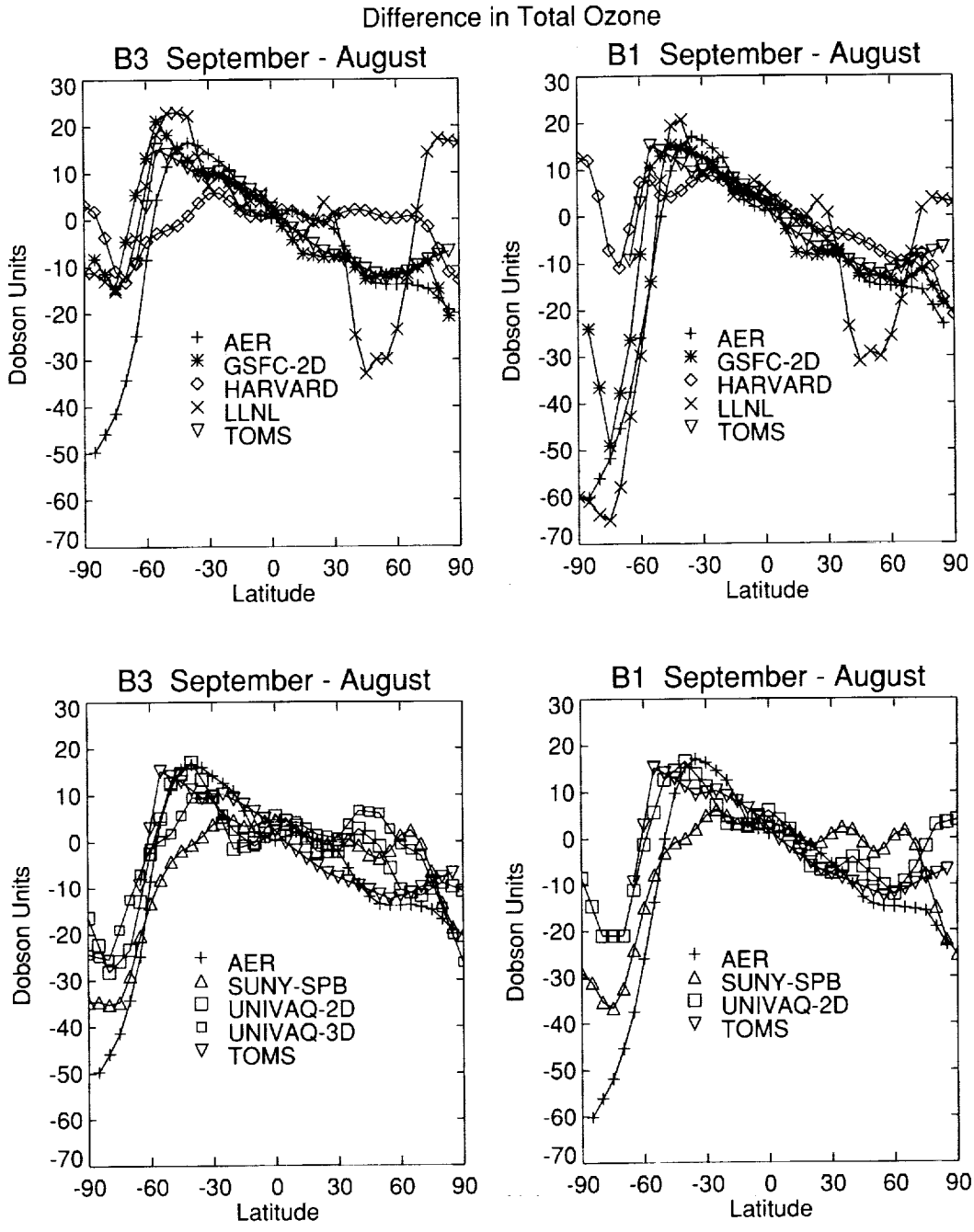

Figure 5.4.3c Concluded.

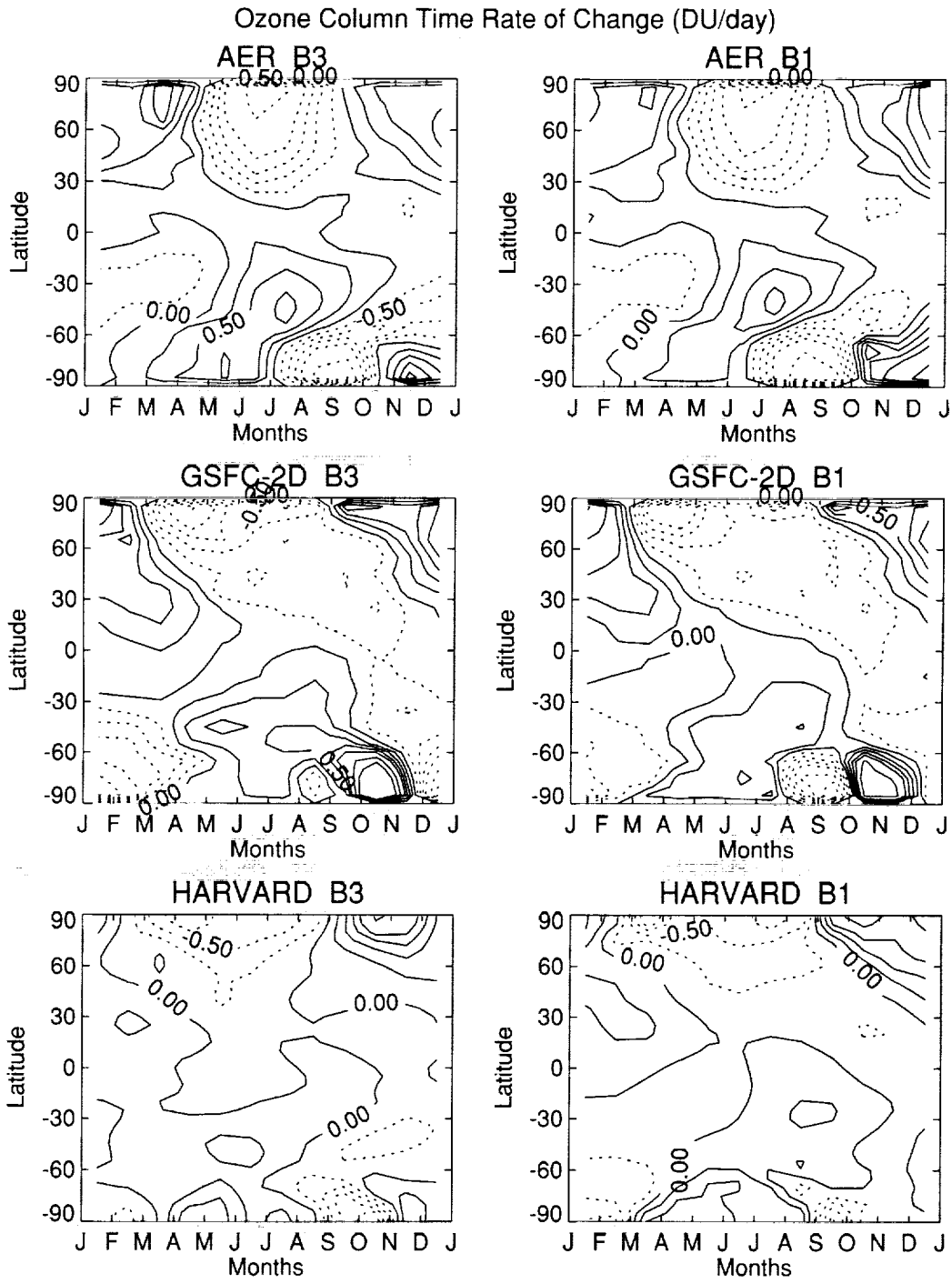

Figure 5.4.4a Column ozone time rate of change (in Dobson Units/day) for runs B-3 and B-1 for 1992 as a function of latitude and time from the AER, GSFC-2D, HARVARD, LLNL, SUNY_SPB, UNIVAQ-2D, and UNIVAQ-3D models. The TOMS (1988-92) average values are also shown for comparison.

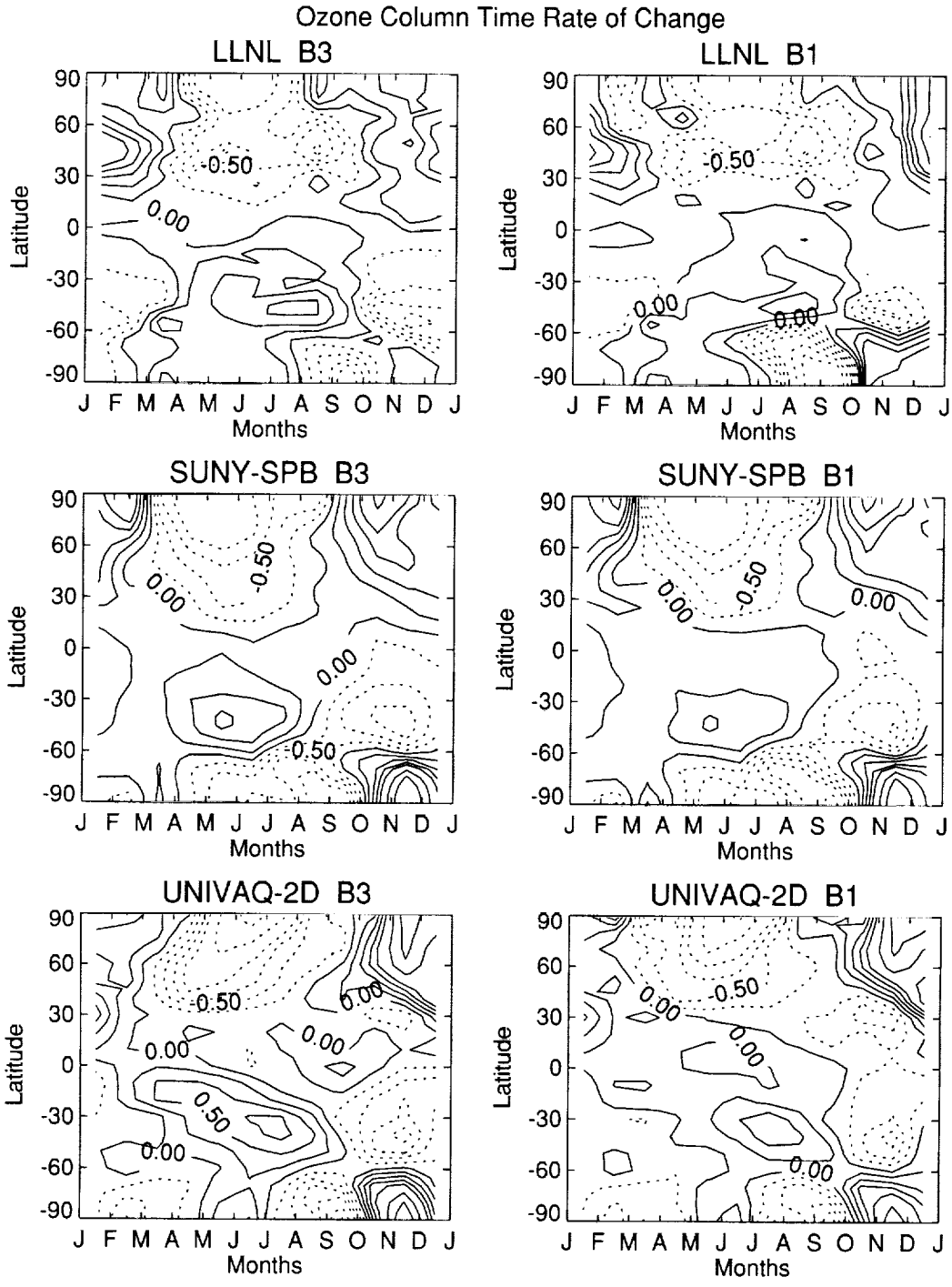

Figure 5.4.4b Continued.

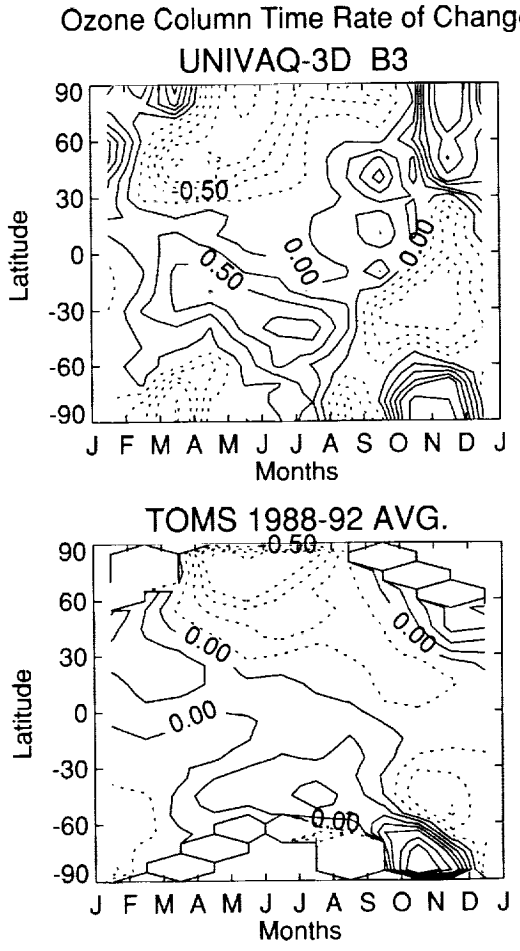

Figure 5.4.4c Concluded.

5.5 Signatures of High Latitude Dynamical Processes and Denitrification

David B. Considine

University of Maryland

5.5.1 Introduction

In order to have confidence in a model prediction of the response of atmospheric O_3 concentrations to a perturbation it is necessary but not sufficient that the model reproduce reasonably well observed O_3 concentrations. If the model happens to get O_3 concentrations about right for the wrong reasons it is unlikely that its response to a perturbation will resemble that of the atmosphere. It is thus important to also determine that the processes regulating model O_3 concentrations are similar to those in the atmosphere.

Polar dynamical processes are difficult to represent in both 2D and 3D models. Wobbling of the polar winter vortex smooths zonal mean gradients of long-lived tracers without any transport across the vortex edge. A 2D model may therefore overestimate the cross-vortex transport of material because vortex wobbling is represented in the model by diffusion, which produces irreversible mixing. In 3D models the amount of wintertime descent and the polar temperatures depend sensitively on planetary and gravity wave dissipation, which can be too weak or in the wrong location.

In this section we primarily examine the degree to which model representations of polar dynamical processes result in adequate simulations of observed atmospheric constituents. Because a direct inter-model comparison of these processes would be very difficult due to differences in model formulation, we look instead for the signature of the processes of interest in the model constituents, emphasizing N_2O distributions. This enables comparison with observations and allows us to ignore the model formulation details. In addition to N_2O distributions we intercompare model Cly with values inferred from atmospheric observations. Without an adequate simulation of Cly a model has no hope of correctly simulating atmospheric O_3 concentrations or its response to a perturbation. We also evaluate the models' ability to reproduce observed HNO_3 concentrations. HNO_3 strongly influences the rate at which O_3 recovers from PSC-induced depletion, so its correct simulation in a model is critical. It is controlled both by dynamical processes and high latitude denitrification from PSCs.

Below we compare the run B-1 model simulations from 8 2D models and 4 3D models. The 2D models submitting B-1 run results are those from the Goddard Space Flight Center (GSFC-2D), the Lawrence Livermore National Laboratory (LLNL), the National Oceanographic and Atmospheric Administration - National Center for Atmospheric Research (NOCAR), the Universita degli Studi, L'Aquila (UNIVAQ-2D), the State University of New York (SUNY-SPB), Atmospheric and Environmental Research, Inc. (AER), Harvard University (HARVARD), and CSIRO. The 3D models submitting B-1 run results are those from GSFC (GSFC-3D), the University of Cambridge (SLIMCAT), and the NASA Langley Research Center (LARC-3D). It should be noted that neither the HARVARD nor the CSIRO models include polar heterogeneous chemical reactions so only their representation of polar dynamics will be considered. We also present N_2O results from the Goddard Institute for Space Studies (GISS8×10) model, which were made for run A-5.

The B-1 run is described in Chapter 1. Briefly, the run was each modeling group's best simulation of 1992. The year was chosen so that observations made by the CLAES instrument on the upper

atmosphere research satellite could be used. Observed zonally averaged temperatures from MLS and surface area density distributions derived from SAGE II satellite observations were provided to each modeling group, but there was no requirement that the groups use these data. Each modeling group included their own parameterization of polar heterogeneous processes.

5.5.2 Vortex and Tropical Boundaries

The wintertime stratosphere is characterized by strong planetary wave dissipation at midlatitudes driving a residual circulation consisting of ascent in the tropics, transport toward the winter pole at high altitudes above the planetary wave dissipation region, and descent at high latitudes over the winter pole. [e.g., Eluszkiewicz et al., 1996; Rosenlof, 1995]. The isopleths of long-lived species such as N_2O reflect this transport pattern [e.g., Bacmeister et al., 1995]. Tropical, midlatitude, and polar regions with relatively weak internal gradients are separated from each other by stronger gradients. This occurs because the time scales for mixing between the regions are longer than the timescales of the processes which establish the tracer values typical for each region. Strong tracer gradients can therefore be used to identify the boundaries of these dynamically distinct regions [Nakamura and Ma, 1997].

The absolute value of the first derivative of a long-lived tracer distribution such as CLAES N_2O [Roche et al., 1996] will have peaks where the gradients are the strongest. It should be easy to identify the tropical and polar boundaries in the atmosphere or a model by plotting the first derivative of a long-lived tracer. Figure 5.5.1 is a six-panel plot of the absolute value of the first derivative with respect to latitude of 1992 CLAES version 8 N_2O at 21.5, 27, and 32 km (46.4, 21.5, and 10.0 mbars, respectively). The left-hand side of the figure shows plots of the northern hemisphere N_2O gradients and the right-hand side shows plots of the southern hemisphere gradients. The figure was obtained by zonally averaging all of the available CLAES data for each yaw cycle in 1992, taking the absolute value of the derivative, and then using the north-looking yaws to construct the northern hemisphere plots and the south-looking yaws to construct the southern hemisphere plots. Averaging over entire yaw cycles results in a smooth and fairly low resolution contour plot. Although low resolution, the figure provides a good picture of the seasonal evolution of the tropical and vortex barriers throughout the lower stratosphere.

Figure 5.5.1 shows that at 21.5 km the northern hemisphere vortex sets up in December at about 70 degrees North. Peak gradients in N_2O move south through January and February to about 60 degrees North. The vortex structure weakens in March and April. There is a weaker but definite tropical barrier centered at about 22 degrees North which is strongest in January and February. Between the vortex and tropical boundaries there is a region of relatively weak N_2O gradients which has been identified as the "surf zone," where planetary wave breaking, dissipation, and mixing is strongest [McIntyre and Palmer, 1984]. The tropical barrier moves north in March, and by the end of April the vortex and tropical barriers have merged. The summer is thus characterized only by a high latitude and a low latitude region, with one transport barrier between them. This single structure persists until the end of October, at which time distinct tropical and vortex edges begin to reform.

The two remaining northern hemisphere plots in Figure 5.5.1 show the evolution of the N_2O gradients at 27 and 32 km. At 27 km there is a more pronounced northern hemisphere vortex than at 21.5 km, but at 32 km the plot shows a considerably weakened vortex. The gradients defining the boundary between the tropics and midlatitudes increase in both the 27 km and the 32 km plots.

The right-hand side of Figure 5.5.1 shows the time evolution of the N_2O gradients in the southern hemisphere. At 21.5 km the boundary between the tropics and midlatitudes is more persistent than in the northern hemisphere. The gradients defining the boundary between the southern hemisphere polar

vortex and midlatitudes are also somewhat different from the northern hemisphere. At higher altitudes the gradients are stronger earlier in the year. Also, at both 27 km and 32 km the peak values of the N_2O gradients are smaller than at 21.5 km.

Because the potential vorticity but not the latitude of an air parcel is conserved in the absence of mixing processes, a parcel's potential vorticity is a better indicator of its tropical, midlatitude, or polar identity than its latitude. Since only the latitude is considered when it is included in a zonal mean, parcels with tracer concentrations characteristic of dynamically different regions can be averaged over. The zonal mean therefore artificially "mixes" these regions, resulting in weakened meridional tracer gradients.

A meridional coordinate which explicitly accounts for potential vorticity conservation would therefore be more appropriate than latitude for separating these regions and quantifying the actual rate of mixing between them. Equivalent latitude is such a meridional coordinate. The equivalent latitude characterizing a parcel of air can be defined as the latitude bounding a circle of area A centered over the pole, where A is the area enclosed by the potential vorticity contour intersecting the parcel in question [Nash et al., 1996]. Averaging tracer observations along lines of constant equivalent latitude produces a 2 dimensional picture of the atmosphere similar to the zonal mean but with meridional gradients that are more characteristic of the actual amount of mixing between air masses.

Figure 5.5.2 shows CLAES N_2O gradients as a function of equivalent latitude in the northern and southern hemispheres at 21.5 km, 27 km, and 32 km. Note that the contouring of this plot is more widely spaced than in Figure 5.5.1 to avoid too tight contours. The equivalent latitude N_2O gradients characterizing the northern hemisphere boundary between the winter polar vortex and the midlatitudes are the most different from the zonal mean gradients shown in Figure 5.5.1. Peak gradients have approximately doubled and the location of the gradient varies less in equivalent latitude than in latitude. The gradients defining the edge of the tropics are somewhat weaker than the zonal mean N_2O gradients at this location. The southern hemisphere polar vortex boundary is very similar in the latitude and equivalent latitude coordinates.

Figure 5.5.2 is probably most appropriate for comparison to atmospheric models. The 2D models participating in this intercomparison are technically zonal mean models, suggesting that Figure 5.5.1 is the correct comparison. However, a zonal mean model reproduces atmospheric zonal mean gradients by irreversible mixing. During times when the atmosphere is zonally asymmetric, zonal means can average over two distinct unmixed regions. This leads to zonal mean gradients which are weaker than the actual gradients separating the two regions. The result is that if a 2D model reproduces the atmospheric zonal mean gradients, the mixing between the two regions will be overestimated. To correctly model atmospheric fluxes under zonally asymmetric conditions it may be necessary to maintain gradients in the 2D models which resemble those in Figure 5.5.2. A zonal mean of a 3D model tracer distribution could average over dynamically distinct regions as is the case with the atmosphere, provided that it reproduces the observed zonal asymmetry. In this situation Figure 5.5.1 would be the more appropriate comparison for 3D models. However, if the 3D model is essentially zonally symmetric, then reproducing the gradients in Figure 5.5.1 would imply an overestimate of the mixing between the two regions similar to the 2D models.

Figures 5.5.1 and 5.5.2 can be compared with N_2O gradients at 22 km, 28 km, and 32 km from the 8 2D and 4 3D models shown in Figure 5.5.3, 5.5.4 and 5.5.5, respectively. The left hand plots in the figures show the northern hemisphere gradients and the right hand plots show the southern hemisphere gradients for each of the models. There is a wide variation in nature of the vortex and tropical boundaries shown in these plots. The LLNL and NOCAR models reproduce the observed N_2O gradients most

convincingly. They both show very strong gradients which sometimes exceed those of the observations, and tropical and vortex boundaries which can be identified fairly easily. These two models tend to place their vortex boundaries equatorward and their tropical boundaries poleward of their observed location. In both hemispheres the model polar vortices set up and decay earlier at higher altitudes, as observed. The GSFC-2D, CSIRO, and LARC-3D models show the development of relatively well-defined and well-placed vortex and tropical boundaries at most altitudes which are generally weaker than is observed. The remainder of the models reproduce the observed tracer gradients less consistently than the above five models. For instance, the SLIMCAT model produces good southern hemisphere vortex gradients which resemble the observations at all altitudes. However, the model northern hemisphere vortex boundary is weak and poleward of its observed location, and it has no well-defined tropical boundaries. The HARVARD model appears to have no northern or southern hemisphere vortices at any altitude. The 3D models tend to have less well-defined tropical boundaries than the 2D models.

Comparing the 3D model output with the CLAES N_2O gradients in Figures 5.5.1 and 5.5.2 may be unfair. The smoothness of the CLAES contour plots results from significant averaging in time. Short time scale dynamical features in the observations have been eliminated in this process. The model outputs to which these data are compared have not been time averaged. This does not much affect the 2D models because they are not designed to reproduce dynamical features on sub seasonal time scales. The 3D models are however, and as a result show more small-scale structure than the smoothed observations.

5.5.3 High Latitude Seasonal Cycle of N_2O

The high latitude seasonal behavior of long lived tracers is strongly affected by the annual formation and breakup of the polar winter vortices, which isolate columns of rapidly descending air from their surroundings. Mixing from lower latitudes also affects the high latitude tracer isopleths, however, and sometimes this effect can be significant even when a well-defined vortex is present. For instance, Strahan et al. [1996] note that CLAES CH_4 isopleths descend more rapidly than N_2O isopleths during times of strong horizontal mixing. They attribute this difference to weaker horizontal CH_4 gradients. The net flux of CH_4 into high latitudes from horizontal mixing is smaller than that for N_2O, resulting in faster isopleth descent.

The seasonal cycle of modeled and observed long-lived tracers will reflect the combined effects of vertical descent and mixing, so comparison of the seasonal cycles can reveal the extent to which models capture the interplay between these high latitude transport processes.

The left-hand plots in Figure 5.5.6 show the seasonal cycle of CLAES N_2O in 1992 at high northern latitudes, at 21.5 km, 27 km, and 32 km in altitude. The right-hand plots show the corresponding cycles in the southern hemisphere. The crosses show averages over the UARS data in approximately 12 day time periods averaged in latitude between 75 degrees and 80 degrees. The asterisks show averages between 75 degrees and 80 degrees of equivalent latitude. The error bars included on the equivalent latitude averages indicate the geophysical variability of the observations included in the averages.

In the northern hemisphere at 21.5 km, N_2O reaches peak values of about 200 ppbv in December. The equivalent latitude averages show decreasing values through January and February, reaching a minimum in March of about 75 ppbv. There is almost a factor of 2 difference between the equivalent latitude and zonal mean averages at this time, indicating a significant zonal asymmetry in the atmosphere. The equivalent latitude averages show an annual amplitude of about 125 ppbv while the zonal mean values have an amplitude of less than half this amount. At higher altitudes the peak values decrease to about 110 and 40 ppbv at 27 and 32 km, respectively. At 27 km there is a factor of 3 to 4

difference in February and March between the zonal mean and equivalent latitude averages, resulting in an equivalent latitude annual amplitude of about 100 ppbv. At 32 km the difference between the zonal mean and equivalent latitude averages is still important, and the annual amplitude is a much smaller 30 ppbv at 32 km. The timing of the mixing ratio peak at 27 and 32 km moves earlier in the year, to near the end of May in both cases.

Figure 5.5.7 shows the northern hemisphere seasonal cycles in N_2O for 8 2D and 4 3D models at 80 degrees, at 22 km, 28 km, and 32 km. At all levels there is a wide variation amongst the models in the amount of N_2O, the magnitude of the seasonal cycle, and the timing of the extrema. The models typically underestimate the amplitude of the seasonal cycle. There is a tendency for the minima to occur in the late winter or early spring which is consistent with the observations. The maxima appear to occur earlier in the year than is indicated by the observations at 22 km, but later in the year at 28 and 32 km than the observed seasonal cycle suggests. Overall, the LARC-3D model compares best with the observations, but in general the models do not convincingly simulate the northern hemisphere high latitude seasonal cycle of N_2O.

The right-hand plots in Figure 5.5.6 show the southern hemisphere high latitude seasonal cycle observed by CLAES at 21.5, 27, and 32 km. The amplitude of the cycle at all altitudes is significantly larger than its northern hemisphere counterpart. This illustrates the point that although wintertime descent is larger in the northern compared to the southern hemisphere [Rosenfield et al., 1994; Rosenlof, 1995], the relative lack of meridional mixing in the southern hemisphere results in larger changes in tracer isopleths [Bacmeister et al., 1995]. There is also much less difference between the equivalent latitude and zonal mean averages during the winter, indicating a more zonally symmetric southern hemisphere vortex.

The CLAES N_2O data for the June/July and August/September yaw cycles are problematic due to a low temperature bias in the CLAES temperature retrieval and frequent occurrence of thick polar stratospheric clouds. The low temperature bias causes higher N_2O values to be retrieved. The bias is about 1-2 Kelvin at typical stratospheric temperatures and is as much as 3 Kelvin inside the southern hemisphere winter vortex. Schoeberl et al. [1996] compared N_2O from CLAES with values inferred from HALOE CH_4 observations on August 17, 1992, and found HALOE to be about 35% lower than the CLAES values. Because the low temperature bias is itself a function of temperature, the N_2O values in the southern hemisphere at high latitudes may be about 10% higher during the colder winter and spring yaw cycles than during other times of year. Polar stratospheric cloud interference tends to reduce N_2O and is probably the cause of the large error bars seen at 21.5 km and 27 km from June to September [A. Roche, personal communication].

CLAES N_2O mixing ratios should be unaffected by PSC formation and changing temperature biases through the end of April. Thus it appears that N_2O mixing ratios increase through at least April at 21.5 km and are relatively constant through this time at 27 km. This occurs even though descent over the southern hemisphere pole is strong from March through September between 20 and 30 km [Rosenfield et al., 1994; Rosenlof, 1995]. Because the N_2O decreases strongly with altitude during the entire time period, the N_2O isopleths must be substantially affected by meridional mixing during the fall. As noted in Strahan et al., [1996], this means that polar descent cannot be reliably estimated at these altitudes from changes in isopleth altitudes.

Figure 5.5.8 shows the seasonal cycles of N_2O in the southern hemisphere from the models. As in the northern hemisphere there is a significant intermodel variability in the N_2O seasonal cycle at all altitudes, and no model represents the seasonal cycle of N_2O particularly well at all altitudes. The amplitude of the seasonal cycle is typically underestimated. There is an interesting but weak anticorrelation

between correctly representing the overall magnitude of the seasonal cycle and its amplitude. For instance, the AER and SUNY-SPB models compare well with annually averaged N_2O mixing ratios but have very weak seasonal amplitudes. The NOCAR model has one of the largest amplitudes, but N_2O mixing ratios are much too low for most of the year. The model meridional N_2O gradients seen in Figures 5.5.3, 5.5.4, and 5.5.5 in comparison with the observed gradients in Figures 5.5.1 and 5.5.2 show that the SUNY-SPB and AER models have very weak meridional gradients throughout the year suggesting large mixing of N_2O at all times. Consequently a fair amount of N_2O is transported to high latitudes but the amplitude is weak. The NOCAR model shows a strong N_2O gradient throughout the year, even during the summer when the observed N_2O gradients are weak. Since there is never a time when meridional mixing of N_2O to high latitudes is large, the overall amount of high latitude N_2O is low. In order to correctly capture the seasonal cycle in N_2O at high latitudes it is necessary to represent well the seasonal variability in meridional mixing in addition to the correct magnitude of the wintertime polar boundary.

At 22 km the LARC-3D model seasonal amplitude is largest and is about 65% of the observed amplitude. Note that if the CLAES N_2O observations are indeed too high due to retrieval errors, the seasonal amplitude seen by the LARC-3D model at 22 km is very good. At 32 km, the N_2O amplitudes in the SLIMCAT and LARC-3D models compare well with the observations. There is a lot of variability in the timing of the peak, but there is a tendency for the peak values to occur earlier at higher altitudes, as is observed in the data. There is also a tendency for the model minima to occur in the late spring as observed, but there is considerable variability in the timing of the minima. At higher altitudes the minima typically occur earlier in the year, as is seen in the observations.

5.5.4 Meridional N_2O Gradients at 20 km from ER-2 Observations

Observations of a number of important atmospheric constituents were made from the ER-2 aircraft during several missions to the northern and southern hemisphere polar regions. The AASE II mission took data in the 1992 northern hemisphere winter and spring [Anderson and Toon, 1993]. We can compare these observations to the model simulations, which were designed to simulate 1992. The AAOE mission measured constituents in the southern hemisphere in the winter of 1987 [Tuck et al., 1989]. Although this is not the year simulated by the models, interannual variability in the southern hemisphere is smaller than in the northern hemisphere. Useful comparisons between these observations and the models should be possible. The aircraft measurements are made at altitudes in the range of 18 kilometers, several kilometers lower than the CLAES observations described above. The ER-2 data thus provide information about an important part of the atmosphere somewhat below the range of the satellite observations.

Figure 5.5.9 compares January northern hemisphere model N_2O mixing ratios as a function of latitude with the N_2O distribution obtained by averaging all of the data from January 1992 ER-2 flights into 5 degree wide latitude bins. Figures 5.5.9a - 5.5.9c show 20 km model results overplotting the ER-2 data, which is the same in each plot. The crosses show the ER-2 data. The error bars show the standard deviation of all the observations in each bin, which indicates the geophysical variability of the data. Figure 5.5.9d shows only the ER-2 data, this time averaged as a function of equivalent latitude. This average shows the expected sharper gradients compared to the latitude averages at both the tropical and vortex edges. Because the data were taken on different days and at similar longitudes, The ER-2 latitude averaged N_2O is not technically a zonal mean.

The ER-2 observations indicate that N_2O values of about 100 ppbv are typical within the 1992 January northern hemisphere polar vortex. The model values vary from about 75 ppbv to about 220 ppbv. Most models err on the high side, due either to too rapid mixing or too weak descent within

the vortex. The NOCAR and the LLNL models have vortex edge gradients that are similar to those seen in the data, although the LLNL edge is about 7 degrees south of its placement in the ER-2 data. The other models show weak edges or none at all. No consistent difference between the 2D and the 3D models is seen in this comparison.

Figure 5.5.10 is similar to Figure 5.5.9 except that it compares model N_2O mixing ratios at 20 km with AAOE observations for the month of September, 1987. The observations also show that N_2O concentrations around 100 ppbv characterize this time of year and altitude. Model values range between about 60 and 250 ppbv. The ER-2 observations suggest a vortex edge at about -55 degrees - -60 degrees, which is consistent with the location of the edge as defined by gradients in the 1992 CLAES N_2O observations at 21.5 km. The most convincing model vortex edges are those seen in the 2D LLNL model and the 3D LARC model. Models which do not resolve the vortex edge well typically have too large high latitude N_2O mixing ratios in comparison with the observations.

5.5.5 Meridional Cly Gradients Inferred from ER-2 N_2O Observations

Woodbridge et al. [1995] provide a method for inferring the amount of Cly that exists at some location from a colocated N_2O observation. Figure 5.5.11 shows the northern hemisphere Cly mixing ratios inferred by this method from the AASE II N_2O data presented in Figure 5.5.9. The Cly mixing ratios calculated by the models at 20 km are also plotted in Figure 5.5.11. The GSFC-2D, LLNL, NOCAR, HARVARD, and AER models all have reasonable amounts of high latitude Cly in comparison with inferred values, while the rest of the models have about 60% of the N_2O-inferred Cly. The AER and HARVARD models do not represent the meridional structure of the Cly distribution well, showing very little evidence of a midlatitude surf zone at this altitude.

Figure 5.5.12 compares ER-2 inferred Cly from AAOE N_2O data in the southern hemisphere with model calculations. ER-2 estimates of Cly in the southern hemisphere are similar to northern hemisphere values. Model Cly mixing ratios range from only 1 ppbv in the UNIVAQ-2D model to over 3 ppbv in the HARVARD model. High latitude Cly concentrations in the GSFC-2D, LLNL, and NOCAR models are within 15% of the ER-2 inferred values, and most of the models fall within 35% of the inferred concentrations.

5.5.6 High Latitude Seasonal Cycle of HNO_3

High latitude gas phase HNO_3 concentrations respond to the amount of descent within the wintertime polar vortex, the amount of mixing from lower latitudes, the sequestration of NOy into condensed phases, and the amount of irreversible denitrification which occurs due to particle sedimentation over the course of the winter. Comparison of model HNO_3 concentrations with observations will not test the individual adequacy of a model's representation of these processes but will show their overall effect.

Figure 5.5.13 compares observed high latitude northern hemisphere HNO_3 with 6 2D and 3 3D time series. The HARVARD and CSIRO models are not included in this comparison because they do not include denitrification in their models. The crosses represent CLAES HNO_3 observations between 75 degrees and 80 degrees North averaged over 10 to 12 day intervals for the year of 1992. The asterisks which lie nearly on top of the crosses represent CLAES HNO_3 observations between 75 degrees and 80 degrees in equivalent latitude, averaged over the same time intervals. The plus/minus 1 sigma error bars associated with the equivalent latitude averages do not account for instrumental error and indicate the geophysical variability of the observations used to construct the average values. There is little difference between equivalent latitude and latitude averages even in February and March when there are large

difference between zonal mean and equivalent latitude averaged N_2O. This is probably due to the relatively weak high latitude meridional and vertical gradients in HNO_3 at these altitudes.

Peak values of about 12 ppbv of HNO_3 occur in January in the northern hemisphere and decrease to minimum values of about 8 ppbv in late July and early August. The models plotted in Figure 5.5.12 generally do a good job of representing the overall magnitude of HNO_3, the amplitude of the seasonal cycle, and the timing of the extrema. A notable exception is the NOCAR model, which overestimates both the magnitude and the amplitude.

Figure 5.5.14 shows a time series of CLAES HNO_3 at about 21.5 km at high southern latitudes, compared with 6 2D and 3 3D models. The figures show that CLAES observed HNO_3 increases from about 7 ppbv to around 11 ppbv during the southern hemisphere summer, peaking in the early fall. At this time HNO_3 mixing ratios begin to decrease rapidly. Note that this is probably not due to dynamical processes because N_2O at this altitude continues to increase throughout the winter. HNO_3 mixing ratios decline throughout the fall and winter, reaching minimum values between 1 and 2 ppbv toward the end of the winter. A recovery to values of about 4 ppbv occurs by the end of spring.

The 9 models included in this comparison show behavior similar to the observations. There is a fairly significant variability in the timing of peak HNO_3 concentrations, with most models late by 1 to several months. The model fall peak mixing ratios are generally within about 50% of the CLAES observations, with a general tendency to be low. The NOCAR and the GSFC-2D models significantly overestimate HNO_3 mixing ratios in the late southern hemisphere spring, with peak values 3 to 5 times higher than the observations. This may be due to descent of high HNO_3 mixing ratios from above in these two models, which would be consistent with the decreasing N_2O mixing ratios observed in these two models at this time and altitude. It may also be due to weak irreversible denitrification resulting in the return of gas phase HNO_3 from the condensed phase when HNO_3-rich PSCs evaporate.

Most of the model HNO_3 time series are similar to the observed HNO_3 time series, with the exception of the NOCAR model. The agreement between modeled and observed HNO_3 is significantly better than the agreement between modeled and observed N_2O. Peak modeled HNO_3 mixing ratios tend to occur later in the year than the observations indicate, with the model minima similarly phase-shifted. The amplitude of the model HNO_3 mixing ratios is generally weaker than that seen in the observations.

5.5.7 Summary and Conclusions

Atmospheric dynamical processes establish the background environment in which polar chemical processes occur and determine how the polar chemistry influences the rest of the globe. It is thus important for the processes to be well-represented in models hoping to accurately predict the response of the atmosphere to perturbations. We have used observations of several atmospheric constituents sensitive to polar processes to evaluate how well the modeled polar processes reproduce the features seen in the observations. We have not attempted to explicitly evaluate the adequacy of any particular polar process.

The meridional first derivative of CLAES N_2O mixing ratios clearly highlights vortex and tropical edges, and is therefore a useful diagnostic of model performance. Significant differences between zonal mean and equivalent latitude averages show that vortex wobble significantly affects northern hemisphere high latitude zonal means during winter. There is not as much of an effect in the southern hemisphere high latitudes or in the tropics of either hemisphere.

The observed structure of long-lived atmospheric tracers are not consistently well-simulated in either 2D or 3D models. There is a significant amount of intermodel variability, with some models

doing much better than others. There is a tendency to underestimate the strength of the gradients in both 2D and 3D models, but the strong gradients seen in the 2D NOCAR and LLNL models indicate that 2D models do not necessarily underestimate the observed gradients. It is probably desirable in a 2D model to reproduce the N_2O gradients seen in the CLAES equivalent latitude averages. Doing so may produce more accurate fluxes between dynamically distinct atmospheric regions. Correctly representing the fluxes is probably more important to predicting how the atmosphere will respond to a perturbation than the correct zonal mean gradients. These conclusions need to be explicitly demonstrated in modeling studies, however.

The seasonal cycle of N_2O is not well-simulated in most models. The seasonal amplitude of the cycle is underestimated by the models at 21.5 and 27 km, while at 32 km there is better agreement. Peak N_2O values generally occur too early in the year compared to the observations. The timing of the minimum varies considerably from model to model. The models generally do succeed in placing higher altitude extrema earlier in the year than at lower altitudes, consistent with observations.

Estimates of Cly inferred from ER-2 observations suggest values between 2.5 and 3 ppbv characterize the polar latitudes in both the northern and southern hemispheres. There is more variability in the model northern hemisphere Cly than in the southern hemisphere. Some models significantly underestimate Cly in both the northern and southern hemispheres, but the GSFC-2D, LLNL, NOCAR, HARVARD, and AER models agree reasonably well with Cly in both hemispheres.

Model simulations of the seasonal behavior of HNO_3 are in reasonable agreement with CLAES HNO_3 mixing ratios at 21.5 km in both the northern and southern hemispheres. The weak meridional gradients in HNO_3 at high latitudes apparently make it easier to simulate well HNO_3 concentrations. There is no evidence from the data of extensive sequestration of HNO_3 at high northern latitudes in 1992.

Observed HNO_3 in the southern hemisphere decreases when N_2O concentrations are still increasing, suggesting that the decreases are due to condensation rather than dynamical processes. The models differ significantly in the timing of the onset of decreasing HNO_3 values, typically being late by up to several months. The GSFC-2D and NOCAR models recover after the annual HNO_3 minimum in the southern hemisphere to values which are 3 to 5 times observed values. This may be due to too rapid descent or to too weak irreversible denitrification. Other models show a slower recovery of HNO_3 in better agreement with the observations.

References

Anderson, J. G., and O. B. Toon, Airborne arctic stratospheric expedition II: An overview, Geophys. Res. Lett., 20, 2499 - 2502, 1993.

Bacmeister, J. T., M. R. Schoeberl, M. E. Summers, J. R. Rosenfield, and X. Zhu, Descent of long-lived trace gases in the winter polar vortex, J. Geophys. Res., 100, 11,669 - 11,684, 1995.

Eluszkiewicz, J., D. Crisp, R. Zurek, L. Elson, E. Fishbein, L. Froidevaux, J. Waters, R. G. Grainger, A. Lambert, R. Harwood, and G. Peckham, Residual circulation in the stratosphere and lower mesosphere as diagnosed from Microwave Limb Sounder data, J. Atmos. Sci., 53, 217 - 240, 1996.

McIntyre, M. E., and T. N. Palmer, The "surf zone" in the stratosphere, J. Atmos. Terr. Phys., 46, 825 - 849, 1984.

Nakamura, N., and J. Ma, Modified Lagrangian -mean diagnostics of the stratospheric polar vortices 2. Nitrous oxide and seasonal barrier migration in the cryogenic limb array etalon spectrometer and SKYHI general circulation model, J. Geophys. Res., 102, 25,721 - 25,735, 1997.

Nash, E. R., P. A. Newman, J. E. Rosenfield, and M. R. Schoeberl, An objective determination of the polar vortex using Ertel's potential vorticity, J. Geophys. Res., 9471-9478, 1996.

Roche, A. E., et al., Validation of CH4 and N2O measurements by the cryogenic limb array etalon spectrometer instrument on the upper atmosphere research satellite, J. Geophys. Res., 101, 9679 - 9710, 1996.

Rosenfield, J. E., P. A. Newman, and M. R. Schoeberl, Computations of diabatic descent in the stratospheric polar vortex, J. Geophys. Res., 99, 16,677 - 16,689, 1994.

Rosenlof, K. H., Seasonal cycle of the residual mean meridional circulation in the stratosphere, J. Geophys. Res., 100, 5173 - 5191, 1995.

Schoeberl, M. R., A. R. Douglass, S. R. Kawa, A. E. Dessler, P. A. Newman, R. S. Stolarski, A. E. Roche, J. W. Waters, and J. M. Russell, III, Development of the Antarctic ozone hole, J. Geophys. Res., 101, 20,909 - 20,924, 1996.

Strahan, S. E., J. E. Nielsen, and M. C. Cerniglia, Long-lived tracer transport in the Antarctic stratosphere, J. Geophys. Res., 101, 26,615 - 26,629, 1996.

Tuck, A. F., R. T. Watson, E. P. Condon, J. J. Margitan, and O. B. Toon, The planning and execution of ER-2 and DC-8 aircraft flights over Antarctica, August and September 1987, J. Geophys. Res., 94, 11,181 - 11,222, 1989.

Woodbridge, E. L., J. W. Elkins, D. W. Fahey, L. E. Heidt, S. Solomon, T. J. Baring, T. M. Gilpin, W. H. Pollock, S. M. Schauffler, E. L. Atlas, M. Lowentein, J. R. Podolske, C. R. Webster, R. D. May, J. M. Gilligan, S. A. Montzka, K. A. Boering, and R. J. Salawitch, Estimates of total organic and inorganic chlorine in the lower stratosphere from in situ and flask measurements during AASE II, J. Geophys. Res., 100, 3057 - 3064, 1995.

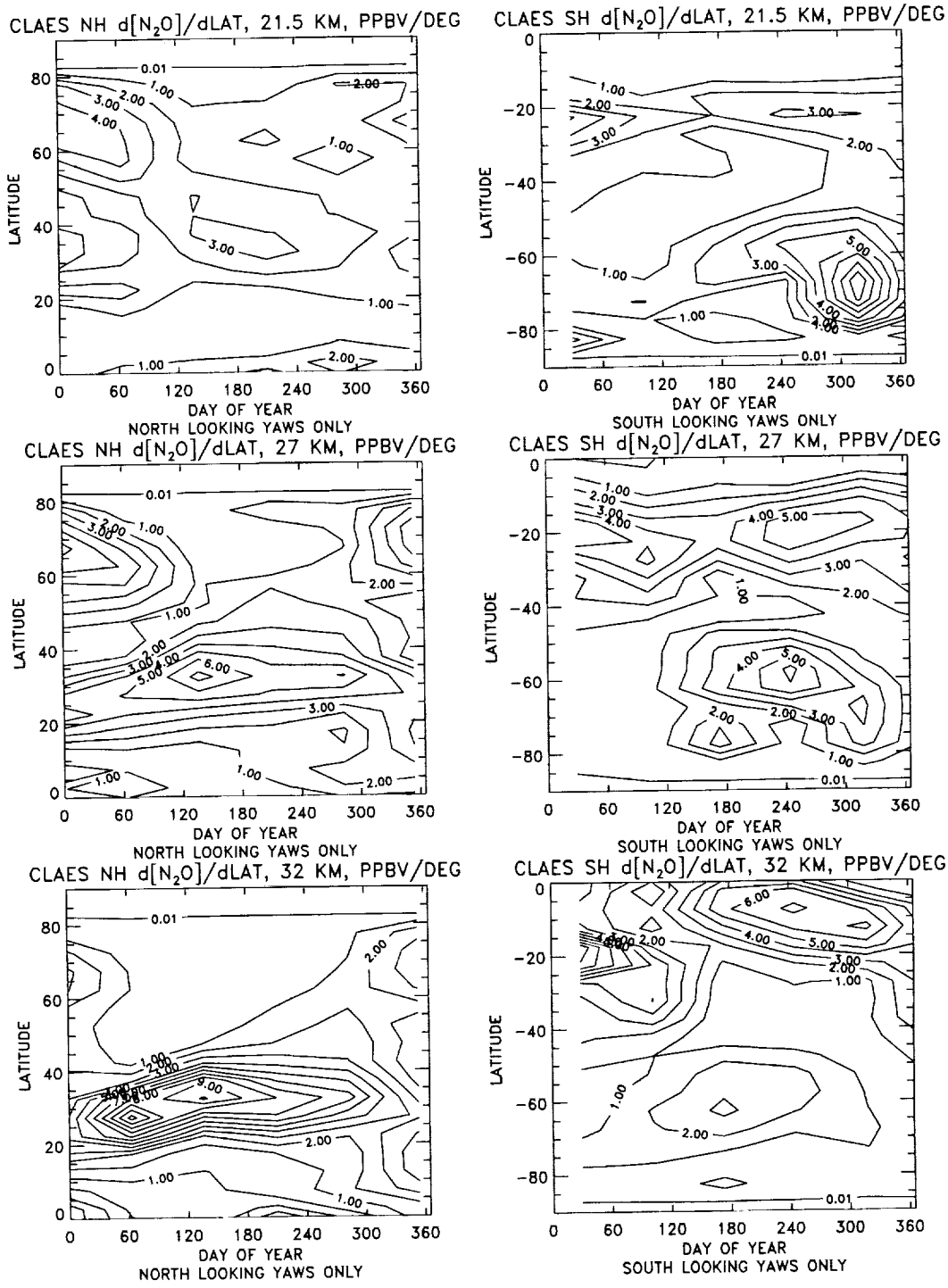

Figure 5.5.1. Absolute value of first derivative of CLAES version 8 N_2O mixing ratios with respect to latitude. The six plots show the seasonal changes in the derivative in the northern hemisphere (left side) and the southern hemisphere (right side) at 21.5 km (top), 27 km (middle), and 32 km (bottom). Contours are 1, 2, 3, 4, 5, 6, 7, 8, 9, and 10 ppbv/degree latitude. The plots were made by first calculating zonal mean averages of N_2O for each yaw cycle with 5 degree latitude resolution, and then taking the first derivative of the resulting distributions. The 5 north-looking yaw cycles in 1992 were used to construct the northern hemisphere plots, while the 5 south-looking yaw cycles were used for the southern hemisphere.

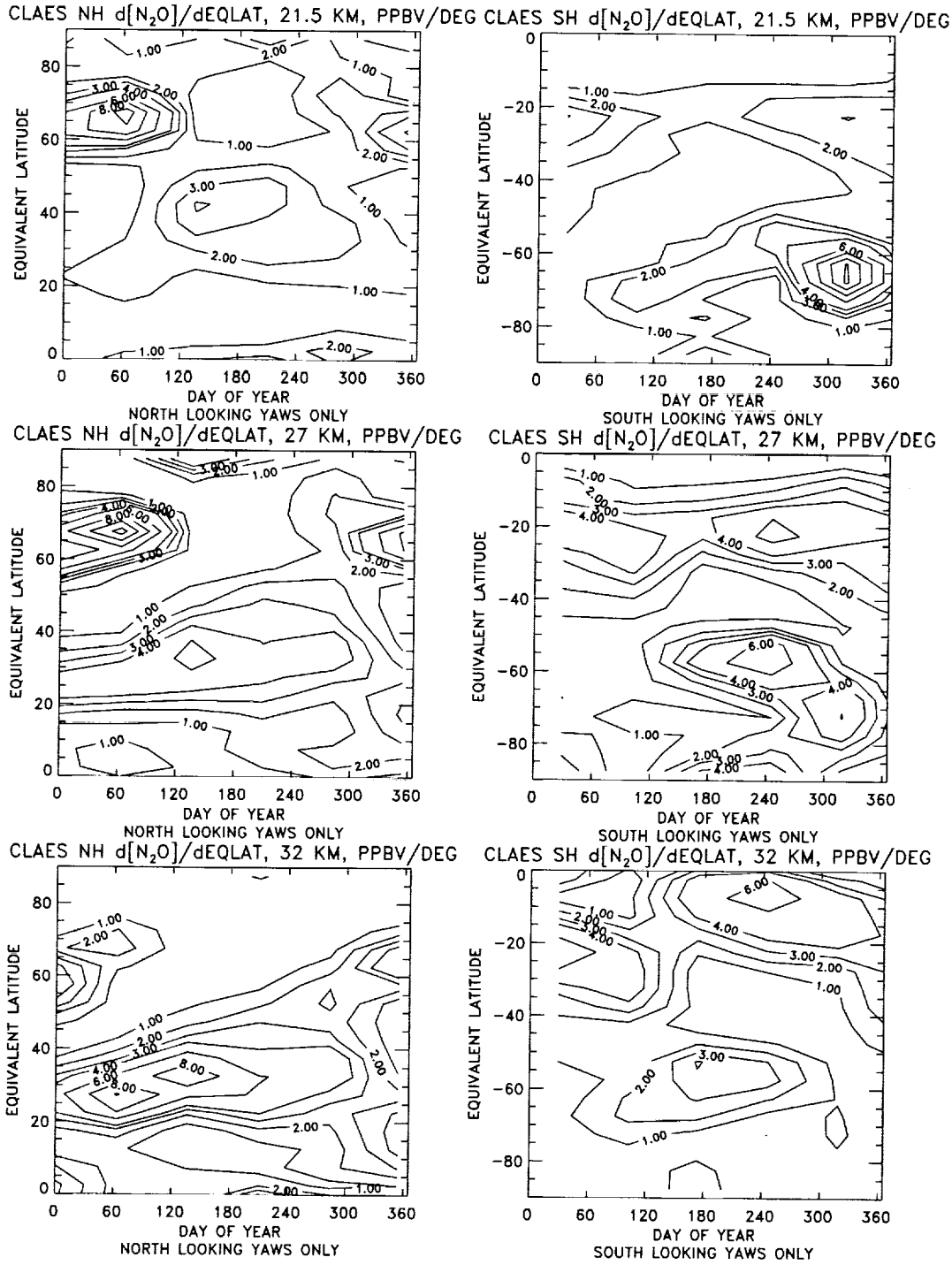

Figure 5.5.2. Absolute value of first derivative of CLAES version 8 N_2O mixing ratios with respect to equivalent latitude. The six plots show the seasonal changes in the derivative in the northern hemisphere (left side) and the southern hemisphere (right side) at 21.5 km (top), 27 km (middle), and 32 km (bottom). Contours are 1, 2, 3, 4, 6, 8, 10, and 12 ppbv/degree latitude. The plots were made by first calculating equivalent latitude averages of N_2O for each yaw cycle with 5 degree latitude resolution, and then taking the first derivative of the resulting distributions. The 5 north-looking yaw cycles in 1992 were used to construct the northern hemisphere plots, while the 5 south-looking yaw cycles were used for the southern hemisphere.

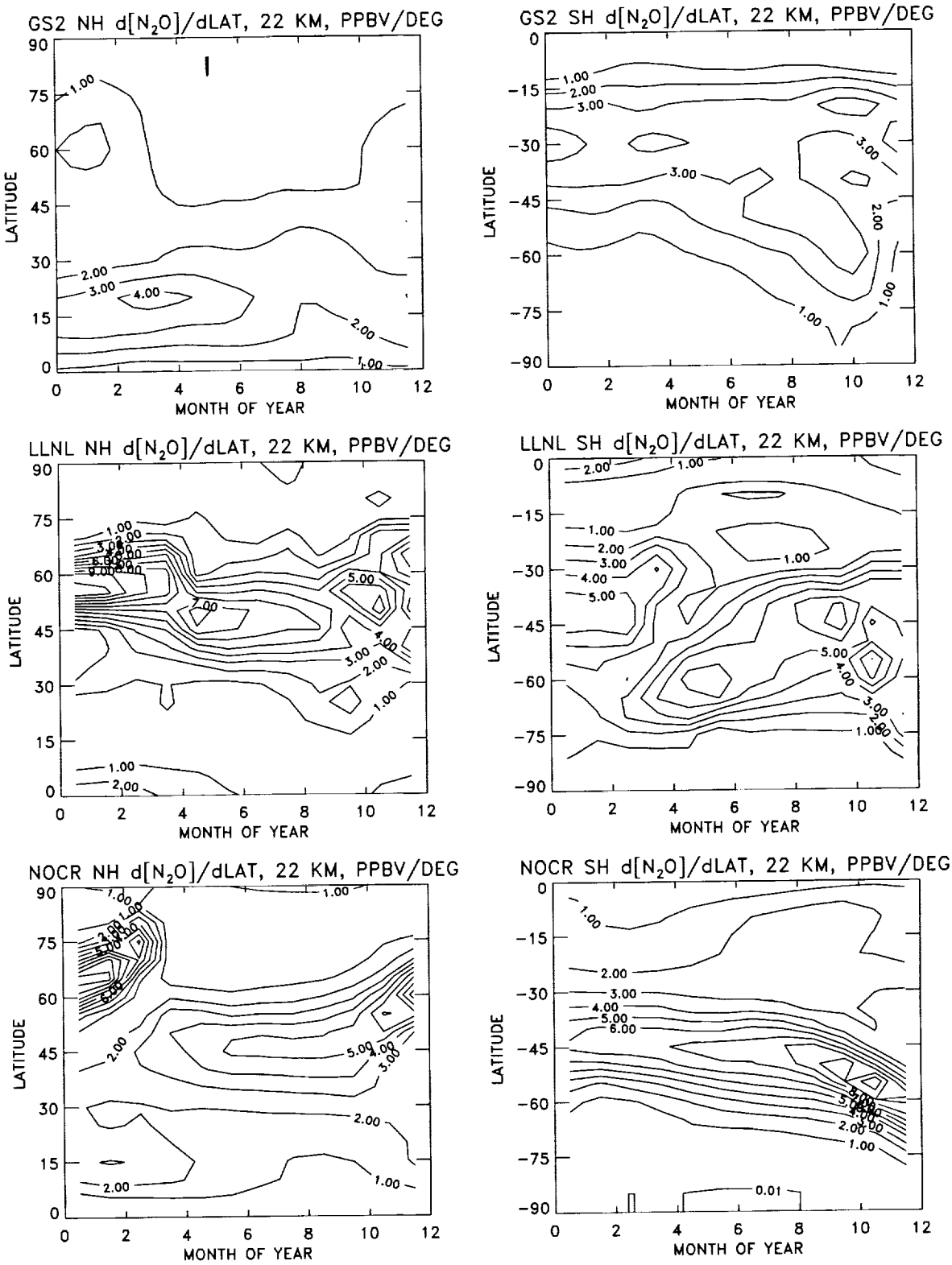

Figure 5.5.3. Absolute value of the first derivative of model N_2O distributions with respect to latitude at 22 km in the northern hemisphere (left side) and southern hemisphere (right side) for the 8 2D and 4 3D models mentioned in the chapter text. Units are ppbv/degree and contours are the same as Figure 5.5.1. The abscissae tick marks indicate the end of the month.

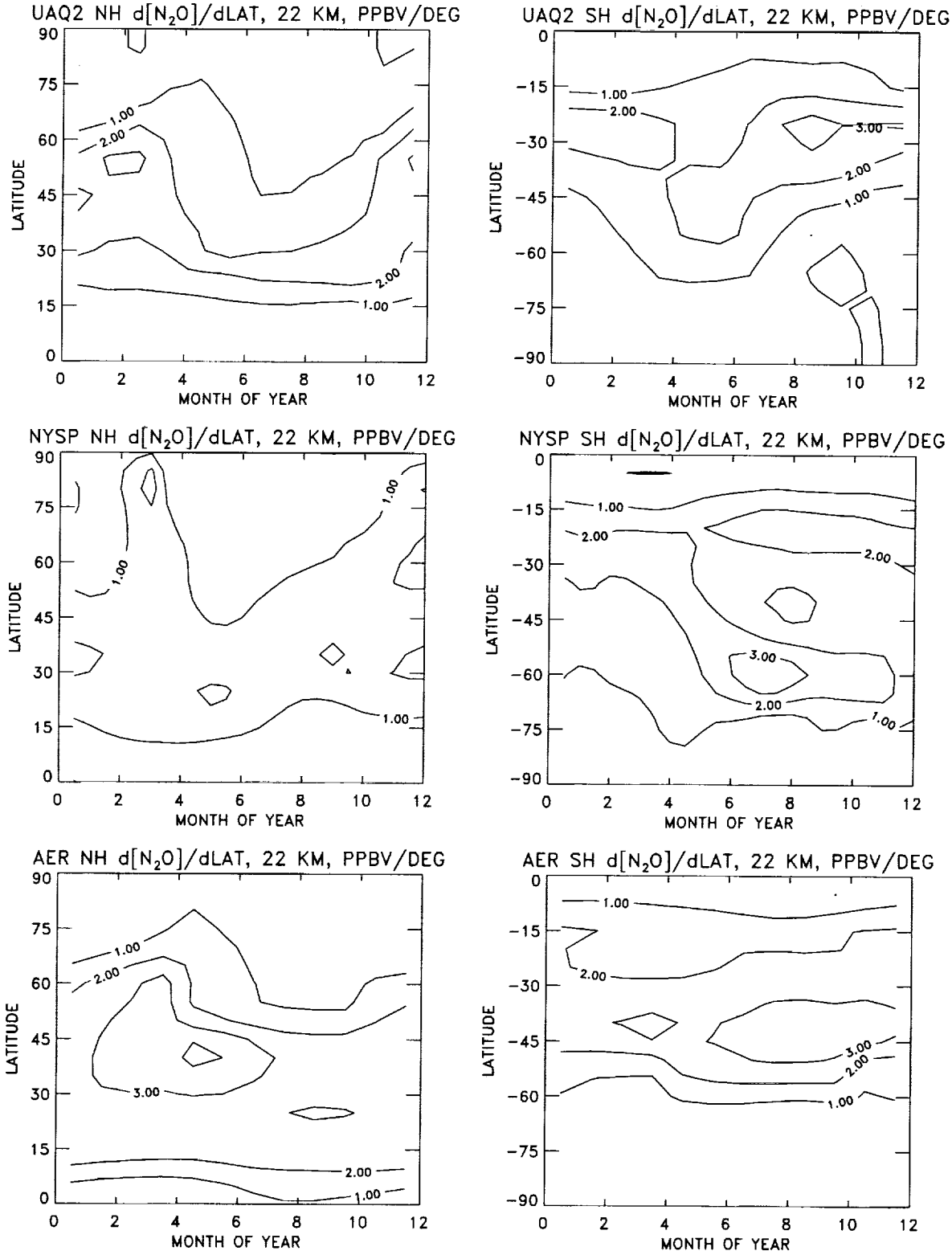

Figure 5.5.3. Continued.

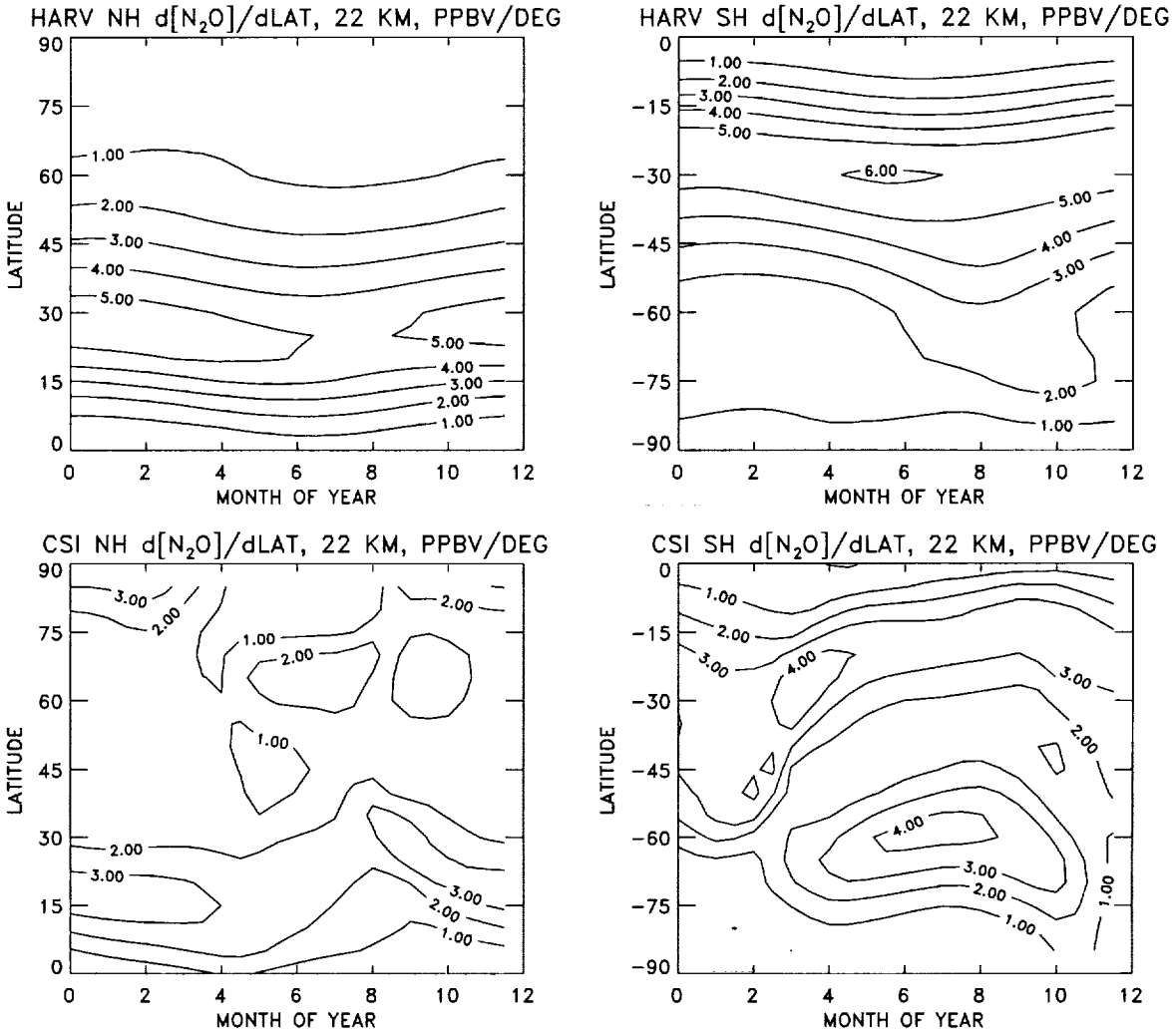

Figure 5.5.3. Continued.

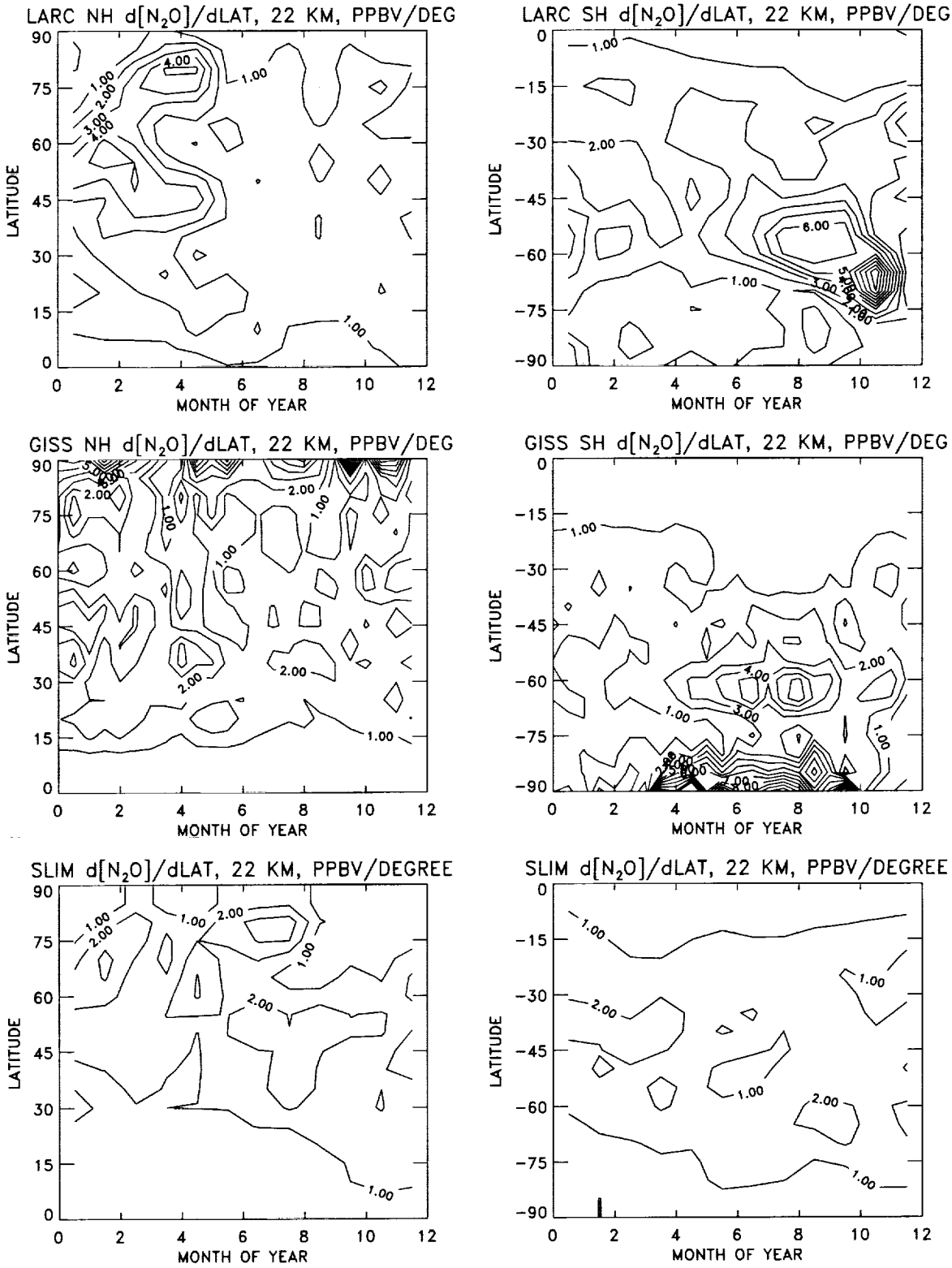

Figure 5.5.3. Continued.

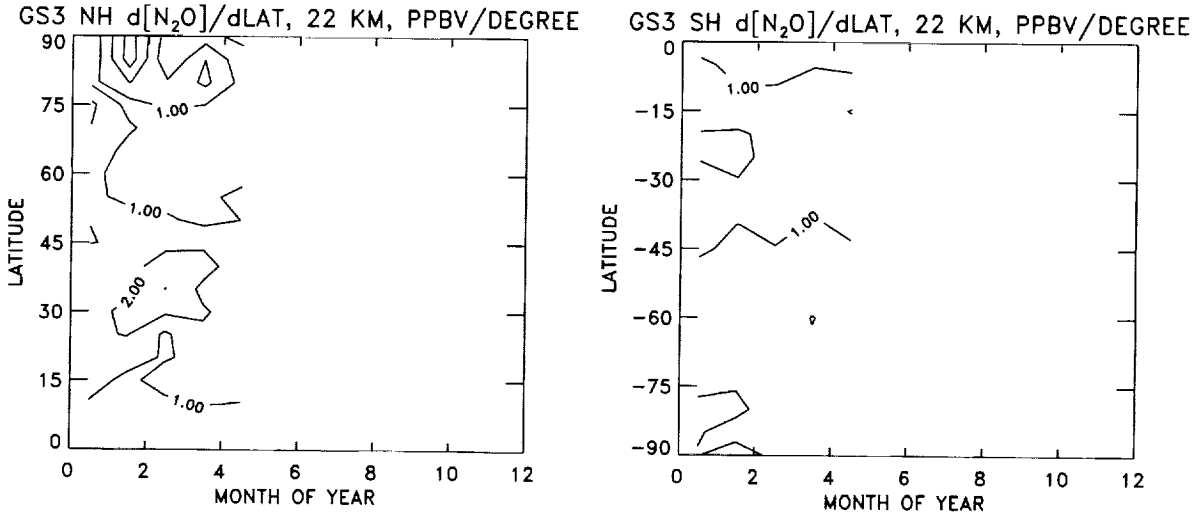

Figure 5.5.3. Concluded.

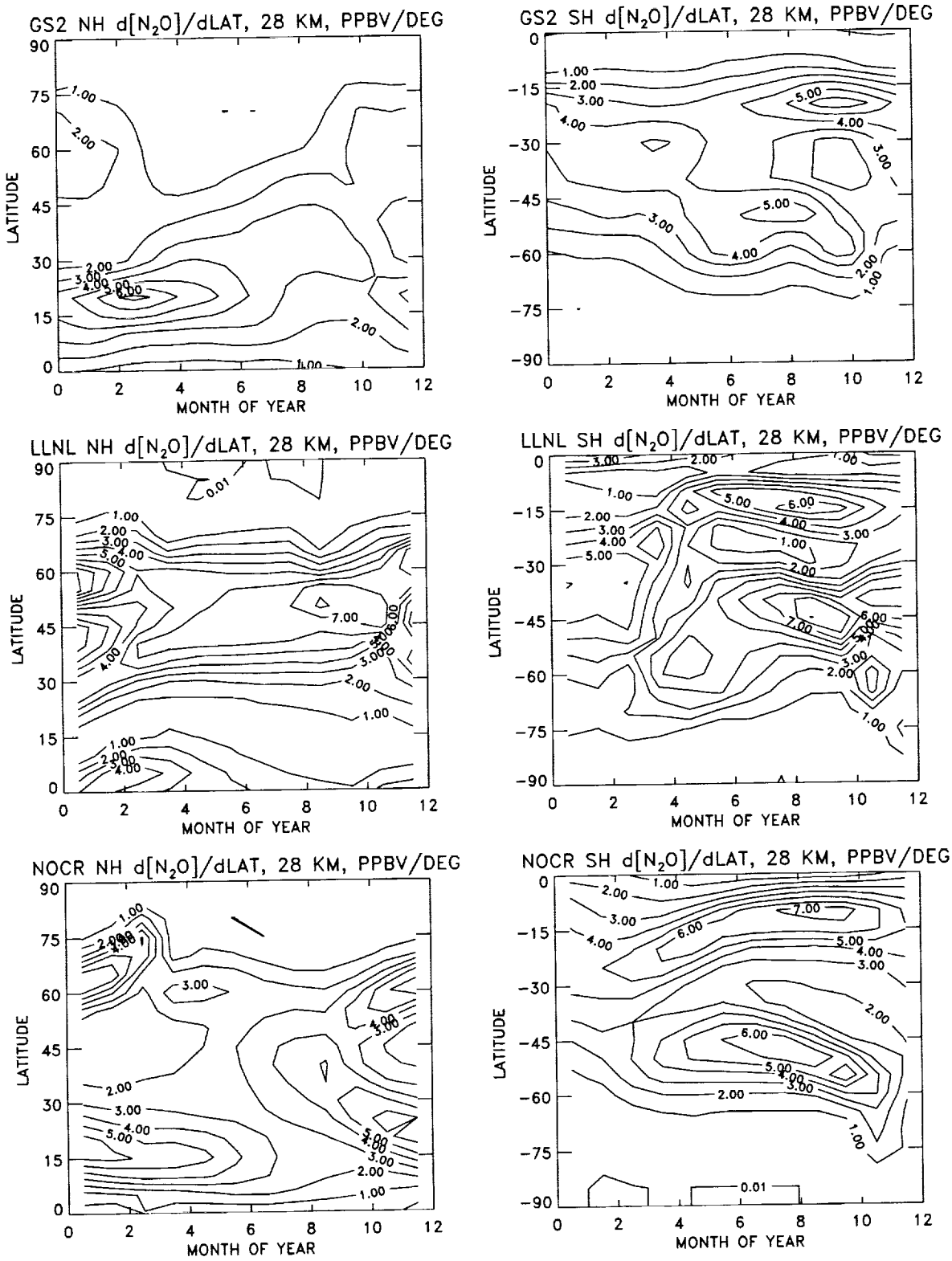

Figure 5.5.4. Absolute value of the first derivative of model N_2O distributions at 28 km in the northern hemisphere (left side) and southern hemisphere (right side) for the 8 2D and 4 3D models mentioned in the chapter text. Units are ppbv/degree and contours are the same as Figure 5.5.1. The abscissae tick marks indicate the end of the month.

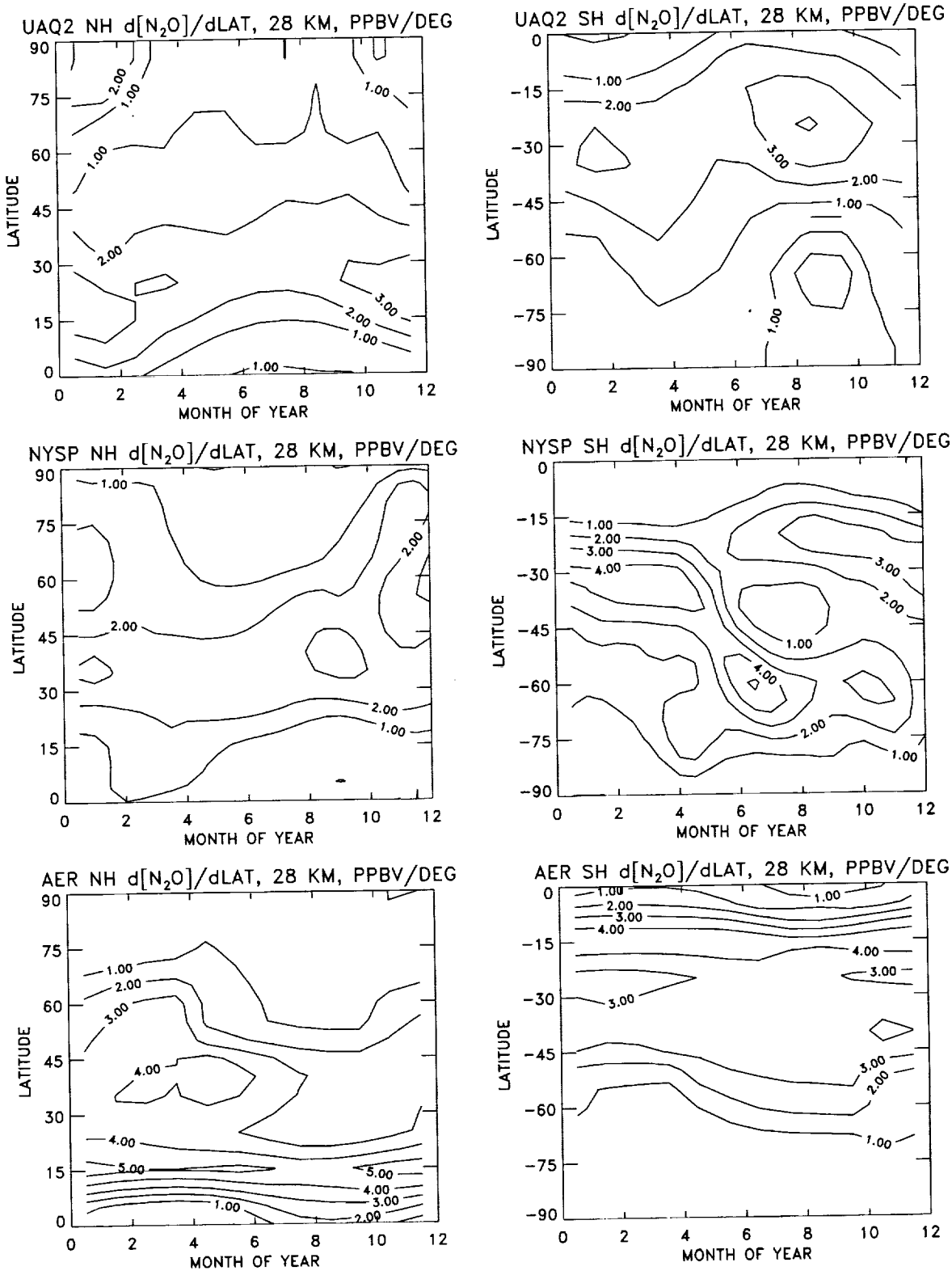

Figure 5.5.4. Continued.

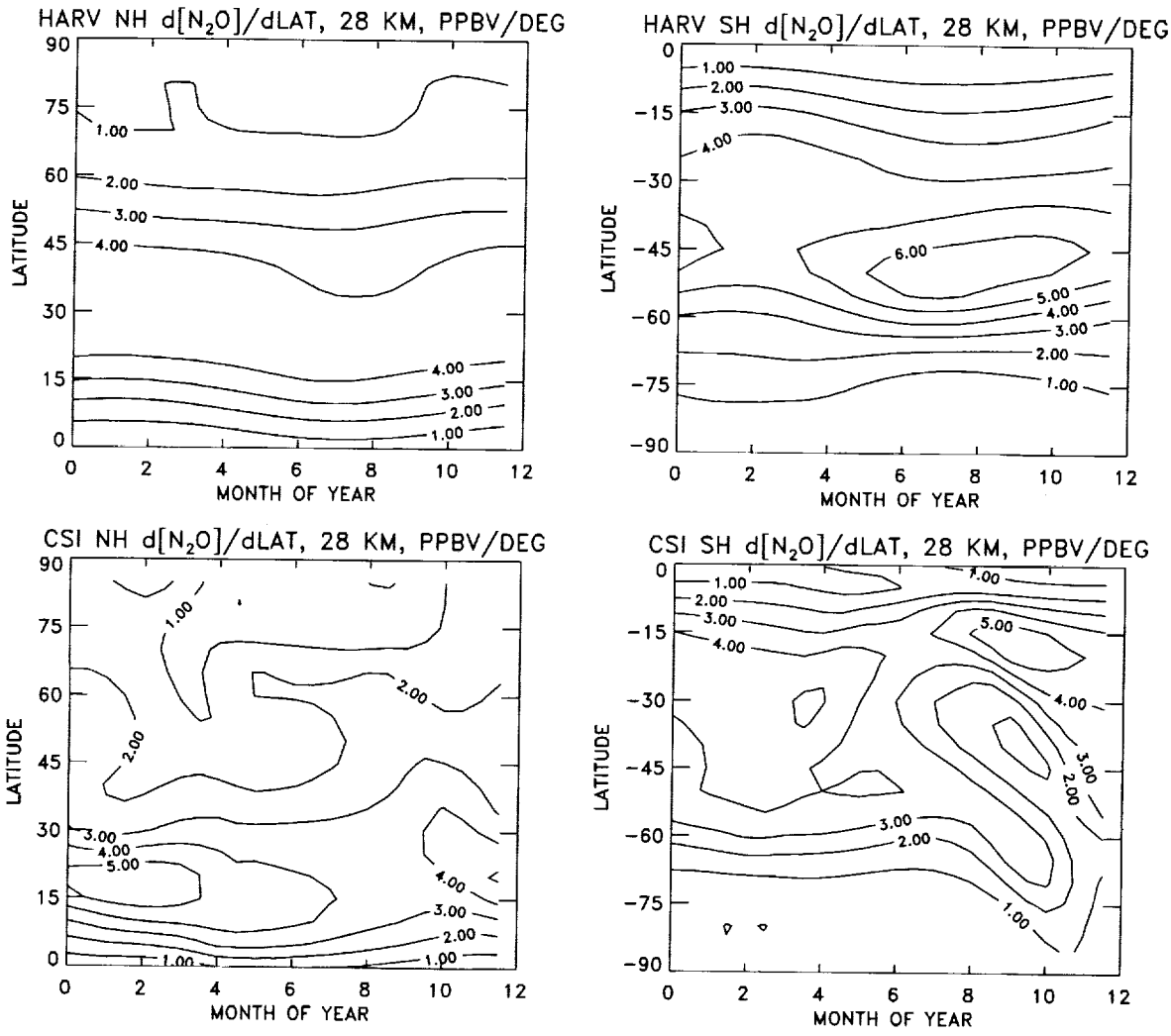

Figure 5.5.4. Continued.

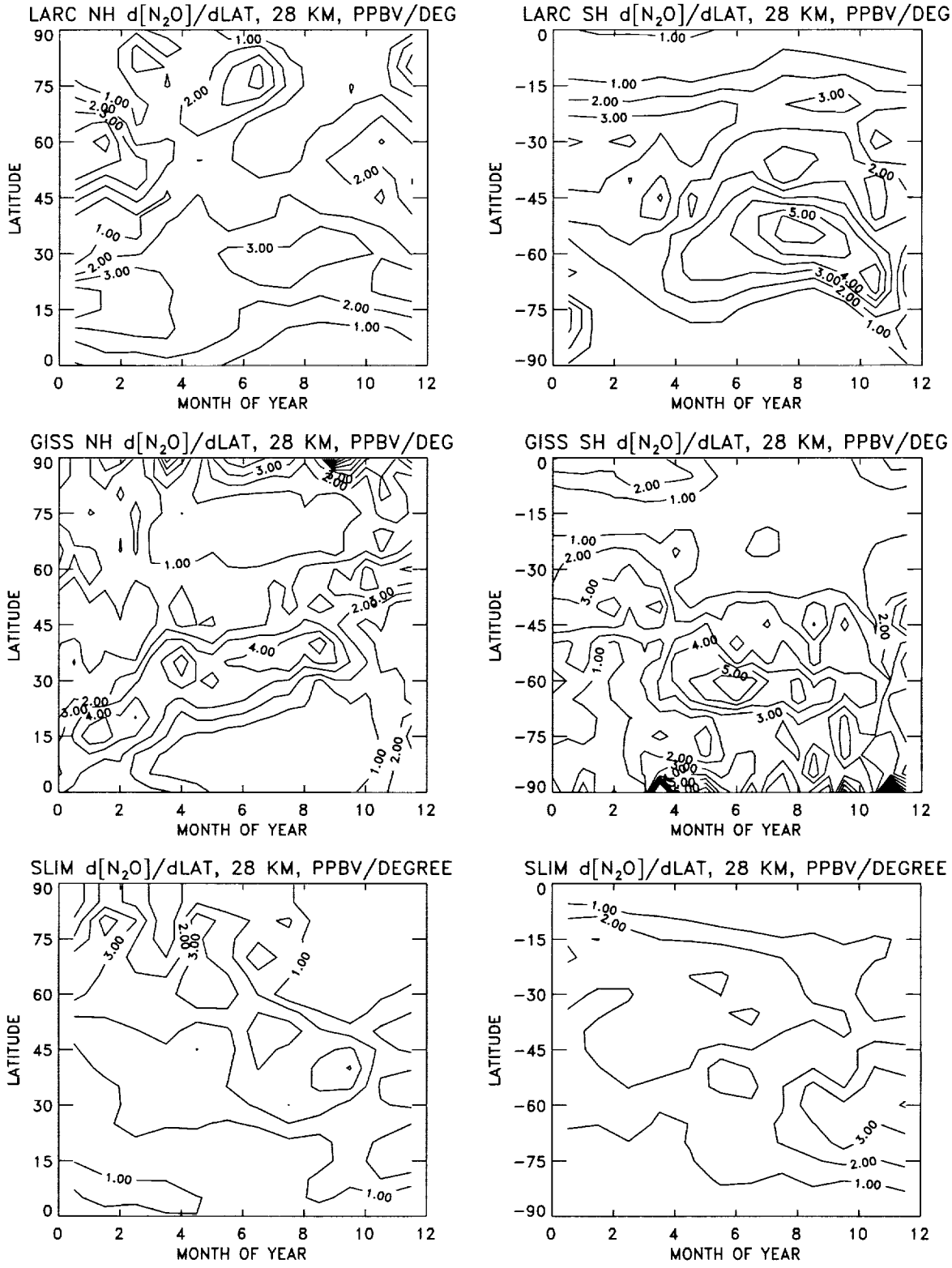

Figure 5.5.4. Continued.

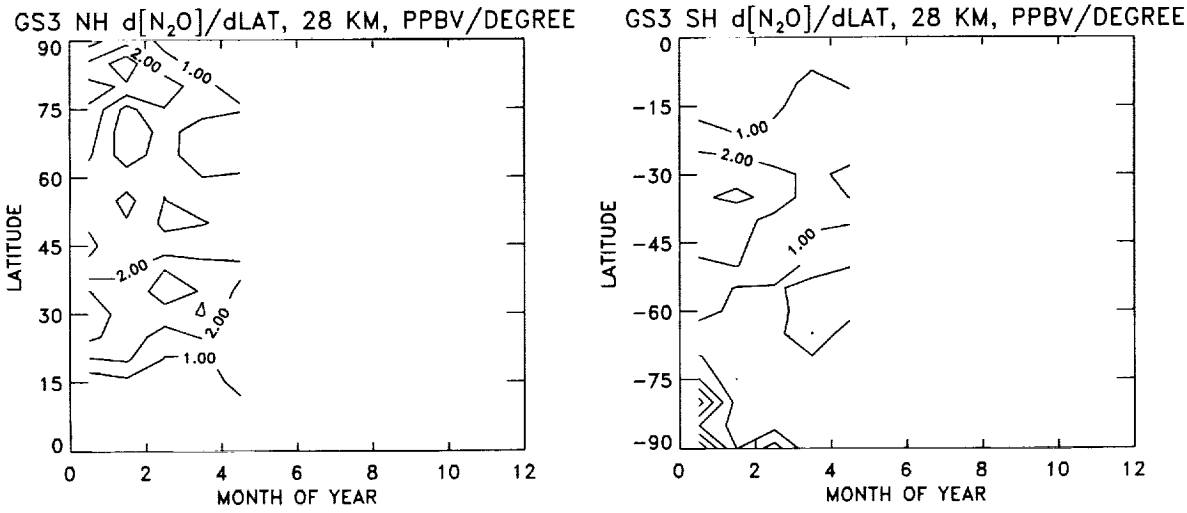

Figure 5.5.4. Concluded.

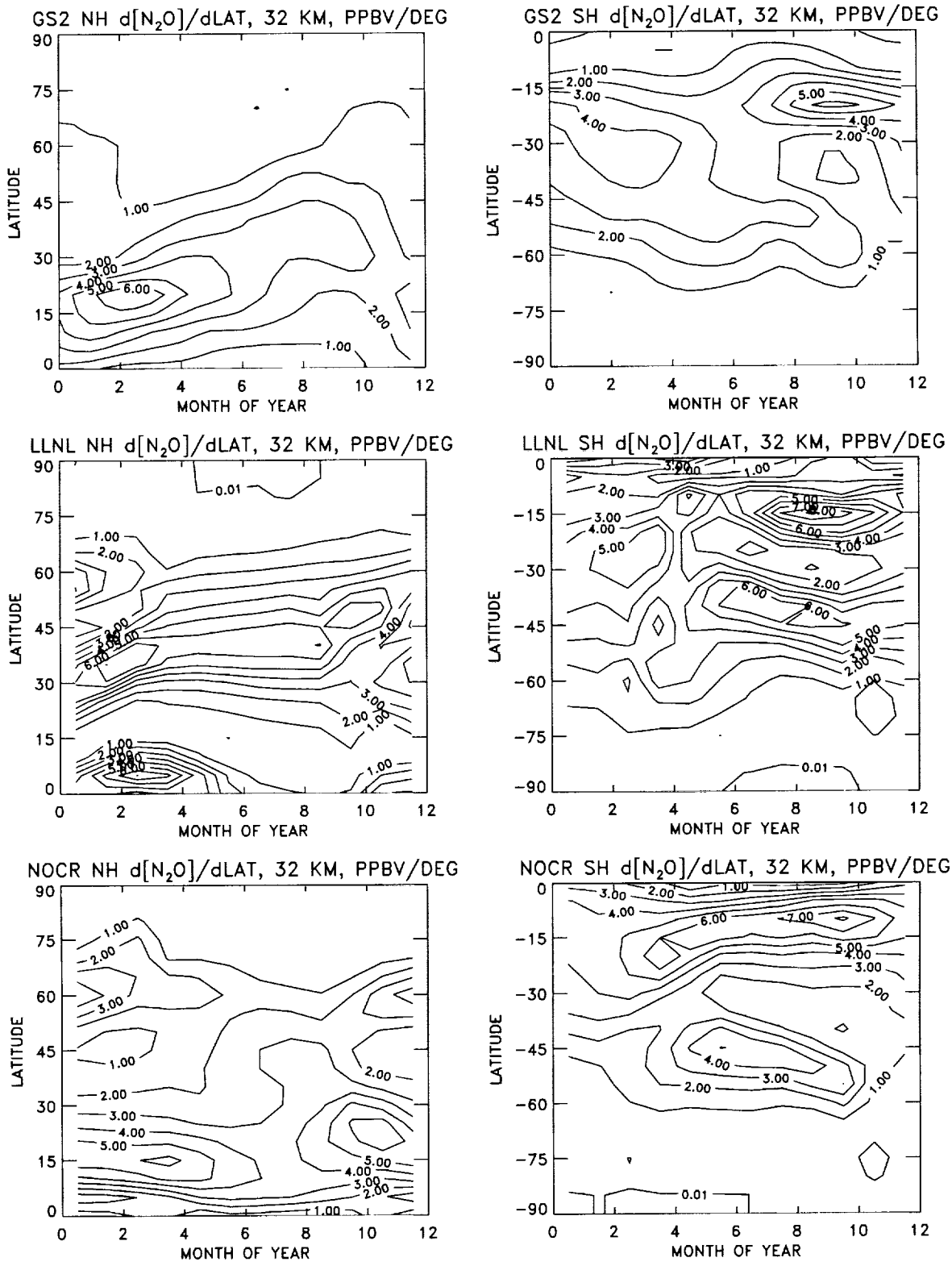

Figure 5.5.5. Absolute value of the first derivative of model N_2O distributions at 32 km in the northern hemisphere (left side) and southern hemisphere (right side) for the 8 2D and 4 3D models mentioned in the chapter text. Units are ppbv/degree and contours are the same as Figure 5.5.1. The abscissae tick marks indicate the end of the month.

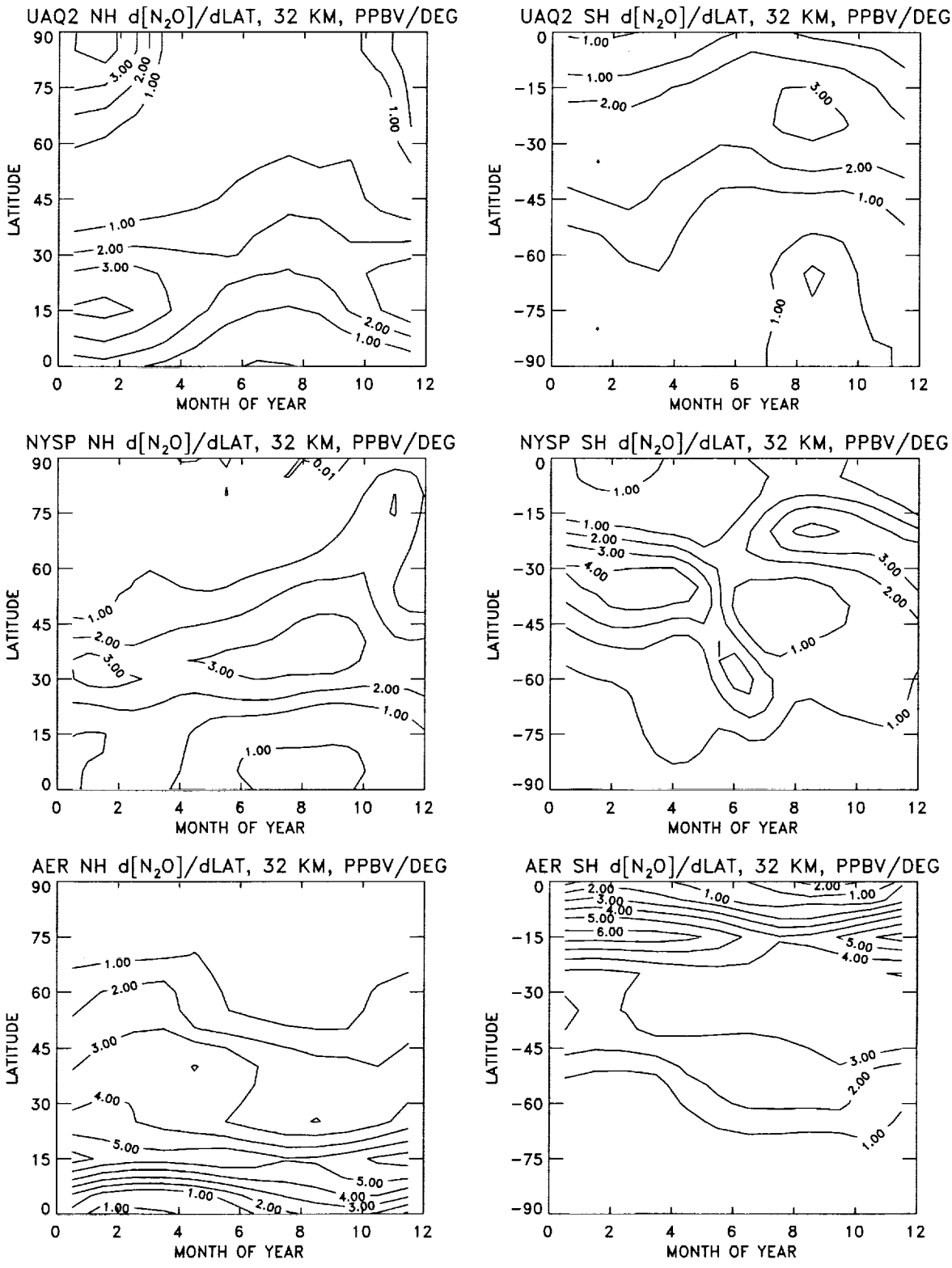

Figure 5.5.5. Continued.

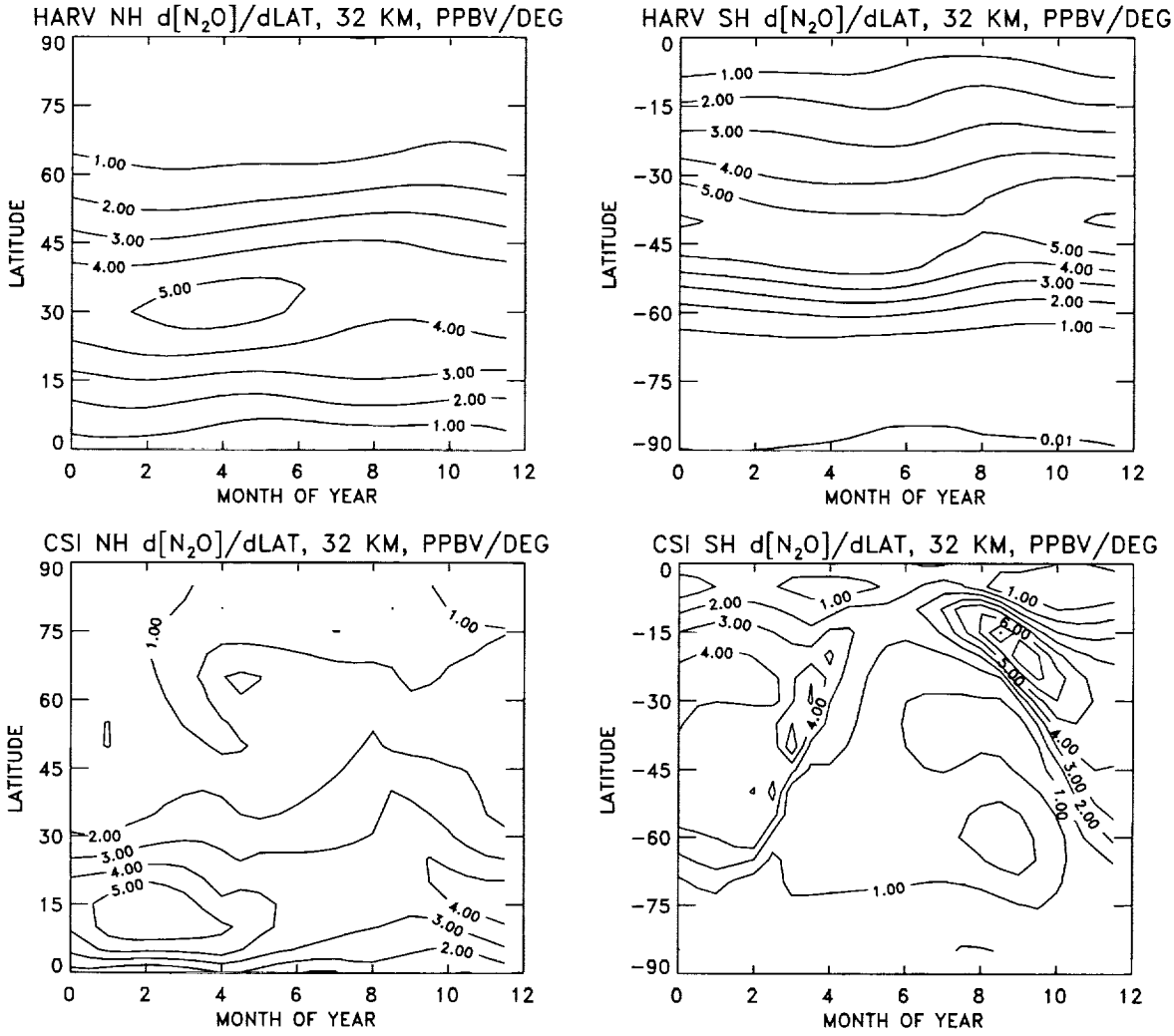

Figure 5.5.5. Continued.

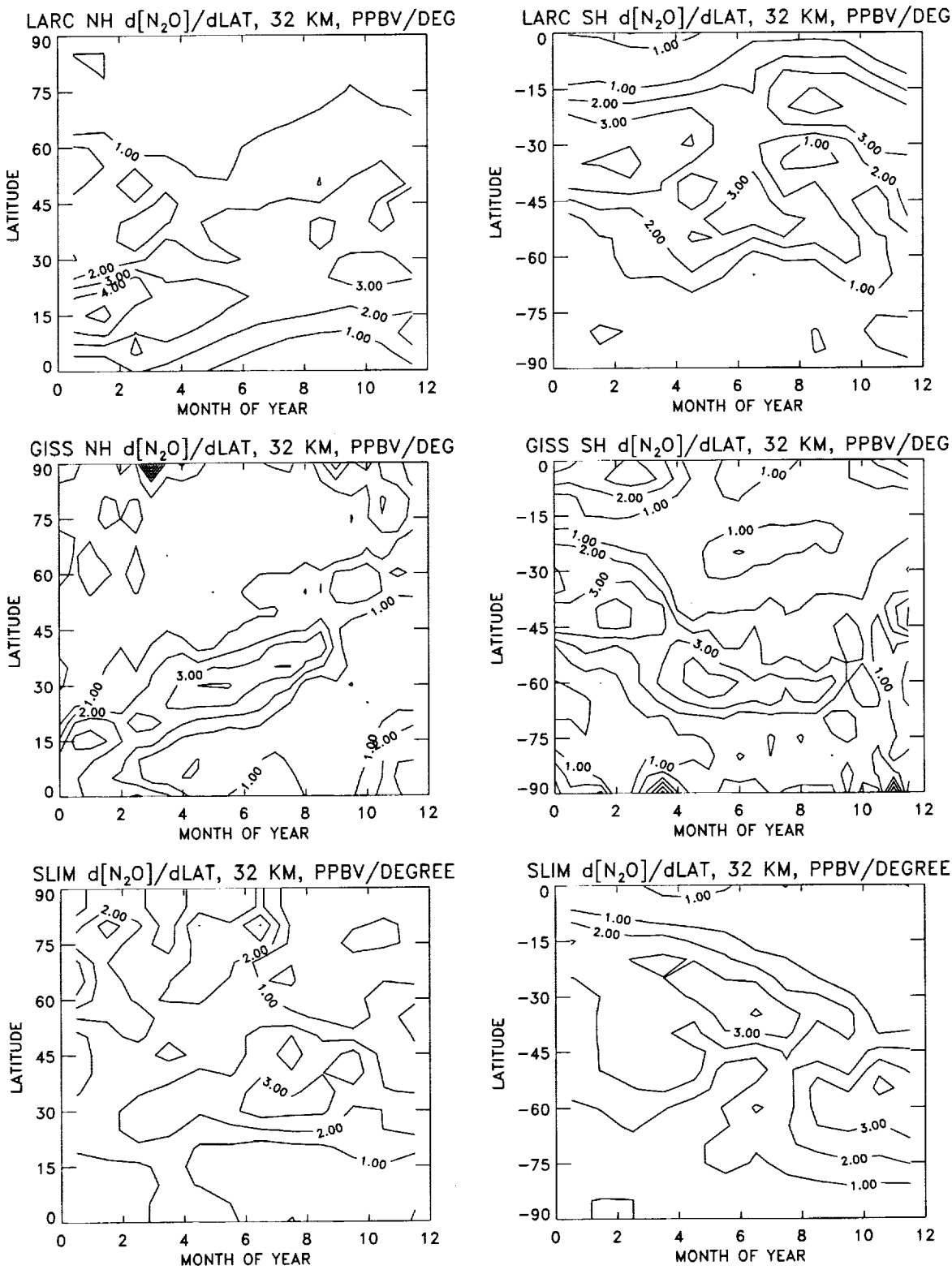

Figure 5.5.5. Continued.

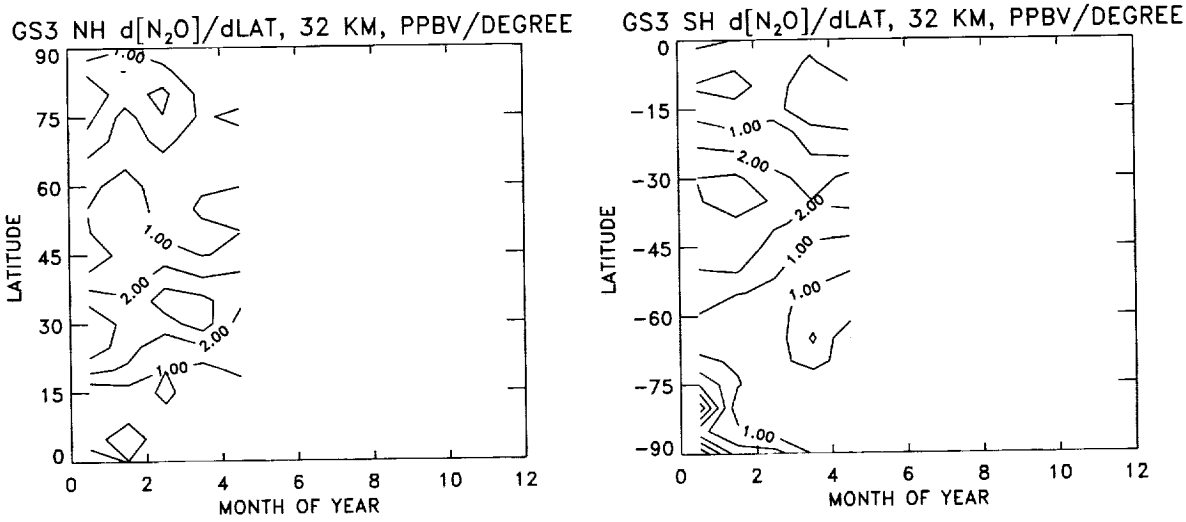

Figure 5.5.5. Concluded.

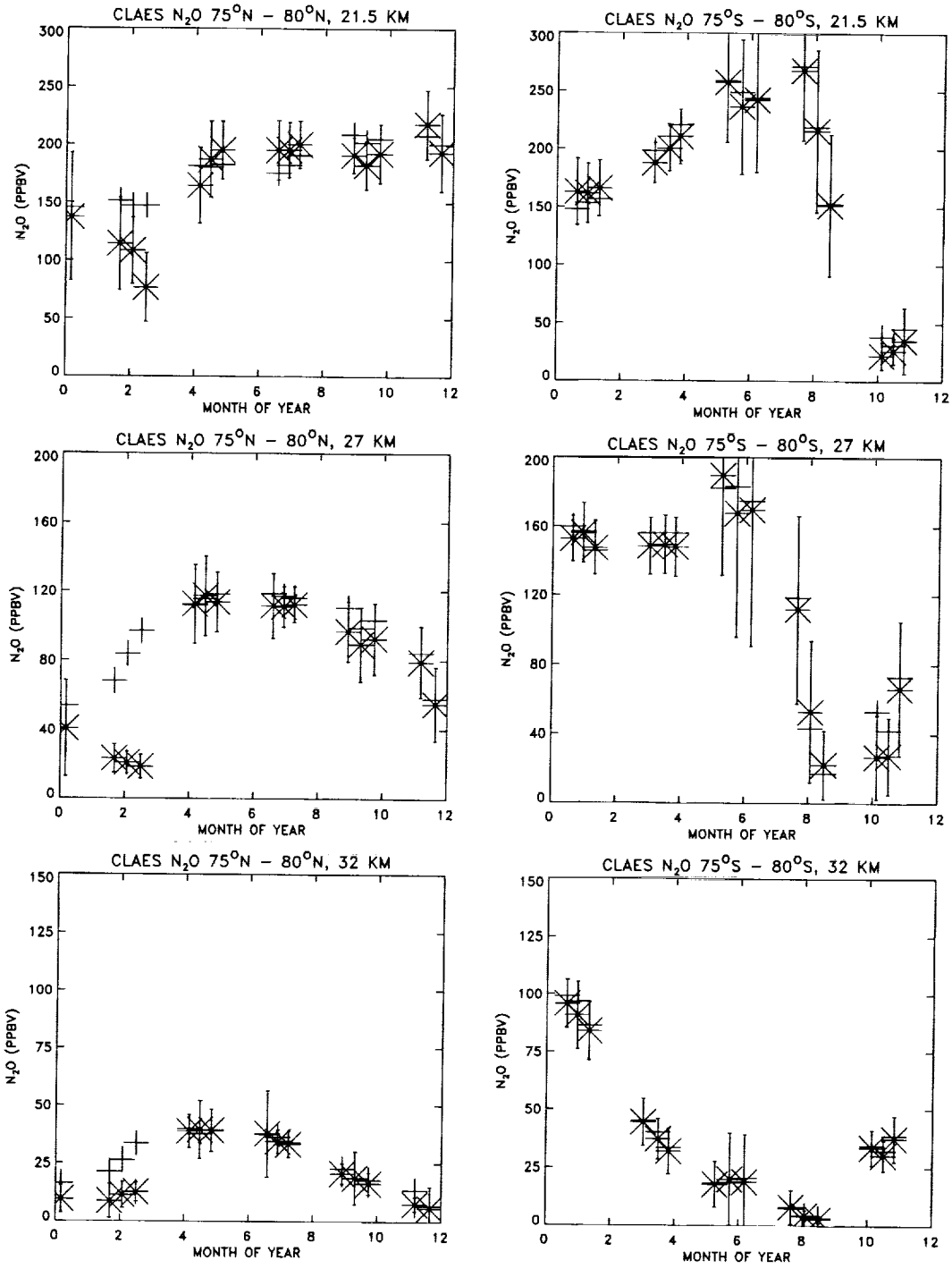

Figure 5.5.6. Seasonal cycle of CLAES version 8 N_2O in 1992 for the northern hemisphere (left side) and southern hemisphere (right side) at 21.5 km (top), 27 km (middle), and 32 km (bottom). Each of the points represent an average using approximately 12 days of data. Crosses indicate zonal mean averages between 75 degrees and 80 degrees. Asterisks represent equivalent latitude averages between 75 degrees and 80 degrees equivalent latitude. Error bars are plotted for the equivalent latitude points and indicate plus/minus 1 standard deviation. No instrumental error has been considered so the error bars indicate the statistical (and perhaps geophysical) variability of the data. The abscissae tick marks indicate the end of the month.

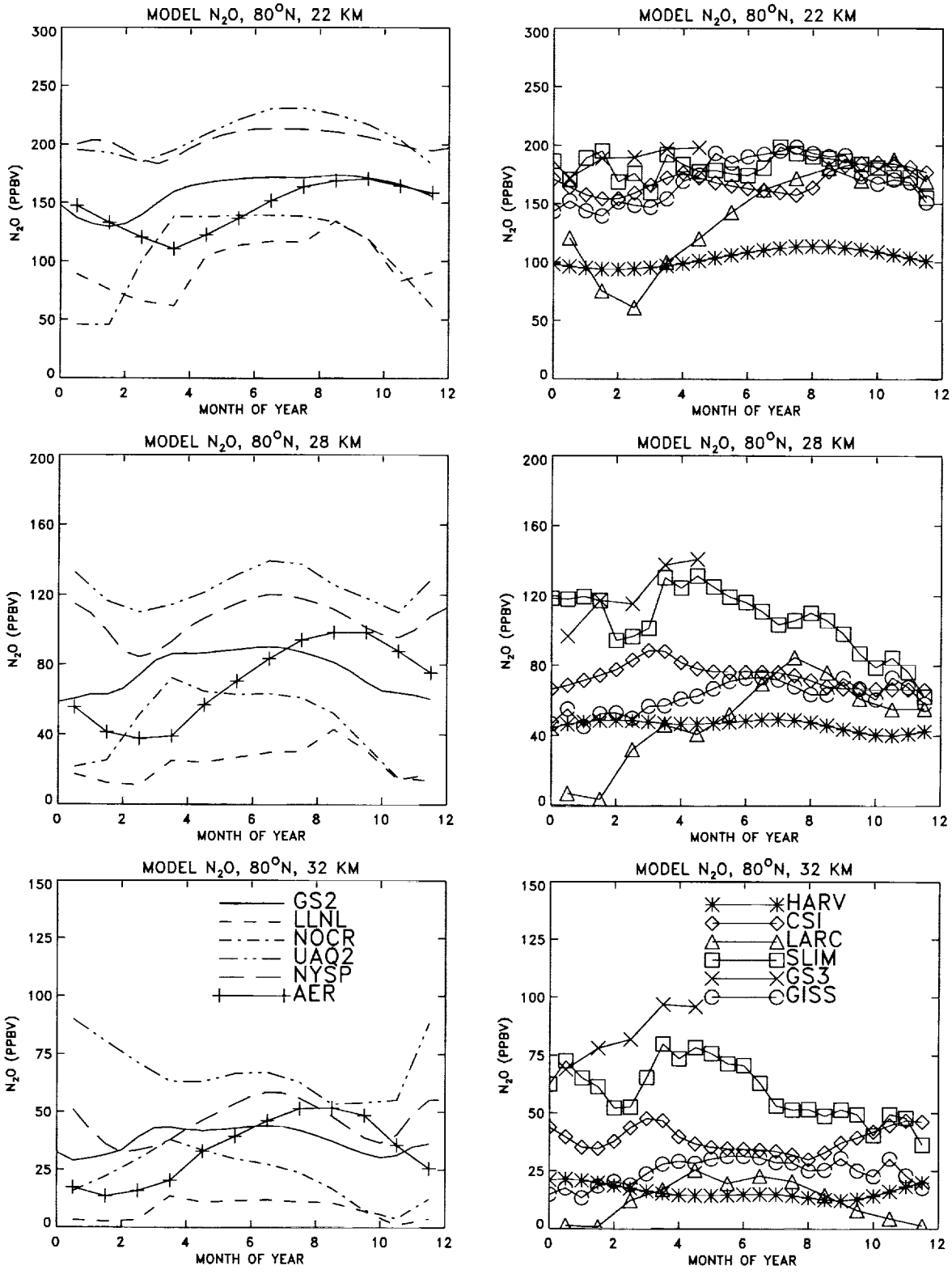

Figure 5.5.7. Seasonal cycle of N_2O at 80 degrees North for 8 2D and 4 3D models (see chapter text to determine which model is 2D and which is 3D). The left hand plots show the behavior of 6 models, and the right hand plots show the behavior of the remainder at 22 km (top), 28 km (middle) and 32 km (bottom). The abscissae tick marks indicate the end of the month.

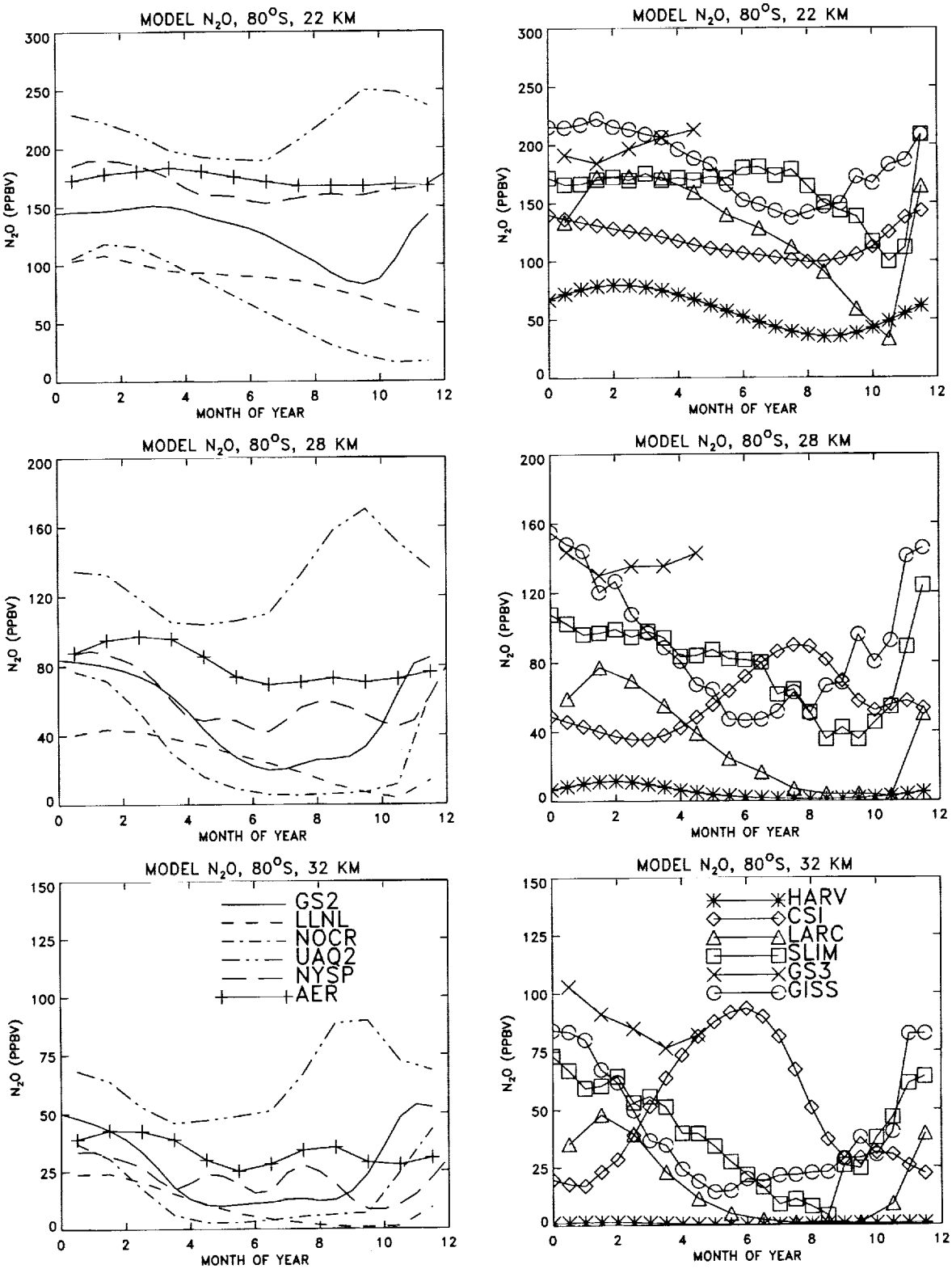

Figure 5.5.8. Same as Figure 5.5.7, but for the southern hemisphere.

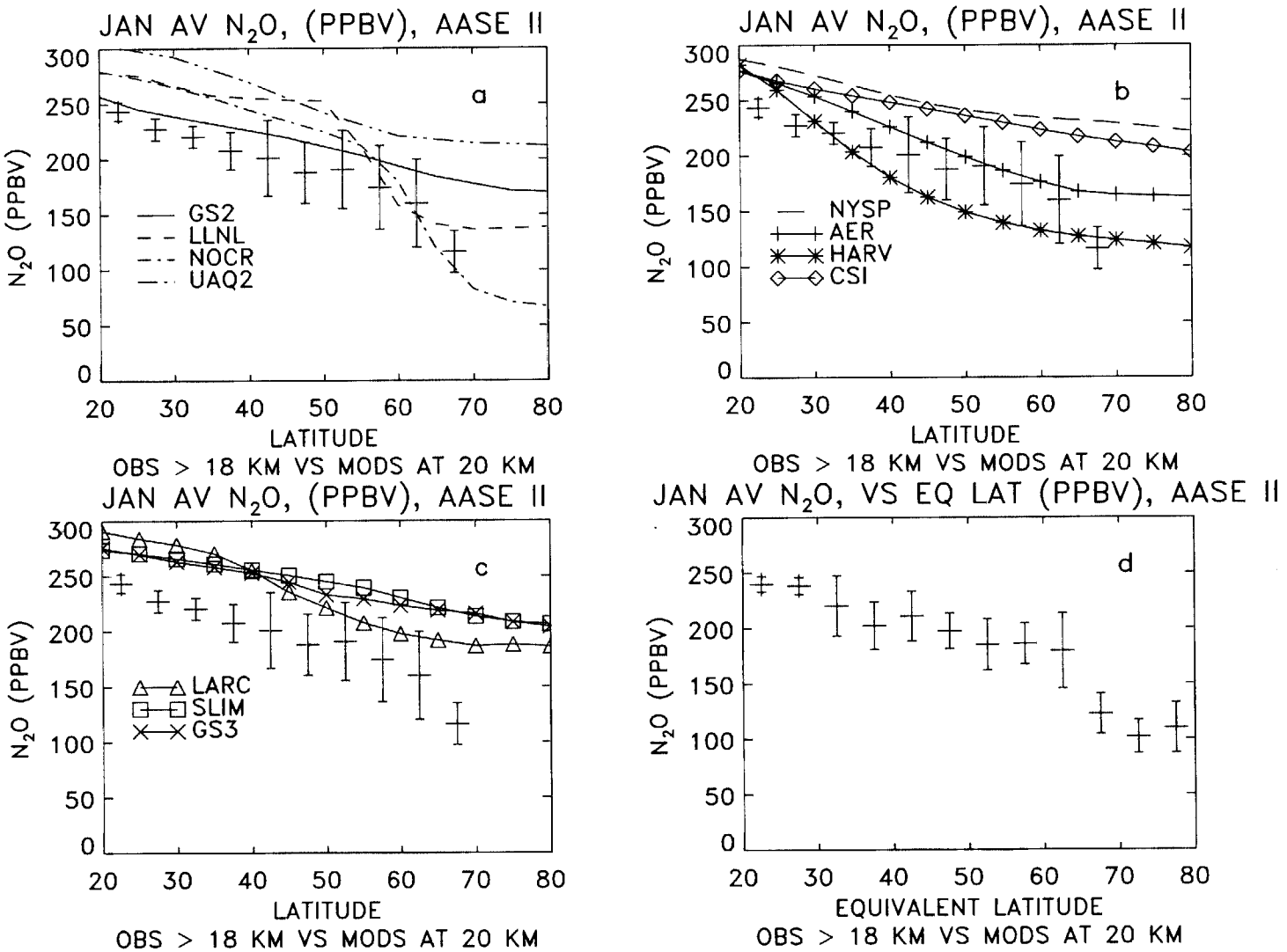

Figure 5.5.9. January N_2O mixing ratios in the northern hemisphere as a function of latitude. Crosses in plots a - c represent averages of all available N_2O data taken by the ER-2 aircraft during the AASE II mission with 5 degree resolution in latitude. The crosses in plot d shows the data averaged with 5 degree resolution in equivalent latitude. The ER-2 data was limited to that taken above 18 km in altitude. Also plotted in the figure are the N_2O mixing ratio distributions for 8 2D and 4 3D models at 20 km.

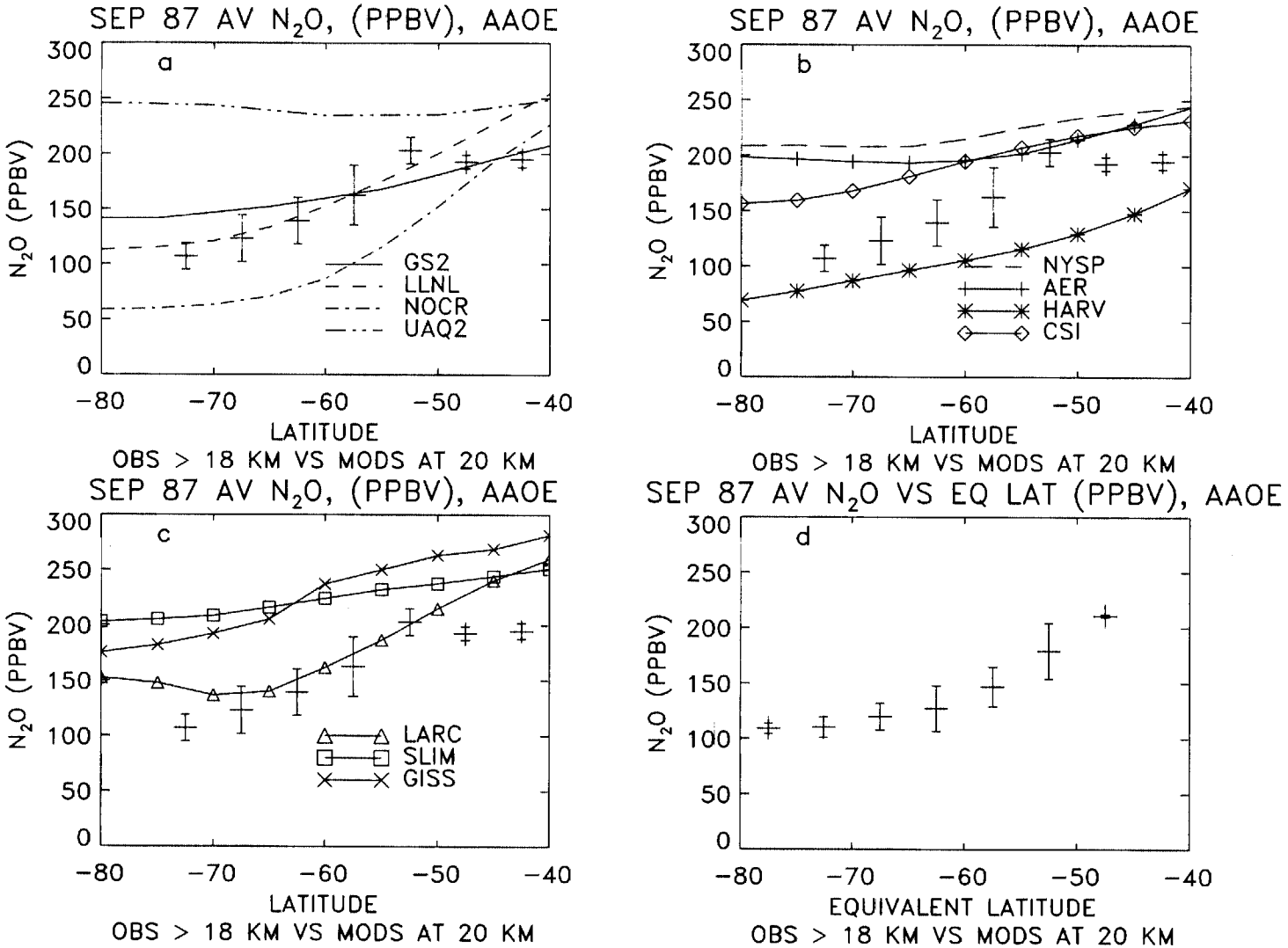

Figure 5.5.10. September N_2O mixing ratios in the southern hemisphere as a function of latitude. Plot is similar to Figure 5.5.9 but the data source is the 1987 AAOE mission.

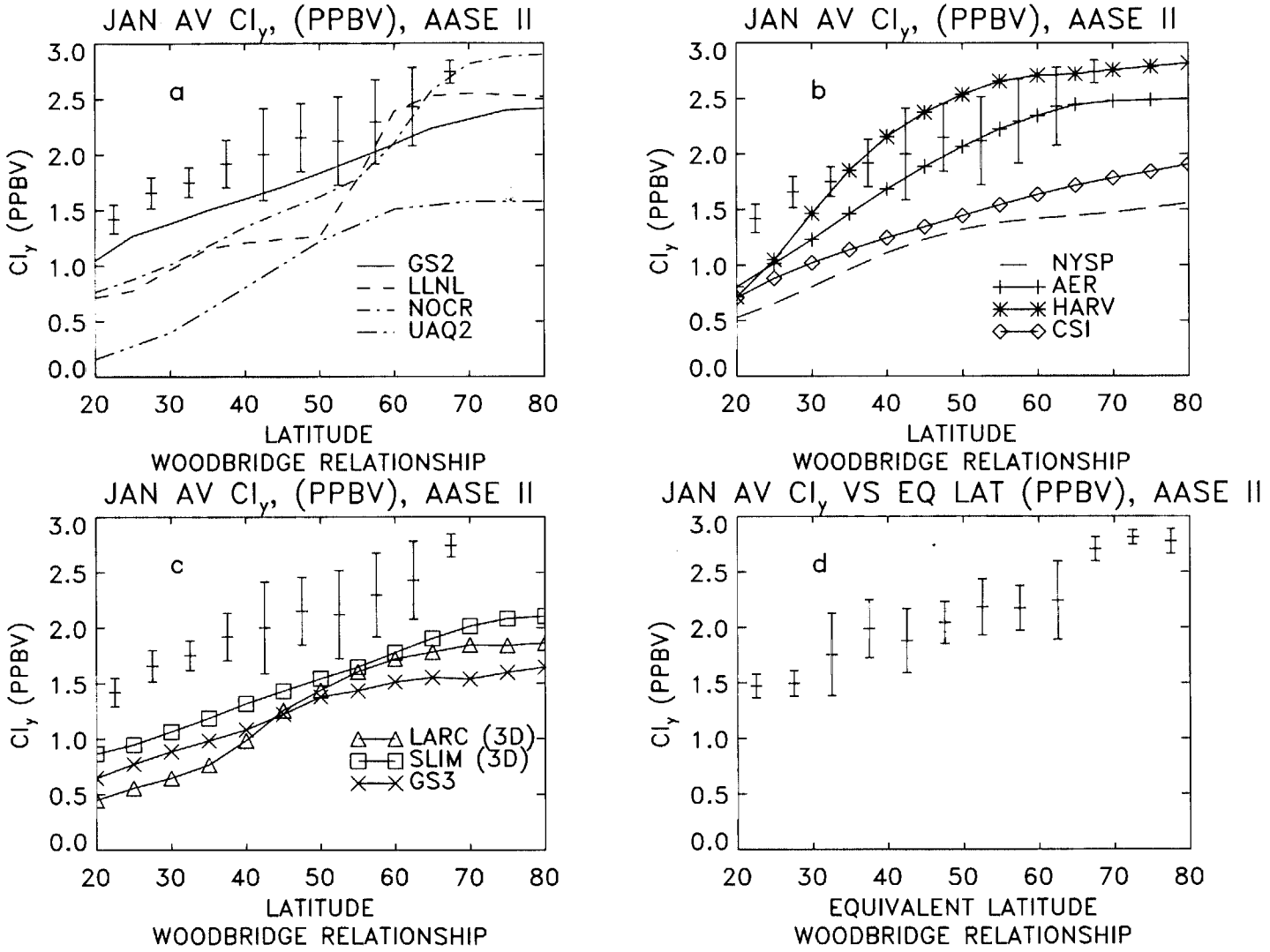

Figure 5.5.11. January Cly inferred from ER-2 N_2O observations taken during the AASE II aircraft mission compared with model calculations using the method of Woodbridge et al., 1995. Cly was first inferred from the N_2O observations, and then averaged as described in caption for Figure 5.5.9.

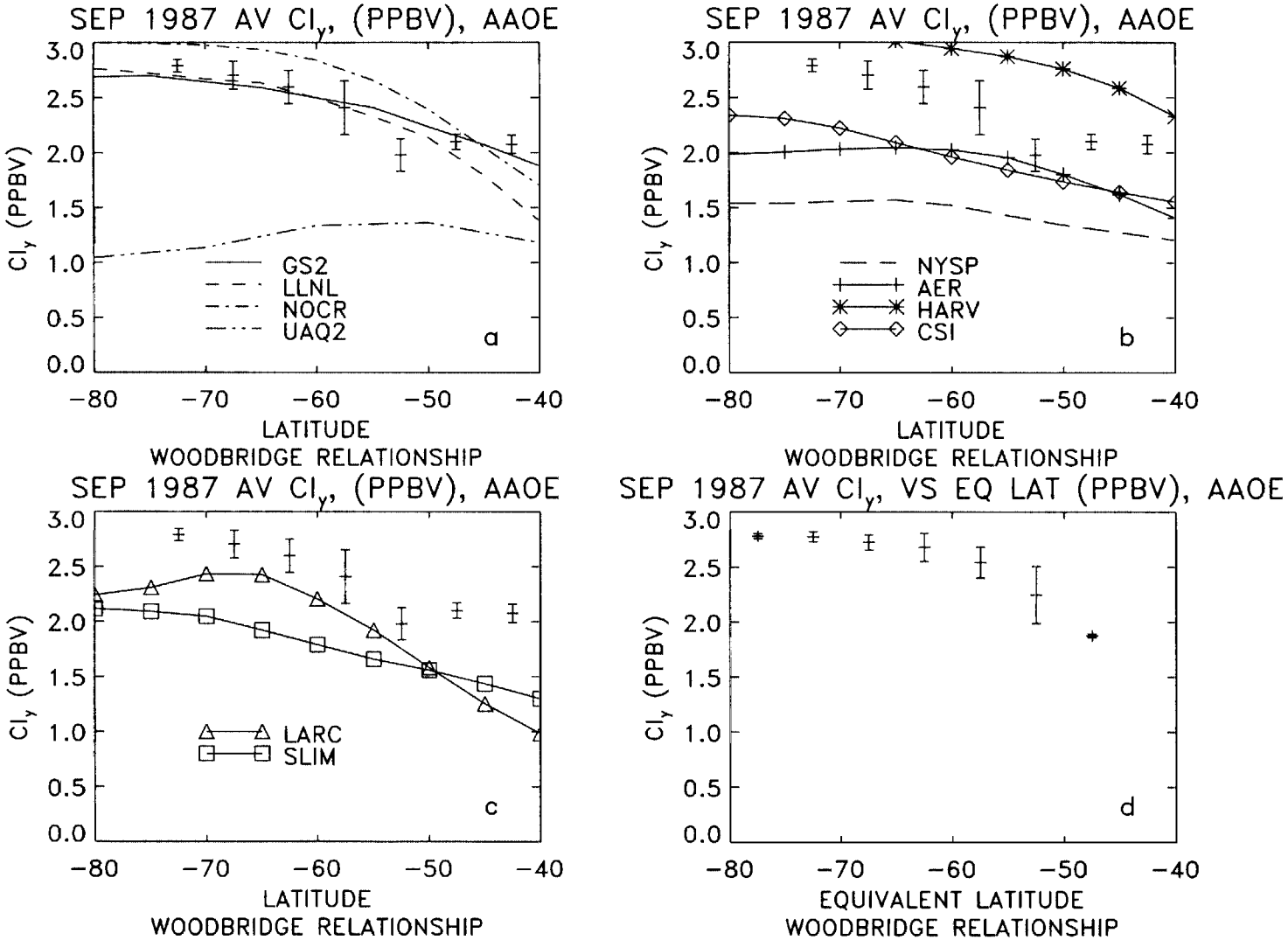

Figure 5.5.12. Cly inferred from ER-2 N_2O observations taken during the AAOE mission in September of 1987. The method for obtaining the values is that described in the text and the caption for Figure 5.5.11.

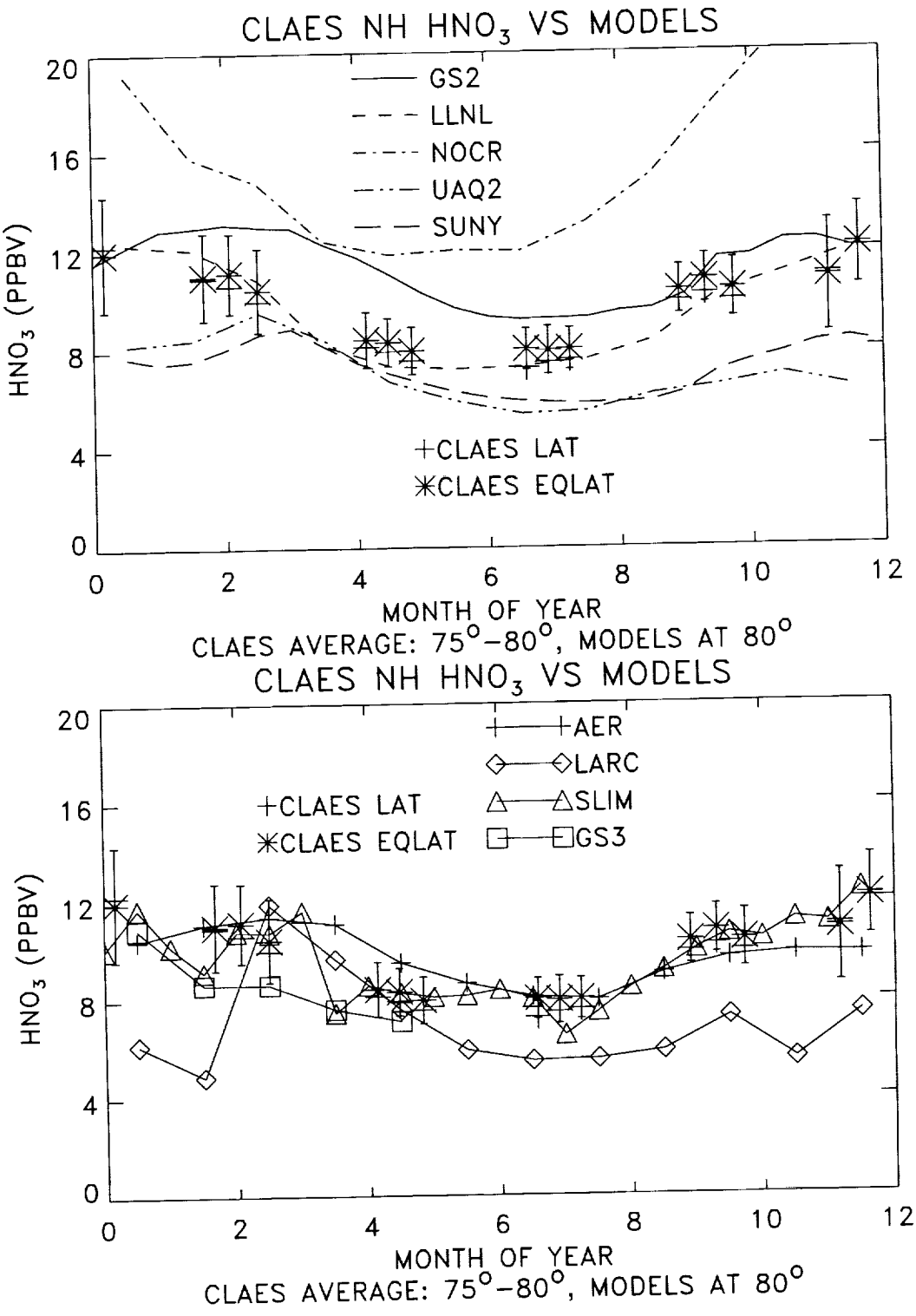

Figure 5.5.13. Seasonal cycle of HNO_3 at high northern latitudes. The heavy crosses represent zonal mean averages of CLAES version 8 HNO_3 between 75 and 80 degrees north. The heavy asterisks represent the data averaged between 75 and 80 degrees in equivalent latitude. Error bars on the equivalent latitude points show the statistical (geophysical) variability of the observations included in the average. Each point represents an average of all data taken during an approximately 12 day period. The data in the top and bottom plots are the same. Model seasonal cycles of HNO_3 are also shown in both the top and bottom plots, as indicated by the plotting legend. The abscissae tick marks indicate the end of the month.

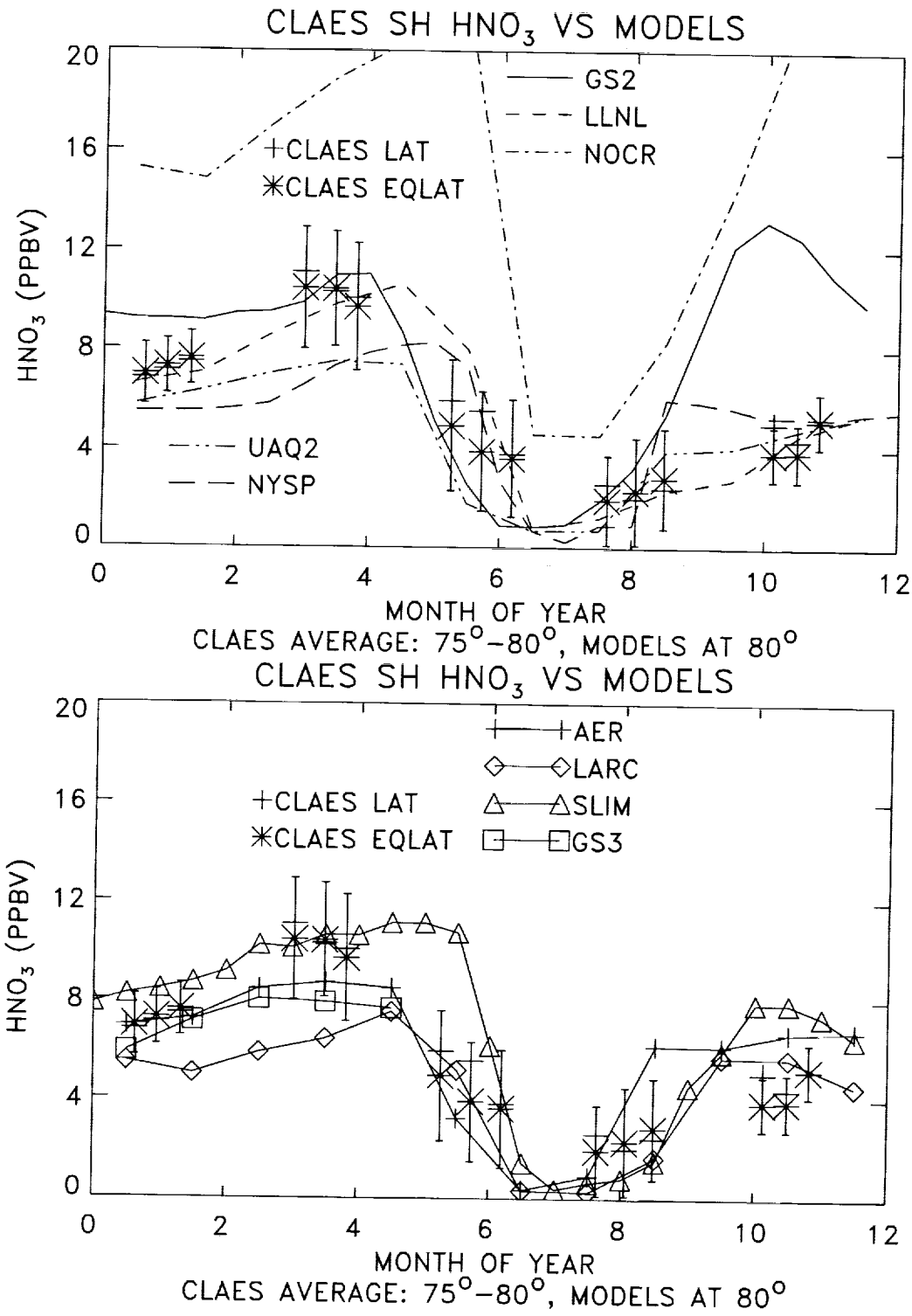

Figure 5.5.14. Same as Figure 5.5.13, for the southern hemisphere.

5.6 Chlorine Partitioning and Ozone in the Polar Vortex

Anne R. Douglass

NASA Goddard Space Flight Center

5.6.1 Introduction

A model calculation of the impact on ozone of polar processes during winter depends on the amount of inorganic chlorine, the extent to which the chlorine is activated, and the partitioning of the chlorine species. In this section, model ozone and ClO in the high latitude winter lower stratosphere are compared with MLS observations of ozone (Froidevaux et al., 1996) and ClO (Waters et al., 1996). The ClO depends on model descent, which affects total inorganic chlorine, the model scheme for release of reactive chlorine from the reservoirs HCl and $ClONO_2$ in the presences of PSC's or cold sulfate, and on the partitioning between ClO and the dimer Cl_2O_2. The ozone depends upon descent as well as chemical loss, which takes place largely through the dimer cycle.

Here, comparisons are made for the northern and southern winters for 6 two-dimensional models (AER, GSFC-2D, SUNY-SPB, UNIVAQ-2D, NOCAR, LLNL) and 3 three-dimensional models (LARC-3D, SLIMCAT, and GSFC-3D (northern winter only)).

5.6.2 Southern Hemisphere - Chlorine

Comparison of Cly

In 5.5 (Dynamical Signatures in Long-Lived Tracers) the model Cly at 20 km is compared with Cly as derived by Woodbridge et al. [1995] from observations of N_2O. The pair of model profiles of Cly for September and November are shown for the altitude range 14-26 km at 75S in Figure 5.6.1. The models are quite different in their Cly profiles. Although several of the models (GSFC-2D, LLNL, NOCAR) have reasonable amounts of Cly at 20 km 75S (> 2.5 ppbv) comparable to the inferred values as discussed above, the profile shapes are quite different. Except for UNIVAQ-2D and SUNY-SPB, all of the models show Cly between 2 and 3 ppbv at 20 km. At lower altitudes, the models diverge. NOCAR only falls to 2 ppbv by 14 km; the other models which are similar to the observations at 20 km are between 0.5 ppbv and 1.5 ppbv at 14 km. All of the models converge at higher altitude. The difference reflects the difference in descent and the amount of horizontal mixing in the models, which is also seen in the comparisons with N_2O. Several of the models (NOCAR, LLNL, GSFC-2D, LARC-3D) show continued descent between September and November, which is identified by an increase of 0.15 ppbv or more at 18 km.

Chlorine Activation

The models differ in the extent to which chlorine is released from its reservoirs HCl and $ClONO_2$ and found in ClO and its dimer. The ratio $(ClO + 2*Cl_2O_2)/Cly$ for September 15 at 75S is given in Figure 5.6.2. The models differ in both the maximum value of the activation and in the vertical extent over which polar processes are important. NOCAR, SLIMCAT, GSFC-2D and UNIVAQ-2D show a ratio as high as 0.8 somewhere in the profile. For UNIVAQ-2D, this is found between 22 and 24 km. For NOCAR and SLIMCAT, the region where activation is important is broad; the ratio is between 0.8 and

0.9 for the range 14 and 22 km. For GSFC-2D, the region of high activation is narrow, 16 - 18 km. For the other models, the activation is significantly lower, and in the case of the AER model, it is confined in altitude as well.

Model Comparisons with MLS ClO

As expected given the Cly profile differences and the differences in the activation, the model ClO profiles show significant variance. The daytime average ClO profiles on Sept. 15 at 65S and 75S are compared with MLS daily zonal averages at 46 hPa for a 10 degree latitude band centered at 65S and 75 S for Sept. 5-21, 1992 in Figure 5.6.3. The daily zonal averages are shown on the figure for both latitudes; the ClO average decreases nearly monotonically with time. From MLS observations [Waters et al., 1996], we expect that ClO is less than a few tenths ppbv at 100 hPa (~16 km), and 22 hPa (~27 km) (not shown on this figure). At 75S, the models tend to underpredict ClO, with the exception of the NOCAR model; however, only NOCAR shows ClO greater than 1 ppbv as low as 15 km. At 65S, the models are more consistent with the observations, partly because there is much less active chlorine (observed or modeled). Again, NOCAR has the highest ClO. This is consistent with the high Cly (and low N_2O) found at high latitudes, and also consistent with the high chlorine activation.

Partitioning of ClO/Cly and Cl_2O_2/ClO

The models also show variance in the partitioning between Cl_2O_2 and ClO, which is shown for September 15 at 75S in Figure 5.6.4. The amount of variance is surprising, given that these two constituents are simply related through the formation reaction for Cl_2O_2 which should be balanced by its thermal decomposition and photolysis. The models also show variance in ClO/Cly (Figure 5.6.5). The NOCAR model has the highest ratio over the largest range. LARC-3D, AER, SLIMCAT and GSFC-2D all show ClO/Cly to be about 0.4 between 18 and 20 km; the models diverge from one another at higher and lower altitude.

The bottom line for this section is that there are several key areas which are different among the models and which affect ClO. The total Cly, the fraction of activation, and the partitioning among chlorine species all differ significantly. In comparing with the MLS ClO, at 75S only the NOCAR and the LARC-3D model have a peak value close to the observations. Knowledge (observations) of the profile of total inorganic chlorine and the efficiency of activation would provide a key discriminator among the models.

5.6.3 Southern Hemisphere - Ozone

The daytime zonal average ozone is given as a function of time at 100, 46 and 22 hPa in Figure 5.6.6 for 65S and Figure 5.6.7 at 75S for 8 models and for MLS observations. The model ozone differs from observations for all models in significant ways. The seasonal change at the highest MLS level shown (22 hPa) is generally underestimated - only the SLIMCAT model shows comparable low values in June and a strong buildup in December. MLS shows low ozone at 46 hPa in early September which decrease steadily. None of the models show as strong temporal decrease of ozone as observed by MLS at 20-22 km. The model ozone difference is generally smaller than observed by MLS. At 100 hPa, several of the models show a strong decrease in ozone, and agree fairly well with MLS at the end of the year. Only the NOCAR model approximates the decrease in ozone between day 250 and day 300, but this model also greatly exceeds the observed ozone around day 180.

The model change in ozone is somewhat related to the model Cl_2O_2 and ClO, but there is significant variance among the models. The maximum change in ozone between October and September for each model is plotted as a function of the September ClO at that level in Figure 5.6.8(a) and as a function of the September Cl_2O_2 at that level in Figure 5.6.8(b). This is a simplistic view of the ozone change, but the average Cly changes in the lower stratosphere over the month (Figure 5.6.1) are small, suggesting limited influence of descent and mixing. The model change is directly related to the magnitude of the ClO and Cl_2O_2, but the broad dependence shown in Figure 5.6.8 reflects the differences in the models that also affect the partitioning. The differences in the models and the modeled ozone change are a result of differences in the total cly, in the polar processes though which chlorine is activated, and the partitioning between ClO and Cl_2O_2.

5.6.4 Northern Hemisphere - Chlorine

Comparison of Cly

The Cly profiles at February at 75N are shown in Figure 5.6.9. The models show a wide range for Cly, and a somewhat different profile shape. As in the southern hemisphere, this is indicative of the difference in the model descent and horizontal mixing. As in the southern hemisphere, the model calculated ozone loss will depend sensitively on Cly, the degree of activation, and the partitioning between ClO and Cl_2O_2.

Chlorine Activation

All of the models show less chlorine activation in the winter northern hemisphere than in the southern hemisphere. There is still significant variance among the models. At 20 km, the percent of chlorine in ClO and the dimer ranges from a low of about 10% (GSFC-2D) to a high near 40% (UNIVAQ-2D). This is shown in Figure 5.6.10.

Model Comparisons with MLS ClO

It is more difficult to compare these models with MLS ClO in the northern hemisphere than in the southern, since the MLS shows much more variability. Figure 5.6.11 shows the model ClO profiles at 65N and at 75 N, and the daily vortex average MLS ClO for each of 4 years. During every year except 1992, the MLS ClO was much higher than is calculated in these models. GSFC-3D and SLIMCAT use winds and temperatures appropriate for 1992, and compare well with each other and with the MLS observations. All of the other models should be producing a climatological value for ClO. One problem is that in February, the vortex average ClO is elevated partly because the vortex is pushed off the pole to lower latitude. In the model, there are never psc's at latitudes lower than 60. In the models, the greatest chance for psc's is in January and February, where there is little sun at high latitudes.

5.6.5 Northern Hemisphere - Ozone

In the northern winter lower stratosphere, ozone can be affected by both transport and photochemistry. Downward motion tends to increase the ozone, and chlorine processes produce ozone loss. In several winters, Manney et al. (1994, 1995) have compared ozone for a conservative calculation with observations from MLS to derive the chemical ozone change.

The MLS zonal average ozone is compared with the model zonal average at 75N for December-April in Figure 5.6.12. For MLS, the vortex average is nearly equal to the zonal average at 75N throughout the time period. The comparisons between MLS and the models at 65N are qualitatively similar. The vortex average from MLS shows very low values at the end of 1996 and 1997 winters, consistent with the high ClO found those years. Since the model chlorine activation is more consistent with 1992 than the later years, it is not surprising that the model ozone does not show such low mixing ratios. It is perhaps more significant that most of the models show a somewhat different seasonal cycle for 1992 when the ozone loss derived by Manney et al. (1994) is not large. MLS ozone increases in March, and in most of the models the ozone mixing ratio peaks in February or by March 1. Exceptions are the two of the 3D models (SLIMCAT model and GSFC-3D), the NOCAR model and the CSIRO model. The differences among the model seasonal change in O_3 are reflected in the differences in the among model seasonal changes in N_2O; it is important to account for effects of both descent and horizontal mixing as discussed above.

These northern hemisphere comparisons also illustrate the difficulty in calculating the effects of polar processes in the northern hemisphere in an assessment model. The effects show large interannual variability, which is not simulated in climatological models. Models using assimilated data for inputs (SLIMCAT and GSFC-3D) may reproduce the interannual variability for observed years, but unless an assessment included meteorological data from many different years for input, these models would not simulate the interannual variability either. If the response of the model to a perturbation is sensitive to the model base calculation for the effects of psc's, then an assessment calculation would need to encompass a wide range of base perturbations to cover observed variability and make a reasonable evaluation of the perturbation sensitivity.

References

Froidevaux, L., W. G. Read, T. A. Lungu, R. E. Cofield, E. F. Fishbein, D. A. Flower, R. F. Jarnot, B. P. Ridenoure, Z. Shippony, J. W. Waters, J. J. Margitan, I. S. McDermid, R. A. Stachnik, G. E. Peckman, G. Braathen, T. Deshler, J. Fishman, D. J. Hofmann, and S. J. Oltmans, Validation of UARS Microwave Limb Sounder ozone measurements, J. Geophys. Res., 101, 10017-10060, 1996.

Manney, G. L., L. Froidevaux, J. W. Waters, R. W. Zurek, W. G. Read, L. S. Elson, J. B. Kumer, J. L. Mergenthaler, A. E. Roche, A. O'Neill, R. S. Harwood, I. MacKenzie, and R. Swinbank, Chemical depletion of ozone in the Arctic lower stratosphere during winter 1992-93, Nature, 370, 429-434, 1994.

Manney, G. L., R. W. Zurek, L. Froidevaux, and J. W. Waters, Evidence for arctic ozone depletion in late February and early March 1994,' Geophys. Res. Lett., 22, 2941-2944, 1995.

Waters, J. W., W. G. Read, T. A. Lungu, L. Froidevaux, V. S. Perun, R. A. Stachnik, R. F. Jarnot, R. E. Cofield, E. F. Fishbein, D. A. Flower, J. R. Burke, J. C. Hardy, L. L. Nakamura, B. P. Ridenoure, Z. Shippony, R. P. Thurstans, L. M. Avallone, D. W. Toohey, R. L. deZafra, and D. T. Shindell, Validation of UARS MLS ClO measurements, J. Geophys. Res., in press, 1996.

Woodbridge, E. L., et al., Estimates of total organic and inorganic chlorine in the lower stratosphere from in situ and flask measurements during AASE II, J. Geophys. Res., 100, 3057-3064, 1995.

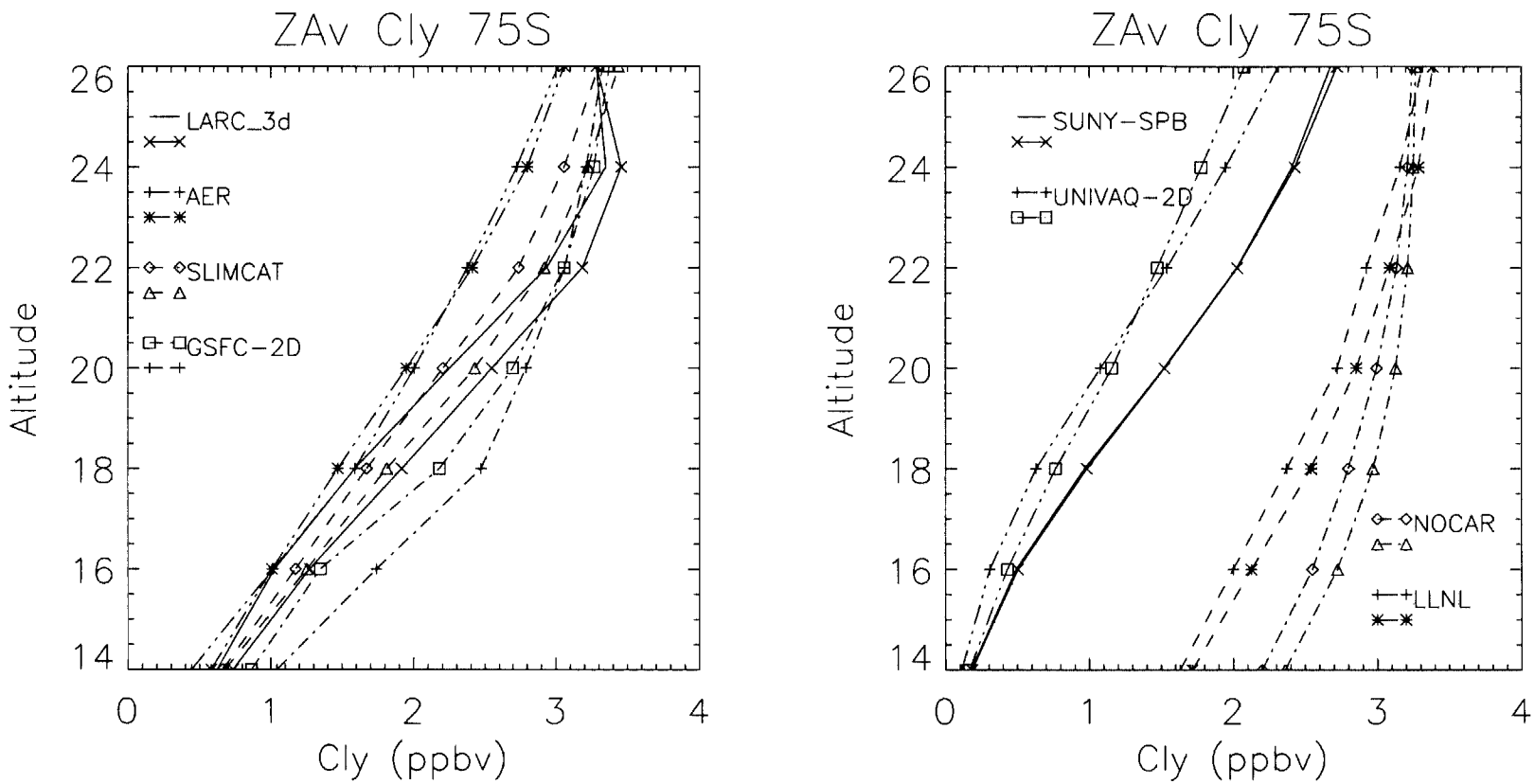

Figure 5.6.1. The total inorganic chlorine from 8 models at 75S is shown as a function of altitude. The pair of lines for each model represents the profiles in September and November, to provide a sense of how the Cly is changing during this important period for ozone loss. Near 20 km, the models show a wide range of values for Cly, from about 1 ppbv to 3 ppbv. Several of the models (NOCAR, LLNL, GSFC-2D, LARC-3D) show continued descent between September and November, which is identified by an increase of 0.15 ppbv or more at 18 km.

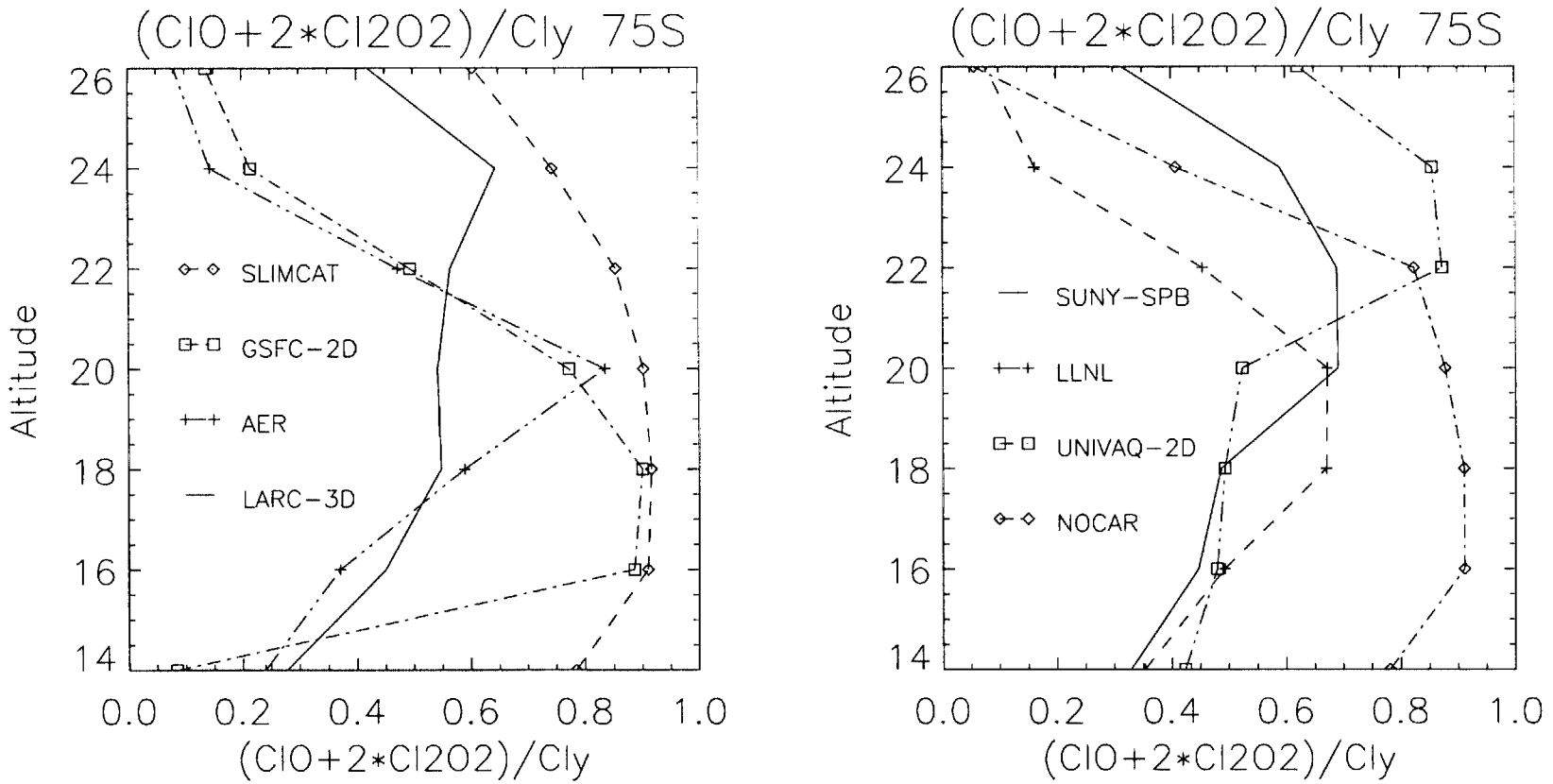

Figure 5.6.2. The profiles of ($ClO+2Cl_2O_2$)/Cly provide a measure of the efficiency of chlorine activation in the models. This varies among the models both in the maximum activation achieved and in the profile shapes.

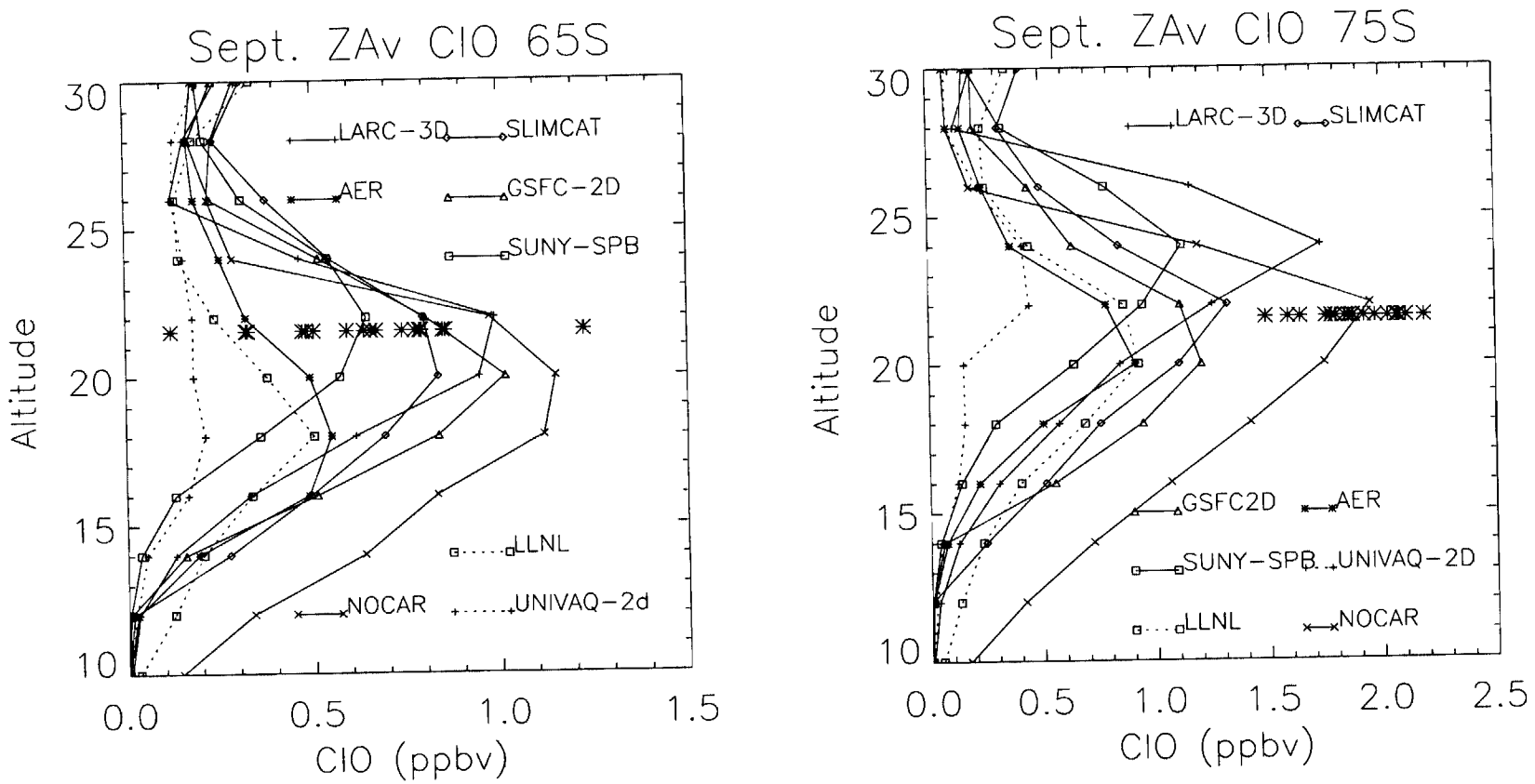

Figure 5.6.3. The models vary in their estimates of ClO, which are given at 65S and 75S for 8 models. Also shown on the figures are the daily zonal average daytime ClO mixing ratios for the month of September. These decrease nearly monotonically throughout the month. At 65S, ClO in many of the models (which are shown for Sept. 15) is near to the MLS measurement. At 75S, only the NOCAR model ClO is near to the MLS mixing ratio.

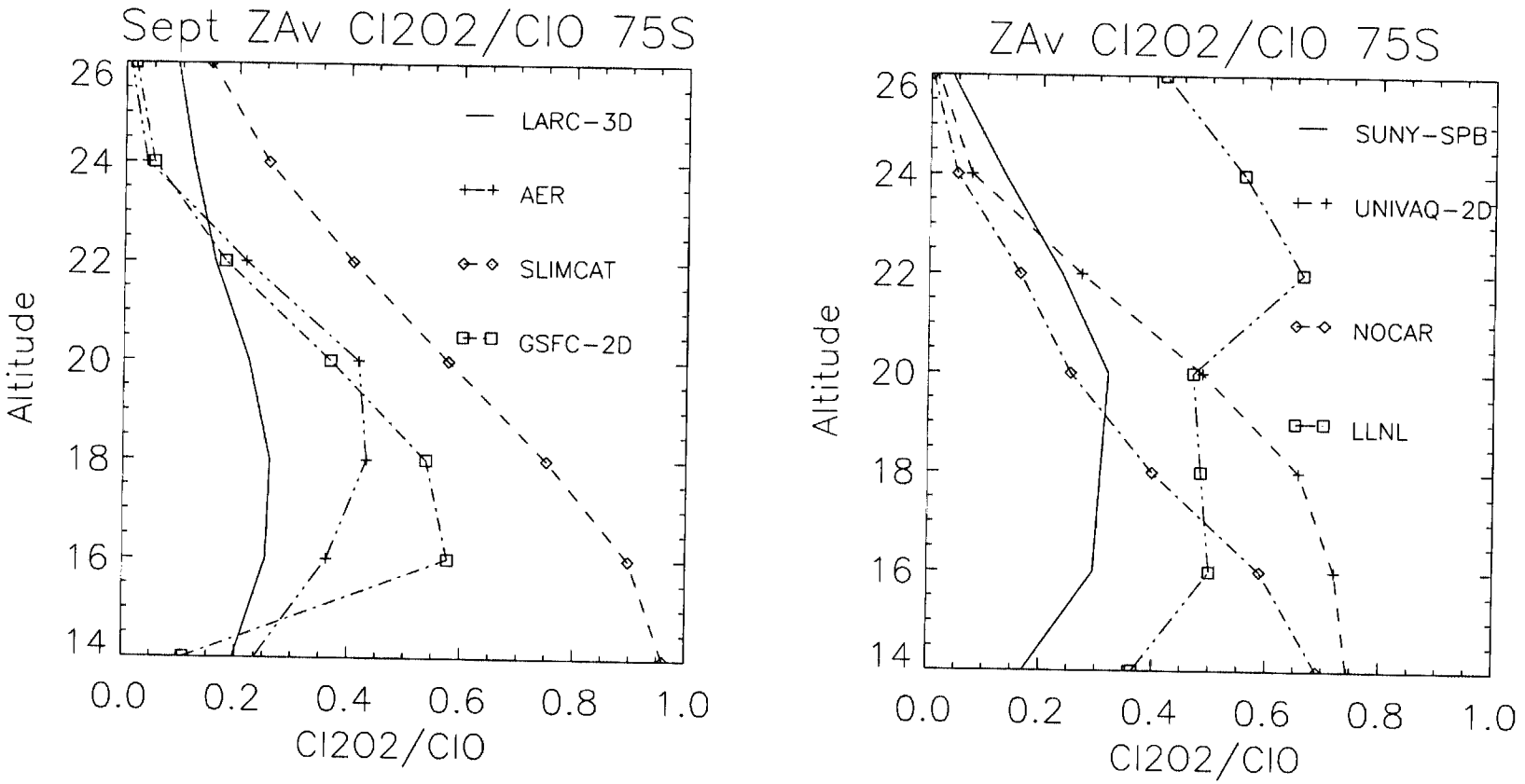

Figure 5.6.4. The models also differ in the ratio Cl2O2/ClO, which should be in photochemical equilibrium in the models. This points to a difference either in the rate of dimer formation or thermal decomposition, or to a difference in the photolysis rate of the dimer.

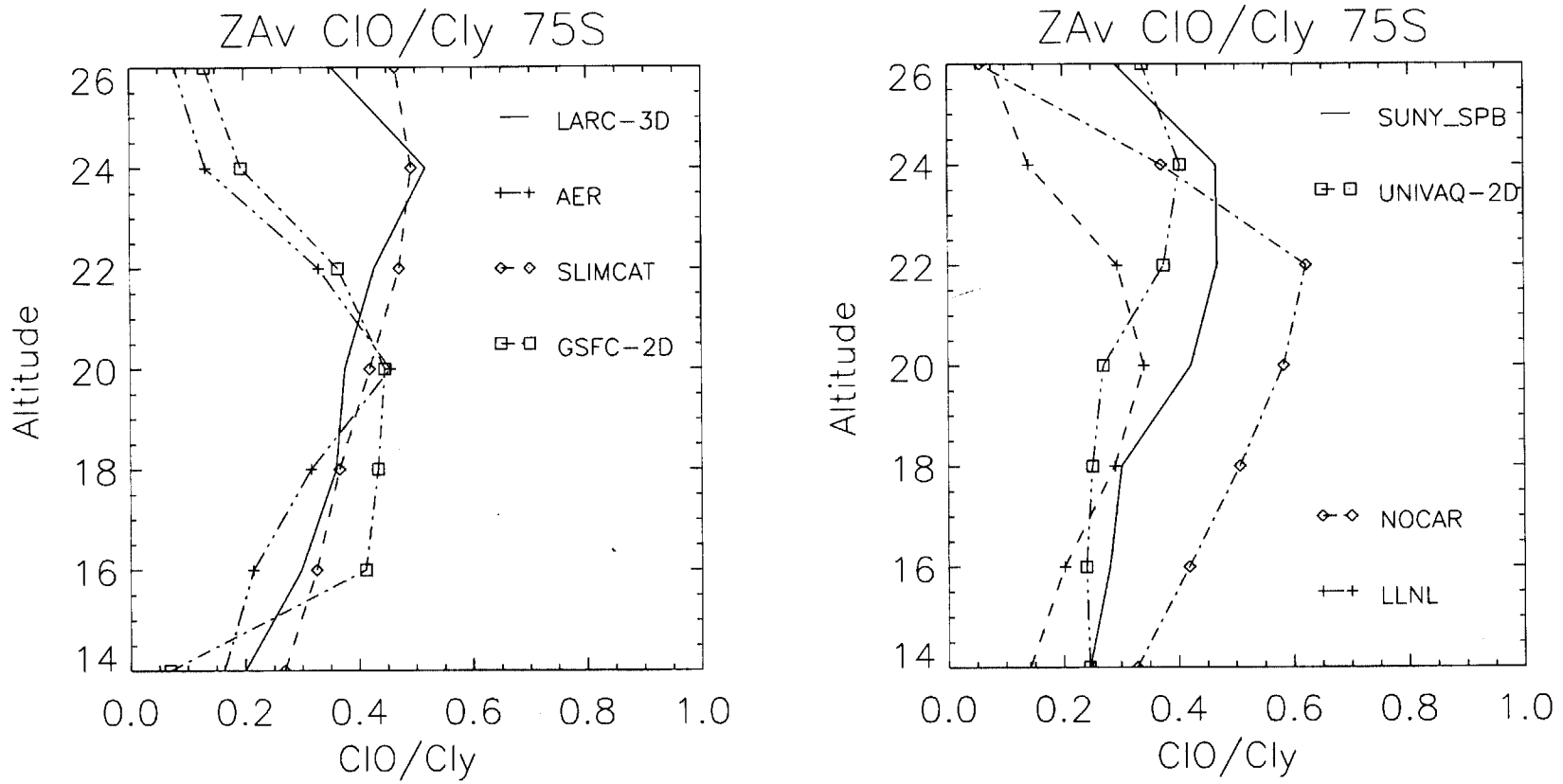

Figure 5.6.5. ClO/Cly varies for the models from about 0.2 to close to 0.6 at about 20 km. This variation is expected given the differences in activation efficiency and in partitioning between ClO and the dimer.

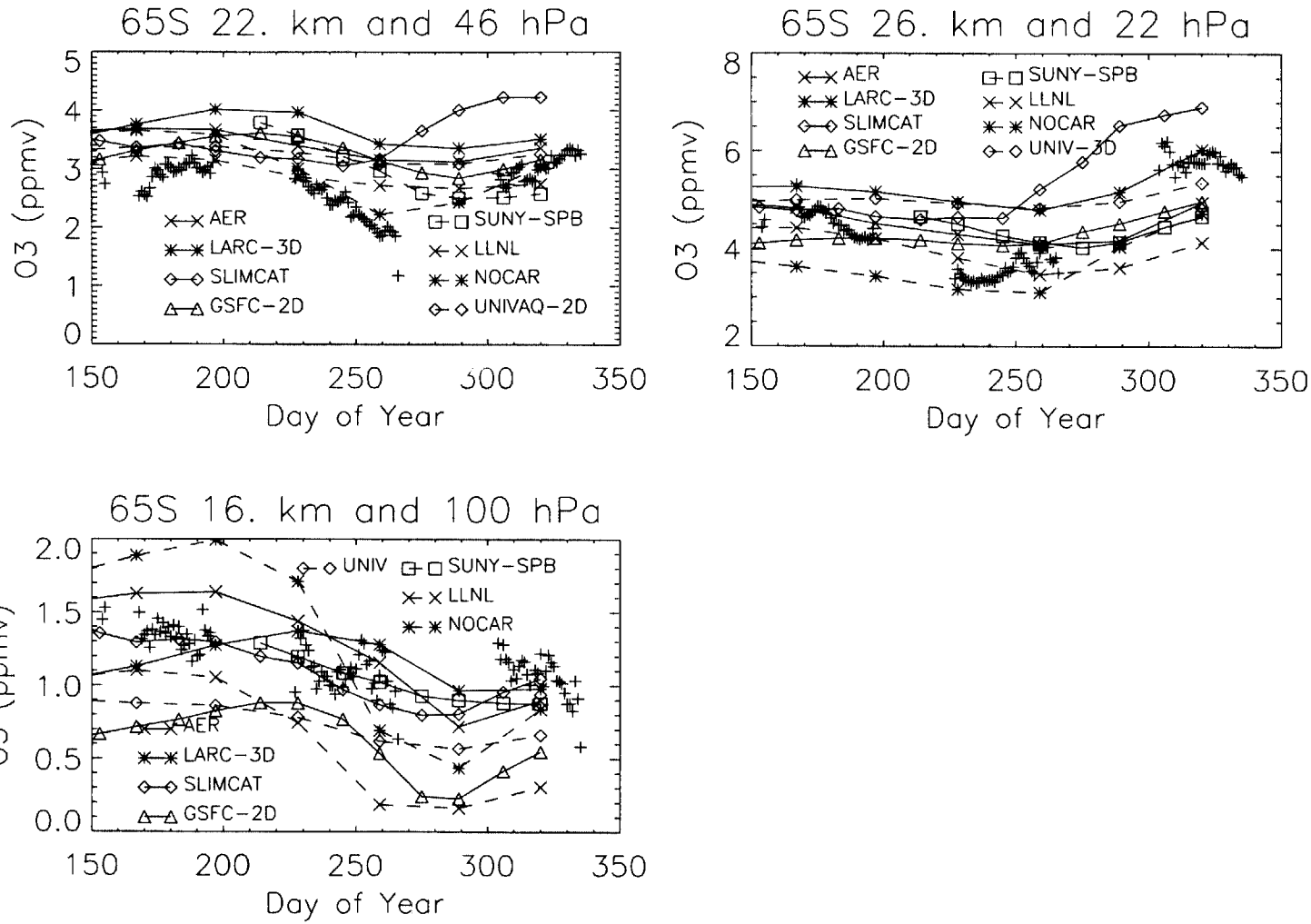

Figure 5.6.6. MLS ozone is compared with the models at 65S at three altitudes. The models are in poor agreement with the seasonal changes inferred from MLS. None of the models matches the steep rate of decrease of O_3 observed at 65S at 22 km.

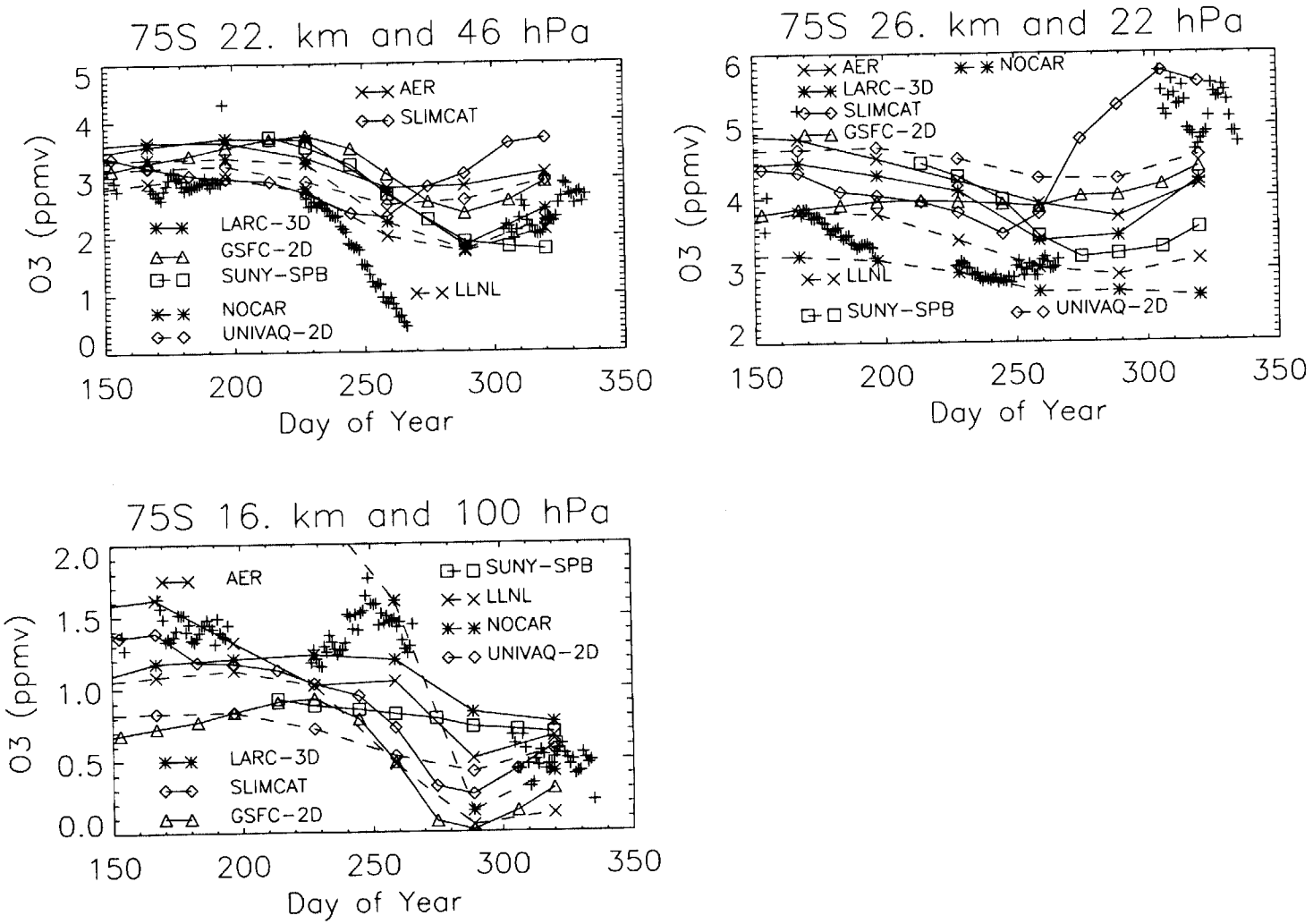

Figure 5.6.7. Same as Figure 5.6.6 for 75S. None of the models matches the steep rate of decrease of O_3 observed at 75S at 22 km. None of the models matches the seasonal behavior observed at 16 km. Only the SLIMCAT model shows fair agreement with the ozone seasonal changes observed at 26 km.

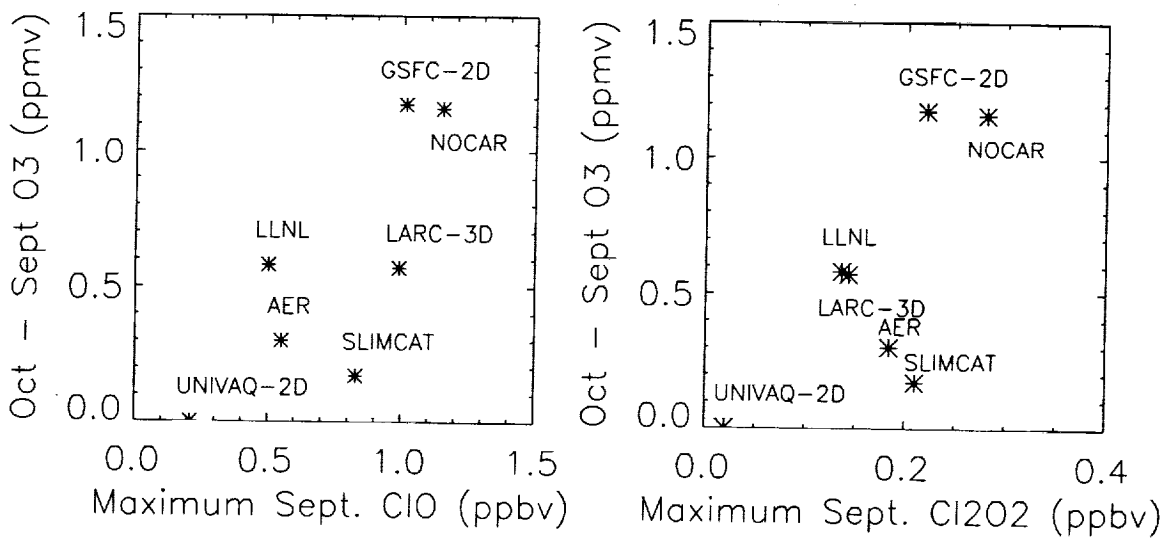

Figure 5.6.8. In the models, the change in ozone between September and October is related to the maximum ClO or to the maximum Cl_2O_2, i.e., larger ozone changes are found for models with more ClO and Cl_2O_2. There is variance in this relationship, reflecting the other differences in the partitioning and photochemistry seen in Figures 5.6.1 to 5.6.5.

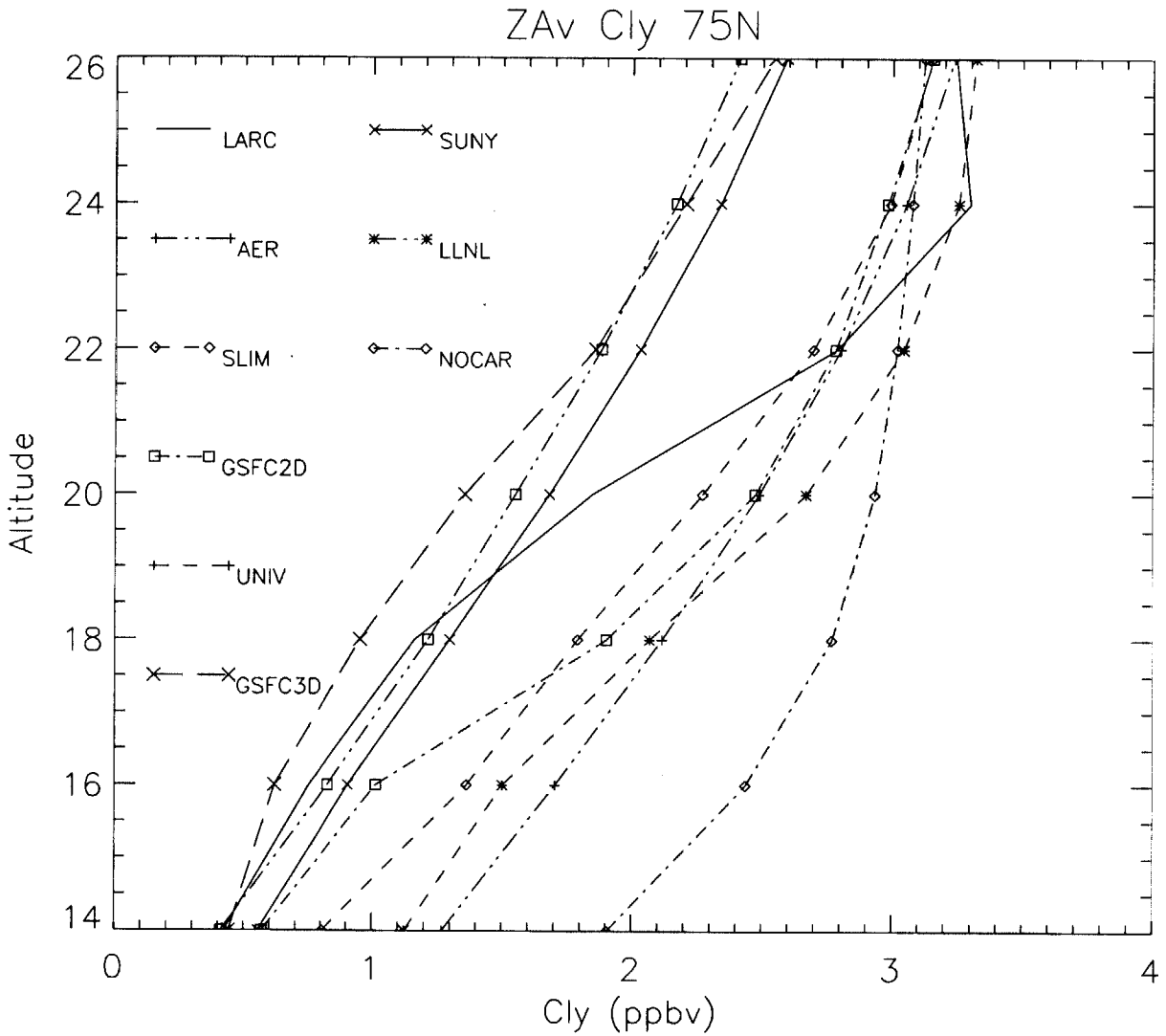

Figure 5.6.9. The Cly at 75N shows a great deal of variance among the models, varying from about 1.3 to about 2.9 at 20 km.

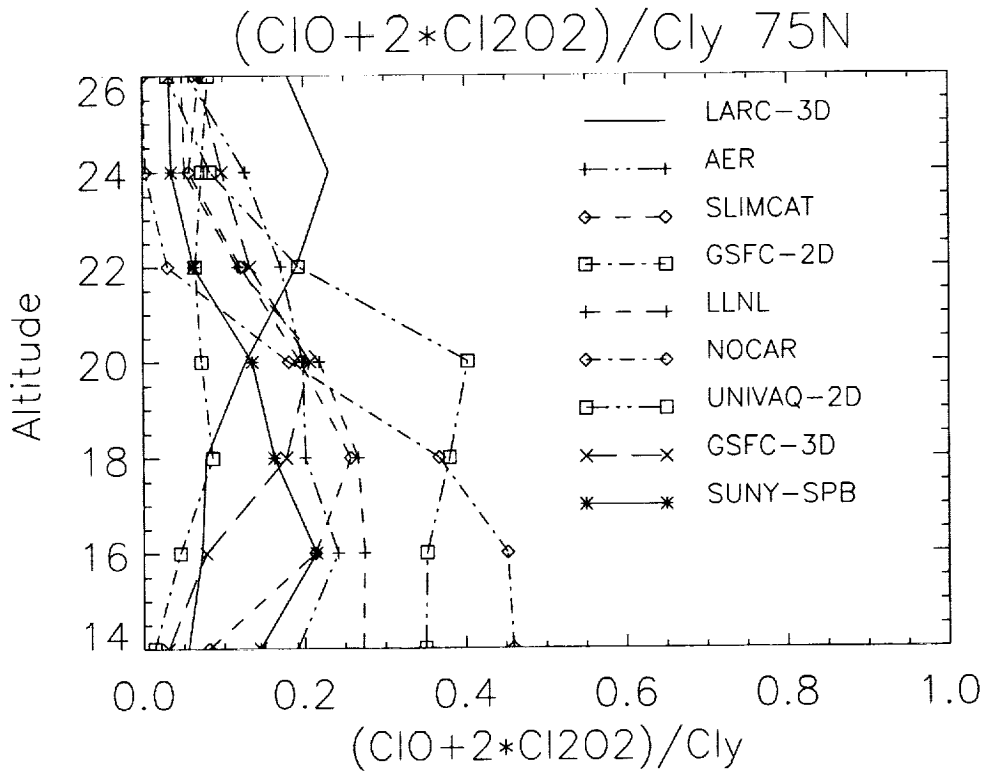

Figure 5.6.10. As in the southern hemisphere (Figure 5.6.2) the efficiency of chlorine activation varies greatly among the models, from about 0.1 to 0.4 at 20 km.

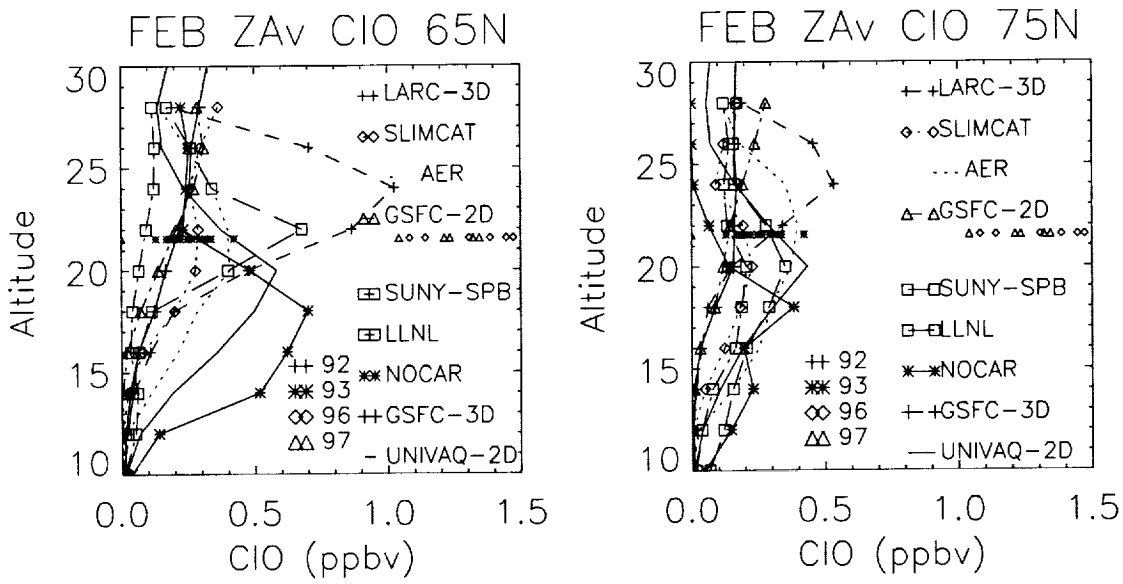

Figure 5.6.11. The daytime zonal average model ClO at 65N and 75N is compared with vortex averaged daytime MLS ClO. The northern hemisphere ClO is highly variable from year to year. The models are in overall fair agreement with MLS for 1992 (which was a year with relatively little chemical ozone depletion (Manney et al., 1994)). None of the models approach the high values seen in 1996 and 1997.

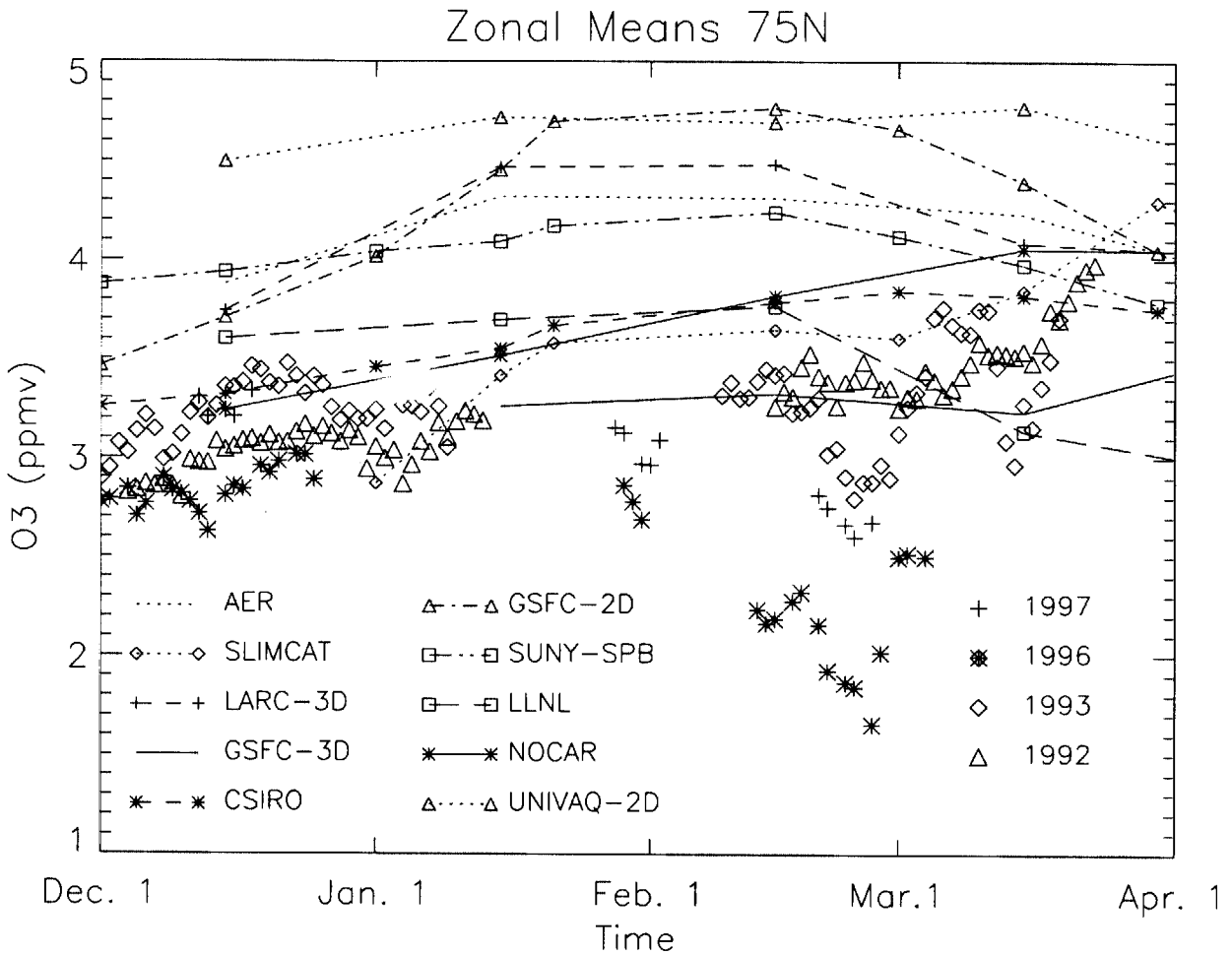

Figure 5.6.12. The MLS ozone at 75N is also highly variable from year to year. Given that none of the models produce high active chlorine, it is not surprising that none of the models produces the very low ozone seen in 1996 and 1997. However, even disregarding that aspect of the comparison, most of the models do a poor job of simulating the ozone seasonal cycle for the years shown.

6. Future Atmospheric Perturbation from NOx Injection in the Lower Stratosphere

Donald Wuebbles

University of Illinois

The High Speed Civil Transport (HSCT) aircraft emissions studies provide a means to evaluate how the models being compared respond to a perturbation. The standard scenario of 500 HSCTS (Baughcum and Henderson, 1998) is used, but with a limited representation of the emissions so as to simplify the interpretation of the model results for the intercomparison. Emissions of nitrogen oxides corresponding to an Emissions Index of 10 are used in addition to two different assumptions about the effects of sulfur emissions. The first case assumes the background level of sulfuric aerosols (SA0) is left unchanged. The second case (SA1) assumes that the distribution of sulfuric aerosols have been modified by the aircraft sulfur emissions, with the distribution of aerosol surface area based on the AER model (Weisenstein et al., 1997). In this case, 50 % of the SO_2 emitted by the aircraft is assumed to be immediately converted to sulfate particles in the plume. Neither case assumes any H_2O aircraft emission. The zonal average of the HSCT NOx emissions used are shown in Figure 6.1, while Figure 6.2 shows the ratio of the aerosol surface area density for SA1 relative to SA0. All HSCT calculations were done relative to a "2015" background atmosphere assuming SA0 sulfuric aerosol surface area.

Nine models participated in the HSCT runs, including seven 2-D models and two 3-D models. The 3-D ECHAM3/CHEM model was only used for the SA1 case while the other eight models ran both cases.

6.1 Change in NOy

Contour plots of the absolute (ppbv) change in NOy for the HSCT perturbation relative to the background atmosphere are shown in Figure 6.3 for the SA1 case. The percentage changes in NOy are shown in Figure 6.4. Only the SA1 results are shown as the changes in NOy for the SA0 and the SA1 cases are essentially the same. The models are similar in having the peak absolute change in NOy at mid- to high latitudes at altitudes near the peak HSCT emissions. The GSFC-2D and Harvard two-dimensional models have the largest changes in NOy with peak mixing ratio changes greater than 2 and 3 ppbv, respectively. These models, along with the three- dimensional ECHAM3/CHEM model, have the largest mixing ratio changes extending into the southern hemisphere. LLNL has a much smaller area of 2 ppbv change in NOy, while SUNY-SPB and UNIVAQ-3D peak at a change of about 1 ppbv. As seen in Figure 6.4, most models have a peak percent change in NOy on the order of 30 %, while the Harvard, UNIVAQ-2D, and ECHAM3/CHEM models having peaks greater than 50 %.

Table 6.1 shows that the HARVARD and GSFC-2D two-dimensional models also have the largest changes in total column NOy while UNIVAQ-3D has the smallest change. Figure 6.5 further amplifies the differences in the aircraft-induced changes in total NOy from the models.

Figures 6.6a, 6.6b, and 6.6c shows the annually-averaged changes in NOy as a function of latitude at altitudes of 14, 20, and 24 km, respectively. Figure 6.7 shows the change in NOy as a function of altitude at 40 N latitude. All of these analyses support the findings above. In addition, there are several other interesting findings. UNIVAQ-2D is only model to have non-zero changes in NOy in the tropics at 14 km, which should be in the troposphere. At 20 km, all of the models have peak changes in NOy at

40-50 N. At latitudes greater than about 40 N (see Figure 6.7), the UNIVAQ-3D model actually determines a decrease in NOy for the HSCT perturbation at altitudes greater than 25 km.

The distributions of the absolute changes in NOy shown in Figures 6.3, 6.6 and 6.7 are very similar to the shape and magnitude of the changes in the HSCT NOx tracer study, run A3. As discussed in the Transport Experiments chapter, there are strong connections between the HSCT NOx tracer experiment (run A3) and the analyses of age of air and other transport indicators determined from the distributions of observable stratospheric tracers. Given these relationships, the derived changes in NOy from the B4 HSCT perturbation runs will be subject to the effects from transport differences discussed in the Transport Experiments chapter. The strong correlation between the change in nitrogen oxides in the A3 and the B4 runs leads to the conclusion that uncertainties in transport processes are having an important impact on the abilities of current stratospheric models to evaluate the effects of HSCTs on stratospheric chemistry.

6.2 Change in NOx and O_3

Figure 6.8 shows contours of the absolute change in NOx in ppbv for each model. Figure 6.9 shows the percentage change in NOx relative to the background atmosphere. Figures 6.10 and 6.11 show the corresponding contour plots for the SA1 case. In examining Figure 6.8, the peak change in NOx is not as isolated to the region of the aircraft emissions as was found with NOy. GSFC-2D has a peak change in NOx of greater than 0.5 ppbv between 30 and 40 km in the equatorial region, whereas peak change in NOy is in the 18-20 km region at mid- to high latitudes (see Figure 6.3). HARVARD has a slightly smaller peak in the 30 km region in the tropics. ECHAM3/CHEM also has large changes, greater than 0.5 ppbv, at these altitudes, near the upper boundary for this model. The other models all have peak changes in NOx that are much smaller, with values of 0.15 to 0.3 ppbv.

For this SA0 case, many of the models have surprisingly similar changes in the percentage change in NOx. Figure 6.9 shows similar 15 % change contours for the AER, GSFC-2D, LLNL, SUNY-SPB, and CSIRO models. These models have peak changes of about 30-40 %. In contrast, the UNIVAQ models, - 2D and -3D, have much larger changes, of over 110 % in the tropical region near 20 km in UNIVAQ-2D (also see Figure 6.12).

Figures 6.8 and 6.10 show that the changes in NOx for the SA0 and SA1 cases have similar contours, but the magnitude of the changes in the lower stratosphere are different in the two cases. This is expected as a result of the interactions of the additional aerosol surface area density leading to additional heterogeneous reactivity in the SA1 case. However, the effects of the two aerosol density cases are substantially different in the various models. A comparison of Figures 6.12 and 6.13, giving the annually-averaged changes in NOx at 20 km for the two cases, shows the AER and LLNL have a decrease in the percentage change in NOx in going from the SA0 case to the SA1 case. In contrast, the GSFC-2D and UNIVAQ-2D models show an increase in the percentage change in NOx such contrasting changes are also shown in Figures 6.14 and 6.15, which show the annually-averaged changes in NOx as a function of altitude at 20 N and 40 N, respectively, for the two aerosol cases. The AER model actually shows a decrease in NOx at many stratospheric altitudes outside the emissions area for the SA1 case. UNIVAQ-3D also shows a decrease but only above 50 N and is the only other model to show this behavior for the SA1 case.

Figures 6.16 and 6.17 show the change in the annually-averaged total NOx for the two aerosol cases. The models generally demonstrate the behavior discussed above. AER is the only model to show a globally-averaged decrease in the change in NOx. However, UNIVAQ-3D had a total column

decrease in NOx at all latitudes greater than 40 N for the SA0 case (and then showed an overall increase for the SA1 case). HARVARD shows the largest annually-averaged globally-averaged increase in NOx for both the SA0 and the SA1 cases (decreasing from 11.0 % for the SA0 case to 8.0 % for the SA1 case).

The ratio of the change in globally-averaged total NOx to the change in NOy is shown in Table 6.2 for both the SA0 and SA1 cases. For the SA0 case, AER has the smallest ratio (0.039)and SUNY-SPB the largest (0.197) For the SA1 case, UNIVAQ-2D and UNIVAQ-3D have the largest ratios, 0.218 and 0.219 respectively, showing significant increases in the fraction of NOx change relative to total NOy change compared to other models.

Percentage changes in ozone as a function of latitude and altitude are shown in Figures 6.18 and 6.19 for the two aerosol cases. The models all show regions of increase in ozone in the troposphere and lower stratosphere, with decreases in ozone above. The altitude of the transition from increase to decrease changes with latitude and with each model. The models generally have larger regions of decrease in the SA1 case, extending to lower altitudes at high latitudes in most of the models. The HARVARD two-dimensional model gives local decreases in ozone approaching 5-6 % in the lower stratosphere at high latitudes in the SA1 case. The other models all have substantially smaller changes in ozone. The AER two-dimensional model has a decrease in ozone of about 2 % at high latitudes while other models give 1 % or less.

As with NOx, the changes in ozone are substantially different between the SA0 and SA1 cases. Figure 6.20 a and b gives the annually-averaged change in ozone as a function of latitude at 20 km for the SA0 and SA1 cases. Figures 6.21, 6.22, and 6.23 give the annually-averaged change in ozone with altitude for 20 N, 40 N, and 60 N for the two cases. The models generally are give changes in ozone that are less positive or more negative, particularly at high latitudes for the SA1 case. The AER and UNIVAQ-2D models give the largest changes in going from SA0 to SA1.

Figure 6.24 and Figure 6.25 give the changes in total ozone for the SA0 and SA1 cases, respectively. For SA0, the models have substantially different patterns in their changes in total ozone. The Harvard model has much larger decreases than the other models, reaching -3 % at high latitudes in September. UNIVAQ-2D has large increases (~1.5 %) in total ozone at the same period. The other models range from small increases to small decreases in total ozone at northern latitudes.The SA1 results in Figure 6.25, as expected, are more negative than the SA0 results. Table 6.3(a-b) gives the globally-averaged changes in total ozone for the two aerosol cases.

The relationship between the changes in NOx and changes in ozone are substantially different in the various models. Figure 6.26 gives representative examples of the change in NOx plotted relative to the change in ozone. Shown in Figure 6.26 are the AER, SUNY-SPB, LLNL, and Harvard models for the SA0 case and AER for the SA1 case. Some models, like SUNY-SPB and UNIVAQ-2D have very compact relationships. Others like LLNL and AER are more intermediate in their spread. HARVARD and GSFC-2D have relationships that are much more spread out. Only one SA1 case is shown because the AER model is indicative of the general conclusion that all of the models tend to maintain very similar changes in NOx relative to changes in ozone relationships for both the SA0 and SA1 cases. This suggests that the primary differences in this relationship between the models is determined by differences in transport processes.

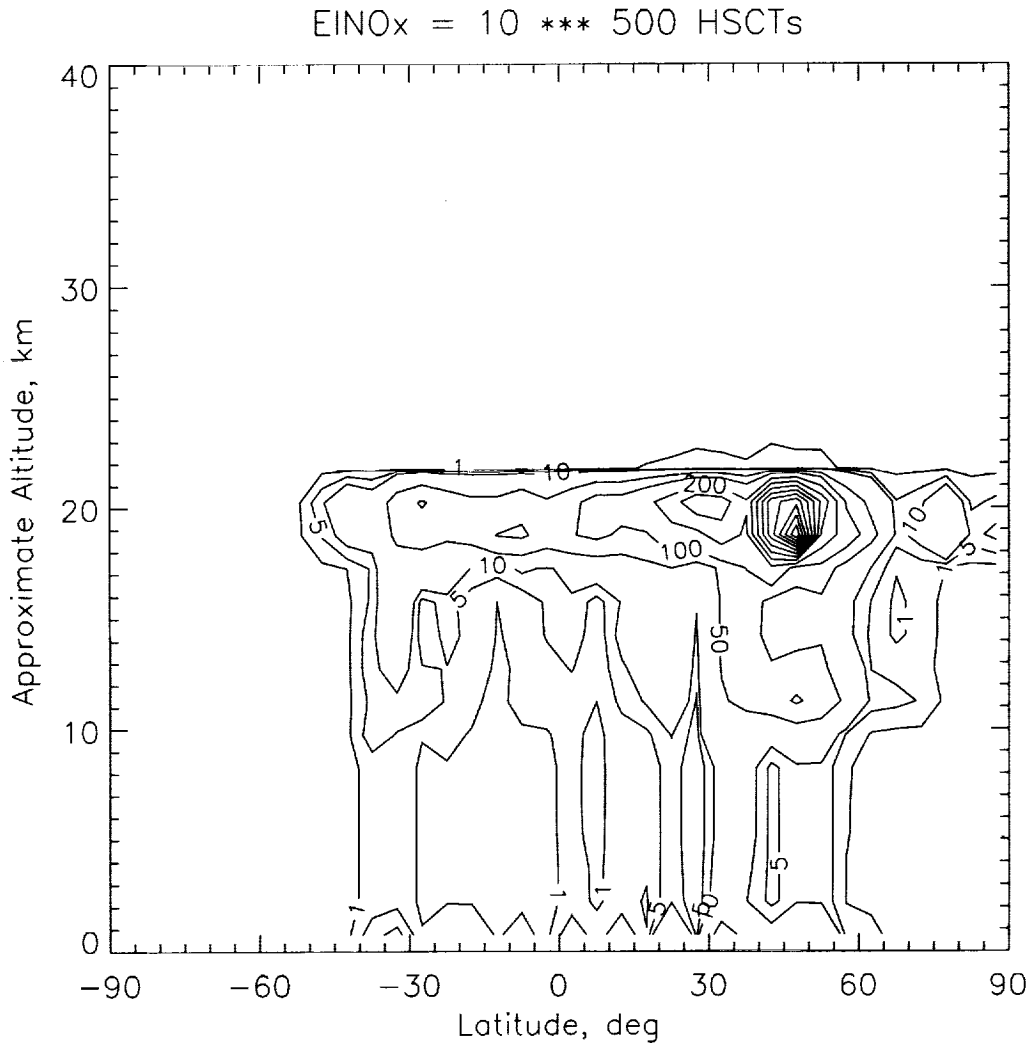

Figure 6.1. Aircraft NOx rate - molecules cm^{-3} sec^{-1}.

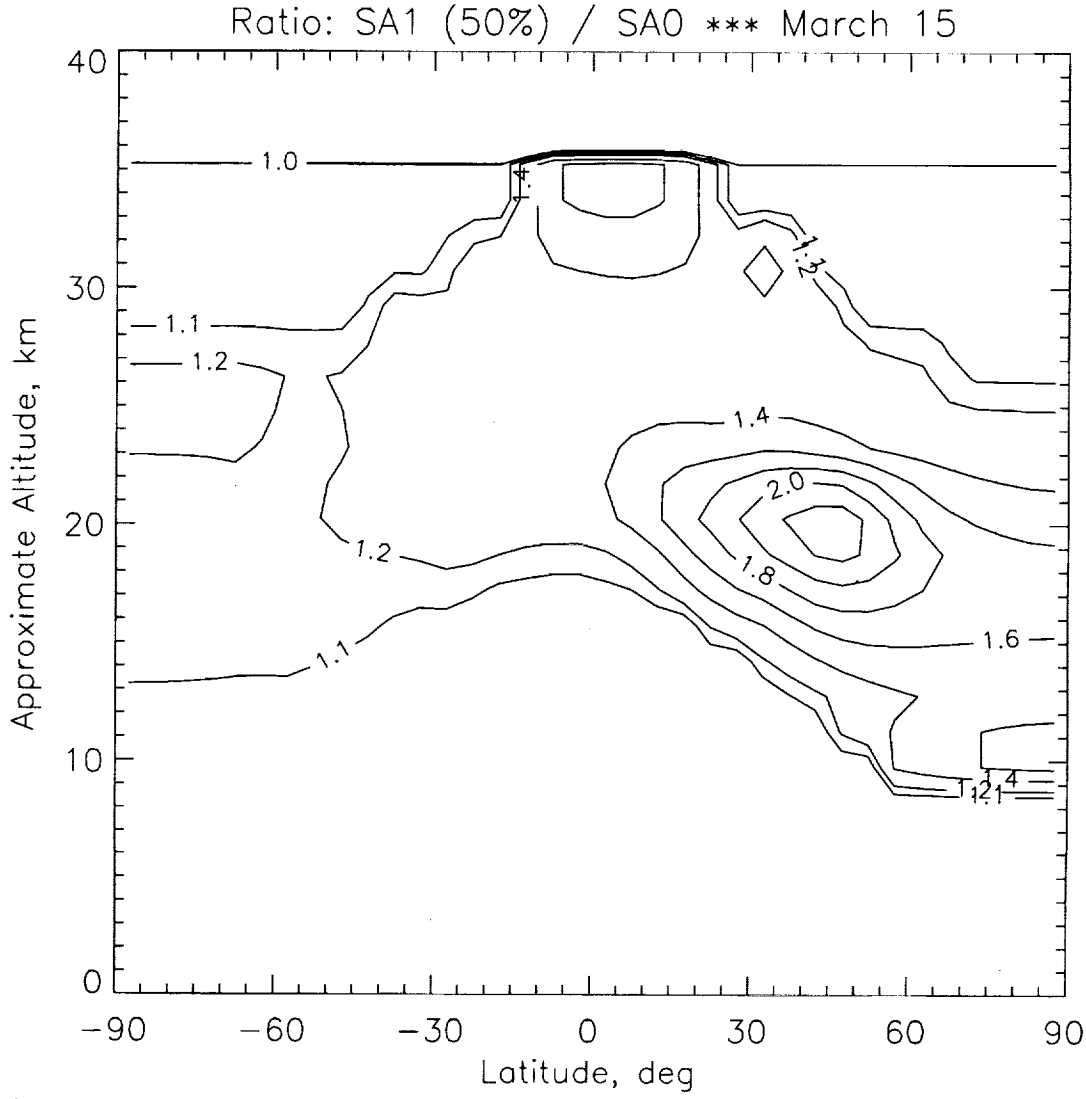
Ratio: SA1 (50%) / SA0 *** March 15
Approximate Altitude, km
Latitude, deg
40
30
20
10
0
−90
−60
−30
0
30
60
90
1.0
1.1
1.2
1.4
2.0
1.8
1.6

Figure 6.2.

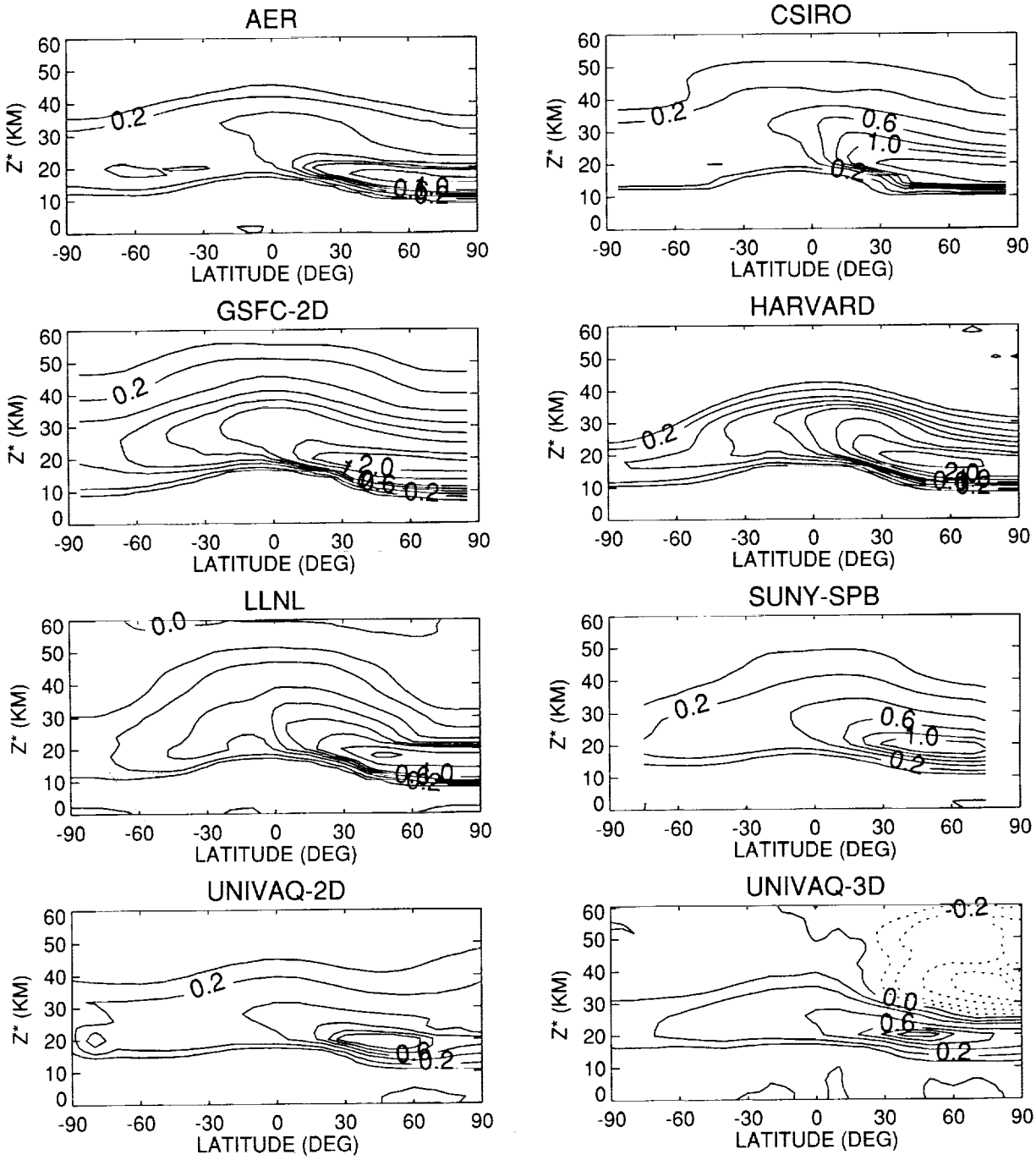

Figure 6.3. NOy DIFF (ppbv); Annual Avg; Run B4 SA1 vs Run B4 Base.

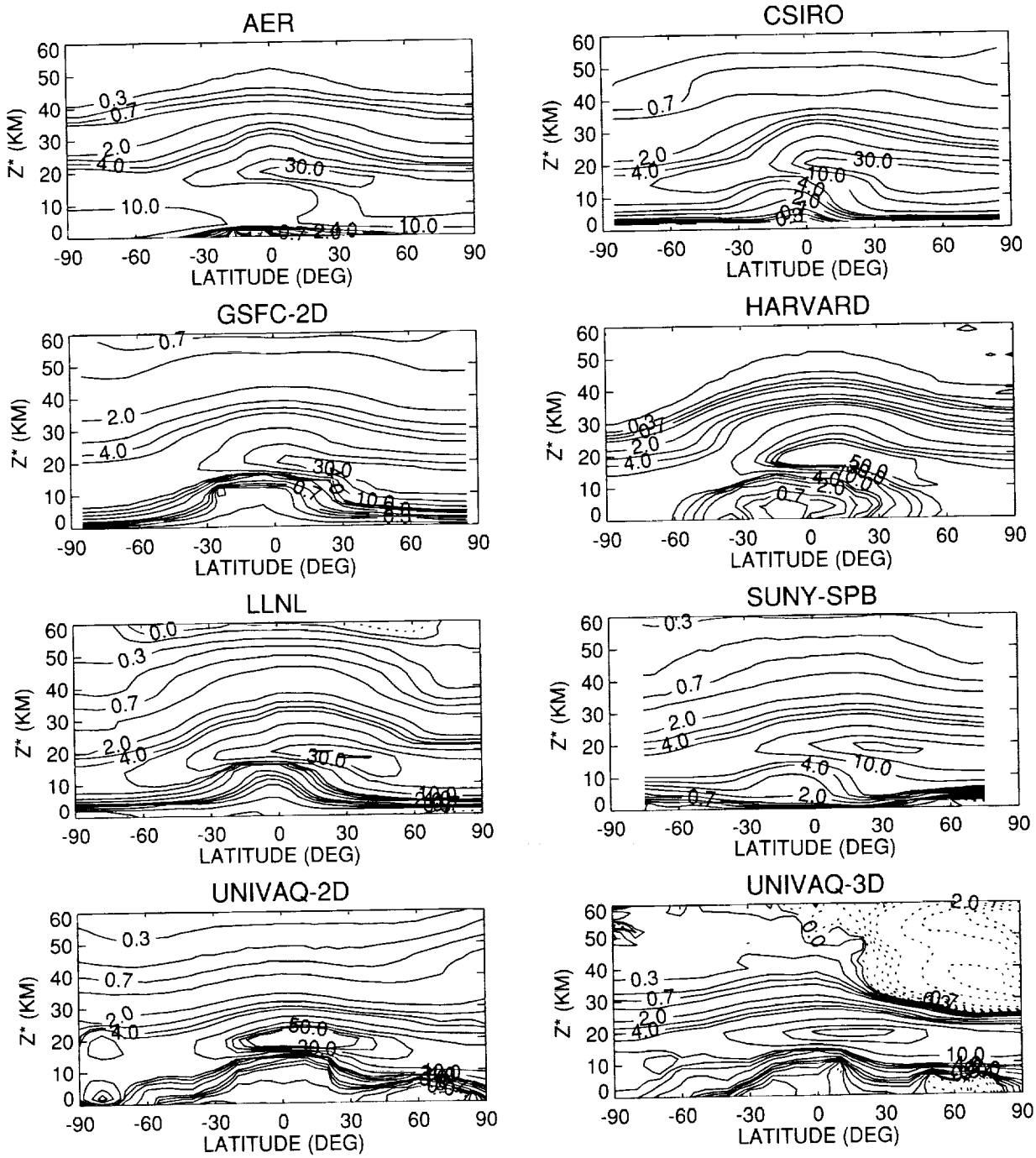

Figure 6.4. NOy PCT DIFF; Annual Avg; Run B4 SA1 vs Run B4 Base.

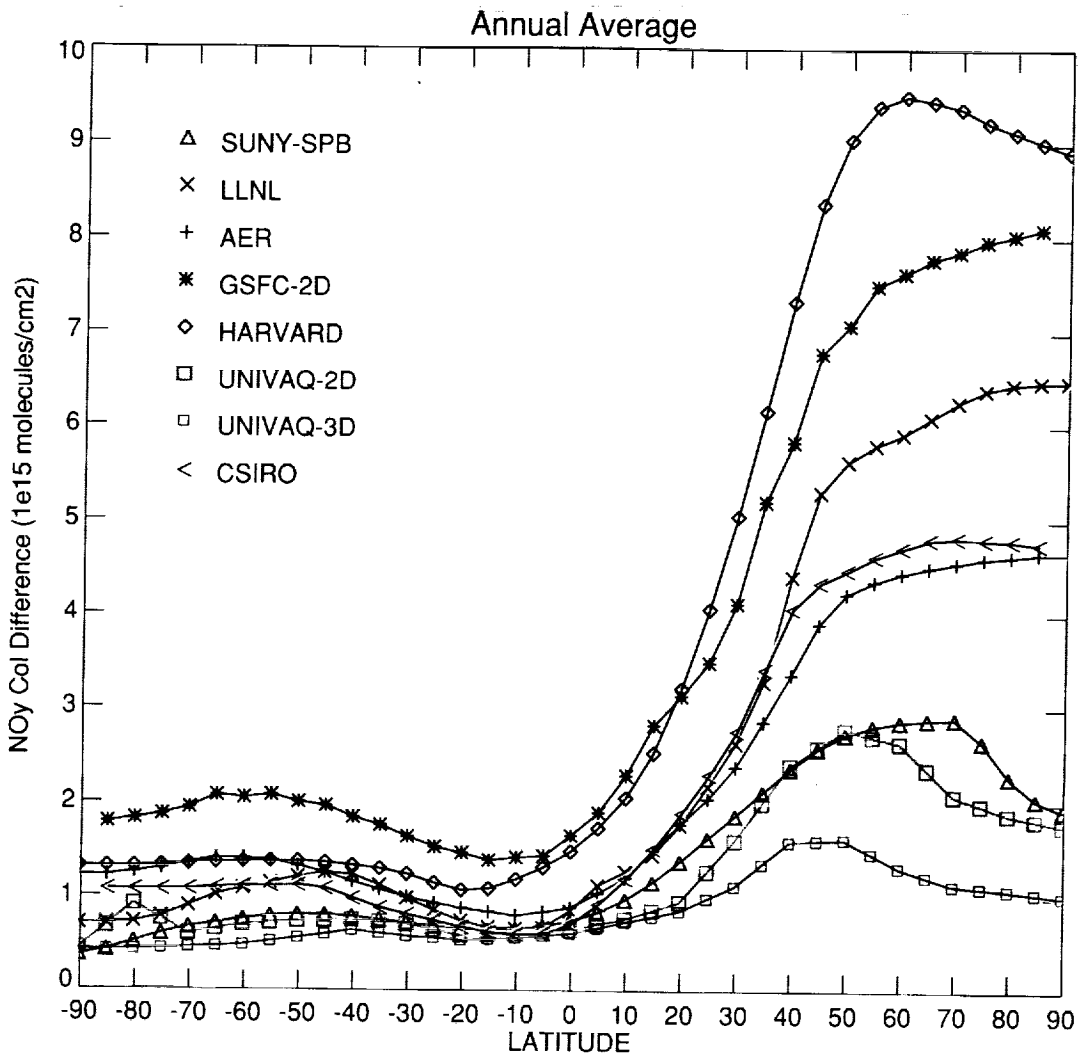

Figure 6.5 Total NOy; Run B4; Year 2015 (SA1).

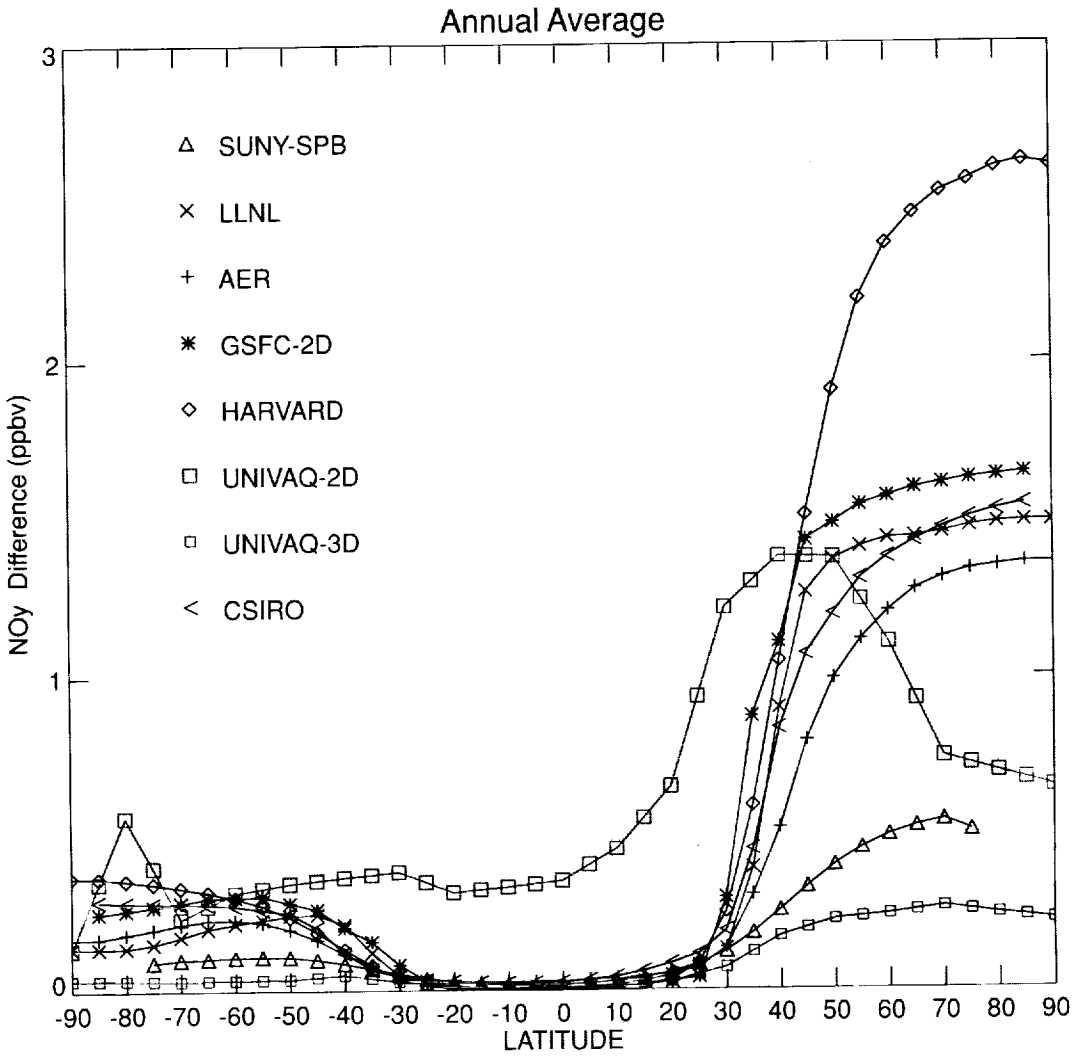

Figure 6.6a. NOy DIFF; Run B4 SA1; Year 2015; Alt 14 km.

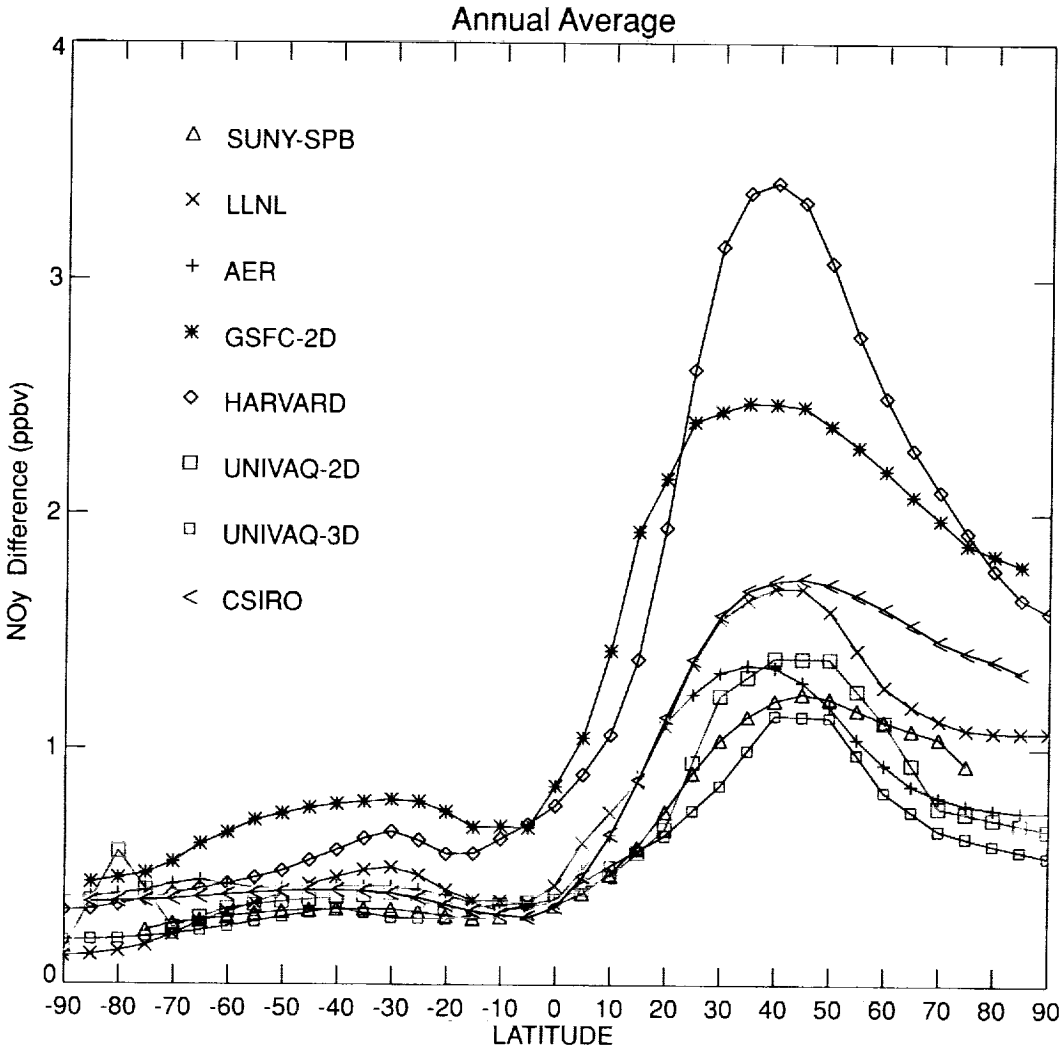

Figure 6.6b. NOy DIFF; Run B4 SA1; Year 2015; Alt 20 km.

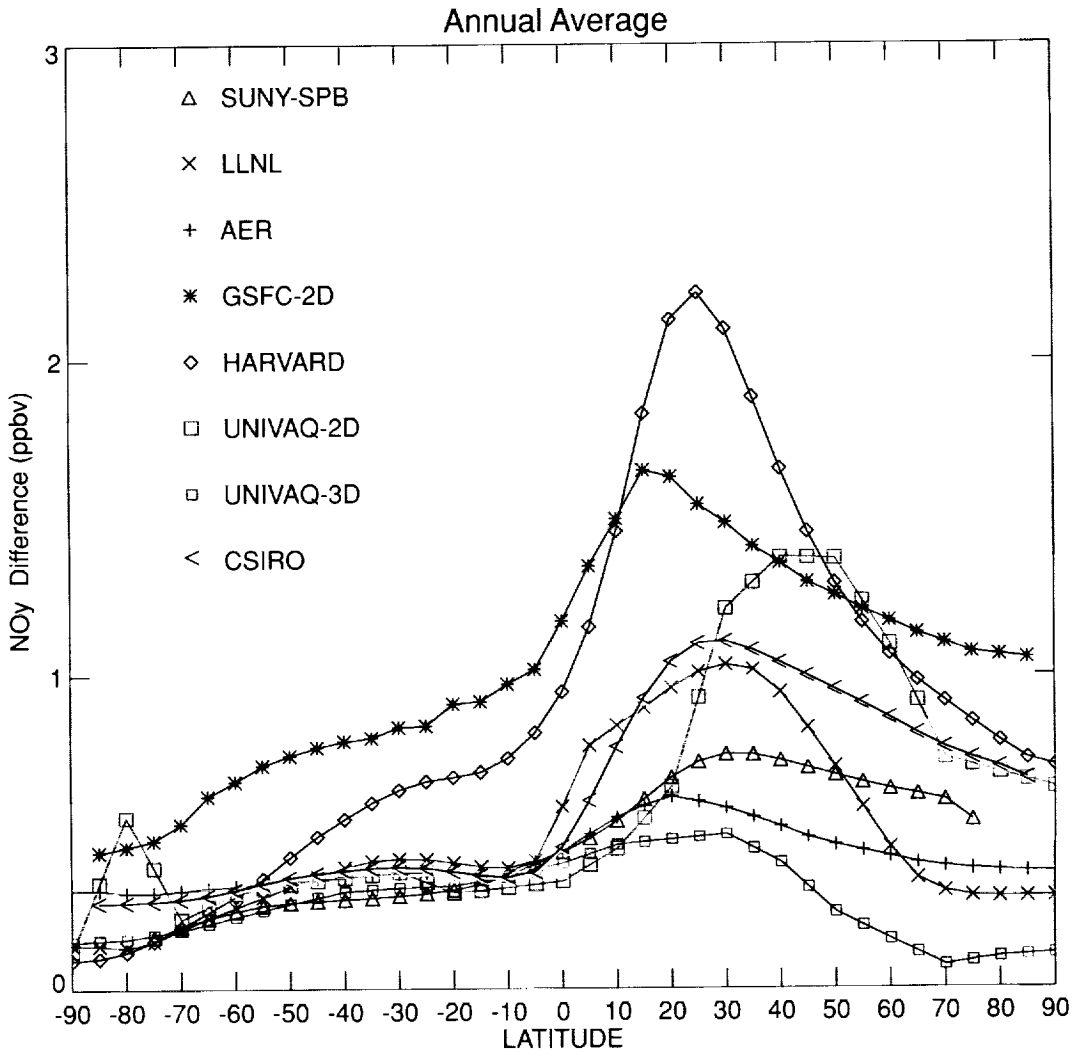

Figure 6.6c. NOy DIFF; Run B4 SA1; Year 2015; Alt 24 km.

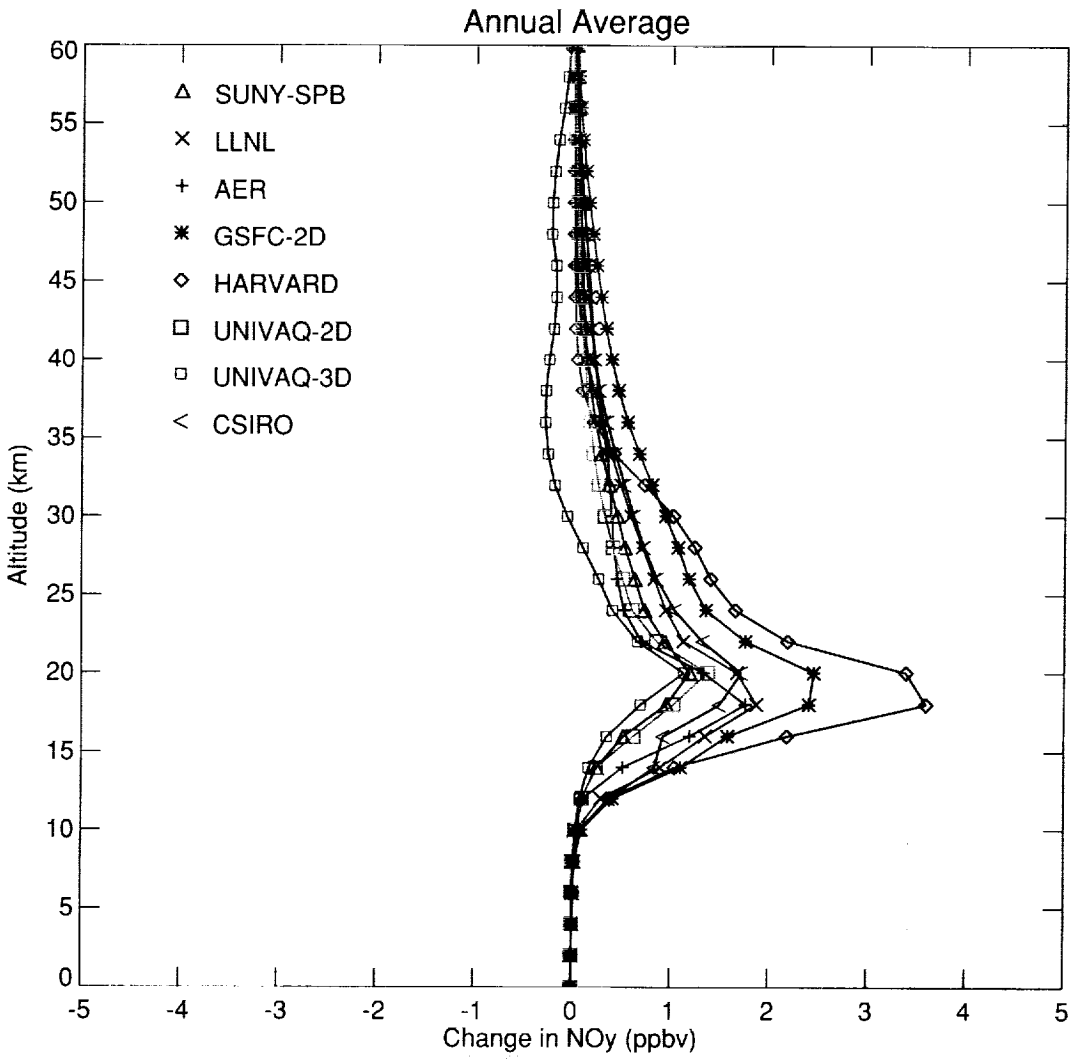

Figure 6.7. NOy DIFF; Run B4 SA1; Year 2015; Lat 40N.

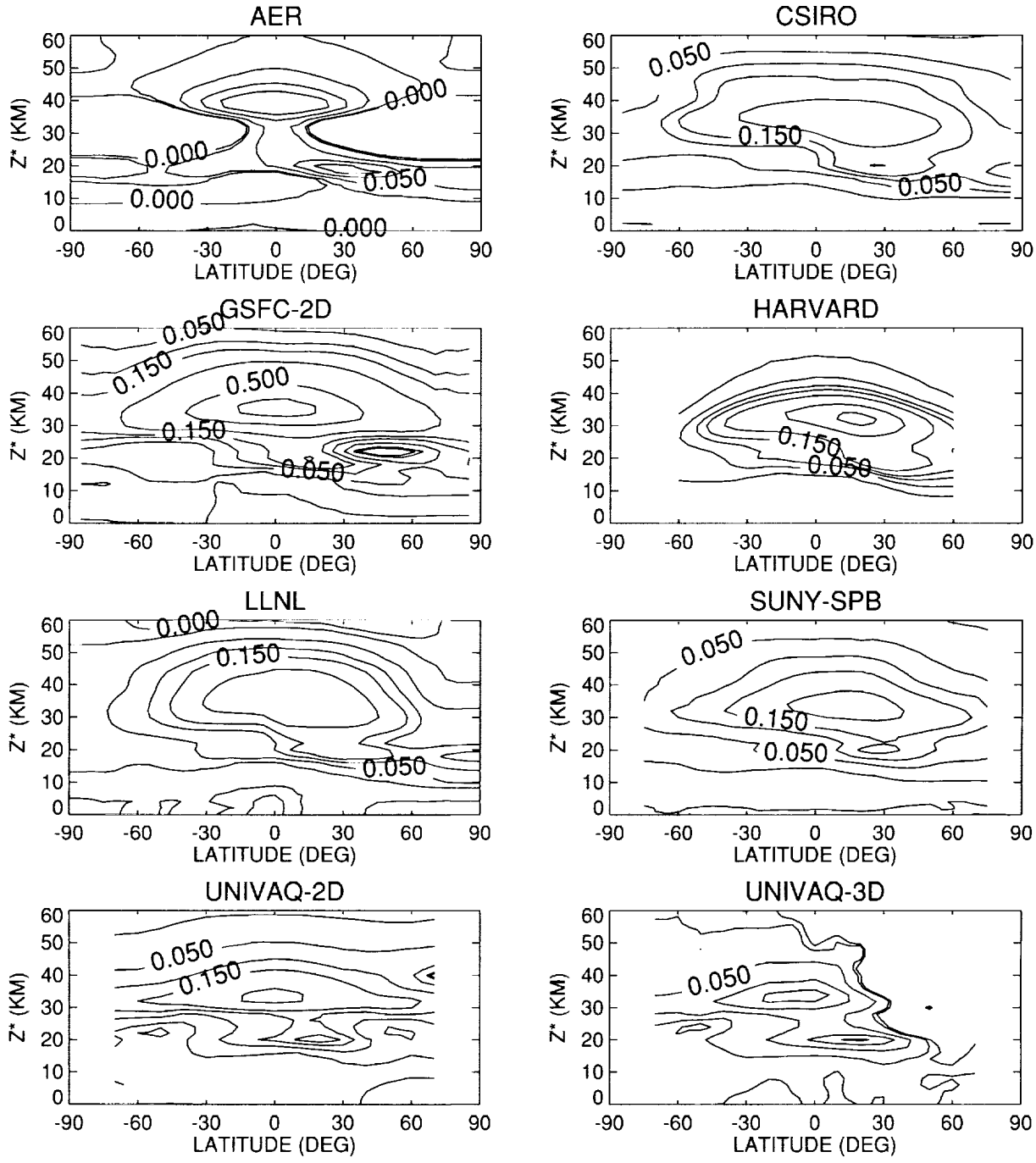

Figure 6.8. NO + NO_2 DIFF (ppbv); Annual Avg; Run B4 SA0 vs Run B4 Base.

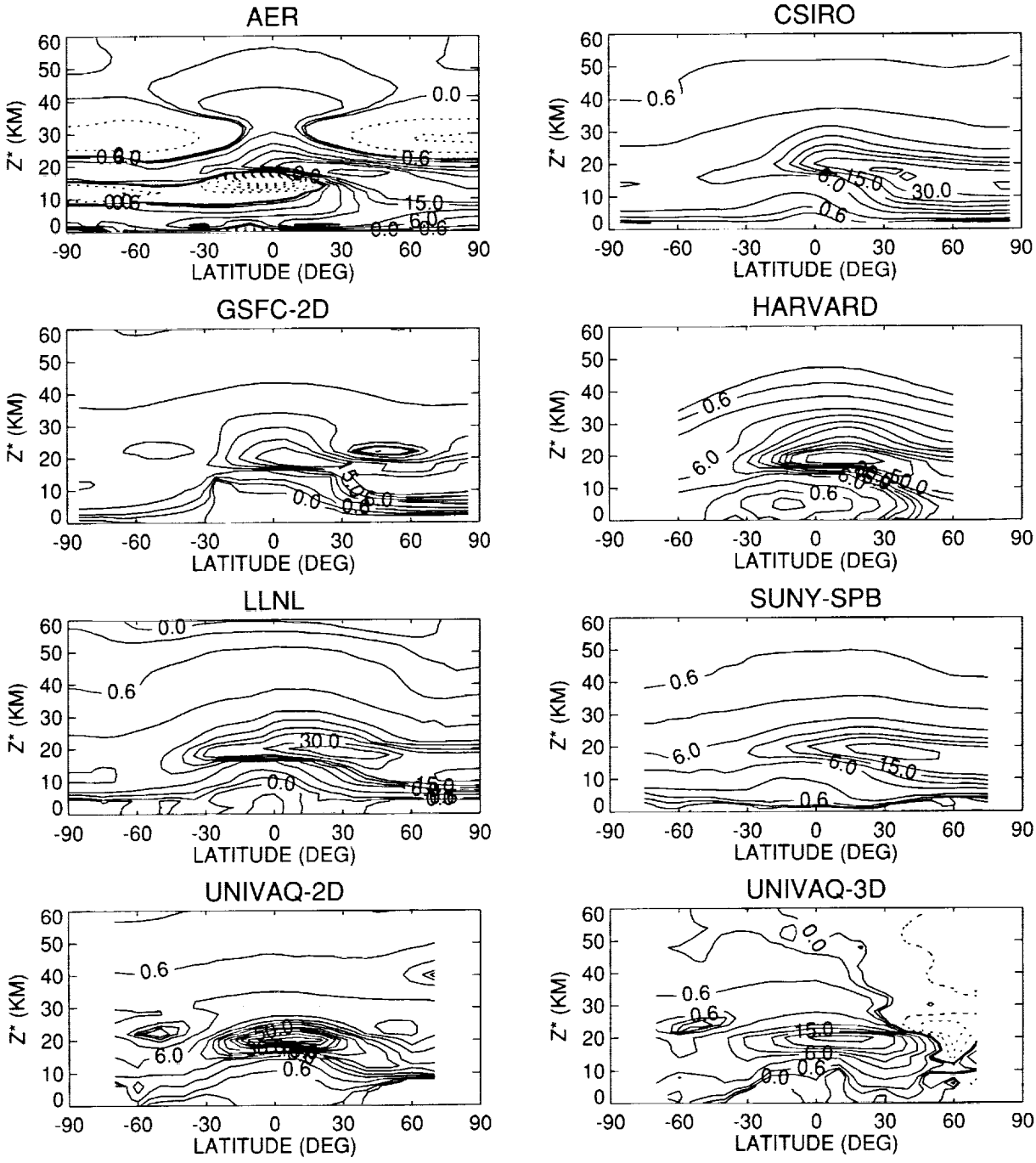

Figure 6.9. NO + NO_2 PCT DIFF; Annual Avg; Run B4 SA0 vs Run B4 Base.

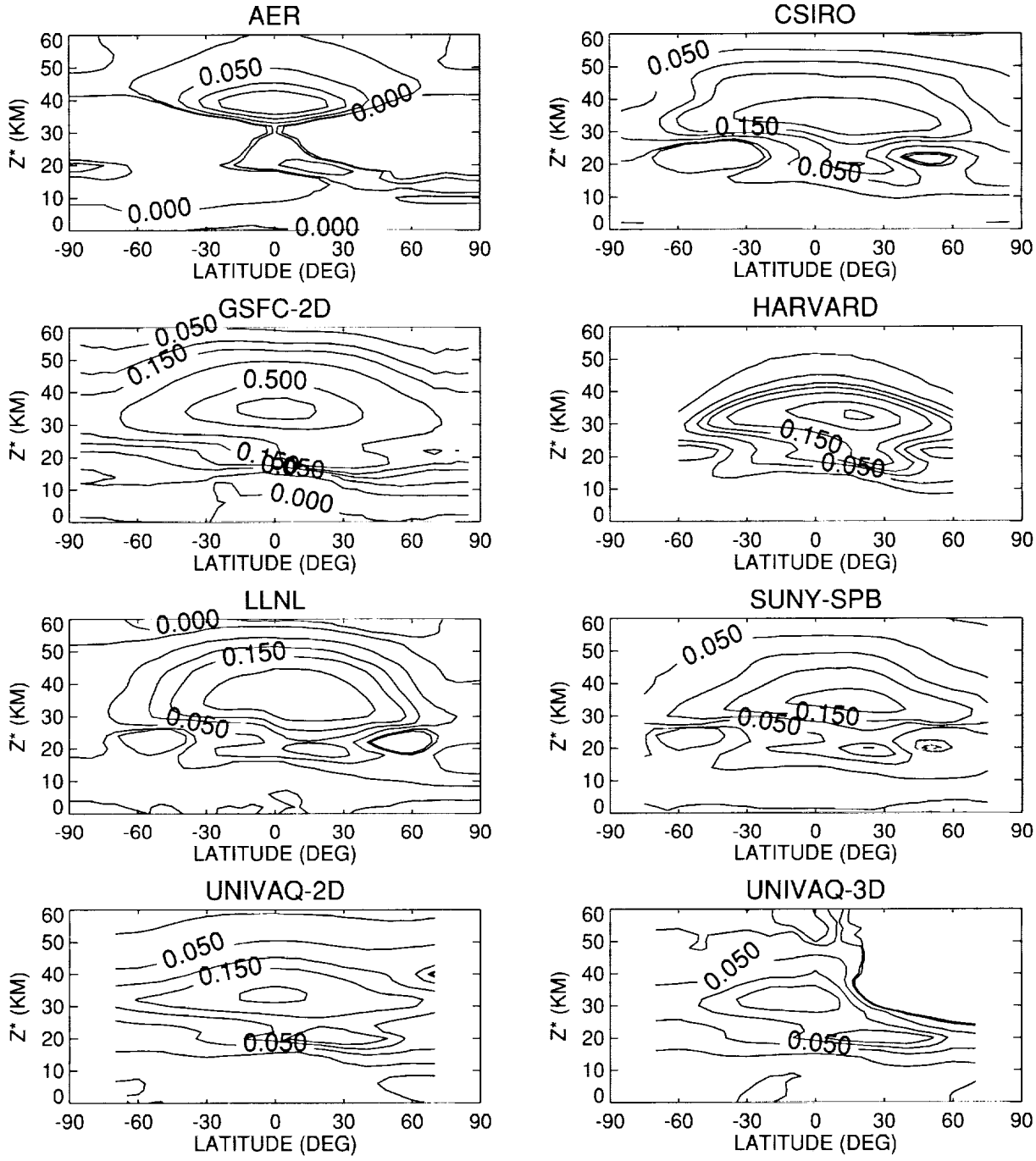

Figure 6.10. NO + NO_2 DIFF (ppbv); Annual Avg; Run B4 SA1 vs Run B4 Base.

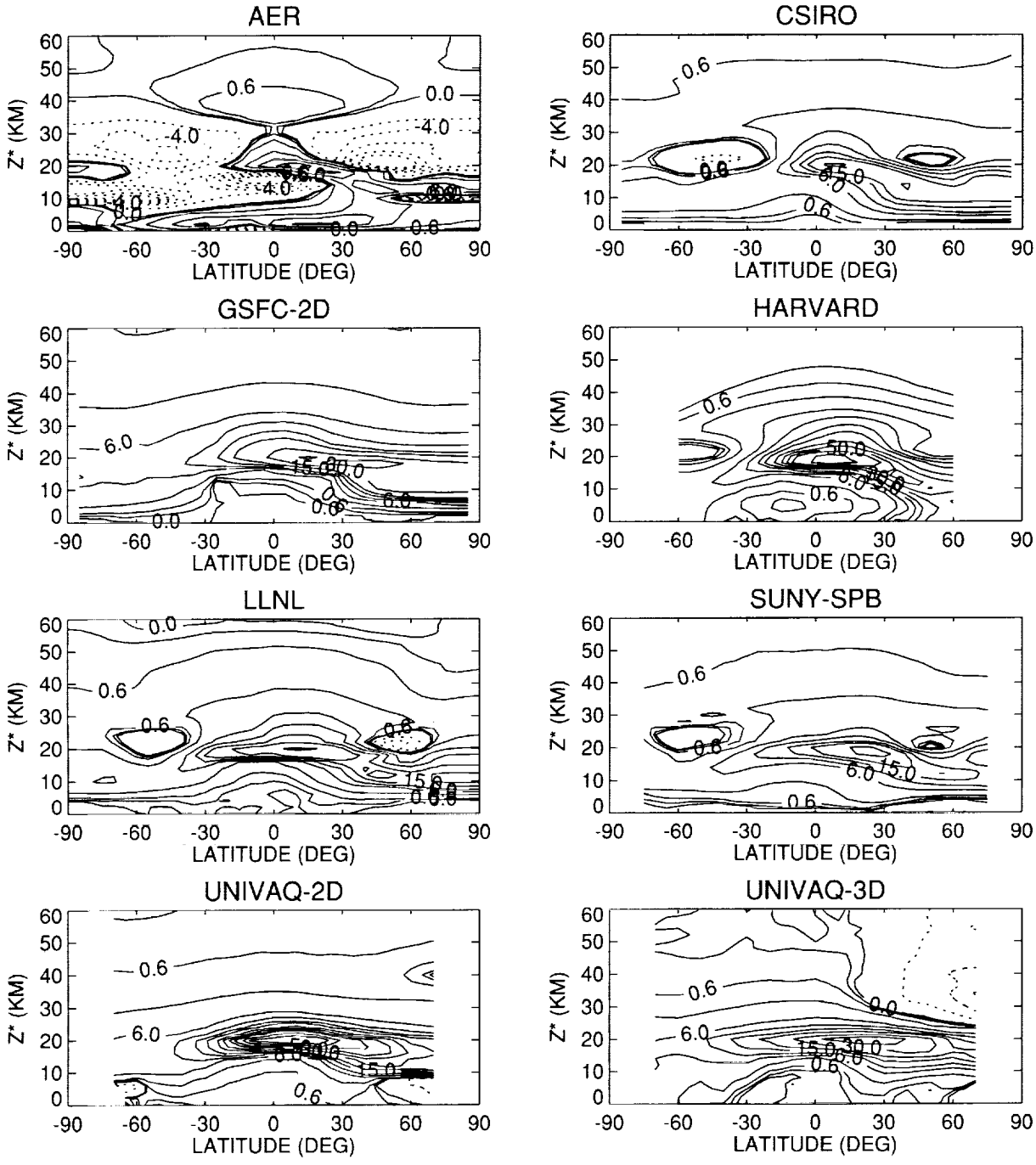

Figure 6.11. NO + NO_2 PCT DIFF; Annual Avg; Run B4 SA1 vs Run B4 Base.

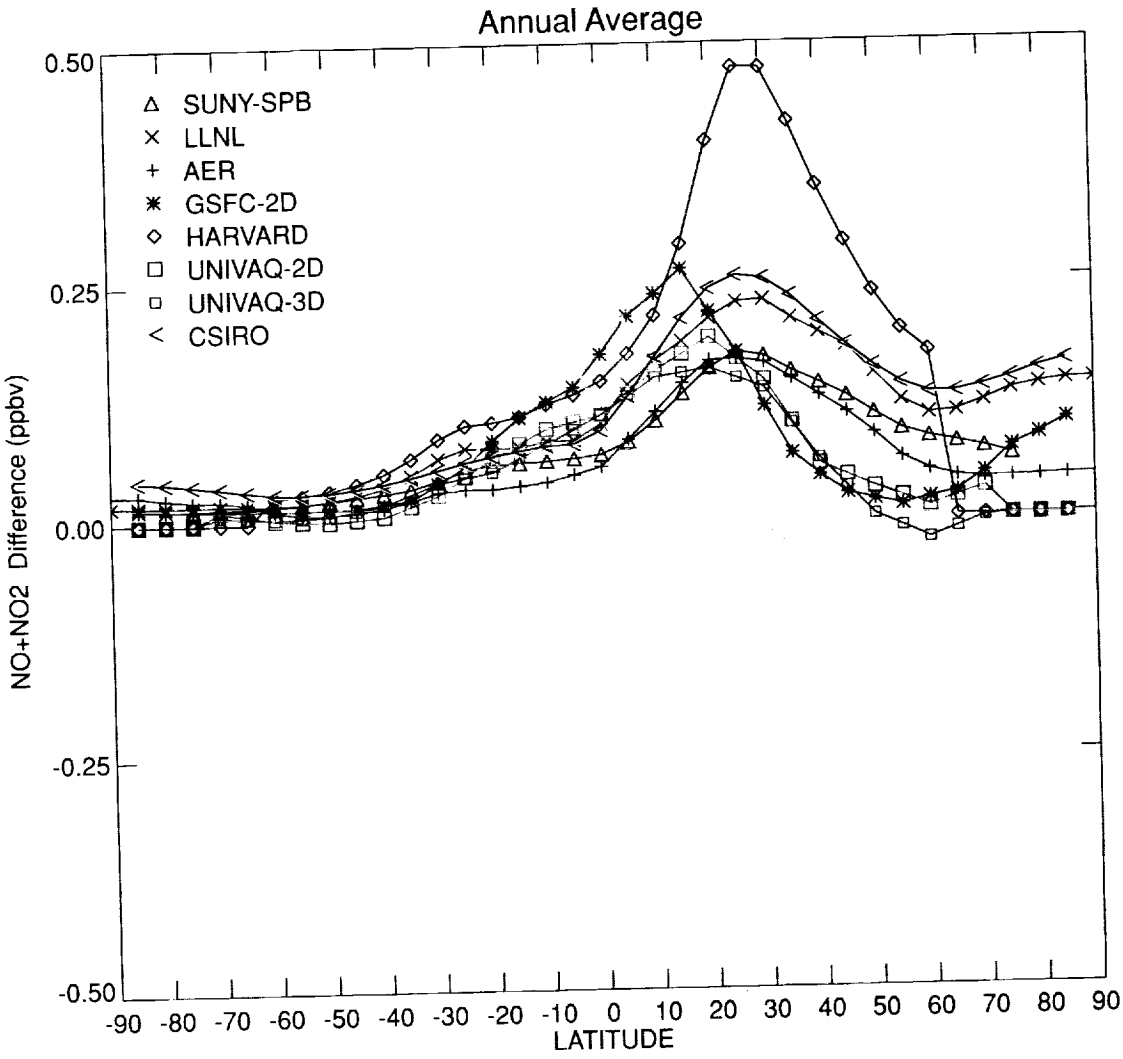

Figure 6.12. NO + NO_2 DIFF; Run B4 SA0; Year 2015; Alt 20 km.

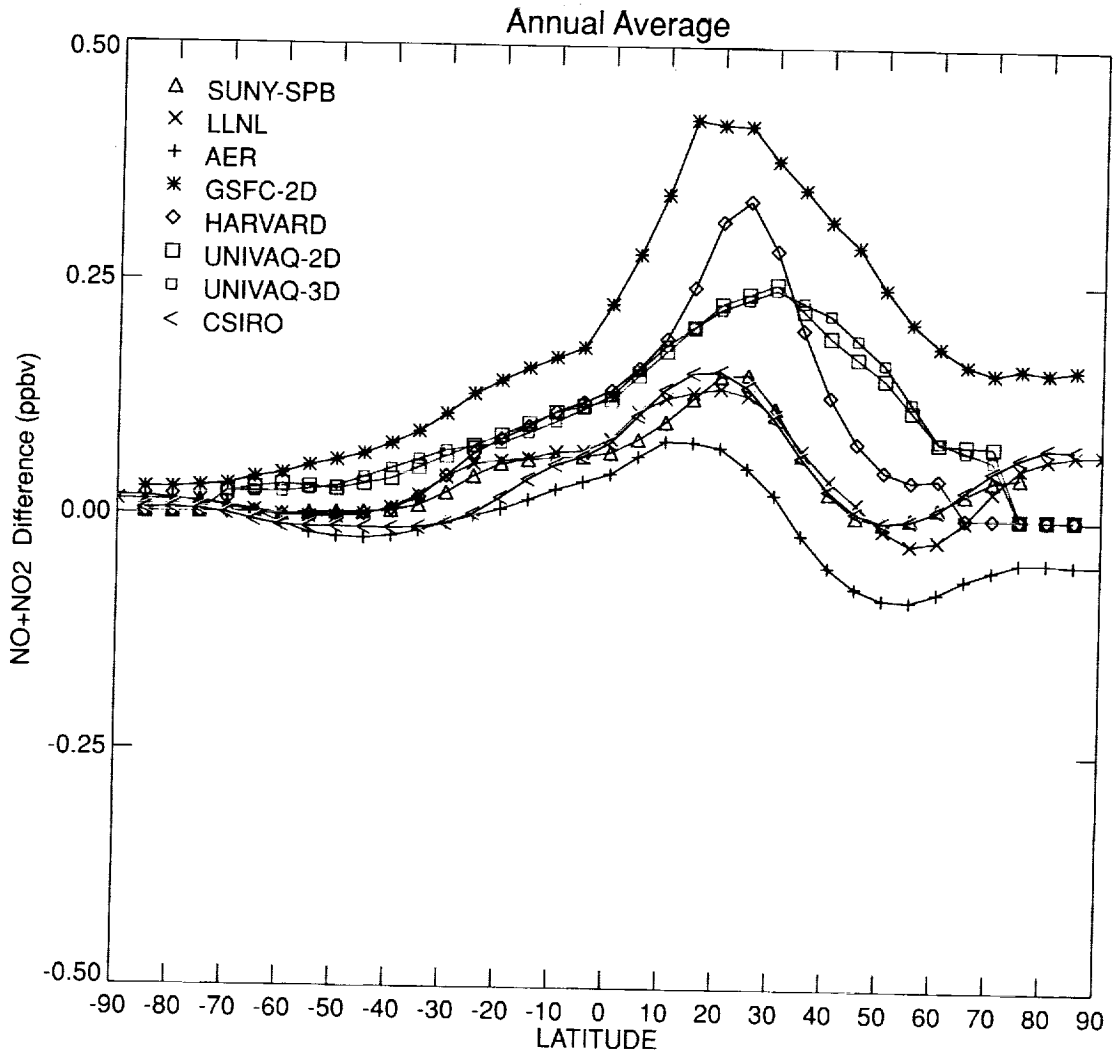

Figure 6.13. NO + NO_2 DIFF; Run B4 SA1; Year 2015; Alt 20 km.

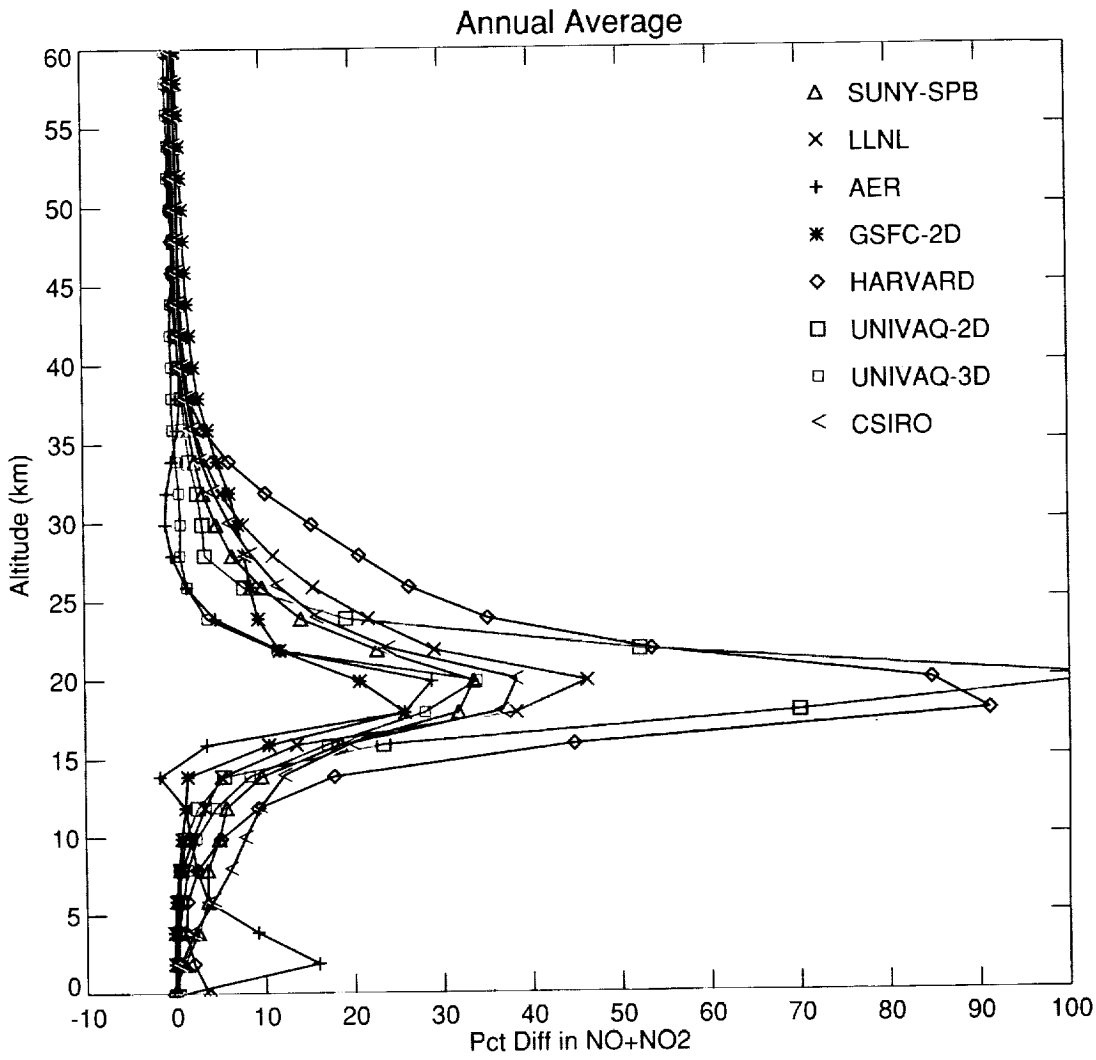

Figure 6.14a. NO + NO_2; Run B4; Year 2015; Lat 20N (SA0).

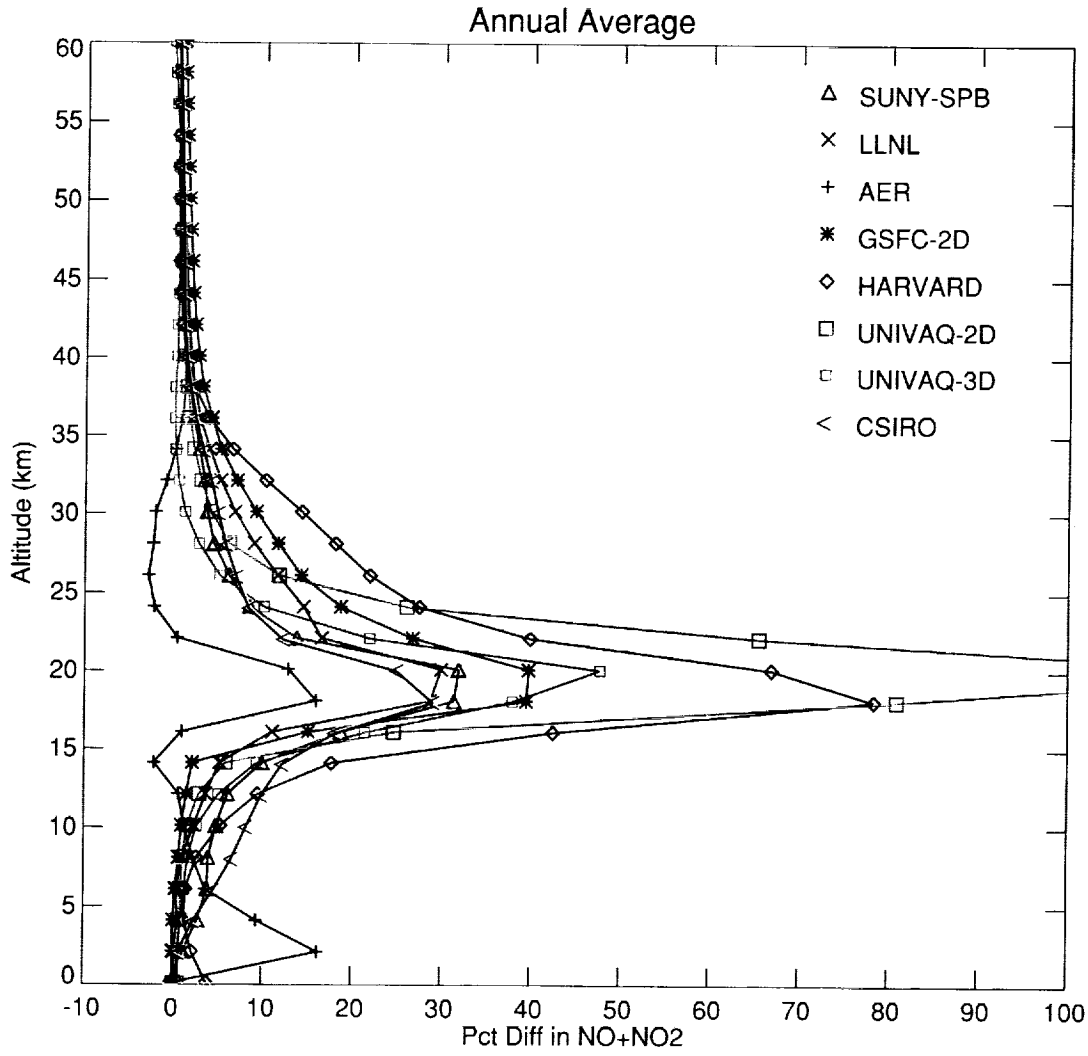

Figure 6.14b. NO + NO_2; Run B4; Year 2015; Lat 20N (SA1).

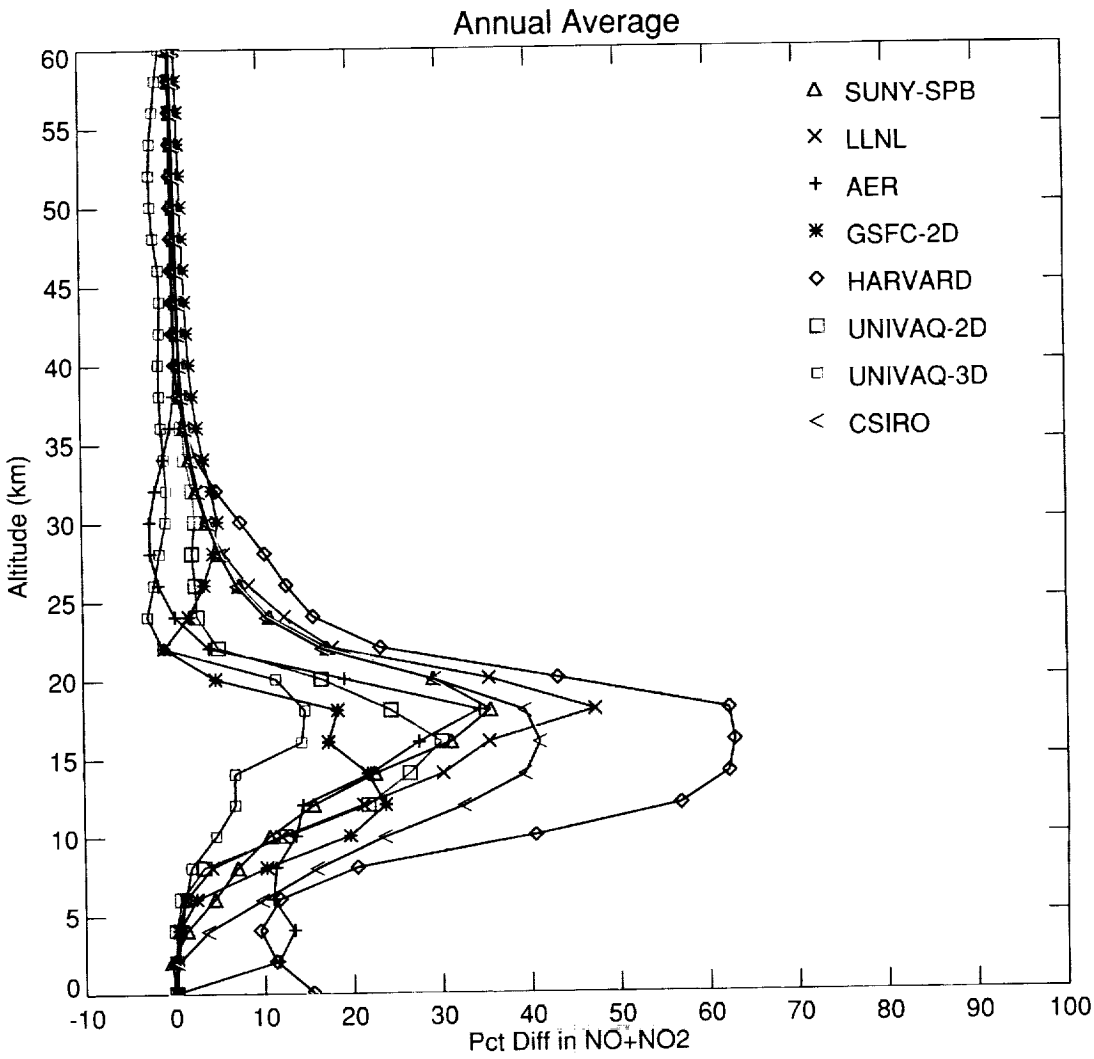

Figure 6.15a. NO + NO_2; Run B4; Year 2015; Lat 40N (SA0).

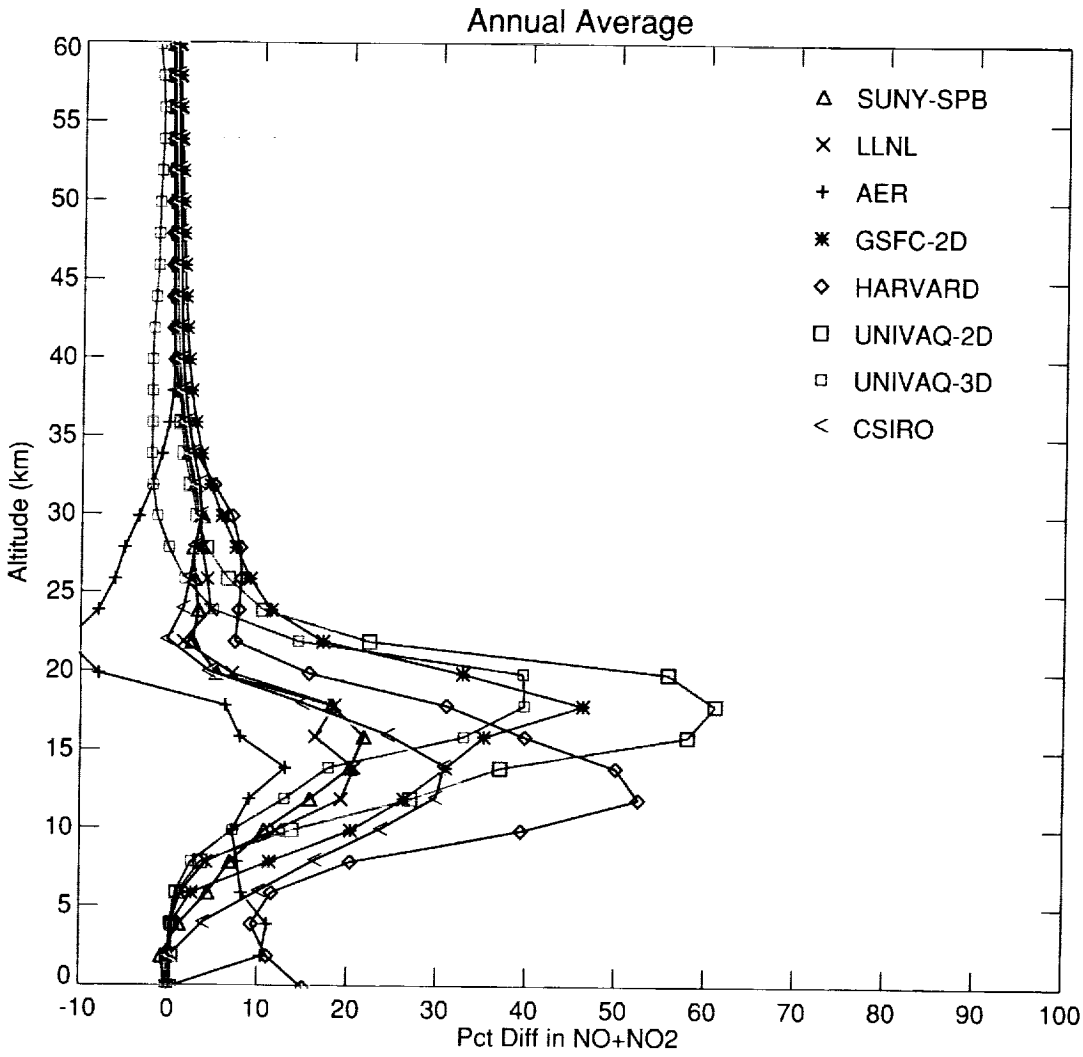

Figure 6.15b. NO + NO_2; Run B4; Year 2015; Lat 40N (SA1).

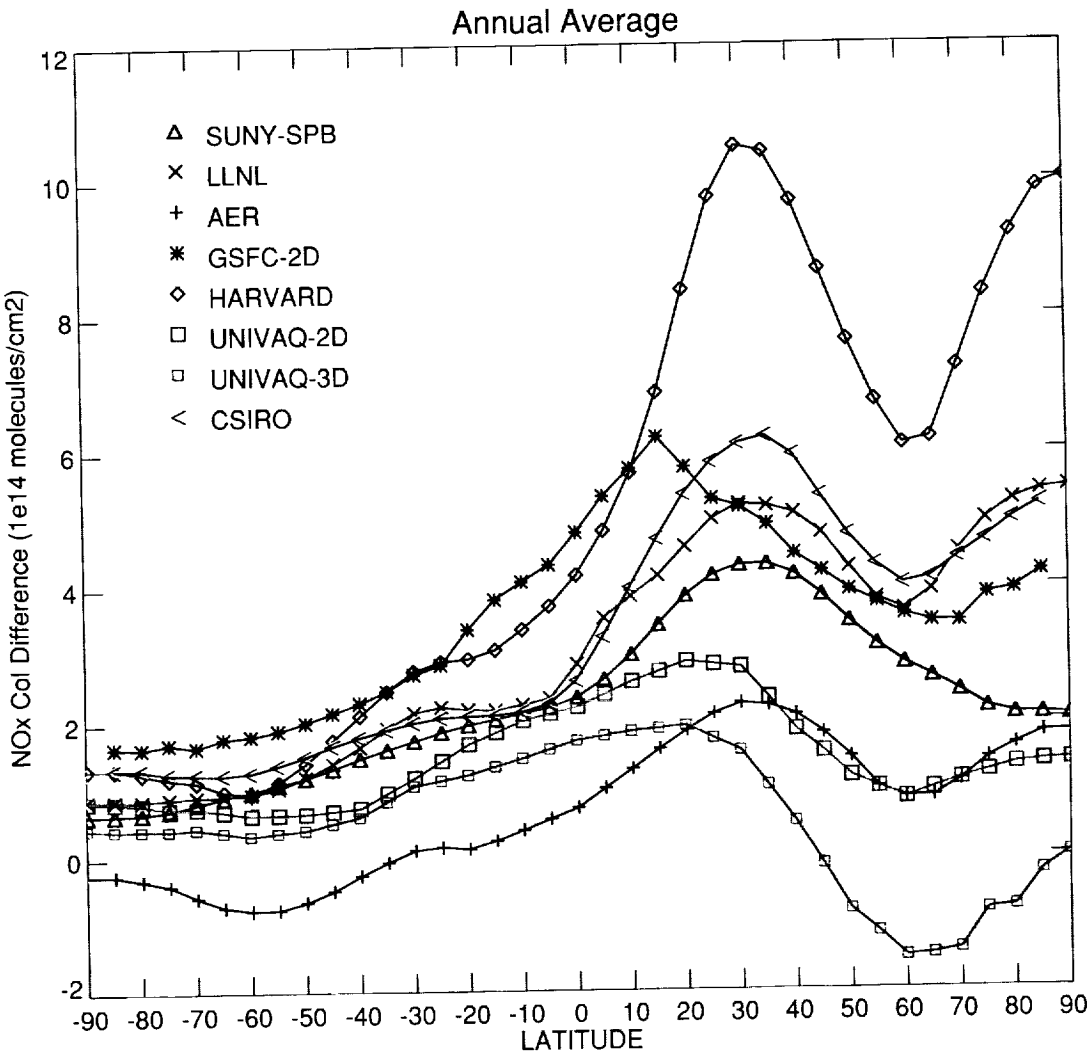

Figure 6.16. Total NOx; Run B4; Year 2015 (SA0).

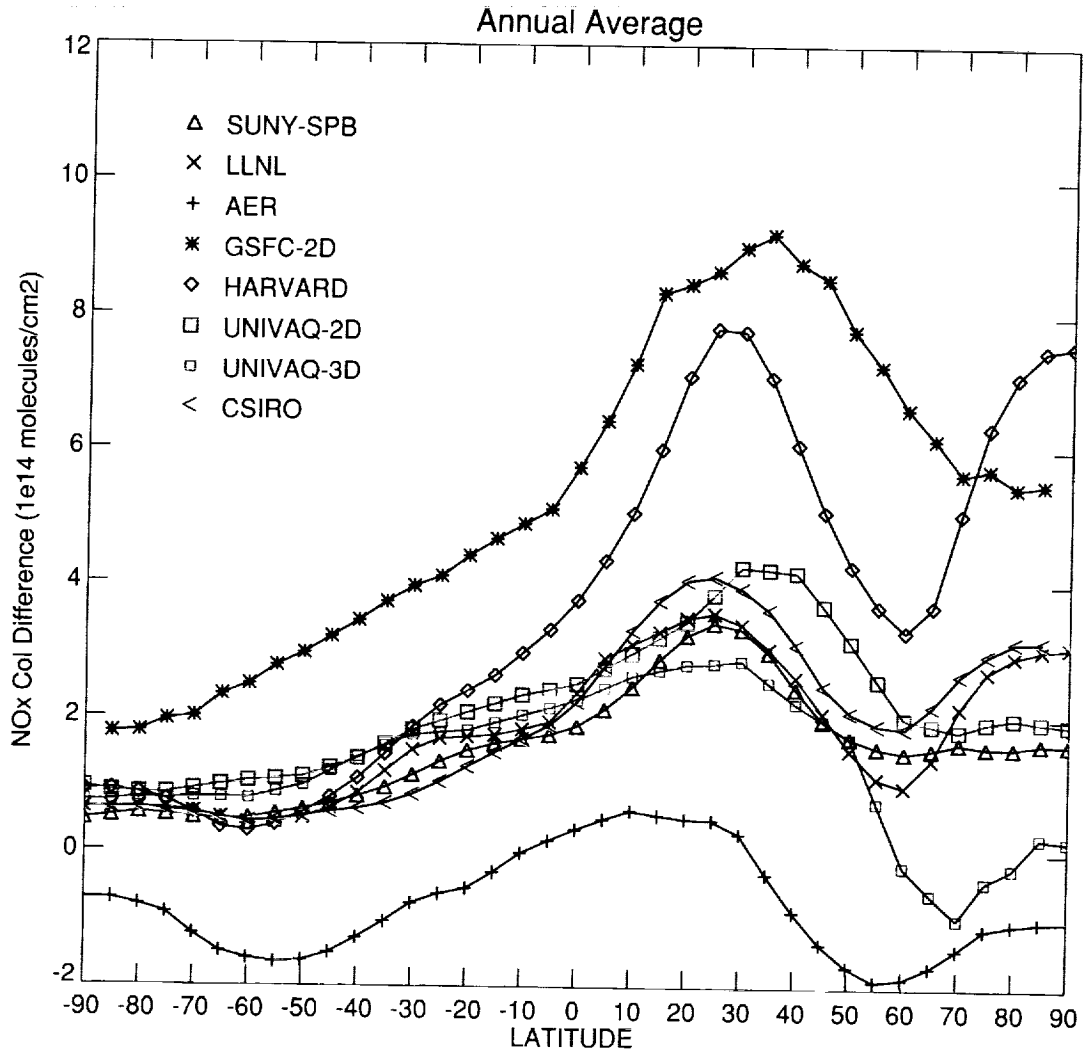

Figure 6.17. Total NOx; Run B4; Year 2015 (SA1).

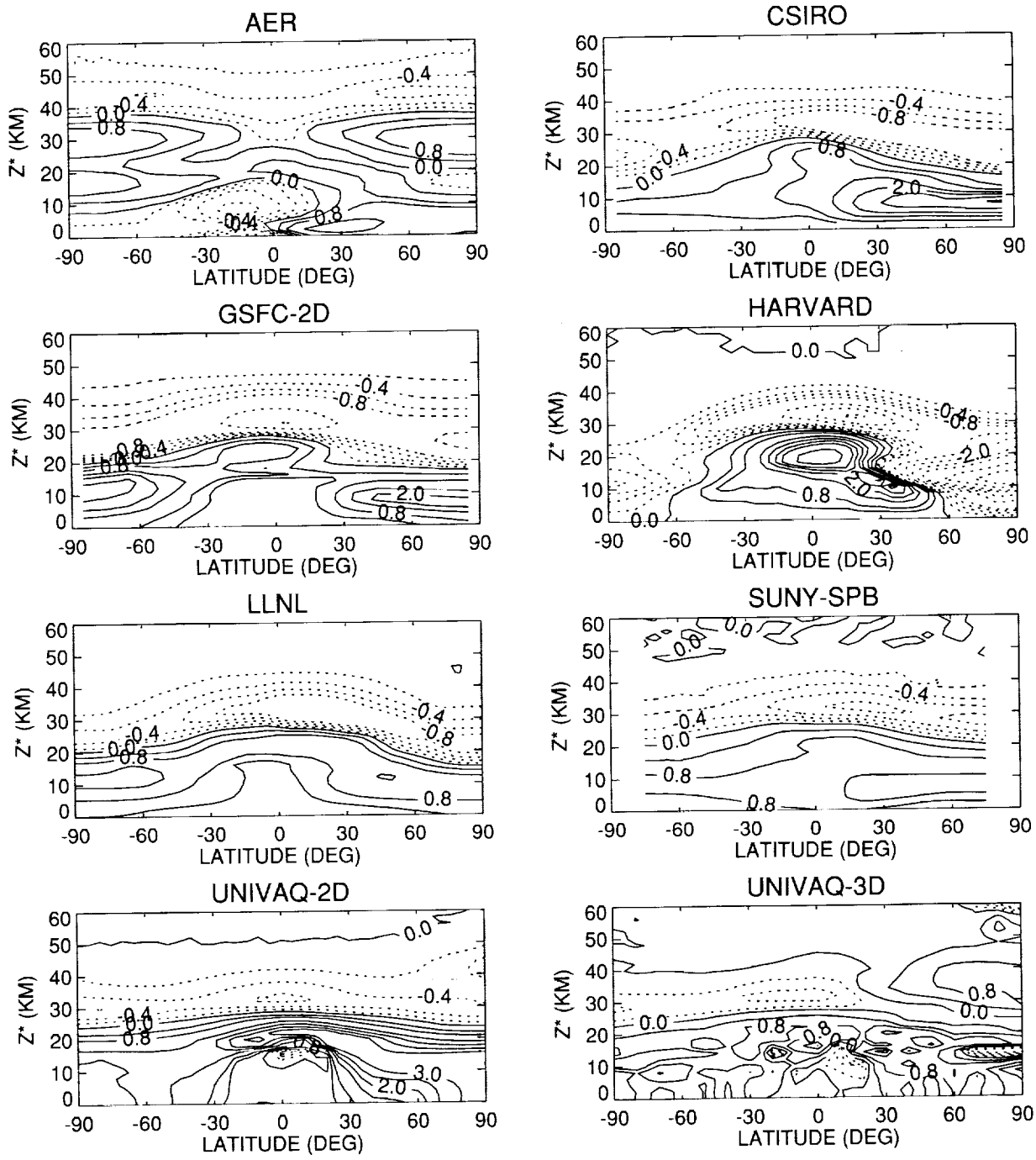

Figure 6.18. O_3 PCT DIFF; Annual Avg; Run B4 SA0 vs Run B4 Base.

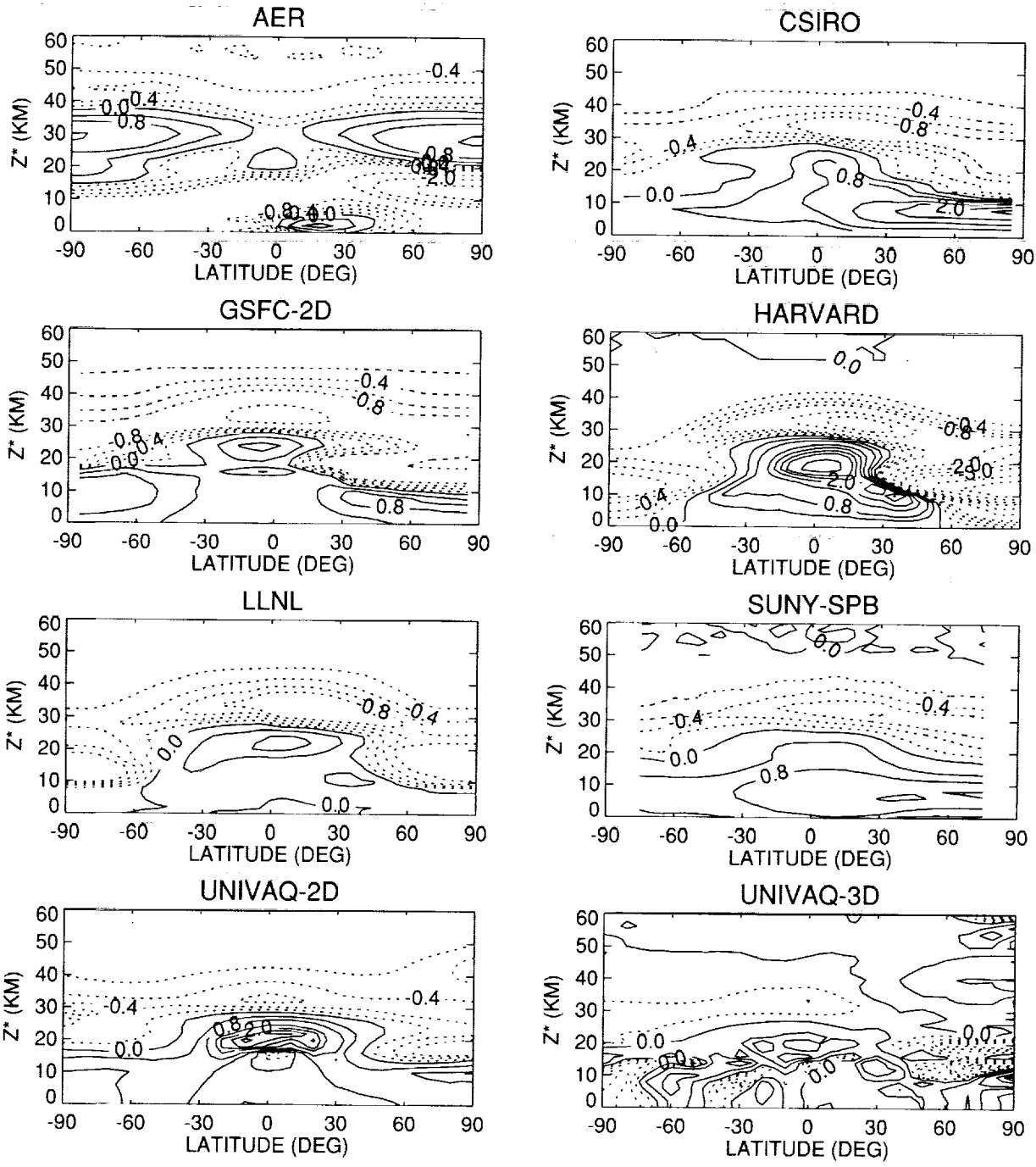

Figure 6.19. O_3 PCT DIFF; Annual Avg; Run B4 SA1 vs Run B4 Base.

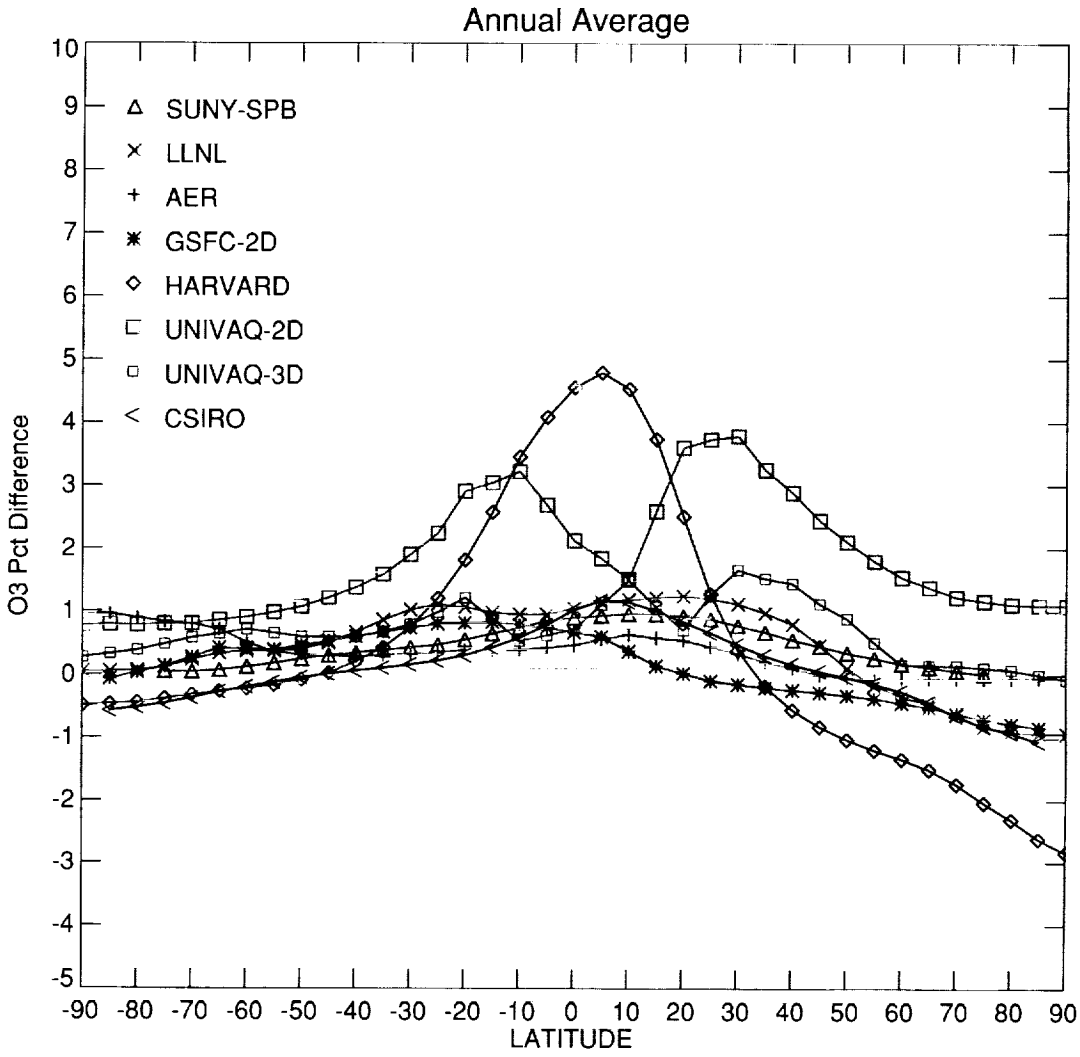

Figure 6.20a. O_3 Pct DIFF; Run B4; Year 2015; Alt 20 km (SA0).

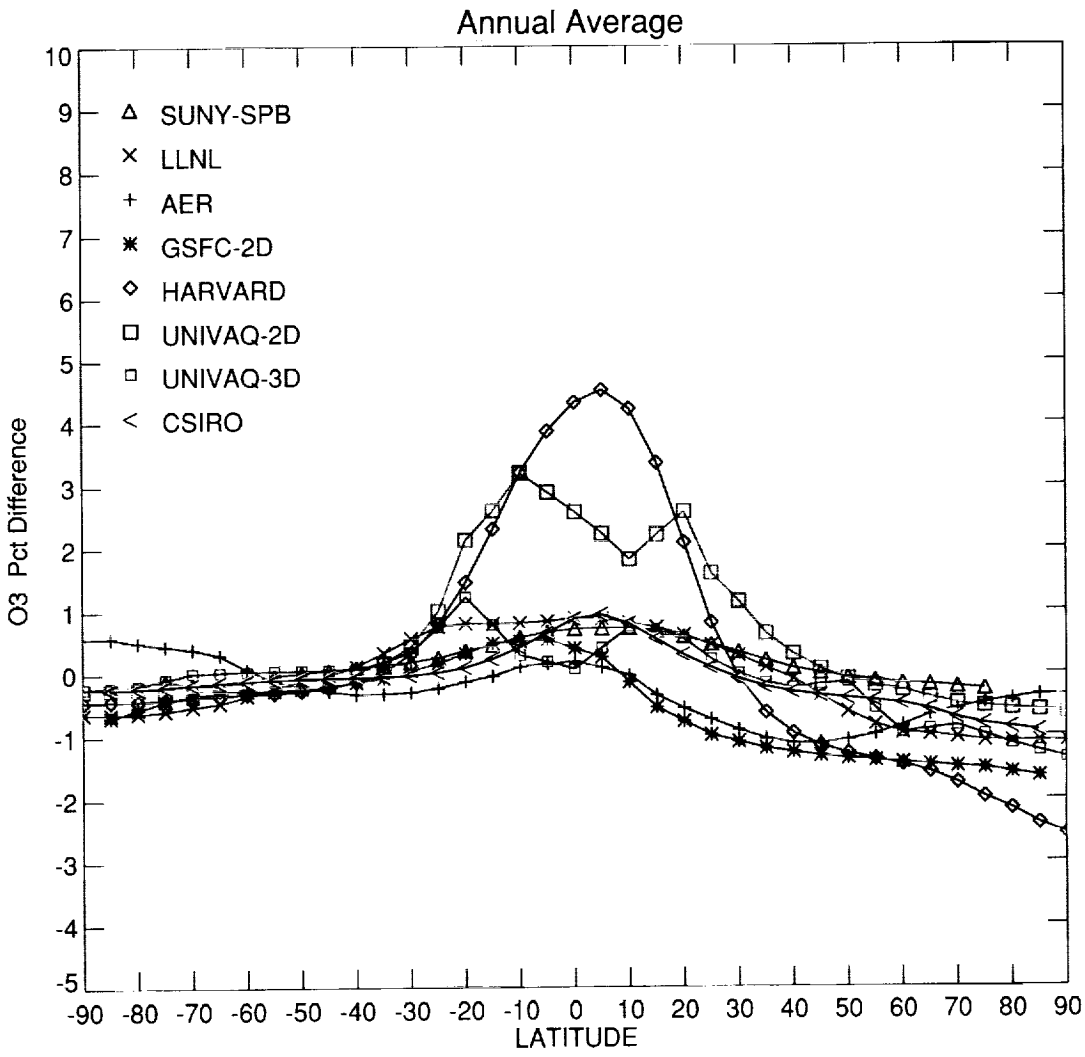

Figure 6.20b. O_3; Pct DIFF; Run B4; Year 2015; Alt 20 km (SA1).

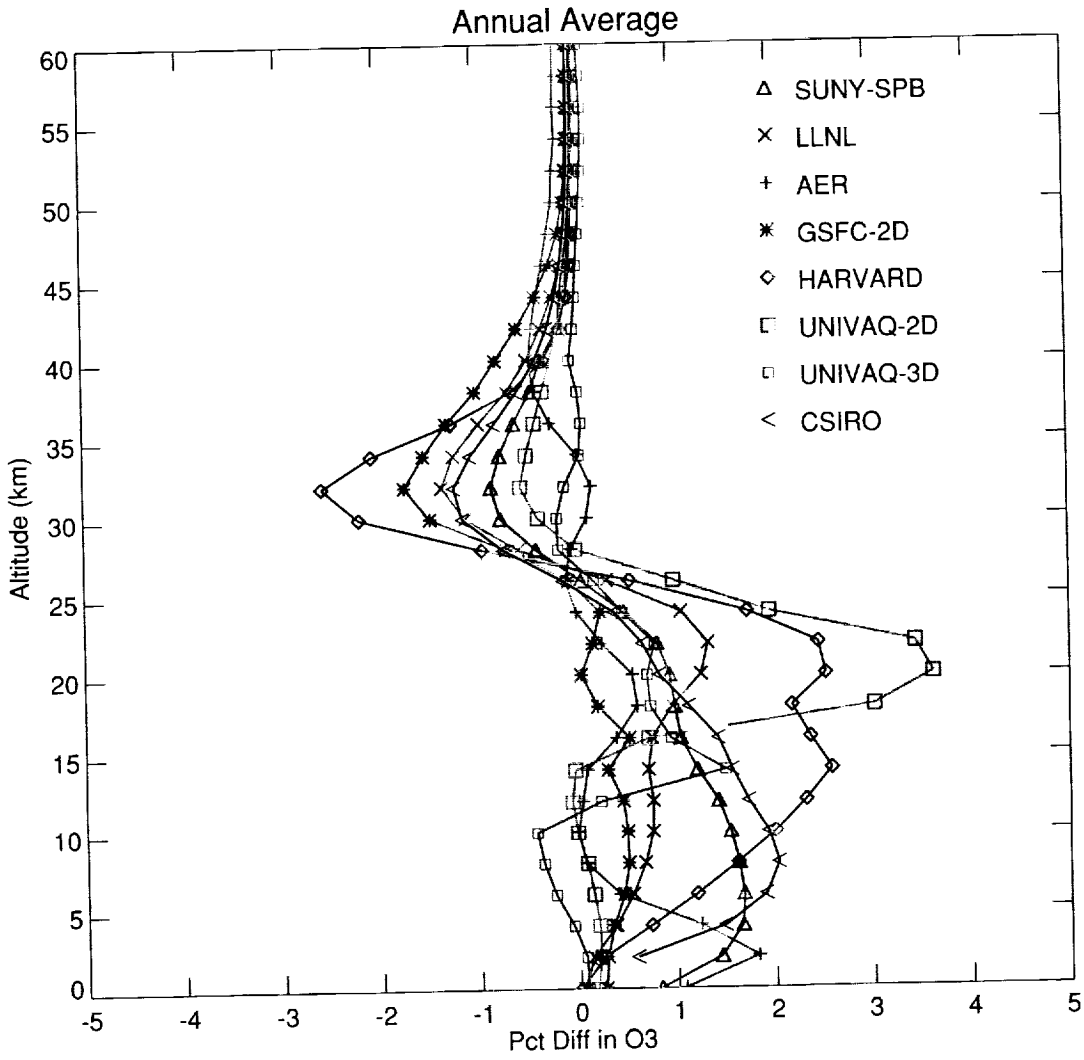

Figure 6.21a. O_3; Run B4; Year 2015; Lat 20N (SA0).

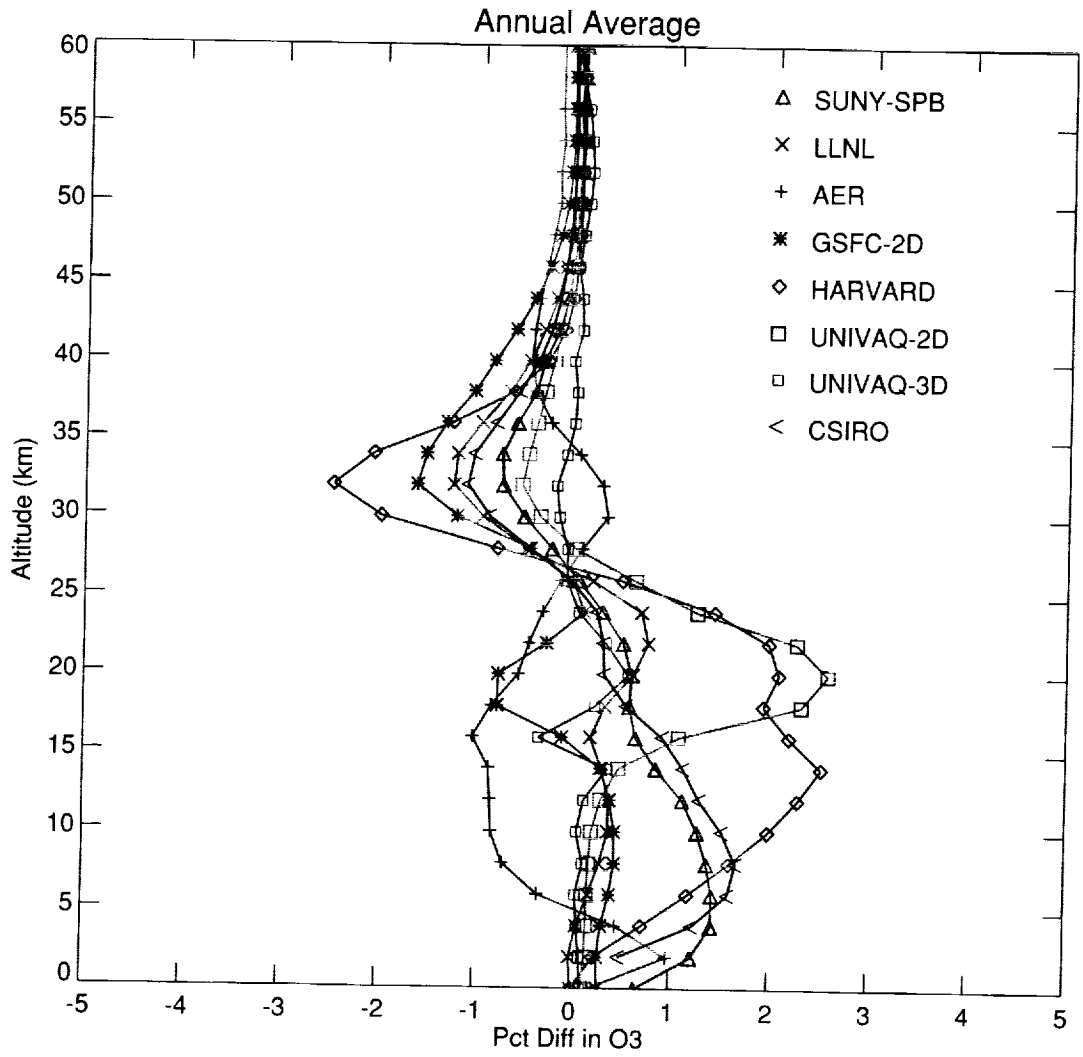

Figure 6.21b. O_3; Run B4; Year 2015; Lat 20N (SA1).

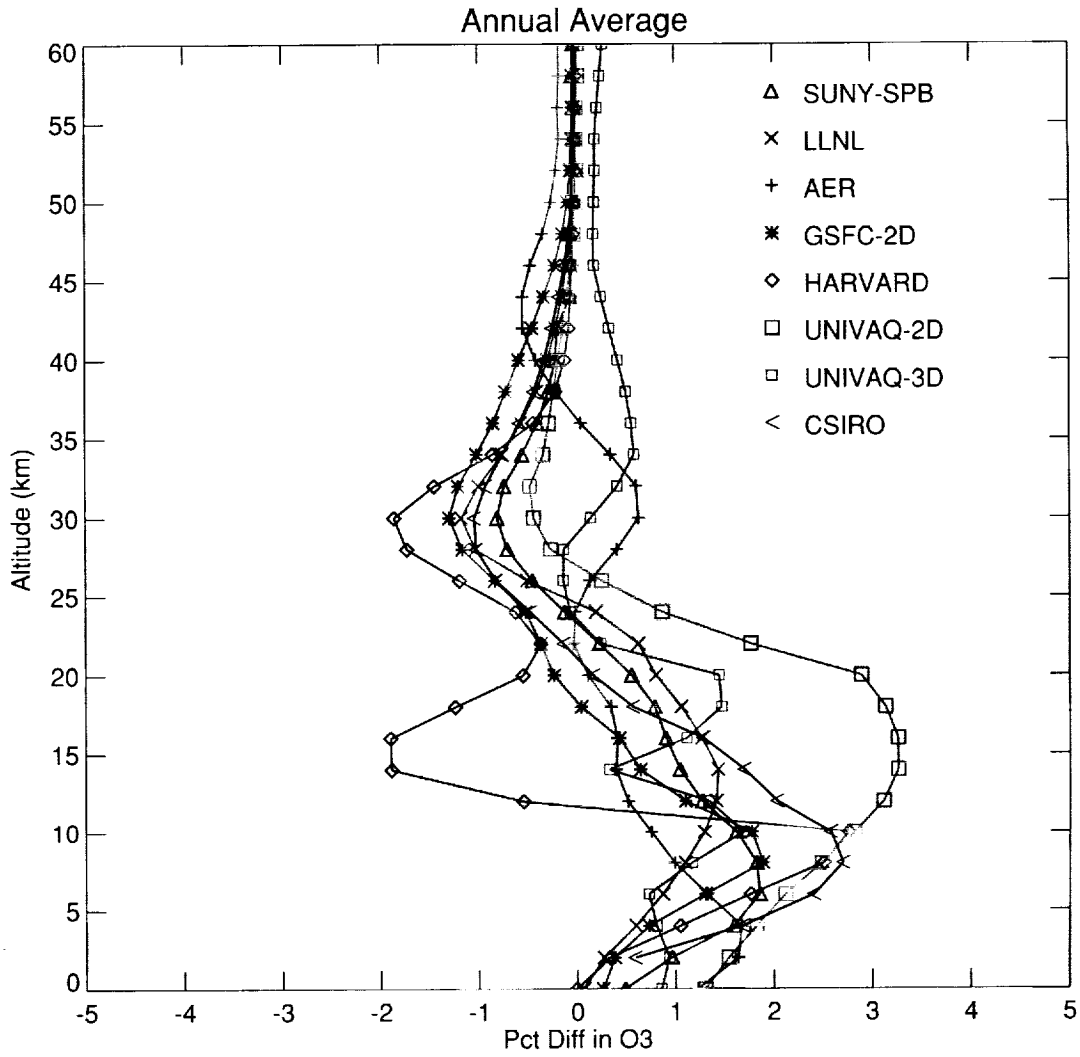

Figure 6.22a. O_3; Run B4; Year 2015; Lat 40N (SA0).

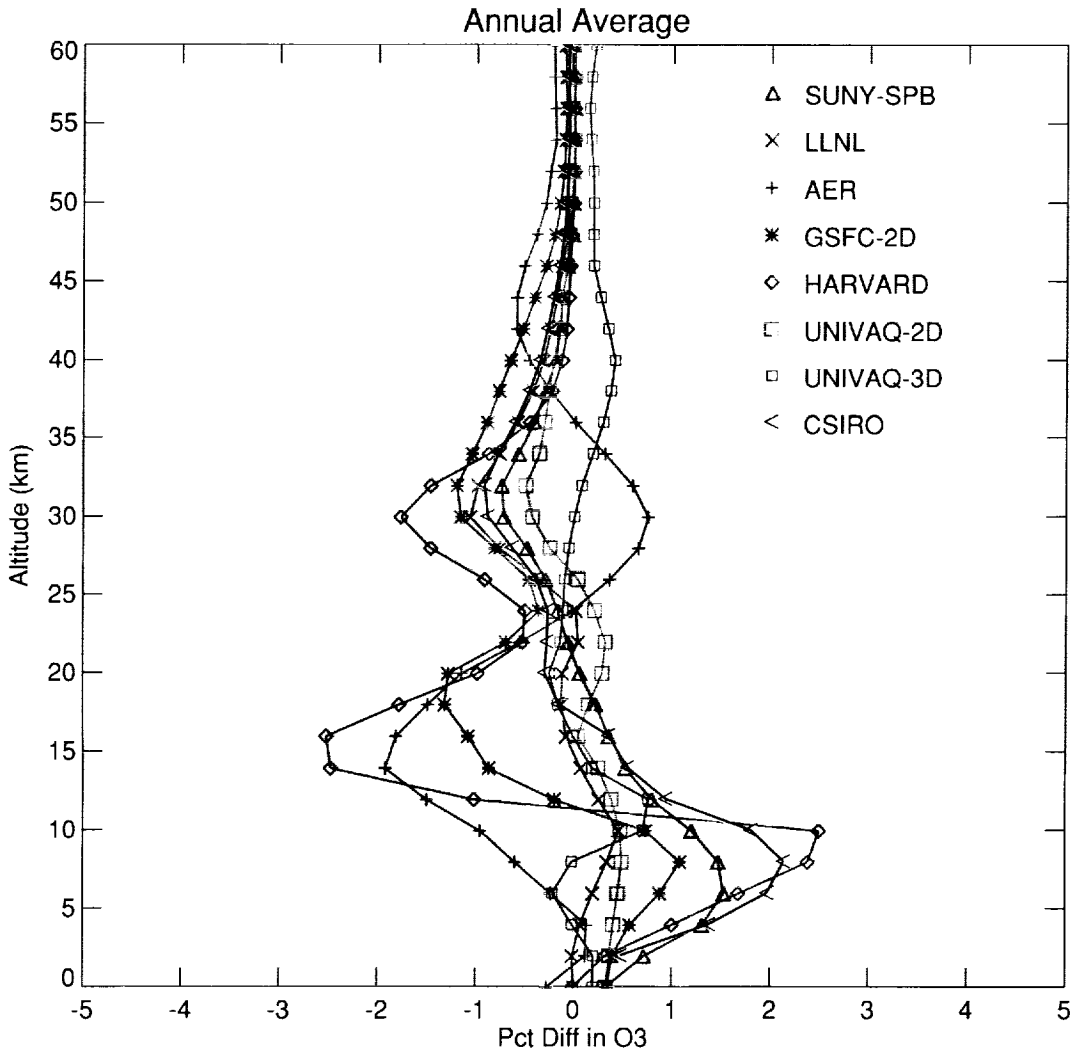

Figure 6.22b. O_3; Run B4; Year 2015; Lat 40N (SA1).

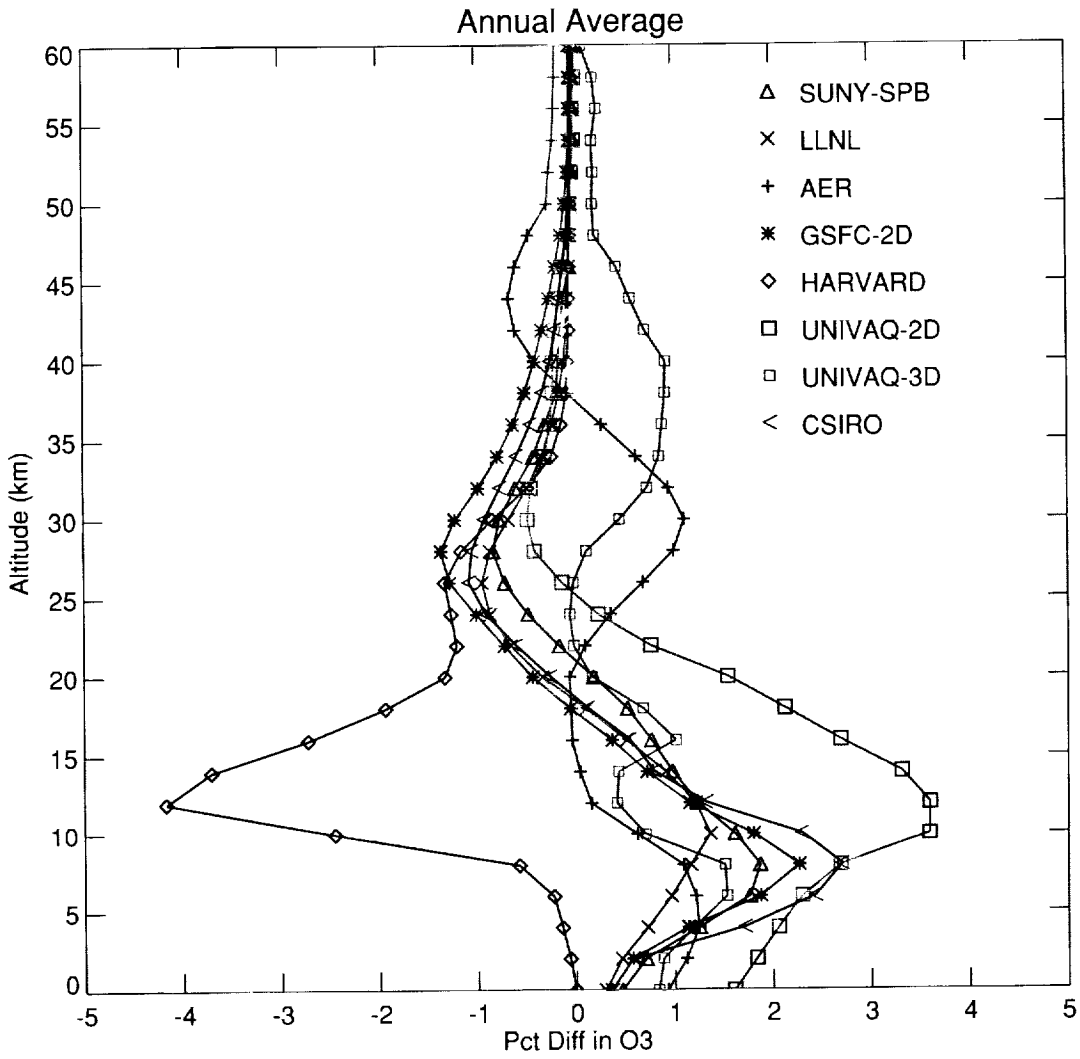

Figure 6.23a. O_3; Run B4; Year 2015; Lat 60N (SA0).

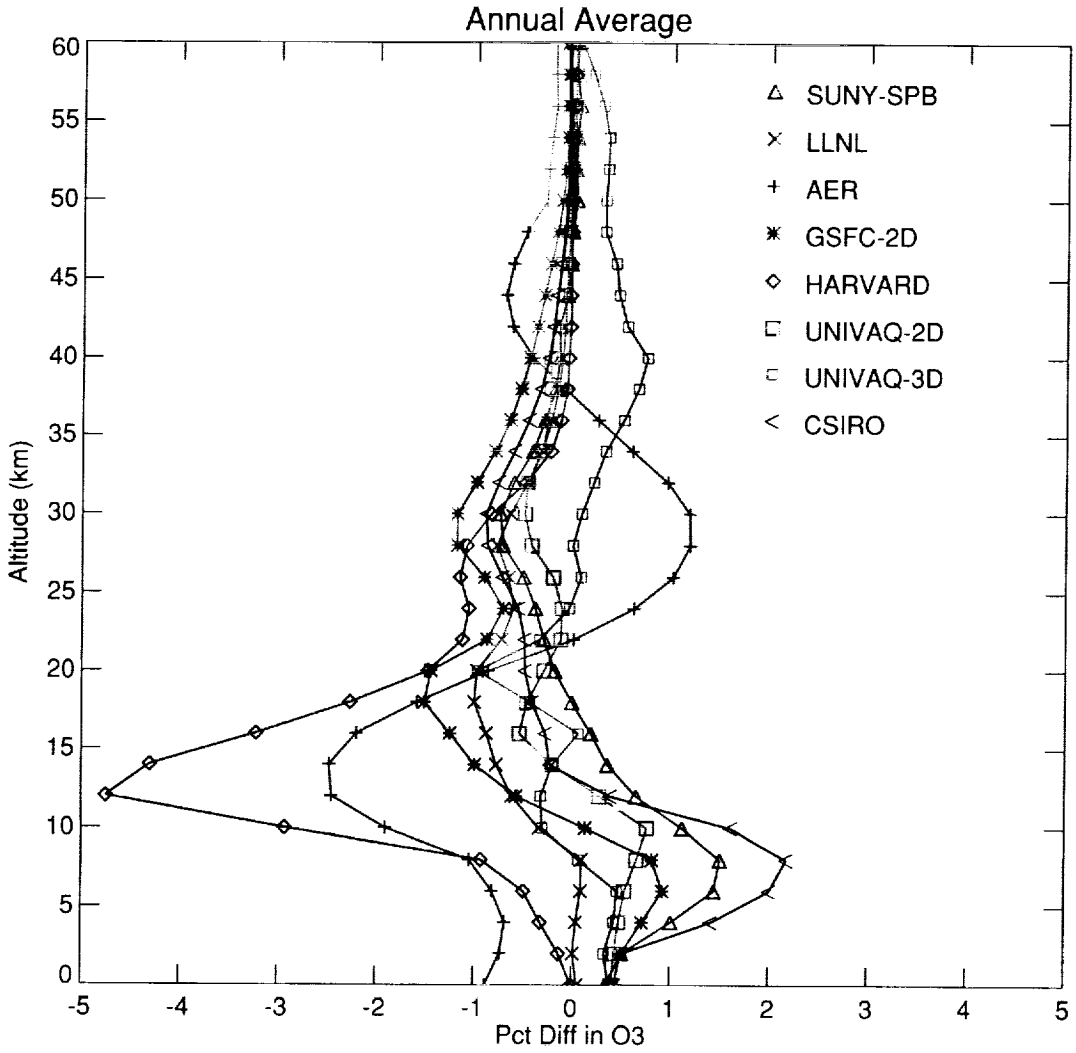

Figure 6.23b. O_3 Run B4 Year 2015 Lat 60N (SA1).

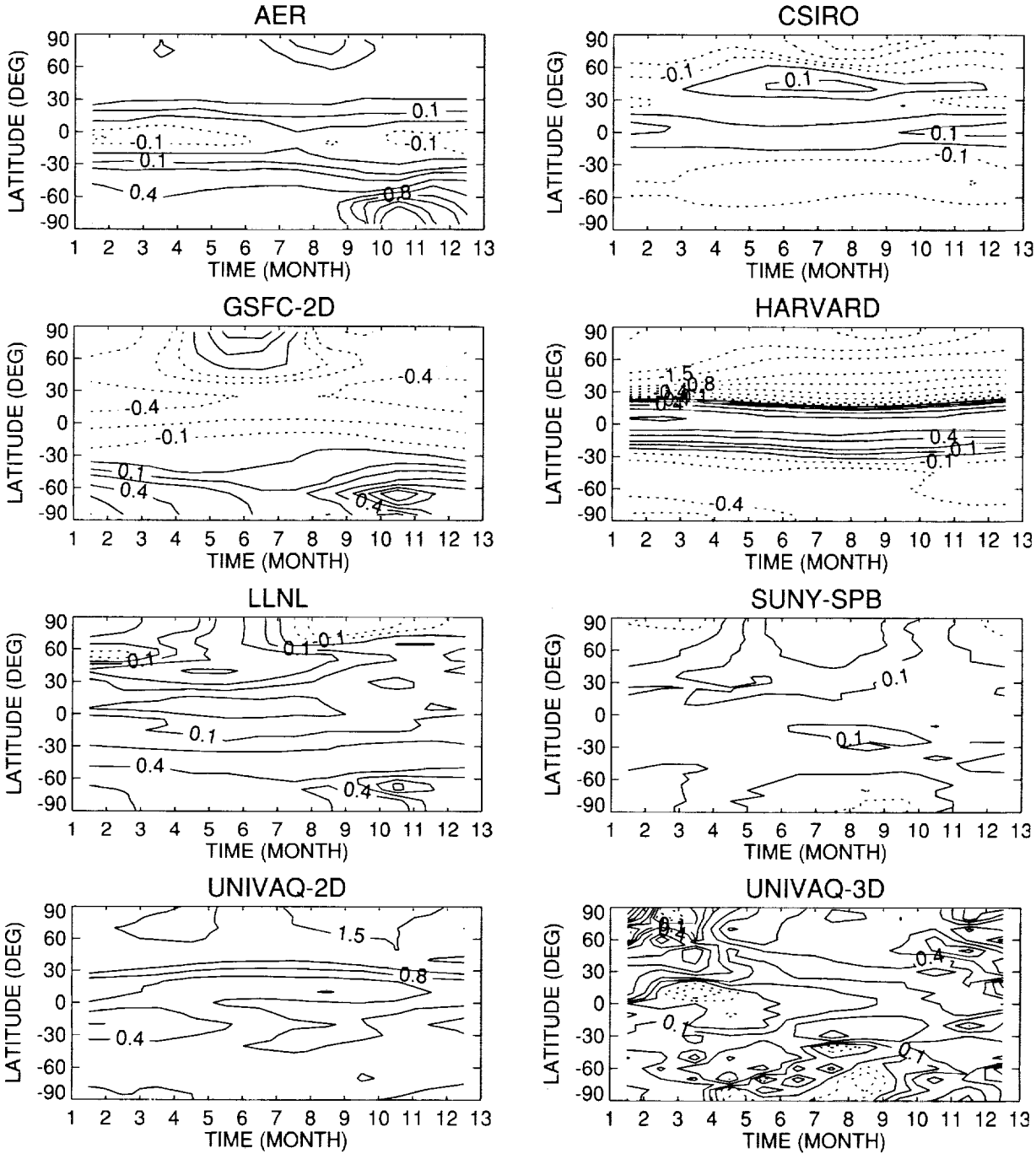

Figure 6.24. Total O_3; Pct DIFF; Run B4 SA0 vs Run B4 Base.

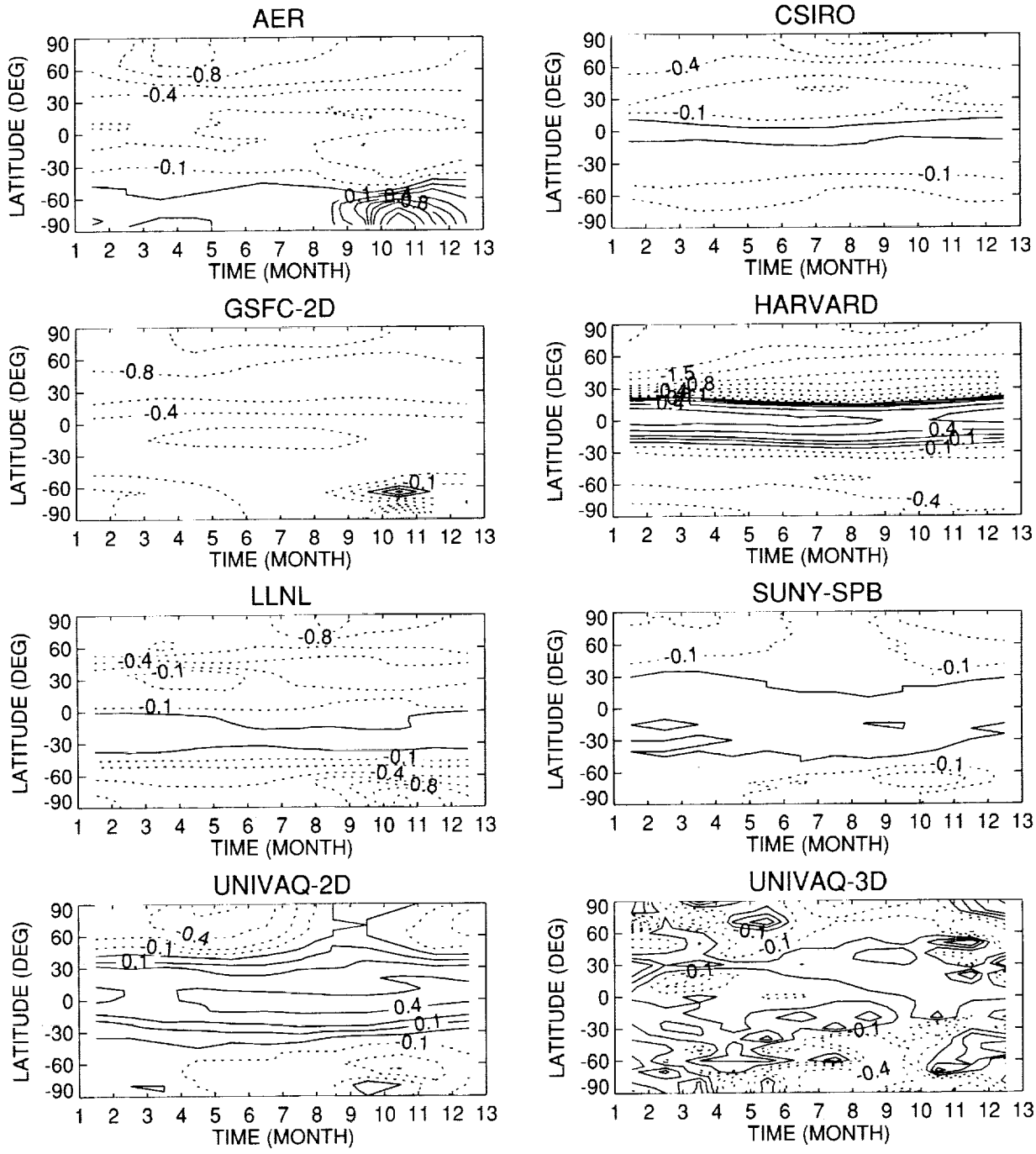

Figure 6.25. Total O_3; Pct DIFF; Run B4 SA1 vs Run B4 Base.

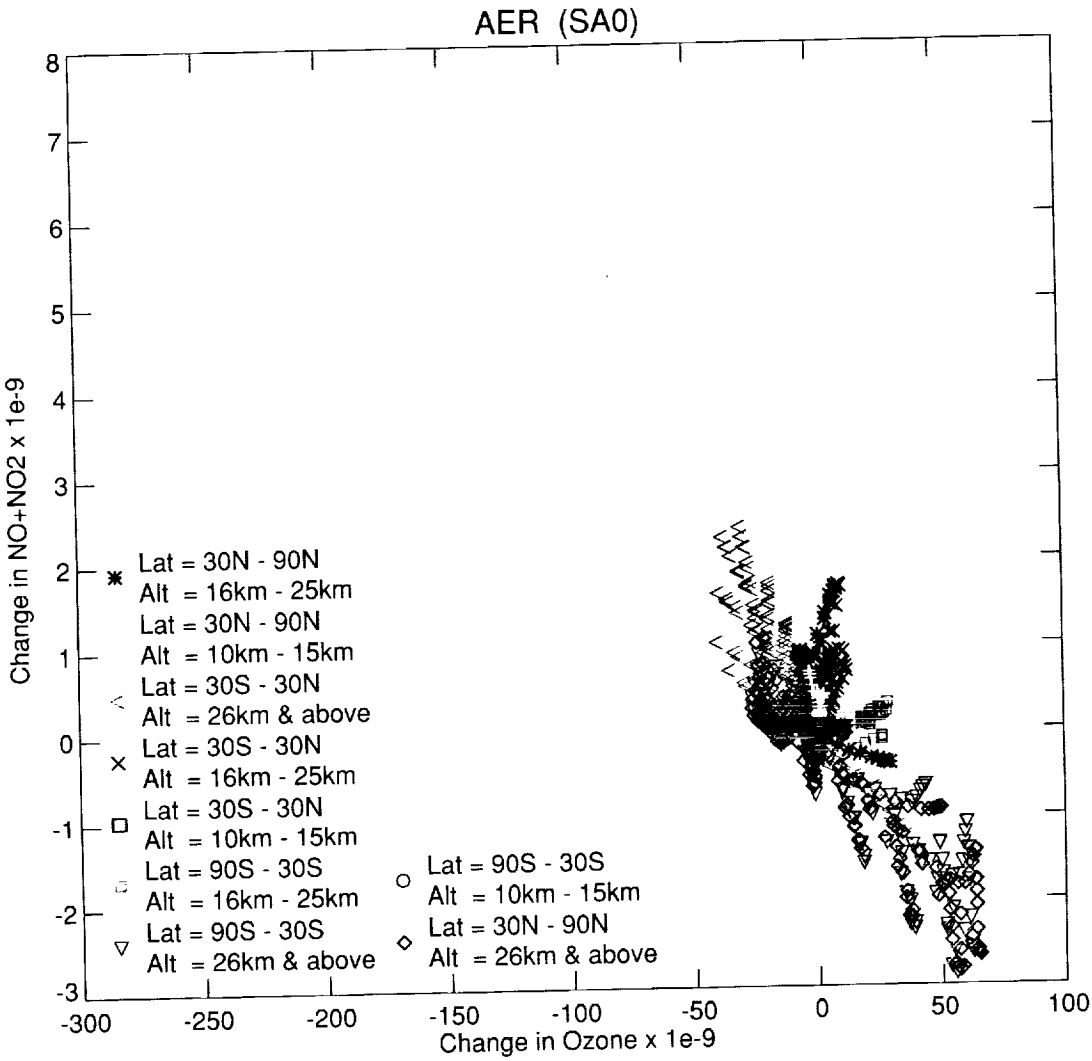

Figure 6.26a. 2015 Annual Average; Change in NOx vs Change in Ozone.

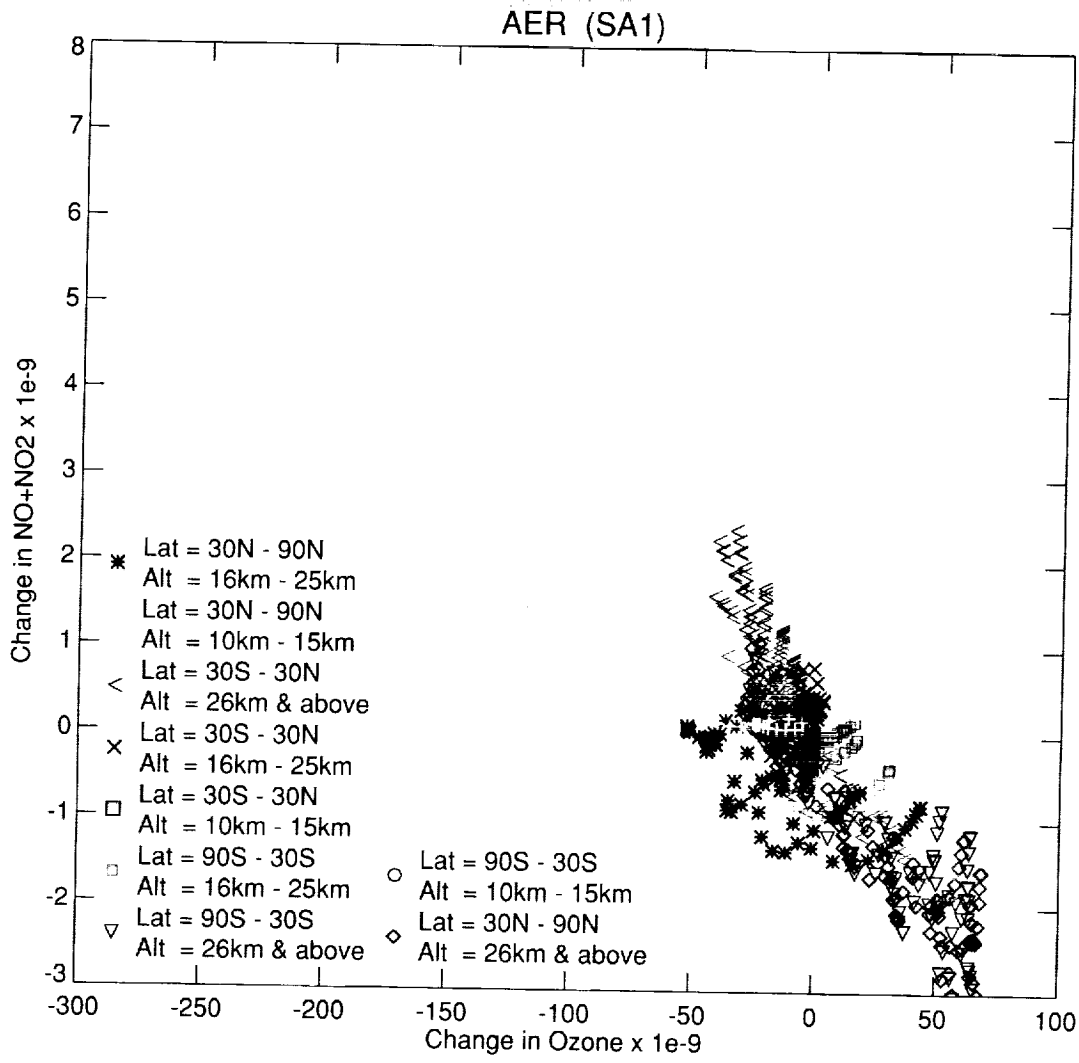

Figure 6.26b. 2015 Average Annual; Change in NOx vs Change in Ozone.

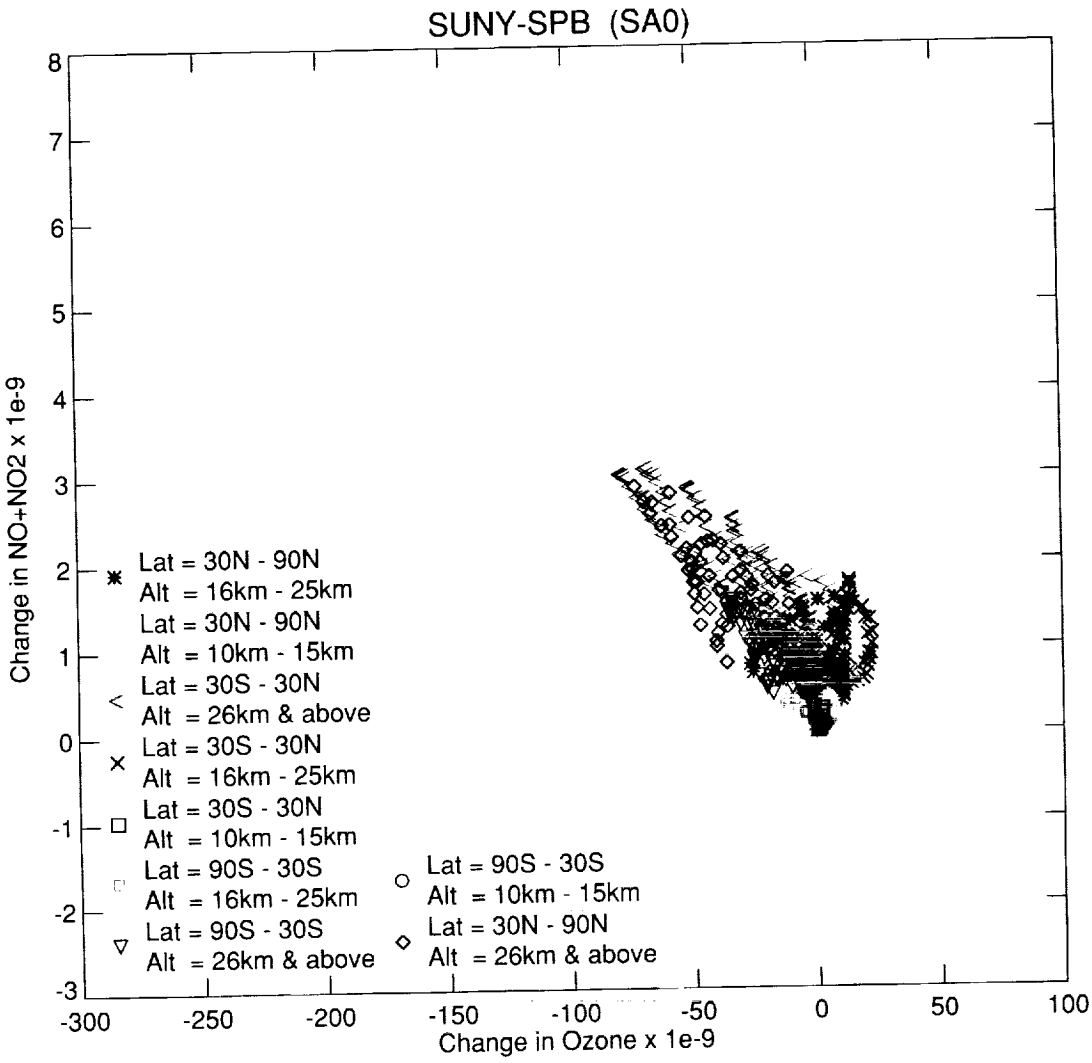

Figure 6.26c. 2015 Annual Average; Change in NOx vs Change in Ozone.

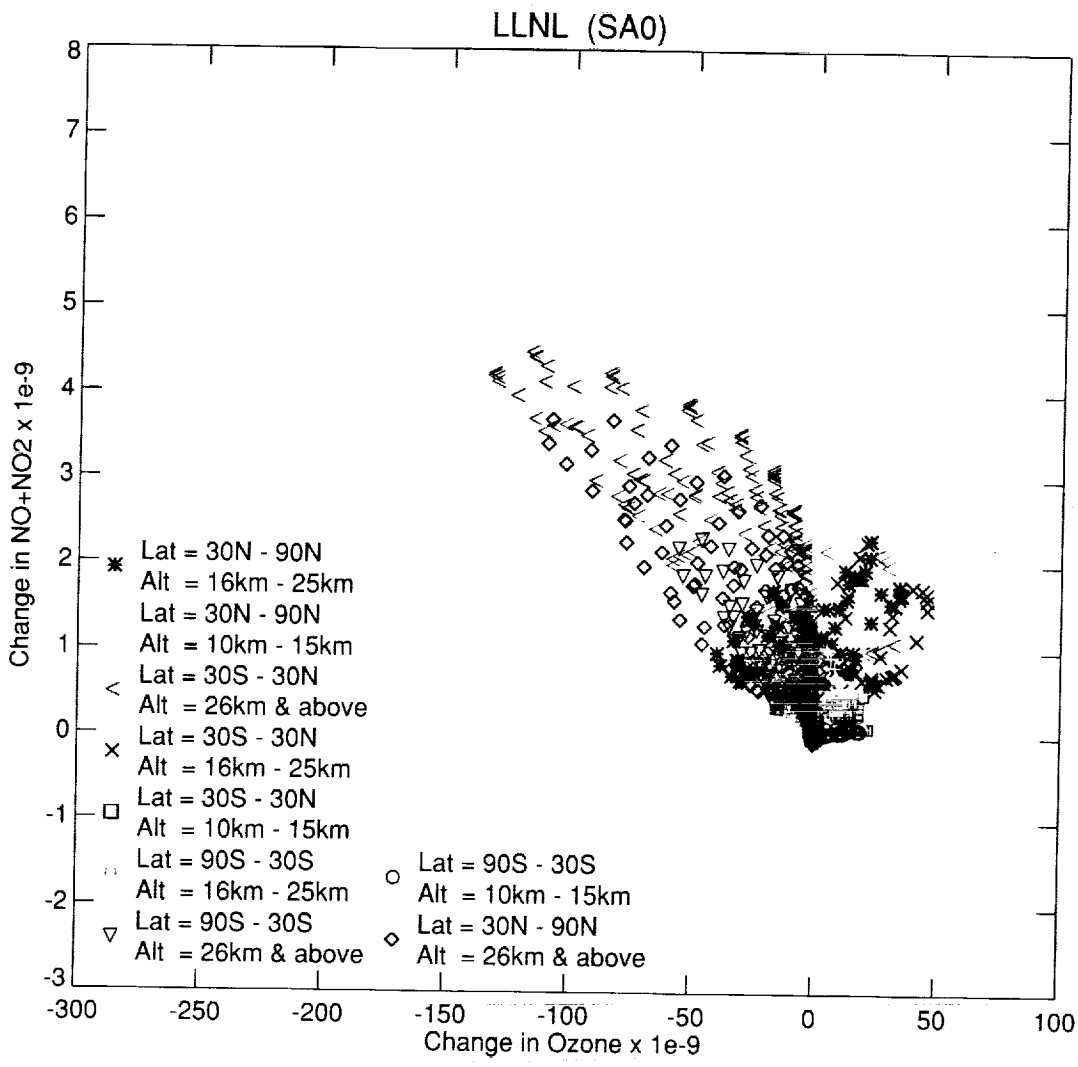

Figure 6.26d. 2015 Annual Average; Change in NOx vs Change in Ozone.

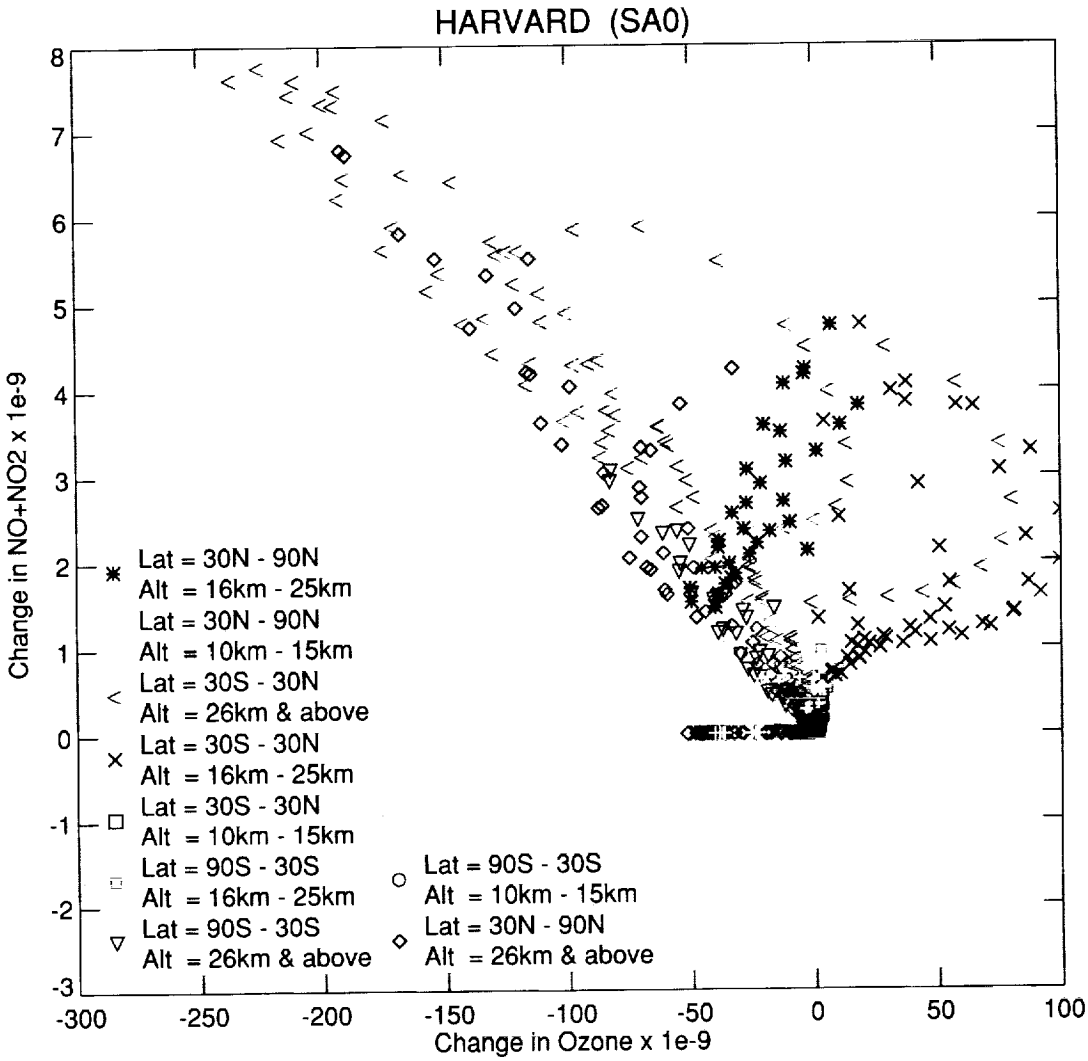

Figure 6.26e. 2015 Annual Average; Change in NOx vs Change in Ozone.

Table 6.1. Change in Total NOy 2015 RUN B4 (SA1 vs Base)

Model	Base Atmosphere	% Change	Absolute Change
AER	1.9662e+16	9.39	1.85e+15
CSIRO	2.1013e+16	8.91	1.87e+15
GSFC-2D	2.8473e+16	11.13	3.17e+15
HARVARD	2.3401e+16	16.64	3.34e+15
LLNL	2.3376e+16	8.95	2.09e+15
SUNY_SPB	1.7111e+16	7.39	1.26e+15
UNIVAQ-2D	1.7067e+16	6.64	1.13e+15
UNIVAQ-3D	2.0776e+16	4.05	8.09e+14

Units = Molecules/cm^2

Table 6.2. Ratio of change in total NOx to change in total NOy for the B4 runs (HSCT with either SA0 or SA1 aerosols)

Model	Ratio (SA0)	Ratio (SA1)
AER	0.039	-0.029
CSIRO	0.179	0.111
GSFC-2D	0.121	0.183
HARVARD	0.152	0.112
LLNL	0.146	0.095
SUNY_SPB	0.197	0.143
UNIVAQ-2D	0.145	0.218
UNIVAQ-3D	0.098	0.219

Table 6.3a. Total O_3 2015 Run B4 (SA0 - Base)

Model	SA0 Atmosphere	Base Atmosphere	Change in O3
AER	3.2139e+02	3.2074e+02	6.5219e-01
GSFC-2D	3.0404e+02	3.0441e+02	-3.7628e-01
LLNL	3.3513e+02	3.3457e+02	5.5954e-01
CSIRO	3.0942e+02	3.0964e+02	-2.1664e-01
SUNY-SPB	3.0878e+02	3.0856e+02	2.1912e-01
UNIVAQ-2D	3.1612e+02	3.1380e+02	2.3214e+00
UNIVAQ-3D	2.9931e+02	2.9856e+02	7.5650e-01
HARVARD	3.0306e+02	3.0410e+02	-1.0412e+00
ECHAM3	3.3076e+02	3.3076e+02	0.0000e+00

Units = Dobson Units

Table 6.3b. Total O_3 2015 Run B4 (SA1 - Base)

Model	SA1 Atmosphere	Base Atmosphere	Change in O3
AER	3.1993e+02	3.2074e+02	-8.1198e-01
GSFC-2D	3.0304e+02	3.0441e+02	-1.3695e+00
LLNL	3.3381e+02	3.3457e+02	-7.5836e-01
CSIRO	3.0919e+02	3.0964e+02	-4.5111e-01
SUNY-SPB	3.0847e+02	3.0856e+02	-9.3781e-02
UNIVAQ-2D	3.1408e+02	3.1380e+02	2.8094e-01
UNIVAQ-3D	2.9849e+02	2.9856e+02	-6.3690e-02
HARVARD	3.0276e+02	3.0410e+02	-1.3373e+00

Units = Dobson Units

Appendix—List of Contributors

S.L. Baughcum	steven.l.baughcum@boeing.com
P.P. Bhatt	p.p.bhatt@larc.nasa.gov
K.A. Boering	boering@cchem.berkeley.edu
G.P. Brasseur	brasseur@ncar.ucar.edu
D.E. Brown	d.e.brown@larc.nasa.gov
C. Bruhl	chb@mpch-mainz.mpg.de
M.P. Chipperfield	martyn@lec.leeds.ac.uk
P.S. Connell	connell2@llnl.gov
D.B. Considine	dbc@welkin.gsfc.nasa.gov
A.R. Douglass	douglass@persephone.gsfc.nasa.gov
V.L. Dvortsov	vdvor@dombai.uars.sunysb.edu
R.S. Eckman	r.s.eckman@larc.nasa.gov
J.W. Elkins	jelkins@cmdl.noaa.gov
E.L. Fleming	fleming@welkin.gsfc.nasa.gov
R.R. Friedl	rfriedl@jpl.nasa.gov
R.R. Garcia	rgarcia@ucar.edu
W.L. Grose	grose@haloe1.larc.nasa.gov
V. Grewe	volker.grewe@dlr.de
T.M. Hall	thall@haggis.giss.nasa.gov
B. Hannegan	bjhanneg@uci.edu
M.H. Hitchman	matt@adams.meteor.wisc.edu
T.Y. Huang	Theresa.Y.Huang@jpl.nasa.gov
C.H. Jackman	jackman@assess.gsfc.nasa.gov
D.B.A. Jones	dbj@io.harvard.edu
I.L. Karol	karol@main.mgo.rssi.ru
S.R. Kawa	kawa@maia.gsfc.nasa.gov
J.A. Kaye	jkaye@hq.nasa.gov
R. Kendall	rose@ember.gsfc.nasa.gov
R. Khosravi	rashid@ucar.edu
D.E. Kinnison	dkin@acd.ucar.edu
M.K.W. Ko	mko@aer.com
L. Kogan	lar@europa.harvard.edu
J. Lerner	cdjal@cleo.giss.nasa.gov
G.J. Labow	labow@chapman.gsfc.nasa.gov
J.A. Logan	jal@io.harvard.edu
R.D. McPeters	mcpeters@qhearts.gsfc.nasa.gov
P.W. Mote	mote@met.ed.ac.uk
N. Andronova	natasha@atmos.uiuc.edu
S. Nossal	nossal@wisp.physics.wisc.edu
S.J. Oltmans	soltmans@cmdl.noaa.gov
J.H. Park	j.h.park@larc.nasa.gov
G. Pitari	pitari@aquila.infn.it
R.A. Plumb	rap@rossby.mit.edu
M.J. Prather	mprather@uci.edu
P.N. Purcell	p.n.purcell@larc.nasa.gov
L. K. Randeniya	Lakshman.Randeniya@tip.csiro.au
W.J. Randel	randel@ucar.edu
P.J. Rasch	pjr@chinook.cgd.ucar.edu
E.E. Remsberg	e.e.remsberg@larc.nasa.gov
D.H. Rind	drind@giss.nasa.gov
C.P. Rinsland	rinsland@riscbox.larc.nasa.gov
H.L. Rogers	helen.rogers@atm.ch.cam.ac.uk
J.M. Rodriguez	jose@aer.com
R.B. Rood	rood@dao.gsfc.nasa.gov
J.E. Rosenfield	rose@euterpe.gsfc.nasa.gov
D. Rotman	drotman@llnl.gov
K.R. Ryan	keith.ryan@tip.csiro.au
E.V. Rozanov	rozanov@uiatma.atmos.uiuc.edu
K.H. Sage	k.h.sage@larc.nasa.gov
R.J. Salawitch	rjs@caesar.jpl.nasa.gov
M.E. Schlesinger	schlesin@atmos.uiuc.edu
C.J. Scott	Courtney_Scott@aer.com
H.R. Schneider	hrs@europa.harvard.edu

S.P. Smyshlyaev	sergey@gclua0.uars.sunysb.edu
R. Soderholm	randy@ember.gsfc.nasa.gov
S. Solomon	solomon@al.noaa.gov
B. Steil	steil@mpch-mainz.mpg.de
X.X. Tie	xxtie@ncar.ucar.edu
P.F. Vohralik	peter.vohralik@tip.csiro.au
D.W. Waugh	waugh@jhu.edu
C.J. Weaver	weaver@aurora.gsfc.nasa.gov
C.F. Wei	c-wei@uiuc.edu
D.K. Weisenstein	dkweis@aer.com
K. Wolfe	kwolfe@al.noaa.gov
D.J. Wuebbles	wuebbles@atmos.uiuc.edu
F. Yang	fanglin@atmos.uiuc.edu
V.A. Yudin	valery@dombai.uars.sunysb.edu
V. Zubov	zubov@main.mgo.rssi.ru
X. Zhu	xzhu@uci.edu

REPORT DOCUMENTATION PAGE

Form Approved
OMB No. 07704-0188

1. AGENCY USE ONLY *(Leave blank)*	2. REPORT DATE	3. REPORT TYPE AND DATES COVERED
	September 1999	Technical Memorandum

4. TITLE AND SUBTITLE
Models and Measurements Intercomparison II

5. FUNDING NUMBERS
WU 622-57-72-70

6. AUTHOR(S)
Jae H. Park, Malcolm K. W. Ko, Charles H. Jackman, R. Alan Plumb, Jack A. Kaye, and Karen H. Sage, Editors

7. PERFORMING ORGANIZATION NAME(S) AND ADDRESS(ES)
NASA Langley Research Center
Hampton, VA 23681-2199

8. PERFORMING ORGANIZATION REPORT NUMBER
L-17895

9. SPONSORING/MONITORING AGENCY NAME(S) AND ADDRESS(ES)
National Aeronautics and Space Administration
Washington, DC 20546-0001

10. SPONSORING/MONITORING AGENCY REPORT NUMBER
NASA/TM-1999-209554

11. SUPPLEMENTARY NOTES
Park: Langley Research Center, Hampton, VA; Ko: Atmospheric and Environmental Research, Inc., Cambridge, MA; Jackman: Goddard Space Flight Center, Greenbelt, MD; Plumb: Massachusetts Institute of Technology, Cambridge, MA; Kaye: Headquarters, National Aeronautics and Space Administration, Washington, DC; Sage: SAIC, Hampton, VA.

12a. DISTRIBUTION/AVAILABILITY STATEMENT
Unclassified–Unlimited
Subject Category 46 Distribution: Standard
Availability: NASA CASI (301) 621-0390

12b. DISTRIBUTION CODE

13. ABSTRACT ***(Maximum 200 words)***
Models and Measurement Intercomparison II (MM II) summarizes the intercomparison of results from model simulations and observations of stratospheric species. Representatives from twenty-three modeling groups using twenty-nine models participated in these MM II exercises between 1996 and 1999. Twelve of the models were two-dimensional zonal-mean models while seventeen were three-dimensional models. This was an international effort as seven were from outside the United States. Six transport experiments and five chemistry experiments were designed for various models. Models participating in the transport experiments performed simulations of chemically inert tracers providing diagnostics for transport. The chemistry experiments involved simulating the distributions of chemically active trace gases including ozone. The model run conditions for dynamics and chemistry were prescribed in order to minimize the factors that caused differences in the models. The report includes a critical review of the results by the participants and a discussion of the causes of differences between modeled and measured results as well as between results from different models. A sizable effort went into preparation of the database of the observations. This included a new climatology for ozone. The report should help in evaluating the results from various predictive models for assessing humankind perturbations of the stratosphere.

14. SUBJECT TERMS
Ozone; Stratospheric chemistry and dynamics; Atmospheric modeling and observation; Assessment of humankind perturbation; Atmospheric perturbation by high speed civil transport aircraft

15. NUMBER OF PAGES
502

16. PRICE CODE
A22

17. SECURITY CLASSIFICATION OF REPORT	18. SECURITY CLASSIFICATION OF THIS PAGE	19. SECURITY CLASSIFICATION OF ABSTRACT	20. LIMITATION OF ABSTRACT
Unclassified	Unclassified	Unclassified	UL